CHEMICAL REVIEWS

Review

pubs.acs.org/CR

Metal Ion Modeling Using Classical Mechanics

Pengfei Li† and Kenneth M. Merz Jr.*

Department of Chemistry, Department of Biochemistry and Molecular Biology, and Institute of Cyber-Enabled Research, Michigan State University, East Lansing, Michigan 48824, United States

ABSTRACT: Metal ions play significant roles in numerous fields including chemistry, geochemistry, biochemistry, and materials science. With computational tools increasingly becoming important in chemical research, methods have emerged to effectively face the challenge of modeling metal ions in the gas, aqueous, and solid phases. Herein, we review both quantum and classical modeling strategies for metal ion-containing systems that have been developed over the past few decades. This Review focuses on classical metal ion modeling based on unpolarized models (including the nonbonded, bonded, cationic dummy atom, and combined models), polarizable models (e.g., the fluctuating charge, Drude oscillator, and the induced dipole models), the angular overlap model, and valence bond-based models. Quantum mechanical studies of metal ion-containing systems at the semiempirical, ab initio, and density functional levels of theory are reviewed as well with a particular focus on how these methods inform classical modeling efforts. Finally, conclusions and future prospects and directions are offered that will further enhance the classical modeling of metal ion-containing systems.

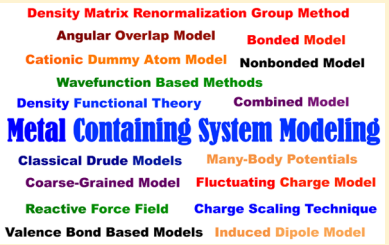

CONTENTS

Received: July 8, 2016
Published: January 3, 2017

DOI: 10.1021/acs.chemrev.6b00440
Chem. Rev. 2017, 117, 1564–1686

1. INTRODUCTION

1.1. Relevance of Computer Modeling of Metal Ion-Containing Systems

1.1.1. Importance of Metal Ions. Metals and metal ions are ubiquitous in nature and account for tremendous chemical diversity. In the periodic table, from element 1 (H) to element 109 (Mt), there are 84 metals, 7 metalloids, and only 18 nonmetals. The sum of the abundances of Al, Fe, Ca, Na, K, Mg, and Ti in the earth's crust is ∼25%. Metals are well-known

DOI: 10.1021/acs.chemrev.6b00440
Chem. Rev. 2017, 117, 1564−1686

substances in our daily lives, composing objects from coins to bridges, but the metal objects we touch are metal crystals or alloys. With low electronegativities, metals are easily ionized and highly reactive, allowing them to participate in many unique reactions or catalytic processes. Metals and their ions are distributed widely and play extremely important roles in chemistry, geochemistry, biochemistry, material sciences, etc. Approximately one-third of the structures in the Protein Databank (PDB) contain metal ions.[1] In biology, Na^+, K^+, Mg^{2+}, and Ca^{2+} help maintain the osmotic pressure of blood;[2−5] they activate/deactivate some enzymes;[6−11] while redox pairs such as Fe^{2+}/Fe^{3+} and Cu^+/Cu^{2+} are essential to metabolic electron transfer processes,[12−15] just to name a few of the myriad of biological functions of metal ions. Metals are widely used materials in our daily lives; for example, coins are made of Cu, Ag, Au, Al, Ni, and Fe, etc. Moreover, industrial catalysis is no less reliant on metal chemistry: more than 80% of currently used large-scale chemical processes rely on solid catalysts, typically based on the chemistry of transition metals (TMs).[16]

1.1.2. Significant Role of Contemporary Computer Modeling. Contemporary computational chemistry is playing an ever-growing role in chemical research, driven by the improved hardware and lithography, which was facilitated by advances in semiconductor materials containing metals and metalloids. As Moore's law describes, the computational power of central processing units (CPUs) doubles every 18 months.[17] The dramatic increase in computational power makes previously unattainable computations feasible, allowing for the ever-expanding role of computation in science. For example, in the 1940s and 1950s, with very limited computational power available, it was hard to simulate systems beyond the hydrogen atom,[18] while it is now possible to deal with systems containing hundreds of atoms using ab initio quantum mechanics (QM) methods and systems containing millions of atoms through the use of classical mechanics. The development and application of new hardware modalities also remarkably increased computational power. For example, application of graphic processing units (GPUs) in computational chemistry speeds up calculations by at least an order of magnitude over traditional CPUs.[19,20] Development of the Anton supercomputer makes possible routine millisecond MD simulations of small proteins.[21]

Computational methods offer atomic/molecular and electronic-level insights, which are hard or impossible to obtain experimentally, thereby providing a complementary tool to experiment. Computational approaches can help us to better interpret chemical phenomena and also provide prospective insights and new hypotheses for experimentalists. Novel molecules can be rapidly designed and characterized for desired properties prior to the initiation of expensive synthetic efforts. Computation is playing an increasing role in structure-based drug design and discovery[22−27] as well as in the materials design field.[28−33] Structure-based drug design computational tools have facilitated in the discovery of novel compounds for diseases including HIV,[22,23,25] cancer,[26] and hypertension.[27] It has also facilitated in the design of novel materials for applications in solar cells,[28] solid catalysts,[29,30] semiconductors, and superconductors.[31−33]

1.2. Challenge of Modeling Metal Ion-Containing Species

1.2.1. High Angular Momenta Atomic Orbitals. Unlike the s and p block elements, TMs have d or f orbitals as their outermost orbitals, which can also participate in chemical bonding. As compared to s and p orbitals, d and f orbitals have more electrons and more complicated shapes (due to their higher angular momenta), which result in more complicated chemical bonding characteristics.

1.2.2. Multiple Oxidation States. Furthermore, there are multiple possible oxidation states for a given TM. For example, Mn has oxidation states ranging from −3 to +7 (with +2, +4, and +7 being the most prevalent), while Fe has oxidation states ranging from −4 to +6 (with +2, +3, and +6 being the most prevalent). Ru and Os have an oxidation state of 8 in RuO_4 and OsO_4.[34] In 2014, Wang et al. characterized the $[IrO_4]^+$ ion experimentally, in which Ir has a +9 formal charge.[35] Recently, Yu and Truhlar predicted that $[PtO_4]^{2+}$ could kinetically exist based on theoretical calculations, in which Pt has a +10 oxidation state.[36] Furthermore, the higher oxidation states result in highly charged systems that can have pronounced long-range effects, which need to be accurately accounted for in simulations.

1.2.3. Electronic State Degeneracy. Another significant challenge for modeling TM containing systems is their complicated electronic structures, wherein various spin states can be present with relatively close energies. On one hand, it is generally hard to predict the ground state of a TM ion and to accurately calculate the relative energies between the different states. On the other hand, different spin states may exist at the same time or are essentially degenerate, further complicating the electronic structure. It is impossible to model this static correlation effect based on single-reference methods using a single Slater determinant. Different methods including density functional theory and multireference methods will likely be required to model these systems accurately. Beyond the state degeneracy issue, electronic effects including the Jahn−Teller effect and the trans effect exist, making it even more challenging to accurately model TM-containing molecules at the classical level of theory.

1.2.4. Complicated Chemical Bonding and Multiple Coordination Numbers. On the basis of the above, TM-containing species have more complicated chemical bonding patterns than their organic counterparts, causing much of their ability to have flexible and dynamic coordination environments. Chemical bonds are often characterized on a continuum from covalent to ionic: at one extreme, bonds are based on electrons shared between two atoms, while at the other electrons are exclusively held by one atom or the other, and the association is electrostatic in nature. The main group nonmetal elements usually have consistent bonding patterns due to the nature of their covalent bonds. For example, hydrogen and halogen atoms usually just form one bond with other atoms, while oxygen atoms usually have one double bond or two single bonds with other atoms. Two carbon atoms can form a triple bond at the most, which can be understood as one σ bond and two π bonds between the atom pair. While chemical bonding in organic species has its nuances, many general-purpose chemical models have been designed for organic species and biopolymers that are broadly descriptive of their behavior. However, metal ions present much more challenging modeling problems due to their larger coordination numbers (CNs), relatively labile chemical bonding, and diversity of electronic states.

For the main group metal elements, their chemical bonding has more ionic character, which causes them to have both higher and more flexible CNs than the main group nonmetal elements. For example, Ca^{2+} encompasses CNs ranging from 5

DOI: 10.1021/acs.chemrev.6b00440
Chem. Rev. 2017, 117, 1564−1686

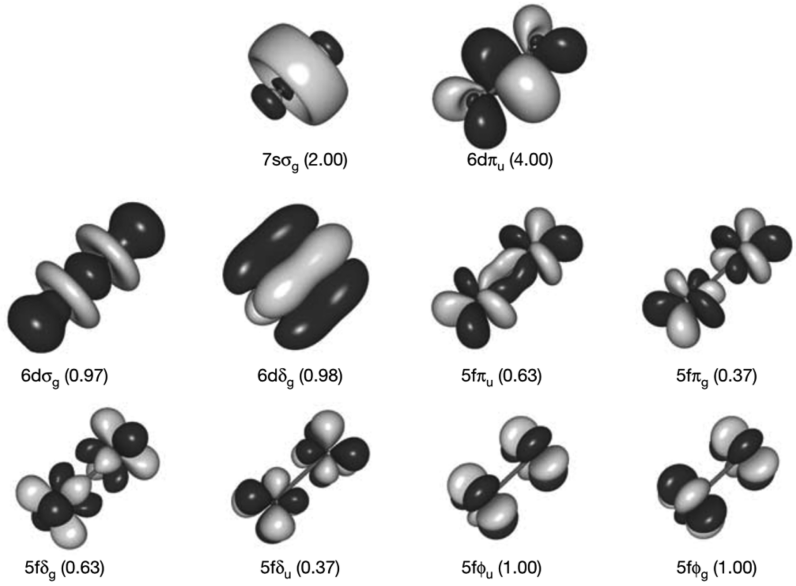

Figure 1. Active molecular orbitals forming the chemical bond between two uranium atoms. The orbital label is given below each orbital, together with the number of electrons occupying this orbital or pair of orbitals in the case of degeneracy. Reprinted with permission from ref 39. Copyright 2005 Nature Publishing Group.

to 10 in aqueous solution.[37] Moreover, more complicated bonding patterns can appear between TMs and their coordinating ligands. Whereas main-group compounds tend to have strictly covalent or ionic bonding, transition metals form bonds to their ligands nearer the middle of the bonding "spectrum". These "coordinate bonds" are typically more flexible and easier to break than a covalent bond, facilitating the use of TMs in catalysts. The coordinate bond shares some characteristics with covalent and electrostatic bonds; depending on the atoms involved, some coordinate bonds are more covalent and some are more ionic. For example, TMs can form both σ and π bonds with coordinate atoms. In contrast, the coordinate bonds in Werner-type compounds are more ionic in nature. Overall, these characteristics give TMs more flexible coordination environments than the nonmetal main group compounds. First, as compared to main group nonmetal elements, higher order bonds can be formed between TMs. For example, Cotton et al. found that there is a quadruple bond between two Re atoms in $K_2[Re_2Cl_8]_2{\cdot}H_2O$.[38] This bond involves a $d_{z^2}-p_z$ hybrid (as a σ bond), two $d_{xz}-d_{yz}$ bonding pairs (as two π bonds), and one $d_{xy}-d_{xy}$ bonding pair (as another σ bond) in the quadruple bond. Recent computations of Gagliardi and Roos have shown that U_2 has a quintuple bond (see Figure 1), which has all known covalent bond types (electron-pair bond, one-electron bond, and ferromagnetically coupled electrons) in it.[39] Nguyen et al. have crystallized a Cr complex with two Cr^+ ions (with a $3d^5$ configuration) with a 5-fold bond, with a bond distance of only ~1.84 Å (see Figure 2).[40] Second, more diversified bond types existed between TMs and ligands. For instance, "yl-ene-yne" type compounds of W and Cr have been characterized, in which there are single, double, and triple bonds formed between the central metal ion and the surrounding coordinating atoms (see Figure 3).[41−43] Moreover, TMs can also have flexible CN values: For example, Cu can have a CN of 5 and 6 in aqueous solution where both configurations have similar energies;[44] zinc ions play structural and catalytic roles with CNs ranging from 4 to 6 in biological systems.[45]

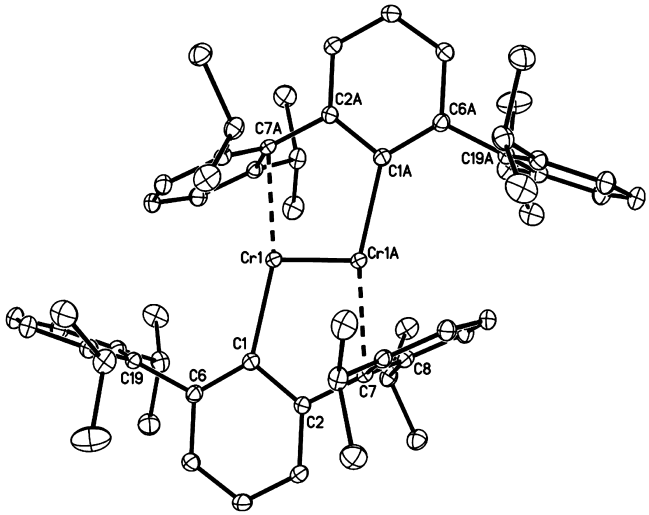

Figure 2. Thermal ellipsoid (30%) drawing of Ar′CrCrAr′ (Ar′ means C_6H_3-2,6(C_6H_3-2,6-Pr^i_2)$_2$, where Pr^i means isopropyl). Hydrogen atoms are not shown. Selected bond distances and angles (deg) are as follows: Cr(1)−Cr(1A), 1.8351(4) Å; Cr(1)−C(1), 2.131(1) Å; Cr(1)−C(7A), 2.2943(9) Å; Cr(1)−C(8A), 2.479(1) Å; Cr(1)−Cr(12A), 2.414(1) Å; C(1)−C(2), 1.421(1) Å; C(1)−C(6), 1.423(2) Å; C(7)−C(8), 1.421(1) Å; C(7)−C(12), 1.424(1) Å; Cr(1A)−Cr(1)−C(1), 108.78(3)°; Cr(1A)−Cr(1)−C(7A), 94.13(3)°; C(1)−Cr(1)−C(7A), 163.00(4)°; Cr(1)−C(1)−C(2), 114.34(7)°; Cr(1)−C(1)−C(6), 131.74(7)°; and C(2)−C(1)−C(6), 113.91(9)°. Reprinted with permission from ref 40. Copyright 2005 The American Association for the Advancement of Science.

The higher CN values dramatically increase the number of possible compounds that can be generated around a metal center. Flexible bonding makes it hard to simulate diverse chemical bonds with one modeling strategy. Moreover, the number of electronic states available to some metal ions coupled with more flexible bonds results in many configurations having very similar energies that in turn require highly accurate and expensive computational methods to differentiate

DOI: 10.1021/acs.chemrev.6b00440
Chem. Rev. 2017, 117, 1564−1686

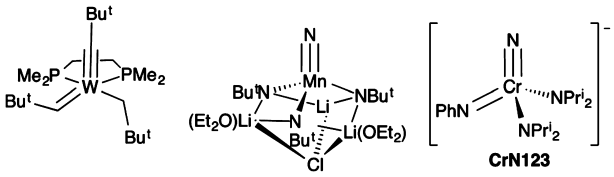

Figure 3. Structures of Schrock and Clark's "yl-ene-yne" complex of refs 41, 42, Wilkinson's nitride-imido complex (half of the dimer is shown and the chloride bridges to one lithium of a chemically equivalent manganese center) of ref 46, and the NCr(NPh) $(NPr^i_2)_2$ anion of ref 43. Reprinted with permission from ref 43. Copyright 2016 PCCP Owner Societies.

the subtle differences. In typical force fields for metal ions, parameters are designed for a specific CN found for the metal ion in an environment. Because an individual metal ion can form many complexes with different CNs, which may or may not be close in energy, and may change from one environment to another, it is hard to simulate these systems accurately. Hence, generating a general force field for metal ions becomes more of a challenge. On the basis of the previous discussion, we hope we have lain bare why it is such a challenge to model metal-containing compounds.

1.3. Impact of the Dearth of Experimental Data

1.3.1. Experimental Challenges. Unfortunately, there are limited experimental data about TM species, which slows the development of accurate theoretical methods to model TM-containing compounds. For example, both the number and the accuracy of experimentally derived heats of formation (HOFs) for TM-containing molecules are modest when compared to what is available for organic compounds. In the work of Jiang et al., they benchmarked the correlation consistent composite approach for transition metals (ccCA-TM) composite method against one of the biggest data sets of experimental HOFs of TM species.[47] 193 out of 225 entries in the data set were used during the benchmark calculations. As compared to the number of possible TM-containing molecules that could exist, this number represents a rather paltry validation set. Figure 4

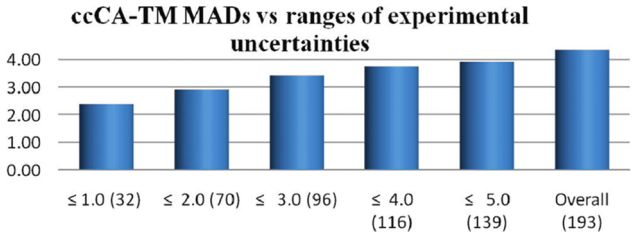

Figure 4. MADs of the ccCA-TM composite method with respect to experimental heats of formation. Unit is kcal/mol along the *Y* axis. The value in brackets represents the number of data points in the subset. Reprinted with permission from ref 47. Copyright 2011 American Chemical Society.

showed the mean absolute deviations (MADs) of the ccCA-TM method toward subsets of the experimental data combined with different upper limits of uncertainties. We can see that there are very few (only 32) experimental data points that have accuracies within what is termed "chemical accuracy" (which is ±1.0 kcal/mol). Meanwhile, they found that the MAD of the ccCA-TM method increases along with the upper error limit of the experimental data set they used (see Figure 4), further demonstrating the challenge of using experimental data with higher uncertainties. These results indicate that to impel theoretical methods forward, extensive and highly reliable experimental data will be essential. Because it is challenging to obtain thermodynamic experimental data for TM species to chemical accuracy, the ability for computational methods to advance will be hindered as well.

Another challenging issue is the way in which accurate hydration free energies (HFEs) are obtained for ions. Chemists determine the HFE of a single ion based on experimentally determined HFE values of salts coupled with theoretical assumptions. In particular, the HFE of the proton is usually used as a reference by which the rest of the HFEs are scaled. However, this value has been assigned a range of values covering more than 10 kcal/mol. Meanwhile, there are also other issues that should be considered, including the difference between intrinsic and absolute HFE values, if one wants to accurately model HFE values. Because molecular dynamics (MD) simulations usually employ periodic boundary conditions (PBCs), which do not have an interface, the intrinsic HFE, other than real HFE values, are usually obtained. Related discussions can be found in the work of Grossfield et al.[48] and in the work of Lamoureux and Roux.[49] Another issue is that ion parametrization is performed under infinite dilution, while in high concentration solutions, ion pair interactions are important.

1.3.2. Inconsistencies between Experimental and Computational Data. Another aspect that restricts the development of TM modeling is inconsistencies between the available experimental and computational data. For example, X-ray diffraction (XRD) data are always based on the crystal phase.[50] These crystals are packaged with numerous adjacent unit cells. In QM or molecular mechanics (MM) modeling efforts, the calculation is usually performed in the gas phase without inclusion of crystal packing effects. Moreover, XRD refinement determines the center of the electronic cloud but not the nuclear position, which can be influenced by lone pairs and highly electron-attracting/-donating groups.[51] In contrast, theoretical methods normally use the position of the atomic nuclei. Meanwhile, using experimental data directly may introduce inaccuracies due to different interpretations of the data. For example, the van der Waals (VDW) radii used in X-ray studies are based on the distance of nearby atoms, which are influenced by the crystal packing, while the theoretical chemist treats the VDW radii sum as the energy minimum of two isolated particles.[51] Under these circumstances, assessment of theoretical results based on experimental data may be biased. Moreover, experimental thermochemical data are more often given as free energy values. However, theoretical computation of free energy changes requires extensive sampling, which is still challenging, especially for macromolecular systems.[50] Therefore, direct comparison between the theoretical and computational data becomes more difficult.

1.4. Scope of This Review

This Review covers the theoretical and computational work on metal ion modeling reported in the past several decades, with a focus on metal ion modeling employing classical force fields. Because quantum calculations are usually used for parametrization and to benchmark metal ion force fields, we briefly review extant QM modeling strategies with respect to metal-containing systems in section 2. Next, we review the widely used nonbonded and bonded approaches to classical modeling of metal ions in sections 3 and 4, respectively. We then

DOI: 10.1021/acs.chemrev.6b00440
Chem. Rev. 2017, 117, 1564−1686

summarize the cationic dummy atom and combined models in section 5. These two models are presented separately from the bonded and nonbonded models because they form a distinct set of "semibonded" models. Subsequently, we review several widely used polarizable models in section 6, while in section 7 we review classical models based on the angular overlap model (AOM) and valence bond (VB) theory. Finally, we summarize our conclusions and perspectives on the prospects of this research field in section 8. While we strive to give a balanced review of the field, we realize that due to the limits of our knowledge omissions might occur, for which we make our apologies. Note that the dates listed in the main text represent the year of publication in the original article, which may differ from the year when the article appeared in press. For example, the original paper describing the 12-6-4 LJ-type nonbonded model for divalent metal ions was published online in October of 2013, while it appeared in print in 2014 in the *Journal of Chemical Theory and Computation*. Hence, we refer to the work as being reported in 2014.

1.5. Previous Reviews

A broad range of reviews regarding the computational modeling of metal ions have been published in the past several decades. Below, we summarize some extant reviews for the sake of the readers who want to trace back through the relevant literature.

1.5.1. Quantum Mechanics Methods. There are a number of reviews concerning TM chemistry that have been published in *Chemical Reviews*. Holm and Solomon coedited a series of reviews largely focused on experimental studies of bioinorganic enzymes.[12−15,45,52−71] Davidson edited a series of reviews on QM modeling of TM-containing systems in 2000,[72−85] which summarized the development of ab initio and DFT methods to date. In total, 13 articles on various topics of QM TM modeling were included.[73−85] Holm and Solomon edited another series of reviews on biomimetic inorganic chemistry,[86−112] of which there were couple of reviews on theoretical topics. Noodleman et al. reviewed QM studies of enzyme reaction mechanisms,[104] and Solomon et al. reviewed the electronic structure of models of clusters found in blue copper proteins from both experimental and theoretical points of view.[108] As a sequel to their successful series of reviews in 1996,[52] Holm and Solomon edited another series of articles on bioinorganic enzymology.[113−123] In the series of reviews about theoretical calculations on large systems edited by Gordon and Slipchenko in 2015,[124] Blomberg et al. reviewed QM studies of the mechanisms of a series of metalloenzymes.[114] Fernando et al. reviewed QM calculations on metal-containing systems including metal, metal oxide, and metal chalcogenide clusters,[125] which focuses on the structure and physical properties of metal-containing clusters, but did not cover the studies of bulk or surface properties in periodic systems. Finally, Odoh et al. recently reviewed QM studies of metal−organic frameworks (MOFs).[126]

Besides the aforementioned collections of relevant review articles, several other germane reviews have been published in the last several decades. Rode et al. summarized their QM simulation work on ion solvation in 2004.[127] They used QM MD simulations, which include "quantum effects" and, consequently, provide detailed insights into the ion solvation process. Deeth reviewed the application of DFT methods to the modeling of the active sites and mechanisms of metalloenzyme systems in 2004.[128] In his review, he discussed factors for designing suitable models and described overall strategies for calculations on these model systems. In 2005, Shaik et al. reviewed the available theoretical work on cytochrome P450 enzymes.[129] In 2006, Noodleman and Han reviewed DFT methods applied to spin-polarized and spin-coupled systems and DFT applications to different states of redox-active and electron transfer metalloproteins,[130] while Neese reviewed the application of DFT and time-dependent DFT methods to bioinorganic chemistry.[131] Hallberg reviewed the DMRG method and its applications to various areas including physics and chemistry also in 2006.[132] In 2009, Cramer and Truhlar reviewed the DFT method and its application to TM chemistry.[133] Multiple topics were covered including the effect of DFT functional choice, available software and validation tests, combined with representative applications to different TM-containing systems. Aullón and Alvarez reviewed the relationship of atomic charge and formal charge in TM compounds based on DFT studies on four-coordinated TM complexes.[134] In 2010, Shaik et al. reviewed QM/MM studies on P450 enzymes.[135] In 2011, Hofer et al. reviewed studies relating to the hydration of highly charged ions.[136] In this Review, they concluded that the combination of accurate QM simulation with experimental research would be necessary to obtain highly reliable insights into the solvation of these ions. In 2012, Sameera and Maseras gave an overview of DFT and DFT/MM studies of TM catalysis,[137] while in 2014, Tsipis reviewed DFT modeling of coordination chemistry.[138] In the latter, several general suggestions were provided regarding how to choose a DFT functional suitable for the problem at hand.

1.5.2. Unpolarized Force Fields. There are a few reviews on classical modeling of inorganic complexes published several decades ago. For example, Brubaker and Johnson reviewed MM modeling in coordination chemistry in 1984.[139] Hancock and Martell reviewed MM modeling strategies for application to ligand design for metal ion complexation in 1989.[140] Comba reviewed MM-based studies on metal ion selectivity in 1999.[141] Limitations and the reasons for the failure of some of the modeling efforts were discussed along with their possible solutions. Norrby and Brandt reviewed parametrization strategies for deriving MM parameters for coordination complexes in 2001.[142] Topics on model setup, target choice, parameter refinement, and force field validation were covered in the review. Banci reviewed MD simulation work on metalloproteins,[143] and Comba and Remenyi reviewed MM-based modeling of inorganic compounds both in 2003.[144] For the later, studies on blue copper proteins were used as a case study, while the pros and cons of QM, QM/MM, and MM models were discussed in detail. Jungwirth and Tobias have reviewed classical modeling of ions (for both unpolarized and polarizable force field models) at the air/water interface.[145] Comba, Hambely, and Bodo coauthored a book entitled "Molecular Modeling of Inorganic Compounds" in 2009.[146] Zimmer reviewed classical MM-based simulations of bioinorganic systems and highlighted work on methyl coenzyme-M reductase and urease as example cases.[147] Sousa et al. discussed the difficulties of modeling metalloenzymes using MD simulation and gave an overview of the typical modeling strategies used to solve this problem in 2010.[148] A modeling study of a zinc-containing metalloenzyme-farnesyltransferase using the bonded approach was used to illustrate this modeling strategy. In 2011, Leontyev and Stuchebrukhov reviewed the "molecular dynamics in electronic continuum" method (a charge scaling technique) they developed.[149] In 2012, Dommert et al. reviewed unpolarized, polarizable, and CG

DOI: 10.1021/acs.chemrev.6b00440
Chem. Rev. 2017, 117, 1564−1686

Table 1. $^3D-^3F$ and $^3D-^1S$ Excitation Energies of Ni Based on Several Different QM Methods and from Experiment[a]

	HF[188]	HF+rel[188]	SDCI+rel[188]	SDCI+rel with Davidson correction[188]	MRCI+rel[188]	MRCI+rel with Davidson correction[188]	exp.[189]
$^3D-^3F$	−1.277	−1.637	−0.340	−0.325	−0.086	−0.195	0.03
$^3D-^1S$	4.199	4.404	2.484	2.261	1.879	1.843	1.74

[a]Units in eV. Herein, +rel means with relativistic correction, the HF and HF+rel calculations used an uncontracted (20s15p10d6f) basis set, while the rest of the calculations used a (7s6p4d3f2g) basis set; the experimental results were obtained after averaging over the *J*-components.

force fields for ionic liquids with a focus on the imidazolium-based ionic liquids.[150] In 2012, Riniker et al. reviewed coarse-grained (CG) models for simulating biomolecules, in which they generalized the "coarse-graining" concept and discussed the basic principles involved in developing CG models based on fine-grained models.[151] Marrink and Tieleman reviewed the popular MARTINI force field in 2013.[152] In 2015, Nechay et al. reviewed their work on metalloprotein modeling using the QM/discrete molecular dynamics (DMD) approach.[153] Li et al. reviewed simulation work on metal ion coupled protein folding.[154] Finally, in 2016, Heinz and Ramezani-Dakhel reviewed molecular simulation work on inorganic−bioorganic interfaces.[155] Kmiecik et al. reviewed CG models for proteins and summarized a range of related applications.[156] Cho and Goddard reviewed studies of metalloproteins from the theoretical and experimental points of view in their book.[157]

1.5.3. Polarizable Force Fields. Because there are very few extant review articles specific to the modeling of metal ions using polarizable force fields, we decided to highlight a number of reviews on polarizable force fields that have appeared regardless of their overall relevance to metal ion-containing systems. In this way, interested readers can gain entry into this rapidly developing field.

In the collection of *Chemical Reviews* articles edited by Holm and Solomon in 1996,[52] one article by Stephens et al. focused on theoretical calculations of the redox potentials of Fe−S proteins using the protein dipole Langevin dipoles model.[13] Halgren and Damm summarized work on polarizable force fields up to ∼2001.[158] In 2002, Rick and Stuart reviewed the strategies of incorporating polarizability into classical modeling while focusing on the use of polarizable force fields in MD and Monte Carlo (MC) simulations.[159] Ponder and Case reviewed the available protein force fields (both unpolarized and polarizable) in 2003.[160] Mackerell gives a short review on polarizable force fields as part of his review of empirical force fields in 2004.[161] Friesner has also reviewed the development of polarizable force fields in 2005.[162] Patel and Brooks summarized their work on the development and application of the CHARMM fluctuating charge (FQ) model in 2006.[163] Gresh et al. gave an overview of the formulation and applications of the sum of interactions between fragments computed ab initio (SIBFA) method in 2007.[164] Warshel et al. critiqued the development of macroscopic polarizable force fields and emphasized the importance of polarization effects in application studies in their review in 2007.[165] Cieplak et al. sketched out the development and application of polarizable force fields for macromolecular simulations in 2009.[166] They reviewed unpolarized force fields, followed by intermolecular interactions studied by QM methods, and then polarizable force fields. Loopes et al. summarized the theories, extended Lagrangian integrators, and application studies of polarizable force fields in 2009.[167] Russo and van Duin described the reactive force field (ReaxFF) method and showed an application to a zinc−oxide nanowire in 2011.[168] Gong outlined modeling work of ion-containing systems using the atom-bond electronegativity equalization method (ABEEM) FQ model in 2012.[169] Lamoureux and Orabi, in 2012, reviewed the cation−π interaction modeling with an emphasis on applications to proteins and the Drude oscillator (DO) model they developed.[170] Shin et al. surveyed the use of ReaxFF for simulating complex bonding and chemistry in 2012, with an emphasis on the application of ReaxFF and the charge optimized many-body models.[171] An overview of the development and application of reactive potentials was given by Liang et al. in 2013, with an emphasis on the comparison of ReaxFF and the charge-optimized-many-body (COMB) force fields with variable-charge schemes.[172] In 2015, Shi et al. gave a conspectus on the recent progress of different polarizable force fields,[173] and in the same year Vanommeslaeghe and Mackerell examined recent developments of the CHARMM unpolarized force field and discussed the CHARMM DO force field, with an emphasis on its parametrization scheme.[174] Recently, Lemkul et al. have reviewed the DO model with emphasis on the application of the Drude-2013 model to biological molecules.[175] Senftle et al. reviewed the ReaxFF model, in which its development, applications, and future directions were discussed.[176]

1.5.4. Other Models. Landis and co-workers reviewed their SHAPES method in 1995,[177] and Deeth and co-workers have written several reviews and book chapters regarding their ligand field MM (LFMM) method.[178−182]

2. MODELING TRANSITION METAL-CONTAINING SPECIES USING QUANTUM MECHANICS

2.1. Challenges

This Review concentrates on force field modeling for metal ions; however, due to the broad adoption of QM methods to derive force field parameters and in QM/MM simulations, we provide a brief review on metal ion modeling using QM methods. A number of more extensive reviews on QM modeling of TM-containing systems are available in the literature for the interested reader.[183−185]

QM and QM/MM methods offer detailed insights into intermediates and transition states in catalysis, where these states are hard to understand using experimental tools.[137] However, it is still challenging to accurately model TM-containing systems using QM calculations. In particular, modeling the multireference characteristic of many TM species using single reference methods is not handled correctly because they do not address static correlation.

Besides modeling molecules, it is hard to simulate the metal atoms from the middle TM series. Here, we treat the Ni atom as an example. The atomic excitation energies of Ni for $3d^94s^1-3d^8s^2$ ($^3D-^3F$) and $3d^94s^1-3d^{10}$ ($^3D-^1S$) excitations calculated by several different QM approaches are shown in Table 1, together with experimental values. Table 1 shows that the HF method gives significant errors predicting these properties, while multireference methods need to be employed to obtain accurate results.

DOI: 10.1021/acs.chemrev.6b00440
Chem. Rev. 2017, 117, 1564−1686

Martin and Hay have studied the excitation energies of low-lying states and ionization potentials (IPs) of TMs.[186] Relativistic effects were taken into consideration based on the scheme of Cowan and Griffin.[187] They found that the relativistic effect stabilized the "s-electron-rich" configurations, while correlation effects favored the "d-electron-rich" configurations. In their work, it was shown that the numerical HF method without relativistic correction predicted excitation energies for the $^3D-^3F$ and $^3D-^1S$ transitions of −1.27 and 4.20 eV, respectively, while the relativistic HF method predicted the two values as −1.63 and 4.41 eV, respectively. Bauschlicher et al. systematically investigated different methods for predicting these excitation energies.[188] They found a single reference SDCI approach offered improvement, but the differences when compared to experiment were still considerable (see Table 1). Finally, they showed that the multireference configuration interaction (MRCI) method coupled with large atomic natural orbital (ANO) basis sets could further reduce the errors (see Table 1).

Because the DFT method considers the electron density−energy relationship directly, it incorporates static correlation effectively when modeling TM containing systems.[133] However, there are a large number of functionals available, and the computational accuracy varies widely among them and is property dependent. Hence, the answer to the question of which functional should be used really depends on the system and property one wants to investigate. In general, correlation functionals, which do not attain the homogeneous gas electron limit, are not suggested for pure metal systems,[190,191] while for mixed systems, such as organometallics, this is not a significant limitation.[84]

2.2. Ab Initio Methods

The Hartree−Fock (HF) method is a self-consistent field (SCF) method that was first proposed by Hartree[192,193] and later developed by Fock,[194] Slater,[195,196] etc., resulting in the HF method widely used nowadays. It uses several approximations to solve the Schrödinger equation efficiently for complex systems, including the Born−Oppenheimer, nonrelativistic, linear combination of atomic orbitals (LCAO), Slater determinant, and mean field approximations. However, because it neglects the correlation energy and is a single reference method, it is generally not used for modeling TM-containing systems. Even with these issues, HF methods can be used for force constant derivation with some success.[197] The MP2, CCSD, and CCSD(T) methods include some portion of the correlation energy and are contemporary post-HF work horses. Among them, CCSD(T) with complete basis set (CBS) extrapolation is treated as the "gold standard" for predicting the properties of small organic molecules.[198] It can achieve chemical accuracy (±1 kcal/mol) for atomization energies and reaction enthalpies for small molecules.[199] However, due to its single reference character, CCSD(T) does not afford an accurate representation of "static correlation". Multiple reference wave function-based methods offer better descriptions but with greatly increased computational cost.[200]

TM-containing systems are more likely to have strong multireference properties due to the near degeneracy of d orbitals. A well-known multireference TM system is Cr_2, its multireference character making it challenging to simulate using methods employing a single Slater determinant.[201] However, we note that multireference is not only a characteristic that is relevant to TMs. For example, the C_2 molecule, which has several low-lying excited electronic states, also has strong multireference character. Abrams and Sherrill have explored the limitations of single-reference methods in modeling the multireference C_2 system.[202]

Jiang et al. studied the multireference character of 3d TM-containing systems and have discussed the criteria for determining this characteristic.[203] Subsequently, Wang et al. performed related studies for 4d TM-containing species and listed criteria for determining the multireference characteristics of these systems.[204]

Weaver et al. have investigated the accuracy of the CCSD and CCSD(T) methods for calculating the HOFs of zinc-containing systems.[205] The basis sets 6-31G** and TZVP, along with two hybrid basis sets LANL2DZ-6-31G** (same as LACVP**) and LANL2DZ-TZVP, were employed. The 6-31G** basis set showed the best performance in general. The CCSD(T)/6-31G** level of theory showed the best performance for predicting the HOFs of nonalkyl zinc species, while none of the investigated theory combinations could reproduce the HOFs of alkyl zinc compounds accurately. Moreover, it was shown that the CCSD/6-31G** level of theory could best reproduce experimental geometries. However, the coupled cluster (CC) methods did not systematically outperform DFT functionals. For the ZnH and ZnF_2 systems, there are many DFT functionals that gave better predictions with the 6-31G** basis set. In a related work by Weaver and Merz, they investigated the CC method for calculating the HOFs of copper-containing systems.[206] The results indicated that there is no correlation between calculating the HOFs accurately and predicting bond lengths precisely. The CCSD(T)/6-31G** level of theory incorrectly predicts the ground state of the CuO compound as a quartet, with an elongated bond length (∼0.29 Å longer than experiment), and afforded an overestimate of the HOF value (∼29 kcal/mol higher when compared to experiment).

In the recent work of Xu et al., they calculated the bond energies of 20 diatomic molecules containing 3d TM elements using four CC-based methods (CCSD, CCSD(T), CCSDT, $CCSDT(2)_Q$) and 42 DFT functionals, and compared them to the most reliable experimental data.[207] They found that the CC methods only offered similar accuracy with, but not necessarily better than, the DFT methods, suggesting that CC methods do not form a benchmark theory for DFT methods. They also found that both CC and DFT methods perform better for single reference systems than for multiple reference systems. Moreover, it was found that CCSD(T) calculations usually underestimate the bond energies, while DFT broken-symmetry calculations usually overestimate these values. Overall, using CCSD(T) results as benchmark values for DFT and other methods should be treated with caution for TM methods.[207]

Given the limited accuracy of direct prediction based on post-HF methods, the scaled approach is an alternative and offers improved results. For example, Hyla-Kryspin and Grimme have investigated the dissociation enthalpy changes of a number of TM complexes using the MP2, MP3, spin component scaled-MP2 (SCS-MP2), SCS-MP3 methods, and the BP86 density functional, and compared them to experimental data.[208] The mean average error (MAE) values of the MP2, MP3, SCS-MP2, SCS-MP3, and BP86 methods are 21.0, 22.3, 11.6, 4.1, and 3.4 kcal/mol, respectively. This indicates the SCS method can correct the erratic behavior of MP2 and MP3 methods, and that DFT showed improved performance in the modeling of these systems.[208]

DOI: 10.1021/acs.chemrev.6b00440
Chem. Rev. 2017, 117, 1564−1686

Carlson et al. have studied a di-iron complex Fe−Fe−Cl and some analogues with weaker metal−metal bonds (Co−Co, Co−Mn, Co−Fe, and Fe−Mn) using multireference wave function-based methods and DFT functionals.[209] They found that a larger active space is necessary to correctly describe the Fe−Fe−Cl system. Full consideration of the 4d orbitals in the active space is needed to correctly describe the electronic delocalization and bonding between the two irons in the Fe−Fe−Cl complex, while truncation of the 4d orbital set causes the inaccurate modeling of some 3d orbitals, and incorrectly predicts the ground spin state. However, for the Co−Co−Cl system, which has more localized metal centers, a full or truncated inclusion of 4d orbitals in the active space affords the same result. They also found that some DFT functionals predict the correct ground spin state, chemical bond, and structural properties of the complexes investigated, while hybrid functionals strongly localized the 3d orbitals and failed to predict the correct spin state ordering, especially for the di-iron complex.

2.3. Composite Methods

The so-called QM composite methods attempt to mimic the accuracy of more expensive high-level QM calculations by using a combination of several procedures with lower computational expense and accuracy.[210] Pople, Curtiss, and co-workers have developed the Gaussian-1 (G1), Gaussian-2 (G2), and Gaussian-3 (G3) approaches and pioneered this field.[211−214] These approaches were intended to create a "black box" to accurately predict energetic properties including HOFs, IPs, electron affinities (EAs), and proton affinities within ±2 kcal/mol of experimental data.[210]

Subsequent to these methods, Curtiss et al. developed the Gaussian-4 (G4) method.[215] Mayhall et al. have calculated the enthalpies of formation of 20 3d TM-containing molecules using several composite approaches and DFT functionals.[216] It was shown that the four composite approaches G4(MP2, rel), G4(rel), G3(CCSD, rel), and G3(CCSD, MP2, rel) have MADs of 2.84, 4.75, 5.81, and 4.85, respectively (here, "rel" represents including corrections for scalar relativistic effects). They proposed that the failure of the G4(rel) method is due to the poor convergence of the MP4 calculations. The B3LYP, PBE, and PW91 functionals showed remarkably different performance: the B3LYP functional yielded a MAD of 4.64 kcal/mol, while the later two functionals showed MADs of more than 20 kcal/mol.

Wilson and co-workers are active in composite approach development for TM systems, and herein we briefly introduce their work. Wilson and co-workers developed the correlation consistent composite approach (ccCA) in 2006.[210] It is a MP2-based composite method without any parameters. It was shown that the method could accurately predict the energetic properties of main group species (with MAD < 1 kcal/mol)[217] and s-block systems (with a bigger deviation but still good accuracy).[218,219] In 2007, they used the ccCA approach to study the HOFs of 17 3d TM species.[220] They noted that the amount and accuracy of experimental thermochemistry data were limited, and it is challenging to achieve "chemical accuracy" for both experimental and theoretical thermochemistry.[220] Hence, in light of this, an average deviation of ±3 kal/mol could be considered as "chemical accuracy" for TM thermochemistry. The ccCA method showed a MAD of 3.4 kcal/mol for a training set of 8 TM-containing molecules, similar to the DK-CCSD(T) approach (a CCSD(T)-based composite approach), which yielded a MAD of 3.1 kcal/mol for the same set. However, the agreement between the theoretical values and experimental data is more system dependent, when compared to that of the main group molecules.

DeYonker et al. have used the ccCA method to calculate the HOFs of 147 main group molecules and 52 3d TM complexes in 2009.[221] They obtained a MAD for the former set of 0.89 kcal/mol, while the MAD and mean square deviation (MSD) for the later set was 2.85 and 3.77 kcal/mol, respectively.[221] It was shown that the DFT results are more system dependent with some of them giving erratic predictions for some cases, while the ccCA method was less system dependent and more consistent. They also pointed out that some of the experimental data need to be revisited based on the ccCA calculations.

Subsequently, Jiang et al. calculated the enthalpies of formation of 225 3d TM species using the ccCA-TM approach and compared them to experimental results.[47] It was shown that the deviation from experiment decreases only when consideration is made for the uncertainty in the experimental data. The MADs for subsets of TM-containing systems, which have uncertainty upper limits of ±5, ±4, ±3, ±2, and ±1 kcal/mol, were 3.91, 3.74, 3.42, 2.90, and 2.37 kcal/mol, respectively (see Figure 4). Hence, they proposed that the large error from theory is due to less reliable experimental data for TM-containing species relative to organic species.[47] They also carried out calculations using the B3LYP and M06 functionals for comparison; the MAD of B3LYP for the subsets with different upper limits in uncertainty (±1 to ±5 kcal/mol) are in the range of 12.9−14.1 kcal/mol, while for the M06 method the corresponding values are in the range of 10.5−11 kcal/mol. These results showed that the accuracy of the ccCA-TM composite method outperforms DFT methods.

Laury et al. have carried out calculations of thermochemical properties of 25 molecules containing 4p elements (Ga−Kr) and 30 molecules containing 4d TMs, using the relativistic pseudopotential ccCA (rp-ccCA) method.[222] The rp-ccCA approach needs less time than the ccCA method because a pseudopotential was also employed. The average uncertainty of the experimental HOFs for the 4d TMs is 3.43 kcal/mol. The values obtained from the rp-ccCA method had MADs of 0.89 and 2.89 kcal/mol for molecules containing 4p elements and 4d TMs, respectively. Overall, these results show the ability of the ccCA approach.

2.4. Semiempirical Methods

TMs have significantly more electrons than the first- and second-row elements in the periodic table, resulting in a significant increase in computational cost. While it is challenging to perform ab initio calculations of TM containing systems, semiempirical (SE) methods are efficient and attractive alternatives. SE methods use a minimal basis set to save computational time. Generally the time complexity of SE methods is $O(N^2)$ or $O(N^3)$, where N is the number of basis set functions.[223] Hence, SE methods are ∼1000 times faster than the DFT method,[223] allowing for the treatment of larger systems using modern computational resources.

2.4.1. Neglect of Differential Overlap-Based Methods.

Pople and co-workers pioneered the development of SE methods and proposed the complete neglect of differential overlap (CNDO),[224,225] intermediate neglect of differential overlap (INDO),[226] and neglect of diatomic differential overlap (NDDO) methods in the 1960s.[227] These methods use strategies, as their names indicate, to neglect all or some of

DOI: 10.1021/acs.chemrev.6b00440
Chem. Rev. 2017, 117, 1564−1686

the differential overlap calculations in the HF method to save on computational time.

Zerner and co-workers pioneered SE method development for TMs: they parametrized the INDO scheme (so-called ZINDO method) not only for the main group elements, but also for the 3d and 4d TMs, and even lanthanides and actinides, from the 1970s to the 1990s.[228−236] It uses a linear combination of two Slater functions to represent the atomic orbitals of the main group elements (K to I) and TMs. It sets the one-center Coulomb integrals on one atom as identical and evaluates them as the difference between the IP and EA of the atom (also known as absolute hardness). Exchange integrals are represented using Slater−Condon parameters. Reference spectra were used to fit some parameters in the scheme. These parameters concentrated more on reproducing spectroscopic and electron-transfer properties.[237] Filatov et al. have proposed and parametrized the CNDO-S^2 procedure for molecules containing H, C, N, O, and Ni atoms in 1987.[238] Nieke and Reinhold parametrized the NDDO method for 3d TMs in 1984.[239] Subsequently, Filatov et al. developed the NDDO/MC (NDDO for metal compounds) method and parametrized it for H, C, N, O, Co, and Ni atoms in 1992.[240]

Jug and co-workers developed the SINDO1 method, which is consistent with the symmetrically orthogonalized INDO (SINDO) method that considers the orthogonality of atomic orbital basis sets in calculating related core-Hamiltonian elements.[241−243] The frozen-core strategy was used, and only the electrons of the valence-shell are represented explicitly in the SINDO1 method.[241−243] Jug and co-workers extended and parametrized the SINDO1 method to 3d TM elements in 1992.[244] 90 bond lengths, 14 angle values, HOFs of 78 molecules, and IPs of 32 molecules from experiment were used as the reference set for parametrization. The obtained results showed that the SINDO1 method could predict the geometry with considerable accuracy and reproduce the HOFs and IPs semiquantitatively. Later, they developed the modified SINDO (MSINDO) method[245−247] and also parametrized it for 3d TMs. HOFs, IPs, geometries, and dipole moments of more than 200 molecules were treated as the reference set for parametrization.[248] Comparison with the SINDO1 method was carried out, and in general the MSINDO method showed substantial improvement over its predecessor. The transferability of these parameters was shown in calculating the binding energies of monohydrates of singly charged 3d TM ions from Ti^+ to Cu^+.

2.4.2. Modified Neglect of Diatomic Overlap-Based Methods. Dewar and co-workers played a significant role in the development of SE methods. They developed the modified intermediate neglect differential overlap (MINDO),[249] MINDO/2,[250] and MINDO/3[251] methods based on the INDO approximation in 1969, 1970, and 1975, respectively. To improve the overall accuracy of their methods, Dewar and Thiel developed the modified neglect of diatomic overlap (MNDO) method based on the NDDO approximation in 1977.[252] Dewar and co-workers parametrized the MNDO method for Sn and Hg in 1984 and 1985, respectively.[253,254] Dewar and Merz parametrized MNDO for Zn in 1986.[255] Thiel and Voityuk extended the MNDO scheme to d orbitals (so-called MNDO/d method) and demonstrated improved results.[256,257] In 1996, they parametrized the MNDO/d approach for the second-row elements (except Ar) and group IIB elements (Zn, Cd, and Hg).[258] Extensive tests were carried out, and it was again shown that the MNDO/d method outperformed other MNDO-type methods lacking d-orbitals.[258]

2.4.2.1. AM1 Model. Dewar and co-workers developed the Austin Model 1 (AM1) method in 1985 to better model hydrogen-bonded systems.[259] Dewar and Merz extended this method for Zn in 1988, which showed better performance than the MNDO method for this same metal.[260] Voityuk and Rösch added d-orbitals to the AM1 method (so-called AM1/d method), parametrized it for Mo, and demonstrated this method's ability to predict the geometries and HOFs of a series of Mo complexes.[261] Imhof et al. parametrized the AM1/d method for Mg in metalloenzymes and demonstrated considerable improvement over the AM1 and MNDO/d methods.[262] Finally, Clark and co-workers developed the AM1* model for a series of elements including the 3d TMs (except Sc) as well as Al, Zr, Pd, Ag, and Au.[263−269]

2.4.2.2. PMx Models. Stewart described the parametric method 3 (PM3) method in 1989[270,271] and extended it to 28 elements including metals such as Be, Mg, Zn, etc., in 1991.[272] Ignatov et al. extended the PM3 method to a s,p,d basis set and carried out test calculations on organometallic complexes of Cr in 1996.[273] Børve et al. applied the PM3(tm) method to several catalysts containing Ti, Zr, or Cr in 1997.[274] Cundari and Deng parametrized the PM3 method for TMs against experimental structures in 1999.[275] Their model showed the ability to predict the geometries of TM complexes, especially for TMs in the left-hand side of the periodic table.[275] Stewart have extended the PM3 method creating PM6 in 2007 that covered 70 elements and showed excellent overall performance in predicting HOFs.[276] PM7 appeared in 2013, and it showed improved performance over PM6.[277] Seitz and Alzakhem used the AM1/SPARKLE, PM3/SPARKLE, and PM6/SPARKLE methods to study more than 650 Ln complexes, which have water coordinating the metal ion in 2010.[278]

2.4.3. Embedded Atom, Finnis−Sinclair, Sutton−Chen, and Tight-Binding Models. There are three different packing patterns for metals: the body-centered cubic (BCC), face-centered cubic (FCC), and hexagonal close-packed (HCP) structures. Metals in these three packing structures have CNs of 8, 12, and 12, respectively. The packing factors of these three packing modes are 0.68, 0.74, and 0.74, respectively. Different metals may have different packing structures. For instance, metals such as Li, Na, K, V, Cr, Ba, etc., have BCC structures, metals including Al, Cu, Ag, Au, Ni, Pt, Pb, etc., have FCC structures, and Be, Mg, Zn, Cd, etc., have HCP structures.

A number of SE models have been developed for metals and their alloys, including the embedded atom model (EAM),[279] Finnis−Sinclair (FS) model,[280] Sutton−Chen (SC) model,[281] and tight-binding (TB) model.[282] These models are many-body potentials and are related to the electronic density. Generally, it is more challenging to model BCC metals than FCC and HCP examples. It is also not an easy task to calculate the relative stabilities of the former over the latter two. Below we briefly review several representative approaches.

2.4.3.1. Embedded Atom Model. Daw and Baskes developed the EAM method based on DFT in 1983.[279] They have applied it to the hydrogen doped Ni system, and their results showed that fracture stress in metallic Ni could be reduced by hydrogen. Subsequently, they described the formalism of the EAM method.[283] The total potential is shown in eq 1. $\rho_{h,i}$ is the host density, which is approximated by a sum of atomic densities (see eq 2). ϕ_{ij} is a short-range pairwise repulsive potential (see eq 3). This potential is

DOI: 10.1021/acs.chemrev.6b00440
Chem. Rev. 2017, 117, 1564−1686

represented by the electrostatic interaction of the effective charges of two interacting atoms. Different properties (such as the lattice, elastic constant, etc.) can be derived from the total energy. They parametrized the potential for Ni and Pd metals and applied it to study related impurity, surface, and defect properties.

$$E_{tot} = \sum_i F_i(\rho_{h,i}) + \frac{1}{2}\sum_{i,j\neq i} \phi_{ij}(R_{ij}) \quad (1)$$

$$\rho_{h,i} = \sum_{j\neq i} \rho_j^a(R_{ij}) \quad (2)$$

$$\phi_{ij}(r) = \frac{Z_i(r)Z_j(r)}{r} \quad (3)$$

Foiles et al. have further developed the EAM model for several FCC metals (Cu, Ag, Au, Ni, Pd, and Pt) and their alloys.[284] The potentials were fitted to several experimental properties. It was shown that the model reproduces various properties including several issues related to impurities and surface properties.

2.4.3.2. Finnis–Sinclair Model. Finnis and Sinclair developed an empirical *N*-body model (the FS model) for TMs in 1984.[280] The components of the potential function are shown below:

$$U_{total} = U_{rep} + U_{attr} \quad (4)$$

$$U_{rep} = \frac{1}{2}\sum_{ij} U(r_{ij}) \quad (5)$$

$$U_{attr} = -A\sum_i f(\rho_i) = -A\sum_i \sqrt{\rho_i} \quad (6)$$

$$\rho_i = \sum_j \phi(r_{ij}) \quad (7)$$

Here, the repulsion term is an additive two-body term, representing core–core interactions, while the attractive term is an *N*-body term that represents the band energy. It mimics TB results by choosing $f(\rho_i)$ as $\sqrt{\rho_i}$, where ρ_i is the site electronic charge density via summation over the neighboring atoms j into a potential ϕ, and where $\phi(r_{ij})$ can be considered as the sum of squares of hopping integrals.[280] Both terms in eq 4 were short-ranged with specified distance cutoffs. The parameters are fitted to lattice constants, cohesive energies, and elastic moduli for 7 BCC TMs. In the original parametrization, they used a parabolic equation for $\phi(r_{ij})$ (a different formulation was used for Cr and Fe) and a quartic polynomial equation for U_{rep}. It was shown that the model could reproduce different experimental properties and also results based on the TB theory, while offering improvement over the simple pairwise potential.

2.4.3.3. Sutton–Chen Model. Sutton and Chen developed the SC potential on the basis of the Finnis–Sinclair potential in 1990.[281] They discussed that the description of the VDW potential is as important as modeling the short-range interactions. The function has the form:

$$U_{total} = \varepsilon_{ij}\left[\sum_{i,j>i}\left(\frac{a_{ij}}{r_{ij}}\right)^{n_{ij}} - c_i\sum_i \sqrt{\rho_i}\right] \quad (8)$$

$$\rho_i = \sum_{j\neq i}\left(\frac{\sigma_{ij}}{r_{ij}}\right)^{m_{ij}} \quad (9)$$

The attractive term is represented by an *N*-body potential; it can be extended to a pairwise potential when an additional atom approaches the surface at long-range, even as the magnitude of the pairwise potential is influenced by other neighboring atoms. By assigning $m = 6$, one has a r^{-6} representation for the attraction energy at long-range. However, it was shown that the potential always favors the FCC and HCP structures over the BCC one. It was also shown that the SC model could be extended to a pairwise LJ $m-n$ model under a reference density (see eq 10).

$$\sqrt{\rho^s + \left(\frac{a}{r}\right)^m} \cong \sqrt{\rho^s} + \frac{(a/r)^m}{2\sqrt{\rho^s}} \quad (10)$$

The only parameters that need to be determined in the equation are ε, σ, m, and n. Sutton and Chen have derived analytical expressions for different experimental properties on the basis of the potential. On the basis of this, they parametrized the potential for 10 FCC metals to reproduce different experimental properties. For these metals, m was determined to be in the range of 7–14, while n was determined to be in the range of 6–8. They also discussed that there are different physical origins for the short-range *N*-body unsaturated covalent bond and the VDW interaction, even if they are merged into one term in the equation for mathematical convenience.

2.4.3.4. Tight-Binding Model. Cleri and Rosato developed the TB model with second moment approximation (TB-SMA) for FCC and HCP TMs.[282] Meanwhile, examples of potential derivations for a few TM alloys were also presented in their work. The potential consists of a band energy term and a repulsive term (see eqs 11–13). The band energy term is a many-body term, while the repulsion term is a pairwise term based on the Born–Mayer equation. In the band energy term (eq 12), ξ represents the effective overlap/hopping integral, which is similar to the format of the FS model that uses the $\sqrt{\rho_i}$ formulation to mimic the results of the TB model. Only A, ξ, p, q, and r_0 are the parameters that need to be determined in the model. They were fitted to reproduce different experimental properties. The model effectively simulates the thermal behavior of TMs. It was shown that through the use of a large cutoff, the model could represent experimental data even at temperatures close to the melting point of the metal, which is usually beyond the capability of a short-range model. However, the potential did not successfully model BCC metals. Other limitations were discussed in the concluding remarks in their work.[282]

$$E_{total} = E_R + E_B \quad (11)$$

$$E_B = -\sqrt{\sum_j \xi_{\alpha\beta}^2\, e^{-2q_{\alpha\beta}(r_{ij}/r_0^{\alpha\beta}-1)}} \quad (12)$$

$$E_R = \sum_j A_{\alpha\beta}\, e^{-p_{\alpha\beta}(r_{ij}/r_0^{\alpha\beta}-1)} \quad (13)$$

2.4.4. Self-Consistent Charge Density Functional Tight-Binding Model. Elstner, Cui, and co-workers have performed extensive work developing the self-consistent charge DFTB (SCC-DFTB) method. Siefert et al. proposed the

DOI: 10.1021/acs.chemrev.6b00440
Chem. Rev. 2017, 117, 1564–1686

density functional tight-binding (DFTB) method in 1986.[285] Elstner et al. followed with the SCC-DFTB method and applied it to organic, biomolecular, and material systems containing light main group elements in 1998.[286] The SCC-DFTB method is based on a second-order expansion of the charge density (see eqs 14−17). It uses Mulliken partial charges to represent the charge densities. "Band-structure" energy and a short-range repulsive term, along with a Columbic interaction between the charge fluctuations, were included in this approach. Akin to HF-based SE methods, SCC-DFTB uses a minimal basis set, which limits its accuracy to some extent. One important difference between the SCC-DFTB and SE methods is the former has $O(N^2)$ parameters (here N is the element numbers), while the latter only uses $O(N)$.

$$E^{\text{SCC-DFTB}} = E^{H0} + E^{\gamma} + E^{\text{rep}} \tag{14}$$

$$E^{H0} = \sum_{i} \sum_{\mu \in a} \sum_{\nu \in b} n_i c_{\mu i} c_{\nu i} H^0_{\mu\nu} \tag{15}$$

$$E^{\text{2nd}} \approx E^{\gamma} = \frac{1}{2} \sum_{ab} \Delta q_a \Delta q_b \gamma_{ab} = \frac{1}{2} \sum_{ab} \Delta q_a \Delta q_b \left[\frac{1}{r_{ab}} - S(r_{ab}, U_a, U_b) \right] \tag{16}$$

$$E^{\text{rep}} = \{E^{\text{SCF}}_{\text{LDA}}(R) - \sum_{i}^{\text{occ}} n_i \varepsilon_i(R)\}|_{\text{reference structure}} \tag{17}$$

$$E^{\text{rep}} = \frac{1}{2} \sum_{ab} V^{\text{rep}}_{ab}[\rho_a^0, \rho_b^0, r_{ab}] \tag{18}$$

Elstner et al. extended the SCC-DFTB method to Zn in 2003,[287] where they used a new functional form for the E^{rep} term (see eq 18). They parametrized it on the basis of B3LYP calculations and tested the parametrization on a series of biologically relevant zinc complexes via calculations on the geometries, relative binding energies, ligand deprotonation energies, and reaction barriers. The results considerably outperformed the PM3 method in many aspects, and good agreement with B3LYP/6-311+G** or MP2/6-311+G** calculations was obtained.

In an examination of the SCC-DFTB and NDDO-based methods, Sattelmeyer et al. showed that the former approach outperformed the latter in some areas when modeling molecules containing C, H, N, and O.[288] They observed that the SCC-DFTB method gives better conformational and intermolecular interaction energies but gives less accurate HOFs of ions and radicals. However, none of these methods accurately modeled hydrogen bonds with strengths less than 7 kcal/mol. Moreover, SCC-DFTB was shown to have considerable errors when dealing with S−O and N−O bonds.[288]

In 2007, Zheng et al. parametrized the spin-polarized SCC-DFTB method for Sc, Ti, Fe, Co, and Ni atoms.[289] They carried out the parametrization based on the B3LYP functional with mixed basis sets (SDD plus 6-31G*) and tested the parameters on a series of TM species. The computed results indicated that the parameters accurately modeled structural properties but only qualitatively reproduced energetic properties (such as bond energies and relative energies between different spin states) when compared to the reference B3LYP/SDD+6-31G* level of theory. A parametrization of the Cu ion was reported in 2012 by Bruschi et al. using the spin-polarized SCC-DFTB method.[290] The results indicated that the SCC-DFTB method was able to reproduce the energetic sequence of the three most stable Cu(HGGG) (Py) (see Figure 5) isomers in comparison to the BP86/TZVP level of theory.

$$E^{\text{SCC-DFTB3}} = E^{H0} + E^{\gamma} + E^{\Gamma} + E^{\text{rep}} \tag{19}$$

$$E^{\text{3rd}} \approx E^{\Gamma} = \frac{1}{6} \sum_{abc} \Delta q_a \Delta q_b \Delta q_c \left. \frac{d\gamma_{ab}}{dq_c} \right|_{q_c^0} \tag{20}$$

Gaus et al. further improved the basic SCC-DFTB approach through the introduction of SCC-DFTB3 (see eq 19, where the E^{H0}, E^{γ}, E^{Γ}, and E^{rep} terms are defined in eqs 15, 16, 20, and 18,

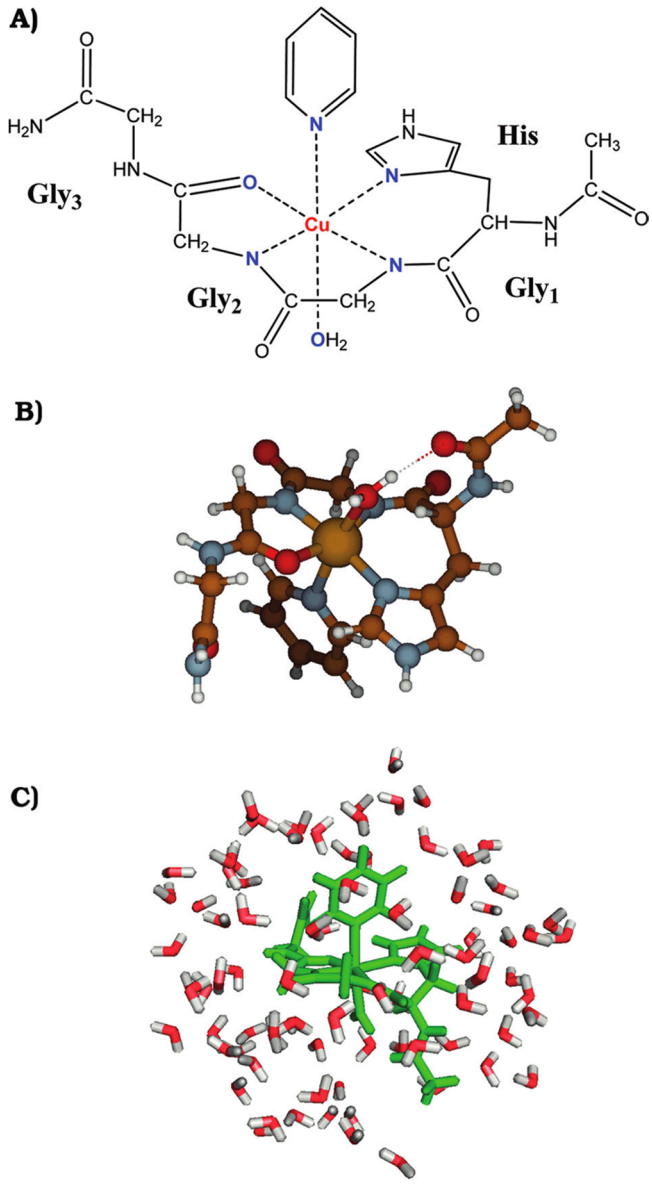

Figure 5. Complex $[Cu(AcHG_1G_2G_3NH_2)(Py)(W)]$ used as a precursor of all of the five- and four-coordinated forms considered in the study of Bruschi et al.[290] (A) Schematic representation of the complex; (B) molecular geometry of the complex alone; and (C) the complex inserted into a sphere of 84 water molecules. Reprinted with permission from ref 290. Copyright 2012 American Chemical Society.

DOI: 10.1021/acs.chemrev.6b00440
Chem. Rev. 2017, 117, 1564−1686

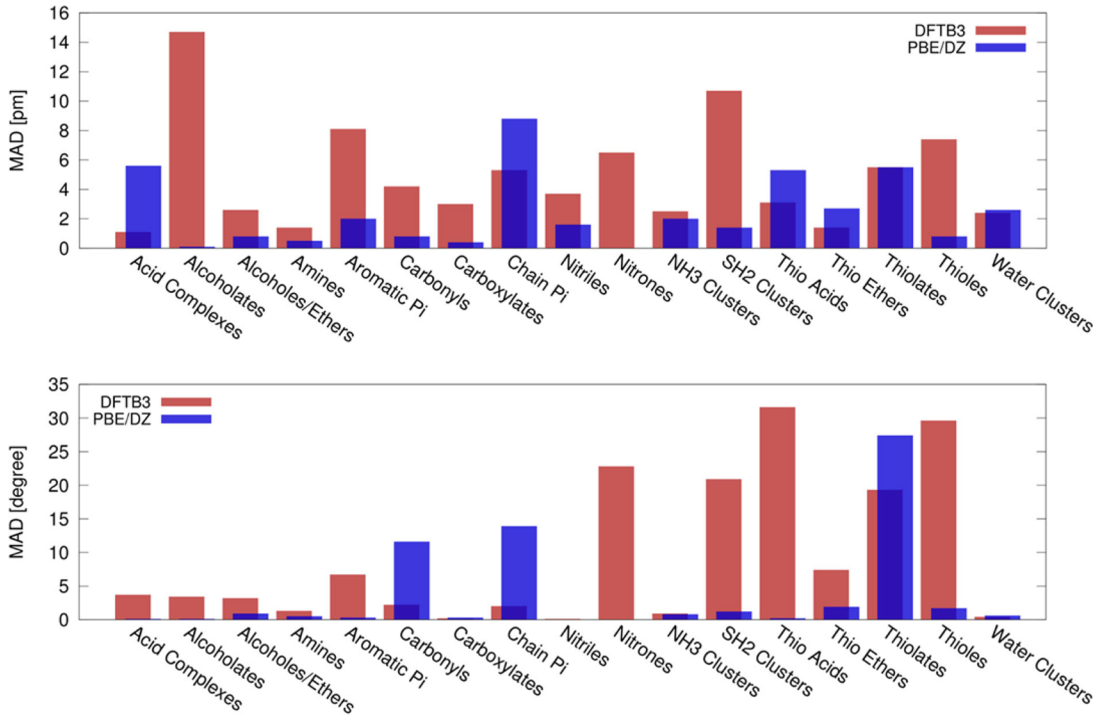

Figure 6. Accuracy of bond distances (upper panel) and bond angles (lower panel) in complexes of calcium with various organic functional groups reproduced by the DFTB3 parametrization from Kubillus et al.[293] The deviations observed with PBE/def2-SVP calculations are shown for comparison. The reference data were obtained with DFT optimizations at the level B3LYP/def2-TZVPP using Turbomole 6.4. Errors expressed as MADs in pm. The test systems contained in each category mentioned here are detailed further in the Supporting Information of ref 293. Reprinted with permission from ref 293. Copyright 2015 American Chemical Society.

respectively) in 2011, and they parametrized the model for H, C, N, O, and P (this work was termed as the SCC-DFTB3/MIO parametrization).[291] An improved description of the Coulombic interaction and a third-order expansion of the DFT energy were used in the SCC-DFTB3 scheme. Afterward, Gaus et al. performed the SCC-DFTB3/3OB parametrization for C, H, N, and O elements with refitting against a different database.[292] The new parametrization showed improved hydrogen-bonded energetics and better geometries for non-covalent interactions, as well as the elimination of overbinding errors.[292] Overall it reaches the accuracy of the DFT/DZP level of theory with a reduced computational cost. Nonetheless, several deficiencies remain. As a method based on DFT, the self-interaction error also exists in SCC-DFTB3. Because of limits from the use of a minimal basis set, the SCC-DFTB3 method fails where the DFT/DZP level of theory fails and will have issues if the system needs d orbitals to accurately represent its electronic structure. Moreover, it was shown that the SCC-DFTB3 method does not accurately predict atomization energies for ionic systems: cations tended to be underestimated and anions were overestimated. However, it is much more affordable being ∼250 times faster than PBE or B3LYP with a small basis set.

Kubillus et al. have extended the SCC-DFTB3 method to Na, K, Ca, F, Cl, and Br.[293] High-level QM calculations were used to generate reference data, and excellent performance was obtained from this parametrization. However, some deficiencies were noted including deviations in ionic bond lengths between alkali ions and anionic oxygen/sulfur atoms and an inability to model solid systems effectively. One example is shown in Figure 6, where their results show that DFTB3 suffers weaknesses when modeling Ca^{2+} interacting with alkyne (cation−π interaction), H_2S-containing systems, and lone pairs (especially oxygen lone pairs). The authors discussed that this arises due to the minimal basis set representation in DFTB and the spherical charge representation of the charge transfer (CT) between atoms in the SCC-DFTB3 model.

The SCC-DFTB3 method has been parametrized for Mg and Zn by Lu et al.[294] Tests calculations in gas or condensed phases were carried out to compare with high-level QM calculations. It was shown the SCC-DFTB3 method reproduced structural properties (see Figure 7), but was less satisfactory for energies.

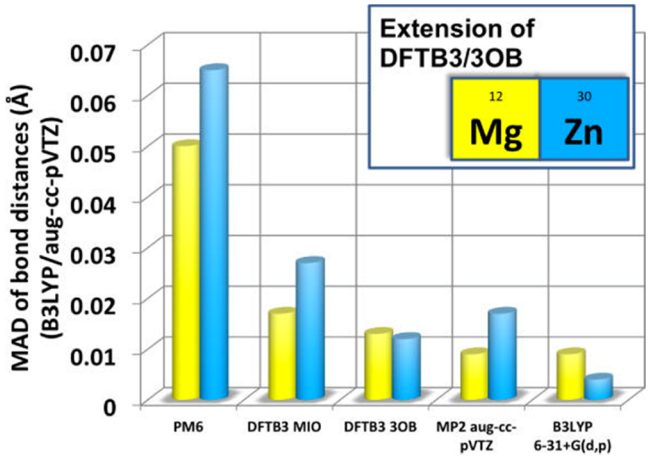

Figure 7. MADs of the bond distances of Mg^{2+} and Zn^{2+} test sets in ref 294 using the PM6, DFTB3/MIO, DFTB3/3OB, MP2/aug-cc-pVTZ, and B3LYP/6-31+G(d,p) methods where B3LYP/aug-cc-pVTZ is used as reference. Reprinted with permission from ref 294. Copyright 2014 American Chemical Society.

DOI: 10.1021/acs.chemrev.6b00440
Chem. Rev. 2017, 117, 1564−1686

DFTB3/MM benchmark calculations were carried out in condensed phase and enzyme systems containing Zn^{2+} or Mg^{2+} ion with encouraging results. However, it was shown that the SCC-DFTB3 scheme had difficulty describing the interaction between the Mg^{2+}/Zn^{2+} ion and highly charged or highly polarizable ligands.[294]

More recently, Gaus et al. parametrized the spin-polarized SCC-DFTB3 for Cu.[295] Orbital angular momentum-dependent Hubbard *U* parameters (which equal twice the chemical hardness) and their charge derivatives were introduced to allow 3d and 4s orbitals to have different responses to charge density redistribution. The B3LYP/aug-cc-pVTZ level of theory was used to calculate the reference data. SCC-DFTB3 showed better performance than PM6 in predicting structural and energetic properties. However, it still gave less accurate results for charged ligands relative to neutral ones, which again may be due to the use of a minimal basis set.

Christensen et al. have incorporated the chemical-potential equilibration (CPE) model into the DFTB3 approach, along with an empirical dispersion correction that has two-body and three-body terms in 2015.[296] The parameters for H, C, N, O, and S were determined for the new method (DFTB3/CPE-D3). CCSD(T) calculated interaction energies and DFT calculated dipole moments were used as targets for the fitting. The DFTB3/CPE-D3 approach showed good improvement in the description of charged species, while retaining its accuracy for describing neutral complexes, when compared to the DFTB3-D3 model. Generally, the DFTB3/CPE-D3 model showed better performance than the PM6-D3H4 method and the PBE-D3 method with a small basis set.

In 2012, Lukose et al. employed the SCC-DFTB method to study Zn, Cu, and Al-containing MOFs,[297] in which they developed the Cu and Al parameters for the dispersion corrected SCC-DFTB method independently. The final results showed that the SCC-DFTB method reproduced both the structural properties and the absorption energies, when compared to benchmark DFT calculations. For example, the XRD patterns from experiment and DFT as well as DFTB optimized structures of the Cu-BTC MOF system are shown in Figure 8, which illustrates the good agreement between DFTB, DFT, and experiment. Because of the speed advantage, they proposed that it is possible to use the SCC-DFTB method to simulate MOF systems, which have unit cells of up to 10^4 atoms.

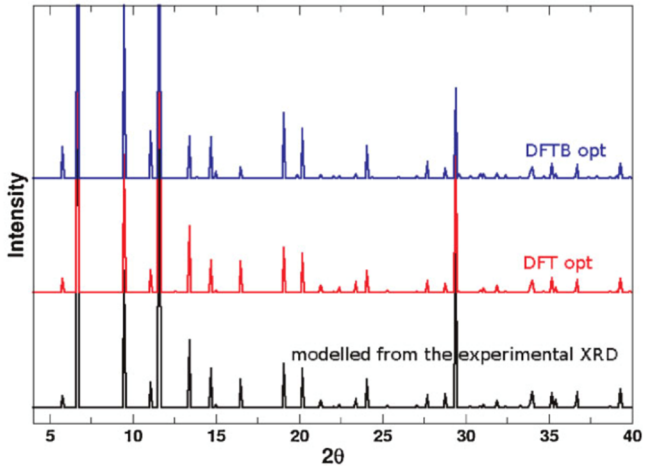

Figure 8. Simulated XRD patterns of the Cu-BTC MOF with the experimental unit cell parameters and optimized at the DFTB and DFT levels of theory. Reprinted with permission from ref 297. Copyright 2011 John Wiley and Sons.

2.5. Density Functional Theory Methods

The Thomas–Fermi model is considered to be the vanguard of modern DFT theory.[298,299] The modern DFT method was formalized in the theorems of Hohenberg–Kohn[300] and then cast into the Kohn–Sham framework[301] in the 1960s. It represents the energy of molecules through the use of functionals of the electron density. There are various levels or rungs of DFT functionals: local density approximation (LDA), local spin density approximation (LSDA), generalized gradient approximation (GGA), nonseparable gradient approximation (NGA), Meta-GGA, meta-NGA, Hybrid GGA, Hybrid meta-GGA, and double hybrid methods, etc. Perdew and Schmidt systematically introduced different levels of approximations for the exchange-correlation energy based on their well-known "Jacob's Ladder of DFT" concept (see Figure 9).[302] DFT has been shown to have good accuracy and has a speed advantage over the high-level post-HF methods and composite approaches, and is generally considered as the modern "work-horse" QM approach. For example, the total citation count for B3LYP[303] and PBE,[304] two widely used functionals, is over 130 000 (ca. 2016, from Google Scholar).

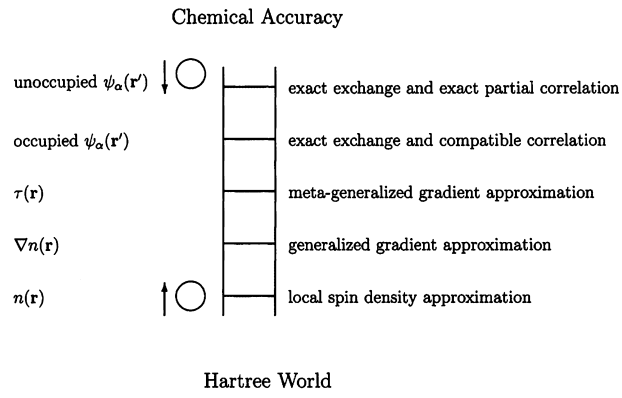

Figure 9. Jacob's ladder of density functional approximations. Any resemblance to the Tower of Babel is purely coincidental. Also shown are angels in the spherical approximation, ascending and descending. Users are free to choose the rungs appropriate to their accuracy requirements and computational resources. However, at present (ca. 2001), their safety can be guaranteed only on the two lowest rungs. Reprinted with permission from ref 302. Copyright 2001 American Institute of Physics Publishing LLC.

Because force fields derived on the basis of QM calculations usually make use of information derived from the Hessian matrix, which can be relatively expensive to compute, DFT has found a home in force field parametrization of TM-containing systems as it affords good accuracy at an affordable computational cost. Another advantage of DFT in modeling TM species is the incorporation of "static correlation", giving DFT an improved ability to model multireference systems over its single referenced brethren based on the HF framework.[133] However, hybrid DFT functionals still have some single reference characteristics due to, in part, the use of exact exchange from HF calculation. Because of its nature, DFT computational errors are more randomly distributed than that observed in HF or post-HF methods.[305] Moreover, DFT is usually not sensitive

DOI: 10.1021/acs.chemrev.6b00440
Chem. Rev. 2017, 117, 1564–1686

to the basis set used and converges quickly to the basis set limit.[131]

Overall, DFT is widely used to model TM-containing systems, but improved performance is not necessarily guaranteed if more sophisticated functionals are employed.[306] Generally, the middle series TMs are hardest to model.[307] If a DFT functional models one property well, this does not automatically mean that it will also perform similarly well on other properties.[307] The accuracy of different functionals has also been shown to be system dependent for TM-containing species, and, overall, it is hard to identify one DFT functional that is accurate for a wide range of TM-containing systems.[308,309] In some work, it was found that nonhybrid DFT functionals offered more accurate results than hybrid ones,[310,311] while other work arrived at the opposite conclusion,[312−316] or no remarkable differences were found between the hybrid and nonhybrid functionals.[306] Even though inclusion of a modest amount of HF exchange can improve results,[309,313,315,317] too much HF exchange is generally not recommended.[313,318] For pure metals, the functionals that achieve the uniform gas limit work better than others.[190,191] According to several publications, the TPSS functional yielded the best results for modeling TM-containing systems.[190,200,312,319−321]

There are very few DFT functionals specifically designed with TM-containing systems in mind. For example, the M06 functional developed by Zhao and Truhlar had TM properties included in its training set.[322] A recent double-hybrid DFT functional mPWPW91DH was designed to predict the electron response properties of TM-containing molecules.[323] Recently, Yu et al. developed the gradient approximation for molecules (GAM) functional based on the NGA with reference database containing TM relevant energetic properties.[324]

Several benchmark studies regarding the performance of different DFT functionals in reproducing excitation energies, bond dissociation energies (BDEs), molecular geometries, HOFs, etc., of TM-containing systems have been reported. These results illustrate the advantages and disadvantages of various DFT functionals and offer insight into optimal methodological choices for particular problems containing TMs. In this active field, Truhlar and co-workers have performed an extensive series of benchmarks on DFT calculations on TM-containing systems.[306,307,309,311,319,325] Wilson and co-workers have also performed a series of benchmarks on DFT functionals for TM species.[313,314,317,326] Below, we briefly explore several examples.

2.5.1. Atomic Properties of Transition Metals. Using 60 different DFT functionals, Luo et al. in 2012 explored their ability to calculate the excitation energies of 4d TM atoms and their monovalent cations, as well as the IPs of the atoms.[306] Analyses of fractional subshell occupancies and spin contamination were carried out, from which they sorted out the biases between s and d orbitals, and biases between low-spin and high-spin states. A general DFT functional should have little or no bias, rather than giving a satisfactory result simply due to error cancellation. The nonhybrid functionals have a tendency to overstabilize the 4d over the 5s orbitals, while HF exchange tends to decrease this bias. Local DFT functionals prefer low-spin states, while those with HF exchange tend to prefer the high-spin states. It was shown that there is no correlation between the general performance of a method and the amount of HF exchange included in the DFT functional. It was also observed that GGA and hybrid-GGA functionals outperform meta-GGA and hybrid meta-GGA methods, implying room for improvement of the meta-GGA and hybrid meta-GGA functionals.

Luo et al. have calculated excitation energies and IPs of 3d TM atoms covering 75 different DFT functionals in 2014.[309] They note that studies on molecular systems enjoy some error cancellation effects that are not present in studies on atomic systems. It was again observed that no DFT functional performed well across a broad range of TMs. They discussed the notion that some amount of HF exchange is important for a balanced representation of the s and d orbitals, to accurately predict excitation energies and IPs.

2.5.2. Systems of Pure Metal or Those Containing Metal−Metal Bonds. Schultz et al. explored a series of TM dimers using 42 different DFT functionals in 2005.[311] Overall, they observed that nonhybrid methods gave much better predictions than did hybrid functionals. For example, the PES and bond length of Cr_2 are shown in Figures 10 and 11,

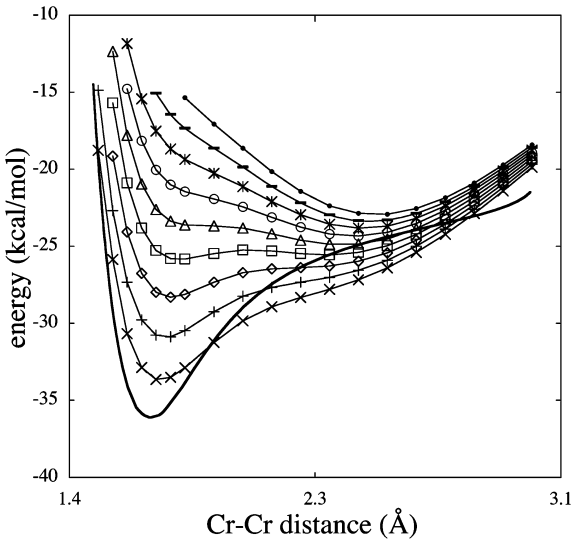

Figure 10. Potential energy curve for Cr_2 computed with the mPW exchange functional and the KCIS correlation function using the following percentages of HF exchange: X = 0 (×), 1 (+), 2 (◇), 3 (□), 4 (△), 5 (○), 6 (*), 7 (−), and 8 (●), and experiment (solid line). Reprinted with permission from ref 311. Copyright 2005 American Chemical Society.

respectively. It was noted that inclusion of some HF exchange improved the accuracy for compounds containing "organic" and main group elements, but this was shown not to be the case for TM-containing systems. It was shown that even for the subset that does not have multireference character, similar trends were not found relative to modeling studies of organic molecules and TM dimers with respect to the accuracy of the different DFT functionals.

Zhao et al. examined 23 DFT functionals with two effective core basis sets (LANL2DZ and SDD) for modeling neutral and ionic Ag_n ($n \leq 4$) clusters.[190] They found that, in general, functionals that achieve the homogeneous electron gas limit (e.g., PW91, PBE, P86, B95, TPSS, VSXC) outperformed the other functionals (e.g., the LYP and B97 series). For example, significant differences in the computed quantities for the Ag_3 and Ag_4 clusters were observed between the two groups. Therefore, care should be taken in choosing the appropriate functional for related studies. It was shown that the PBE1PBE

DOI: 10.1021/acs.chemrev.6b00440
Chem. Rev. 2017, 117, 1564−1686

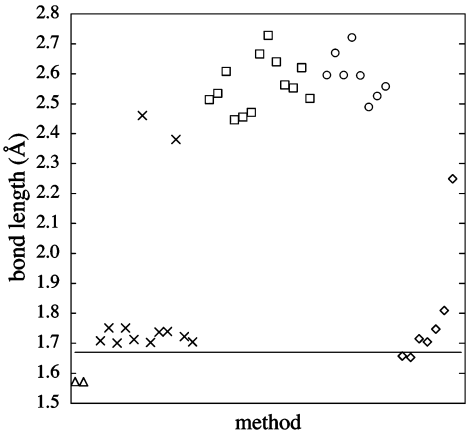

Figure 11. Optimized bond lengths for the LSDA (△), GGA (×), hybrid GGA (□), meta GGA (◇), and hybrid meta GGA (○) with TZQ basis level and the experimental bond length (line) for Cr_2. Reprinted with permission from ref 311. Copyright 2005 American Chemical Society.

(also known as the PBE0) functional predicted both the geometry and the energetic properties with good accuracy.

Paier et al. examined the ability of the B3LYP functional to predict the properties of solids (e.g., lattice parameters, bulk moduli, atomization energies, and reaction energies) in 2007.[191] It was shown that the B3LYP functional gives comparable results for lattice constants as does the PBE functional but with different characteristics. B3LYP gave better predictions for systems with large energy gaps and strong electron localization, but showed reduced accuracy for metals (via an overestimation of the lattice constants due to an underestimation of the formation energies), when compared to the PBE functional. Moreover, the B3LYP functional predicts much poorer atomization energies than PBE0 and HSE03 (both hybrid functionals), which were developed to accurately model the uniform electron gas. They discussed that this was because of B3LYP's weakness in attaining the uniform electron gas limit, reducing its ability to describe "free-electron-like" systems such as metals and semiconductors with small energy gaps. Lastly, it was shown the B3PW91 functional, which achieves the uniform electron gas limit, also offered obvious improvement in the reproduction of atomization energies over the B3LYP functional.

Gorelsky observed that the hybrid DFT functionals predict both the geometry and the energy poorly for the $[V(C_5H_5)_2]Pn$ complex (with a V^{2+}–V^{2+} bond and Pn represents pentalene; Figure 12 shows the complicated electronic structures of two V^{2+} ions), while GGA functionals gave better results.[310] The hybrid functionals were not recommended to study 3d TM complexes with weak or intermediate metal–metal bonds.

To explore the bulk properties of 3d, 4d, 5d TM clusters, Janthon et al. used a number of different DFT functionals.[325] The mean absolute percentage errors (MAPEs) for various DFT functionals regarding their ability to predict interatomic distances, cohesive energies, and bulk moduli are summarized in Figure 13. Hybrid functionals showed the best performance for calculating the interatomic distances, but poorly predict the cohesive energies and only show moderate performance in predicting the bulk moduli. It was proposed that this is due to the static correlation errors caused by inclusion of HF exchange.

2.5.3. Geometries of Transition Metal-Containing Species. Bühl and Kabrede have explored the ability of multiple DFT functionals to predict the geometries of 32 3d TM complexes.[312] They found that hybrid functionals modestly outperform the corresponding nonhybrid variants, while TPSS, a meta-GGA functional together with its hybrid variant, showed the best results.

Waller et al. have evaluated the performance of 15 DFT functionals in their ability to model the geometries of 19 4d TM complexes.[328] They found that the GGA functionals all have bigger deviations than the corresponding hybrid ones. It was also shown that the overall deviation from experimental values did not decrease after adding zero-point vibrational corrections, which were calculated at the BP86/SDD level of theory, to the equilibrium bond lengths.

2.5.4. Energetic Properties of Transition Metal-Containing Species. Zhao and Truhlar assessed seven DFT functionals for their ability to predict reaction energies of 3d TM containing systems in 2006.[319] They found that M05 gave the best performance, B97-2 performed the best in predicting

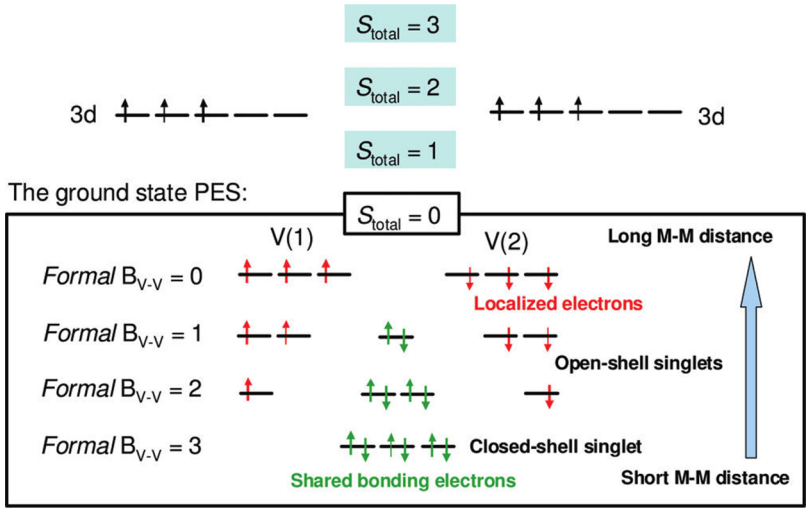

Figure 12. Multiple electronic configurations that originate from the electronic interaction of two V^{II} ions. Reprinted with permission from ref 310. Copyright 2012 American Chemical Society.

DOI: 10.1021/acs.chemrev.6b00440
Chem. Rev. 2017, 117, 1564–1686

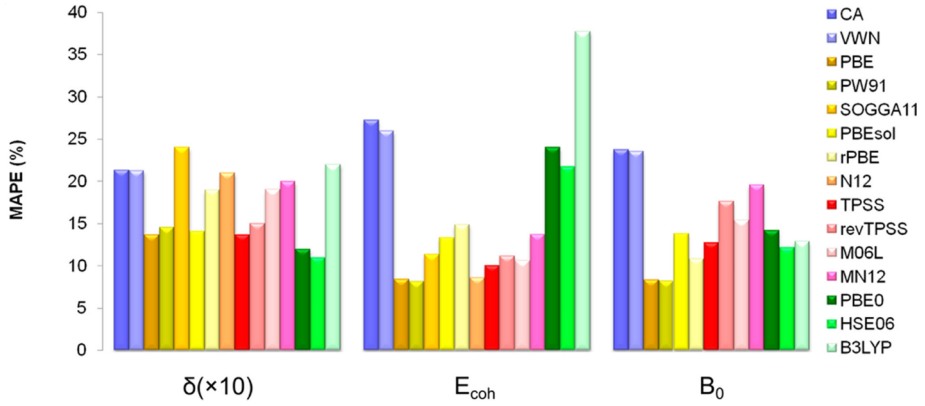

Figure 13. MAPEs for the interatomic distances, δ; cohesive energies, E_{coh}; and bulk moduli, B_0, of 27 transition metals with respect to experimental values extrapolated to 0 K and adjusted to remove zero-point vibrational contributions. MAPEs of δ has been multiplied by a factor of 10 for a better presentation. Data for LDA xc functionals, PBE, PW91, PBEsol, and RPBE are adapted from Janthon et al.[327] Reprinted with permission from ref 325. Copyright 2012 American Chemical Society.

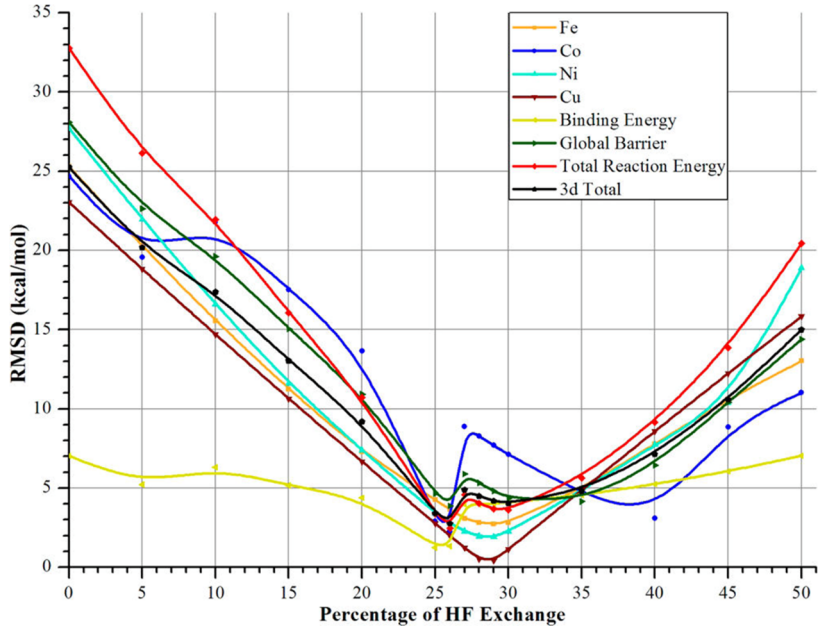

Figure 14. RMSDs of PBE versus percentage of HF exchange for 3d species. Reprinted with permission from ref 317. Copyright 2014 American Chemical Society.

the binding energies, and TPSS works best for three TM dimers (Sc_2, Ni_2, and V_2), which have significant multireference characteristics.

Furche and Perdew explored the performance of several different DFT functionals for their ability to predict a series of properties (structures, dipole moments, bond energies, harmonic frequencies) of 3d TM-containing molecules in 2006.[320] It was shown that BP86 (a GGA functional) and TPSS (a meta-GGA functional) yielded the best performance. They also proposed that the self-interaction error in one-electron and three-electron bonds appears to be the dominant error in the prediction of TM reaction energies when employing semilocal functionals.

Kasper et al. examined different properties of diatomic molecules of 3d TMs with H, N, C, O, S, F, Cl, and Br atoms employing five different DFT functionals in 2007.[308] They found there is no universal functional and that the performance of different DFT functionals is system dependent. It was observed that hybrid DFT functionals usually underestimate the BDEs due to its preference for open-shell electronic structures, while GGA functionals usually overestimate them. It was also shown that the late TMs were better modeled using hybrid functionals, while the results of GGA functionals showed less preference. The hybrid DFT functionals also predict larger dipole moments than GGA ones, implying a less covalent bonding picture. The hybrid and GGA functionals differ significantly when modeling states with large spin contamination, hinting at the challenges faced by DFT in explaining the electronic structures of these systems.

In 2013, Zhang et al. explored how well 42 DFT functionals (in total 11 functional types including DFT-D) and the HF method reproduced select bond energies within 70 3d TM complexes.[307] The meta-GGA, meta-NGA functionals showed improved performance over GGA and NGA methods, while there is no systematic improvement for the hybrid methods over nonhybrid ones. It was shown the TMs in the middle of the series (V, Cr, and Mn) are harder to model than the earlier and later ones. M−O and M−H bonds are hard to describe

DOI: 10.1021/acs.chemrev.6b00440
Chem. Rev. 2017, 117, 1564−1686

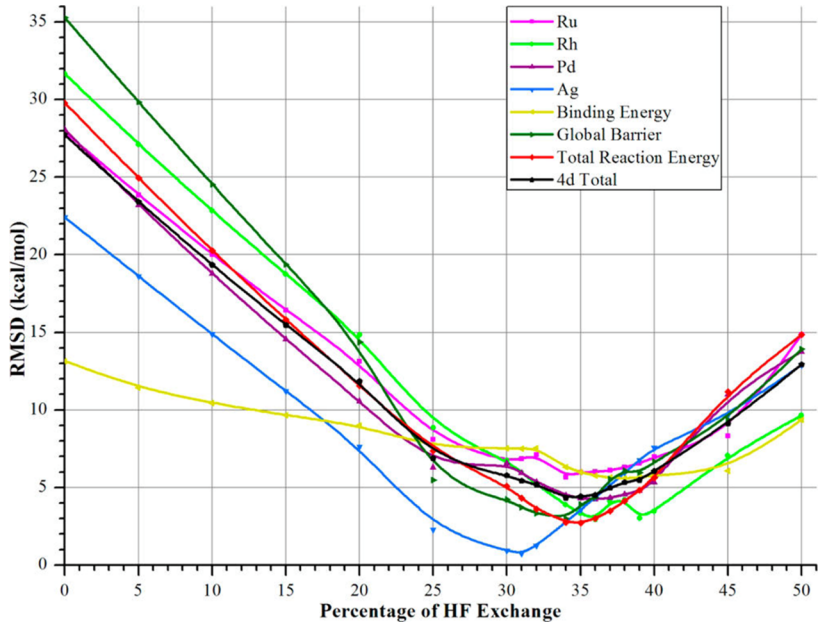

Figure 15. RMSDs of PBE versus percentage of HF exchange for 4d species. Reprinted with permission from ref 317. Copyright 2014 American Chemical Society.

accurately, which may due to their multireference character. It was also demonstrated that DFT functionals, which yield good performance for the prediction of bond energies, may not be good for other properties.

Liu et al. used the catalytic properties of several 3d and 4d TMs for C−O bond dissociation as a benchmark set.[317] Calculations over eight DFT functionals were compared to values computed at the CCSD(T)/CBS level of theory. It was shown that reactions for earlier TMs have smaller activation energies and are more exothermic than the later ones, for both 3d and 4d species. Again, the percentage of HF exchange is crucial. The best results were obtained for 26% and 34% HF exchange 3d and 4d TM systems (see Figures 14 and 15), respectively. This interesting observation suggests that a higher percentage of HF exchange might be needed for systems with heavier metal ions.

Weymuth et al. benchmarked nine popular DFT functionals for the prediction of ligand dissociation energies in large TM complexes.[315] They found that for this end point, the performance of nonhybrid functionals was improved after incorporating some HF exchange. They also found that dispersion corrections decreased the performance of DFT functionals when predicting the dissociation energies of some ligands.

Riley and Merz investigated the accuracy of 12 DFT functionals covering GGA, hybrid-GGA, meta-GGA, and hybrid-meta-GGA functionals for 3d TM-containing molecules.[316] They used 94 experimental HOFs and 58 experimental IPs as reference data. They found that generally the hybrid DFT functionals performed better than the nonhybrid ones. The triple-ζ TZVP basis set generally outperformed the 6-31G** basis set. At least for the 6-31G** basis set, all of the DFT calculations give large HOF errors (6−12 kcal/mol bigger than the errors for organic molecules) when compared to experiment. The errors of the computed IPs are large as well (in the range of 0.85−1.20 eV), being about 3−4 times greater than the errors observed for organic molecules (in the range of 0.25−0.35 eV).

In subsequent work, Yang et al. explored the performance of the same 12 DFT functionals but with mixed basis sets (an ECP basis set with double-ζ - LANL2DZ for the TMs and 6-31+G** for the main group elements).[321] Interestingly, the mixed basis set strategy showed better performance than the single basis set strategy employed previously. Moreover, they found the GGA and meta-GGA functionals generally outperformed the hybrid functionals in predicting HOFs but showed less ability to predict IPs. The TPSSTPSS (with both exchange and correlation functionals labeled as TPSS) was able to predict both the HOFs and the IPs with reasonable accuracy. In related work from this group, Weaver et al. investigated 14 different DFT functionals, as well as the MP2, CCSD, CCSD(T), CASSCF, and CASPT2 methods for their ability to calculate the HOFs of zinc-containing molecules.[200] The aug-cc-pVDZ and aug-cc-pVTZ basis sets were used in this research. TPSSTPSS and TPSSKCIS showed the best performance for the prediction of HOFs. It was shown that properly chosen DFT functionals yielded better performance than MP2 and CC methods.

Tekarli et al. have studied the HOFs of 19 3d TM complexes spanning over 44 different DFT functionals and compared them to experiment.[313] Overall, the top five best performing DFT functionals are all hybrid ones, clearly indicating that it is beneficial to include some amount of exact HF exchange. However, the hybrid functionals with more than 40% HF exchange performed poorly. CO-containing complexes proved to be very challenging for 42 out of the 44 functionals. The B97-1/cc-pVQZ level of theory showed outstanding performance, predicting HOFs ±1 kcal/mol with respect to composite methods based on high-level QM computations. The impact of the cc-pVTZ basis set versus cc-pVQZ was also explored, and it was shown that GGA and meta-GGA methods were less sensitive to basis set choice than the generalized gradient exchange (GGE), hybrid-GGA, and hybrid meta-GGA methods.

More recently, Jiang et al. have computed the HOFs of 193 3d TM-containing molecules using 13 DFT hybrid functionals

DOI: 10.1021/acs.chemrev.6b00440
Chem. Rev. 2017, 117, 1564−1686

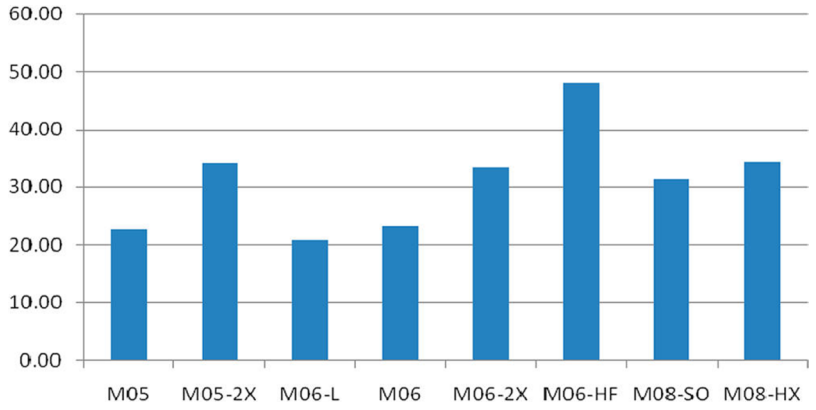

Figure 16. Average unsigned heat of formation errors (kcal/mol) for the complete set of complexes, highlighting the performance of different M0X suite of functionals with LANL2DZ basis set, containing transition metals taken in the study of Shil et al.[318] Reprinted with permission from ref 318. Copyright 2013 American Chemical Society.

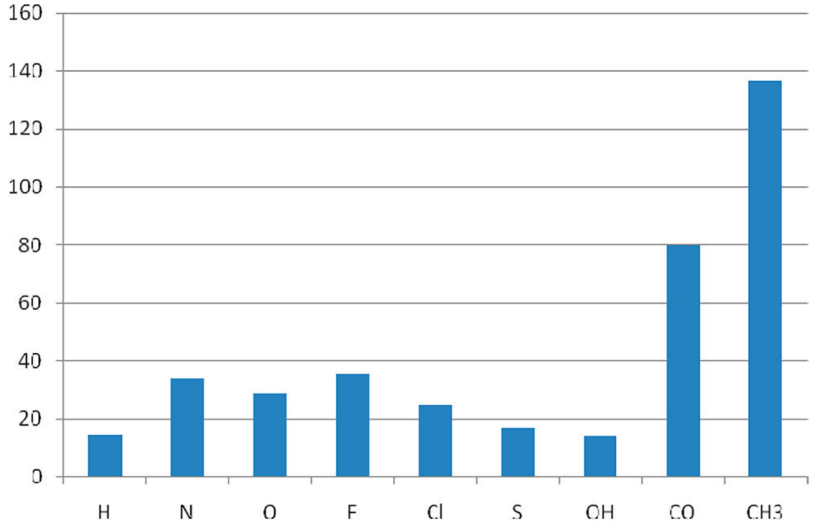

Figure 17. Average unsigned heat of formation errors (kcal/mol) for different transition metal bonding partners treated in the study of Shil et al.[318] Reprinted with permission from ref 318. Copyright 2013 American Chemical Society.

and compared them to experiment.[326] They observed that the B97-1 and mPW2-PLYP functionals gave the best performance (with MADs of 7.2 and 7.3 kcal/mol, respectively).

Shil et al. have benchmarked eight different "Minnesota" DFT functionals with 54 experimental HOFs and 47 experimental IPs of 3d TM complexes.[318] It was demonstrated that the performance of any given DFT functional decreased with an increase of the percentage of HF exchange. The meta-GGA method M06-L performed the best, while the hybrid metal-GGA method M06-HF, which use 100% HF exchange energy, gave the worst results. The unsigned average errors of HOFs for different functionals with respect to different ligating atoms are shown in Figures 16 and 17. From these figures, we see that the M06-HF has the largest errors, while the DFT functionals yield the biggest errors for CH_3 and CO coordinated TM complexes. Moreover, the largest errors were also found in the prediction of the HOFs of Fe complexes and the IPs of Ni complexes. This may be due to the multireference character afforded by partially filled d orbitals.

Laury and Wilson investigated the HOFs of 30 4d TM-containing molecules with 22 different DFT functionals in 2013.[314] The MAD values are shown in Figure 18. This work found that the double hybrid DFT functionals B2GP-PLYP and

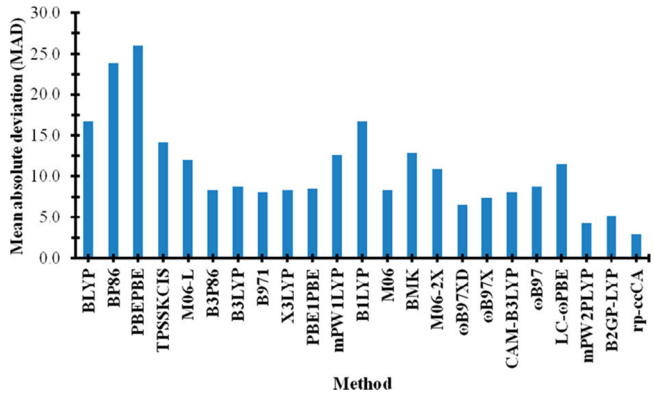

Figure 18. MADs of 22 DFT functionals and the rp-ccCA method for the HOFs of 30 molecules containing 4d TMs. Reprinted with permission from ref 314. Copyright 2013 American Chemical Society.

mPW2-PLYP showed the best performance with MADs of 4.25 and 5.19 kcal/mol, respectively. The GGA functionals showed the largest errors, and are not recommended for computing thermochemical properties of 4d molecules. The hybrid-GGA methods showed good performance, with MADs of 6−10 kcal/mol. The mPW2-PLYP method with the cc-pVQZ-PP and

DOI: 10.1021/acs.chemrev.6b00440
Chem. Rev. 2017, 117, 1564−1686

effective core potential (ECP, for 4d metals) basis sets were proposed to be a good choice for calculating thermochemical properties of 4d TM-containing species.

Grimmel et al. benchmarked a number of DFT functionals that range from LDA to double hybrid ones for predicting properties of Ln-containing molecules.[329] 54 experimental HOFs of Ln species were employed as the reference data set. They proposed that 5.0 kcal/mol represented the "lanthanide chemical accuracy" based on the uncertainty of the experimental values. The results show that generally the nonhybrid functionals outperformed the hybrid ones. The TPSS functional yielded the best performance among the functionals they investigated.

2.6. Density Matrix Renormalization Group Method

The density matrix renormalization group (DMRG) method was proposed by White in the early 1990s.[330,331] It was developed on the basis of the renormalization (RG) method[332,333] and is an efficient method for modeling 1D systems and 2D systems. The number of degrees of freedom in Hilbert space for a many-body system grows rapidly as its size increases, but the DMRG method decreases the effective number of degrees of freedom. The computational complexity of the DMRG method is $O(M^2K^4 + M^3k^3)$, where M represents the number of DMRG states and k indicates the number of one-particle orbitals.[334] Generally, the DMRG method has a number of advantages over traditional QM methods. For example, the DMRG method follows both the size consistency and the variational theorem.[335] Configuration interaction doubles (CID) and the quadratic configuration interaction singles doubles (QCISD) methods only obey the latter but not the former, while perturbation theory obeys the former but not the latter.[335] Full CI obeys both features, but it has exponential scaling, while the DMRG method has polynomial scaling.[336] The DMRG method includes the static correlation effect efficiently. For example, when compared to the CASSCF multireference method, the DMRG method can handle a much larger active space.[336] However, the DMRG method is still computationally expensive when using larger basis sets to capture dynamic correlation effects.[334] Even though the development of the DMRG method is still in its infancy, some progress has been made on TM-containing systems, and the method shows promise for future QM studies of TMs.

White and Noack performed the first application of the DMRG method on a 1D toy model.[337] Nishino illustrated the application of the DMRG method to the interaction round a face (IRF) model.[338] Fano et al. applied the DMRG method to cyclic polyene $(CN)_n$ systems (with n up to 34) using the Pariser−Parr−Pople SE Hamiltonian.[339] They explored the Hilbert space with a dimension of 5×10^{18} and showed that the DMRG method offered high accuracy, comparable to full CI and CC methods. However, they also pointed out that the DMRG method keeps a large number of matrixes when the interaction term relevant four orbitals are located in different blocks.[339] White and Martin applied the DMRG method to ab initio quantum chemistry.[340] They performed a study of H_2O with a standard Gaussian basis and obtained a total energy comparable to those obtained using CI and CC methods.[340] Daul et al. illustrated the ability of the DMRG method to solve the full CI interaction problem. They applied the DMRG method to the paramagnetic HHeH molecule and discussed the basis set dependency, scaling issue, and also compared the DMRG method to other QM methods.[335] Chan and Head-Gordon illustrated the formulation of the DMRG method in detail and tested its applications to water, ethane, and the nitrogen dimer systems.[334] They found that the DMRG method offered excellent accuracy, especially when the static correlation is strong. However, they pointed out that it is computationally expensive for the DMRG method to evaluate the dynamic correlation effect with larger basis sets.[334]

Marti et al. applied the DMRG method to CoH, NiCO, and dinuclear Cu clusters in 2008.[341] Natural orbitals from CASSCF calculations instead of HF orbitals were used because they afforded better energies. They pointed out that the DMRG method could include more active orbitals than many QM methods, offering improved performance in modeling static correlation effects. They found that the total energy of the system decreases with an increase in the number of DMRG states, while the relative energy is easier to converge than the total energy. They also pointed out that one niche of the DMRG method in quantum chemistry is TM chemistry because it can handle much larger active spaces (bigger than 18 electrons and 18 orbitals) than the CASSCF method and qualitatively offers large-scale CASSCF wave functions and energies.[341]

Kurashige and Yanai applied the DMRG method to study the PESs of the Cr dimer and isomerization of the $[Cu_2O_2]^{2+}$ cluster in 2009.[342] They showed that the method offered excellent results for predicting these properties. Yan et al. studied the 2D kagome lattice in 2011 using the DMRG method, which proved its high accuracy for modeling the ground state.[343] In 2013, Kurashige et al. applied the DMRG method to the Mn_4CaO_5 cluster in the PSII system.[344] They considered more than 10^8 quantum degrees of freedom, and the work marks the first treatment of the PSII system beyond the DFT single-electron picture.[344] Sharma et al. explored the 2Fe-2S and 4Fe-4S clusters using the DMRG method in 2014.[345] They found that the Heisenberg double exchange model largely underestimates the number of low-lying states, which are due to the neglect of iron d−d excitations, that are proposed to be important in these systems. Meanwhile, they found that the electronic energy levels are concentrated on the Fe−S clusters and vary on the vibrational fluctuation scale, offering an explanation of the wide existence of these clusters in nature.[345]

Recently, Olivares-Amaya et al. have presented benchmark results on a series of systems including the Cr dimer, Mn-oxo-salen, and Fe-porphine. They also offered a series of suggestions for doing DMRG calculations in practice.[346] The BLOCK code, which was developed by Chan's group, is now available in ORCA,[347] Q-Chem,[348] Molpro,[349] and from Chan's group.

2.7. Valence Bond Theory-Based Models

Besides the wave function-based QM methods and DFT, there are also VB-based QM methods available. Valence bond (VB) theory, which was proposed by Pauling, has played a key role in understanding chemical structure and reactivity.[350] VB theory has two fundamental concepts: hybridization and resonance. It considers hybridization between different atomic orbitals while representing a molecule as a sum of its resonance structures with different weights. It offers a very intuitive perspective on chemical bonding and reactivity. For example, the hybridization concept is useful in determining molecular geometries (e.g., the VESPR theory). Even though MO theory is more widely used in contemporary computational chemistry, VB theory offers a

DOI: 10.1021/acs.chemrev.6b00440
Chem. Rev. 2017, 117, 1564−1686

more straightforward view of chemical bonds. VB theory uses localized hybrid orbitals (HOs) based on natural bond orbitals to model electronic structure, rather than the delocalized MOs obtained using the LCAO strategy employed in MO theory. However, these two perspectives on electronic structure are interchangeable via a unitary transformation of the density matrix of the natural localized molecular orbitals (NLMOs) to that of the delocalized canonical molecular orbitals (CMOs).[351] Hence, all of the physical properties calculated on the basis of NLMOs or CMOs should be identical, even though the two models afford different "localizations". For simple cases, one Lewis structure is enough to obtain accurate results, while for more complicated systems, excellent results can be obtained using relevant resonance structures.[352−354]

Examples of VB-based QM studies of metal ion-containing systems include the following: Goddard and co-workers developed the generalized VB (GVB) method[355] and applied it to metal-containing molecules.[356] Åqvist and Warshel reviewed the modeling of enzyme reactions (including those contain metals) and highlighted applications based on the empirical valence bond (EVB) method.[357] Maupin, Voth, and co-workers studied the proton transfer mechanisms in human carbonic anhydrase II (HCAII)[358] and its H64A mutant[359] using the multistate empirical valence bond (MS-EVB) method. Wu et al. reviewed modern VB methods in 2011, and highlighted VB modeling on $(CO)_4Fe(CH_2{=}CH_2)$.[360]

2.8. Basis Set Choices

Cundari et al. employed the B3LYP functional with the LANL and CEP-31G basis sets to study the HOFs of TM complexes in 2005.[361] It was shown that the former outperformed the latter in general. The results indicated that employing effective-core potentials for light elements (with atomic number less than 10) in the CEP-31G basis set was the major source of error. It was suggested that all electron basis sets be used for the main group elements when calculating the thermochemical properties of TM complexes.

In 2008, Williams and Wilson studied a set of group XI TM-containing molecules using MP2 and CCSD(T) methods with various cc-pV*n*Z-PP (where n = D, T, Q, and 5) basis sets on the metal ion, ligand, or both simultaneously.[362] The results showed that changing the ligand basis set but not the metal ion basis set has a much larger influence on the calculated geometry and dissociation energies than changing the metal ion basis set but not the ligand basis set. This indicated that the choice of basis set for the ligand is more important than that for the metal ion.

Xu and Truhlar have investigated the performance of HF-based effective core potentials when employing HF and DFT methods for 3d TM-containing systems.[363] To evaluate the performance of different basis sets, 10 test cases were constructed, and the results were compared to the data obtained on the basis of a basis set incorporating the relativistic effect (NCBS-DK), and a basis set that did not consider relativistic effects (NCBS-NR). The all-electron def2-TZVP basis set was suggested to be used in relativistic and nonrelativistic DFT calculations for 3d TMs due to its excellent performance. These results also demonstrated that different DFT functionals affect the optimal choice of the ECP basis set.

2.9. Error Analysis

There have been few benchmark studies comparing accuracies of different kinds of QM methods and force fields for simulations of TM-containing systems. Related research efforts are encouraged because they can afford insights into the advantages and disadvantages of the relevant methods.

Amin and Truhlar have investigated the accuracy of 39 DFT functionals, the HF method, and 7 SE methods on their ability to predict the geometries, BDEs, and dipole moments of a series of zinc compounds.[364] CCSD(T) and CCSD results were treated as the standard for comparison. They observed that all SE methods have 1.5−2.1 times bigger errors than the HF method, while DFT yields errors less than one-half of that of the HF method. The results demonstrated that DFT functionals for zinc compounds are consistent with what has been observed for main group compounds (functionals that offer good accuracy for organic molecules usually also yield good performance for zinc complexes). Moreover, it was shown that the performance of DFT functionals was improved via an admixture of exact exchange. In Lin and Wang's research, they found that QM/MM simulation, with the SE method PM3 for the QM region (which contains three His residues, one zinc ion, and one ligand) and the AMBER ff03 force field for the MM region, gave larger structural distortions than the additive force field when compared to the XRD structure.

There are two main simulation issues nowadays: the accuracy of the potential and the extent of sampling. Some benchmark studies of protein systems showed encouraging results regarding unpolarized force fields. It was shown that some unpolarized force fields outperformed SE methods but were still inferior to DFT functionals in predicting the relative conformational energies of tetrapeptides[365] and protein−ligand interactions.[305] However, Faver et al. pointed out that it is still hard to predict the native structures of proteins on the basis of the current generation unpolarized force field models due to error accumulation.[366] Even though QM methods offer considerable accuracy for simulating TM-containing systems and more QM simulations have been performed in recent years (e.g., the CPMD[367] and nanoreactor[368]), classical models are still widely used due to their speed advantage, thereby accessing larger system sizes, longer simulation time scales, and broader conformational spaces, which are not accessible to QM-based simulations.[147] In the following, we briefly review popular classical models: the nonbonded, bonded, cationic dummy atom, combined, and polarizable models.

3. CLASSICAL MODELING OF METAL IONS: THE NONBONDED MODEL

3.1. Widely Used Potentials

There are two potentials widely employed to model the nonbonded interactions of ions: the 12-6 Lennard-Jones (LJ) potential[369] and the Born−Mayer potential.[370] The history of the evolution of these models is fascinating and involves some of the leading luminaries that laid the theoretical foundation to model intermolecular interactions.

In 1903, Mie proposed the Mie potential (see eq 21),[371] in which there are two parameters in the equation, n and m, representing the inverse-powers of the repulsion and attraction interactions, respectively.

$$U(r) = \left(\frac{n}{n-m}\right)\left(\frac{n}{m}\right)^{m/(n-m)} \varepsilon\left[\left(\frac{\sigma}{r}\right)^n - \left(\frac{\sigma}{r}\right)^m\right] \quad (21)$$

It is a generalized form of the familiar Lennard-Jones expression. The modeling of periodic as well as charged systems was advanced in 1921 when Ewald described the so-called Ewald summation method to calculate the electrostatic energy

DOI: 10.1021/acs.chemrev.6b00440
Chem. Rev. 2017, 117, 1564−1686

inside periodic systems.[372] This approach and its variants are widely used in molecular simulations to calculate long-range electrostatic interactions.[373]

Lennard-Jones proposed the LJ equation (see eqs 22 and 23) to model the intermolecular interactions between argon in 1924,[374,375] where 5 was found as the best value for m while for n good agreement was found for all models when $n > 9$ with the best being $n = 14\frac{1}{3}$. Hirschfelder et al. discovered that a 12-6 LJ equation could produce a good model for both helium and argon in 1938.[369]

$$f(r) = \frac{\lambda_n}{r^n} - \frac{\lambda_m}{r^m} \text{ (force equation)} \tag{22}$$

$$U(r) = \frac{\lambda_n}{(n-1)r^{n-1}} - \frac{\lambda_m}{(m-1)r^{m-1}} \text{ (potential equation)} \tag{23}$$

London proposed the London equation (see eq 24) in 1930 to describe the magnitude of the dispersion interaction between two particles A and B using QM with second-order perturbation theory,[376] in which the α_i and α_j are the dipole polarizabilities of particles i and j, while I_i and I_j are the first IPs of the particles.

$$U(r) \approx -\frac{3}{2}\frac{I_i I_j}{I_i + I_j}\frac{\alpha_i \alpha_j}{r_{ij}^6} \tag{24}$$

Slater and Kirkwood proposed the Slater–Kirkwood formula (see eq 25) in 1931 and applied it to Ne, Ar, N_2, H_2, O_2, and CH_4.[377] In their work, they used an exponential term to represent the repulsion interaction. In their formulation, ε is the mutual energy, v_0 is the highest quantum state electron number of the molecule, a_0 is the Bohr radius, E_0 is the ground-state energy of a hydrogen atom, while r_{ij} is the distance between two particles.

$$\varepsilon = -\frac{1.36\nu_0^{1/2}a_0^{3/2}a^{3/2}E_0}{r_{ij}^6} \tag{25}$$

Buckingham proposed what came to be know as the Buckingham potential (see eq 26) in 1938 and applied it to gaseous He, Ne, and Ar.[378] Similar to Slater and Kirkwood's work, he used the exponential term to describe the repulsion interactions in the potential.

$$U(r) = A\, e^{-r/\rho} - \frac{B}{r^6} \tag{26}$$

In 1918, Born and Lande proposed what came to be know as the Born–Lande equation (see eq 27) for calculating interactions inside ionic solids.[379] As shown in eq 27, it uses a Born equation to describe the electrostatic potential (ESP), while an inverse-power term represents the repulsive interaction.

$$U(r_{ij}) = -\frac{N_A M z^+ z^- e^2}{4\pi\varepsilon_0 r_{ij}} + \frac{A}{r_{ij}^n} \tag{27}$$

where N_A is Avogadro's number, M is the Madelung constant, which depends on the lattice geometry, z^+ and z^- are the charges for the positive and negative ions, respectively, e is the charge of a proton, ε_0 is the vacuum dielectric constant, while n is the Born exponent. By taking the derivative $dU(r_{ij})/r_{ij} = 0$ when $r_{ij} = r_0$ (r_0 is the equilibrium distance between the two particles), one obtains:

$$A = -\frac{M z^+ z^- e^2 r_0^{n-1}}{4\pi\varepsilon_0 n} \tag{28}$$

$$U(r_{ij}) = -\frac{N_A M z^+ z^- e^2}{4\pi\varepsilon_0 r_{ij}}\left(1 - \frac{1}{n}\left(\frac{r_0}{r_{ij}}\right)^{n-1}\right) \tag{29}$$

Pauling estimated n in the Born–Lande equation over a range from 5 to 12 for different noble gas atoms and for the Cu^+, Ag^+, and Au^+ ions.[380] In 1932, Born and Mayer proposed the Born–Mayer potential (see eqs 30 and 31; eq 31 was obtained similar to eq 29 based on eq 27) where they used an exponential term $e^{-r/\rho}$ instead of the inverse-power term r^{-n} to represent the repulsion interaction.[370] ρ is a constant that depends on crystal compressibility, and a value of 30 pm gave a good description for the alkali metal halides.[370] Finally, r_i and r_j are the ionic radii of the ions, while A_{ij} was a factor determined by Pauling, generally set to 1.00 for a cation–anion pair, 0.75 for an anion–anion pair, and 1.25 for a cation–cation pair.[370]

$$U(r_{ij}) = -\frac{N_A M z^+ z^- e^2}{4\pi\varepsilon_0 r_{ij}} + A_{ij}\, e^{-(r_i + r_j - r_{ij})/\rho} \tag{30}$$

$$U(r_{ij}) = -\frac{N_A M z^+ z^- e^2}{4\pi\varepsilon_0 r}\left(1 - \frac{\rho}{r_0}\right) \tag{31}$$

In the subsequent year, Mayer added a r^{-6} (representing dipole–dipole interactions) and a r^{-8} (representing quadruple–dipole interactions) dispersion term into the Born–Mayer potential (see eq 32),[381] where the dispersion parameters were estimated from the formula given by Margenau.[382] The potential showed improvement for the CsCl lattice type (i.e., the CsCl, CsBr, and CsI ionic compounds). Huggins and Mayer determined the ionic radii (which were used to determine the strength of the repulsion term) for five alkali metal ions (Li^+, Na^+, K^+, Rb^+, and Cs^+) and four halide ions (F^-, Cl^-, Br^-, and I^-).[383] On the basis of these values, experimental lattice constants were reproduced for 20 alkali metal–halide ionic solids.

$$U(r_{ij}) = -\frac{N_A M z^+ z^- e^2}{4\pi\varepsilon_0 r_{ij}} + A_{ij}\, e^{(r_i + r_j - r_{ij})/\rho} - \frac{B_{ij}}{r_{ij}^6} - \frac{C_{ij}}{r_{ij}^8} \tag{32}$$

Tosi and Fumi revisited ionic compounds using two different potentials (i.e., using the exponent and inverse-power as the repulsion terms, respectively) and determined the crystal radii of NaCl-type alkali halides in 1964.[384,385]

3.2. 12-6 Lennard-Jones Potential

3.2.1. Functional Format. The popular 12-6 LJ potential approximates the repulsion interaction, which is best modeled via exponential decay along with the particle distance (i.e., as described by the Buckingham potential and Born–Mayer potential; see eqs 26 and 30).[386] However, when applying these potentials to a molecular structure where two particles are too close with each other, the Buckingham or Born–Mayer potential can yield a negative interaction energy, while the 12-6 LJ potential prevents this from happening. Moreover, the 12-6 LJ potential is calculated 4 times faster than the Buckingham potential.[387] Another consideration is the 12-6

DOI: 10.1021/acs.chemrev.6b00440
Chem. Rev. 2017, 117, 1564–1686

LJ potential needs less parametrization work than the Buckingham potential (two versus three parameters, respectively), which also supports its wide utilization in molecular simulations. Furthermore, the 12-6 LJ potential yields accuracy similar to that of the Buckingham potential after careful parametrization when used in a molecular force field. For example, Lifson and Warshel found that applying the Coulombic equation and a Urey–Bradley-type force field plus the 12-6 LJ potential in the CFF formulation offered improvement in modeling the intermolecular interactions in cycloalkane and *n*-alkane (with $n = 5-12$) systems in 1968.[388] Jorgensen also found that a 12-6-3 potential gave almost the same accuracy as the exponential function to describe the short-range interactions between two water molecules in 1979.[389]

The 12-6 nonbonded potential for ions represents ionic interactions between a metal ion and the surrounding particles as a sum of the electrostatic and VDW terms. This model closely reproduces the situation for monovalent ions that have low electronegativities (e.g., alkali metal ions). However, the quality of this representation degrades for systems containing divalent or highly charged ions, where the POL and CT effects are significant.[390,391]

The form of the 12-6 LJ nonbonded potential, between particles *i* and *j*, is given in eq 33. Three different forms are in common usage, and each is given in eq 33. Q_i and Q_j are the partial charges on the two particles. In the nonbonded model, the metal ion is generally modeled using an integer partial charge equal to its oxidation state. The only parameters that need to be determined are A_{ij} and B_{ij}, $R_{\min,ij}$ and ε_{ij}, or $\sigma_{\min,ij}$ and ε_{ij} depending on the form of the equation.

Figure 19 visualizes the differences and physical meaning of the $R_{\min,ij}$ and ε_{ij}, and σ_{ij} and ε_{ij} forms, which are in common usage. $R_{\min,ij}$ is the distance at which the LJ potential has its minimum value, while σ_{ij} is the distance at which the LJ potential is equal to zero. ε_{ij} is the well depth of the LJ potential curve, representing the VDW interaction strength between the two particles. If we have *N* atom types employed in a force field, there will be $\frac{N(N+1)}{2}$ unique atom pair types. All forms of the LJ potentials have two parameters (A_{ij} and B_{ij}, $R_{\min,ij}$ and ε_{ij}, or σ_{ij} and ε_{ij}) for each atom type pair, which leads to $N(N+1)$ LJ parameters that need to be parametrized. This represents a tremendous parametrization effort; hence, a number of combining (or mixing) rules were introduced to reduce the overall parameter space. By obtaining the $A_{ii}/B_{ii}/R_{\min,ii}/\sigma_{ii}/\varepsilon_{ii}$ and $A_{jj}/B_{jj}/R_{\min,jj}/\sigma_{jj}/\varepsilon_{jj}$ values, first the pairwise $A_{ij}/B_{ij}/R_{\min,ij}/\sigma_{ij}/\varepsilon_{ij}$ parameters are obtained from the former two using an appropriate combining rule. This decreases the number of parameters to 2*N*. Popular force fields such as AMBER,[392−400] CHARMM,[401−406] OPLS-AA,[407−411] etc., treat several different atom types of the same element with identical LJ parameters, further decreasing the parametrization effort.

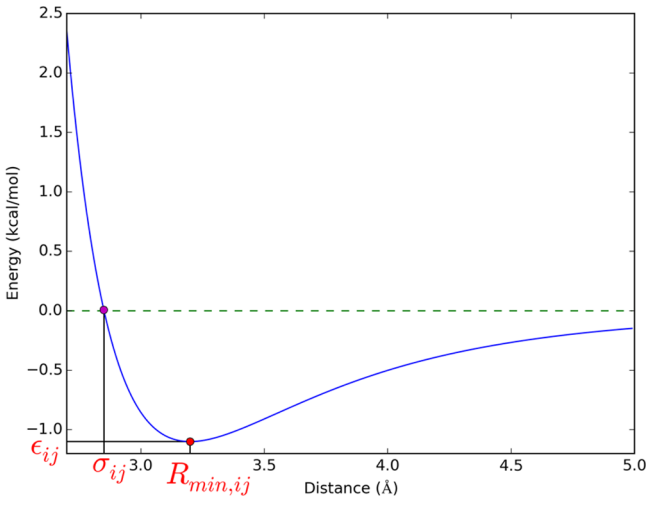

Figure 19. Representation of $R_{\min,ij}$, σ_{ij}, and ε_{ij} in a 12-6 LJ equation. Here, we illustrate the LJ potential between two particles, which have the same $R_{\min,i}$ (1.6 Å) and ε_i (1.1 kcal/mol) values.

$$U(r_{ij}) = E_{ele} + E_{VDW} = \frac{Q_i Q_j}{4\pi\varepsilon_0 r_{ij}} + \frac{A_{ij}}{r_{ij}^{12}} + \frac{B_{ij}}{r_{ij}^{6}}$$
$$= \frac{Q_i Q_j}{4\pi\varepsilon_0 r_{ij}} + \varepsilon_{ij}\left[\left(\frac{R_{\min,ij}}{r_{ij}}\right)^{12} - \left(\frac{R_{\min,ij}}{r_{ij}}\right)^{6}\right]$$
$$= \frac{Q_i Q_j}{4\pi\varepsilon_0 r_{ij}} + 4\varepsilon_{ij}\left[\left(\frac{\sigma_{ij}}{r_{ij}}\right)^{12} - \left(\frac{\sigma_{ij}}{r_{ij}}\right)^{6}\right] \quad (33)$$

Below we summarize some of the most widely used combining rules.

(1) For A_{ij} and B_{ij} terms, the geometric combining rule is generally used:

$$A_{ij} = \sqrt{A_{ii} \times A_{jj}} \text{ and } B_{ij} = \sqrt{B_{ii} \times B_{jj}} \quad (34)$$

(2) For $R_{\min,ij}$ and $\sigma_{\min,ij}$, the arithmetic (Lorentz), geometric (Good–Hope), and sixth power (Waldman–Hagler) combining rules are used extensively.

Lorentz combining rule:

$$R_{\min,ij} = \frac{1}{2}(R_{\min,ii} + R_{\min,jj}) \text{ or } \sigma_{ij} = \frac{1}{2}(\sigma_{ii} + \sigma_{jj}) \quad (35)$$

Good–Hope combining rule:

$$R_{\min,ij} = \sqrt{R_{\min,ii} \times R_{\min,jj}} \text{ or } \sigma_{ij} = \sqrt{\sigma_{ii} \times \sigma_{jj}} \quad (36)$$

Waldman–Hagler combining rule:

$$R_{\min,ij} = \sqrt[6]{\frac{R_{\min,ii}^6 + R_{\min,jj}^6}{2}} \quad (37)$$

(3) For ε_{ij}, the geometric (Berthelot) and sixth power (Waldman–Hagler) combining rules are widely used.

Berthelot combining rule:

$$\varepsilon_{ij} = \sqrt{\varepsilon_{ii} \times \varepsilon_{jj}} \quad (38)$$

Waldman–Hagler combining rule:

$$\varepsilon_{ij} = \sqrt{\varepsilon_{ii} \times \varepsilon_{jj}}\,\frac{2R_{\min,ii}^3 R_{\min,jj}^3}{R_{\min,ii}^6 + R_{\min,jj}^6} \quad (39)$$

Note: For clarity, we will use the following nomenclature throughout.

$$A_i = \sqrt{A_{ii}} \quad (40)$$

$$B_i = \sqrt{B_{ii}} \quad (41)$$

DOI: 10.1021/acs.chemrev.6b00440
Chem. Rev. 2017, 117, 1564−1686

$$R_{\min,i} = \frac{R_{\min,ii}}{2} = R_{\min}/2 \text{ (only for the Lorentz combining rule)} \quad (42)$$

$$\sigma_i = \frac{\sigma_{ii}}{2} = \frac{\sigma}{2} \text{ (only for the Lorentz combining rule)} \quad (43)$$

$$\varepsilon_i = \varepsilon_{ii} \quad (44)$$

The Lorentz combining rule (or arithmetic combining rule) depends on the hard sphere assumption, in which particles are treated as rigid balls. The optimal distance of the VDW interaction is the sum of VDW radii of the particles i and j. The geometric combining rule relies on a "soft sphere" assumption. In eq 45, we exemplify this rule for the determination of ε_{ij}: the smaller of ε_{ii} and ε_{jj} has a bigger weight in the determination of the final value of ε_{ij}.

$$\varepsilon_{ij} = \sqrt{\varepsilon_{ii} \times \varepsilon_{jj}} = \frac{1}{2}\sqrt{\frac{\varepsilon_{jj}}{\varepsilon_{ii}}} \times \varepsilon_{ii} + \frac{1}{2}\sqrt{\frac{\varepsilon_{ii}}{\varepsilon_{jj}}} \times \varepsilon_{jj} \quad (45)$$

3.2.2. Parametrization Strategies. The parameters of ions are usually determined by reproducing one or several theoretical/experimental end points using force field (FF) calculations either through single point energy calculations or via MC[412] or MD[413] simulations. Target values used for model construction and validation can be classified as thermodynamic quantities (e.g., interaction energy, calculated potential energy surface (PES), HFE, hydration entropy, crystal lattice energy (LE), etc.), structural properties (e.g., QM calculated equilibrium distance, ion−oxygen distance of the first solvation shell (IOD), CNs of the first solvation shell, crystal lattice constant (LC), etc.), and kinetic or dynamic properties (e.g., exchange rate of first solvation shell water, diffusion coefficient (DC), etc.). From the phase state point of view, the parametrization end points can be classified as solid-state properties (LC, LE, etc.), liquid phase properties (HFE, solvation entropy, IOD, DC, mean residence time of first solvation shell (MRT), activity coefficient (AC), etc.), gas-phase properties (interaction energy of monohydrates, PES, etc.), and interface properties (osmotic pressure, etc.). From another perspective, the reference properties can be classified as single ion properties (HFE, IOD, CN, etc.), ion-pair properties (AC, Kirkwood−Buff integral (KBI), etc.), along with mixed system properties (osmotic pressure of a biomolecular system, etc.). Typical ion parametrization efforts fit two or more properties for a single-ion at a time and then afterward test their transferability to other systems or properties. For example, if an ion model was parametrized in aqueous solution using a specific water model, its transferability to other water models, with other ions (to explore ion-pair properties), in combination with other atom types in a mixed system (such as a biological system) would ultimately need to be addressed to fully validate the model.

In the pioneering efforts on ion parametrization, when computational resources were at a premium and free-energy simulation methods were not widely available, researchers usually parametrized the potential by reproducing QM-derived interaction energies and equilibrium distances or by fitting the potential to a simulated PES obtained from QM calculations on the monohydrates. However, potentials derived in this way had errors arising from the neglect of three-body and higher order effects. This causes an overestimation of the interaction energy between the solvated ion and water and then, ultimately, the ion's HFE. This error increases dramatically for the divalent and highly charged metal ions, for which the CN values predicted from molecular simulations based on the conventional pair potential are generally higher than the experimentally determined CN values. Work has been done to add the three-body term and higher order terms into the function, and remarkable progress has been made in this area.[414−417] However, the computational complexity and parametrization effort increase considerably at the same time. Hence, work focusing on adding these effects into a pair potential, yielding an effective pair potential, has been the preferred approach. This potential can be parametrized in multiple different ways, such as fitting to a QM-based effective potential, or parametrizing it directly to reproduce experimental results.

3.3. Early Studies

The modern computer was invented in the last century; for example, the ENIAC (electronic numerical integrator and computer) was announced in 1946.[418] In the 1960s, supercomputers began to become available to investigators at major universities and institutes. Concomitant with hardware developments, QM methodologies and software were becoming widely available, allowing force fields to be parametrized on the basis of accurate QM calculations, while ever more sophisticated and realistic simulation of ionic compounds, aqueous solutions, proteins, etc., began to regularly appear in the literature.

3.3.1. Studies Based on the Monte Carlo Method. The MC method analyzes a system by generating a structural ensemble whose energy follows a Boltzmann distribution. The modern MC method was proposed by Metropolis and Ulam in 1949.[412] This paper was then followed by a number of applications on molecular or molecular-like simulations. Rosenbluth and Rosenbluth performed a MC simulation for a three-dimensional system with a hard sphere potential and a two-dimensional system with a LJ potential in 1954.[419] Wood and Parker performed a MC simulation of an Ar gas system using a 12-6 LJ potential in 1957.[420] Several properties such as the radial distribution function (RDF), excess internal energy, compressibility factor, etc., were obtained, and a liquid−solid transformation was observed during the simulation. The simulated results agreed with one set of experimental results but disagreed with another.[420] Barker simulated proton−electron plasma at various temperatures and densities using the MC method in 1965.[421] In these simulations, he employed a Columbic potential coupled with the Ewald sum method to estimate long-range electrostatic interactions during the simulation. The results supported the usefulness of the MC method. Woodcock and Singer carried out a MC simulation for solid KCl using a Born−Mayer−Huggins potential in 1971.[422] They calculated a series of properties such as pressure, entropy, internal energy, etc., for different volumes, temperatures, and pressures. The results showed good agreement with experimental results. Furthermore, some experimentally inaccessible data (such as the contribution of different energy terms, properties at extreme temperatures/pressures, etc.) were obtained using these simulations. They found that the r^{-8} (dipole−quadrupole) term is only responsible for −0.5% of the internal energy along their simulation, and hence could be safely neglected during the simulation.

Clementi and co-workers fit a series of potentials based on QM calculations and performed a range of related MC or MD simulations for ion-containing systems (e.g., ionic solu-

DOI: 10.1021/acs.chemrev.6b00440
Chem. Rev. 2017, 117, 1564−1686

tion,[423−429] ion-nucleic acid,[430−434] and ion-transmembrane channel[435−438] systems) in the 1970s and 1980s.

3.3.2. Studies Based on Molecular Dynamics Simulation. The MD simulation method integrates Newton equations of motion to simulate a system by propagating the positions, velocities, and accelerations of particles as a function of time. MD not only provides thermodynamic and structural properties akin to MC simulations, but it can also directly simulate time-related properties. Alder and Wainwright reported the first MD simulation for a hard sphere system in 1957,[413] and they proposed a propagation algorithm for MD simulations in a later work.[439] Gibson et al. described a MD simulation exploring the mechanism of damage of solid Cu using a Born−Mayer potential in 1960.[440] Later, Rahman simulated liquid Ar using the MD method in 1964.[441] Periodic boundary conditions combined with a truncated LJ equation were used to carry out the simulation. The simulated pair-correlation function was in good agreement with experiment, while the calculated self-diffusion constant was 15% smaller than the experimental value. Woodcock performed the first ionic compound MD simulation (on LiCl, NaCl, and KCl compounds) in 1971, again using a Born−Mayer potential.[442] The potential parameters were from Tosi and Fumi's previous work,[384] while the Ewald method was used to model the electrostatic interactions. Various properties such as the specific heat capacity, entropy, and diffusion coefficient, etc., were obtained for the three liquid alkali metal halides at 1273 K and showed good agreement with experimental results.

Rahman and Stillinger performed the first simulation of liquid water system in 1971, in which they used a five-site water model with a tetrahedral configuration (so-called the ST2 water model).[443] The two-body potential was parametrized to reproduce the water dimer interaction energy from ab initio QM calculation. Both structural (e.g., pair-correlation functions, CNs, distribution functions, etc.) and kinetic properties (such as center-of-mass motion mean-square displacement, autocorrelation functions of the velocity, dipole relaxation function, etc.) were calculated, and good agreement was obtained when compared to experimental results.[443]

Heinzinger and Vogel performed the first MD simulation of an ionic solution system (LiCl in water) in 1974.[444] In their work, they used the ST2 water model proposed by Rahman and Stillinger.[443] The 12-6 LJ nonbonded model was used for the ions, and the LJ parameters were obtained directly from the LJ parameters for He and Ar (as they are isoelectronic with Li^+ and Cl^- ions, respectively) determined by Hogervorst[445] (where the parameters were obtained by parametrizing against experimental viscosity values). The combining rules were taken from Kong,[446] while a switching function was utilized for the evaluation of the Columbic terms. The simulated structure of the first hydration shell showed good agreement with experimental XRD and neutron diffraction data, and the simulation was able to predict the faster rotation of the first solvation shell water molecules of the Li^+ ion (relative to other water molecules in the system), in agreement with nuclear magnetic resonance (NMR) results.

Jorgensen and co-workers parametrized the LJ potential for Na^+ using the transferable intermolecular potential function (TIPS) format,[447] and the Li^+, Na^+, F^-, and Cl^- ions for the TIP4P water model based on QM calculated energetic and structural information in the 1980s.[448]

Bounds parametrized Li^+, Na^+, K^+, Ca^{2+}, and Ni^{2+} using QM calculations and simulated them with the TIP4P water model of Jorgensen and co-workers[449] via MD simulations in 1985.[450] Ca^{2+}/H_2O and Ni^{2+}/H_2O potentials were derived from ab initio SCF calculations.[450] Exp-4-6-1 and exp-1 formatted functions were used for the ion−oxygen and ion−hydrogen interactions, respectively. A higher CN for Ni^{2+} (as high as 8) was predicted from the simulation, which is greater than the experimentally determined CN of 6. High pressure affected the second-coordination shell of Cl^-, while high temperature and pressure showed little effect on the structure of Ca^{2+} in aqueous solution.

In 1986, Teleman and Ahlstrom simulated the Ca^{2+} EDTA complex and the Ca^{2+}-aqueous system based on the VDW parameters derived from the Kirkwood−Slater formula.[451] The simulated CN of Ca^{2+} in both water and EDTA is ∼7. The observed structural properties were "plausible", while the simulated dynamics were deemed "fast" relative to experiment.

It was observed in the late 1980s that there are considerable errors when applying the conventional pair potential to calculate HFEs for ions. For example, Migliore et al. calculated the HFEs of the Li^+, Na^+, K^+, F^-, and Cl^- ions on the basis of the parameters fitted to the configuration interaction (CI) QM calculations. They found that the errors in the simulated HFEs are considerable, ranging from −30% for Cl^- to 21% for Na^+ when compared to experimental values.[452] Straatsma and Berendsen studied the HFEs of Na^+, K^+, Ca^{2+}, F^-, Cl^-, and Br^- ions using the thermodynamic integration (TI) approach, and they observed that the simulated HFEs of these ions (except for the Ca^{2+} ion) were too negative when compared to experiment.[453] These results indicated that many-body effects are important and that a potential fitted from a monohydrate in the gas phase does not have good transferability to the liquid phase.

3.3.3. Many-Body Effects. As described above, the conventional pair potential, when fitted to QM calculated results on monohydrates in the gas phase, yields a notable overestimation of the ion−water interaction in the aqueous phase, in part due to the neglect of many-body effects. For starters, the first, second, third, and *n*th water binding energies to the metal ion tend to decrease. The QM fitted potential generally only considers the first water molecule, which will lead to an overestimation of the effective potential for ion−water interactions in aqueous systems. This leads to higher HFE values and may cause an increase in CN over that observed experimentally. This error can be decreased using error-canceling strategies, for example, using small basis sets, which underestimate the interaction energy of the monohydrates.

Another concern has to do with the $M^{q+}-H_2O$ system becoming the $M^{(q-1)+}-H_2O^+$ species at long distances, because the *q*th IP of the metal ion is higher than the first IP of the water molecule.[454] A positive charge on both the ion and water will cause repulsion between them. Marcos et al. proposed that for $Zn(H_2O)^{2+}$, the crossing of the two $^1A_1$ symmetry states ($Zn^{2+}-H_2O$ and $Zn^+-H_2O^+$) appears at 4.5 Å.[455] For $Be(H_2O)^{2+}$, Corongiu and Clementi found its crossing occurs at ∼9 bohr (∼5.3 Å). Curtiss et al. found that the crossing distances for $Fe(H_2O)^{2+}$ and $Fe(H_2O)^{3+}$ were >6 Å and "close to" 1.852 Å, respectively.[456] However, in an aqueous system, the other *n*−1 water molecules in the first solvation shell (assuming there are *n* water molecules in the first solvation shell) will stabilize the charge on the ion, preventing the formation of the $M(H_2O)_n^{(q-1)+}-H_2O^+$ species at long-range. Using a restricted Hartree−Fock (RHF) method, the $M^{q+}-$

DOI: 10.1021/acs.chemrev.6b00440
Chem. Rev. 2017, 117, 1564−1686

H_2O electronic configuration can be retained at long-range (even if this is in fact not natural) to obtain the PES, but this kind of strategy may fail when using correlated methods.[454]

Using some fitting strategies (e.g., using small basis sets), the error can be decreased to some extent; however, the HFE and CN values may still be overestimated for some ion-aqueous systems, especially for the highly charged ions, for which the many-body effect is significant. There are several ways to address the many-body problem: (A) adding the many-body terms; (B) using an effective potential; and (C) using a combined model for the hydrated complex (discussed in section 5.2).

3.4. Many-Body Potentials

In 1980, Clementi et al. studied the nonadditivity of the $Li(H_2O)_2^+$ system using QM calculations after which an atomic charge-induced bond dipole term and a short-range correction term were added to the pair potential to represent the three-body effect.[457] Overall, they found the three-body term was 10−15% of the total interaction. On the basis of this three-body potential, Corongiu et al. calculated the HFE value of Li^+ using MC simulations with the free-energy perturbation (FEP) method and obtained a HFE for the Li^+ ion of −114 ± 8 kcal/mol, in good agreement with two different experimental values (−118 or −123 kcal/mol).[458] However, using a conventional pair potential, which only considered the two-body effect, they overestimated the HFE value (−142 ± 2 kcal/mol).

As compared to the monovalent ions, the three-body effect would be expected to be even more significant for highly charged ions in aqueous solution. Bounds simulated Ni^{2+} in aqueous solution using an ab initio pair potential and predicted a higher CN (8 versus 6 from experiment) and an IOD value larger than experiment (2.17 Å versus 2.07 Å),[450] and González-LaFont et al. predicted a higher CN value for the Fe^{2+} ion (8 versus 6) also using an ab initio pair potential.[459]

Natália et al. studied Ni^{2+} in aqueous solution using a conventional two-body potential and a potential with a three-body term.[460] The conventional two-body potential overestimated the CN, giving a value of 8 instead of 6 and an IOD of 2.09 Å rather than 2.07 Å. The potential with the three-body term correctly simulated the CN and IOD values, but still overestimated the hydration enthalpy by ∼158 kcal/mol. Nonetheless, this was a smaller extent than the value given by the two-body potential (which overestimated the value by ∼295 kcal/mol). They proposed that further improvement could be achieved via addition of a short-range correction term and through the use of the Ewald summation method instead of a truncated potential.

Curtiss et al. have also investigated the Fe^{2+} and Fe^{3+} ions in aqueous solution using a pair potential fitted from ab initio calculations.[456] Higher CN and longer IOD values were simulated for the Fe^{2+} and Fe^{3+} ions as well. Subsequently, they parametrized an empirical pair potential that accurately reproduced the CN values of the Fe^{2+} and Fe^{3+} ions.[456]

Yamaguchi et al. simulated $BeCl_2$ in aqueous solution based on an ab initio pair potential and obtained a CN value for the Be^{2+} ion of 6, which is inconsistent with experimental XRD data, which gave a CN of 4.[461] Through an addition of a three-body term into the potential, Probst et al. were able to reproduce the CN of the Be^{2+} ion correctly.[414]

Cordeiro and Gomes have examined three-body, four-body, and higher order terms for $Cu(H_2O)_n^{2+}$, where $n \leq 8$.[415] During these studies, they found that three-body terms, which contribute repulsive interactions to the pair potential, are non-negligible. The potential with a three-body term correctly simulated the CN value (as 6) and offered improvement over the conventional two-body pair potential based on ab initio calculations (which gave a CN of 8). They also found a rapid convergence of the many-body expansion in that the four-body and higher order terms are much smaller than the three-body term. Rode and Islam found similar issues using an ab initio pair potential when they simulated the Cu^{2+} ion in aqueous solution.[416] To tackle these issues, they proposed a three-body term they called the nearest neighbor ligands correction (NNLC) that affected the first solvation shell. This strategy was not only able to reproduce the experimental CN, but it also reduces the potential parametrization burden and simulation time when compared to a potential with more typical three-body terms.

To gain deeper insights into the Cu^{2+} aqueous system, Cordeiro and Gomes reinvestigated it through a comparison of several different potentials.[417] These potentials included the conventional two-body fitted ab initio potential, the effective two-body ab initio potential (fitted from the interaction of Cu^{2+} with its first solvation shell waters), the conventional potential with a three-body term, and the effective potential with a three-body term. They found that both the effective pair potential and the three-body term decreased the average interaction energy between the ion and surrounding water molecules. They also found that the conventional potential overestimated the interaction energy by ∼30% over the effective potential in the first solvation shell, while they were nearly identical outside the first solvation shell. However, the conventional and effective two-body potentials overestimated the CN values as 8−9 and 8, respectively. Both the conventional potential with a three-body term and an effective potential with a three-body term offered improvement with the latter better describing the energetics of the system. Furthermore, they noted that in the three-body term, the ion−water−water term dominates the water−water−water term.

3.5. Effective Two-Body Potentials

There are two different ways to incorporate many-body effects into effective two-body potentials. One is based on fitting to QM-derived data, and the other involves fitting the potential directly to experimental HFE, IOD, etc., values as demonstrated by Aqvist.[462] The methods based on fitting to QM data may still not reproduce the HFE or IOD values accurately due because the reference QM model they fitted to may still only have finite accuracy, with the resultant error propagating with the increasing size of the simulated system. Hence, people prefer to use the latter method in parametrization efforts because it accurately reproduces thermodynamic, structural, or both properties simultaneously.

3.5.1. Quantum Mechanics-Based Parameters. There are different approaches to fit effective two-body potentials based on QM data, for example, (1) fitting the potential between an ion and water within a implicit solvation model, as proposed by Floris et al.,[463] (2) fitting the potential to reproduce the average interaction between an ion and its first solvation layer, as proposed by Cordeiro et al.,[417] and (3) fitting the potential to reproduce the PES between the ion, which has $n-1$ water molecules bound to it (where n is the CN value) with fixed geometry, and the last water, as proposed by Periole et al.[464] The accuracy of the first method depends on the

DOI: 10.1021/acs.chemrev.6b00440
Chem. Rev. 2017, 117, 1564−1686

accuracy of the implicit solvation model, while for the second and third approaches, errors associated with only considering the first solvation shell can reduce their accuracy.

3.5.1.1. Effective Potential Based on Implicit Solvation Model. Floris et al. proposed a QM method to obtain the effective pair potential, which considers many-body effects implicitly.[463] They applied their methodology to Fe^{2+} and Fe^{3+} aqueous systems initially and were able to reproduce the experimental CNs.[463]

$$U_{AB} = \langle\psi|\hat{H}^{(0)}|\psi\rangle_{AB} - \langle\psi|\hat{H}^{(0)}|\psi\rangle_{A} - \langle\psi|\hat{H}^{(0)}|\psi\rangle_{B} \quad (46)$$

As given in eq 46, the interaction energy U_{AB} of two solutes in solvent can be obtained on the basis of QM calculations, where $\hat{H}^{(0)}$ is the Hamiltonian of the solute in vacuo while ψ is the wave function for the solute in solution, which was modeled using the polarizable continuum model (PCM). They found that, for Fe^{2+} ion, the conventional pair potential fitted using the dihydrate complex in vacuo yielded a lower binding energy by ~15 kcal/mol than the conventional pair potential fitted from the monohydrate in vacuo. Using their approach with an effective pair potential fitted using both the monohydrate and the dihydrate data simultaneously further decreased the binding free energy by ~4 kcal/mol. However, this method depends on the accuracy of the implicit solvation model itself and the parameters employed in the solvation model. The broad range of available solvation models has been extensively reviewed by others.[465] In the work of Floris et al., they used the $U_{WMW} = 2U_{MW} + U_{WW}$ relationship (where M = metal and W = water) to determine the ionic radii for Fe^{2+} and Fe^{3+} ions.[463] Finally, they fitted their potential based on a range of ion−water structures and the SPC water model. The resultant potential reproduced the experimental CNs for the Fe^{2+} and Fe^{3+} ions (as 6) and the octahedral geometry of the first solvation shell.

Subsequently, Floris et al. have used their approach to study the aqueous hydration of a range of ions including Li^+, Be^{2+}, Mg^{2+}, Ca^{2+}, Ni^{2+}, Zn^{2+}, Al^{3+}, and Ln^{3+}.[454,466,467] The results obtained further confirmed that their approach offers improvements over the conventional pair potential.

D'Angelo, Chillemi, and co-workers studied Co^{2+}, Zn^{2+}, and Ni^{2+} in aqueous solution using an effective pair potential based on the method developed by Floris et al.[468,469] The PES was evaluated using restricted-open-shell-Hartree−Fock (ROHF) calculations coupled with the PCM solvent model. Even with the complicated potential equation they used (Exp-1-4-6-8-12 potential for the ion-oxygen and a 1-4-6-8-12 potential for ion-hydrogen; see eq 47), MD simulation of Zn^{2+} in water predicted a more asymmetric and a sharp first peak in the metal−oxygen RDF when compared to the EXAFS results. They also used this method to investigate Hg^{2+}, trivalent metal ions in the lanthanide series (Ln^{3+}), and trivalent metal ions in the actinide series (An^{3+}) in aqueous solution and obtained useful insights.[470−475] Besides aqueous solution, they also utilized this method to explore Zn^{2+} and Hg^{2+} in methanol.[476,477] While their approach proved powerful, it has some issues affecting its usability; because of its complicated form, the number of parameters will increase dramatically in mixed systems such as proteins and nucleic acids, reducing its broad applicability.

$$U(r_{ij}) = \frac{q_i q_o}{4\pi\varepsilon_0 r_{io}} + \frac{A_o}{r_{io}^4} + \frac{B_o}{r_{io}^6} + \frac{C_o}{r_{io}^8} + \frac{D_o}{r_{io}^{12}} + E_o\, e^{-F_o/r_{io}} + \sum_{ih=ih1,ih2} \frac{q_i q_h}{4\pi\varepsilon_0 r_{ih}} + \frac{A_h}{r_{ih}^4} + \frac{B_h}{r_{ih}^6} + \frac{C_h}{r_{ih}^8} + \frac{D_h}{r_{ih}^{12}} \quad (47)$$

3.5.1.2. PES Scanning Method. Pang et al. parametrized the Fe^{2+} ion with a 12-6 LJ potential for a nonheme site.[478] The parameters were derived on the basis of the QM PESs between Fe^{2+} and the ligating ligands (two His residues, one Asp residue, one water, and one α-ketoglutarate ligand). They applied a weak harmonic restraint to favor the monodentate Asp binding mode over the bidentate mode frequently preferred by the 12-6 LJ nonbonded model.

3.5.1.3. SLEF Model. Wu et al. have developed the nonbonded short−long effective function (SLEF) model and parametrized it for zinc-containing proteins via reproduction of QM/MM-derived forces for zinc metalloenzymes with different binding modes (with CNs equal to 5, 6, and 7).[479] The SLEF model, instead of the standard Columbic formula, was used to represent the electrostatic interactions between the Zn^{2+} ion and the surrounding particles (see eq 48). The short-range part decays exponentially, while the long-range part contains a term similar to a DFT dispersion correction damping function. As shown in Figure 20, the PES between the zinc ion and the TIP3P water model shows that SLEF strengthens the short-range interactions (from 1.5 to 2.0 Å) and weakens the midrange (from 2.5 to 4.5 Å) interactions, while retaining the strength of the long-range (beyond 4.5 Å) interactions, relative to the standard Columbic model. This behavior implicitly incorporates POL and CT effects into the modeling of the metal ion. Exploratory MD simulations were carried out for Zn^{2+} metalloenzymes with CN values of 5, 6, or 7, and comparisons were made between SLEF and standard 12-6 LJ models. The SLEF model showed improved performance and was able to reproduce different binding modes as shown by QM/MM MD and experimental results.

$$U(r_{ij})_{SLEF} = \frac{1}{4\pi\varepsilon_0}\left[\frac{q_{Zn}q_j}{\sqrt{r_{ij}^2 + \frac{\alpha q_j^2\, e^{\beta r_{ij}^2}}{(R_{min,i}+R_{min,j})}}} + \frac{q_{Zn}q_j}{r_{ij}} \times \frac{1}{1+e^{-2(2r_{ij}/3-1.0)}}\right] \quad (48)$$

Afterward, Gong et al. developed a second-generation approach (SLEF2, see eq 49) where they optimized the parameters (α, β, γ, λ, and R_{Zn}) on the basis of 5 zinc proteins and tested them in 16 proteins.[480] The MD simulations employing the SLEF2 model showed good agreement with XRD structures, while the MD simulations based on the 12-6 LJ model with parameters from Stote and Karplus showed a preference for higher CN values (e.g., 5 or 6).

DOI: 10.1021/acs.chemrev.6b00440
Chem. Rev. 2017, 117, 1564−1686

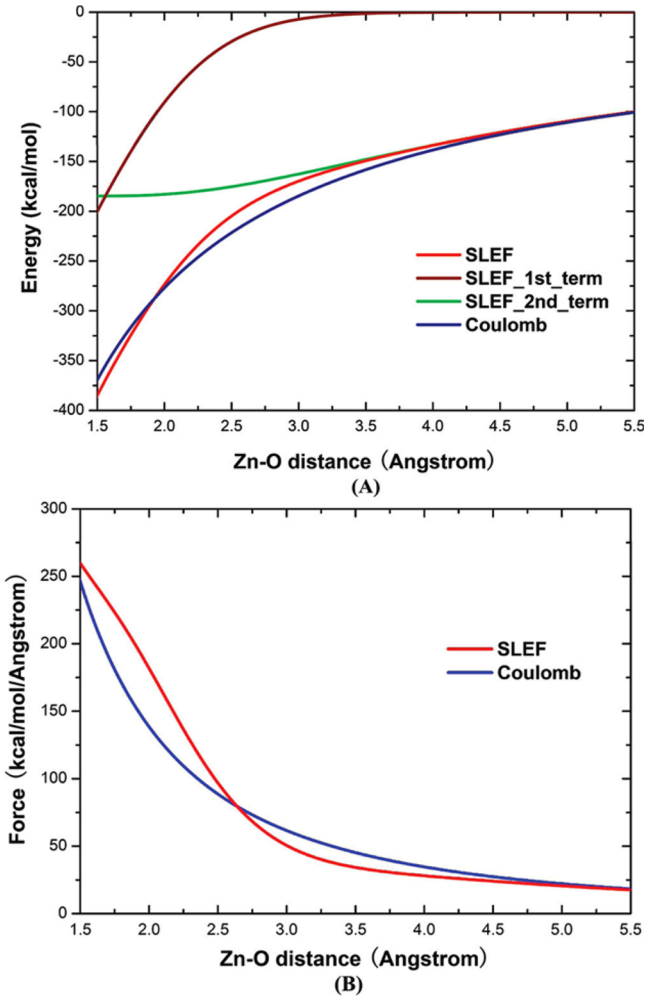

Figure 20. Illustration of the difference between SLEF and the conventional $1/r$ Coulomb function in describing charge interactions between Zn^{2+} and the oxygen of TIP3P water: (A) energy and (B) force. The parameters in the SLEF1 force field were employed. Reprinted with permission from ref 479. Copyright 2011 American Chemical Society.

$$U(r_{ij}) = \frac{1}{4\pi\varepsilon_0}\left[\frac{q_{Zn}q_j}{r_{ij}} \times \left(\frac{1}{1+\alpha\times\frac{(|q_i|+|q_j|)^2}{(R_i^*+R_j^*)^2}\times e^{\beta r_{ij}^2}} + \frac{1}{1+\frac{|q_i|+|q_j|}{q_{Zn}}\times e^{1-\lambda r_{ij}}}\right)\right] \quad (49)$$

3.5.1.4. QPCT Model. Zhu et al. created the quantum calibrated polarizable-charge transfer (QPCT) force field for zinc-containing proteins,[481] in which they added a CT term into the nonbonded model to fit to the QM calculated interaction energy (see eq 50). In this model, they calculated the amount of CT between a zinc ion and one of its ligands (with the remaining ligands fixed) using a natural population analysis (NPA, see Figures 21 and 22). Using this information, they carried out a fit to eq 51 (where A_0, A_1, and A_2 are the parameters to fit), which represents the relationship between the CT amount and the zinc to ligand distance. The E_{CT} term

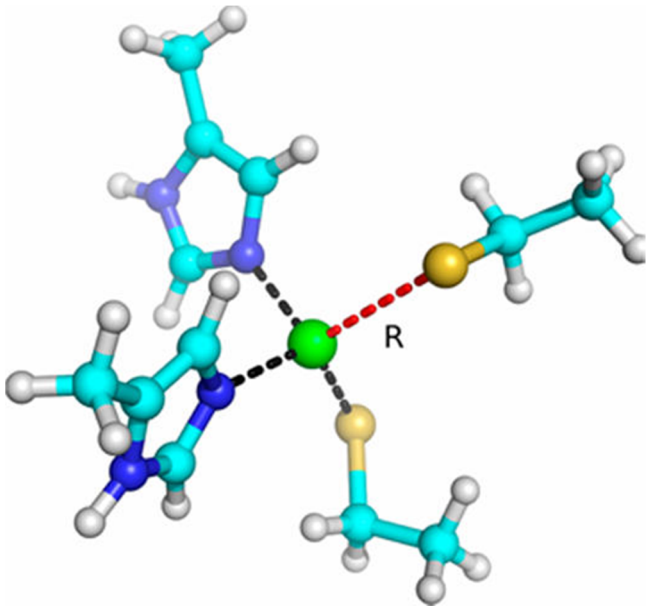

Figure 21. Model system $[Zn(Et)_2(Im)_2]^0$ representing the $ZnCys_2His_2$ binding structure used in fitting the CT and binding energy as a function of the distance between zinc and the ligated atom. Reprinted with permission from ref 481. Copyright 2013 American Chemical Society.

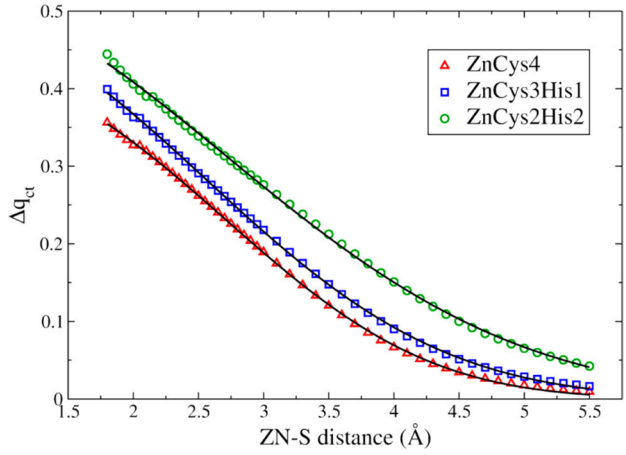

Figure 22. QM calculated CT (Δq_{ct}, NPA charge) at the MP2/6-311++g(2df,p) level as a function of the coordinate bond length for ethylthiolate in $ZnCys_2His_2$, $ZnCys_4$, and $ZnCys_3His_1$ systems. Solid lines denote analytical fitted curves of QM results. Reprinted with permission from ref 481. Copyright 2013 American Chemical Society.

(see eq 52, where B_0, B_1, B_2, and B_3 are parameters to fit) was fit to the difference between the QM calculated interaction energy and sum of the electrostatic and VDW terms ($E_{qm}-E_{ele}-E_{VDW}$). An example describing the various terms (E_{qm}, E_{ele}, E_{VDW}, and E_{CT}) is depicted in Figure 23. The E_{CT} term is cut off when the bond distance between the zinc ion and a coordinated atom is larger than the sum of their VDW radii. The semifluctuating charge (SFC) model[482] considered the polarization of, for example, the N−H, C−O, O−H, S−H, and C−N bonds. These authors have shown that the model was able to accurately simulate different zinc complexes with only a 1% additional computational cost over an unpolarized force field. However, this model assumes that the bond distances between the zinc ion and its ligands are fluctuating around equilibrium values

DOI: 10.1021/acs.chemrev.6b00440
Chem. Rev. 2017, 117, 1564−1686

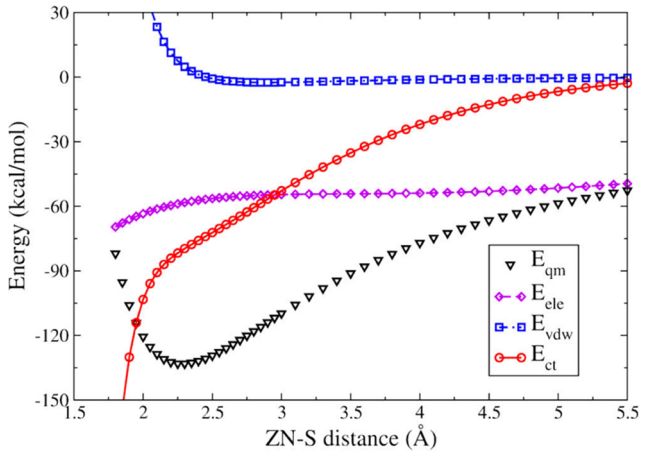

Figure 23. Interaction energies of ethylthiolate (*Et*) and $[Zn(Et)(Im)_2]^+$ as a function of coordinate bond length. E_{qm} is the binding energy of Et and the $[Zn(Et)(Im)_2]^+$ calculated by Gaussian 09 at the MP2/6-311++g(2df,p) level. E_{ele} is the electrostatic interaction between *Et* and the $[Zn(Et)(Im)_2]^+$. E_{vdw} is the van der Waals interaction energy between *Et* and the $[Zn(Et)(Im)_2]^+$, and E_{ct} is "charge-transfer" energy between Et and the $[Zn(Et)(Im)_2]^+$ ($E_{ct} = E_{qm} - E_{ele} - E_{vdw}$). Reprinted with permission from ref 481. Copyright 2013 American Chemical Society.

without large changes. Moreover, the energy terms contained in this function (electrostatic, VDW, and CT terms) are effective ones, which cannot be directly compared to energy decomposition results from QM calculations. Meanwhile, because of the nonadditivity of the CT effect, this model, which is based on the assumption of additivity, may not accurately predict the total interaction energy of a given complex. Hence, it might not be suitable to study ligand exchange processes.

$$E_{Zn-L} = E_{ele} + E_{VDW} + E_{CT} \quad (50)$$

$$\Delta q_{CT} = A_0\, e^{-(R_{Zn-L}/A_1)^{A_2}} \quad (51)$$

$$E_{CT} = -e^{(B_0 \times \Delta q_{CT} + B_1)} + B_2 \times (\Delta q_{CT})^2 + B_3 \quad (52)$$

3.5.2. Experimental Data (Especially Free-Energy)-Based Parameters. The free energy is a comprehensive thermodynamic property that is a combination of the enthalpy and entropy for a given system. There are two free energies of interest in chemistry: the Helmholtz free energy from a canonical ensemble (abbreviated NVT) and the Gibbs free energy from an isothermal−isobaric ensemble (abbreviated NPT). For most chemistry applications, these two quantities are generally considered as interchangeable. There are various ways to use simulations to estimate the free energy change of a given process: two of the most important first-principles approaches include the FEP[483] and TI methods,[453] which are widely used to compute absolute and relative free energies in drug design and other application areas. More approximate methods that also estimate free energy changes include the molecular mechanics Poisson−Boltzmann surface area (MM/PBSA),[484] molecular mechanics generalized Born surface area (MM/GBSA),[465] and linear response methods.[465]

The FEP method has been reviewed in detail in the past.[485] Here, we will highlight work of relevance to the study of metal ions using either the FEP or the TI approach. The FEP method was first proposed by Zwanzig in 1954.[483] Valleau and Card used MC simulations coupled with the FEP method to investigate the free energy change of Columbic fluids in 1972.[486] Torrie and Valleau evaluated the configurational Helmholtz free energy change of a LJ fluid system in 1974.[487] Mezei et al. estimated the HFE and hydration entropy of water using MC simulations combined with the TI method in 1978.[488] In this effort, good agreement was obtained between the simulated and experimental values. Tembe and McCammon reported the simulation of the relative binding free energy of a protein−ligand system using the thermodynamic cycle and FEP method in 1984, which opened the use of FEP method to drug design optimization applications.[489] Jorgensen and Ravimohan determined the relative HFE between methanol and ethane using the TIP4P water model in 1985, yielding good agreement with experiment.[490] Their simulations showed that the hydrogen-bond network is dramatically diminished only after a 25% decrease in the atomic charge of methanol.

Lybrand et al. studied the relative HFE of Cl^- and Br^- using MD simulations and the FEP method.[491] The SPC water model[492] was used with LJ parameters for Cl^- taken from the GROMOS force field. The LJ parameters of Br^- were determined such that they reproduced the experimental interaction energy difference between $Cl(H_2O)^-$ and $Br(H_2O)^-$. The estimated relative HFE value was in good agreement with the experimental value (3.15 kcal/mol calculated versus 3.3 kcal/mol experimental). This was followed by calculations on the relative binding free energy between Cl^- and Br^- ions to SC24 (a macrotricyclic receptor) in water using MD-FEP simulations.[493] The resultant relative binding free energy was in good agreement with experiment, further demonstrating the validity and usefulness of the FEP method. In a related effort, Mazor et al. studied the relative HFE of Na^+ and K^+ and their relative binding free energy to 18-Crown-6 in methanol using the TI method, and the calculated values were in good agreement with experiment (relative HFE, 19.6 kcal/mol calcd versus 17.3 kcal/mol exp; relative binding free energy, −3.5 kcal/mol versus −2.47 kcal/mol).[494]

Jorgensen et al. reported the estimation of the absolute HFEs of methane, water, and Cl^- using the TIP4P water model in 1989.[495] The final results gave good agreement with experiment (methane, 2.27 ± 0.3 kcal/mol calcd versus 2.005 kcal/mol exp; water, −6.1 ± 0.3 kcal/mol versus −6.3 kcal/mol; Cl^-, −79.3 ± 2 kcal/mol versus −77 kcal/mol), validating that the FEP method could evaluate absolute HFEs of both neutral, polar, and charged species.

In the previous efforts, the ion parameters were generally created for the study itself or were largely unvalidated in terms of their broader performance. In a pioneering work, Åqvist carefully parametrized a series of ions to match their experimental HFE values. He systematically parametrized the 12-6 LJ potential for the alkali and alkaline-earth metal ions using the FEP method to best reproduce experimental HFEs in 1990.[462] He argued that for simulations with solutions and biomolecules, targeting the absolute HFEs is the most reliable way to parametrize ion potentials other than to reproduce relative solvation energies between ions. Stote and Karplus parametrized the LJ potential for the Zn^{2+} ion with a modified TIP3P water model in 1995.[496] Initial parameters were derived from an ion−water PES calculated by Clementi et al. and then refined by treating the experimental RDF (the first and second peaks along with the CN value) and HFE as parametrization targets. MC simulation was used to obtain the RDF and CN, while the FEP/MC method was used to obtain the HFE. Good

DOI: 10.1021/acs.chemrev.6b00440
Chem. Rev. 2017, 117, 1564−1686

results were obtained in the test simulations of carboxypeptidase A and carbonic anhydrase, where the nonbonded model yielded accuracy comparable to that of the AMBER force field employing the bonded model. Using the Ca^{2+} LJ parameters from Åqvist and Zn^{2+} LJ parameters from Stote and Karplus, Donini and Kollman used the MM/PBSA method to predict the binding affinity of different ligands to a matrix metalloproteinase (MMP).[497] The correct ranking of the binding affinities of six ligands was obtained from the simulations, while a better ligand was predicted via modifying the best-binding ligand.

Halgren determined the VDW parameters for a series of ions including H_3O^+, Li^+, Na^+, Mg^{2+}, Ca^{2+}, high-spin Fe^{2+} and Fe^{3+}, Cu^+, Cu^{2+}, Zn^{2+}, F^-, Cl^-, Br^-, and OH^- in an extension of MMFF94.[498] Here, the buffered 14-7 VDW potential function was used. The VDW radius was determined on the basis of the polarizabilities (see eq 53, where C_i is a scaling factor). The polarizability of Zn^{2+} was determined on the basis of the XRD structures, while the polarizabilities of the other ions were derived on the basis of energetic and structural properties of mono- and tri-hydrates for monovalent ions, or tri- and hexahydrates for highly charged ions.

$$R_{min,i} = \frac{C_i \alpha_i^{0.25}}{2} \tag{53}$$

Peng et al. parametrized the alkali metal ions and halide ions using the 9-6 LJ nonbonded model by treating the experimental LC and LE values as targets.[499] The Waldman−Hagler combining rules were employed in their work. These parameters obeyed the trend of the noble gas atoms—the VDW radii $R_{min}/2$ and dispersion coefficient C_6 increase inside the group, and the isoelectronic relationship that $R_{min}/2$ and C_6 of the particles, which share the same electronic structure, follow the sequence anion > neutral particle > cation. These parameters showed good agreement with the QM calculated interaction energies of the monohydrates and experimentally determined IOD values (where the SPC water model was employed in the simulations).

Jensen and Jorgenson parametrized the alkali-metal ions, halide ions, and ammonium ions using the 12-6 LJ potential and the TIP4P water model in 2006.[500] MC simulations and FEP calculations were used to reproduce the experimental IOD and HFE values, respectively. Geometric combining rules were employed in the simulations. The final parameters were also able to reproduce QM calculated interaction energies of monohydrates and the experimental CN values of these ions. This represented the first self-consistent 12-6 LJ parameter set for halide ions that was parametrized for aqueous-phase simulations.

In an extensive and systematic effort, Babu and Lim parametrized the 12-6 LJ potential for 24 divalent metal ions in 2006.[501] The nonbonded interaction was truncated using an atom-based switching function. Lorentz−Berthelot (LB) combining rules and the TIP3P water model were used during these simulations. The FEP method was used to calculate the relative HFEs, and the experimental HFE values were taken from Marcus' data set.[502] Final parameters were determined via their ability to reproduce the relative HFE to Cd^{2+}. Overall, their parameter set was able to simultaneously reproduce the relative HFEs, the IOD values, and CNs relative to experiment to a good level of accuracy.

Carlsson and Åqvist calculated the absolute hydration entropies of five alkali metal ions in 2009.[503] The hydration entropies were evaluated on the basis of the van't Hoff plots with HFEs calculated under different temperatures. The simulated hydration entropies agreed well with experiment. They found that the entropy change associated with the creation of a neutral VDW sphere in water solution is correlated with the accessible surface area of the ion in question. It was also shown that without temperature-dependent parameters, neither the continuum Born model nor the linear response approximation could simulate the entropy change associated with charging a VDW sphere in aqueous solution.

Won systematically parametrized 12-6 LJ parameters for monovalent, divalent, and trivalent metal ions to reproduce their experimental HFE values in 2012 using the FEP method.[504] The LB combining rules and the TIP3P water model were employed in the parametrization effort. Meanwhile, during the simulations, the long-range electrostatic interactions were modeled using the solvent boundary potential along with switching functions for the nonbonded interactions (electrostatic and VDW interactions). To address the nonunique parameter problem (discussed below), for a certain ion, the value of ε was derived from the hydration shell radius and thickness, from which the $R_{min}/2$ was determined empirically to reproduce the experimental HFE value.

In 2012, Mao and Pappu developed nonbonded parameters for alkali metal and halide ions for hard-sphere and 12-6 LJ models.[505] The parameters were designed to reproduce the lattice energies and interionic distances of a number of ionic salts. LB combining rules were used in their work, and they used the parameter consistency criteria proposed by Peng et al.[499] (mentioned above) as constraints for the parametrization process. Because no water model was considered during the parametrization process, their parameters are independent of water model choice. It was shown that generally the final LJ parameters reproduced the lattice structures (correctly predicts the favorability of FCC over BCC structures for 17 out of 20 salts), and the HFEs of ions (with RMSDs of 1.0, 4.1, and 2.4 kcal/mol for TIP3P, SPC/E, and $TIP4P_{EW}$ water models, respectively, where the simulated HEFs were determined using the HFE hypersurfaces determined by Joung and Cheatham[506] and the experimental HFEs were from Schmid et al.[507]), showing excellent transferability. They also discussed that the simulated HFE is particularly sensitive to the LJ parameters of small ions.

Darden et al. developed the particle mesh Ewald (PME) method on the basis of the fast Fourier transform in 1993.[373] It offered a substantial speed improvement (proportional to N log N rather than N^2 for Ewald sums, where N is the number of particles in the system) coupled with good accuracy. MD simulations of proteins and nucleic acids using this algorithm showed improved stability.[508] This method can also be used to calculate multipole interactions in periodic systems and has been used with polarizable force fields.[509] In recent years, the PME method has became the standard technique for MD simulations, essentially rendering the earlier parameters sets somewhat obsolete. In what follows, we introduce several representative works of the reparametrization of the nonbonded model of ions specifically for the PME approach.

In light of this, Joung and Cheatham reparametrized the alkali metal and halide ions in conjunction with the PME method.[506] They systematically reparametrized the 12-6 LJ

DOI: 10.1021/acs.chemrev.6b00440
Chem. Rev. 2017, 117, 1564−1686

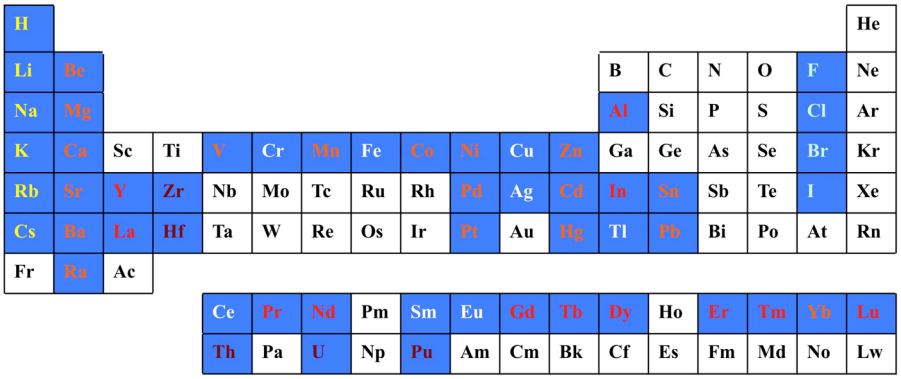

Figure 24. Atomic ions that were parametrized for the 12-6 model by Li, Merz, and co-workers.[390,391,510] These ions are shown with a blue background. The monovalent anions, monovalent cations, divalent cations, trivalent cations, and tetravalent cations are shown in light green, yellow, orange, red, and dark red, respectively. The ions that have multiple oxidation states are shown in white, which are Cr^{2+}/Cr^{3+}, Fe^{2+}/Fe^{3+}, Cu^{+}/Cu^{2+}, Ag^{+}/Ag^{2+}, Ce^{3+}/Ce^{4+}, Sm^{2+}/Sm^{3+}, Eu^{2+}/Eu^{3+}, and Tl^{+}/Tl^{3+}. Besides these atomic ions, the H_3O^{+} and NH_4^{+} ions were also parametrized in their work. Reprinted with permission from the Ph.D. dissertation of Li.[511] Copyright 2016 Pengfei Li.

nonbonded model for alkali metal and halide ions for three widely used water models (TIP3P, SPC/E, and TIP4P$_{EW}$) in 2008.[506] Importantly, they accounted for long-range electrostatic interactions using the particle mesh Ewald (PME) method as opposed to using a cutoff scheme. The values targeted in the parametrization effort were the experimental HFE, LE, and LC values. These parameters were also able to reproduce the interaction energies of monohydrates and the IOD values.

In recent years, Li, Merz, and co-workers systematically developed 12-6 LJ parameters for monovalent to tetravalent ions for use with the PME model (see Figure 24).[390,391,510] They demonstrated that it is difficult to find accurate 12-6 LJ parameters for divalent metal ions even with the PME method.[390] Moreover, the error of the 12-6 LJ nonbonded model increases along with the charge of the ion of interest (i.e., from monovalent to tetravalent).[390,391,510] They developed different parameter sets for various metal ions (from monovalent to tetravalent) aimed at reproducing different experimental properties (HFEs, IODs, relative HFEs, CNs).[390,391,510] Many of their conclusions will be covered in sections 3.6 and 3.7.

Fitting LJ parameters for metals proceeds differently from that of the ions. Pairwise potentials including 9-6 LJ and 12-6 LJ models yield impressive performance for metals as well. Recently, metal−protein systems and their associated interactions have attracted considerable attention. CVFF/CHARMM-METAL[512] and Gold-protein (GolP)[513] are two widely used FF models used to simulate this class of systems. The former was parametrized for a number of FCC metals and surfaces (they specifically examined (111) and (100) surfaces), but did not consider polarization explicitly. The later model includes the polarization effect with the Drude rod (DR) model (see section 6.2.2), and it considers interactions with different natures (e.g., chemisorbed, π systems) separately in the parametrization process, but specific for the Au(111) surface. However, none of them included covalent interactions between metal surfaces and adsorbates. We introduce the CVFF/CHARMM-METAL force field below (which is an unpolarized force field and a part of the INTERFACE force field developed by Heinz et al.), while the GolP force field, which is a polarizable force field, is discussed in section 6.2.2.

Heinz et al. parametrized the 12-6 LJ and 9-6 LJ potentials for FCC metals in 2008.[512] They noted that the parametrization strategy based on deriving the LJ parameters on the basis of density and vaporization energies worked well for the nonpolar organic liquids, but it is not suitable for metallic and mineral systems. The former systems usually have a boiling point ±200 K over room temperature, while for the latter ones they have boiling points up to 4000 K. The assumption that vaporization energies can be employed as the fitting target resulted in low-quality LJ parameters, while density and surface tension properties under standard conditions afforded better fitting targets resulting in higher quality LJ models. In the LJ equation, the R_{min} and ε are related to the density and surface free energy of the lowest energy (111) surface, respectively. In their work, they used both the geometric combining rules (as in OPLS-AA) and the sixth power combining rules (as in COMPASS), and both of them offered good performance. They found the two parameters are only slightly correlated with each other, implying their different physical roles. Both the 12-6 LJ and the 9-6 LJ equations were parametrized; the latter one has ∼1.7% increase in R_{min} and an ∼18% decrease in ε due to its less repulsive and more attractive characteristics. It was shown that through use of this strategy, it was possible to decrease the deviation from experiment by about 1 order of magnitude when compared to fits based on the density and vaporization energy. Results show that the newly developed parameters give deviations in the densities (0.1%), surface energies of (100) surfaces (3%), metal−water interface energies (10%), and mechanical properties (25%), when compared to experiment.[512] The 12-6 LJ model outperformed the 9-6 LJ model in reproducing mechanical properties. As compared to semiempirical quantum mechanical methods like the EAM and TB approaches, the new parameters showed comparable accuracy and were up to 1 million times faster.[512] The INTERFACE force field model is discussed further in the bonded model section (Section 4) of this Review.

3.6. Transferability, Physical Meaning, and Balance of the Parameters

3.6.1. Condition Changes. The wide range of parameters that have been developed, to date, employ different simulation conditions (e.g., different cutoff values, long-range interaction algorithms, etc.), which limits the transferability of the derived parameters. This was touched on by Marrone and Merz as well as by Åqvist in the early 1990s.[514−516] When cation and anion parameters, developed on the basis of different parametrization

DOI: 10.1021/acs.chemrev.6b00440
Chem. Rev. 2017, 117, 1564−1686

schemes, are used in combination, an imbalance between the parameter sets may occur. For example, Auffinger et al. showed that for the simulation of KCl solutions, the K^+ parameters of Dang and Kollman[517] showed better performance than the AMBER ones adopted from the work of Åqvist.[518] They also suggested that simulating mixed solutions at concentrations >0.25 M was a better measure of parameter quality than examining them at minimal salt conditions. Importantly, these 12-6 LJ parameters may not be compatible with new simulation protocols including those using the PME algorithm. Examples about parameters designed specifically for the PME approach were introduced in an earlier section (section 3.5).

3.6.2. Parameter Uniqueness Problem. Using the 12-6 LJ model for ions can lead to multiple combinations of LJ parameters (such as $R_{min}/2$ and ε) that give similar HFE and IOD values,[390] leading to what we will call the parameter uniqueness problem. The problem here is which one to chose to obtain a consistent set of parameters. The multiple parameter sets arise because similar A_{ij} and B_{ij} terms can be obtained between the ion and water-oxygen atoms: for a certain $R_{min}/2$ and ε, there will be a corresponding bigger $R_{min}/2$ and smaller ε, or a smaller $R_{min}/2$ and bigger ε, which yield similar A_{ij} and B_{ij} terms (see eqs 54 and 55). Meanwhile, the number of atom types would increase dramatically in biomolecular systems. When two different ion parameter sets, which give similar A_{ij} terms between an ion and oxygen in water, are applied to the same biomolecule, they may give quite different A_{ij} terms between the same atom type on the biomolecule and the metal ion after applying the combining rules. So how to select the final parameter combination is a problem that needs to be addressed.

$$A_{ij} = \varepsilon_{ij} R_{\min,ij}^{12} \tag{54}$$

$$B_{ij} = 2\varepsilon_{ij} R_{\min,ij}^{6} \tag{55}$$

There are various ways to solve this problem. (1) The easiest way is fixing the value of $R_{min}/2$ or ε. For example, Dang and co-workers parametrized a series of ions by uniformly treating their ε values as 0.1 or 0.2 kcal/mol.[519−524] Jensen and Jorgensen parametrized their cations and anions using two different ε values: a smaller one for cations (e.g., 0.0005 kcal/mol) and a large one for anions (0.71 kcal/mol).[500] (2) A second approach is to parametrize the $R_{min}/2$ or ε value first and then determine its partner empirically. For example, Won determined the ε values first based on the radius of the charged sphere (r in eq 56) and the thickness of the spherical hydration shell (Δr in eq 56), and afterward obtained the $R_{min}/2$ value based on the ε value.[504] (3) A third approach is to parametrize the potential with two or more different target values. This may not work when the two parametrization targets are correlated with each other like HFE and IOD.[390] In Joung and Cheatham's work, they parametrized the potential primarily to reproduce the HFE value and selected the final parameter set that gave the best compromise between the LE and LC.[506] (4) Finally, the $R_{min}/2$ and ε parameters can be optimized simultaneously. For example, Babu and Lim parametrized the $R_{min}/2$ and ε parameters over a series of ions based on a reference ion.[501] Li et al. proposed the noble gas curve (NGC, see eq 57) to describe the relationship between the $R_{min}/2$ and ε values quantitatively.[390] On the basis of this, the two-dimensional problem can be solved as a one-dimensional one (discussed further below).

$$\varepsilon = 0.063\sqrt{r/\Delta r} \text{ (Won)} \tag{56}$$

$$\varepsilon = 57.36 \times e^{-2.471 \times R_{min}/2} \text{ (NGC)} \tag{57}$$

3.6.3. Values of the Parameters. *3.6.3.1. Magnitude and Range of LJ Parameters.* The parameters inside the LJ equation can be assigned a physical meaning. For example, $R_{min}/2$ represents the VDW radius of the ion, while ε represents the interaction well depth (or mutual energy). On the basis of their physical meaning, we can estimate the appropriate magnitudes and ranges for atomic particles. $R_{min}/2$ should have a magnitude appropriate for an atomic particle with respect to their known physical sizes and should be in the range of 0.8−3.0 Å, while ε should be less than 10 kcal/mol or even smaller than 1 kcal/mol due to the overall weakness of the VDW interaction.

3.6.3.2. Insights from Experiment and Theory. Even though it is hard to obtain the VDW radius of a certain ion from experiment directly, we can use the VDW radii of noble gas atoms, as well as that of the element's neutral form, to estimate its magnitude and range. Moreover, it is possible to obtain theoretical estimates of the VDW radii of some ions.[525] All of these values can help us to estimate, determine, and evaluate the final VDW parameters. Using the noble gas atoms as an example: the experimentally determined VDW radii of He, Ne, Ar, Kr, and Xe are 1.40, 1.54, 1.88, 2.02, and 2.16 Å, respectively,[526] while their experimentally determined $R_{min}/2$ parameters for the 12-6 LJ equation are 1.485, 1.55, 1.88, 2.00, and 2.20 Å, respectively.[527] Even though the two sets are not identical (except for the Ar atom), largely because the 12-6 LJ potential is not entirely physically accurate, they are very close in value to one another (with an unsigned average error of ∼0.02 Å).

3.6.3.3. Behavior within a Group. Noble gas atoms have increasing $R_{min}/2$ and ε values inside the group. This is because the bigger atom has a more dispersed and polarizable electron cloud. For instance, the $R_{min}/2$ parameters of He, Ne, Ar, Kr, and Xe were summarized above, while the experimental ε parameters are ∼0.02, ∼0.08, ∼0.28, ∼0.40, and ∼0.55 kcal/mol, respectively.[527] This trend is also predicted by the Slater−Kirkwood formula[377] that shows that the mutual energy is correlated with the polarizability of the particle (see eq 25). In eqs 54 and 55, the A_{ij} and B_{ij} terms will also increase along with the $R_{min}/2$ and ε values. This trend should also be seen inside the alkali ion, alkali-metal ion, and the halide ion groups; that is, the R_{min}, ε, A, and B values are expected to increase inside these groups as well.

3.6.3.4. Particles Sharing the Same Electronic Structure. Another boundary condition that can be exploited in ion parametrization is the trend among ions that share the same electronic structure. For instance, F^-, Ne, and Na^+ share the same electronic structure, but the $R_{min}/2$ of F^- should be the biggest because it has the smallest nuclear charge resulting in the largest electron dispersion extent. This means F^- will also have the largest ε, A, and B values as well.

3.6.3.5. From Qualitative to Quantitative Relationships. The previous two relationships can help us estimate or evaluate the final parameters qualitatively but not quantitatively. Because the value of ε increases along with the $R_{min}/2$ value, Li et al. proposed the use of the NGC (see Figure 25),[390] which is fitted from experimentally determined $R_{min}/2$ and ε parameters of the noble gas atoms, to quantify the correlation between $R_{min}/2$ and ε. This approach converts the two-dimensional para-

DOI: 10.1021/acs.chemrev.6b00440
Chem. Rev. 2017, 117, 1564−1686

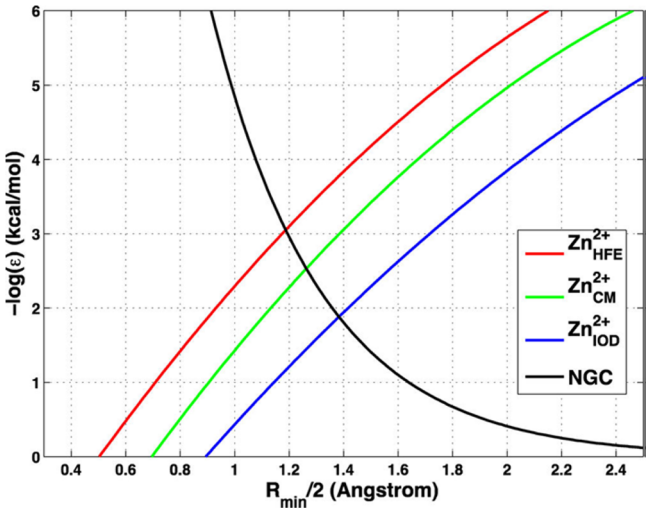

Figure 25. Determination of the three parameter sets for the Zn^{2+} ion in TIP3P. Reprinted with permission from ref 390. Copyright 2013 American Chemical Society.

metrization problem (via scanning $R_{min}/2$ and ε at the same time) into a one-dimensional problem (only scan $R_{min}/2$, while the ε values are calculated from $R_{min}/2$ according to the NGC). Moreover, parameters determined using this technique satisfy the two trends described above. Meanwhile, the final determined $R_{min}/2$ values based on the NGC were also very close to theoretically estimated VDW radii, further supporting this overall strategy. In addition, the final parameters evaluated in this manner showed excellent transferability when applied to ion-pair solutions,[510] further demonstrating the strength of this approach.

3.7. Limitations of the 12-6 Lennard-Jones Model

The 12-6 LJ nonbonded model remains a fast and practical way to simulate ions using classical force fields. Ramaniah et al. studied K^+ in aqueous solution using the Car−Parrinello MD method (CPMD) in 1999.[528] The BLYP functional was used for the system containing a K^+ ion and 59 water molecules. In total, 0.168 ps of equilibration and 1.98 ps of sampling were performed in the NVE ensemble. Good agreement between the CPMD and classical MD simulations was obtained for the structural properties of aqueous K^+, validating in part the classical representation of the K^+ ion. Moreover, it has also shown that it is possible to simultaneously simulate two or more experimental properties for some of the monovalent ions (e.g., Na^+, K^+, Rb^+, Cs^+) using the 12-6 LJ nonbonded model.[510] Even so, akin to the situation for unpolarized water models where it remains a challenge to reproduce various experimental properties, it also remains for the classical nonbonded model of ions.

3.7.1. Combining Rule Approximations. There are various combining rules that are employed with the LJ equation. These combining rules are based on empirical relationships or on approximate theoretical derivations.[446,529−537] For example, the Lorentz combining rules are based on the hard sphere approximation.[529] Because ion parameters are usually designed for aqueous phase-single ion systems, it is a challenge to accurately simulate VDW interactions inside mixed systems based on the single particle LJ parameters and combining rules coupled with the two-body potential. For example, the LJ parameters generated directly on the basis of combining rules can yield erratic results when simulating counterions at high concentrations, and this can be solved by refitting the LJ parameters between a cation and anion (which is equivalent to using modified combining rules), or via the charge scaling technique introduced in section 3.9.

Fyta and Netz found that the Kirkwood−Buff integrals of some ion pairs were hard to reproduce simply by using the LB combining rules with ion parameters based on single-ion properties.[538] This is because the LB combining rules give a smaller C_{12} for the smaller alkali metal−halides (e.g., NaF), while a bigger C_{12} for the larger alkali−halide pairs (e.g., CsCl). They introduced scaling factors into the LB combining rules for the alkali metal-halide LJ parameters, which allowed them to reproduce the Kirkwood−Buff integrals.

Luo and Roux have shown the LJ parameters based on LB combining rules failed to reproduce the osmotic pressure of high concentration solutions, and they successfully refitted the LJ parameters between the cations Na^+, K^+, and the anion Cl^- to reproduce osmotic pressure up to solubility limits (see Figure 26).[539] Furthermore, the inaccuracy of the combining rules for highly concentrated solutions exists not only for the nonbonded model, but also for other models including the cationic dummy atom model (CDAM) and polarizable models. Related discussions can be found in section 5.1 and section 6.

3.7.2. Influence of the Water Model. Moreover, the water model, which was used to do the original parametrization work, is another factor that influences the overall quality of the ion parameters. Joung and Cheatham performed an investigation on their previously developed parameters (which were obtained by fitting to experimental HFE, LE, and LC values) to

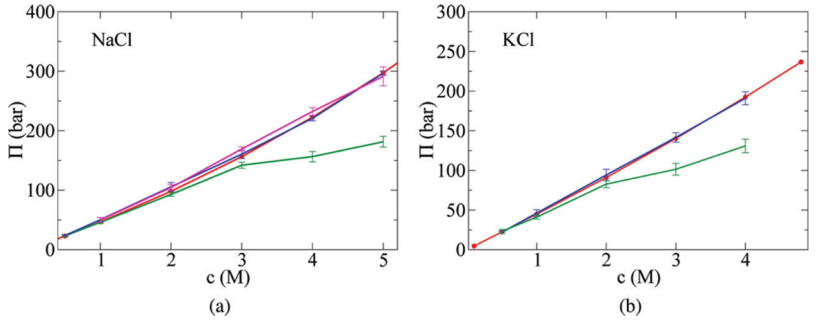

Figure 26. Osmotic pressure as a function of the NaCl (a) or KCl (b) salt concentration. The red line is the experimental values; green line is obtained from MD simulations with the LB combination rules; blue line and magenta line are from simulations with adjusted R_{min} LJ parameters using NBFIX. In panel a, the blue line is the original Na^+ (1) from ref 540, and the magenta line is the reparametrized Na^+ (2) from ref 541. The error bars are calculated from 10 separate trajectories of 1 ns. Reprinted with permission from ref 539. Copyright 2010 American Chemical Society.

DOI: 10.1021/acs.chemrev.6b00440
Chem. Rev. 2017, 117, 1564−1686

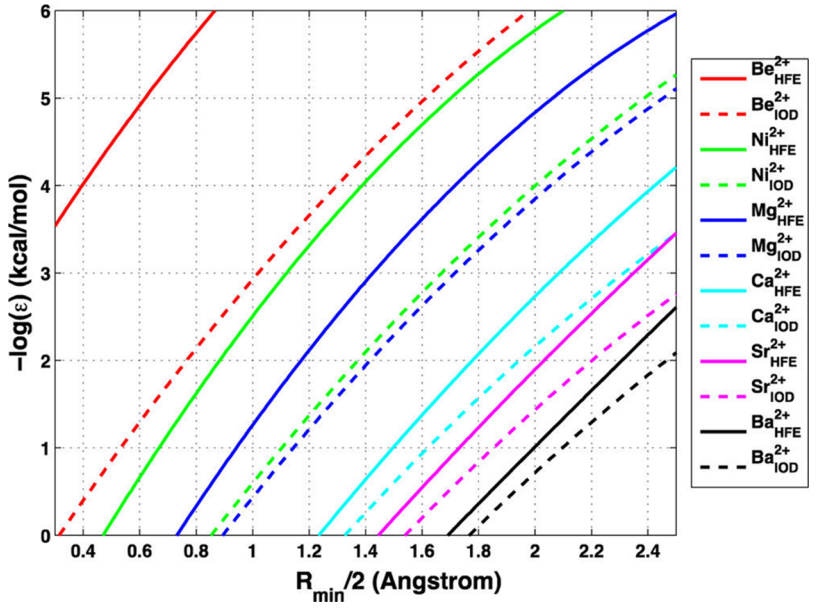

Figure 27. HFE and IOD fitting curves of six representative divalent metal ions using TIP3P water model. Reprinted with permission from ref 390. Copyright 2013 American Chemical Society.

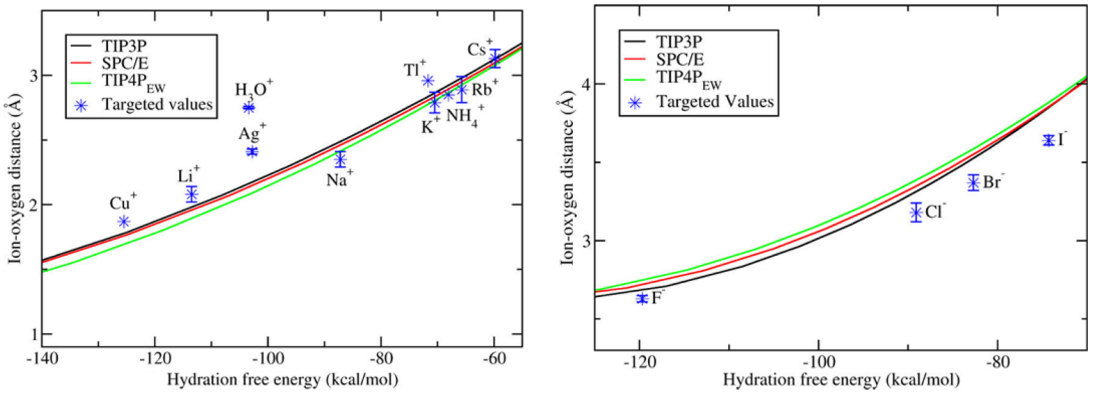

Figure 28. Fitting curves between the HFE and IOD values for the positive (left) and negative (right) monovalent ions with three water models together with the targeted values of the ions investigated in the work of Li et al.[510] Reprinted with permission from ref 510. Copyright 2015 American Chemical Society.

reproduce several experimental solution properties such as solubility, activity coefficients, diffusion coefficients, association constants, and residence time of atomic pairs.[542] They reached the conclusion that the water model has a significant influence on the reliability of the ion force field; therefore, concomitantly developing a reliable water model is very important. They also found that the SPC/E and TIP4P$_{EW}$ water models were preferred over the TIP3P water model to simulate solutions with high salt concentrations. Moreover, the nature of the ion−ion interaction is crucial to reproduce solution properties such as cation−anion residence time, association constant, solubility, etc.

Note that there are water model-independent ion parameters available including those from Peng et al. (9-6 LJ model)[499] and Mao and Pappu (hard-sphere model and 12-6 LJ model)[505] where the parameters were fit for crystalline properties. These parameters could be a choice if the water−ion parameters coupling issue can be ignored in the particular application.

3.7.3. Limitations of the 12-6 Lennard-Jones Potential for Ions. Li et al. observed that it is difficult (and in some cases likely impossible) to find LJ parameters that simultaneously reproduce experimental HFE and IOD values for the divalent and higher-charged metal ions in PME-based simulations.[390,391] Figure 27 showed that it is impossible to simultaneously obtain a LJ parameter combination to reproduce both the HFE and the IOD values of these divalent ions. Moreover, with increasing ion radii, the error of the 12-6 model decreases (the HFE and IOD fitting curves are the closest for the biggest ion, Ba^{2+}). It is possible to reproduce both properties simultaneously for some monovalent cations (including Na^+, K^+, Rb^+, Cs^+), while for cations that can strongly polarize the surrounding water molecules (like Li^+, Ag^+, Tl^+) difficulties arise (see Figure 28, left panel). Meanwhile, as shown in the right panel of Figure 28, it is also hard to reproduce both properties simultaneously for halide ions due to the charge hydration asymmetry.[510] Generally, it was found that the error of the 12-6 LJ nonbonded model is approximately proportional to the square charge of the metal ion (see Figure 29).[510]

These drawbacks of the 12-6 LJ nonbonded model leads to fine-tuning or refitting the parameters to meet different demands in a simulation. Generally, because most of the parametrization was performed to reproduce structural (e.g.,

DOI: 10.1021/acs.chemrev.6b00440
Chem. Rev. 2017, 117, 1564−1686

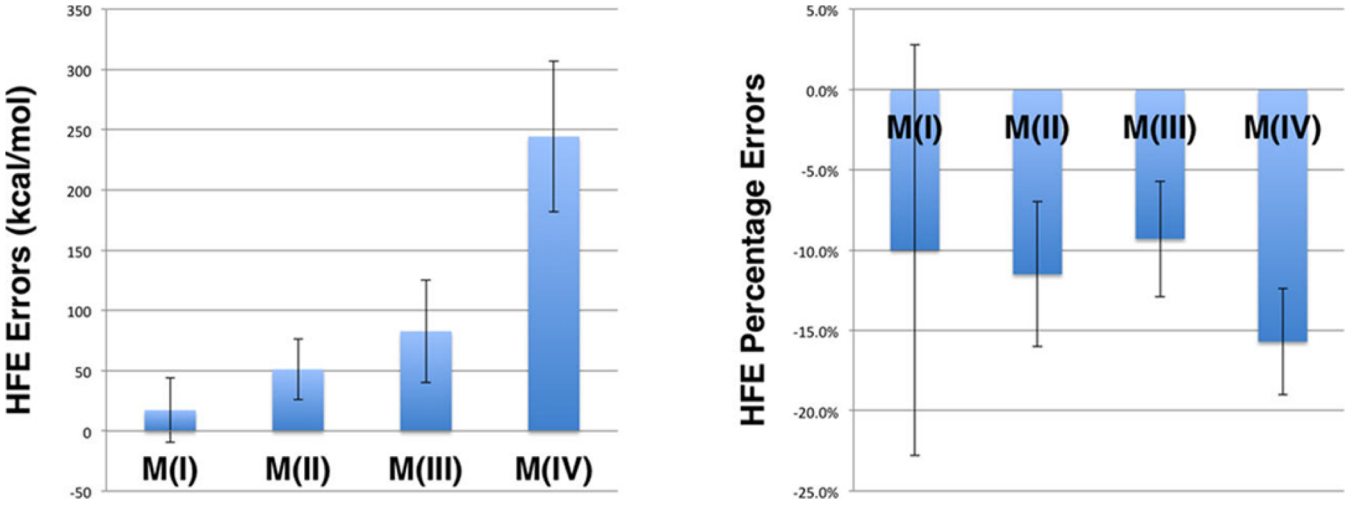

Figure 29. HFE absolute errors (left) and percentage errors (right) for the IOD parameter sets for the mono-, di-, tri-, and tetravalent cations in the TIP3P water model. The ratio is roughly 1.0:3.0:4.8:14.2 for the errors in the HFE values for the mono-, di-, tri-, and tetravalent cations. This agreed well with the ion-induced dipole interaction (eq 59) that predicts that strength of the ion-induced dipole is approximately proportional to the square of the ion's charge (ratio of $1^2:2^2:3^2:4^2$). Reprinted with permission from ref 510. Copyright 2015 American Chemical Society.

IOD, LC, etc.), thermodynamic (e.g., HFE, LE, etc.), and microscopic (e.g., monohydrate interaction energy) properties, the parameters underperform in reproducing kinetic (e.g., exchange rate, activation energy) or macroscopic properties (e.g., osmotic pressure). Instead of changing the two parameters in the LJ equation simultaneously, researchers tend to fine-tune one specific parameter (e.g., $R_{min}/2$, σ, C_6). Generally, larger adjustments are needed for the highly charged ions, for which the 12-6 LJ nonbonded model yields its most significant errors.

Allnér et al. parametrized the Mg^{2+} ion by adjusting the C_6 value to reproduce the experimental exchange rate of its first solvation shell water molecules.[543] They refitted the parameters because previous Mg^{2+} parameters gave Mg^{2+}−water exchange rates several orders of magnitude smaller than the experimental value. The potential of mean force (PMF) between the Mg^{2+} and oxygen atom in water was calculated, which was coupled with transition state theory to estimate the exchange rate. Tests were carried out for Mg^{2+} binding to a monophosphate model system and Mg^{2+} binding to the RNA purine riboswitch add A-riboswitch.[543] The parameters generated by these authors showed improved performance in the reproduction of kinetic properties.

Yoo and Aksimentiev parametrized the Li^+, Na^+, K^+, and Mg^{2+} ions for nucleic acid systems to reproduce the experimental values for osmotic coefficients.[544] Available parameters were unable to reproduce the arrangement and inner pressure of a DNA array consists of 64 parallel duplex DNA. Multiple LJ σ parameters involving nonbonded interactions were adjusted (see Figure 30), and the dipoles of the six coordinated water molecules to the Mg^{2+} ion (still represented by the nonbonded model) were enlarged by 1 D to follow the results of the AMOEBA polarizable force field. With these modifications, they were better able to reproduce the experimental osmotic coefficients and DNA array properties. Venable et al. also revised the LJ radii for the Na^+ ion and other organic groups to reproduce experimental osmotic pressures in sodium acetate and electrophoretic results on vesicles of palmitoyl-oleoylphosphatidylcholine.[545] Even with only small adjustments (changing the LJ radii by only 0.02−0.12 Å), the

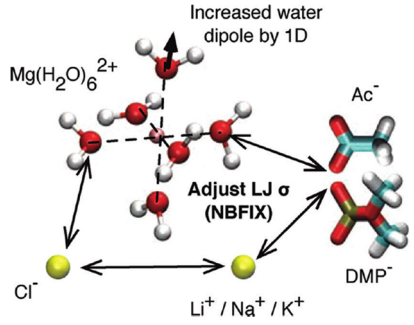

Figure 30. Illustration of the reparametrization scheme used in the work of Yoo and Aksimentiev.[544] Oxygen is colored in red, magnesium in pink, carbon in cyan, phosphorus in tan, hydrogen in white, and salt ions in yellow. Reprinted with permission from ref 544. Copyright 2012 American Chemical Society.

new parameter set alleviated the issue of Na^+-lipid overbinding and increased the surface area by 5−10% per lipid.

Torras and Aleman parametrized the Cu^+, Cu^{2+}, and Zn^{2+} ions in acetonitrile using the 12-6 LJ potential in conjunction with Ewald sums to estimate long-range electrostatic interactions.[546] The parametrization targets were experimental solvation free energies, ion−N distance at the first peak of the RDF, and the CN value of the first solvation shell. The TI method combined with MD simulations was used to obtain the solvation free energy. To reproduce the experimental solvation free energy, the ion−N distance was underestimated about 0.21, 0.28, and 0.12 Å for Cu^+, Cu^{2+}, and Zn^{2+}, respectively, when compared to the experimental values. They needed to increase ε to rather large values (63.0, 285.0, and 410.0 kcal/mol for Cu^+, Zn^{2+}, and Cu^{2+}, respectively) and keep the $R_{min}/2$ values relatively small (0.230, 0.4565, and 0.413 Å for Cu^+, Zn^{2+}, and Cu^{2+} ions, respectively) to reproduce the experimental HFEs.

de Araujo et al. parametrized the 12-6 LJ potential for Cd^{2+} and Pb^{2+} to reproduce the experimental HFE, experimental, and QM/MM calculated RDF and CN values.[547] The HFE values were evaluated using the linear interaction energy (LIE) method. The parameters were optimized using the TIP3P water

DOI: 10.1021/acs.chemrev.6b00440
Chem. Rev. 2017, 117, 1564−1686

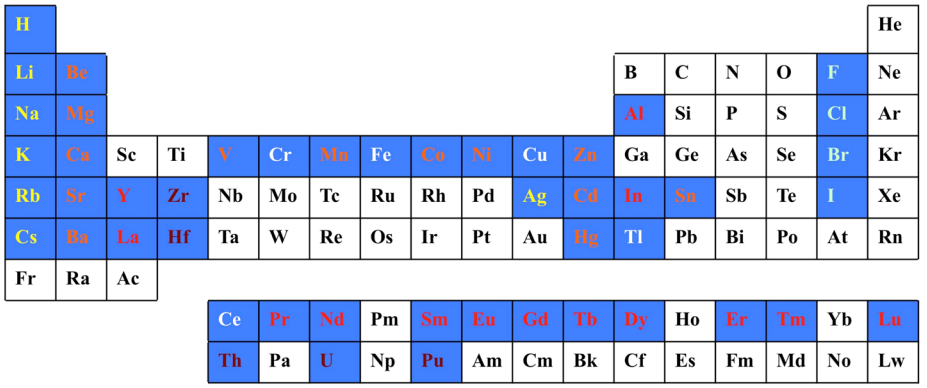

Figure 31. Atomic ions that were parametrized for the 12-6-4 model by Li, Merz, and co-workers.[391,510,549] These ions are shown with a blue background. The monovalent anions, monovalent cations, divalent cations, trivalent cations, and tetravalent cations are shown in light green, yellow, orange, red, and dark red, respectively. The ions that have multiple oxidation states are shown in white, which are Cr^{2+}/Cr^{3+}, Fe^{2+}/Fe^{3+}, Cu^{+}/Cu^{2+}, Ce^{3+}/Ce^{4+}, and Tl^{+}/Tl^{3+}. Besides these atomic ions, the H_3O^+ and NH_4^+ ions were also parametrized in their work. Reprinted with permission from the Ph.D. dissertation of Li.[511] Copyright 2016 Pengfei Li.

model and were subsequently tested in another three water models (SPC, SPC/E, and TIP4P). The calculated HFE values have errors in the range of 57.04−253.21 kJ/mol (~13.63 to ~60.52 kcal/mol) when compared to available experimental values. The four-site TIP4P water model had the largest error relative to the other three three-site water models. The results showed that Cd^{2+} has a smaller diffusion coefficient and a longer MRT in its first solvation shell when compared to the Pd^{2+} ion.

Williams et al. created 12-6 LJ parameters for the Fe^{3+}-ethylenediamine complex with H_2O, Cl^-, TcO_4^-, and SO_4^{2-} ions.[548] The resultant LJ parameters showed limited transferability for the highly charged Fe^{3+} ion. They optimized the LJ parameters for different ligand types via reproduction gas-phase interaction energies from DFT calculations. The final optimized σ values for the Fe^{3+} ion for different ligands were 1.465 Å (for O in H_2O), 1.820 Å (for O in SO_4^{2-}), 2.600 Å (for O in TcO_4^-), 3.095 Å (for Cl^-), and 1.700 Å (for other atom types), whose variation arises due to different polarization magnitudes between Fe^{3+} and its ligands. PMF profiles generated using the umbrella sampling method were used to estimate the affinities between the complex and its ligands. The calculated results agreed well with the ligand exchange mechanism proposed from experiments. Moreover, they found that both the relative solvation enthalpy and entropy are important for the ligand exchange process.

3.8. 12-6-4 Nonbonded Model

Li and Merz proposed a 12-6-4 LJ-type nonbonded model in 2014.[549] Overall, they parametrized the 12-6-4 model for various ions from monovalent to tetravalent for three widely used water models (see Figure 31).[391,510,549] It was based on the consideration that classical force fields do not explicitly consider the charge-induced dipole and dipole−induced dipole interactions (see Figure 32), and that the former term is proportional to r^{-4} (the latter term is also included in the r^{-4} term akin to how the dipole−dipole interaction is present in the point charge model). Hence, a C_4 term was used to represent the ion-induced dipole interaction and was added to the standard 12-6 LJ equation (see eq 58). It was shown that after carefully designing the parameters, both the experimental HFE and IOD values could be simulated at the same time, even for the halides and highly charged ions. Through a consideration of the physical origin of the C_4 term (see eq 59 for the charge-induced dipole interaction energy and eq 60 for the C_4 term), a different combining rule was proposed (see eq 61), and it gave excellent transferability when applied to various systems (such as proteins, ionic solutions, and DNA systems).[391,510,549] For example, in the work of Li et al., the 12-6-4 model showed improvement over all 12-6 models tested in reproducing the KBIs of ionic-pair solutions.[510] Panteva et al. found that the 12-6-4 model was an improvement over 12-6 models in simulating the Mg^{2+} ion in aqueous solution.[550] They also observed that the 12-6-4 model of Mg^{2+} with the SPC/E water model largely reproduced all relevant experimental properties (such as RDF, HFE, exchange barrier of first solvation shell water, diffusion constant, etc.) simultaneously. This independently validated that the 12-6-4 model, which provides a better physical description than the 12-6 LJ model, was capable of simultaneously reproducing various properties.

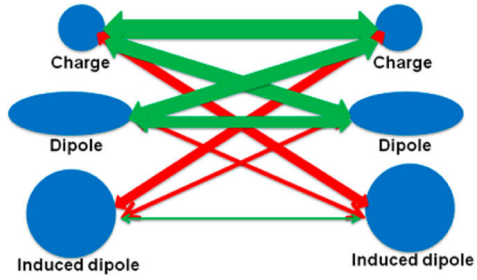

Figure 32. Scheme representing intermolecular interactions: the green double-headed arrow and red double-headed arrow represent the interactions, which are included and not included in the 12-6 nonbonded model, respectively. Reprinted with permission from ref 549. Copyright 2014 American Chemical Society.

DOI: 10.1021/acs.chemrev.6b00440
Chem. Rev. 2017, 117, 1564−1686

Table 2. Comparison of DFT, Polarizable, and 12-6-4 Models for Simulating the Mg^{2+} Ion in the Aqueous System[a]

model	IOD (Å)	CN	exchange rate (s^{-1})	diffusion coefficient (10^{-5} cm^2/s)	HFE (kcal/mol)
CPMD/PBE[551]	2.13	6	$<3.2 \times 10^{11}$		
SWN4-NDP[552]	2.06	6		0.82	−447.2
AMOEBA-J[553]	2.07	6	4.4×10^{9}	0.3	−431.1 ± 2.9
AMOEBA-P[554]	2.08	6	$<2.0 \times 10^{8}$		
FQ-DCT[555]	2.06	6		0.34 ± 0.4	−461.6
12-6-4 TIP3P	2.09[549]	6[549]	5.2×10^{7}[550]	0.813 ± 0.059[550]	−436.6[549]
12-6-4 SPC/E	2.09[549]	6[549]	5.5×10^{5}[550]	0.748 ± 0.044[550]	−436.7[549]
12-6-4 $TIP4P_{EW}$	2.09[549]	6[549]	1.1×10^{7}[550]	0.801 ± 0.052[550]	−437.9[549]
experiment	2.09 ± 0.04[556]	6[556]	$(6.7 \pm 0.2) \times 10^{5}$[557]	0.706[558]	−437.4[502]

[a]The two AMOEBA models were differentiated by the first character of the names of the first authors. The exchange rate in the CPMD/PBE simulation is calculated on the basis that water exchange was not observed under 3.1 ps simulation. The exchange rate in the AMOEBA-J simulation is calculated on the basis of the relaxation time of the first solvation shell water molecules as 228 ps. The exchange rate of the AMOEBA-P simulation is calculated on the basis that water exchange was not observed under 5 ns simulation.

$$U(r_{ij}) = \frac{Q_iQ_j}{4\pi\varepsilon_0 r_{ij}} + \frac{A_{ij}}{r_{ij}^{12}} + \frac{B_{ij}}{r_{ij}^{6}} + \frac{C_{ij}}{r_{ij}^{4}} = \frac{Q_iQ_j}{4\pi\varepsilon_0 r_{ij}} + \varepsilon_{ij}\left[\left(\frac{R_{\min,ij}}{r_{ij}}\right)^{12} - 2\left(\frac{R_{\min,ij}}{r_{ij}}\right)^{6}\right] + \frac{C_{ij}}{r_{ij}^{4}} = \frac{Q_iQ_j}{4\pi\varepsilon_0 r_{ij}} + \varepsilon_{ij}\left[\left(\frac{R_{\min,ij}}{r_{ij}}\right)^{12} - 2\left(\frac{R_{\min,ij}}{r_{ij}}\right)^{6} - 2\kappa R_{\min,ij}^{2}\left(\frac{R_{\min,ij}}{r_{ij}}\right)^{4}\right] \text{ with } \kappa = \frac{C_{ij}}{B_{ij}} \quad (58)$$

$$U_{q-\alpha_0} \approx -\frac{1}{2}\alpha_0\left(\frac{q}{4\pi\varepsilon_0\varepsilon_r r^2}\right)^2 \cos\theta \quad (59)$$

$$C_4 \approx -\frac{1}{2}\alpha_0\left(\frac{q}{4\pi\varepsilon_0\varepsilon_r}\right)^2 \cos\theta \quad (60)$$

$$C_4(\text{atom type}) = \frac{C_4(H_2O)}{\alpha_0(H_2O)} \times \alpha_0(\text{atom type}) \quad (61)$$

In Table 2, we compare the 12-6-4 models to polarizable and the PBE functional for the simulation of aqueous Mg^{2+} system. It was shown that the 12-6-4 models outperform all of the other models listed. This may due to that the 12-6-4 potential better encapsulates the physics associated with Mg^{2+} interacting with water molecules.

Recently, Panteva et al. studied the divalent metal ion−nucleic acid systems employing the 12-6-4 model.[559] They refit the original 12-6-4 potential to best reproduce binding free energies between different divalent metal ions (Mg^{2+}, Mn^{2+}, Zn^{2+}, and Cd^{2+}) with different nucleic acid sites and applied these parameters to the study of metal ion transfer in the hammerhead ribozyme catalytic reaction.

3.9. Charge Scaling Technique

3.9.1. Method Introduction. Unpolarized force fields use simple point charges with VDW spheres that do not afford a good description of short-range and long-range polarization effects (the long-range effect could also be called the charge screening effect). For example, it is hard to reproduce the dielectric constants of organic solvents and water, which results in errors in the description of the long-range interaction between solvated groups. To address this problem, the charge scaling (CS) technique has been developed to simulate long-range screening effects.

Leontyev and Stuchebrukhov created the molecular dynamics electronic continuum (MDEC) method for organic molecules,[560] water,[561] and ionized groups.[562] Widely used water models including TIP3P (with a dipole moment of 2.35 D),[449] SPC/E (2.35 D),[563] TIP4P/2005 (2.305 D),[564] $TIP4P_{EW}$ (2.32 D),[565] and TIP5P (2.29 D)[566] all underestimate the dipole moment of water, when compared to experiment and ab initio MD simulations, which place the dipole moment of water in the liquid phase around ∼3.0 D.[561] Leontyev and Stuchebrukhov explained this by noting that the water dipole moment in the typical unpolarized water models (∼2.3 D) is scaled by a factor of $1/\sqrt{\varepsilon_{el}}$ due to the screening effect of the electronic polarization, where ε_{el} is the high-frequency (electronic) dielectric constant of water, and in their work they used a value from experiment (ε_∞ = 1.78, where ε_∞ is the optical dielectric constant of water) as ε_{el} for charge scaling.[561] They also proposed that ionized groups (e.g., ionized groups in amino acids, ions) should be scaled down by ∼0.7, while this factor ranges from ∼0.7 to ∼0.9 for neutral groups.[567] Furthermore, they also developed a fluctuating charge type water model that is compatible with widely used unpolarized force fields such as CHARMM and AMBER, based on the charge scaling concept.[568] Other than immediately responding to the change of environment, their model represents the water dipole response to environmental changes in a mean-field manner. Even though their model does not simulate the out-of-plane polarizability of water, it does simulate the different extents of the polarization for water molecules coordinated to ions, around protein surfaces, and in the bulk phase. This model can be viewed as a bridge between unpolarized and polarized force fields.

3.9.2. Advantages. The CS technique retains the simulation performance of unpolarized force fields because no additional terms added, while at the same time it better models a number of properties than unscaled unpolarized force fields and even some polarizable force fields (sometimes a reparametrization of the LJ parameters is needed). For example, the CS unpolarized force field reproduces the PMF between one cation and one anion in benzene solution calculated based on the Drude oscillator model.[567] It also reproduces the dielectric constants of alkanes, which are hard to reproduce by using unscaled unpolarized force fields.[567] Even scaling down charges will underestimate HFEs of ions; it was noted that by

DOI: 10.1021/acs.chemrev.6b00440
Chem. Rev. 2017, 117, 1564−1686

adding up the electronic free energy term, which usually accounts for more than 50% of the total HFE, the experimental HFEs of polyatomic ions can be well reproduced using this model.[567] Other studies have shown that the CS technique allows unpolarized force fields to better simulate electric conductivity,[569] dependency of the water diffusion constant on salt concentration,[570] structures of highly concentrated ionic solutions,[571] and even interfacial affinities at the water/decane interface.[572] Herein, we use the water diffusion dependency on salt concentration as an example to illustrate the potential of this method.

Researchers have found that it is challenging to reproduce the increase in the water diffusion coefficient along with the concentrations of ionic solutions with salts that have low charge densities (e.g., CsI), while unpolarized force fields and even some polarizable models predict a decreasing trend as the salt concentration increases. Studies have shown that the charge-transfer effect is important in predicting these trends and that the CS technique can be used to solve this issue.

Kim et al. have studied water diffusion in salt solutions using both MD and NMR techniques.[573] They found that both unpolarized models (4 total) and polarizable models (the SWM4-DP and AMOEBA models) could not reproduce the increase of the water diffusion constant concomitant with the CsI salt concentration. Ding et al. have shown that ab initio MD simulation (revPBE DFT functional[574] was used in their work) could qualitatively reproduce the different dependencies of water diffusion constant on the salt concentrations of NaCl and CsI.[575] They noted that ab initio MD simulation can simulate the dynamic heterogeneity of waters, which is essential in reproducing these trends.

Kann and Skinner have studied ionic solutions using a CS unpolarized model.[570] They used the factor $\sqrt{\frac{\varepsilon_{sim}}{\varepsilon_{exp}}}$ (where ε_{sim} and ε_{exp} are the simulated and experimental static dielectric constants of water) to scale the ions' charges. This kind of scaling well reproduces ionic interactions in the aqueous phase since $\frac{q_{eff}^2}{\varepsilon_{sim} r} = \frac{q^2}{\varepsilon_{exp} r}$. They used the ion parameters from Mao and Pappu[505] because these parameters were designed to reproduce the lattice energies and interionic distances, and therefore are not dependent on the water model employed. When their scaling model was used with the TIP4P/2005[564] or E3B[576] water model, it reproduced the trend of the water diffusion constant in different concentrated CsI solutions qualitatively. Moreover, the CS ion model with the E3B water model reproduced the reduced mass densities, first peaks of the ion-oxygen RDFs, and diffusion coefficients of ions in various salt solutions. Meanwhile, they discussed that the CS technique may not be well suited to more complicated systems with multiple dielectric environments, and they also noted that the CS technique needs further modification to accurately predict thermodynamic properties.

Li and Wang developed unpolarized models for Na^+, K^+, Cl^-, and Br^- ions,[577,578] where a different potential function, other than the standard 12-6 LJ nonbonded model, was used. The adaptive force matching method was employed to reproduce MP2 calculated properties. In their model, these ions have charges other than their formal charges: with cations they have a charge of +0.804e, while anions all have a charge of −0.804e, respectively. These parameters reproduced several properties including salt concentration-dependent water diffusion constant trends. Yao et al. have simulated NaCl and KCl solutions using the FQ-DCT model (see section 6.4.2).[579] It was found the FQ-DCT model, which incorporates charge-transfer effect in its formulation, qualitatively reproduced the slightly increasing trend of the water diffusion constant with the KCl salt concentration. They discussed that explicit consideration of the charge-transfer effect is important to simulate the different dependencies of water diffusion constant with respect to the concentrations of the Na^+- and K^+-containing salt solutions.

3.9.3. Limits. Even though encouraging results were obtained using charge scaled unpolarized force fields, this model's success is limited and likely will not replace polarizable force fields, which consider polarization effects explicitly. This is mainly because that the charge scaled method is based on an average point of view. Even though it yields excellent performance for the prediction of some statistical properties, it fails to represent the microscopic interactions in the local region.

For example, Schroder compared a CS unpolarized force field with the DO polarizable model for ionic liquids by investigating structural and dynamical properties.[580] He found that the CS unpolarized force field cannot reproduce the broad range of dipolar distributions simulated by the polarizable force field. Furthermore, inconsistencies in the computed RDFs exist within an 8 Å range, but diminish at longer distances. Schroder also noted that the polarization effects of charge−dipole and dipole−dipole have r^{-3} and r^{-6} dependencies, respectively, while the charge scaled unpolarized force field has a r^{-1} dependence. However, at the macroscopic level, he found that the CS method reproduced the frequency-dependent generalized dielectric constant via the application of a scaling factor of $(S^{eff})^{-2}$ (herein S^{eff} is the charge scaling factor), and this factor can be explained using the electronic continuum model.

Pegado et al. have simulated $NaSO_4$ solutions using a CS unpolarized force field and the DO polarizable force field.[581] Experimental and ab initio MD results were used as reference to evaluate the performance of these force field models. They found that the CS model has a comparable solvation structure, while the DO model predicted an overstructured solvation shell, when compared to the ab initio MD results. They also found the CS model underestimated ion association while the DO model overestimated ion association, when compared to experimental results. Vazdar et al. have found that a CS unpolarized model offered consistent results with experiment and polarizable simulations about the interfacial affinities of halide ions at a water/decane interface (water and decane have electronic dielectric constants of 1.78 and 2, respectively), while simulations based on unscaled model yielded incorrect behavior. However, the unpolarized model overestimates the surface affinities of these ions at the water/vapor interface where the electronic dielectric constant jump is too precipitious.[572]

3.10. Ion Models in Coarse-Grained Force Fields

Coarse-grained (CG) simulation has become popular in recent years to model macromolecules due to its improved computational performance relative to traditional all-atom simulations. The smallest units in CG models are groups/beads rather than atoms. CG force fields generally use similar functional forms (e.g., bond, angle, dihedral, electrostatic, and VDW terms) as all-atom force field models. The united-atom model is an early example of CG force fields, where CH, CH_2, and CH_3 groups were treated as "united" atoms.[392] Different CG models have

DOI: 10.1021/acs.chemrev.6b00440
Chem. Rev. 2017, 117, 1564−1686

different coarse-graining levels, but to retain a correct physical representation certain criteria should be met during the coarse-graining process.[151] The number of particles in the system decreases along with the increase in the coarse-graining level, and CG models can usually employ much larger simulation time-steps (e.g., a 20−40 fs time-step is used with the MARTINI force field,[152,582] as compared to the 1−2 fs time-step usually used in all-atom simulations). All of these savings dramatically increase the simulation time scale of CG models. Furthermore, it is also possible to build a QM/MM/CG multiscale model to increase the speed of QM/MM simulations.[583] The nonbonded model of ions is usually employed in CG force fields. Ion modeling in CG force fields usually treats the atomic ion with its first solvation sphere as a united CG particle.[152,582,584] Because atomic ions are independent from other particles while CG and all-atom models use similar functional forms, CG models of ions can be used both in CG models and in cases where all-atom models are used to represent other features of the system of interest.[585] Moreover, an all-atom ion model can be used with CG representations for other groups.[586] However, it was noted that because it is still challenging to simulate atomic ions accurately in the all-atom force field model, the CG model affords only qualitative accuracy.[582]

Singh et al. simulated a DNA fragment using MD simulations with and without hydrated counterions in 1985.[585] The AMBER ff84 force field[392] was used to model DNA, while a 12-6 LJ nonbonded model with $R_{min}/2$ = 5.0 Å, ε = 0.1 kcal/mol, and a 131 amu mass was used to model the hydrated Na^+ ion to mimic the hydration effect and prevent contact ion pair formation with the negatively charged phosphate groups. Results showed that even though the average structures of the two simulations were similar, the simulation with the counterions predicted a better helical structure when compared to experiment.

Marrink et al. developed a CG force field for lipids (a prototype of the MARTINI force field), in which Na^+ and Cl^- ions were also parametrized.[584] The hydrated Na^+ or Cl^- ions were treated as a "Q" type CG bead and further clarified as a "da" subtype group (a group with both options of acting as a hydrogen-bond donor and acceptor). The interaction between the ions and their environments was represented by a 12-6 LJ model in which the Na^+ and Cl^- ions were treated with the same VDW parameters. Partial charges of the hydrated Na^+ and Cl^- ions, which were optimized to reproduce the pair distribution functions from all-atom simulations, were determined to be +0.7e and −0.7e, respectively. The authors discussed that these reduced partial charges simulate the charge screening effect of the first solvation shell. Meanwhile, a relative dielectric constant ε_r = 20 was used to calculate the electrostatic interaction in the force field to include explicit screening. Because of the short-range nature of electrostatic interactions in the model, the authors noted that it is limited to modeling ionic solutions with moderate to high concentrations. In the MARTINI force field, Marrink et al. used formal charges for the CG beads of hydrated Na^+ and Cl^- ions, together with a reduced relative dielectric constant of ε_r = 15 for the electrostatic calculation in their force field.[582] These two effects counteract each other and yield reasonable agreement with CNs for ion pairs and ion−solvent simulated using an all-atom model.

Khalili et al. created Ca^{2+} parameters for ion−amino acid interactions in the united residue (UNRES) CG force field.[586] The Ca^{2+} ion was represented independently rather than as a hydrated ion. The functional forms for ASP/GLU-Ca^{2+}, ASN/GLN-Ca^{2+}, and normal side chain-Ca^{2+} interactions were treated differently on the basis of the natures of their interactions, while the Ca^{2+}−Ca^{2+} interaction was described using a 12-6 LJ nonbonded model. The parameters were fitted to the restricted free energy surfaces, which were obtained using RHF/6-31G** calculations and with a consideration of the degrees of freedom lost during the coarse-graining process. Calculations showed the CG model is effective in predicting the positions of Ca^{2+} ions in proteins.

4. CLASSICAL MODELING OF METAL IONS: THE BONDED MODEL

4.1. Functional Form and Early Metalloprotein Modeling

4.1.1. Functional Form. The modern bonded model (see eq 62) has the following form: it consists of bond, angle, and dihedral terms for the bonded interaction, with addition of the electrostatic (fourth term) and VDW (fifth term) for the nonbonded interactions. The force field contains a number of parameters to be determined: the k_r (bond force constant) and r_{eq} (equilibrium bond length) for each bond type; k_θ (angle force constant) and θ_{eq} (equilibrium angle value) for each possible angle type; V_n (torsion barrier), n (periodicity), and γ (phase) for each possible dihedral type; partial charge q for each atom; and VDW parameters A_{ij} and B_{ij} for each atom pair type (these parameters can be calculated on the basis of $R_{min}/2$ and ε for each atom type through various combining rules, as discussed in the nonbonded model approach section).

$$U = \sum_{\text{bonds}} k_r(r - r_{eq})^2 + \sum_{\text{angles}} k_\theta(\theta - \theta_{eq})^2 + \sum_{\text{torsions}} \sum_{n=1,2,3,4} V_n[1 + \cos(n\phi - \gamma)] + \sum_{i,j>i}^{N} \left(\frac{q_i q_j}{4\pi\varepsilon_0 r_{ij}} + \frac{A_{ij}}{r_{ij}^{12}} - \frac{B_{ij}}{r_{ij}^{6}} \right) \quad (62)$$

Lifson and co-workers developed the bonded model for different organic molecules and biomolecules in 1960s and 1970s.[388,587−595] Their pioneering force field work facilitated the computer modeling of biomacromolecules.[596] Bixon and Lifson studied the cycloalkanes in 1967.[587] Besides the bonded interactions, only the nonbonded interaction between hydrogen atoms was modeled with an exp-6 representation, while the rest were set to zero. They noted that the dihedral term was the softest term in the energy function and that the conformational strain energy is the most sensitive to the barrier height of the dihedral angles rather than other force constants.

Lifson and Warshel proposed the "consistent force field" (CFF) for cycloalkanes and n-alkanes in 1968.[388] The force field parameters were optimized to best reproduce several experimentally observed values. In this work, they found notable improvements by (1) incorporating the Coulombic term and(2) using a Urey−Bradley function (for 1−3 interactions) and the 12-6 Lennard-Jones equation instead of the exp-6 representation.[388] In 1969, Levitt and Lifson followed up this work by performing the energy minimization on myoglobin and lysozyme using a united atom model, in which each heavy atom and its connected hydrogen atom(s) were represented by one united particle.[597] They used the force field shown in eq 62 without the Coulombic term coupled with a

DOI: 10.1021/acs.chemrev.6b00440
Chem. Rev. 2017, 117, 1564−1686

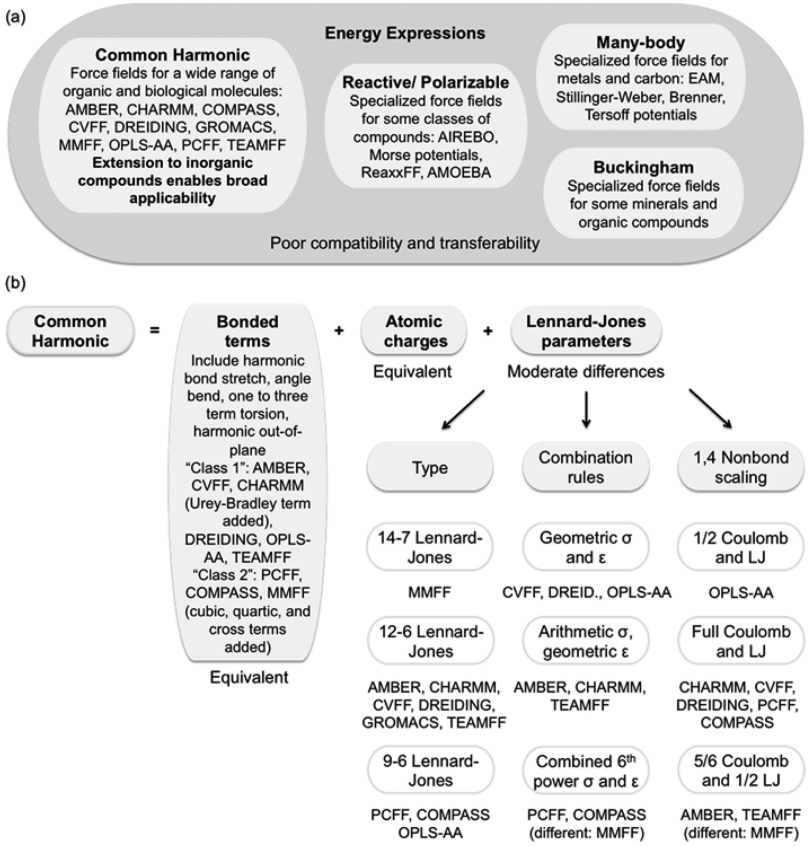

Figure 33. Available force fields and challenges in transferability. (a) Parameters for different energy expressions can hardly processed into a uniform force field for both organic and inorganic components. (b) Harmonic force fields like AMBER, CHARMM, OPLS-AA, and PCFF are similar and contain quality parameters for organic compounds. Bonded terms and atomic charges for newly added compounds are derived in similar manners. Moderate differences in the type of LJ potential, combining rules, and the scaling of nonbonding interactions between 1,4-bonded atoms (1,4 nonbonded scaling) can be overcome by adjustments in $\sigma_{0,ii}$ and $\varepsilon_{0,ii}$ to reproduce the same bulk and interfacial properties. Reprinted with permission from ref 598. Copyright 2013 American Chemical Society.

restraint term to prevent the final structure deviating far away from the experimental structure. Minimizations were performed with a steepest descent algorithm, and different restraint values were investigated. However, they noted that the force field parameters used had limited accuracy and needed further improvement. Extension of this force field to other organic/biological molecules including amides, lactam rings, alkanes, olefins, peptides, and proteins was reported in a series of papers from the Lifson laboratory.[588−592] In the CFF parametrization work on peptides and proteins by Hagler et al. in 1974, the authors found that the 12-6 and 9-6 LJ functional forms worked equally well when combined with the Coulombic term. Moreover, they observed that an explicit hydrogen-bond term was not needed in their model.[591] In subsequent work of Lifson et al., they also observed that hydrogen bonds were well described using a model consisting of an electrostatic term and a VDW interaction term.[595]

Unlike the bonded terms that are localized, the nonbonded terms are long-range and affect a model's ability to accurately reproduce interfacial properties.[598] Atomic charges play a significant role in determining the quality of a force field.[598] To reproduce different properties simultaneously, it is essential to assign chemically reasonable atomic charges and VDW parameters. For example, partial charges represent electronic localization in the system, and VDW radii should be consistent with experimental values and their intrinsic trends, while the ε values should be relatively small due to VDW interactions being intrinsically weak.

To date, eq 62 and its variants (e.g., instead of 12-6 LJ using a 9-6 LJ for the VDW interaction) represent the most widely used form for a classical force field (see Figure 33). Heinz and co-workers developed the INTERFACE force field, which uses the harmonic force field format (represented by the bond and angle terms in eq 62), for a series of material systems such as silicates, metals, apatites, cement minerals, clay minerals, etc.[598] In their work, they discussed that even more sophisticated force fields exist, which usually require more parameters and are less transferable. The harmonic force field form has been parametrized for a wide range of biological and material systems (including AMBER,[392−400] CHARMM,[401−406] OPLS-AA,[407−411] and GROMOS,[599−605] for biologically related systems, while COMPASS,[606,607] CVFF,[608] PCFF,[609] and TraPPE[610] are more materials orientated). Their electrostatic terms usually use the same Coulombic form, but their LJ terms vary to some extent. For example, different VDW potentials, combining rules, and 1-4 nonbonded scaling schemes are used among them (see Figure 33).

4.1.2. Early Work on Metalloprotein Modeling. Karplus, Case, and co-workers pioneered the early classical modeling of metalloproteins focusing on heme proteins.[611−614] Gelin and Karplus performed molecular modeling studies of a hemoglobin in 1977.[611] In this work, they performed a structure minimization and then static analysis based on a

DOI: 10.1021/acs.chemrev.6b00440
Chem. Rev. 2017, 117, 1564−1686

united atom force field. A proposed reaction path for a oxygen transferring from the heme group to surface of the deoxyhemoglobin α chain subunit was presented. On the basis of theoretical calculations and their comparison to experimental data, it was shown how the ligation of the heme group changes its geometry and then induces subunit structural changes. The results indicated that if the subunit is in the deoxy state rather than oxy state, the ligation-induced tertiary structural changes would require more energy.

Case and Karplus performed MD simulations to investigate the binding processes of CO and O_2 to myoglobin.[612] Results from MD simulations based on a diabatic representation (a ligand moves around a rigid protein) highlighted two binding paths. An adiabatic representation (allowing protein relaxation during the simulation) was employed to calculate the binding energy barriers. The calculated barriers, which were obtained from an analysis of the conformational relaxation, yielded qualitative agreement with experiment. Moreover, differences between myoglobin and hemoglobin were discussed in the work.

Following this work, Case and McCammon performed MD simulations exploring how an O_2 molecule enters and exits the heme pocket inside myoglobin.[613] The path was between the distal His and Val residues, while the reaction coordinate was chosen as the distance between the ligand and a "dividing plane" defined by three atoms in the protein. Umbrella sampling was used to compute the potential of mean force (PMF) for the process. The PMF profile predicted a 7 kcal/mol barrier for O_2 exiting the heme pocket, while the potential energy profile showed an energy decrease along the reaction path. These results indicated that entropy played a defining role for the kinetic barrier. The reactive trajectories, which started from snapshots at the top of the barrier, showed that only a small proportion of O_2 molecule recrossed the "dividing plane", suggesting the transition state theory (TST) could be applied to this process.

Subsequently, Kottalam and Case carried out MD simulations to investigate the process of O_2 exiting from the heme pocket of sperm whale myoglobin.[614] Umbrella sampling studies were performed to generate PMF profiles at different temperatures. The rate constants were calculated on the basis of the TST approximation and full MD simulations, respectively. The computed rate constants at room temperature agreed well with the available experimental data. The transmission coefficients computed using the TST approximation were in the range of 0.8−0.9. It is interesting that for lower temperatures (between 180 and 270 K), there are higher activation energies (~5 kcal/mol) than at room temperature (<1 kcal/mol). The authors proposed that this non-Arrhenius behavior may due to a "mechanism" change at different temperatures: the rate-limiting step at low temperatures is governed by the opening of the heme pocket to affect ligand escape, while at higher temperature this barrier is decreased due to protein dynamics and the rate limiting-step is influenced by the frequency at which the ligand can escape along the correct pathway.

4.2. Bond and Angle Parameters

In classical force fields, the bond and angle terms are represented as being independent from the nonbonded terms (electrostatic and VDW). Hence, bond and angle parameters can be transferred between force fields using similar potential function representations. However, many classical force fields include 1-4 nonbonded interactions fully or to some extent (via scaling), thereby coupling the dihedral term to the electrostatic and VDW terms. This then requires that dihedral terms be refit during the parametrization process (as discussed in the dihedral section—Section 4.3—in detail) to ensure a high-quality force field.

The bond and angle terms are represented with harmonic terms in the AMBER,[392−400] CHARMM (with an additional 1-3 harmonic term),[401−406] OPLS-AA,[407−411] GROMOS,[599−605] CVFF,[608] and DREIDING[615] force fields. Higher power terms and cross terms were added to more sophisticated force fields including the MM series (MM2,[51,616] MM3,[51,617−621] and MM4[622−627]), MMFF94,[498,628−633] COMPASS,[606,607] and PCFF.[609] There are a number of ways to obtain parameters: based on experimental information (e.g., vibrational spectra from infrared (IR) or Raman studies), theoretical calculations (e.g., the PES scanning, the *Z*-matrix, and the Seminario methods), or empirical relationships (e.g., Badger's rule).

Even though the Morse potential can represent the anharmonicity of bond vibrations and is generally thought of as a more accurate description for bonded interactions, it has been largely supplanted by the harmonic model for several reasons: (1) only two parameters define a harmonic term (the equilibrium distance and the force constant), while a Morse potential needs three (the equilibrium distance, well depth, and the potential width); (2) most simulations work at equilibrium, which is well represented by a harmonic model, while the Morse potential allows for bond disassociation leading to possible departures from equilibrium; (3) if needed, the anharmonicity of bond vibrations can be incorporated using higher order terms from the Taylor expansion (e.g., by adding the third-order and fourth-order terms).

One basic assumption in force field models of macromolecules is that the parameters from a small representative system can be transferred into much larger systems. Experiment supports this hypothesis that certain bond types (e.g., the C−C single bond between two sp^3 carbon) have similar bond lengths and strengths in different environments. Because of limitations in computational power, macromolecules are usually built up using fragment groups whose parameters were fitted to QM or experimental results. During the parametrization process, the equilibrium bond distances and angle values are usually taken directly from the QM optimized or experimentally determined structures. This is a reasonable approach, but not entirely accurate as equilibrium bond and angle values obtained in this way represent a compromise between various interactions, and hence, likely deviate from the values for the isolated bonds and angles.

Moreover, in experimental spectra and QM calculations, unlike classical force field models, the bonded and nonbonded interactions are not isolated but are coupled together, causing both the Wilson method (see section 4.2.1), the PES scanning method (see section 4.2.2), the *Z*-matrix method (see section 4.2.3), and the Seminario method (see section 4.2.4) to all have issues with double counting. Ideally, it is best to fit bond and angle parameters to various experimental and QM calculated data by "freeing" all degrees of freedom (without any restraints or constraints) in the parameter space. However, this is challenging because too many degrees of freedom are present (discussed in detail in section 4.2.5). There are empirical ways (see section 4.2.7) available to efficiently estimate force field parameters, but the parameters may have limited accuracy. In short, compromises between accuracy and effort are made, and

DOI: 10.1021/acs.chemrev.6b00440
Chem. Rev. 2017, 117, 1564−1686

researchers need to make a choice about which method to use to achieve the desired accuracy.

4.2.1. Parametrization Based on Experimental Spectra. Urey and Bradley described what came to be known as the Urey–Bradley force field (see eq 63) in 1931,[634] in which they used the first two terms of a Taylor expansion to represent the relationship between the configurational energy and the bond as well as 1-3 distances while assigning a harmonic function for the angle term. Vibrational frequencies can be calculated on the basis of the potential, and they found that experimental frequencies were best reproduced via addition of a $1/r^n$ term (with $n = 5-9$) and an electrostatic term $(1/r)$ into the potential.

$$V = V_0 + \sum_1^4 \frac{\partial V}{\partial r_i}\Delta r_i + \frac{1}{2}\sum_1^4 \frac{\partial^2 V}{\partial r_i^2}\Delta r_i^2 + \frac{1}{2}\sum_1^4 k_2 r_0^2 \Delta\theta_i^2 + \sum_1^6 \frac{\partial V}{\partial r_j}\Delta r_j + \frac{1}{2}\sum_1^6 \frac{\partial^2 V}{\partial r_j^2}\Delta r_j^2 \quad (63)$$

Wilson proposed a method in 1939, which directly generated the expanded secular equation for the vibrational frequencies of a given molecule.[635] As shown in eq 64, the B matrix is a vector matrix that transforms a Cartesian coordinate (x_i) representation to an internal coordinate one (R_k), from which the G matrix is created (see eq 65). On the basis of the assumption that the molecular kinetic energy only consists of harmonic vibrations, and through the construction and solution of the secular equation: $|F - G\lambda| = 0$ (where F is the force constant matrix), force constants could be directly evaluated.

$$R_k = \sum_{i=1}^{3n} B_{ki} x_i \ (k = 1, 2, ..., 3n - 6) \quad (64)$$

$$G_{kl} = \sum_{i=1}^{3n} B_{ki} B_{li}/m_i \ (k, l = 1, 2, ..., 3n - 6) \quad (65)$$

However, in the spectroscopic force field, the F matrix contains the bond, angle, and torsion terms along the diagonal and the cross interactions in the off-diagonal terms. These terms contain the nonbonded interactions implicitly, reducing the transferability of the parameters to disparate systems.[51]

Simanouti explored the use of the Urey–Bradley force field and Wilson's method for a range of molecular systems.[636−638] For example, in one publication, 102 fundamental frequencies of 16 small molecules (with CX_4, CX_3Y, CX_2Y_2, CXY_3 structures) were well reproduced (1.4% mean deviation relative to experiment) based on 28 force constants.[636] He also found that the experimental frequencies of CH_4, CD_4, C_2H_6, C_2D_6, $(CH_2)_n$, and $(CD_2)_n$ were well reproduced using the same force constant parameter set.[636] In a subsequent work, he proposed a force field for a range of carbides and silicides.[638]

Nakagawa and Shimanouchi detected of a series of aquo complexes of TMs using IR spectra.[639] On the basis of their experimental studies, they calculated the bond stretching force constants for various metal–oxygen bonds. The strength of these force constants varied according to the sequence: $Cr^{3+} > Ni^{2+} > Mn^{2+} \approx Fe^{2+} > Cu^{2+} \approx Zn^{2+} > Mg^{2+}$. Their results showed that the largest force constant (the force constant of the Cr^{3+}–O bond) is smaller than the force constants found between metal ions and nitrogen atoms in amine/nitro complexes, and between metal ions and carbon atoms in cyanide complexes.

Moreover, it is possible to calculate the IR/Raman spectra using a force field and to fit the force field parameters to reproduce experimental spectra. For example, in the INTERFACE force field developed by Heinz et al.,[598] the equilibrium bond lengths and angle values were obtained from crystal structures, while the bond and angle force constants were fitted to reproduce experimental IR/Raman spectra. The calculated spectra were based on the Fourier transform of the velocity autocorrelation function. Deviations of less than 50 cm^{-1} in the frequencies were achieved when compared to experiment, while the intensities were poorly reproduced because of the classical representation.

4.2.2. Potential Energy Surface Scanning Method. A straightforward way to obtain force field parameters is fitting the force constants based on QM calculated PESs. To illustrate this approach, we give two examples.

In 2012, Shahrokh et al. developed a force field for different heme states representing the cytochrome P450 catalytic cycle.[640] The parametrization was performed in an AMBER-compatible manner using the B3LYP/LACVP level of theory for the reference QM calculations. Their approach involves two different models (a truncated one and full description) for each state. The bond and angle force constants were obtained on the basis of the QM PES scans of the truncated model. The restrained electrostatic potential (RESP) charges obtained from the full model showed better performance than those from the truncated model in docking studies. They observed different docking patterns of substrate with different models and states, and the parameters showed stability at the nanosecond time scale under a variety of circumstances (with explicit or implicit solvent, with and without the enzyme environment).

Neves et al. developed bonded models for 12 Mn containing complexes from 9 protein systems in 2013.[641] They used the PES scanning method to determine force constants of the bonds and angles involving the metal ion. Partial charges were derived using the RESP charge fitting algorithm. MD simulations were carried out for these systems, and the resultant trajectories were analyzed. Good agreement between the QM and MM models was obtained on the basis of comparisons of the optimized structures and the calculated normal-mode frequencies. They also performed linear and quadratic fits of the bond force constants and equilibrium distances between the Mn ions and their ligating O and N atoms. These fits provide a basis for an empirically derived force field for Mn containing complexes.

The PES scan approach has as its main merit its overall simplicity, but unlike the Z-matrix or Seminario methods, which can obtain all needed bonded parameters in "one-shot", the PES scanning method requires an independent PES scan for each bond and angle involving the metal center. This makes this approach computationally more expensive than alternatives. Moreover, double counting is still an issue. Fitting all of the energy changes along a PES scanning into a single bond or angle term is not entirely valid because along the PES scanning not only the bond length or angle magnitude changes, but also the related nonbonded interactions (even they are assumed small). Hence, this approach double counts the nonbonded interactions into the degrees of freedom on fitting. This problem could be solved through considering changes of the nonbonded interactions or by using an alternative strategy such as the automated parametrization method (see section 4.2.5).

4.2.3. Z-Matrix Method. There are a number of ways to calculate the Hessian matrix (see eq 66, where F_{ij} is an element

DOI: 10.1021/acs.chemrev.6b00440
Chem. Rev. 2017, 117, 1564−1686

in Hessian matrix with respect to the coordinates of atoms i and j). For example, one can calculate the numerical derivative of the energy or calculate the analytical derivative of the energy (as with the gradients, most modern implementations of QM methods obtain the second derivatives analytically[642,643]).

$$F_{ij} = \left(\frac{\partial^2 E}{\partial q_i \partial q_j} \right)_0 \tag{66}$$

Pulay developed a method to calculate force constants on the basis of HF calculations in 1969.[644] He proposed a method that calculated the derivative of energy analytically and then the second derivative numerically. He called his approach the "force method" in the original article. After calculating the force analytically, one can transform it from Cartesian coordinates to internal coordinates using the Wilson B matrix. This transformation is nonunique so the force constants obtained are dependent on the choice of internal coordinate. He also noted that without explicit electron correlation, the HF method leads to an ionic dissociation picture of a bond and tends to overestimate the bond force constants.

$$V = V_0 - \sum_i \phi_i q_i + \frac{1}{2} \sum_{ij} F_{ij} q_i q_j + \frac{1}{6} \sum_{ijk} F_{ijk} q_i q_j q_k + \ldots \tag{67}$$

Ten years later, Pulay et al. proposed a set of standardized internal coordinates to calculate force constants.[645] The internal coordinate systems (with coordinates q_i) are complete and nonredundant, which makes eq 67 unique. Their local internal valence coordinates contain the bonds, angles, dihedrals, and their linear combinations. To facilitate force field function construction, a standardized coordinate system was proposed: (1) preferential treatment of the hydrogen atoms due to their small mass; (2) recommended the use of deformational symmetry coordinates with the corresponding planar ring of D_{nh} symmetry for ring systems; and (3) use of the Simons−Parr−Finlan expansion for the bond stretching coordinate. The resultant force constant matrix can then be used for efficient geometry optimization and transition state searches.

Because of the lack of correlation, the HF method overestimates vibrational frequencies as well as the force constants. Furthermore, anharmonicity lowers the frequencies, thereby further enlarging the overestimation of the vibrational frequencies.[646] To ameliorate this problem, a scaling factor of 0.9 for the frequencies[647] and $0.9^2 = 0.81$ for the force constants[648] was introduced. However, for strongly correlated systems, including organometallics, this scaling strategy may fail. Presently, for this class of problem, DFT offers a better alternative.

Rauhut and Pulay have determined scaling factors for two popular DFT functionals: BLYP and B3LYP, combined with the 6-31G* basis set.[646] They developed the scaling factors for two different strategies to reproduce experimental vibrational frequencies. The first one uses a uniform scaling factor, while the second one employs multiple scaling factors for different types of internal coordinates (e.g., different bonds, angles, etc.). The uniform scaling factors were 0.995 and 0.963 for frequencies based on the BLYP/6-31G* and B3LYP/6-31G* levels of theory, respectively (for comparison, the HF/6-31G* and MP2/6-31G* scale factors were 0.89[647] and ∼0.95[649]). Through the use of the multiple scale factor strategy, the B3LYP/6-31G* level of theory gave better performance than the BLYP/6-31G* level of theory.

One drawback of the Z-matrix method is its dependence on the chosen internal coordinates.[650] For instance, for the three-membered HCON molecule, HF/STO-3G calculations give different force constants for the same CO bond under different internal coordinate choices: the force constant equals (1) 0.54 au when the internal coordinates (excluding hydrogen atoms) are CO, CN, and NCO; (2) 0.57 au when CO, NO, and CON are chosen; and (3) 0.26 au when the redundant internal coordinates CO, NO, CN, CNO, NOC, and OCN are used.[650] Moreover, in the bonded model, only harmonic terms (which are the diagonal terms in the Z-matrix) are considered, and neglect of the cross terms causes an incomplete description of the potential energy surface (even if some of the cross terms are small). Therefore, force constants obtained using the Z-matrix method may need further adjustments to reproduce QM calculated results (e.g., vibrational frequencies and relative energies). Moreover, the dihedral force constants obtained using the Z-matrix are for the harmonic potential, which are inapplicable to the Fourier expansion series used in contemporary bonded models. This is not only because of the different functional forms, but also because in the dihedral interactions of many force fields, the 1-4 nonbonded interaction is considered either fully or partially, making the dihedral terms obtained from Z-matrix method and force field models incompatible.

Ryde has used the Z-matrix method in his modeling studies of alcohol dehydrogenase, a zinc-containing enzyme, in 1995.[648] He used the Z-matrix method to obtain the force constants on the basis of HF calculations and then scaled these values by a factor of 0.81 (square of the frequency correction factor). Charges were assigned on the basis of Mulliken charges obtained at the HF level with appropriate adjustments. Minimization results showed that four-coordination was preferred over five-coordination by at least 36 kJ/mol (∼8.6 kcal/mol). He also noted that to correctly simulate the dynamics of the metal site, it is important to use specific force constants for bond stretching, while the application of bond length constraints restricts the sampling space yielding unphysical results.

Tuccinardi et al. studied MMPs, which have a zinc ion in its catalytic site, using a classical force field.[651] The RESP algorithm was used to obtain the partial charges. They obtained the metal−ligand bond force constants on the basis of the Z-matrix method, and represented the angle force constant by scaling down relevant bond force constant by an order of magnitude. These parameters were further optimized to reproduce QM calculated relative energies between different conformations.

Merz and co-workers have studied several metalloproteins based on the Z-matrix method.[652−654] For example, Op't Holt and Merz performed classical modeling on the human antioxidant protein HAH1.[654] The Cu^+ binding site of HAH1 as well as the proposed transfer mechanism for the Cu^+ ion between the HAH1 and MNK4 proteins are shown in Figures 34 and 35, respectively. However, the original calculated force constants were too weak to reproduce the geometry of the binding site, and were increased to closely reproduce the Cu^+−S distance in the complex. A larger VDW radius parameter for the Cu^+ ion was used to prevent close contact between the metal ion and H/S atoms in nearby Cys residues, which are not bound to the metal ion. MD simulations were carried out, and

DOI: 10.1021/acs.chemrev.6b00440
Chem. Rev. 2017, 117, 1564−1686

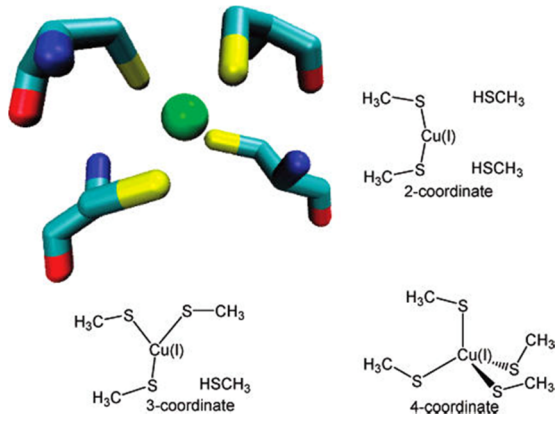

Figure 34. Cu^+ binding site from the HAH1 crystal structure, including Cys side chains, and the three QM models used to represent two-, three-, and four-coordinate Cu^+ environments. Reprinted with permission from ref 654. Copyright 2007 American Chemical Society.

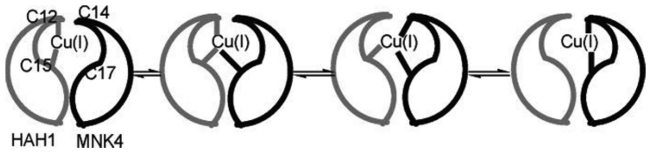

Figure 35. Proposed mechanism for transfer of Cu^+ between HAH1 and MNK4. A possible four-coordinate intermediate that would reside between the two three-coordinate states in the middle has been left out. In the HAH1 homodimer used as a mimic of the HAH1-MNK4 heterodimer in MD simulations, C14 and C17 of the target domain are replaced by Cys 12 B and Cys 15 B, respectively. Reprinted with permission from ref 654. Copyright 2007 American Chemical Society.

they generally reproduced the XRD structure for the protein and its metal site. Both the QM and the MM results suggested that the Cu^+ ion prefers two-coordination or three-coordination over four-coordination.

4.2.4. Seminario Method. The Seminario method and its associated software, FUERZA, were described in 1996.[650] This method reproduced the vibrational frequencies of several small molecules (including a Rh complex) as demonstrated by Seminario.[650] It uses a sub matrix of the Cartesian Hessian matrix to calculate force constants. It reduces the $3N \times 3N$ matrix problem into a problem involving $3N$ 3×3 matrixes. The parametrization process is straightforward and does not involve an iterative process. The parameters derived on the basis of the Seminario method employ a harmonic approximation for the bond, angle, dihedral, and improper torsion terms (see eq 68). The geometric parameters r_{eq}, θ_{eq}, ϕ_{eq}, and ω_{eq} can be obtained on the basis of QM optimized or XRD structures, and the force constant parameters k_b, k_θ, k_ϕ, and k_ω are derived on the basis of eqs 69−72. In these equations, k_{AB} is the force constant between atom A and B, while u_{AB} is the unit vector between the two atoms. λ_i and v_i are the eigenvalues and eigenvectors of the sub Hessian matrix between atoms A and B. In total, there are three eigenvectors of each sub Hessian matrix. u^N is the unit vector perpendicular to the BCD plane. u^{PA} and u^{PB} are the unit vectors perpendicular to unit vector u^{AB} and u^{CB}; R_{AB} and R_{CB} are the bond distances between atoms AB and CB; u_{NABC} and u_{NBCD} are the unit vectors perpendicular to planes ABC and BCD, respectively.

$$U(r) = \sum_{\text{bonds}} \frac{1}{2}k_b(r - r_{eq})^2 + \sum_{\text{angles}} \frac{1}{2}k_\theta(\theta - \theta_{eq})^2 + \sum_{\text{dihedrals}} \frac{1}{2}k_\phi(\phi - \phi_{eq})^2 + \sum_{\text{improper torsions}} \frac{1}{2}k_\omega(\omega - \omega_{eq})^2 \quad (68)$$

$$k_{AB} = \sum_{i=1}^{3} \lambda_i^{AB} |u^{AB} \cdot v_i^{AB}| \quad (69)$$

$$\frac{1}{k_\theta} = \frac{1}{R_{AB}^2 \sum_{i=1}^{3} \lambda_i^{AB} |u^{PA} \cdot v_i^{AB}|} + \frac{1}{R_{CB}^2 \sum_{i=1}^{3} \lambda_i^{AB} |u^{PC} \cdot v_i^{CB}|} \quad (70)$$

$$\frac{1}{k_\phi} = \frac{1}{R_{BA}^2 |u_{AB} \times u_{BC}|^2 \sum_{i=1}^{3} \lambda_i^{AB} |u_{NABC} \cdot v_i^{AB}|} + \frac{1}{R_{CD}^2 |u_{BC} \times u_{CD}|^2 \sum_{i=1}^{3} \lambda_i^{DC} |u_{NBCD} \cdot v_i^{DC}|} \quad (71)$$

$$k_\omega = h_{ABCD}^2 \left[\sum_{i=1}^{3} \lambda_i^{AB} |u^N \cdot v_i^{AB}| + \sum_{i=1}^{3} \lambda_i^{AC} |u^N \cdot v_i^{AC}| + \sum_{i=1}^{3} \lambda_i^{AD} |u^N \cdot v_i^{AD}| \right] \quad (72)$$

Note that the Seminario method incorporates the influence of the environment implicitly in its parametrization. The force constants can be considered as "effective force constants" and may not be accurate for isolated bonds, angles, dihedrals, and improper torsion terms. Moreover, the dihedral and improper torsion parameters obtained from the Seminario method are not directly applicable to force fields such as AMBER, CHARMM, OPLS-AA, GROMOS, etc., due to differences in functional forms (herein harmonic terms are used while these force fields all use a Fourier expansion). Furthermore, explicit 1-4 nonbonded interactions in these force fields create further complications. In related applications, only the bond and angle parameters based on the Seminario method are used, while the dihedral and improper torsion terms involving metal ions are set to zero.[1,655−660]

The Seminario method showed its versatility in applications to various systems. For example, Seminario and co-workers derived force field parameters for oligopeptides,[661] polypeptides,[662] nitro compounds,[663] Si nanoclusters,[664] and gallium nitride nanoclusters[665] on the basis of the Seminario method. Some other applications including ionic liquids,[666] carbon nanotubes,[667] and MOFs[668] were also reported. Below we highlight some examples about metal-containing systems.

Nilsson et al. developed the program, Hess2FF, on the basis of the Seminario method in 2003.[669] They pointed out that the sub matrix could be selected in two different ways for each atom pair, the (i,j) or (j,i) submatrix, and found it led to less than 5% uncertainty in determining the force constants. They averaged the final result on the basis of various possible permutations. They refined five heterocompounds in protein systems (three containing one iron or zinc ion) by utilizing the Hess2FF software. They calculated the Cartesian Hessian matrix using the B3LYP functional, AM1, and PM3 SE-QM methods, as well as the universal force field (UFF),

DOI: 10.1021/acs.chemrev.6b00440
Chem. Rev. 2017, 117, 1564−1686

DREIDING, and MMFF94 force fields. They found that the B3LYP functional performed best according to the R_{free} factor, and it was recommended for high accuracy calculations. On the basis of force field parameters obtained from B3LYP calculations using mixed basis sets (6-31G* basis set for main group atoms and a double-ζ with polarization basis set for the TMs), they performed XRD structure refinement using the Crystallography and NMR System (CNS) force field, and obtained high-resolution structures with decreasing R_{free} factors. In particular, a 1.70 Å resolution structure of cytochrome c_{553} matched a 0.97 Å resolution structure more closely after the refinement with parameters obtained by Hess2FF. In the refinement process, they used the harmonic approximation for the dihedral term and did not include electrostatic term. However, they proposed that the electrostatic term should not be neglected for polar systems in classical simulation.

Lin and Wang parametrized 18 zinc-containing complexes, in which the metal associated bond and angle parameters were obtained from the Seminario method and charge parameters were derived using the RESP algorithm based on the B3LYP/6-311++G(2d,2p) level of theory.[655] The metal related torsion parameters were set to zero, while the remaining force field parameters were obtained from GAFF. They tested their models with different combinations of the bonded/nonbonded model with RESP charge/formal charge schemes. Ultimately, they found that the bonded model using a RESP charge model performed the best among all strategies examined. They performed normal-mode analysis for four different systems, and good agreement was obtained between MM and QM calculated results. Some inconsistencies existed for the high frequency modes, and they showed that the agreement could be improved by tuning bond parameters involving hydrogen. They also noted that these modifications were not necessary when the SHAKE algorithm was used to constrain X−H bonds during MD simulations.

Peters et al. developed the metal center parameter builder (MCPB) within the modeling toolkit plus plus (MTK++) package to facilitate the building of metal centers in metalloprotein systems.[1] To balance the accuracy and computational cost, a side chain model was created to obtain metal−ligand related bond and angle parameters based on the Seminario method, while a large model (with metal site residues capped by ACE and NME residues) was built to derive partial charges for the metal center based on the RESP algorithm. Furthermore, four charge fitting algorithms (ChgModA, where all of the charges are flexible in the metal cluster; ChgModB, where the charges of the heavy backbone atoms in the metal cluster are fixed; ChgModC, where the charges of all backbone atoms in the metal cluster are fixed; ChgModD, where the charges of all backbone atoms and the C_β atom in the metal cluster are fixed) were tested, and it was found that the ChgModB performed the best when combined with the Seminario method. This may be due to the fact that the charges of the backbone heavy atoms were taken into account in the parametrization of the backbone torsion parameters. On the basis of the Semnario/ChgModB method, they developed the zinc AMBER force field (ZAFF) for 10 different zinc sites with tetrahedral coordination.

Subsequently, there were a number of parametrizations of metalloprotein systems described in the literature based on MCPB. For example, Merz and co-workers studied the Zn-containing protein *CzrA*,[656] the Cu-containing metallochaperone *CusF*[657] and *CusB*,[658] and the Ni-containing enzymes, urease[659] and *Helicobacter pylori* (Hp) urease,[660] based on the MCPB software package using the Seminario method and RESP algorithm. MD simulations were performed, and insights into the structure, function, and dynamics of these metalloproteins were obtained. Below we highlight several of these studies.

In one example of their work, *Klebsella aerogenes* (KA) urease was studied,[659] which is a homotrimer of heterotrimers (in total there are nine monomers; see Figure 36), with each homotrimer having an active site that contains a dinickel metal center (see Figure 37). MD simulation of KA urease predicted a "wide-open" state for the flap over the active site (see Figure 38), which was not observed in the available crystal structures. Results showed that the "wide-open" state could be accessed from the "open" state through a relatively low free energy barrier (see Figure 39). This results in a more extensive active site region, which offers further opportunities for structure-based drug design.

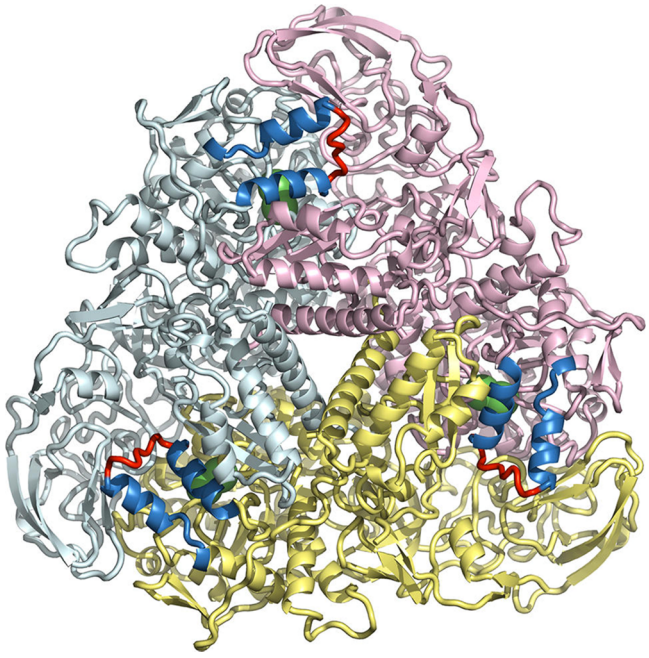

Figure 36. Initial structure of *K. aerogenes* urease in the open state, as used in the simulations of ref 659. The trimeric subunits are shown in yellow, pink, and cyan. The flaps are shown as α-helices (blue) and loops (red). Nickel ions are shown as green spheres. Reprinted with permission from ref 659. Copyright 2012 American Chemical Society.

In another example, the homodimeric Zn^{2+}/Co^{2+}-responsive transcriptional repressor from *Staphylococcus aureus* (so-called *CzrA*) was studied using MD simulations.[656] *CzrA* has several allosteric states as shown in Figure 40. Each of its two metal binding sites has 3 HIS residues and 1 ASP residue coordinating to the metal center (see Figure 41). The MD simulation of the DNA bound *CzrA* system captured the switching between its closed to open state due to Zn^{2+} binding. Analysis suggested Zn^{2+} binding quenches the conformational sampling of the *CzrA* system through a hydrogen-bonding pathway or network, which is in agreement with experimental results. The root-mean-square fluctuations (RMSFs) of different residues for apo-*CzrA* and its Zn bound form are shown in Figure 42. From this figure, it is clearly seen that the α2,

DOI: 10.1021/acs.chemrev.6b00440
Chem. Rev. 2017, 117, 1564−1686

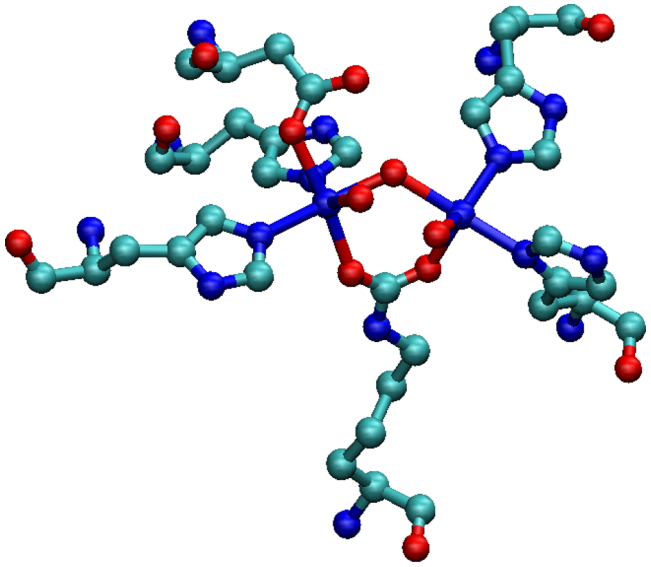

Figure 37. Heavy atoms of the metal site residues in native KA urease. The two nickel ions in the metal center are six-coordinated (left one) and five-coordinated (right one), respectively. The structure is from PDB entry 1FWJ, and this figure was made using VMD.[670]

α3+αR, and β1+β2 domains have significantly decreased RMSF values after Zn binding.

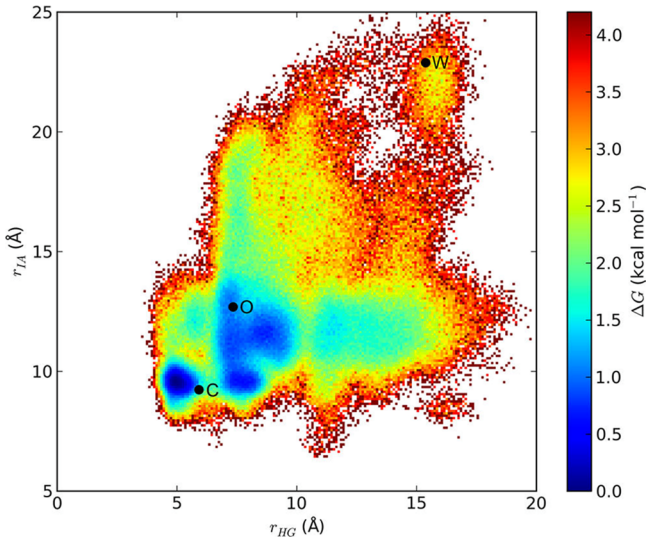

Figure 39. Relative free energy map for opening of the urease flap. The points labeled as "C", "O", and "W", respectively, represent the closed, open, and wide-open structures shown in Figure 38. Points C and O represent the initial XRD structures of the closed- and open-flap models (PDB entries 1FWJ and 1EJX, respectively); for the latter structure, the flap was added by homology modeling. Point W is a representative wide-open conformation selected from the simulation trajectory of 1FWJ. Reprinted with permission from ref 659. Copyright 2012 American Chemical Society.

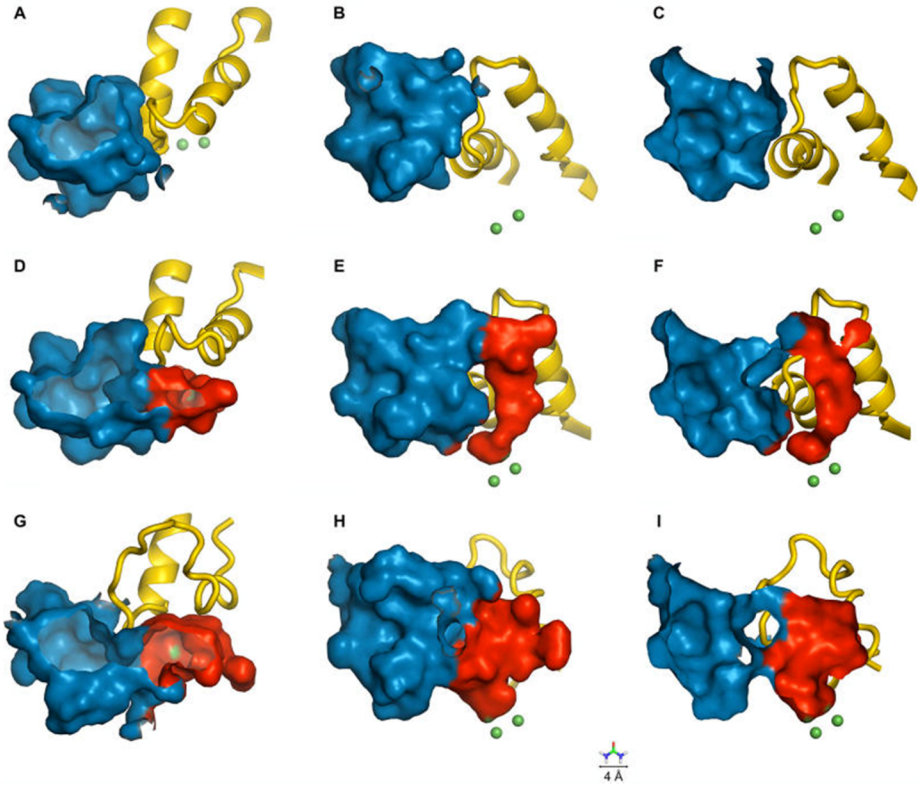

Figure 38. Flap, active site, and ancillary binding pocket of *K. aerogenes* urease. The flap is shown in yellow, the active site in red, and the ancillary binding pocket in blue. The nickel ions are shown as green spheres, and the exposed nickel surfaces in (D)−(I) are also shown in green. The three rows from top to bottom show the closed flap (A−C), the open flap (D−F), and the wide-open flap (G−I). In each row, three views are shown: from the top, looking down into the binding pockets (A, D, G); from the side (B, E, H); and from the side in a cutaway view (C, F, I). To show the scale, a urea molecule (4 Å across) is depicted at the bottom of the figure. Reprinted with permission from ref 659. Copyright 2012 American Chemical Society.

DOI: 10.1021/acs.chemrev.6b00440
Chem. Rev. 2017, 117, 1564−1686

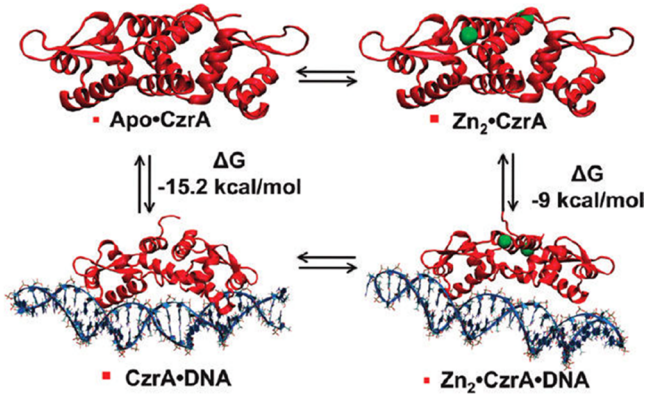

Figure 40. Four allosteric forms of CzrA examined in the study of Chakravorty et al.,[656] and the associated thermodynamic parameters of the CzrA mechanism. The protein, CzrA, is shown in red, Zn^{2+} ions are in green, and the DNA molecules are blue. These cartoon depictions are snapshots from their MD simulations of these allosteric forms. A negative cooperative allosteric effect of ~6 kcal/mol is observed on Zn^{2+} binding to CzrA. Reprinted with permission from ref 656. Copyright 2012 American Chemical Society.

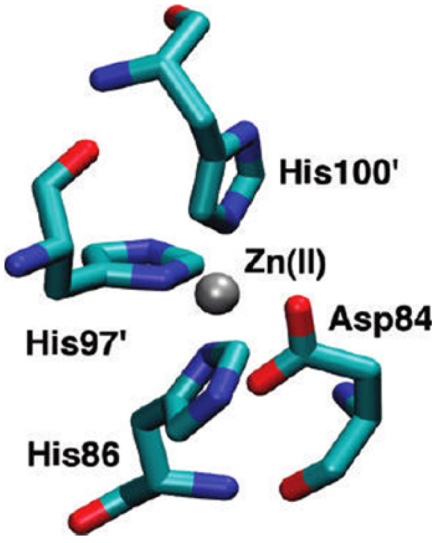

Figure 41. Snapshot of the CzrA metal binding site from the initial structure. The zinc ion is represented as a silver sphere. The metal binding residues include Asp84, His86, His97′, and His100′. These residues also represent the QM region of the QM/MM MD calculations in the study of Chakravorty et al.[656] Reprinted with permission from ref 656. Copyright 2012 American Chemical Society.

Li and Merz recently developed the MCPB.py program within the python metal site modeling toolbox (pyMSMT) software package.[671] It offers a simple and clear workflow for the parametrization process, and supports many more metal-containing systems than did the earlier MCPB program. It supports more than 80 metals with various oxidation states (see Figure 43) and a number of AMBER force fields. Moreover, it supports multiple coordination modes, as well as organometallic systems. Two examples (one for a metalloprotein and the other for an organometallic system) were described on the basis of the Seminario/ChgModB method. MD simulation of the metalloprotein and a normal-mode analysis of an organometallic compound yielded satisfactory results.

Recently, Zheng et al. introduced the visual force field derivation toolkit (VFFDT) to derive bond and angle

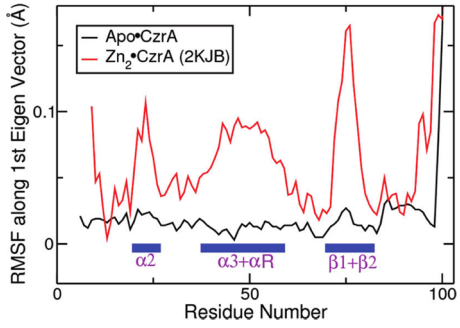

Figure 42. Plot of RMSF values for the lowest mode of the protein from simulation of Apo·CzrA starting from the apo-crystal structure, and simulation of allosteric switching for Zn·CzrA starting from the 2KJB NMR structure of apo-CzrA in a closed conformation. Reprinted with permission from ref 656. Copyright 2012 American Chemical Society.

parameters on the basis of the Seminario method.[672] It can perform parametrization based on the Hessian matrix obtained from several QM packages: Gaussian 03/09,[673,674] GAMESS-US,[675] Q-Chem,[348] ORCA[347] (version 3.0), and MOPAC[676] (version 2009/2012). The visualization interface is an attractive characteristic, and it serves as a complementary tool to the antechamber, MCPB, and MCPB.py programs in the AmberTools software package.

4.2.5. Automated Parametrization Method. Even though force field parameter derivation based on the Hessian matrix is quite straightforward and the results are encouraging, there remains a double counting issue with this approach. This is because the information contained within the Hessian matrix is balanced between the bonded and nonbonded interactions present in the system of interest, causing the nonbonded interactions to be double counted (implicitly considered in the bonded terms while explicitly considered in the nonbonded terms) in the force field modeling.[677] However, this problem can be overcome by using, what we term, the automated parametrization method (APM). There is no assumption that the equilibrium geometric parameters are the same as the experimental or QM calculated geometries. Moreover, the final comparison is usually made between the same properties from experiment (or QM calculations) and MM calculated ones.

Basically, if the parameter space dimension is low, one can scan the parameter space. However, if the dimensionality is high, it is really hard to simply scan because the parameter combinations increase exponentially. One can use a coarse grid at the initial stages of the scan and then a finer one when the optimal parameter region is identified. Yet this still does not effectively deal with high dimension parameter spaces. There are different ways to decrease the parameter space dimensions, for example, dividing the parameter set into several subsets and fitting them sequentially with the other subsets fixed, then iterate until converged results are obtained. It is also possible to decrease the parametrization effort using physical/chemical criteria to shrink the parameter space to scan. For example, in the development of the optimal point charge (OPC) water model, the authors used the lowest order multipole moments of water as a filter for parameter selection.[678]

One widely used method to handle high dimension parameter spaces is to perform parameter optimization akin to geometry optimization. The difference is that parameter optimization minimizes the merit function (e.g., the least-squares difference between the simulated and reference

DOI: 10.1021/acs.chemrev.6b00440
Chem. Rev. 2017, 117, 1564−1686

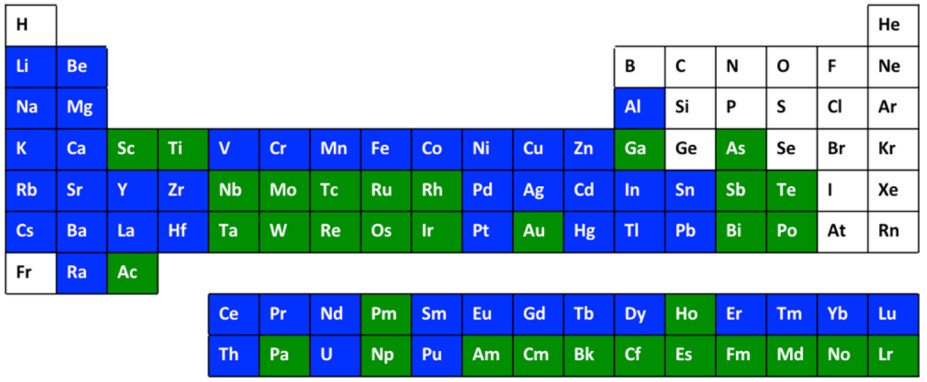

Figure 43. Metal ions currently supported by the MCPB.py program. The metals with a blue background use the VDW parameters from Li et al.,[390,391,510] whereas the metals with a green background use the VDW parameters adapted from UFF. Reprinted with permission from ref 671. Copyright 2016 American Chemical Society.

properties) with respect to the parameters, while geometry optimization minimizes the total energy with respect to the Cartesian or internal coordinates. Moreover, in parameter fitting, the derivatives usually need to be calculated numerically. Like optimizing the geometry, it is hard to find the global minima in the variable space during the parameter optimization procedure. Presently, parameter optimization processes typically need "tricks" and human intervention.

To solve the large dimension problem, there are several points that need attention. (1) A good merit function needs to be used. Similar to solving linear simultaneous equations, for which the number of equations should be comparable or more than the number of unknown values, a large quantity of reference data is need to ensure that the parameters are not overfit. Furthermore, different kinds of properties are needed to balance the optimization to decrease the "biases" in parameter fitting. Meanwhile, different modifications can be made to the merit function to obtain fits. For example, different weights can be applied to increase the priority of the properties near equilibrium because of their higher occurrences. Moreover, constraints and/or restraints can be applied to keep the parameters in a physically reasonable range. (2) An efficient optimization algorithm/procedure needs to be used. Various algorithms can be used to minimize merit function: for example, steepest descent, conjugated gradient, simplex, genetic algorithms, the Newton−Raphson method, etc. Each algorithm has its own set of pros and cons. The answer to the question of which algorithm to choose is problem dependent. (3) Similar to geometry optimization, a good initial guess is important as well. If a bad initial guess is made, the parametrization can be easily trapped in poor or "high-energy" local minima. These suggestions are not only for the bonded model parameter optimization, but can also be applied to parameterization of other the bonded model using APM.

Several freely available APM-based programs have been described including Paramfit[679] and ForceBalance.[680] Interested readers should consult the literature for further details. Below we introduce several examples of the APM.

In the early development of the CFF model, Lifson and coworkers optimized the force field parameters to best reproduce various observables based on a least-squares refinement. For example, in the initial work on CFF for cycloalkanes and *n*-alkanes, Lifson and Warshel attempted to optimize the force field parameters to best reproduce the experimental excess enthalpy, equilibrium coordinates, and normal-mode frequencies (with different weighting factors for these data).[388] Parameters were determined after convergence was reached in the least-squares refinement.

Norrby and Liljefors developed a generalized automatic parametrization procedure for force fields in 1998.[50] The illustrative example shown was ethane using the MM3* force field (which uses form similar to the MM3 force field). The reference data contain experimental/QM calculated structural data (bond lengths, bond angles, and dihedral angles) and relative energies, as well as a mass-weighted Hessian matrix based on QM calculation. They discussed that the Cartesian root-mean-square deviation (RMSD) may not be a good metric for evaluating the force field quality, and hence bond, angle, and dihedral values were treated as the fitting targets. They also discussed that the B3LYP/6-31G* level of theory offered the best price/performance ratio for obtaining QM source data. The final target is to minimize the merit function χ^2 (a least-squares function, see eq 73), while different weights were applied to different properties (100 $Å^{-1}$, 2 deg^{-1}, 1 deg^{-1}, 100 kJ^{-1} mol, and 0.01 kJ^{-1} mol $Å^2$ amu^{-1} for the bond, angle, dihedral, relative energy, and mass-weighted Hessian matrix, respectively). They recommended using a strategy by which optimization was done using a modified simplex algorithm followed by optimization using the Newton−Raphson algorithm with Lagrange multipliers.

$$\chi^2 = \sum_i w_i^2 (y_i - \hat{y}_i)^2 \tag{73}$$

Rydberg and co-workers developed a transition-state force field for cytochrome P450 systems using the method developed by Norrby and Liljefors (see above).[681] Parameters were trained on the basis of calculated transition state structures and Hessian matrixes of 14 substrate models using the B3LYP functional. Another 10 substrate models were used as a test set. Partial charges were determined using the RESP algorithm, while GAFF was used for the substrates. The transition-state force field (or Q2MM method) was not able to calculate the absolute activation energy, but it could evaluate relative barriers, and predict selectivity. The final parameters showed excellent performance for both the training and the test sets: with RMSDs of 0.01 Å and 1.2° for bonds and angles, and has a 0.99 correlation coefficient between the MM- and QM-derived Hessian matrix elements. The transition state structures for aliphatic hydrogen abstraction were well reproduced, but the DFT calculated energies based on them are still ∼24 kJ/mol

DOI: 10.1021/acs.chemrev.6b00440
Chem. Rev. 2017, 117, 1564−1686

(~5.7 kcal/mol) higher than using the DFT optimized ones. This error decreased to 9 kJ/mol (~2.2 kcal/mol) when a parameter optimization strategy was also applied to the substrate (instead of using GAFF), further demonstrating the deficiency of the MM optimized structures. The authors proposed that this is due to the simplicity of the bonded model approach.

Hu and Ryde compared different MM models for simulating biologically related zinc complexes in 2011.[677] They suggested using a nonbonded model with restraints or a bonded model based on the Seminario method for structural metal sites, while the method of Norrby and Liljefors affords a better model for catalytic metal sites. However, while the later method afforded a better model, it is more labor intensive than the former methods after QM calculations. Furthermore, the APM requires significant human intervention. For instance, chemical intuition is needed to check whether unphysical local minima were obtained during the parametrization process.[50] It was found that for the bonded model to perform optimally, new atom types should be assigned to all of the atoms in the metal site. Moreover, attention should be paid to ensure the hydrogen atoms in negatively charged ligands have been assigned appropriate partial charges (i.e., not negative values).

4.2.6. Burger Method and Partial Hessian Fitting Method. *4.2.6.1. Burger Method.* Burger et al. proposed a new parametrization method and developed related software (so-called *parafreq*) in 2012.[682] It solves each internal coordinate separately instead of solving the full Hessian in internal coordinates. It can determine each bond and angle parameter on the basis of the differences between QM and MM calculated Hessian matrixes and the Wilson B matrix. Dihedral terms were determined via fitting to relaxed QM PES scans. Results showed that this method better reproduced QM-derived frequencies than the GAFF, Seminario, and *Z*-matrix methods.

4.2.6.2. Partial Hessian Fitting Method. Recently, Wang et al. developed the partial Hessian fitting (PHF) method to fit the bond, angle, dihedral, and improper torsion parameters in the bonded model.[683] In this method, they aimed at reproducing the partial Hessian matrix between two particles that are in the bond, angle, dihedral, or improper torsion interaction. Nonbonded interactions with RESP charges and the 12-6 LJ potential were determined in the first stage. Afterward, the dihedral force constants were determined to minimize the least-squares difference between QM and MM calculated partial Hessian matrixes between the two terminal particles (which are 1-4 to each other). The angle, improper torsion (if desired), and bond force constants then were derived sequentially to minimize the least-squares difference of QM and MM calculated partial Hessian matrixes between each of the two terminal atoms. QM optimized bond lengths and angle values were used for the initial equilibrium bond and angle values. To prevent distortion caused by too strong of a 1-4 interaction, a scheme called "Katachi" was used to optimize equilibrium bond and angle values to make the MM optimized structure reproduce the QM optimized bond and angle values within 0.0001 Å and 0.002°, respectively. Twenty-three compounds including three secondary building blocks of MOFs were tested. It was shown that the PHF-K method (with the "Katachi" scheme) outperformed the Seminario-K method and GAFF. The PHF method "decouples" the bond, angle, dihedral, improper torsion, and nonbonded parameters, and can be extended to classical force fields that do not use quadratic representations. In comparison, the Seminario method suffers from the double counting problem and is restricted to the harmonic potential form. Meanwhile, the authors also noted that neither the PHF nor the Seminario method can reproduce the QM calculated low-frequency normal modes.

4.2.7. Empirical Approaches. Intuitively, we expect that the larger is the electronic overlap between two atoms, the stronger is the bond, which results in a larger force constant. For instance, in GAFF,[397] the equilibrium bond distances between two sp, sp2, aromatic, and sp3 carbons are 1.1983, 1.3343, 1.3984, and 1.5375 Å, respectively, while the corresponding force constants are 923.7, 569.4, 461.1, and 300.9 kcal/mol·Å^{-2}, respectively.

A number of authors have developed different empirical rules to estimate the relationship between bond length and the corresponding force constant. A range of different dependencies of the force constant to the bond length were explored, including linear,[641,663] quadratic,[641] cubic,[684] and even up to the sixth power.[498]

Using the harmonic spring model, the following relationship is obtained, where $\omega_e c$ represents the vibrational frequency.

$$\omega_e c = \nu = \frac{1}{2\pi}\sqrt{\frac{k}{\mu}} \tag{74}$$

Mecke proposed that a relationship exists between ω_e and r_e values for various states of a molecule in 1925.[685] In 1929, Morse proposed a formula (see eq 75), which is generally valid except for a few exceptions.[686]

$$\omega_e r_e^3 = 3000 \tag{75}$$

In 1934, Badger proposed (now known as Badger's rule, see eq 76) a model for diatomic molecules that described the relationship between a bond length and its associated force constant.[684] In eq 76, the r_e and k_0 are the bond length and bond force constant, respectively, and d_{ij} is a constant that is only relevant to the locations of the two atoms (row i and row j) in the periodic table. This formula can be applied to both ground and excited states (although exceptions exist). Moreover, it was shown this rule could also be extended to polyatomic molecules in that internuclear distances could be obtained based on vibrational frequencies.[687]

$$k_0(r_e - d_{ij})^3 = 1.86 \times 10^5 \tag{76}$$

There are empirical methods used to determine the bond and angle parameters in classical force fields. For example, to extend MMFF94,[498] missing bond parameters can be obtained using eqs 77 and 78. According to eq 77, the bond length can be estimated using the covalent radii of atoms i and j, the difference of the Pauling electronegativities χ_i and χ_j, and a so-called "shrinkage" factor δ. C is a proportionality constant, which was set to 0.050 if either i or j is a hydrogen atom, and 0.085 otherwise, while n is an exponent that was assigned a value of 1.4. The shrinkage factor, which is employed because the MMFF94 force field optimized bond lengths are generally larger than the reference values (from MP2/6-31G* optimized geometries), was set to 0.008 Å. Meanwhile, eq 78, which is an inverse sixth power modification of the Badger's rule, was utilized to determine the bond force constant.

$$r_{ij}^{\mathrm{ref}} = r_i^{\mathrm{ref}} + r_j^{\mathrm{ref}} - c(\chi_i - \chi_j)^n - \delta \tag{77}$$

DOI: 10.1021/acs.chemrev.6b00440
Chem. Rev. 2017, 117, 1564−1686

$$K_r = K_{ij}^{ref}\left(\frac{r_{ij}^{ref}}{r_{ij}}\right)^6 \tag{78}$$

$$K_{ijk}^{\theta} = \frac{\beta Z_i C_j Z_k \, e^{-2D}}{(r_{ij}^{eq} + r_{jk}^{eq})\theta_{ijk}^{eq\,2}} \tag{79}$$

$$D = \frac{(r_{ij}^{eq} - r_{jk}^{eq})^2}{(r_{ij}^{eq} + r_{jk}^{eq})^2} \tag{80}$$

For the angle parameters, an approach proposed by Halgren (see eqs 79 and 80) was used.[688,689] In these equations, Z_i, C_j, and Z_k are parameters related only to the atomic number, D is a factor to represent relative dissimilarity between two bond lengths, and β is a scale factor, which is assigned a value of 1.75 (in the general situation), 85% × 1.75 (if i, j, and k are all in a four-member ring), or 5% × 1.75 (if i, j, and k form a three-member ring).

In GAFF, different empirical equations from MMFF94 are used to derive bond and angle parameters.[397,690] Wang et al. employ eqs 81 and 82 to derive the missing bond parameters, where r_{ij} and K_r are the equilibrium bond length and bond force constant, respectively. K_{ij} is an empirical parameter for elements i and j, while m is an empirically derived power parameter. m and $\ln(K_{ij})$ were determined on the basis of least-squares fitting of $\ln(K_r)$ versus $\ln(r_{ij})$ using data from the AMBER force field. It was observed that optimal m values were 5, 4, and 4 for C−C, C−N, and C−O bonds, respectively. Ultimately, an average value of 4.5 was chosen for m to perform the force constant fitting procedure.

$$K_r = K_{ij}\left(\frac{1}{r_{ij}}\right)^m \tag{81}$$

$$K_{ij} = \frac{K_{ii}|r_{ij}^{ref} - r_{jj}^{ref}| + K_{jj}|r_{ij}^{ref} - r_{ii}^{ref}|}{|r_{ij}^{ref} - r_{jj}^{ref}| + |r_{ij}^{ref} - r_{ii}^{ref}|} \tag{82}$$

$$K_{ijk}^{\theta} = 143.9 \times \frac{Z_i C_j Z_k \, e^{-2D}}{(r_{ij}^{eq} + r_{jk}^{eq})\sqrt{\theta_{ijk}^{eq}}} \tag{83}$$

$$D = \frac{(r_{ij}^{eq} - r_{jk}^{eq})^2}{(r_{ij}^{eq} + r_{jk}^{eq})^2} \tag{84}$$

Equations 83 and 84 were used to derive missing angle force constants. Herein, Z_i, C_j, and Z_k are the empirical parameters for the first, second, and third atoms i, j, and k in an angle. r_{ij}^{eq} and r_{jk}^{eq} are the equilibrium distances of the bonds ij and jk, while θ_{ijk}^{eq} is the equilibrium value of angle ijk. In the AMBER force field, it was shown for situations where (1) both i and k are hydrogen atoms, (2) only one of the two is a hydrogen atom, and (3) in the remaining situations, the force constant is about 30−35, 50, and 70 kcal/mol·rad^{-2}, respectively.

In the work of Bellido and Seminario on nitro compounds, which used the Seminario parametrization scheme, a linear relationship was found between the bond force constants and bond distances for bonds without hydrogen atoms (see eq 85 and panel A of Figure 44).[663] However, there were no clear trends observed between the angle values and the angle force constants except the C−C−C angle in octanitrocubane (see panel B of Figure 44).

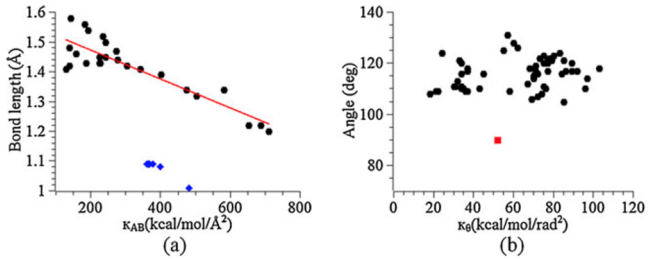

Figure 44. (a) Bond length versus bond force constant; blue ◆ are bonds with hydrogen atoms. (b) Angle versus angular force constant; the red ■ represents the angle between carbon atoms in octanitrocubane. Adapted with permission from ref 663. Copyright 2011 Springer.

$$r_{AB}^{eq} = -4.86 \times 10^{-4} \times K_{AB} + 1.57 \tag{85}$$

Moreover, in the work of Agulira-Segura and Seminario, they found that in general the force constant decreases with the increasing of equilibrium distance for the Si−Si bond.[664]

In the work of Neves et al., the bond and angle force constants were obtained on the basis of the PES scanning method (see section 4.2.2).[641] They performed linear fitting between the bond force constants and the bond distances for the Mn ions and their ligating atoms in different residues. The results are shown in Figure 45. The R^2 values of these fits are 0.82, 0.86, 0.90, and 0.91, respectively. They also performed quadratic fits between the Mn ions with ligating oxygen and nitrogen atoms (see Figure 46). The R^2 values of these two fits were 0.92 and 0.91, respectively. Similar to Bellido and Seminario, Neves et al. did not find a clear relationship between the equilibrium angle values and the angle force constants (see Figure 47). However, even with the use of different methods (Seminario versus PES scanning), the results were consistent in showing that the angle force constants were usually under 100 kcal/mol·rad^{-2}.

4.3. Dihedral and Improper Torsion Parameters

4.3.1. Dihedral and Improper Torsion Parameters in Alkane Chains and Protein Systems. The physical meaning of dihedral interactions is the repulsion between electrons clouds in chemical bonds rather than in atoms.[691] It is essential to have the dihedral term to represent the flexibility of the bond rotations within an organic molecule. Overall, dihedral rotation barriers are small for typical organic molecules. For example, there is only a ∼3 kcal/mol (∼5 × RT at T = 300 K) energy difference between the staggered and eclipsed conformations of ethane. Thus, even the high energy eclipsed conformation is accessible at room temperature. In their early force field work on n-alkanes, Bixon and Lifson described the dihedral term as the softest term in the potential function, but makes a significant contribution to the strain energy.[587]

$$U_{dihedral} = \sum_{dihedrals}\sum_{n=1,2,3,4} V_n[1 + \cos(n\phi - \gamma)] + \sum_{i,j>i}^{N}\left[f_{ele}\frac{q_i q_j}{4\pi\varepsilon_0 r_{ij}} + f_{VDW}\left(\frac{A_{ij}}{r_{ij}^{12}} - \frac{B_{ij}}{r_{ij}^{6}}\right)\right] \tag{86}$$

Fourier expansion is widely used to represent dihedral interactions. Different terms in the Fourier expansion were used

DOI: 10.1021/acs.chemrev.6b00440
Chem. Rev. 2017, 117, 1564−1686

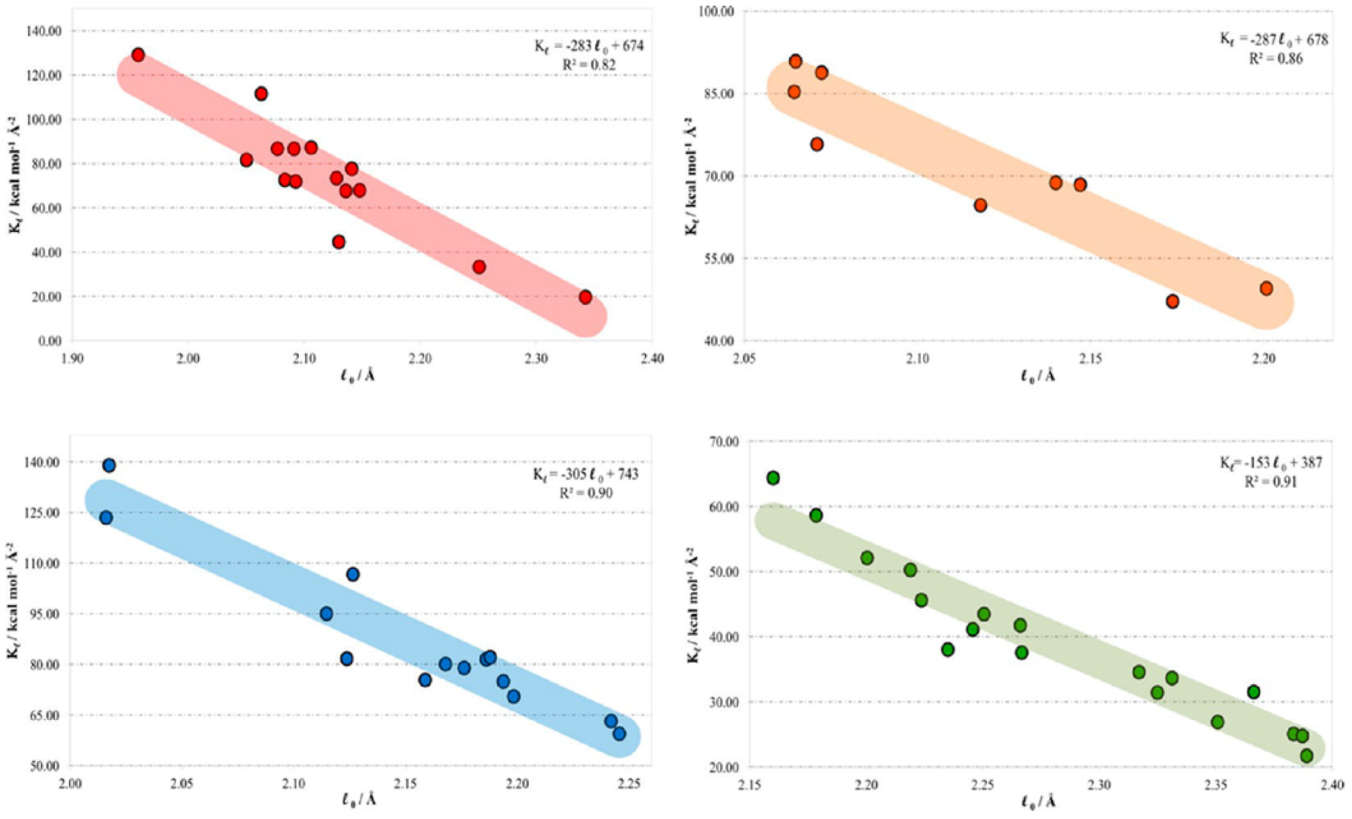

Figure 45. Linear regression for the main ligands in Mn-coordination spheres: aspartate, glutamate, histidine, and water, shown in red, orange, blue, and green, respectively. Reprinted with permission from ref 641. Copyright 2013 American Chemical Society.

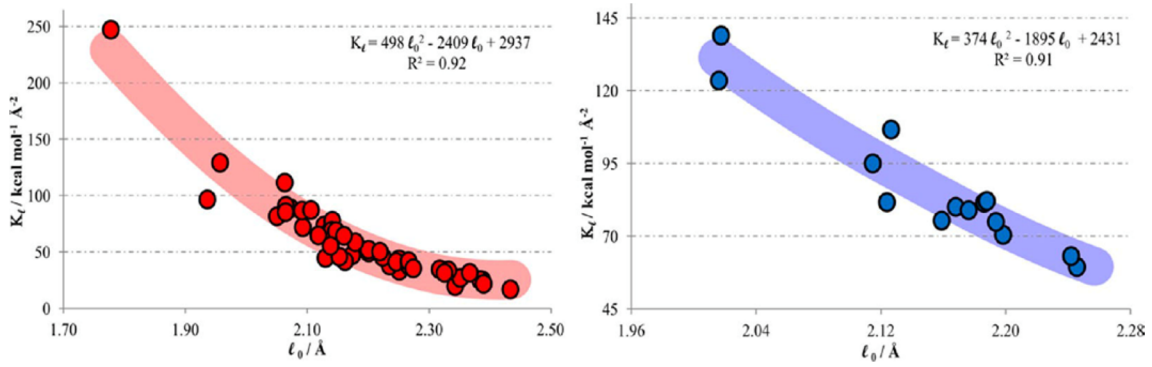

Figure 46. Second-order polynomial regression for the main donor atoms in Mn-coordination spheres (oxygen and nitrogen are shown in red and blue colors, respectively). Reprinted with permission from ref 641. Copyright 2013 American Chemical Society.

to represent the influence of different structural features (see the first term in eq 86). In some force field models, 1-4 nonbonded terms (see the second term in eq 86, where f_{ele} and f_{VDW} are the scaling factors for the 1-4 electrostatic and 1-4 VDW interactions, respectively) are also included to represent eclipsing interactions. Briefly, assigning a periodicity of 1 represents the cis−trans preference (the phase is 0° if trans is more stable than cis, and is 180° for the reverse) where there is only one maximum and one minimum. Assigning a periodicity of 2 yields two maxima and two minima, which represents the rotation in an ethene (with a phase of 180°) and also an out-of-plane improper torsion term (with a phase of 180°). A periodicity value of 3 represents three maxima and three minima, which represents, for example, the rotation of an ethane that has two sp^3 hybrid carbons (with a phase of 0°). In reality, multiple terms in the Fourier expansion may be needed to obtain an accurate representation of a specific dihedral, which have, for example, a specific trans−cis preference, different hybridizations of the central two atoms (e.g., sp^2 and sp^3), etc. Moreover, the Fourier equation has also been used to represent the angle bending interaction and offers better performance than the harmonic potential (e.g., in the SHAPES force field,[197] see section 7.1.2).

The 1-4 nonbonded interactions are considered explicitly or implicitly in classical force fields. Hence, the dihedral terms are usually lumped together with the 1-4 nonbonded interactions (containing the 1-4 electrostatic and 1-4 VDW interactions) to facilitate the accurate reproduction of the total bond rotation barrier. There are different scaling factors used for the 1-4 nonbonded interactions. For example, the scaling factor of 1-4 electrostatic interactions (f_{ele} in eq 86) in the AMBER force field (FF94) was set to 1/1.2, which was fitted from the 1,2-

DOI: 10.1021/acs.chemrev.6b00440
Chem. Rev. 2017, 117, 1564−1686

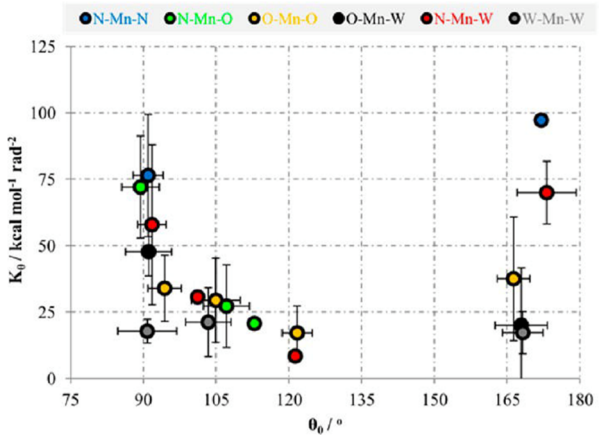

Figure 47. Average equilibrium angles and force constants for main donor atoms concerning the equilibrium angles for the main geometries in manganese. Reprinted with permission from ref 641. Copyright 2013 American Chemical Society.

enthanediol molecule and while also showing transferability to other small molecules like amines, butane, and alcohols.[692] The scaling factor of the 1-4 VDW interaction (f_{VDW} in eq 86) was set to 1/2 in the FF94 AMBER force field.[394] However, the scaling of 1-4 electrostatic and 1-4 VDW integrations is all assigned a value of 1 in the GLYCAM force field.[693] In the CHARMM force field (CHARMM 19 force field),[694,695] the 1-4 scaling factors for both the electrostatic and the VDW interactions are 0.4, while in its current version (CHARMM 22/27),[401,402,696,697] the 1-4 interactions were evaluated without scaling (or with a scaling factor of 1). Clearly, attention should be paid when transferring dihedral parameters between different force fields.

The torsion parameters play an important role in the reproduction of secondary structures and the energy balance between different relevant configurations in biomacromolecules. For example, dihedral parameters relevant to the protein backbone atoms such as C−N−C_α−C, N−Cα−C−N, C_β−C_α−N−C, and C_β−C_α−C−N play, one can say, an outsized role in the simulation of the protein folding processes. Several related force fields have been developed on the basis of QM calculated results, including the AMBER ff03,[396] AMBER ff99SB,[398] AMBER ff02.pol.r1,[698] CHARMM CMAP,[403] and AMBER ff14SB.[400]

4.3.2. Dihedral and Improper Torsion Parameters in Metal-Containing Complexes. Comba et al. suggested that if metal is in not in the central bond of a dihedral, the dihedral parameters could be treated the same as other dihedrals with the same central bond. If the metal ion is in the central bond of a dihedral, the dihedral parameters are usually assumed to be negligable.[146] Overall, the dihedral and improper torsion terms involving metal ions are usually treated as having a zero barrier height when using classical potentials. For example, in the early work of Hancock, the torsion parameters were typically omitted.[691] In the extensive work of Lin and Wang,[655] and Peters et al.,[1] modeling Zn complexes in protein system, and the work of Rui et al.[641] modeling Mn-containing protein complexes, setting the torsion terms to zero had no adverse effects. Moreover, in a range of work on metalloproteins from Merz and co-workers,[652−654,656−660] torsion terms involving metal ions were also treated as having zero barrier heights. In the INTERFACE force field for different material systems, there is generally no dihedral or improper torsion parameter assigned. Furthermore, adding dihedral parameters may cause a problem in MM modeling including metal ions.[699] Neglecting these terms can be ascribed to various factors including rigidity of the overall complex, high periodicity of TM-based torsion motions, functional form issues, 1-4 nonbonded interaction coupling, small barrier heights, etc., but probably the latter is most often invoked.

4.3.2.1. Rigidity. Bonds become harder to rotate when molecular structures become more "compact". The bond in a diatomic molecule (e.g., F_2) can be viewed as rotating freely, while for the ethane molecule, which has two connected sp^3 carbon atoms with each having 3 bound hydrogen atoms, a rotation barrier (~3 kcal/mol) is introduced.[587] TMs usually have large CNs, yielding compact structures, even more so when the ligands are large, and the metal sites in protein systems are even more rigid due to restrictions introduced by the protein matrix. In these situations, large-scale bond rotations are not expected to occur, making the neglection of torsion terms involving metal ions largely inconsequential.

4.3.2.2. High Periodicity and Small Amplitudes. The torsion parameters are usually not considered in TM complexes because of their high periodicity and the notion that the barrier heights are generally low.[139] Because of the high periodicity of TM complexes, higher Fourier terms may be needed to accurately model the torsion PES. An octahedrally coordinated metal ion has 4-fold rotation barriers; hence a Fourier term with periodicity of 4 will be needed to accurately model this torsion motion. Importantly, more terms in the Fourier function directly result in more complicated parametrization efforts.

Moreover, the torsion barriers for TM complexes are usually small. For example, it was shown experimentally that there is a high frequency rotation of the Cr−N bond in the $Cr(NH_3)_6^{3+}$ system, even at temperatures as low as 20 K.[700] In the review of Brubaker and Johnson in 1984, the barriers of dihedral and improper torsion potentials are generally small.[139] Weaver et al. investigated the performance of CCSD and CCSD(T) methods for predicting the HOFs of Zn-containing systems in 2009.[205] In this work, they carried out a PES scan of the H−C−Zn−C−H twisted dihedral angle (note this is a 1-5 interaction, see Figure 48) for the $Zn(CH_3)_2$ complex using the CCSD/6-31G** level of theory. The computed barrier is very small (less than 0.03 kcal/mol, see Figure 49) and is just ~1% of the barrier observed for the H−C−C−H dihedral angle of ethane (~3 kcal/mol).

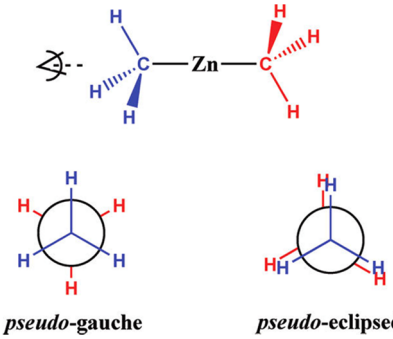

Figure 48. Newman projections depicting viable $Zn(CH_3)_2$ conformations. Reprinted with permission from ref 205. Copyright 2009 American Chemical Society.

DOI: 10.1021/acs.chemrev.6b00440
Chem. Rev. 2017, 117, 1564−1686

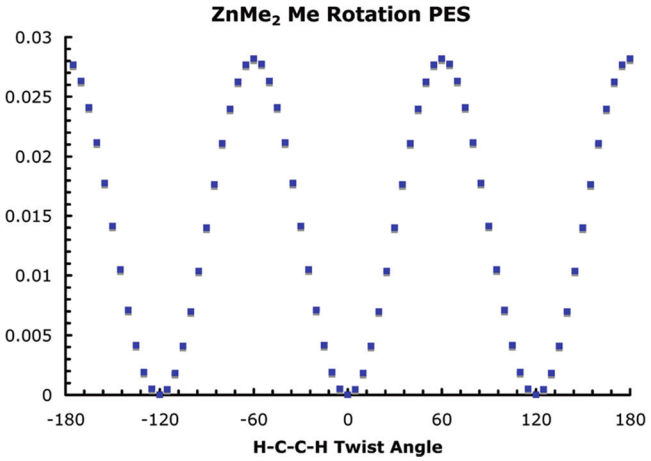

Figure 49. Relative conformational energy versus H−C−C−H twist for $^{1}Zn(CH_3)_2$ (CCSD/6-31G**); unrelaxed scan in 5° increments. Minima at −120°, 0°, and 120° correspond to the pseudoeclipsed conformation; maxima at −60°, 60°, and 180° correspond to pseudogauche. Reprinted with permission from ref 205. Copyright 2009 American Chemical Society.

4.3.2.3. Different Functional Forms. Another reason torsion terms are neglected is that the torsion parameters obtained using "one-shot" methods (such as the Z-matrix and Seminario methods) are for the harmonic equation and cannot be readily applied to Fourier terms directly. For example, Nilsson et al. parametrized the harmonic dihedral parameters (using the CNS force field) for several heterocompounds using the Seminario method and then applied them to XRD refinement with excellent performance.[669] However, this option is not readily available to fit complex Fourier expansions, making the development of this class of Fourier potentials an even greater challenge.

4.3.2.4. 1-4 Interactions. Moreover, dihedral parameters usually need to be fit under the total or partial consideration of 1-4 nonbonded interactions, making the parametrization process even more complex and time-consuming. Because the scaling factor may vary among different force fields, care should be taken when transferring these parameters for relevant dihedral terms.

4.3.2.5. Examples Obtaining the Torsion Parameters for Metal-Containing Complexes. Burger et al. parametrized the dihedral terms for the dizinc complex of bis-dipicolylamine based on a relaxed PES scan.[682] Scans along the dihedral with QM and MM (with dihedral terms set to zero for the latter) methods were performed, while the difference was used to fit the Fourier expansion through a least-squares algorithm. A cutoff value of 0.1 kcal/mol for the V_i term ($V_i/2$ is the rotation barrier) was used to truncate the Fourier expansion. Some other details of their work can be found elsewhere in the present text (section 4.2.6).

In some studies of metal-containing complexes, dihedral or improper torsion terms were included to constrain the planarity of the complex. For example, Hambley investigated the ligand rotation barriers of several Pt complexes (diammine- and bis(amine)bis(purine)-Pt^{2+} complexes) using a classical mechanics force field,[701] in which an improper torsion parameter with a 602 kJ/mol (~144 kcal/mol) barrier was added to retain the planarity of the Pt complexes. The calculated ligand rotation barriers agreed well with experimental results. Finally, it was shown that the rotation barriers are predominantly influenced by the interaction between the ammine/amine ligands and the 6-position group of the coordinated purine ligands. This research relates to cisplatin and its congeners, while related discussion of the impact of their work on broadening the understanding of this drug class is included in their work.

4.4. Charge Parameters

Similar to force field development for organic molecules, electrostatic terms were usually not considered in early modeling studies of TM complexes.[139,691] Later, as was also concluded for the modeling of macromolecular systems including proteins, the partial charge term is necessary for the accurate representation of long-range electrostatic interactions.[702]

There are a number of approaches to determine charge parameters: empirical methods, methods based on QM fitting, experimental derivation, FQ method, etc. Empirical charges were mainly used in the early stages of modern force field development, which can be fitted to reproduce experimental structures, energetics, and dipole moments.[591,592,595] CFF[591,592,595] and OPLS[703,704] are two well-known force fields that used empirical charges. However, empirically derived charges offered challenges when trying to represent transition and excited states, while QM calculations could readily generate the needed parameters. Moreover, it is time-consuming to fit empirical charges because of the need of extensive testing using minimization, MC, or MD simulations to reproduce requisite experimental properties. Given these considerations, QM-derived charges tend to be the preferred approach in the design of modern force field models. An intriguing approach involves obtaining charges based on experimental data, and they have been shown to yield excellent performance in classical modeling studies.[598] Finally, the FQ model is also widely used in contemporary molecular simulation studies, but we defer discussion of this method until section 6.1.

4.4.1. Quantum Mechanics-Derived Charges. There are a number of ways to obtain QM-derived partial charges, all with their associated pros and cons. For example, charges can be obtained using molecular orbital (MO) analysis (e.g., Mulliken,[705−708] NPA,[709] AOIM[710]), based on ESP fitting (e.g., Singh−Kollman,[711] CHELP,[712] CHELPG[713]), based on the electron density in real space (e.g., AIM,[714] Hirshfeld,[715] ADCH[716]), and then a number of ways to derive charges using postprocessing or scaling techniques (e.g., AM1-BCC,[717,718] CM1,[719] CM2,[720] CM3,[721] CM4,[722] CM5,[723]). The Mulliken charge, which is based on the Mulliken population analysis, is widely used because it is easy to obtain and has a well-understood physical meaning. However, raw Mulliken charges are not suitable for modeling atomic partial charges directly for use in force field methods. This is because the Mulliken charge is basis set sensitive and does not accurately reproduce the multipolar properties of molecules. Scaling procedures can be effectively applied to Mulliken charges for subsequent use in MM modeling. For example, AM1-BCC charges were based on Mulliken population analysis and then scaled to reproduce HF/6-31G* calculated RESP charges. The CM1 charge model was derived from Mulliken charges and then fitted to experimental properties. Mulliken charges are also used in the SCC-DFTB method (see Section 2.4.4) for the description of changes in the charge.

Partial charges, based on ESP fitting, can accurately reproduce the multipolar properties of molecules and could

DOI: 10.1021/acs.chemrev.6b00440
Chem. Rev. 2017, 117, 1564−1686

reproduce intermolecular or intramolecular electrostatic interactions, leading to the conclusion that they provide an excellent choice for partial charges in MM calculations.[711]

4.4.1.1. Electrostatic Potential Map. Bonaccorsi and co-workers developed the idea of using electrostatic potential maps (EPMs) to study molecular properties in the early 1970s.[724−730] They applied the method to various small molecule systems including diatomic and triatomic molecules,[726] three-membered ring molecules,[724,725,728] and nucleic acid bases,[730] and the results were insightful in further our understanding of protonation properties or identifying electrophilic sites. Kollman et al.[731] and Morokuma et al.[732,733] used the EPM method to explore hydrogen-bond interactions and found them to be helpful in predicting the directionality and strength of hydrogen bonds. Kollman and co-workers carried out pioneering studies using QM-derived ESPs maps to explore Coulombic interactions in biological systems. Hayes and Kollman employed ESP maps to investigate protein−ligand interactions between carboxypeptidase A (CPA) and the Gly-Tyr substrate in 1976.[734] They predicted that an *o*-OH-Gly-Tyr analogue would have a stronger binding interaction to CPA than Gly-Tyr.[734] In another work, they also explored important electrostatic contributions in the binding pocket that might facilitate catalysis.[735] Later, Nuss and Kollman used ESP maps to study the interactions between different base pairs.[736] The predicted interactions correlated well with relative biological activities but not as well with relative binding affinities.[736]

After the application of the EPM method to explore chemical phenomenon, partial charges derived by fitting were determined to reproduce the EPMs and to mimic the charge distribution in a molecule. For example, Bonaccorsi et al. utilized 13 charge points in a single water molecule to represent the QM calculated charge distribution of a water molecule.[727] These partial charges were placed on the nuclear centers and the centroids of localized orbitals. These partial charges reproduced the QM-derived EPM reasonably accurately. Afterward, Almlöf and Wahlgren fit the atomic charges of the H_3O^+ ion via a least-squares fit of the QM calculated potentials on points surrounding the hydronium ion.[737]

4.4.1.2. QM-Derived ESP Charges. The ESP of a point r in space can be calculated using QM methods based on eq 87, where Z_A is the nuclear charge, R_A is the position of the nuclei, while r' is a dummy integration variable. i and j are atomic orbital indices, while P_{ij} is the density matrix. The classical ESP of the same point (at r) is represented by eq 88, where R_A is also the nuclear coordinate. q_A is the atomic charge, for which we want to finally fit, based on a linear least-squares fitting between the $V_{QM}(r)$ and $V_{MM}(r)$ values.[738] The total net charge is applied as a restraint during the fitting process, while other restraints (e.g., dipole moment, etc.) may also be applied when so desired. The location of the ESP points depends on the algorithm being employed, and different weights can be applied to select ESP points during the fitting process (e.g., making the points that are closer to the nuclei have larger weights).[738]

$$V_{QM}(r) = \sum_A \frac{Z_A}{|r - R_A|} - \sum_{ij} P_{ij} \int \frac{\chi_i \chi_j}{|r - r'|} \, dr' \tag{87}$$

$$V_{MM}(r) = 332.1 \sum_A \frac{q_A}{|r - R_A|} \tag{88}$$

Scrocco and Tomasi,[739] Momany,[738] Cox and Williams,[740] and Smit et al.[741] all carried out pioneering works on the determination of atomic partial charges of small molecules based on the EPM. The critical issue was to locate the position and necessary density of points to obtain the best fit of atomic charges to the EPM. It was proposed that the points should not be too close to the nuclei, where the ESP is usually positive.[740] It was also shown that the root-mean-square (RMS) error of the fit increased when using points close to the nuclei in the fitting process.[711,740] Furthermore, it was found that it was not necessary to considered points that were too far away from the nuclei. Overall, it was found that picking points between the VDW surface and up to 3 or 7 Å away from this surface gave satisfactory results. A total net charge restraint was needed for the ESP fitting procedure, and further constraints could be added for the dipole moment or higher multipole moments as needed. Meanwhile, different weights could be applied to points in different areas of the EPM. For example, Momany used smaller weights on points closer to the VDW surface during the fitting procedure.[738] Generally, there are two different ways to choose ESP points: cube-based or layer/shell-based. There is not a clear sense of which approach is the best, and it depends somewhat on the properties to be reproduced.[742] Momany selected points between the VDW surface and several angstroms away from it, and used a density of 0.5 Å between each point.[738] Cox and Williams used a boundary that was 1.2 Å away from the VDW surface, with a shell thickness as 1.0 Å and cubic grid spacing of 1.0−1.2 Å.[740] Singh and Kollman picked points on a shell around the molecule at 1.4, 1.6, 1.8, and 2.0 times the VDW radius with a density of 1−5 points per unit area.[711] The CHarges from Electrostatic Potentials (CHELP) method selected points symmetrically placed on spherical shells around the atomic nuclei with 14 points on each shell. In total, there were 4 shells selected with the innermost as the VDW surface of the molecule and the other shells placed at 1, 2, and 3 Å away from the VDW surface, respectively.[712] The CHarges from ELectrostatic Potentials using a Grid-based (CHELPG) method selects points between the VDW surface of the molecule and a surface 2.8 Å away using a cubic grid with a spacing of 0.3 Å between points.[713]

Singh and Kollman described an algorithm for charge derivation based on fitting point charges to ab initio-derived ESPs and applied it to a selection of small molecules in 1984.[711] The Singh−Kollman approach has also been used in the charge determination for united atom models and lone pair sites.[711] On the basis of united atom fits, the ff84 AMBER force field was developed for proteins and nucleic acids.[392] Chirlian and Francl created the CHELP algorithm and related software to fit atomic charges based on QM calculated ESPs in 1987.[712] They found that the results based on calculations using the HF method with different basis sets (including STO-3G, 3-21G, and 6-31G*) could accurately reproduce QM-derived dipole moments. Finally, they selected the HF/3-21G level of theory as the best method to use based on its speed and overall accuracy. Breneman and Wiberg noted that the CHELP algorithm was inadequate to describe the charge invariance of internal rotations and developed the CHELPG method to alleviate this issue.[713] Besler et al. carried out a study of ESP charge fitting on a series of organic molecules using the MNDO, AM1, HF/STO-3G, and HF/6-31G* levels of theory in 1990.[743] In this work, they found that the MNDO method showed better performance than AM1 and HF/STO-3G calculations when compared to the HF/6-31G* results. Moreover, HF/6-31G* quality ESP charges could be obtained

DOI: 10.1021/acs.chemrev.6b00440
Chem. Rev. 2017, 117, 1564−1686

by scaling the MNDO results, which afforded a quick way to derive reliable atomic charges for a classical force field.

Merz and co-workers incorporated the ESP approach in their investigations of human carbonic anhydrase II (HCAII, a zinc-containing enzyme) in the early 1990s.[702,744,745] In their modeling of the metal-containing active site, they used equilibrium bond distance and angle values from QM optimizations based on the MNDO method, the bond and angle force constants from experiment, while the LJ parameters for the zinc ion were obtained such that they reproduced the QM calculated geometries and interaction energies of the $Zn^{2+}-CO_2$ and $Zn^{2+}-H_2O$ complexes. It was shown that the metal site experiences a strong electron transfer effect from the coordinating groups to the zinc ion. For example, the MNDO ESP calculations of the $[(imidazole)_3Zn-OH]^+$ complex showed a charge of +0.5 on zinc, which is much smaller than its formal oxidation state +2.[744]

By combining the MD and FEP methods, Merz calculated the binding energies of the CO_2 molecule to two different binding sites in the HCAII system.[744] The results showed good agreement with the experimental values and suggested that the first binding site of CO_2 is catalytically important, while the second binding site, which is further away from the metal site, served to increase the surface area for CO_2 to be recognized and bound by HCAII. In related work, Merz and co-workers performed FEP calculation on several sulfonamide inhibitors bound to HCAII.[745] Experimental relative binding affinities were reproduced via a consideration of the pK_a differences between the sulfonamide and sulfonate groups. They concluded that a single hydrogen interaction, which is present in the sulfonamides but not sulfonates, was responsible for the higher binding affinity of the former.

Hoops et al. carried out an investigation of different charge modeling strategies on a zinc center coordinated by the side chain nitrogen atoms of three HIS residues and one hydroxide oxygen.[702] They calculated the ESP charges of the $[Zn(NH_3)_3H_2O]^{2+}$ (high pH form) and $[Zn(NH_3)_3OH]^+$ (low pH form) systems employing the MNDO, HF/STO-3G, HF/MINI-4, HF/MIDI-4, and HF/6-31G* levels of theory based on MNDO optimized geometries. From this study, they found that calculations based on the HF/STO-3G level of theory gave the smallest positive charges for the zinc ion (+0.68e and +0.48e for the high and low pH forms, respectively), while the calculation based on HF/MINI-4 gives the most ionic picture of the zinc ion (+1.64e and +1.72e for the high and low pH forms, respectively), and the other three calculations gave results between these extremes. All of these results indicated that it is not appropriate to assign a +2 point charge to the zinc ion in the bonded model. It was also found that the highest correlation between ESP charges derived from the HF/6-31G* level of theory was with MNDO. ESP charge fits based on MNDO calculations were also performed on the small (with HIS residues represented by imidazole groups) and large models (with the HIS residues capped by acetyl and methyl groups), based on which subsequent minimizations and MD simulations were performed. The bonded model, which assigned a +2 charge to the zinc ion combined with the charge model for the metal bound amino acid residues taken from the AMBER force field (referred to as the "Zn^{2+} bonded model" herein), was also tested. The Zn^{2+} bonded model showed a five-coordinated trigonal-bipyramidal geometry after structure minimization, while the other two models (they were also using the bonded strategy but with ESP partial charges) conserved the tetrahedral geometry of the metal site. It is intriguing that the model based on ESP charges fitted from the small model showed better results than that based on the ESP charges derived from the large model. The authors proposed that it might be due to the higher charge of the zinc ion in the large model.

However, ESP charges have drawbacks associated with their conformation dependence because they are usually derived on the basis of single conformation while charges fluctuate considerably in dynamic processes.[692,746,747] For example, Merz carried out ESP charge derivation of amino acids and monosaccharides based on the HF/6-31G*, MNDO, AM1, and PM3 methods.[746] He found that the MNDO-derived ESP charges correlated well with those obtained using the HF/6-31G* method, while the other two empirical methods (AM1 and PM3) performed quite poorly. He then developed an atom-by-atom transferable charge model for the monosaccharides, while for the amino acids large statistical fluctuations made that hard to accomplish. He found that the transferable model performed a little bit better than the MNDO-based method, while it had a much better performance than the transferable model after the MNDO results were scaled. 50 ps QM MD simulations on the Ala dipeptide were also performed using the MNDO method, and snapshots from the trajectory were used to derive ESP charges. Considerable charge fluctuations were found for the atoms in the Ala dipeptide. Moreover, he proposed that it is hard to derive the ESP charges for macromolecules directly due to large computational costs, while an ESP method based on transferable groups (could be atom, functional group, or residue based) could be developed to alleviate this problem.

Besides the drawback discussed above, the ESP approach often underestimates the charge on buried atoms (such as a quaternary carbon atom) and assigns unexpected large values for the charges of nonpolar atoms.[394] Moreover, the ESP charge model did not yield identical charges for atoms that rapidly exchange: for example, the methylene hydrogen atom charges in butane should be identical, but the ESP fitting procedure yields different values depending on the conformation used in the ESP fit.

4.4.1.3. QM-Derived RESP Charges. Bayly et al. noted that either the unconstrained ESP charges or ESP charges fit with a constraint on the methyl carbon atom in methanol would reproduce the ESP of methanol.[748] On the basis of this observation, they then proposed the RESP charge fitting algorithm, which was validated via the examination of multiple simple organic molecules.[748] They also found that hyperbolic restraints performed better than harmonic ones. Fitting was done at the HF/6-31G* level of theory, as in the past, because of the tendency of it to overestimate dipole moments of molecules in gas phase, thereby qualitatively mimicking solvation effects. For example, the HF/6-31G* level of theory overestimates the dipole moment of water in the gas phase as ~2.2 D, yielding a value more consistent with that of liquid water. From their studies, they observed that charges on important polar atoms were negatively impacted when carrying out fits that enforced charge equalization for atoms that exchange rapidly during MD simulation. To overcome this effect, one can average over the two charges, but this artificially enhances the dipole moment and reduces the overall quality of the ESP fit. On the basis of these observations, a two-stage algorithm was used to fit atomic partial charges. The first stage employed a small restraint on the heavy atoms, offered an

DOI: 10.1021/acs.chemrev.6b00440
Chem. Rev. 2017, 117, 1564−1686

excellent fit for the polar groups. The second stage used a larger restraint on the carbon atoms of CH_2 and CH_3 groups while equalizing the atomic charges of the attached hydrogen atoms.

Subsequent work by Cornell et al. further explored the ESP and RESP charge algorithms for small organic molecules.[692] They found that RESP charges with a 1/1.2 scaling factor for 1-4 electrostatic interactions performed well in reproducing high-level ab initio results. Overall, the RESP-derived charges outperformed ESP charges in the ability to reproduce conformational properties of small organic molecules. Both methods gave good agreement with experimental HFEs. Moreover, RESP-derived charges reproduced both inter- and intramolecular structural properties and energies quite well, thereby offering an excellent tool for the development of a general force field for both biological macromolecules and small organic molecules.

For example, Cieplak et al. parametrized the charge parameters of nine different nucleic acid fragments (4 deoxyribonucleosides, 4 ribonucleosides, and dimethylphosphate) and 20 different amino acid fragments with multiple-molecule RESP charge fits in developing the AMBER ff94 force field.[749] In the creation of the atomic charge model for ff94, two configurations with different dihedral angles of each amino acid were employed in the fit. The resultant parameters showed less conformational dependence when compared to ESP-derived charge parameters. Other force field development work has extensively employed the RESP fitting procedure. In another example, Wang et al. investigated the performance of the RESP model in evaluating the conformational energies of organic and biological related molecules. They found that by employing HF/6-31G* RESP charges, they were able to use fewer torsion terms in the force field.[750] After refitting the torsion parameters, they described the AMBER ff99 force field, which takes advantage of this observation and uses a reduced torsion parameter set. Following this work, Wang et al. developed the GAFF for organic molecules, which contains H, C, N, O, S, P, F, Cl, Br, and I.[397] HF/6-31G* RESP charges were used, and AM1-BCC charges were proposed as an alternative choice for point charge derivation for larger systems. Results from three test sets showed that GAFF reproduced X-ray-derived structures, experimental relative energies, and high-level QM optimized structures and intermolecular energies.

The RESP algorithm has become the standard approach for fitting the partial charges of metal−protein complexes. Unlike flexible amino acids in proteins, the amino acids ligating to a metal ion are usually more rigid, leaving only one configuration for the derivation of the RESP charge model for metal ion complexes. For metal ions, the DFT functional B3LYP with the 6-31G* basis set has emerged as the method of choice for RESP charge evaluation because of its overall accuracy and speed. However, in some cases, effective core potential basis sets for metal ions offered better performance.[321] In particular, the choice of QM method plays a crucial role when parametrizing negatively charged clusters.[677,751] For example, B3LYP/6-31G* produces a negative charge on the hydrogen atoms of $Zn(Cys)_4^{2-}$ clusters, while a B3LYP/LANL2DZ basis set addresses this problem.[677]

4.4.2. Experimentally Derived Charges. It is possible to derive atomic charges from experimental XRD results and dipole moments.[752] Even for elements with high oxidation states, their atomic charges are usually between +2 and −2.[752] For example, for the central atoms in $[VO_4]^{3-}$, $[CrO_4]^{2-}$, and $[MnO_4]^{2-}$, which have +5, +6, and +7 formal charges, respectively, atomic charges of +1.05, +1.09, and +0.96 are found on the basis of theoretical calculations.[134] The central atoms in OsO_4 and $[IrO_4]^+$, which have +8 and +9 formal charges, have atomic charges of +1.475 and +1.470, according to the natural population analyses.[134] The $[PtO_4]^{2+}$ complex, which was predicted to exist, has a +1.28 charge on the Pt atom based on calculations by the Hirshfeld method even though its formal charge is as high as +10.[36] It was shown that except for extremely ionic compounds such as NaCl and CaF_2, there is usually a deviation of the atomic charges from the formal ones. For example, LiF has +0.95e on Li and −0.95e on F, while +1.6e and −1.6e are found on Mg and O in MgO.[752] Because there may be large deviations between theoretically derived charges based on different model choices, experimentally derived charges provide a reference to evaluate methodological choices or to scale atomic point charges. For example, the INTERFACE force field[598] uses semiempirical charges derived using experimentally determined atomic charges and an extended Born cycle. It affords a charge for the Si atom, which is tetrahedrally coordinated to 4 oxygen atoms, of +1.1e (±0.1e). This charge assignment reproduces surface energies within ±10% of experiment. In earlier studies, the atomic charges on Si ranged from +0.5e to +4.0e, with some of these charge assignments yielding significant deviations from experimental surface energies.[753]

4.4.2.1. Charge Derivation from XRD Experiments. In a normal XRD refinement, a free atom density function is used (shown in eq 89).[754] N_c and N_{val} are the core and valence electron numbers. ρ_c and ρ_{val} are spherically distributed electron density functions of core and valence electrons in free atoms (see eq 89). Atomic positions and B factors (which are also called temperature factors, representing the uncertainty of each atomic position) are modified during the refinement process to minimize a differential equation between the experimental and predicted values. The R factor is determined on the basis of the relative difference between the observed and calculated values from the model (shown in eq 90).

$$\rho(r) = N_c\rho_c(r) + N_{val}\rho_{val}(r) \tag{89}$$

$$R = \frac{\sum ||F_{obs}| - |F_{calc}||}{\sum |F_{obs}|} \tag{90}$$

Furthermore, XRD refinement can be performed using the "κ refinement" approach (based on eq 91, no multipolar term),[755] and the Hansen−Coppens model (see eqs 92 and 93).[756]

$$\rho(r) = N_c\rho_c(r) + P_{val}\kappa'^3\rho_{val}(\kappa' r) \tag{91}$$

$$\rho(r) = N_c\rho_c(r) + P_{val}\kappa'^3\rho_{val}(\kappa' r) + \sum_l \kappa''^3 R_{nl}(\kappa'' r) \sum_m P_{lm} Y_{lm}(\theta, \phi) \tag{92}$$

$$R_{nl}(r) = N_l r^{nl}\, e^{-\zeta r} \tag{93}$$

In eqs 91 and 92, P_{val} and P_{lm} are adjustable parameters. The third term in eq 92 is a nonspherical multipolar term. This term is omitted in the "κ refinement" (see eq 91). κ' and κ'' are the contraction−expansion coefficients of the spherical term and the nonspherical multipolar term, respectively. A value greater than 1 means a contracted atomic orbital, and less than 1 means an expanded orbital. The cubic powers of κ' and κ'' are for normalization. The $N_{val}-P_{val}$ difference (where P_{val} value is fitted on the basis of eqs 91 or 92) represents the atomic charge

DOI: 10.1021/acs.chemrev.6b00440
Chem. Rev. 2017, 117, 1564−1686

on an atom. The parameters can be transferred between the same atom types in different systems and used for low-resolution structure refinement. A deformation density map can be obtained on the basis of the difference between electronic densities determined experimentally and those superpositioned by the free atom density. Both the static deformation density map (assuming atoms are fixed and B factors are zero) and the dynamic deformation density map, which are based on Fourier transformations, can be calculated. These maps yield detailed insights into chemical bonding.

There are a number of systems that have been investigated on the basis of the method described above. For example, Lecomte et al. have analyzed atomic charges based on XRD refinement of a series of peptides and crambin (with 46 residues).[757−759] Pearlman and Kim determined atomic charges of DNA constituents experimentally.[754,760] Research studying inorganic crystals such as α-AlO(OH),[761] $AlPO_4$,[762] α-Al_2O_3,[763] and dipotase[764] has been conducted in an effort to determine atomic charges.

Pichon-Pesme et al. have shown that multipolar parameters from high-resolution structures can both be transferred to and help in the refinement of low-resolution structures.[757] They applied multipolar parameters from several high-resolution peptide structures to refine the XRD structures for pGlu-Phe-D-Pro-ϕ[CN_4]-Me, resulting in more physically meaningful mean-square displacement factors (U^{ij}).

It was shown that the atomic charges obtained from "κ refinement" of the LBZ helix octapeptide were more consistent with the atomic charges present in the AMBER ff94 force field than charges from multipolar refinement.[758] The protein backbone CONH, and C atoms in CH_3 groups, had the largest charges in terms of absolute values and were in the best agreement. However, unrealistically small charge values appeared in the work on crambin, which suggests accurate atomic charge refinement needs ultrahigh resolution data.[759] In the work on crambin, experimental static deformation density maps agree with static map calculations based on the HF/6-311G++ level of theory (see Figure 50). In the work of Pearlman and Kim on DNA constituents,[754] they found that their charges qualitatively but not quantitatively agreed with theoretically derived ESP charges based on HF/STO-3G calculations performed on the same crystal structures.

Atomic charges can also be fit from the ESPs on or outside the VDW surface, being derived in a way akin to the ESP or CHEPLG method. The ESP can be obtained on the basis of the electronic densities (see eqs 94−97).

$$V(r) = V_{\text{core}}(r) + V_{\text{val}}(r) + \Delta V(r) \tag{94}$$

$$V_{\text{core}}(r) = \frac{Z}{|r - R|} - \int_0^\infty \frac{\rho_c(r')\, \mathrm{d}^3 r'}{|r - R - r'|} \tag{95}$$

$$V_{\text{val}}(r) = -\int_0^\infty \frac{P_{\text{val}} \kappa'^3 \rho_{\text{val}}(\kappa' r')\, \mathrm{d}^3 r'}{|r - R - r'|} \tag{96}$$

$$\Delta V(r) = -4\pi \sum_{lm} \frac{\kappa'' P_{lm}}{2l+1} \left[\frac{1}{\kappa''^{l+1} |r - R|^{l+1}} \times \int_0^{\kappa''|r-R|} t^{l+2} R_{nl}(t)\, \mathrm{d}t + \kappa''|r - R|^l \times \int_{\kappa''|r-R|}^\infty \frac{1}{t^{l-1}} R_{nl}(t)\, \mathrm{d}t \right] Y_{lm}(\theta', \phi') \tag{97}$$

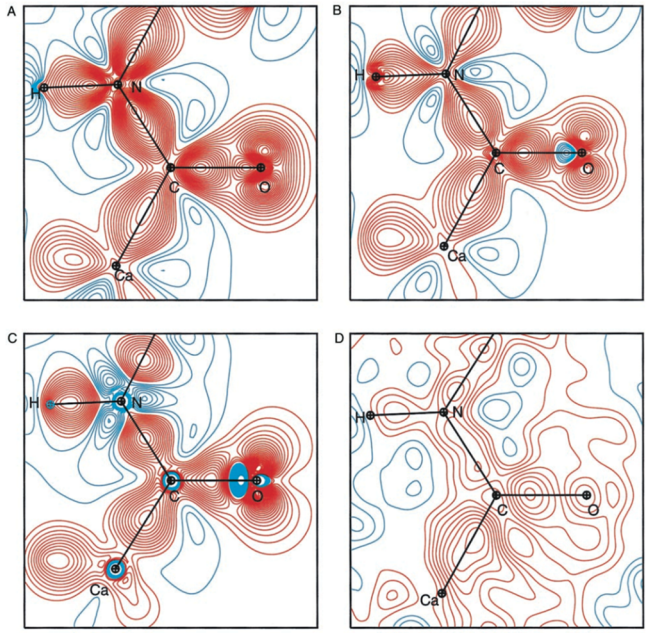

Figure 50. Deformation map in peptide bond plane. (A) Static map obtained from database parameters. (B) Experimental static map obtained using atomic charges and multipole parameters refined against the crambin diffraction data. (C) Theoretical static map computed for the pseudomonopeptide (*Z*)-*N*-acetyl-α,β-dehydrophenylalanine methylamide.[765] (D) Experimental dynamic map for the peptide Ala-9-Arg-10 of crambin. The contour level is 0.05 $e^-/Å^3$. Positive, red lines; negative, blue lines. Reprinted with permission from ref 759. Copyright 2000 National Academy of Sciences, U.S.A.

Herein, $V(r)$ is the ESP of a point with position r, which consists of $V_{\text{core}}(r)$, that is the ESP caused due to the core electrons, $V_{\text{val}}(r)$, which is the ESP induced by valence electron, and $\Delta V(r)$, that is the ESP generated by the nonspherical part of the electron density. Atomic charges are fit on the basis of the electronic potential at many points on a shell or several shells outside a molecule. The fitting quality is then evaluated on the basis of the ability of calculated ESPs to reproduce the original ESPs.

In the work of Ghermani et al., they fit the charges of a pseudopeptide (*N*-acetyl-α,β-dehydrophenylalanine methylamide) along the lines of ESP charge fitting, and regenerated the EPM based on the fitted point charges.[766] The EPM was also constructed on the basis of atomic charges obtained as $q = Z - P_{\text{val}}$ from "κ refinement". They found the former agreed well but the latter differed significantly from the EPM generated from the electronic density directly. Additionally, they showed that the fit quality improves with the addition of atomic multipole moments over only using monopole charges. Results showed that ESP fitting without multipole moments yielded charges on oxygen, hydrogen, and a residual factor (*R*-factor) of −0.89e, +0.44e, and 0.19, respectively. On the other hand, a fit using multipole moments (dipole for hydrogen, and up to quadrupole for oxygen) gave values of −0.54e and +0.27e, 0.0017, respectively, for these quantities.

In a later work, Bouhmaida et al. fit atomic charges and multipole moments (up to octupoles) of the same pseudopeptide based on ESPs calculated from electron density obtained using the Hansen−Coppens model (which contains multipolar terms, see eqs 92 and 93).[767] They found that the fitted monopole charges agreed well with the charges calculated

DOI: 10.1021/acs.chemrev.6b00440
Chem. Rev. 2017, 117, 1564−1686

directly from the $N_{val}-P_{val}$ (see eqs 89 and 92). The atomic charge term and multipole moment terms in the electronic density function can be separated because the former is related to the spherical density term, while the latter is related to the multipolar terms. They also found similar charges and multipole moments between symmetry related or chemically equivalent atoms, implying that these parameters are transferable.

Given the promise of this approach, why has it not found broader application? Atomic charge derivation based on XRD refinement requires structures with very high resolution and low *B* factors. This makes the method limited to crystals with relatively small unit cells. To date, only a few systems have been investigated. Besides using XRD experiments, experimental dipole moments can also be exploited to determine atomic point charges.[752]

4.4.2.2. Charges Based on an Extended Born Cycle. Heinz and Suter developed a semiempirical method to estimate atomic charges.[752] It is based on experimentally determined atomic charges, an extended Born cycle (see Figure 51), and

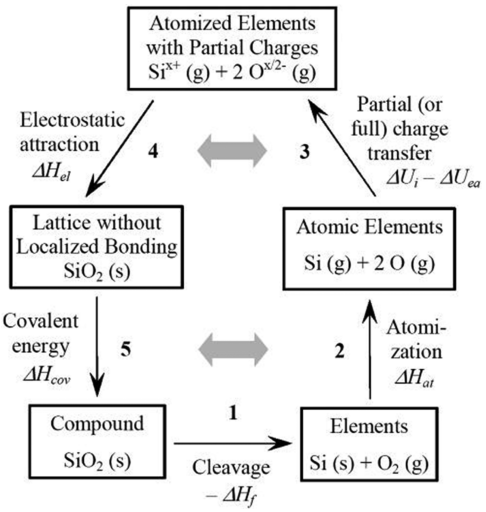

Figure 51. Extended Born model for the example of silicon dioxide (SiO_2). Single-headed arrows describe reversibly taken steps, as indicated in the text of ref 752. Partial ionization energies and electron affinities are involved in step 3. The LE is divided into an electrostatic/repulsive component in step 4 plus a covalent component in step 5. The respective stoichiometric coefficients must be remembered. The shaded, double-headed arrows indicate the complementary electrostatic (top) and covalent (bottom) contributions to the cycle. Reprinted with permission from ref 752. Copyright 2004 American Chemical Society.

chemical knowledge. The extended Born model they use gives a qualitative estimate of the extent of covalent and ionic character in a chemical bond. The atomization energy (E_{at}), IP, and EA values of different elements were used in the extended Born cycle. The E_{at} + IP-EA value can be used as a general factor to evaluate the covalent extent of a chemical bond. Chemical knowledge was used to facilitate charge estimation: for example, (1) covalently bound atoms usually have smaller CNs and less ionic charges than atoms in ionic bonds; (2) larger E_{at} generally indicates a stronger covalent bond; (3) increase in IP is correlated with decreasing atomic charge (a larger IP value means it is harder to lose an electron); and (4) increase in the polarizability α generally combines with a decrease in the IP value for atoms located in higher rows. On the basis of the set of rules sketched out above, they determined that the charge on the Si atom in silicates, which is tetrahedrally coordinated to four oxygen atoms, is +1.1e (±0.1e). This charge assignment offered good performance (<10% deviation from experimental surface energies) in computer simulations, in contrast to the wide range of values (+0.5e to +4.0e) employed in early work, which gave significant deviations in computed surface energies relative to experiment.[753]

In the INTERFACE force field, Heinz et al. parametrized atomic charges on the basis of experimentally determined charges, together with the covalent and ionic extent of the chemical bonds estimated using the extended Born cycle, combined with chemical knowledge (see Figure 52).[598] It was shown that it was possible to get a converged charge set with uncertainties from ±0.1e to ±0.2e for highly charged species and <10% for less charged species (with charges below ±1.0e). The INTERFACE force field was able to simulate various properties simultaneously, even properties it was not fit against. Results showed that the INTERFACE force field reproduced cell parameters and densities with deviations of 0.2%−1.0%, surface properties with deviations of 0−10% (some other force fields have deviations of up to 500% due to poorly derived partial charges and overfitting of the LJ parameters), elastic constants, and moduli with deviations of less than 20%. Overall, this force field provides a platform by which mechanisms of interfacial processes could be explored, and affords the ability to predict properties that are hard to measure via experiment. Its overall performance is largely due to the parametrization of its nonbonded interactions using a thermodynamically consistent scheme, which imparts realistic physical and chemical meaning to the parameters.

4.4.3. Charge Derivation for Periodic Systems, Especially Metal−Organic Framework Systems. MOFs have attracted a lot of attention due to their potential application to an array of problems. Because a plethora of MOFs could, in principle, be generated on the basis of the broad array of potential linkers and metal ions available, a strategy to scan this space by purely experimental means would, to say the least, be very time-consuming. However, using computational tools to screen potential MOFs in silico could handle the "filtering" work, allowing experimental efforts to focus on more promising regions of the MOF "genome".

Hamad et al. systematically reviewed charge derivation strategies for MOF systems.[768] There are various ways to derive atomic charges for MOFs using QM-based methods, FQ models, and empirical methods. Generally, QM methods are the most accurate, but the most time-consuming, while other methods are more efficient and are best used in "screening" methods for rapid structure filtering. There are different QM-derived charges used in MOF simulations,[768] including Mulliken, NPA, AIM (or called Bader charges), density-derived electrostatic and chemical (DDEC),[769] ESP, repeating electrostatic potential extracted atomic (REPEAT),[770] and density-derived atomic point (DDAP)[771] charges. Other charge methods have also been exploited, for example, the extended charge equilibration (EQeq) method, which is based on the FQ model (see section 6.1),[772] and connectivity-based atom contribution (CBAC) charges based on atomic connectivities.[773] Below we introduce some representative methods and note that these methods can also be applied to periodic systems other than MOFs.

4.4.3.1. Cluster Method. ESP charges are one of the most commonly used charge sets in MOF simulations. However,

DOI: 10.1021/acs.chemrev.6b00440
Chem. Rev. 2017, 117, 1564−1686

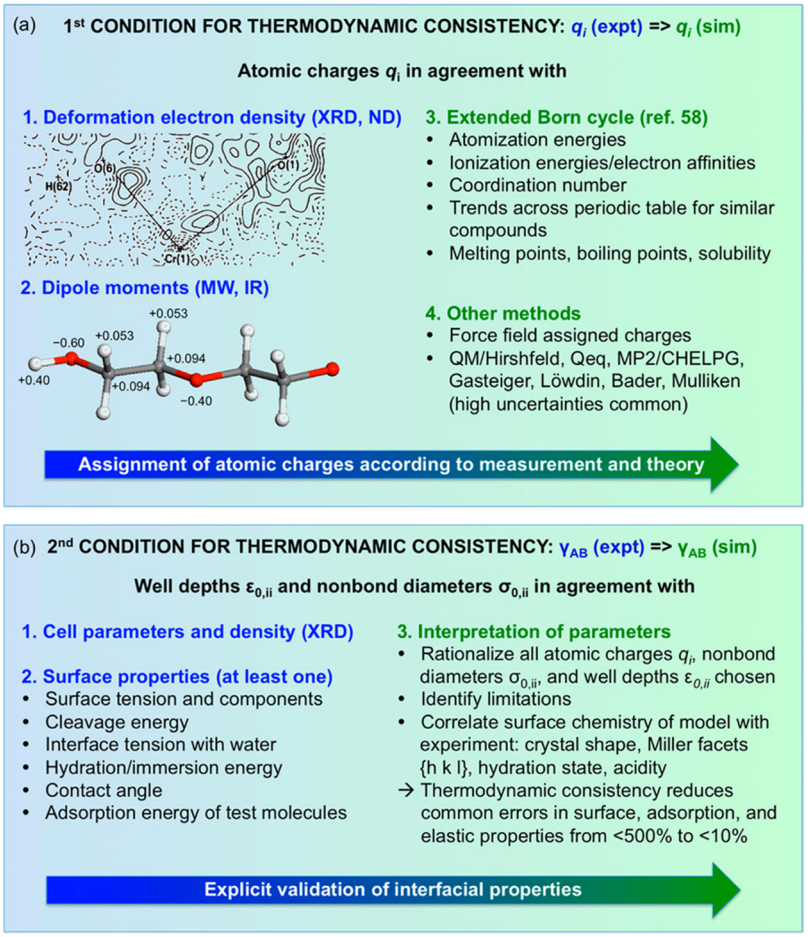

Figure 52. Most important criteria for obtaining thermodynamically consistent force field parameters. (a) Atomic charges and (b) computed interfacial properties in the models should quantitatively agree with atomic-scale and macroscale experimental data. The color scheme and single-headed arrows emphasize the feed of information from experiment (blue) into models and theory (green). Reprinted with permission from ref 598. Copyright 2013 American Chemical Society.

because MOFs are always periodic, it is hard to perform the ESP charge fitting directly, which leads to the need for the cluster approach.[768] Implementing the cluster approach is straightforward and can be readily handled by many extant programs. As shown in Figure 53, dangling hydrogen or methyl groups can be added to cap the system cut from the crystal structure. Different sizes of the excised MOF repeat structure can be used until the charge fitting results converge.

4.4.3.2. REPEAT Method. As shown in eq 98, the REPEAT method uses a modified error function for charge derivation,[770] while a FQ style penalty function was used to better fit the charges of buried atoms.

$$F(\{q_j, \delta_\phi\}) = \sum_{\text{grid}} \left(\phi_{\text{QM}}\left(\vec{r}_{\text{grid}}\right) - \phi_q\left(\vec{r}_{\text{grid}}\right) - \delta_\phi\right)^2 + \lambda\left(\sum_j q_j - q_{\text{tot}}\right) + \sum_j w_j\left(E_j^0 + \chi_j q_j + \frac{1}{2} J_j^{00} q_j^2\right) \quad (98)$$

$$\delta_\phi = \frac{1}{N_{\text{grid}}} \sum_{\text{grid}} \left(\phi_{\text{QM}}\left(\vec{r}_{\text{grid}}\right) - \phi_q\left(\vec{r}_{\text{grid}}\right)\right) \quad (99)$$

Here, δ_ϕ represents the relative difference between the QM-derived ESP values versus the ESP values based on the fit charges (see eq 99). Minimization of F with respect to both charges and δ_ϕ was performed in the charge derivation process. The scheme could be modified by symmetry relationships between atomic sites as needed. This method gives results similar to the CHELPG method for nonperiodic systems. It was also shown that the REPEAT method solved issues relating to the ESP method producing unphysical charges for periodic systems.

4.4.3.3. Connectivity-Based Atom Contribution Charge. Xu and Zhong developed the CBAC charge model in 2010.[773] It is based on the idea that there are a limited number of atom types in MOF systems. They identify 35 atom types (2 Zn, 1 Cu, 2 Co, 1 Cr, 8 O, 12 C, 6 N, 2 H, 1 Cl) in their work. The definitions and charges of these atom types are shown in Figure 54. A training set of 30 MOFs and a test set of 13 MOFs were used in the work. QM-derived charges were calculated on the basis of the UB3LYP/LANL2DZ-6-31+G* level of theory using the CHELPG method. In these calculations, the MOF clusters were terminated with metallic Li (for zeolitic imidazolate frameworks (ZIFs), and materials from Institute Lavoisier (MILs)) and methyl groups (for the remaining MOFs). It was shown that the fluctuation of the QM-derived charges is relatively small for the same atom type. Because the total charges of MOFs based on CBAC charges are not always zero, small adjustments in the CBAC charges may be required. It was found that this "fine-tuning" of the charges only caused modest changes to the calculated results. Excellent agreement between

DOI: 10.1021/acs.chemrev.6b00440
Chem. Rev. 2017, 117, 1564−1686

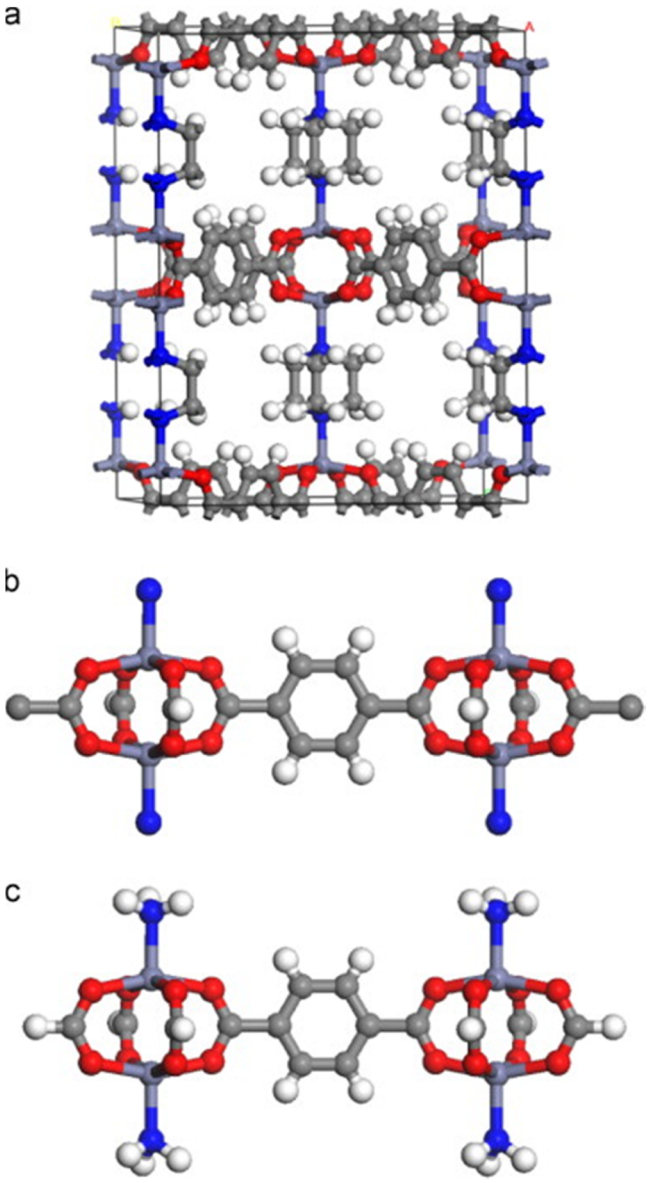

Figure 53. (a) Ball-and-stick representation of the atoms of the unit cell of DMOF-1 (Zn, O, N, C, and H atoms are represented as light blue, red, dark blue, gray, and white atoms, respectively). (b) Cluster created by cutting directly a piece of framework. This cluster cannot be used to model the environment of the BDC (1,4-benzenedicarboxylate) ligand and calculate its charges, because there are cleaved bonds that will have very different electronic structures than in the bulk structure. (c) Same cluster shown in (b), although the cleaved bonds have been saturated with H atoms to achieve electronic structures in the terminal N and C atoms that are similar to those in the crystal structure. Reprinted with permission from ref 768. Copyright 2015 Elsevier.

QM-derived and CBAC charges was observed on a test set of molecules. Comparison to experimental data was also performed, and good results were obtained. Extension of the database to new atom types (1 V and 2 O) was also tested, and the calculated results agreed well with available experimental data (see Figure 55).

4.5. van der Waals Parameters

The VDW parameters of metal ions in bonded models are usually extracted from the nonbonded model. This is reasonable for most cases because 1-2 and 1-3 nonbonded interactions are not included in the bonded model and the VDW interaction decays rapidly at long-range. With that said, specific adjustments might be needed in a range of situations. For example, in the work of Op't Holt and Merz, the VDW radius of the Cu^+ ion was enlarged to prevent close contact with H or S atoms in the surrounding Cys residues, which were not directly bound to the ion.[654] In another approach, the VDW parameters can be fit to QM-derived PES. For example, in the work of Šebesta et al.,[775] they parametrized the LJ potentials of TMs based on QM calculated PESs between the TM complexes and small molecules. They found that there is a flat minimum on the surface of their "least-square" fits (see Figure 56).

4.5.1. Hybrid Model. The standard bonded model does not allow for ligand exchange processes by its very construction, while there is no such restriction for the nonbonded model. If there is a desire to have one ligand exchange, a bonded/nonbonded hybrid model can be employed. However, the VDW parameters of the metal ion or ligating atoms may need to be adjusted when using this strategy. This is because the nonbonded model assumes an integral charge, which is equal to its oxidation state, but the bonded model usually uses partial (nonintegral) charges obtained using ESP or RESP fitting protocol. Because the partial charge on a metal ion is usually less than its oxidation state, this may result in an underestimation of the interactions between the central metal ion and its ligating residues represented by the nonbonded model. For instance, Lin and Wang have tested the nonbonded model using RESP charges on the metal site. They found the central zinc ion "escaped" the metal binding site rapidly during MD simulation.[655] In the work of Chakravorty et al. on the *CusF* system (a copper metallochaperone), they fine-tuned the VDW parameters of Cε3 and Cζ3 in Trp44 to reproduce the interaction between Cu^+ and the Trp44 because the original VDW parameters underestimated the interaction strength.[657]

4.5.2. Physically Meaningful Lennard–Jones Parameters. As we discussed for the nonbonded model, it is essential to treat the VDW parameters within a physically meaningful range. For example, in the INTERFACE force field, Heinz et al. initially used VDW diameter parameters obtained from the literature,[776,777] while their final parametrized values usually only gave small deviations (±5%) from the literature values.[598] The well depth (ε) is the most "adjustable" parameter in the LJ functional form and is related to the atomic polarizability. The INTERFACE force field was designed on the basis of the following considerations: (1) using the ε values of rare gases to determine the range of the ε parameters, as suggested by Halgren; (2) charge state considerations, where anions usually have higher polarizabilities and bigger ε values than the corresponding neutral compounds, while for cations the opposite behavior is observed; (3) volume density of the nonbonded neighbor atoms (including 1-4 interaction), whose increase usually decreases ε; and (4) a bigger ε value may be needed for some polar atoms or ions to make the LJ potential more repulsive at short-range. These nonbonded parameters were fitted to reproduce experimental bulk and interfacial properties. It was also shown that the combining rules only induce small deviations (usually below 10%) in property predictions.[598] This is likely because the VDW parameters are in a physically reasonable range, which gave stable derived parameters based on different combining rules.

DOI: 10.1021/acs.chemrev.6b00440
Chem. Rev. 2017, 117, 1564–1686

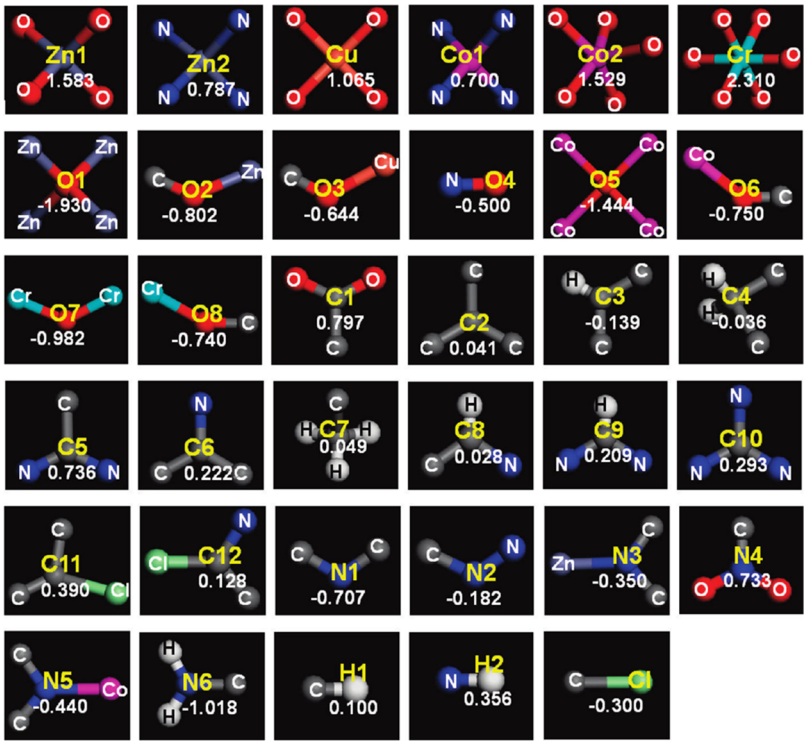

Figure 54. Definition of CBAC atom types and their charges. Reprinted with permission from ref 773. Copyright 2010 American Chemical Society.

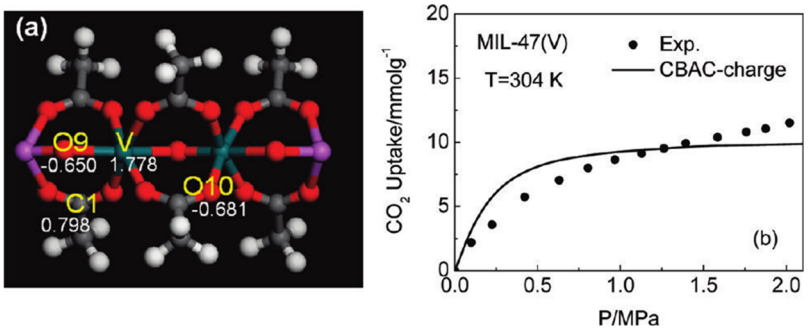

Figure 55. (a) Cluster used for calculating the atomic partial charges for atoms V, O9, and O10. (b) Comparison of simulated and experimental[774] CO_2 excess adsorption isotherm in MIL-47(V) (V, green; O, red; C, gray, H, white; Li, purple). Reprinted with permission from ref 773. Copyright 2010 American Chemical Society.

4.6. General Force Field Development

If there are N atom types in a force field, the bond, angle, and dihedral terms approximately scale as $O(N^2)$, $O(N^3)$, and $O(N^4)$, respectively. With more than 100 elements in the periodic table and with the potential for multiple atom types per element (generally the more atom types in a force field, the more accurate it is), the number of parameters rapidly increases. However, it is difficult to perform parametrization for every possible bond, angle, and dihedral combinations independently. Hence, general force field models usually employ empirical rules and a simplified philosophy to facilitate the derivation of force field parameters. For example, the equilibrium bond lengths are obtained by summing the covalent bond radii of the two connected atoms combined with some corrections (e.g., offset values, electronegativity, or bond order corrections).[615,778] Bond force constants can be obtained using Badger's rule or via another empirical relationship. The equilibrium angle values can be obtained using valence shell electron pair repulsion (VESPR) theory.[51] The torsion parameters are based on the hybridizations of the two central atoms.[615] The VDW parameters can be obtained using experimental results such as IPs,[778] or the VDW radii of noble gas atoms (through interpolation/extrapolation).[51] Even though the accuracy of these force fields may be limited, these models can provide qualitative insights at minimal computational expense on a broad range of systems. Below we highlight some of the features of several general force fields.

4.6.1. Tripos 5.2 Force Field. For the sake of completeness, we describe the Tripos 5.2 force field reported by Clark et al. in 1989.[779] It is a general force field designed initially for organic molecules (but offers avenues to the modeling of metal systems) and is embedded in the Sybyl program. This force field served as a prototype[397,778] for the development of generalized force fields and was designed to predict molecular geometries and relative energies. Geometry minimization was performed for a number of organic molecules (as well as crambin and several peptides), and good agreement

DOI: 10.1021/acs.chemrev.6b00440
Chem. Rev. 2017, 117, 1564−1686

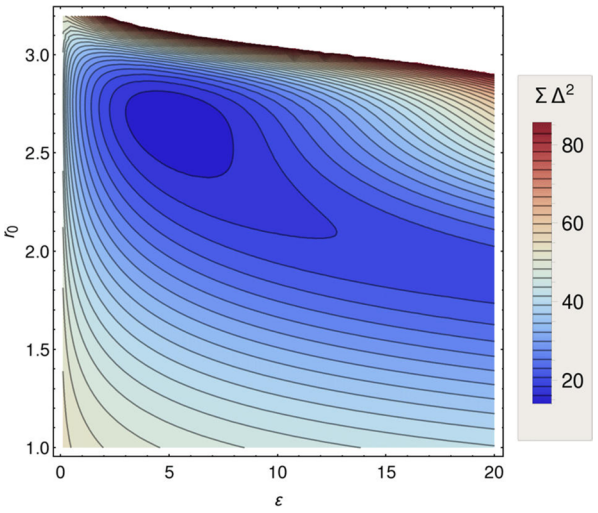

Figure 56. Surface of the least-squares fits ($\sum\Delta^2$) of atomic LJ parameters ε and r_0 (which is σ in eq 33) for Pt(II) complexes interacting with the testing molecules. Reprinted with permission from ref 775. Copyright 2016 American Chemical Society.

was obtained with the available crystal structures. It is suitable for both protein and ligand simulations.

4.6.2. DREIDING Force Field. Mayo et al. created the DREIDING force field in 1990.[615] The equilibrium bond distances were calculated as the sum of atomic radii with an offset value. It uses the harmonic cosine equation for the angle bend term because it gives a zero slope when the angle approaches 180°. The equilibrium angle values were taken from the structures of the parent hydrides (e.g., MH_2) found in the literature.[780−783] A single Fourier equation was used for the dihedral interaction, while the 1-4 nonbonded interaction is generally left unscaled. For improper torsion interactions, they averaged over three inversion terms (eqs 100−102) for nonplanar equilibrium geometries and eq 101 for planar equilibrium geometries (when $\varphi_I^0 = 0°$). Herein, I is the central atom and φ_I is the improper torsion angle. Simple rules were used to assign bond and angle force constants, torsion, and improper torsion terms (e.g., a bond force constant is based on the bond order times a single predefined bond force constant).

$$E_{IJKL} = \frac{K_I}{2(\sin \varphi_I^0)^2}(\cos \varphi_I - \cos \varphi_I^0)^2 \quad (100)$$

$$E_{IJKL} = K_I(1 - \cos \varphi_I) \quad (101)$$

$$E_{IJKL} = \frac{2K_I}{(\sin \varphi_I^0)^2}\left[\sin\left(\frac{1}{2}\varphi_I^0\right)\right]^2 \quad (102)$$

$$E_{\mathrm{VDW}}^{\mathrm{LJ}} = AR^{-12} - BR^{-6} = D_0[\rho^{-12} - 2\rho^{-6}] \quad (103)$$

$$E_{\mathrm{VDW}}^{\mathrm{X6}} = A\, \mathrm{e}^{-CR} - BR^{-6} = D_0\left[\left(\frac{6}{\zeta - 6}\right)\mathrm{e}^{\zeta(1-\rho)} - \left(\frac{\zeta}{\zeta - 6}\right)\rho^{-6}\right] \quad (104)$$

Either a 12-6 LJ (default) or exp-6 (X6) was used to describe the VDW interactions (see eqs 103 and 104). Here, ρ equals $r_{ij}/r_{\mathrm{min},ij}$ while ε is the well depth. ζ is the scaling factor, which is dimensionless. Using $\zeta = 12.0$, E^{LJ} and E^{X6} have the same long-range attraction, while at $\zeta = 13.772$ the two representations have the same behavior where the sum of VDW radii of the two particles meet. DREIDING uses an arithmetic combining rule for the VDW radii and a geometric combining rule for the well depth when using the 12-6 LJ potential. For the X6 potential, a geometric combining rule for the A and B parameters and an arithmetic combining rule for C parameters are used. Charges are ignored or determined by the Gasteiger scheme. A hydrogen-bonding potential was employed and followed a CHARMM-like style. All reported calculations were performed in a vacuum with a dielectric constant of 1. It was shown that the DERIDING force field could reproduce crystal structures, relative energies, and rotational barriers for organic molecules. Metal ion parameters were initially reported (Na^+, Ca^{2+}, Fe^{2+}, and Zn^{2+} ions) for the DREIDING force field, but they were not rigorously tested in the original paper.

4.6.3. Universal Force Field. Rappé et al. reported the development of the UFF in 1992.[778] It contains 126 atom types across the periodic table. The parameters were determined on the basis of general rules and are adjusted according to the element, hybridization, and connectivity of the atom types. The bond length is obtained as the sum of the atomic radii plus terms including bond order and electronegativity corrections. For the corrections, a Pauling-type bond order correction and an electronegativity correction from O'Keeffe and Brese were employed. Force constants were developed on the basis of Badger's rules. Cosine Fourier expansions were used for the angle bending terms, which better represent large amplitude angle motions than the harmonic potential. The angle force constants were obtained on the basis of the angular generalization of Badger's rules. Cosine Fourier expansions were employed to describe the torsion terms, while mixing rules were employed to determine the torsion barriers. Torsion interactions without a main-group element in the central bond were set to zero. The improper torsion terms were represented by cosine Fourier expansions containing one or two terms. The 12-6 LJ potential with geometric combining rules were used for both the VDW radii and the well depth. These parameters were derived by initially fitting experimental data to the exp-6 expression, and subsequently the 12-6 LJ values were derived using the mathematical relationship between the 12-6 LJ and exp-6 equations. Point charges were derived on the basis of the EEM (so-called FQ model, see section 6.1). A number of tests were performed with several TM complexes. In general, it was shown the UFF reproduced bond distances within ±0.1 Å and angles within ±5° to ±10°.

In a separate effort, Rappé et al. applied the UFF specifically for metal complexes.[784] The results support the use of the bond order correction employed in the force field. Using multiple metal-C and metal-P bond orders yielded improvement for TM-phosphine and TM-carbonyl systems where back bonding plays an important role. It was found that half-integer bond orders better account for the trans influence in metal phosphines. However, the force field showed weakness reproducing high-valent TM-π bonding systems and in systems that have strong ionic bonds (rather than covalent). Nonetheless, the authors noted that multiple bond order models are likely to better simulate the high-valent metal-π bonding effect.

4.6.4. General MM2 and MM3 Force Fields. Allinger et al. described a general approach to generate MM2 and MM3 force field parameters in 1994.[51] It supported atoms from H to Hs (no. 108 in the periodic table). It uses quadratic and cubic terms to describe the bond interactions in the MM2 force field while adding quartic terms in the MM3 force field. An

DOI: 10.1021/acs.chemrev.6b00440
Chem. Rev. 2017, 117, 1564−1686

electronegativity correction was added to the covalent atom radii sum to represent the equilibrium bond length. For the angle terms, equilibrium angle values were obtained on the basis of the observed configurations (e.g., tetrahedral, trigonal planar, pyramidal, etc.). Second- and sixth-order terms were to model the angle interaction in MM2, while second- to sixth-order terms were employed in the MM3 force field. Torsion parameters were assigned on the basis of the hybridizations of the central two atoms. The improper torsion parameters were determined on the basis of the central atom. Bond moments, which can be obtained from earlier published work or obtained as the difference between the electronegativity of the two connected atoms, were used to represent the electrostatic interactions. The Exp-6 expression was used to represent the VDW interactions. However, almost all of the supported atom types are neutral in these force fields, and even though charged species are supported in the program, results computed for these species may need to be carefully validated.

4.7. Drawbacks of the Bonded Model

The bonded model is widely used in classical force fields. It has a simple and physically satisfying format, which leads to models that can readily simulate macromolecule systems with considerable accuracy. Despite its remarkable success, it still has several drawbacks when it comes to modeling TM containing complexes. The widely known drawback is the use of harmonic potentials for the bond and angle terms, which makes it impossible to readily simulate ligand switching or CN changes. As discussed above (see section 4.5), a hybrid model can be utilized to overcome these issues for specific ligands. A nonbonded model (see section 3), cationic dummy atom model (see section 5.1), can also be used at this point but with modest accuracy. Furthermore, reactive potentials (see section 6.5), which represent a more advanced modeling strategy, can be employed to overcome these issues.

Hu and Ryde pointed out that distorted structure occurs when modeling a structure with two or more water molecules bound to the same metal ion when using the bonded model.[677] This is because 1-3 nonbonded interactions are usually not considered while the 1-4 nonbonded interactions are included in most bonded models. Because a water molecule usually has a zero VDW parameter on its hydrogen atoms, a serious problem occurs when it has two water molecules bound to the same metal ion: there will be a strong 1-4 electrostatic attraction but no 1-4 VDW repulsion between the hydrogen atoms in one water molecule and the oxygen atom in the adjacent water molecule. If the two water molecules are not on the opposite sides of the central metal ion, the attraction becomes strong enough to distort the angle. At this time, a nonbonded model with QM-derived constraints (which assigns only nonbonded interactions between the coordinated water molecules), a Urey–Bradley model (which includes the 1-3 nonbonded interaction with an added harmonic term based on the distance of the 1-3 atoms), or a reactive force field model (which includes the nonbonded interactions between each atom pair) are possible alternatives to address this problem.

The accuracy of the bonded model is also limited (see section 4.2.5), as demonstrated by Rydberg et al.[681] Overall, the simplicity of the model's functional form for TMs limits its ability to reproduce some QM-derived results precisely. For instance, the bonded model uses a fixed partial charge model, which does not include POL and CT effects explicitly, but these effects are clearly important in TM-containing systems. See section 6 for a discussion on popular polarizable models currently in use.

5. CLASSICAL MODELING OF METAL IONS: THE CATIONIC DUMMY ATOM AND THE COMBINED MODEL

5.1. Cationic Dummy Atom Model

The CDAM was originally described for the Mn^{2+} ion[785] and then extended to other metal ions. Now parameters are available for the Mg^{2+} and Ca^{2+} ions, as well some 3d TM ions including Mn^{2+}, Fe^{2+}, Co^{2+}, Ni^{2+}, Cu^{2+}, and Zn^{2+}. We are unaware of CDAM parameters for monovalent ions, which may be due to the observation that the nonbonded model is accurate enough for most situations. Moreover, to date, CDAM parameters have not been developed for highly charged ions, which is certainly an interesting future research direction for this model.

In the CDAM representation shown in Figure 57, there are six dummy sites connected to the central metal ion. The

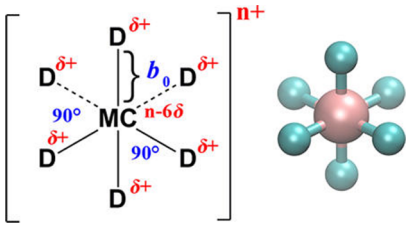

Figure 57. Geometry of the cationic dummy atom model with octehdral shape and a charge of *n*+, in which the central metal ion with a charge of $n - 6\delta$ bonds covalently to six dummy sites each with a charge of $+\delta$. Reprinted with permission from ref 786. Copyright 2016 American Chemical Society.

number of dummy sites can vary according to the CN of the metal ion being studied. The equilibrium bond distances between the metal ion and the dummy sites are usually set at 0.9 Å (with the exception of the Cu^{2+} ion, see below). The dummy sites have fractional masses, while the total mass of the central nucleus and its associated dummy sites is equal to the mass of the ion, with the total charge of metal ion and its allied dummy sites summing to the formal charge of the ion. To reproduce experimental HFEs, the charge of the central nuclei can hold a negative charge enhancing the positive charges on the dummy sites. The charges of the dummy sites are set equal to each other except for the Cu^{2+} ion (to reproduce the Jahn–Teller effect). VDW parameters were not assigned to the dummy sites initially, while in recent work a small repulsive term has been introduced. It has been shown that CDAM simultaneously reproduces experimental HFE and IOD values, thereby offering an improvement over nonbonded models.[787] However, even though CDAM has more atom sites, this does not guarantee that better results will always be obtained over the standard (12-6 LJ) nonbonded model for ions.[788] The nonbonded model assigns an integral charge to the metal ion, while the CDAM approach assigns fractional charges to the dummy sites, which may decrease the interaction strength between the ion and specific residues.[788] Moreover, the negative charge on the nucleus clouds the physical meaning of the model, which in turn hampers its predictive ability. Meanwhile, because an assumed CN is assigned to the ion, the CDAM may not be able to simulate processes involving CN

DOI: 10.1021/acs.chemrev.6b00440
Chem. Rev. 2017, 117, 1564–1686

changes. Nonetheless, whether to use the traditional nonbonded or CDAM comes down to the quality of the parameter sets used in the evaluation process.

Åqvist and Warshel investigated metal ion substitution effects on the activation energy of catalysis by staphylococcal nuclease (SNase) using the EVB approach.[785] In their work, they parametrized the Mg^{2+}, Sr^{2+}, and Ba^{2+} ions using the 12-6 LJ nonbonded model to reproduce the experimental relative HFEs to the Ca^{2+} ion and the first peak of the metal ion-oxygen RDFs. Their results showed that all three of the ions increase the activation energies over Ca^{2+}, implicating Ca^{2+} as the optimal catalytic ion for SNase. The predicted trends agreed well with the available experimental results. As an outcome of this effort, they found that it was hard to reproduce the relative HFE and RDF for the Mn^{2+} ion simultaneously. To address this issue, they introduced CDAM to model the Mn^{2+} ion. The model consists of a central site with charge (−0.1e) and VDW parameters, connected to six octahedrally coordinated dummy sites each with a charge of +0.35e, yielding a total charge of +2e. It was shown that the model reproduced the relative HFE to Ca^{2+} as well as a RDF consistent with its ionic radius. They proposed that the crystal field stabilization energies of the TM ions yield more negative HFE values than seen for "spherical" ions that have similar radii. They also discussed that based on ligand field theory, the electron density of the central ion would partly shift to the d orbitals along the bisectors of the ligands, which decreases the shielding effect and causes stronger interactions with ligands than seen in "spherical" ions. They also note that simulating divalent ions is more difficult than for monovalent ions largely due to their higher HFEs. The calculated activation energy for the reaction with Mn^{2+} is ∼6 kcal/mol higher than that of Ca^{2+}, which agreed well with the experimental kinetic results that indicate that the reaction using Mn^{2+} is at least 36 000 times less efficient than the one using Ca^{2+}. It is impressive that good agreement could be obtained with experimental data based on these simple models. Moreover, they had an insightful discussion about the catalytic mechanism of enzymes similar to SNase in the work.

$$R{-}OH + B \overset{M}{\rightleftharpoons} R{-}O^- \text{ and } BH^+ \qquad (105)$$

The upper part of Figure 58 shows the free energy changes of the proton-transfer reaction (see eq 105) for different combinations of B (base) and M (catalytic metal ion). The lower part of Figure 58 shows enzyme examples, indicating the effect that the presence of metal ion has on the reaction free energy. For example, the presence of a zinc ion decreases the free energy of reaction from 21 to 13 kcal/mol for the transfer of a proton to a water molecule (like the situation in carbonic anhydrase).

CDAM parameters have been developed for the Zn^{2+} ion, and the resultant parameters were applied to a study of human carbonic anhydrase I (HCAI) using the EVB approach.[790] Six dummy atom sites were used in the model with each having a +0.5e charge. The derived parameters reproduced both experimental HFE and IOD values. The simulated results agreed well with experimental data and indicated the importance of electrostatic interactions related to the catalytic Zn^{2+} ion.

Oelschlaeger et al. parametrized the CDAM for Mg^{2+} and applied the parameters to a study of Human DNA polymerase β.[791] The target values they used were the HFE together with QM calculated energies and structures. They assigned a mass of

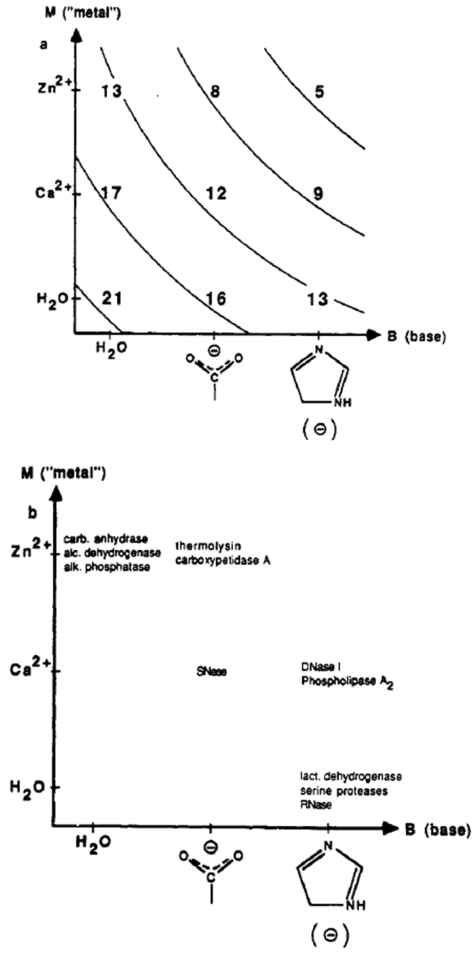

Figure 58. (a) Diagram showing the effects of metal ion and general-base catalysts on the reaction of eq 105. The abscissa denotes increasing general-base strength, represented by a water molecule, a carboxylate ion, and an imidazole ring. The ordinate represents increasing metal ion electrophilicity, where a water molecule denotes the case where no metal is present. The energy values, ΔG_{ij}, correspond to the proton-transfer reaction $(M^{2+}{}_i)H_2O + B_j \rightleftharpoons (M^{2+}{}_i)OH^- + BH^+{}_j$, where each entry is obtained from $\Delta G_{ij} = -2.3RT(pK_j - pK_i)$. For example, in the case of a metalloenzyme using Ca^{2+} and glutamate, respectively, as M and B, *i* denotes $Ca^{2+}(H_2O)$ and *j* denotes (Glu)-COOH (the pK_a's for metal bound water are taken from ref 789). (b) The figure shows a number of different enzymes that catalyze reactions involving a proton-transfer step like eq 105, plotted according to their use of metal ion and general-base catalysis (SNase, DNase I, and RNase denote staphylococcal nuclease, deoxyribonuclease I, and ribonucleases [e.g., A and T_1], respectively). Reprinted with permission from ref 785. Copyright 1990 American Chemical Society.

3.0 amu to each dummy site, which did not have VDW interactions. The central nucleus was assigned a charge of −1.0e, while each dummy site was assigned a charge of +0.5e. It was shown that the CDAM better represented the structures and energies of the Michaelis and transition state complexes than the traditional nonbonded model.

Saxena and Sept parametrized CDAM for Ca^{2+} and Mg^{2+} ions.[792] Because the most common geometry for Ca^{2+} sites in biological systems is the pentagonal bipyramid, they placed 7 dummy sites around the central nuclei (see Figure 59), while an octahedral geometry was used for the Mg^{2+} ion. The central nucleus was treated as neutral and the dummy sites had

DOI: 10.1021/acs.chemrev.6b00440
Chem. Rev. 2017, 117, 1564−1686

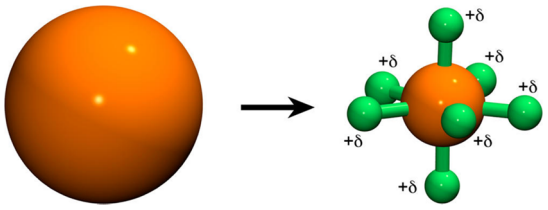

Figure 59. Illustration of the multisite ion model for calcium in the study of Saxena and Sept.[792] Instead of a simple sphere, the charge centers are now distributed to multiple sites depending on the coordination geometry of the ion. Reprinted with permission from ref 792. Copyright 2013 American Chemical Society.

uniform charges. The parametrization effort targeted the reproduction of experimental HFEs, but was also found to be able to reproduce experimental RDFs. By calculating relative binding energies of Mg^{2+} and Ca^{2+} to different systems, it was shown that the CDAM model outperformed all tested nonbonded models. In a related effort, Saxena and García refined the original CDAM parameters for Mg^{2+} and Ca^{2+}.[793] This was done because the initial parameter set could not simulate solutions with high salt concentrations (see sections 3 and 6 for further discussion on this point). They fine-tuned the C_{12} parameter between the dummy atom sites and the Cl^- ion without influencing the interaction between the nuclei or dummy sites with water molecules. The C_{12} parameter was refitted to reproduce experimental osmotic pressures of $MgCl_2$ solutions at different concentrations. It was shown that the new parameter set eliminated artifacts associated with ion aggregation seen with the original parameter set. The new parameter set also reproduced the experimental osmotic pressure values of $CaCl_2$ solutions, demonstrating their excellent transferability.

Duarte et al. developed CDAM parameters for Mg^{2+}, Ca^{2+}, Mn^{2+}, Fe^{2+}, Co^{2+}, Ni^{2+}, and Zn^{2+} ions.[787] All of these models used an octahedral geometry with every nuclei assigned with a −1.0e charge and every dummy site assigned a +0.5e charge. The experimental HFE and IOD values were the parametrization targets. It was shown that the resultant parameter sets reproduced both values simultaneously. Tests on metal-containing enzyme systems also demonstrated the stability of the parameter set.

Liao et al. developed a CDAM model for the Cu^{2+} ion, which incorporated the Jahn−Teller effect.[794] They found that by assigning larger charges to the equatorial dummy sites, they were better able to simulate the Jahn−Teller effect. Intriguingly, along with the uneven charge assignment, they found the "compressed" octahedral structure performed better than a symmetrical or elongated octahedral environment. They arrived at final charges for the axial and equatorial dummy sites of +0.05e and +0.725e (with the metal core assigned a charge of −1) and axial and equatorial bond lengths of 0.8 and 1.0 Å, respectively. The higher charges on the equatorial sites were also helpful in reproducing the square-planar structure of four-coordinated Cu^{2+}. The final parameter set was able to reproduce the experimental HFE and IODs (both of two different Cu−O distances due to the Jahn−Teller effect) simultaneously and performed well on two different copper-containing enzyme systems.

Lu et al. performed simulations on glycogen synthase kinase 3β (GSK3β),[788] which has two Mg^{2+} ions in two different sites that serve as cofactors to catalyze the process of γ-phosphate transfer from ATP to the Ser and Thr residues in the substrate. They studied the parent system and one system in which the Mg^{2+} ion in site 1 is substituted by a Ca^{2+} ion. They found that the Mg^{2+} ion nonbonded model outperformed the CDAM one based on two 20 ns simulations on the parent system. The CDAM model distorted coordination modes for the two Mg^{2+} ions, and disrupted an important hydrogen bond in the active site, while the nonbonded model better reproduce the XRD determined active site structure, even though the CDAM model offered closer metal−oxygen coordination distances when compared to the X-ray structure.

Pang et al. performed a series of studies applying the CDAM approach to zinc-containing metalloproteins.[795−801] Herein, we show an example of the extensive work carried out by them. Peng developed a tetrahedrally coordinated CDAM for the Zn^{2+} ion in 1999.[795] The nucleus was treated as neutral, while the +2e total charge was assigned to four dummy sites (each has a 0.1 amu mass) equally, to mimic the $4s4p^3$ empty orbitals. There is no VDW interaction assigned to the dummy sites. This CDAM model was developed to decrease the underestimation of ion−water interactions in the nonbonded model. Their resultant CDAM model predicted shorter Zn−S distances than experimental data, but it significantly improved the prediction of the HFE value (as −448 kcal/mol, ∼8% smaller than experiment). It was also shown the CDAM model better reproduced the interaction energy of the Zn^{2+}−water dimer than the nonbonded model. Tests carried out on carboxypeptidase, carbonic anhydrase II, and rubredoxin demonstrated the stability of their CDAM model. Besides these systems, they have also applied the CDAM model to study farnesyltransferase,[796] phosphotriesterase,[797] and endopeptidase.[798−801]

Recently, Jiang et al. refined the Mg^{2+} parameters of the CDAM model for TIP3P water through a simple parameter screening strategy.[802] A revised experimental HFE value was used, and an energy correction protocol was employed to improve the parameters' transferability among different simulation strategies. The new parameters reproduced both thermodynamic and structural properties, and it offered improvement over previously developed nonbonded models from Åqvist and Allner, as well as the CDAMs from Oelschlaeger and Duarte, in terms of reproducing the ATP/GTP-Mg^{2+}-protein environment in three metalloenzymes (where the metal center has one or two ions). However, the new model failed to reproduce the Mg^{2+}−Mg^{2+} distance and was biased toward monodentate binding to carboxylate groups. Use of a bonded model was suggested to diminish these artifacts. Following this work, Jiang et al. systematically parametrized 11 6-coordinated divalent metal ions for the TIP3P, SPC/E, and $TIP4P_{EW}$ water models.[786] The experimental HFEs for the ions were obtained by assigning the HFE of the proton as −265.9 kcal/mol. A negative charge of −1.0e or −2.2e was assigned to the atomic cores of these divalent metal ions, while 0.9−1.3 Å bond lengths were used for the bonds between atomic core and the dummy atomic sites. An energy correction protocol was also employed in this work, and the final parameter sets reproduced experimental HFE, IOD, and CN values simultaneously.

5.2. Combined Model

As shown in Figure 60, the combined model considers the ion and its first solvation shell as a unified unit in the molecular modeling process.[803] Because of this, simulating water exchange in the first solvation shell is not possible. This representation is

DOI: 10.1021/acs.chemrev.6b00440
Chem. Rev. 2017, 117, 1564−1686

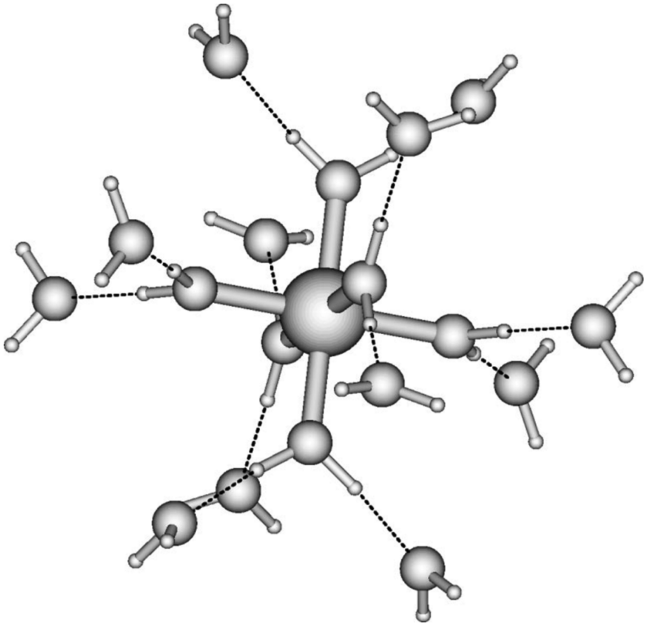

Figure 60. Structure of the minimum corresponding to 12 water molecules interacting with the Cr^{3+} hydrate using the HIW_P and the MCHO potentials in the study of Martínez et al.[803] Drawn bonds between the cation and oxygens of the first-shell water molecules represent the feature of the HIW_P to consider the hydrate as a single unit. Reprinted with permission from ref 803. Copyright 2000 American Institute of Physics Publishing LLC.

reasonable for highly charged ions under relatively short simulation time scales because of the long MRT of first solvation shell waters. Typically the parametrization is based on appropriate quantum calculations. To date, there are combined models for main group ions such as Be^{2+},[804] Mg^{2+},[804] and Al^{3+},[804,805] TM ions including Cr^{3+},[803,806−809] Zn^{2+},[810−812] Cu^{2+},[44] Pd^{2+},[813,814] and Pt^{2+},[814] and even the Th^{4+} ion.[815] The combined model, by its very design, incorporates many-body effects (e.g., CT and POL effects) in the first solvation shell directly and addresses the (potential) electronic state crossing problem. In the early development of the combined model, the hydrating ions were treated as rigid,[807,810] while in subsequent work intramolecular potentials for the hydrated ion were also added to construct flexible models.[805,809] However, because it is usually parametrized using QM calculated results, the accuracy of the resultant potential will be directly influenced by the accuracy of the QM computations. Marcos, Martinez, and co-workers have done a series of related work on the combined model, and, herein, we explore several examples.

The first combined model of an ion was proposed by Pappalardo and Marcos.[810] They fitted a potential for the Zn^{2+} hydrate ion based on QM calculations. They obtained a hydration energy for Zn^{2+} of −517.6 kcal/mol based on the combined model, which is much closer to the experimental value of −491 kcal/mol, than the values based on a two-body conventional potential (−844.6 kcal/mol) and on a potential that included three-body corrections (−848 kcal/mol). They found that water molecules in the second shell have less directionality when employing the combined model than when using a nonbonded model. They proposed that the use of a flexible water model could reduce the extent of this exaggeration in the second shell of water molecules. Later, they performed a series of simulations that demonstrated that the difference between the hydration energy predicted by their model and that from the Clementi potential is mainly due to differences in the ion−water interaction.[816] The latter model overestimated the ion−water interactions, yielding a too negative hydration energy. Results also showed that geometric relaxation caused only limited (∼2.5%) changes in the hydration energy. As another benefit, they proposed that the combined model better incorporates long-range interactions.

Martínez et al. described a fully flexible combined model for the Cr^{3+} ion[809] in which an intramolecular interaction potential was used to represent the interaction between the Cr^{3+} ion and its first solvation shell waters. The potential was fit on the basis of a QM-derived PES between $Cr(H_2O)_5^{3+}$ and H_2O. CHELPG charges were assigned to all of the atoms, and LJ parameters from the TIP4P water were used to describe the VDW interaction between the first solvation shell water molecules. A 4-6-12 potential (between Cr^{3+} and the oxygen atoms in the first solvation shell) was used to describe the interaction (except electrostatic) between Cr^{3+} and its first solvation shell water molecules. It was found that the C_4 term was negative, while both the C_6 and the C_{12} were positive. The TIP4P water model was used for the remaining water molecules. The potential between the hydrated ion and other water molecules was taken from related work.[807] It is noted that this fully flexible model can be treated as a nonbonded model (but the parameters of the first solvation shell water molecules and bulk water molecules are different) because there are no bonded terms for the intramolecular interactions between the Cr^{3+} ion and its first solvation shell water molecules. Because of the high charge on the Cr^{3+} ion (+2.457e, based on the CHELPG algorithm), it is unlikely that exchange of the first solvation shell water molecules happens during the routine MD time scale nowadays. It was shown that a 4-6-7 potential offered improved performance over the 4-6-12 potential in the reproduction of intermolecular vibrational frequencies. Their results showed that the flexible model gave dynamics properties similar to those of the earlier rigid model. The results also support a proposed definition of the hydrated ion that suggests that such an ion could be considered as "hydrated" if its rotational motion obeys the Debye rotational model.

6. CLASSICAL MODELING OF METAL IONS: THE POLARIZABLE MODEL

The importance of the polarization effect has been discussed in detail for some years.[158,159,162] For example, according to symmetry adapted perturbation theory (SAPT) theory, the polarization energy can range from very small to values around 10−20% for the total interaction energy.[817] It has been shown that the polarization effect becomes more pronounced in highly charged systems, where the electronic cloud is more polarized.[391] Furthermore, the polarization effect is also important in hydrogen-bond formation, cation−π interactions, and receptor−ligand recognition. The polarization effect can be qualitatively represented using overpolarized charge parameters within an unpolarized two-body model, but it is still hard to simulate the charge delocalization effect accurately by using the classical additive potentials. This is because that the polarization effect becomes nonadditive when there are more than two molecules in the system.[159]

In unpolarized models, the charge distribution is fixed, and two identical amino acids, but in different environments, are assigned the same charge parameters. This is not particularly physically meaningful because surrounding particles influence

DOI: 10.1021/acs.chemrev.6b00440
Chem. Rev. 2017, 117, 1564−1686

their charge distributions. This kind of difference can be considerable, for example, between an amino acid in a buried site versus that on the protein surface. Unlike unpolarized models, polarizable models allow the electronic distribution to change, which allows inclusion of the charge delocalization effect in response to the environmental changes. This facilitates the polarizable model's ability to reproduce both gas- and liquid-phase properties simultaneously. For example, it is hard to model gas-phase properties of water using typical unpolarized water models because of the overestimation of the polarization effect. The water dimer energy predicted by the TIP3P water model is −6.5 kcal/mol, while many polarizable water models yield values close to −5.0 kcal/mol, an accepted value predicted by QM modeling.[167]

There are three basic types of polarizable models in common usage: the FQ model, the DO model, and the induced dipole model (IDM). Meanwhile, there are also three ways to propagate simulations using polarizable force fields: self-consistent field (SCF), matrix inversion, and extended Lagrangian methods. To help conserve energy, smaller time-steps may be needed during simulations using polarizable models relative to unpolarized ones. Early on, the SCF method was used to propagate MD simulations using polarizable models.[818−820] It performs an energy minimization inside each time-step until converge is reached; however, multiple steps are needed to converge inside each time-step increasing the cost. Besides the SCF method, the matrix inversion method can be used.[821−823] However, inversion of a large matrix representing a macromolecule is time-consuming. Recently, the extended Lagrangian method[824−827] has become the preferred method for MD simulation with polarizable force fields due to its reduced computational cost and good accuracy. It traces its origins to the CPMD approach and includes a polarizable degree of freedom into the dynamics.[367] For example, similar to CPMD simulations, a fictitious charge mass (energy·time^2/charge^2) can be employed in the FQ model.[828] However, in the Lagrangian method, extra works usually need to be performed to assign proper weights to the pseudo particles (e.g., Drude particles), use, and fine-tune two separate thermostats for atoms and pseudo particles. To date, polarizable models have been developed for metal ions with s, p, d, and f orbitals.

6.1. Fluctuating Charge Model

6.1.1. Model Introduction. The FQ model is one of the simplest polarizable models extant. Even though it utilizes a point monopole representation, it still allows charge fluctuation on the basis of changes in the chemical environment. It uses a Taylor expansion of the atomic chemical potential up to second-order terms in atomic charges. Many FQ models have been developed, including the EEM,[829−832] OPLS-AA-FQ,[833] CHARMM-FQ,[828,834] the ABEEM/MM model,[835−852] etc. These models are generally based on the CPE scheme. Dipole moments are usually overestimated in the FQ model,[828] and artifacts are observed if CT is allowed between far distant atoms. Hence, to make this approach work effectively for macromolecules, extra constraints are applied to alleviate these problems.[166,167] Along with these issues, the FQ model has difficulties in simulating out-of-plane polarizabilities.[166] The FQ method is much faster (by several orders of magnitude) than ab initio or DFT methods, while still generating reliable partial charges for a range of chemical compounds. This opens a range of applications involving screening or filtering compounds.[772]

6.1.2. Historical Development. Jensen has discussed the origin and development of the electronegativity concept from its early stage.[853,854] In 1932, Hund proposed that if two atoms have equal $(E_{IP} + E_{EA})/2$ values, they could be treated as having an approximately equal contribution to the bond formation between them.[855] Pauling proposed the electronegativity concept in 1932,[856] which was used to represent the relative attraction of valence electrons for each atom in a covalent bond. He calculated atomic electronegativity values on the basis of experimental bond energies. The square of the electronegativity difference between two elements A and B was determined using $(\chi_A - \chi_B)^2 = \Delta E_{AB}^{bond} = E_{AB}^{bond} - (E_{AA}^{bond} + E_{BB}^{bond})/2$.

Later, Mulliken defined the "absolute" electronegativity scale on the basis of an average of the *IP* and *EA*, and obtained values in agreement with Pauling's data.[857] He proposed that when A and B have equal electronegativities, the difference between the two states A^+B^- and A^-B^+ can be neglected, yielding $IP_A - EA_B = IP_B - EA_A$, so $IP_A + EA_A = IP_B + EA_B$. So $IP_A + EA_A$ or $(IP_A + EA_A)/2$ can be used to define the absolute electronegativity.

Sanderson proposed the seminal concept of electronegativity equilibration in the early 1950s.[858] He proposed that when two atoms approach one another to form a bond, the one with the larger electronegativity attracts more electrons. This increases its atomic radius and decreases its attraction to valence electrons. The opposite occurs for the atom with the smaller electronegativity. This process will adjust the radii of the two atoms to equalize their electronegativity, and the final bond length equals the sum of the adjusted radii. He then proposed the stability ratio function as a measure of the electronegativity. The effective radii of atoms can then be obtained using eq 106:

$$r = \sqrt[3]{\frac{Z}{4.19 ED_i SR_m}} \tag{106}$$

$$ED = \frac{3Z}{4\pi r^3} \tag{107}$$

As shown in eq 107, *ED* is the average electronic density (in units of electron/Å^3), while *r* represents the nonpolar covalent or ionic radius. In eq 106, ED_i is the average electronic density of the corresponding noble gas atom (representing the maximum inertness of an atom), and SR_m is the stability ratio ED/ED_i in the molecule, which represents the chemical reactivity or electronegativity of a particle that has the same electron count as the corresponding noble gas atom.[858] The bond length is the sum of the effective atomic radii of two connecting atoms. The calculated bond lengths based on this model agreed well with experimental results: the mean deviation was 0.05 Å for 95% of the bonds explored. In a later publication, calculations on alkaline halogen compounds were performed.[859] Even though these are highly polarized systems and their bond length is usually less than their sum of covalent radii, Sanderson showed that the calculated results agreed well with experimental data. Slight improvement in the modeling was obtained by using ionic instead of covalent radii.

In 1978, Parr and co-workers proposed that electronegativity equals the negative of the chemical potential for the ground state, based on the viewpoint of DFT.[860] They showed that the energy determines the chemical bond formation, while the electronegativity difference determines whether CT occurs upon bond formation. This proved the assumption of Sanderson. Subsequently, Parr and Pearson proposed the concept of chemical hardness and defined its formulation.[861] It

DOI: 10.1021/acs.chemrev.6b00440
Chem. Rev. 2017, 117, 1564−1686

is defined as the second derivative of the energy with respect to the number of electrons in the system, thereby representing the resistance of the chemical potential to changes in the number of electrons. This quantity can be directly calculated on the basis of the finite difference formula $\eta = \frac{1}{2}(IP - EA)$. It represents one-half of the energy needed for the following process to occur: A + A → A^+ + A^-. They also laid the theoretical framework of the hard soft acid base (HSAB) principle based on the concepts of electronegativity and chemical hardness. Reasonable results were obtained from their calculations on chemical hardnesses for a number of atoms, ions, and compounds.

Hinze et al. proposed the concept of orbital and bond electronegativities in the early 1960s.[862−865] Years later, Gasteiger and Marsili developed the partial equalization of orbital electronegativity (PEOE) charge (so-called Gasteiger charges).[866,867] This was followed by the work of Mortier et al., who developed the electronegativity equalization method (EEM) for the determination of atomic charges.[829] Rappé and Goddard described the charge equilibration (QEq) approach[868] and applied it to the UFF.[778,784,869,870]

6.1.3. Formulation of the Fluctuating Charge Method. It is noted that different FQ methods may have subtle differences in formulation and implementation. Herein, we treated the QEq method as an example. Formally, the QEq method proceeds as follows:

$$E(Q) = E^0 + \left(\frac{\partial E}{\partial Q}\right)_0 Q + \frac{1}{2}\left(\frac{\partial^2 E}{\partial Q^2}\right)_0 Q^2 \tag{108}$$

$$E(+1) = E^0 + \left(\frac{\partial E}{\partial Q}\right)_0 + \frac{1}{2}\left(\frac{\partial^2 E}{\partial Q^2}\right)_0 \tag{109}$$

$$E(-1) = E^0 - \left(\frac{\partial E}{\partial Q}\right)_0 + \frac{1}{2}\left(\frac{\partial^2 E}{\partial Q^2}\right)_0 \tag{110}$$

$$E(0) = E^0 \tag{111}$$

$$IP = E(+1) - E(0) = \left(\frac{\partial E}{\partial Q}\right)_0 + \frac{1}{2}\left(\frac{\partial^2 E}{\partial Q^2}\right)_0 \tag{112}$$

$$EA = E(0) - E(-1) = \left(\frac{\partial E}{\partial Q}\right)_0 - \frac{1}{2}\left(\frac{\partial^2 E}{\partial Q^2}\right)_0 \tag{113}$$

where

$$\left(\frac{\partial E}{\partial Q}\right)_0 = \frac{1}{2}(IP + EA) = \chi^0 \tag{114}$$

$$\left(\frac{\partial^2 E}{\partial Q^2}\right)_0 = IP - EA = J^0 = 2\eta^0 \tag{115}$$

$$E(Q) = E^0 + \chi^0 Q + \frac{1}{2}J^0 Q^2 = E^0 + \chi^0 Q + \eta^0 Q^2 \tag{116}$$

$$E(Q_1 \ldots Q_N) = \sum_i \left(E_{i0} + \chi_i^0 Q_i + \frac{1}{2}J_{ii}^0 Q_i^2\right) + \sum_{i,j>i} J_{ij} Q_i Q_j = \sum_i (E_{i0} + \chi_i^0 Q_i + \eta_{ii}^0 Q_i^2) + \sum_{i,j>i} 2\eta_{ij} Q_i Q_j \tag{117}$$

$$\chi_i(Q_1 \ldots Q_N) = \frac{\partial E}{\partial Q_i} = \chi_i^0 + J_{ii}^0 Q_i + \sum_{j\neq i} J_{ij} Q_j = \chi_i^0 + \sum_j J_{ij} Q_j = \chi_i^0 + 2\eta_{ii}^0 Q_i + \sum_{j\neq i} 2\eta_{ij} Q_j = \chi_i^0 + \sum_j 2\eta_{ij} Q_j \tag{118}$$

Herein, the χ^0 and η^0 are the electronegativity and chemical hardness (which is related to the Hubbard U parameter) parameters, respectively. Here, we assume $J_{ij} = J_{ii}^0$. The constraints used in solving the equations are (1) the electronegativity values of all atoms in the system are the same (eq 119) and (2) the total charge is conserved (eq 120).

$$\chi_1 = \chi_2 \ldots = \chi_N \tag{119}$$

$$Q_{tot} = \sum_{i=1}^{N} Q_i \tag{120}$$

In total, there are N equations and N variables. The charge distribution is approximated via the solution of these linear equations.

The typical FQ model does not describe the bond formation/dissociation process well, while the split charge equilibration (SQE)[871,872] and the atom-condensed Kohn−Sham DFT approximated to second-order (ACKS2)[873] methods offer improvements.

In the FQ model, the electrostatic and electronegativity terms facilitate charge separation, while the chemical hardness term is a damping term in opposition. The electronegativity and chemical hardness parameters can be determined using QM calculations, extracted from experimental data, or treated as empirical parameters. Patel and Brooks proposed the following relationship between the polarizability tensor and chemical hardness matrix elements, thereby bridging between the FQ model and the IDM:[828]

$$\bar{\bar{\alpha}} = \Delta\bar{r}\bar{\bar{\eta}}^{-1}\Delta\bar{r}^T \tag{121}$$

Here, the $\Delta\bar{r}$ is the atomic coordinates relative to the geometric center, based on which one can derive parameters for the chemical hardness or values for the polarizability.

6.1.4. Studies of Berne and Co-workers. Rick et al. developed FQ versions of the SPC and TIP4P water models (the SPC-FQ and TIP4P-FQ models).[874] The FQ models outperformed their unpolarized counterparts. By employing the extended Lagrangian method, the new models only had a modest increase in computational cost (∼10%) over the unpolarized models.

Stuart and Berne explored the Cl^- ion in aqueous solutions using a mixed polarizable model (with TIP4P-FQ model for water and a DO model for the Cl^- ion), and compared it to an unpolarized model.[875] They observed that the Cl^- ion prefers to localize near the air−liquid interface in water clusters of varying size (up to 255 water molecules) when using the polarizable force field. However, this phenomenon was not observed in simulations using an unpolarized model. They

DOI: 10.1021/acs.chemrev.6b00440
Chem. Rev. 2017, 117, 1564−1686

proposed that this might be because the fluctuating dipole of the water molecules allowed them to remain mobile while the polarizability of the Cl^- played a lesser role. They then went on to investigate surface curvature effects in aqueous systems with Cl^- using the same polarizable model.[876] The results showed that the solvation depth profile is dependent on the interface curvature, which agrees with the "structure-breaking" behavior of the Cl^- ion.

6.1.5. ABEEM Model. Yang and co-workers have developed the ABEEM model and validated it on several large molecules.[835] It places charges on both atoms and bonds, with the positions of charges on the bonds based on the covalent radii ratio of the two connected atoms. They have performed the model parametrization based on QM calculations on over 100 molecules.[835] Tests were carried out on several large organic molecules, and the obtained results agreed well with QM-derived results. They followed this up with the ABEEM-7P water model.[840] It uses a flexible representation for the water molecule, places VDW interactions, not only on the oxygen atom, but also on the hydrogen atoms, and has an independent parameter that describes the hydrogen-bond interaction. The ABEEM-7P water model was shown to reproduce the properties of water clusters (including 2−6 water molecules).[840] A subsequent study was performed to examine the energetic, structural, and dynamic properties of the ABEEM-7P water model in the liquid phase under different temperatures.[839] Overall, it was shown that the calculated properties agreed well with experimental observations.

Li and Yang studied $Li^+(H_2O)_n$ (with n = 1−6 and 8) clusters using the ABEEM/MM model.[841] The ABEEM-7P water model was used in the modeling. Parameters related to Li^+ were fitted to QM and experimental data on $Li^+(H_2O)_n$ clusters. Charge constraints were placed on the Li^+ and its first solvation shell water molecules, while a neutrality constraint was used for each water molecule beyond the first hydration shell. The model predicted geometries, binding energies, and vibrational frequencies that agreed well with experimental and QM-derived data. They also performed MD simulations on the Li^+-aqueous system based on the ABEEM/MM model.[842] They calculated RDFs, DCs, and residence times of solvated water molecules in the first solvation shell at different temperatures (in the range of 248−368 K). Their reported results agreed well with available experimental data, and it was also shown that the ABEEM/MM model outperformed available unpolarized models.

Yang and Li have studied solvated monovalent ion systems (both as ionic clusters and as ion-aqueous systems) using the ABEEM/MM force field.[843] The investigated systems contain Li^+, Na^+, K^+, F^-, Cl^-, and Br^-, and they studied ionic clusters containing 1−6 water molecules. It was shown that the parameters derived for small clusters were transferrable to the liquid phase. The ABEEM/MM force field was able to reproduce both ionic clusters and liquid properties simultaneously. In subsequent research on ionic clusters and solutions of divalent ions (Be^{2+}, Mg^{2+}, and Ca^{2+}),[844] they fit the electronegativity, chemical hardness, and VDW parameters using QM calculations on ion−water clusters. MD and FEP approaches were employed to simulate different properties of these ion-aqueous systems. A charge constraint was applied to the ion and its first solvation shell water molecules, while the remaining water molecules were constrained to individually have a net zero charge. Generally the ABEEM/MM force field yielded results in agreement with QM and experimental data. However, the CN for the Be^{2+} ion was overestimated, implying a more sophisticated potential will be needed to better model this system.

Continuing their research theme, Yang and Cui fit the electronegativity and chemical hardness parameters of 3d TMs in the ABEEM force field.[848] The target atomic charges, which they tried to reproduce, were obtained on the basis of Mulliken analyses at the B3LYP/6-31G* level of theory. More than 300 organometallic compounds were contained in the training set. As shown in Figures 61 and 62, even though the absolute values

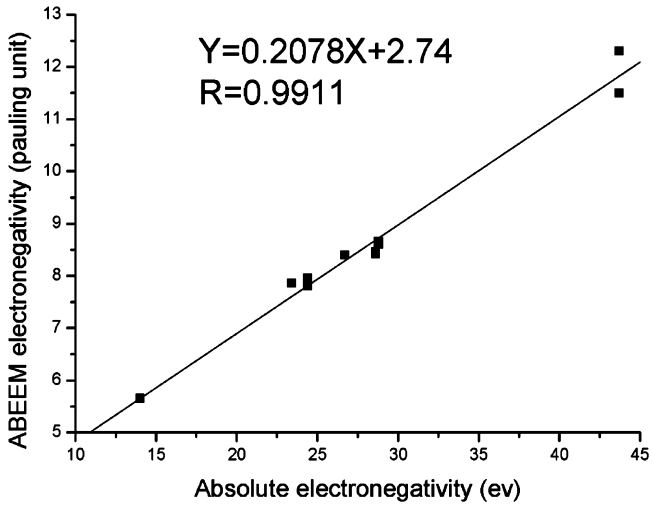

Figure 61. Correlation diagram between the absolute electronegativity parameters and the ABEEM parameters χ^* for some metal ions. Reprinted with permission from ref 848. Copyright 2007 American Chemical Society.

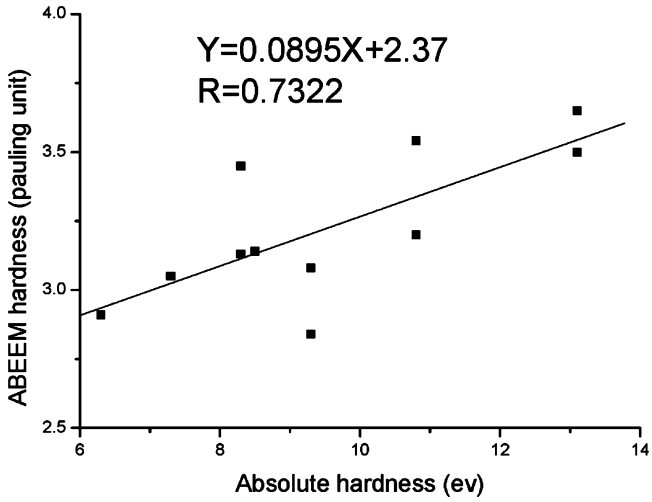

Figure 62. Correlation diagram between the absolute hardness parameters and the ABEEM parameters $2\eta^*$ for some metal ions. Reprinted with permission from ref 848. Copyright 2007 American Chemical Society.

were not close, the final derived electronegativity and chemical hardness parameters follow the trend of experimentally determined values. Further tests were carried out on several large biorelated organometallic compounds, and good agreement was obtained with the B3LYP/6-31G*-derived Mulliken charges. In a subsequent work, Cui et al. parametrized the ABEEM/MM model for the heme group.[849] It was shown that

DOI: 10.1021/acs.chemrev.6b00440
Chem. Rev. 2017, 117, 1564−1686

through a better consideration of the charge delocalization effect, the ABEEM/MM model outperformed the unpolarized CHARMM force field in reproducing crystal structures.

Further extending their work on TMs, Yang et al. fit the reference charge, electronegativity, and chemical hardness parameters for 3d, 4d, and 5d TMs in the ABEEM$\sigma\pi$ force field.[852] More than 700 structures were contained in the training set. The target values were the Mulliken charges obtained at the HF/STO-3G (for 3d and 4d TM complexes) or HF/CEP-4G (for 5d TM complexes) level of theory, and the dipole moments calculated using larger basis sets. It was argued that smaller basis sets give a more reliable prediction of partial charges in these systems, while bigger basis sets may overestimate these values. It was shown that the ABEEM$\sigma\pi$ force field, which fit parameters as described above, showed much better agreement with dipole moments calculated at the HF/6-311+G(d,p) level of theory than those based on the HF/STO-3G level of theory. Finally, 5 Mo^{4+} ion-containing metalloproteins were minimized using the ABEEM$\sigma\pi$ force field, and the structures obtained agreed with the available PDB structures.

Comba et al. have parametrized a FQ model (other than the ABEEM model) for complexes containing Fe^{2+} (low-spin and high-spin), Fe^{3+} (low-spin and high-spin), Co^{3+} (low-spin), and Cu^{2+} ions.[877] Spectroscopy data from the National Institute of Standards and Technology (NIST) were used to generate the isolated atom parameters through a quadratic fitting strategy. Four training sets with 96 structures in total were used to fit the electronegativity and chemical hardness parameters. These parameters were fit to reproduce the reference charges using an iterative Hirshfeld method coupled with the B3LYP/6-31G* or B3LYP/TZVP level of theory. Ultimately, atomic charges were calculated for a test set containing 13 structures based on the FQ model, and the obtained values agreed well with QM calculated charges generated by the iterative Hirshfeld method. Afterward, Comba et al. applied this FQ model to the ^{64}Cu complexes in a quantitative structure−activity relationship (QSPR) related study for the lipophilicity predictions.[878]

6.1.6. Periodic Systems. Besides FQ models developed for nonperiodic TM complexes, there are also examples of FQ models developed for periodic metal-containing systems. There are numerous examples of periodic systems that we would like to model using classic methods, but given their sizes how to assemble their charge distributions is a challenge. The FQ model offers some respite to this problem, and in what follows we give some examples of this approach.

Ramachandran et al. created the periodic charge equilibration (PQEq) method to derive the charges for periodic systems.[879] They applied the method to systems related to zeolite Y and found that the zeolite lattice has little influence on the charge distributions of absorbed *n*-octane, water, and benzene, but a considerable effect on the charge distribution of the transition state in the hydride transfer reaction between the $C_4H_9^+$ ion and *n*-octane.

Wilmer et al. proposed the EQeq method.[772] It calculates the electronegativity and chemical hardness parameters on the basis of measured IPs. The model only uses two global parameters: the dielectric strength (treated as 1.67 in this work) and a modified parameter related to hydrogen atoms, which corrects the tendency of hydrogen atoms having negative charges by assigning the IP of the neutral hydrogen atom to −2 eV instead of the experimental value of +0.754 eV.

$$E_{sys}(Q_1, Q_2, ..., Q_N) = \sum_{k=1}^{N}\left(E_{Ak}(Q_k^*) + \chi_{Q_k^*}(Q_k - Q_k^*) + \frac{1}{2}J_{Q_k^*}(Q_k - Q_k^*)^2 + E_{Ck} + E_{Ok}\right) \quad (122)$$

The energy of the system is represented by eq 122, where E_{Ck} is the electrostatic energy of the *k*th atom interacting with the other atoms. The representation of E_{Ck} is different for nonperiodic and periodic systems. E_{Ok} is a damping function for the electrostatic interaction between two point charges with very close contact (where the point charge approximation is not yet valid). Importantly, only linear equations need to be solved making this method much faster than DFT calculations, while still offering good results in test cases involving CO_2 adsorption in MOFs.

Afterward, Martin-Noble et al. found that the EQeq method failed to predict the partial charges of TMs with high oxidation states in the amine-templated metal oxide (ATMO) complexes.[880] They then added a correction term into the EQeq scheme on the basis of the relationship between the bond order and bond distance proposed by Pauling (see eq 123, where *n* means the bond order, *r* means the bond distance, with r_0 and *b* as two parameters; this relationship was also used in the bond valence sum (BVS) model[881] and CM5 charge correction[723]). The new method was termed as the EQeq+C method. After parametrization toward the partial charges of ATMO complexes calculated by the Hirshfeld-I (i.e., the iterative-Hirshfeld) method, and the partial charges of MOFs based on the REPEAT method, the EQeq+C method showed remarkable improvement over the original EQeq method. Transferability of the new method was also shown on a series of unrelated dipeptides.

$$n = e^{-(r-r_0)/b} \quad (123)$$

6.2. Drude Oscillator and Drude Rod Models

6.2.1. Drude Oscillator Model. The DO model, which has also been called the "shell" model, was proposed by Drude in 1902.[882] As shown in Figure 63, it uses a Drude particle as the satellite particle of an atomic core to represent its induced electronic cloud. In the absence of an electric field, the Drude particle is located at the atomic core. Once the atom is placed in an electric field (*E*), the Drude particle will have distance *d* from the atomic core:

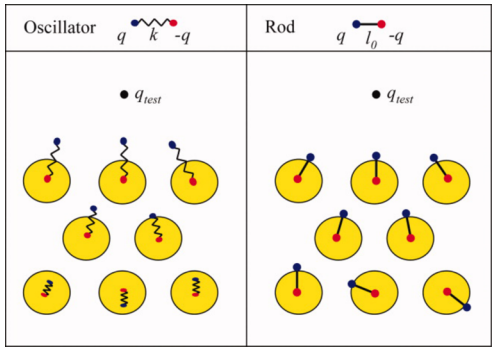

Figure 63. Schemes of the DO and DR models for Au particles. Reprinted with permission from ref 884. Copyright 2008 John Wiley and Sons.

DOI: 10.1021/acs.chemrev.6b00440
Chem. Rev. 2017, 117, 1564−1686

$$d = \frac{q_D E}{k_D} \quad (124)$$

The atomic induced dipole then is treated as:

$$\mu = q_D d = q_D \times \frac{q_D E}{k_D} = \frac{q_D^2 E}{k_D} \quad (125)$$

On the basis of the induced dipole formula, one obtains:

$$\alpha = \frac{q_D^2}{k_D} \quad (126)$$

Here, α is the atomic polarizability, k_D is the force constant between the atomic core and the Drude particle, while q_D is the charge of the DO. After the system is induced by an electric field, the charge on the atomic core will change to $q-q_D$ (where q is the total partial charge of an atom). In the DO model, both positive and negative charges can be placed on the Drude particles.

To date, DO models have been created for alkali metal, alkaline earth metal, and halide ions, as well as the Zn^{2+} and Cf^{3+} ions.[49,552,883] Among them, most of the VDW parameters are obtained by reproducing liquid-phase properties.[49,552]

6.2.1.1. Early Work. Initially, the DO model was applied to ionic materials. For example, Dick and Overhauser used the Born−Mayer potential with the DO model to study crystalline systems in 1958.[885] It was shown that this model could be used for the derivations of the generalizations of the Szigeti relationship, Clausius−Mossotti relationship, and the Lorenz−Lorentz relationship. It also partially explained the deviation from unity for the e^*/e value from the second Szigeti relationship.[886,887] In 1959, Hanlon and Lawson applied the DO model to derive the effective charge in the Born−Szigeti equation for NaCl crystals.[888] The deviation of the effective charge from the formal charge was found to be proportional to the difference between the electronic polarizabilities of the cation and anion. Moreover, results showed that the predicted dipole moments agreed semiquantitatively with experimentally observed values. In 1974, Jacucci et al. studied crystalline NaCl using the DO model[889] in which only polarizabilities of the Cl^- ions were considered. The total potential was treated as the sum of the Tosi−Fumi potential and the polarization energy. DO parameters were assigned close to Sangster's work, and other parameters from the Tosi−Fumi potential were used in the modeling. The Drude particle around the Cl^- ion was assigned a −3e charge, and the k_D value was 8.5×10^5 cm^{-2}. Polarization only caused a ∼0.1% change in the total energy and had a small influence on the acoustic and transverse modes in the optical phonon spectrum.[889] However, polarization has a large impact on the longitudinal modes, yielding improved agreement with experiment relative to an unpolarized model. Lindan and Gillan developed a new method to simulate ionic materials using the DO model, and applied it to the CaF_2 system in 1992.[890] The simulation used a conjugated gradient minimization technique to obtain relaxed structures inside each MD step. They found that incorporating polarization had a limited effect on the system, and they noted that because Ca^{2+} and F^- are less polarizable ions, the observed results were not unexpected.

Mitchell and Fincham assigned fractional masses to the Drude particles, making them propagate in the same way as the atomic cores.[891] A smaller time-step, ∼3 times smaller than that used in unpolarized models, was necessary in their method. Their model is ∼3 times faster than the conventional DO model using the conjugate gradient relaxation approach. This is because the simulations employing the conjugated gradient relaxation approach were able to use the same time-step as employed in an unpolarized model, but needed ∼10 conjugate gradient iterations inside each time-step, which greatly increased the computational cost. They noted that when the Drude particles were assigned proper masses, the vibrational frequencies between the atomic core and the Drude particle were much higher than the lattice vibrational frequencies, allowing the new method they developed to give results similar to those of the conventional DO model, which assigned no mass to the Drude particles. They tested the new method by calculating the ion diffusion coefficients of the Na^+ and Cl^- ions in molten NaCl and the F^- ion in superionic CaF_2, as well as by predicting phonon frequencies found in the MgO system. Good agreement was obtained when comparison was made to previous simulations based on the conventional DO model.

6.2.1.2. Recent Applications to Metal-Containing Systems. Multiple DO models have been developed for a variety of systems in recent years. Lamoureux, Roux, Mackerell, and coworkers are active in this field. They have developed DO models for water,[892,893] ions,[49,552,894−896] small organic molecules,[897−904] amino acids,[905] nucleic acids,[906,907] lipids,[908] carbohydrates,[909] etc. In most cases, the Drude particles were assigned to the heavy atoms. Here, we focus our review on representative work of metal-containing system modeling by the DO approach.

Lamoureux and Roux proposed a new simulation algorithm for the DO model.[910] They used two different thermostats on the atom core and on the Drude particle. The thermostats for the atom core and Drude particles were set to room temperature and 1 K, respectively. An extended Lagrangian algorithm instead of a SCF algorithm was used to propagate the dynamics, with the Drude particles being assigned small masses. Importantly, relatively large time-steps (1 or 2 fs) could be used with the new algorithm. A water model, which adopted the SPC geometry and added an additional Drude particle, was used in their simulations. It was shown that simulations using this algorithm and the SCF algorithm agreed in their predictions of liquid properties. Moreover, it was also shown that simulations, which used their new algorithm but employed the same thermostat on the atom centers and the Drude particles, generated less accurate results and suffered from numerical stability issues.

Lamoureux et al. described the "simple water model with four sites and Drude polarizability" (SWM4-DP) model in 2003.[892] The water model uses a rigid gas-phase geometry and placed a $+q$ charge on each of the two hydrogen atoms, $-2q$ on the additional dummy site along the HOH bisector, $-q_D$ on the oxygen atom core, and $+q_D$ on the Drude particle, which is connected to the oxygen atom, respectively. A 12-6 LJ potential was assigned to the oxygen atom core. Because of the constraints used, there were only four parameters that needed to be optimized: the distance between the oxygen atom core and its Drude particle, the polarizability of water, and the two 12-6 LJ parameters on the oxygen atom. The water model was parametrized to reproduce the properties of liquid water under different conditions, and the extended Lagrangian algorithm was used to perform the MD simulations. It was found that the water model reproduced various experimental properties (i.e., vaporization enthalpy, static dielectric constant, self-diffusion

DOI: 10.1021/acs.chemrev.6b00440
Chem. Rev. 2017, 117, 1564−1686

constant). However, some compromises were made during the parameter design process. For example, the polarizability of the isolated water molecule was 1.04 Å^3, instead of 1.44 Å^3 obtained from experiment. They noted that this is because the "Pauli" repulsion opposes the polarizability induction. They further discussed that compromises were made for a number of reasons including the "too repulsive" nature of the 12-6 LJ potential, adopting the gas-phase geometry for condensed phase applications and the point charge representation for the short to middle range interactions. The Exp-6 potential and a smeared charge representation were suggested as possible improvements to the water model.

The SWM4-DP model was followed by the SWM4-NDP (N indicates negative) model,[893] where a positive charge is assigned to the oxygen atom and negative charge to the Drude particle. Overall, the SWM4-DNP model is comparable to the SWM4-DP model. Highlights of the newer model were its ability to reproduce the experimental viscosity and the HFE of water, suggesting the SWM4-NDP model a suitable choice for the simulation of aqueous phase systems and dynamic processes.

Lamoureux and Roux created consistent parameter sets for the alkali and halide ions for use with the SWM4-DP water model.[49] The polarizabilities of the alkali ions were taken from earlier work, while the polarizabilities of the halide ions were scaled down by a factor 0.724 from the gas-phase ionic polarizabilities determined previously. This factor comes from the polarizability of the SWM4-NP water model divided by the experimental value of the polarizability of water. No scale factor was applied to the polarizabilities of the alkali ions because of their small magnitudes. Hence, scaled or not would have had a limited influence on the simulation results. The Drude particle charge was determined on the basis of $q_D = \sqrt{\alpha k_D}$, and the VDW parameters of the ions were fit to reproduce ion−water binding energies in gas-phase monohydrates, the HFEs of the ion pairs, and the relative HFEs of ions in the same series. The final data imply an intrinsic HFE of the proton of −247 kcal/mol (giving a real HFE of −259.45 kcal/mol, with a phase potential for the SWM4-DP water model of −12.45 kcal/mol). Even though encouraging results were obtained, the model showed less accuracy in the modeling of small ions like Li^+ and F^-, as well as the minimized hydrates of the halide ions. Meanwhile, the limited accuracy of the LB combining rules was also discussed as an issue that limits the predictability of the model.

Yu et al. parametrized the alkali metal ions, alkaline earth metal ions, the zinc ion, and halide ions for the SWM4-NDP water model.[552] Small masses were assigned to the Drude particles (0.4 amu for each). The fitting targets they used were the total HFEs of the neutral salts and relative HFEs between ions in the same series. Monohydrate properties were also used in the parameter determination. Generally, the model simultaneously reproduced various gas-phase and liquid-phase properties obtained from experiment and QM calculations. Their data defined the real HFE of the proton as −258.8 kcal/mol (its intrinsic HFE is −246.2 kcal/mol, with an offset from the real HFE by the phase potential of −12.6 kcal/mol for the SWN4-NDP water model). The final results agreed well with the experimental HFEs of single monovalent ions from Noyes[911] but differed substantially from some others. A Thole-like damping function between the divalent cations and water molecules was used to prevent the polarization catastrophe, which is observed when the IOD is smaller than 1.97 Å. However, the model showed less accuracy for simulating divalent cations, which may be because of the strong CT effect between these ions and the surrounding water molecules.

Archontis et al. simulated 1.2 M NaI solutions using the SWM4-DP water model and ion parameters from Lamoureux and Roux.[912] A double layer was observed near the solution interface, with I^- ions closer to the surface than the Na^+ ions. They also observed that all of the solution species near the surface have their dipole moments perpendicular to the surface, while in bulk, the dipole vectors are randomly distributed. An additional simulation was performed with an isolated I^- ion in a water slab. This showed that the induced dipole interaction plays a major role in stabilizing the I^- ion at the interface, while permanent charge-dipole interactions between the I^- ion and water molecules favor placement of I^- in bulk.

Interactions between different monovalent cations (the Li^+, Na^+, K^+, and NH_4^+ ions) and benzene along with NH_4^+ interacting with a water molecule were studied by Orabi and Lamoureux using the DO model.[894] The parameters were developed by reproduction of QM-derived results. The parameters reproduced not only the interaction energies and PESs of the cation−π dimer, but also the cooperative behavior of the cation−π−π trimers and anticooperative behavior of the π−cation−π trimers. Simulation and related analysis of the ion-benzene dimer in aqueous solution showed that the small ions Li^+ and Na^+ favor solvation in water, while the bigger ions K^+ and NH_4^+ have favorable interactions with benzene of 1.2 and 1.4 kcal/mol, respectively. Simulation of K^+ or NH_4^+ with two benzene molecules in aqueous solution indicated that the cation−π and π−π interactions are all enhanced when compared to those predicted with a pairwise model (the heights of the first peaks of the RDFs defining benzene−benzene and benzene−ion interactions all increased when compared to systems having one K^+ or NH_4^+ and one benzene in aqueous solution).[894] This illustrated the cooperativity of the two different interactions in aqueous solution. This same team developed parameters for alkali ions interacting with the NH_3 molecule.[895] The model was parametrized via reproduction of MP2-derived ion-NH_3 dimer properties. The resultant model reproduced the QM calculated binding energies for the $M^+(NH_3)_n$ (with n = 2−4) and $M^+(NH_3)_n(H_2O)_m$ (with n, m = 1−3 with $n + m \leq 4$) systems, as well as the relative solvation free energies of these ions in ammonia. The PMFs of these ions in NH_3/H_2O mixed aqueous solutions showed Li^+ and Na^+ bind to NH_3 only in their second solvation shells, and K^+ and Rb^+ slightly favor NH_3 over water, while Cs^+ binds to NH_3 only in its first solvation shell.

Same as with unpolarized models, balancing the parameters used to simulate mixed systems employing the DO model can pose a challenge. For instance, in the simulation of ionic solutions, one may need to optimize the VDW parameters between the counterions if ion parameters were fit for a single ion under infinite dilution conditions. For DNA in ionic solutions, one needs to balance the interactions between the counterions as well as the interactions between DNA and ions, which again can afford a challenge.

Luo et al. noted that most parametrization efforts were performed to reproduce isolated ion properties, which may not yield accurate models for the simulation of finite concentration solutions.[896] To further explore this issue, they simulated NaCl and KCl solutions at different concentrations using the SWM4-

DOI: 10.1021/acs.chemrev.6b00440
Chem. Rev. 2017, 117, 1564−1686

NDP water model[893] and ion parameters developed by Yu et al.[552] The osmotic pressures of KCl solutions were reproduced with only slight deviations from the experimental results for concentrations above 2 M. However, their results showed that even at 1 M, simulation of the NaCl solution underestimated the osmotic pressure. They attempted to optimize the parameters by changing the Thole-damping factors or adjusting the pairwise LJ parameters. Even though both strategies worked well to better reproduce experimental osmotic pressures, changing the Thole-damping factor, while reducing the interaction energy, did not shift the minimum position (unlike modifying the LJ parameters). It was also shown that the second virial coefficients predicted by the new parameter set were much smaller than those predicted by the original parameters, but afforded better agreement with CPMD simulation results. Overall, this work showed that examining osmotic pressure affords another route to validating computational models of ion solvation.

Galbis et al. created a DO model for the Cf^{3+} ion,[883] in which the mobile charge densities in harmonic oscillators (MCDHO) water model[913] was used, while the atomic core and DO particle of the Cf^{3+} ion were assigned with charges of +4e and −1e, respectively. QM calculations based on two different levels of theory (MP2 and BP86) were performed but offered different CN and IOD values. Two different methods, the "Heuristic method" and "Systematic method", were used to generate a number of geometries, and potential fits were performed on the basis of the MP2 and BP86 calculated data, respectively. Afterward, MC simulations were performed on the basis of their derived potential using the NVT ensemble. It was shown that the two obtained potentials (MP2 and BP86), which were all based on the "Systematic method", gave similar structural results in the MC simulation, even though the MP2 and BP86 calculations showed different CN preferences. Extended X-ray absorption fine structure (EXAFS) spectra were calculated on the basis of different potentials and compared to experimental data. The results supported a CN of 8 for the Cf^{3+} ion. An analysis of the O−Cf^{3+}−O angles was performed, suggesting that a square antiprism structure (for CN = 8) was preferred in the aqueous solution.

Savelyev and Mackerell balanced DO model parameters to better represent the interactions between ions, water, and DNA.[896] The QM-derived data on small model molecules, experimental hydration, and osmotic properties were used as fitting targets. Partial reoptimization of the valence angle parameters in the bases, modification of the charges of select atoms in the DNA backbone, and adjustments of the LJ parameters between DNA and water as well as the LJ parameters between DNA and ions were performed to improve the model. Results showed that the new model better reproduced the ion distributions predicted by counterion condensation theory than the CHARMM36 unpolarized force field, highlighting the advantage of the DO model over the unpolarized one for the description of DNA in ionic solutions.

Besides modeling the ion−aqueous and ion−molecule systems, the DO model has also been applied to the ion-containing material systems. Herein, we introduce an example using the DO model to simulate the MOF systems. Yu et al. developed a DO model for N_2 and CO_2 molecules based on the SAPT analysis of each molecular dimer.[914] In total, there are four terms in the model, which are related to the exchange, electrostatic, induction, and dispersion interactions, respectively. Each term in the model was fit to the QM calculated counterpart separately. In general, the resultant force field reproduced various properties of gaseous N_2 and CO_2 as compared to experimental data. On the basis of this work, McDaniel and Schmidt created the ZIF FF to simulate CO_2 and N_2 adsorption in the ZIF systems.[915] An extension of the Williams−Stone method was used to represent the dispersion interactions and was able to accurately reproduce the calculated dispersion energies on the basis of the SAPT theory. Simulated CO_2 and N_2 adsorption isotherms for nine different ZIFs agreed well with the available experimental data. Results implied that UFF overpredicted the gas absorption in ZIFs with sodalite (SOD) and gmelinite (GME) topologies due to the systematically overestimation of the asymptotic dispersion interactions. They noted that UFF benefits from error cancellation between the electrostatic and dispersion interactions when simulating ZIFs with RHO topology. They also proposed that the modest performance of the UFF dispersion term arises from its unphysical LJ form, and usage of the environment independent dispersion parameters.

6.2.2. Drude Rod Model. In comparison to the DO model, the DR model[884] places a rigid bond between each atomic core and its Drude particle (see Figure 63), which gives it a permanent dipole. The orientation of the Drude particle responds to the direction of the electric field. Iori and Corni applied the DO and DR models to gold surfaces.[884] Both models place $-q_D$ and $+q_D$ charges on the gold atoms and their Drude particles, respectively. There are three parameters in the DO model: k_D, q_D, and m. The harmonic oscillator frequency of the DO model was obtained using eq 127. The DR model also has three parameters l_0, q_D, and m, yielding a permanent dipole $\mu = q_D l_0$, while its polarizability and harmonic frequency were obtained using eqs 128 and 129, respectively.

$$\omega = \sqrt{\frac{k_D}{m}} \tag{127}$$

$$\alpha = \frac{\mu^2}{3k_BT} = \frac{q_D^2 l_0^2}{3k_BT} \tag{128}$$

$$\omega = \sqrt{\frac{2k_BT}{l_0^2 m}} \tag{129}$$

They found that the DR model offered a better accounting of gold surfaces. They also discussed the numerical instabilities encountered in the DO model in simulating the interactions between the Drude particles and nearby atomic cores. Moreover, PME calculations would be inaccurate when two charges are very close when using the DO model. However, the DR model addresses these problems effectively. They used q_D = +0.3e, m = 0.5 amu, and l_0 = 0.7 Å for the DR model based on several validation studies. MD results of the DR model agreed well with results based on a continuum model, validating its ability to account for the polarization effect in these systems.

Iori et al. described the GolP force field for modeling protein interactions with the Au(111) surface in aqueous solution.[513] The interaction potential function form is:

$$E_{int} = E_{pol} + E_{VDW} + E_{chemisorb} + E_{\pi} \tag{130}$$

Here, E_{pol} is represented by the DR model, while the other three terms were described by 12-6 LJ potentials to represent the various interactions. On the gold metal surface, VDW points were placed in virtual sites (see Figure 64) instead of at

DOI: 10.1021/acs.chemrev.6b00440
Chem. Rev. 2017, 117, 1564−1686

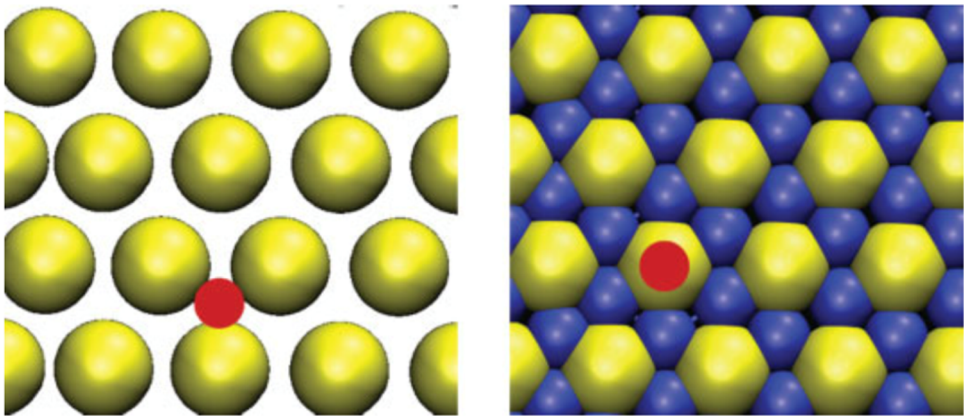

Figure 64. Using the real gold atoms as LJ interaction site drives adsorption in the hollow position (left panel), while the use of VS (in blue) drives adsorption on-top (right panel). Reprinted with permission from ref 513. Copyright 2008 John Wiley and Sons.

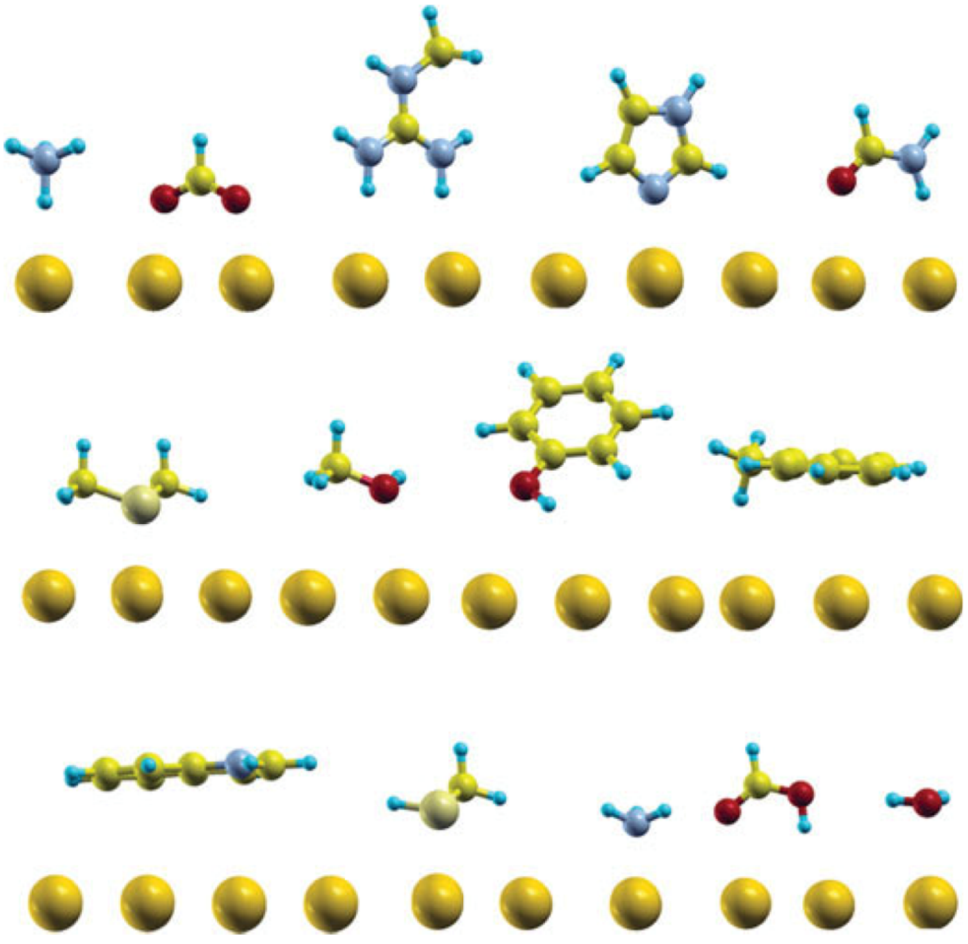

Figure 65. Lateral view of the adsorption geometry obtained by DFT calculations for all 14 molecules in Table 1 of ref 513. Only the uppermost gold layer is shown in the figure. Reprinted with permission from ref 513. Copyright 2008 John Wiley and Sons.

the gold atoms to reproduce the correct absorption behavior: on-top adsorption is favored over absorption in hollow sites. This also has a physical meaning because in metals the free-electron density in the hollow sites is higher than that on the lattice atoms. PW-DFT calculations were performed for Au(111) interacting with different amino acids to clarify the chemisorption effects. Instead of carrying out DFT calculations for all of the 20 different amino acids at various conformations on the Au(111) surface, calculations were performed between an Au cluster and fragmented small molecules (see Figure 65). It was shown that the imidazole, NH_3, CH_3SH, and CH_3SCH_3 molecules were chemisorbed, rather than physisorbed. It was found that it was hard to reproduce the interaction energies of ethane, 1,3-butadiene, and benzene with the Au(111) surface using a single VDW term because of their strong π interactions with coinage metals. Incorporating an independent term, modeling π interactions with the metal surface (E_π, see eq 130) was included and parametrized via modification of the LJ parameters. QM calculated data and experimental results were used in developing the parameter sets. Validation tests between

DOI: 10.1021/acs.chemrev.6b00440
Chem. Rev. 2017, 117, 1564−1686

Table 3. Representative Examples of IDMs

	permanent multipole	polarizability	CT term	induced multipole	VDW
AMBER ff02.pol[920]	monopole	isotropic	no	dipole	12-6
CHARMM/PIPF[923]	monopole	isotropic	no	dipole	12-6
CHARMM/CTPOL[924]	monopole	isotropic	yes	dipole	12-6
OPLS-AA/PFF[162]	monopole	isotropic	no	dipole	X-12-6
OPLS-AAP/CM1AP[919]	monopole	isotropic	no	dipole (electric field was calculated according only to the permanent point charges)	12-6
AMOEBA[921]	monopole, dipole, quadrupole	anisotropic	no	dipole	buffered 14-7
SIBFA[164]	monopole, dipole, quadrupole	anisotropic polarizability on bond centers and lone pairs, quadrupole polarizability on Cu^+	yes	dipole (with additional quadrupole on Cu^+)	X-6

small molecules and the Au(111) surface were carried out to explore the capabilities of the model to describe these interactions. These results demonstrated that the GolP FF generally reproduced available experimental data.[513]

6.3. Induced Dipole Model

6.3.1. Model Overview. Barker described the IDM in 1953,[916] while Warshel and Levitt performed the first classical simulation of a biomacromolecule based on a polarizable model using induced dipoles.[917] Stillinger and David developed a polarizable water model in 1978 based on the IDM.[918] In the IDM, the total energy is also represented by the sum of bonded and nonbonded interactions (see eq 131). Its difference from the unpolarized model is that the electrostatic energy of each site is calculated on the basis of its induced dipole and electric field on that site (see eq 132).

$$E_{\text{total}} = E_{\text{bonded}} + E_{\text{nonbonded}} = E_{\text{bonded}} + E_{\text{ele}} + E_{\text{VDW}} \tag{131}$$

$$E_{\text{ele}} = -\frac{1}{2}\sum_i \mu_i E_i \tag{132}$$

The induced dipole of a particle is usually represented as its polarizability α_i times the total electric field E_i (see eq 133) at its site. In a more accurate approach, the induced dipole is calculated on the basis of eq 134, where β_i is the hyperpolarizability. However, there are more parameters in this formulation, and the linear representation (eq 133) is more widely used.

$$\mu_i = \alpha_i \cdot E_i \tag{133}$$

$$\mu_i = \alpha_i \cdot E_i + \beta_i E_i^2 \tag{134}$$

The electric field can be calculated using the permanent point charges (see eq 135, which is used in the OPLS-AAP/CM1AP force field[919]), permanent point charges and induced dipole moments (see eq 136, which is used in the AMBER ff02.pol force field[920]), sum of the permanent multipole expansion and induced dipole moments (see eq 137, which is used in AMOEBA force field[921]), or via a more complicated procedure: by using the permanent and induced multipole expansions (see eq 138, which is used in the SIBFA model to describe Cu^+ in Cu^+-containing systems[922]). Herein, T represents the interaction matrix, μ represents the dipole moment, while M means the multipole expansion. For instance, the AMOEBA force field[921] uses a permanent multipole expansion up to the quadrupole (see eq 139).

$$E_i = E_i^0 \tag{135}$$

$$E_i = E_i^0 - \sum_{k\neq i} T_{ik}^{\alpha\beta}\mu_k \tag{136}$$

$$E_i = \sum_{j\neq i} T_{ij}^0 M_j^0 - \sum_{k\neq i} T_{ik}\mu_k \tag{137}$$

$$E_i = \sum_{j\neq i} T_{ij}^0 M_j^0 - \sum_{k\neq i} T_{ik} M_k \tag{138}$$

$$M_i^0 = [q_i^0, \mu_{i,x}^0, \mu_{i,y}^0, \mu_{i,z}^0, Q_{i,xx}^0, Q_{i,xy}^0, Q_{i,xz}^0, ..., Q_{i,zz}^0]^T \tag{139}$$

As was partially discussed above, there are different strategies to represent the induced dipole: for example, (1) whether or not higher multipole moments are considered—inclusion of the multipole moments improves the representation of the charge anisotropy distribution inside a molecular system; (2) assigning anisotropic or isotropic polarizability to the atomic or bond centers—inclusion of the anisotropic polarizability will also improve the ability to model anisotropic charge distribution; (3) whether or not the hyperpolarizability, which models the nonlinear property of the polarizability toward the electrostatic field, is considered in the model; (4) calculating the induced dipole on the basis of fixed charges, or was it also influenced by the other induced dipoles in the system; performing the simulation in the former way decreases the computational cost, but sacrifices accuracy; and (5) inclusion or exclusion of higher order inductions (e.g., the induced quadrupole, octupole, etc.). Frustratingly, there is no quick answer to what is the best combination of these terms, but we briefly summarize a few representative examples of IDMs that have developed over the years (see Table 3). In general, higher order terms offer better accuracy, but increase the difficulty of parametrization and decrease the speed of calculation. However, the accuracy of different models also relies on the parametrization schemes used, so researchers need to determine the combination that best meets their own requirements.

There are a series of QM-based methods available, which can be taken advantage to develop IDMs. In general, IDMs can use related parameters (e.g. polarizabilities,[925] permanent multipole moments[926,927]) from different QM analyses. Moreover, the remaining parameters can also be optimized against QM calculated data (e.g., energies and geometries) and/or QM energy decomposition analysis (e.g., the constrained space-orbital variation (CSOV) analysis,[928−930] reduced variational

DOI: 10.1021/acs.chemrev.6b00440
Chem. Rev. 2017, 117, 1564−1686

space (RVS) analysis,[931] and SAPT analysis[817]) and/or experimental results.

6.3.2. Cation−π Interaction. Caldwell and Kollman explored the nonadditivity of cation−π interactions in 1995.[932] Unpolarized models are largely unable to accurately model cation−π systems. For example, the OPLS force field for benzene coupled with the Li^+ parameter set from Åqvist predicts an enthalpy of complex formation of −19.8 kcal/mol rather than the experimental value of −38.3 kcal/mol.[932] They also observed that the atomic charges of benzene derived using the RESP algorithm better reproduced the quadrupole moment of benzene and the enthalpy of complex formation than the charges from the OPLS force field, which were parametrized to reproduce aqueous phase properties. IDMs outperformed unpolarized models, but they found that it was hard to reproduce both the interaction enthalpy and the energy minimum distance simultaneously. For example, the minimum energy distances of five cation−benzene complexes were underestimated by ∼0.2 Å on average using the IDM. Even fine-tuning the LJ parameters (by making them more repulsive) corrected this deficiency, as it negatively affected the predicted interaction enthalpies.[932] They also proposed that the CT effect may need to be included to improve the model.

6.3.3. AMOEBA Force Field. Ponder, Ren, and co-workers have created the atomic multipole optimized energetics for biomolecular simulation (AMOEBA) force field.[48,921,933] It has bonded terms (bond, angle, dihedral, and improper torsion terms) represented using classical models. The bond and angle parameters are fit on the basis of QM-derived values (e.g., geometries and vibrational frequencies). The dihedral terms are fit to reproduce QM calculated PESs. The electrostatic interaction is represented by permanent monopoles (point charges), dipoles, and quadrupoles derived from the distributed multipole analysis (DMA) procedure,[926] along with the polarizable dipoles. Its VDW interaction uses a buffered 14-7 potential, and the VDW parameters were fit to reproduce QM calculated gas-phase properties (such as interaction energies) and then refined toward experimental condensed phase properties (such as densities and heats of vaporization).

A number of researchers have parametrized Na^+, K^+, Cl^-, Mg^{2+}, Ca^{2+}, Zn^{2+}, and Th^{4+} ions in aqueous solution for the AMOEBA force field.[48,553,554,934,935] The parameters were fit to QM calculated ion−water dimer results. It was shown that it is possible to reproduce both gas-phase properties (ion−water dimer properties) and liquid-phase ones (e.g., HFE) simultaneously. Creation of a Zn^{2+} ion model using the AMOEBA force field to simulate a metalloprotein system has also been reported.[936] Generally, the polarizable force fields have several advantages when it comes to simulating metal ions in protein systems. For example, it can simulate the tetrahedral structure of a number of zinc sites, while the unpolarized model tends to give octahedral structures. It can also more accurately model the chelation coordination mode of carboxylate oxygens while unpolarized force fields treat the two terminal oxygen identically, thereby favoring bridged structures.[936]

Ren and Ponder developed the AMOEBA water model by fitting the permanent monopole, dipole, and quadrupole of the water monomer based on the DMA employing high level QM calculations.[921] A modified Thole damping function was used to prevent the so-called polarization catastrophe at short-range. Both the hydrogen and the oxygen atoms were assigned a buffered 14-7 VDW potential. The quadrupole of the water molecule was scaled by 73% to better reproduce the water dimer structure from experiment and high-level QM calculations. It was shown that the water model well reproduced both cluster and bulk properties of water, which is hard to simulate using classical unpolarized force fields.

Grossfield et al. parametrized the Na^+, K^+, and Cl^- ions for the AMOEBA force field.[48] They used polarizability parameters of 0.12, 0.78, and 4.00 $Å^3$ for the three ions, respectively. They calculated the ion pair solvation free energies using FEP and MD methods, and the results agreed well with available experimental data. Because of uncertainties in the HFE of the proton, upon which many solvation free energy scales are determined, they proposed that the HFEs of the ions calculated by the AMOEBA force field, validated using gas-phase QM/experimental results (ion−water dimer interaction energies, HFEs of ion pairs, and relative HFEs between the same series of ions), represent the best estimate of the HFEs for these ions. On the basis of this hypothesis and their computational results for K^+ and Cl^-, they predicted that the HFEs of H^+ and OH^- are −252.5 and −116.8 kcal/mol, respectively.

Jiao et al. have performed the parametrization and simulation of Mg^{2+} and Ca^{2+} ions in aqueous solution using the AMOEBA force field.[553] They derived the polarizabilities on the basis of the B3LYP/6-31G* level of theory. They used Thole damping function to prevent the polarization catastrophe between the divalent ion and water. VDW parameters and damping factors were optimized to reproduce QM calculated distances and interaction energies of the ion−water dimers. Stronger damping (using a smaller damping factor) was employed between the divalent ion and water (0.095 and 0.159 for Mg^{2+} and Ca^{2+} ions, respectively) relative to the value used for the AMOEBA water dimer (0.39). The HFEs of these two ions were calculated and agreed well with experimental data. It was also shown that the Bennett acceptance ratio (BAR) method is more efficient than the FEP method.

Piquemal et al. incorporated the AMOEBA force field into the AMBER software package and parametrized the same two divalent metal ions (Mg^{2+} and Ca^{2+}) with the AMOEBA water model.[554] The difference is that they used the CSOV energy decomposition method during the parametrization. The CSOV method decomposes the interaction energy into Coulombic, exchange-repulsion, POL, and CT terms. On the basis of the POL term, they fitted the Thole parameters. Meanwhile, they found that the CT term is small (∼2% and ∼3% of the total interaction energies for the Mg^{2+}−water and Ca^{2+}−water systems, respectively), and absorbed it into the VDW interaction. They determined the Thole damping factors to be 0.076 and 0.088 for Mg^{2+} and Ca^{2+}, respectively. They compared a small simulation box (60 water molecules) versus two larger simulation cells (216 and 512 water molecules) using the AMOEBA force field, which resulted in different outcomes from the simulations: the Ca^{2+} ion had a CN of 7.7 (versus 7.2 in the small box) and an increased residence time for the first solvation shell (∼30% larger than the small box) in the larger simulation cells. As illustrated in earlier research, it is challenging to simulate the Ca^{2+} ion in aqueous solution even with the state-of-the-art CPMD approach due to the flexibility of the CN. CPMD simulation with the BLYP functional and a small simulation box (1 ion with 31 water molecules) gave a CN between 7 and 8,[937] while simulation with the PBE functional and a larger box (1 ion with 60 water molecules) underestimated the CN of Ca^{2+} (6.2 and 7 using a flexible and rigid water model, respectively).[938] The latter CN is significantly lower than the experimental value of ∼8 in a 1

DOI: 10.1021/acs.chemrev.6b00440
Chem. Rev. 2017, 117, 1564−1686

Table 4. Polarization Energies and Charge-Transfer Energies from RVS Energy Decomposition of Zn^{2+} in the Presence of Water Clusters of Sizes 1, 4, 5, and 6 at the HF/CEP-41G(2d) Level (or HF/aug-cc-pVTZ/6-31G**, Results in Parentheses)[a]

	complex			
	$[Zn(H_2O)]^{2+}$	$[Zn(H_2O)_4]^{2+}$	$[Zn(H_2O)_5]^{2+}$	$[Zn(H_2O)_6]^{2+}$
E_{pol} (RVS)	−37.6	−118.7 (−135.3)	−110.8 (−127.5)	−104.3 (−117.5)
E_{CT} (RVS)	−10.9	−28.7 (−9.3)	−24.5 (−6.7)	−21.8 (−4.51)
$(E_{CT}/(E_{pol} + E_{CT})) \times 100$	22.5	19.4 (6.4)	18.1 (5.0)	16.6 (3.7)

[a]Percentages of induction energies due to charge transfer are presented in the last row. All are in units of kcal/mol. Reprinted with permission from ref 934. Copyright 2010 American Chemical Society.

M $CaCl_2$ solution.[37] Ikeda et al. calculated the free energy difference between the different coordination modes of Ca^{2+} in aqueous solution using CPMD. They showed that the free energy differences between different CNs are very small and that the CN of Ca^{2+} has several minima in aqueous solution.[939]

Wu et al. developed an AMOEBA parameter set for the Zn^{2+} ion in aqueous solution.[934] The CSOV method was used again to parametrize the system. The VDW parameters were derived on the basis of QM calculations on Zn^{2+}−water dimer. It was shown from simulations that the experimental HFE, CN, and residence time of the first solvation shell water molecules matched well with experiment. They also analyzed the CT and POL effects using the RVS approach. The results show that the POL energy dominates the induction energy and the CT effect decreases as more water molecules coordinate to the Zn^{2+} ion (see Table 4). They suggested that the CT term should be subsumed into the VDW interaction or treated explicitly, rather than fitting them into polarization terms, to avoid overfitting.

Marjolin et al. parametrized the Th^{4+} ion in water using the AMOEBA force field.[935] The CSOV decomposition method was again used, and on the basis of these studies, the damping factor was determined to be 0.2. The PES for the Th^{4+}−water dimer interaction was determined using MCSCF/MRCI method and was subsequently used to determine the VDW parameters. Simulations using this model agreed well with experimental structural properties. However, they predicted the HFE of Th^{4+} to be −1635 (±18) kcal/mol based on the BAR method. This value is higher than the experimental value (e.g., −1391 kcal/mol from Marcus[502]).

Ren et al. developed the AMOEBA force field for small organic molecules, and have shown that it reproduces both gas- and liquid-phase properties simultaneously.[940] Shi et al. computed the HFE values for small organic molecules employing the AMOEBA force field based on different parametrization strategies.[941] Excellent agreement was obtained between theory and experiment. To facilitate the parametrization process for small molecules in AMOEBA, Wu et al. developed the Poltype software.[942] Parameters obtained in this way gave a RMS of ∼1 kcal/mol for the HFEs of neutral molecules, while the relative errors for cations and anions were less than 3%. Shi et al. developed the AMOEBA protein force field in 2013.[933] Group-based multipole interactions were used, and they set the scaling factors to 0, 0, 0.4, and 0.8 for the 1-2, 1-3, 1-4, and 1-5 multipole interactions, respectively. Torsion parameters were fitted to high level QM calculations and then tuned on the basis of experimental data.

Using the AMOEBA protein force field described briefly above, Zhang et al. studied Zn^{2+} ions in proteins.[936] They refined the polarizabilities and the VDW parameters of some atom types on the basis of their interactions with Zn^{2+} and water. The two metal sites in MMP-13 are known experimentally to be tetrahedral, while octahedral structures were usually predicted using a classical unpolarized force field. They found that the metal site structure is sensitive to the polarizabilities of the coordinating ligands: for example, an octahedral instead of a tetrahedral structure could be obtained by scaling down the polarizabilities of atoms on the imidazole ring of the coordinating HIS residues by ∼20−30%. On the basis of their model, the relative binding affinities were calculated for four inhibitors (see Figure 66) bound to MMP-

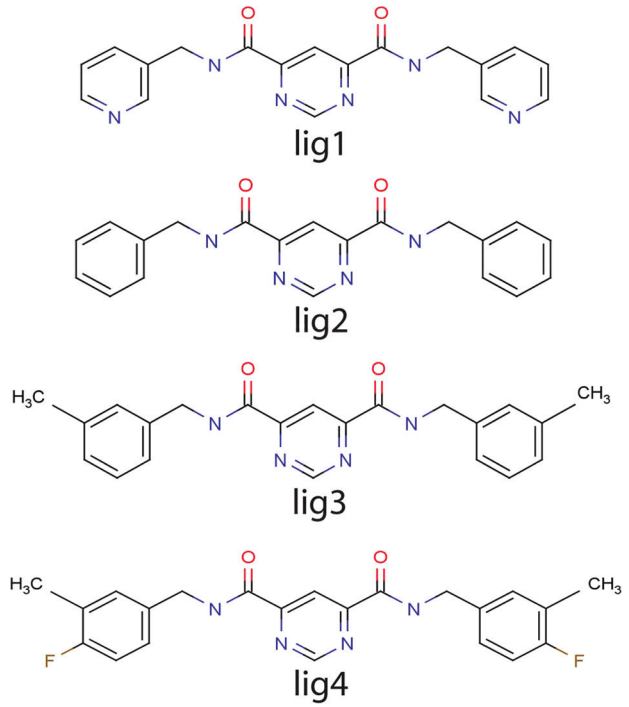

Figure 66. Pyrimidine dicarboxamide inhibitors binding with MMP-13. Reprinted with permission from ref 936. Copyright 2012 American Chemical Society.

13 using the BAR method. Note that the ligand is not directly bound to the zinc ion with the smallest distances between the ligand heavy atoms and the zinc ion being 4.7 Å. The rank order was well predicted, and the RMSD of the relative binding affinities was 0.72 kcal/mol, when compared to experimental results (see Figure 67). They found that the binding affinity increases along with the molecular polarizability of the ligand. For comparison, they calculated the relative binding affinities where they treated either the charge or the polarizability of the Zn^{2+} ion as zero. From this computational experiment, they found that the relative binding affinities were overestimated yielding a RMSD of ∼2.2 kcal/mol when the charge of the Zn^{2+} ion was neglected (see Figure 67). Moreover, it was shown that the rank order was not well reproduced when the polarizability

DOI: 10.1021/acs.chemrev.6b00440
Chem. Rev. 2017, 117, 1564−1686

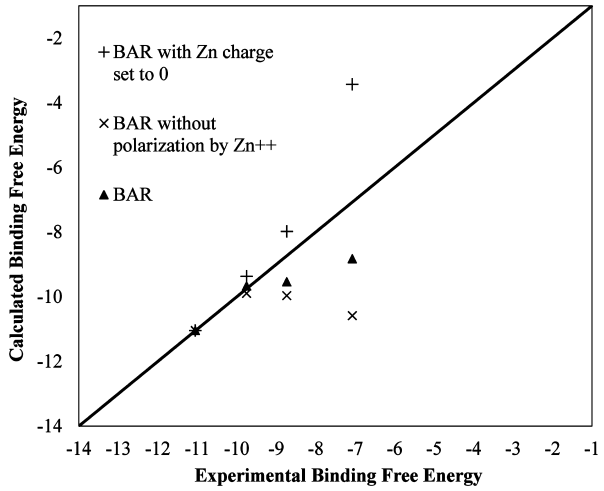

Figure 67. Comparison of calculated and experimental relative binding free energies (kcal/mol). Ligands 4, 3, 2, and 1 can be identified from the *x* axis in order from left to right, respectively, with the corresponding experimental binding free energies −11.05, −9.75, −8.73, and −7.07 kcal/mol. Reprinted with permission from ref 936. Copyright 2012 American Chemical Society.

of the Zn^{2+} ion was neglected (see Figure 67). This indicates that the polarization effect is ligand dependent, which is hard to model using an unpolarized force field by scaling the charges.

Semrouni et al. parametrized different spin states (singlet, triplet, quintet) of the Fe^{2+} ion for simulation in aqueous solution using the AMOEBA force field.[943] They parametrized the Fe^{2+}−water potential on the basis of the interaction between $Fe(H_2O)_5^{2+}$ and a water molecule. An energy decomposition scheme was used during the parametrization process. They assigned the same polarizability (0.55 $Å^3$) and Thole damping factor (0.113) but different VDW parameters to the three spin states. They performed a MD simulation on the quintet Fe^{2+} ion in aqueous solution, and good agreement was obtained with experiment for structural properties. However, the model underestimated the HFE value by ∼8.6%.

6.3.4. PFF Force Field. The polarizable force field (PFF), which was developed by Kaminski, Friesner, and co-workers, utilizes a permanent monopole and a permanent dipole with an induced dipole term to perform the modeling.[944] The PFF water model has five sites with two representing the lone pairs.[945] An exponential-12-6 term was used for the VDW interaction. As discussed in the nonbonded model section, the exponential form is more physically meaningful for modeling the exchange−repulsion interaction, but it can cause issues at close range. The r^{12} term used in the PFF prevents very close contact between particles, thereby alleviating this issue. Ponomarev et al. studied the Cu^+ ion interaction with water and benzene as well as in aqueous solution using an unpolarized force field and the PFF model, respectively.[946] They found that the unpolarized force field, without further fitting, underestimated the interaction by nearly a factor of 2 and 4 for the Cu^+−water and Cu^+−benzene cases, respectively. Even after refitting the VDW parameters in the unpolarized force field, the interaction energy between Cu^+ and water/benzene, as well as the HFE of Cu^+, were still underestimated. Even though the PFF parameters were only fit to the Cu^+−water system, it is encouraging that this model has excellent transferability to Cu^+−benzene and Cu^+−aqueous systems: they reproduced the interaction energy and distance of the Cu^+−benzene complex, and the HFE of Cu^+. Their work showed that inclusion of polarization is necessary to model highly polarized systems (e.g., cation−π systems) and that the PFF has better transferability than for an unpolarized force field.

Click et al. performed calculations on CopZ, a copper chaperone in *Bacillus subtilis*, in which Cu^+ is bound by a CXXC motif (the two Cys residues are Cys13 and Cys16), using OPLS and PFF, respectively.[947] Through local geometry optimization and the Poisson−Boltzmann finite element (PBF) continuum solvation model, they calculated the pK_a values for several related species. The Cu^+ parameters for the OPLS and PFF models were from Ponomarev et al. (discussed above).[946] They refitted the nonbonded parameters of atoms in CH_3SH and CH_3S^- to reproduce their interaction with water (as evaluated using QM calculated distances and interaction energies) for both the OPLS and the PFF force fields. They also parametrized the PBF hydration parameters for the Cu^+ ion, CH_3SH, and CH_3S^- residues to reproduce experimental HFEs. Generally, the PFF model showed improvement over OPLS. The PFF and OPLS force fields predicted the pK_a value of the methyl-capped Cys dipeptide as 7.35 and 19.05, respectively, as compared to the experimental value of 8.14. PFF predicted the pK_a1 and pK_a2 for the CopZ Cys13/Cys16 complex as 5.70 and 8.79, while OPLS predicted them to be 25.03 and 56.03, comparing that experiment gave values of ∼4 and ∼6. PFF predicted the binding free energy of Cu^+ with CopZ as ∼33 kcal/mol, being ∼50% greater than the experimental value, whereas the OPLS force field predicted a positive value. Furthermore, PFF better reproduced the experimental geometry for the metal site than did OPLS.

6.4. More Sophisticated Models

Beyond inclusion of just CT or POL effect, there are models that consider both terms: for example, the charge-transfer polarizable (CTPOL) force field developed by Sakharov and Lim,[924] the FQ discrete charge-transfer (FQ-DCT) model developed by Rick and co-workers,[948] and the SIBFA model developed by Gresh and co-workers.[164] Paesani and co-workers have developed the many-body polarizable (MB-pol) water model,[949−951] based on which the i-TTM[952,953] and many-body-energy (MB-nrg)[954] ion models were developed. Even though there is no explicit CT term included in the MB-pol model formulation, the CT effect is implicitly considered in the many-body terms.

6.4.1. CTPOL Model. Sakharov and Lim developed the charge-transfer polarizable (CTPOL) force field for proteins that contain $Zn(Cys_2His_2)$ or $Zn(Cys_4)^{2-}$ metal site in 2005.[924] In the CTPOL force field, a linear model was used to represent the CT effect between Zn^{2+} and its ligating atoms when their bond distance is less than the sum of their VDW radii. The polarization effect was modeled using an IDM and included only locally for Zn^{2+} and the side chain atoms of the ligating residues. The polarizabilities of ligating N and S atoms were fitted empirically to reproduce the X-ray determined Zn^{2+}−N and Zn^{2+}−S distances in the $Zn(Cys_2His_2)$ metal site. Comparison was made between the CTPOL force field and two 12-6 LJ nonbonded models developed earlier. It was also shown that the new force field preserved the tetrahedral coordination of the $Zn(Cys_2His_2)$ metal site during the simulation, while the two 12-6 nonbonded models overestimated the CN as 6 (two additional water molecules complete the coordination sphere; see Figure 68). Another test

DOI: 10.1021/acs.chemrev.6b00440
Chem. Rev. 2017, 117, 1564−1686

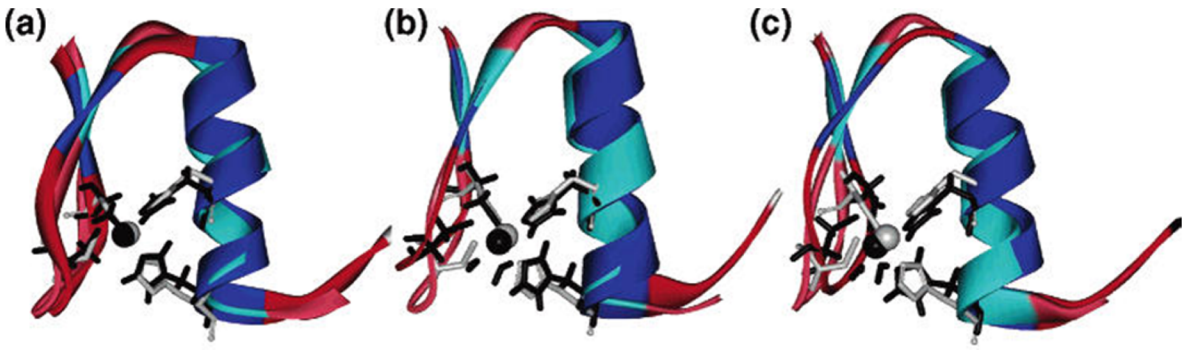

Figure 68. Crystal structure (light color) of the Zif268 Cys_2His_2 Zn-finger domain superimposed upon the average MD structure (dark color) derived from simulations using (a) the CTPOL force field, and (b) and (c) two 12-6 LJ nonbonded models. The metal-binding site is in black (MD) or gray (X-ray), while the regular secondary structures are in dark blue (MD) and light blue (X-ray), whereas the loops are in red (MD) and pink (X-ray). Reprinted with permission from ref 924. Copyright 2005 American Chemical Society.

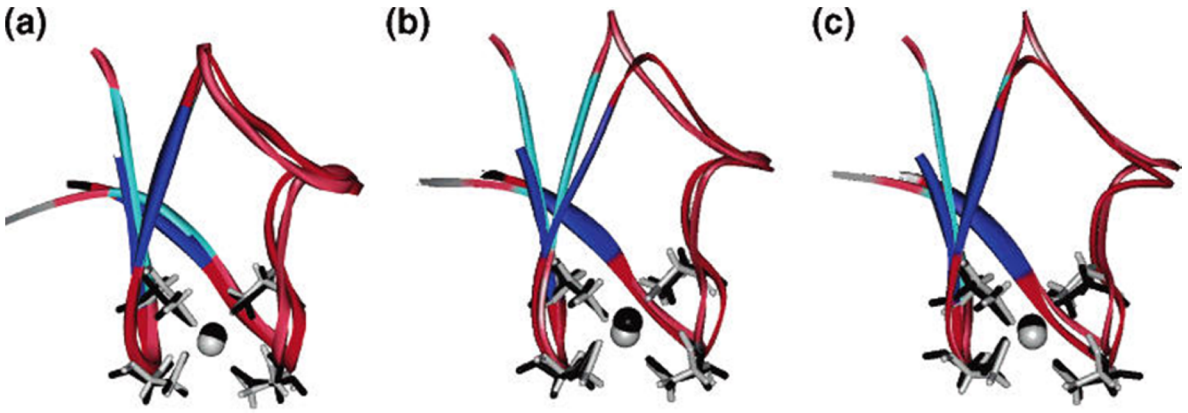

Figure 69. Crystal structure of the Zn-Cys_4 adenylate kinase lid domain superimposed upon the average MD structure derived from simulations. Panel a is for the CTPOL force field, while panels b and c are for two 12-6 LJ nonbonded models. The metal-binding site is in black (MD) or gray (X-ray), while the regular secondary structures are in dark blue (MD) and light blue (X-ray), whereas the loops are in red (MD) and pink (X-ray). Reprinted with permission from ref 924. Copyright 2005 American Chemical Society.

showed that the new force field better reproduced the tetrahedral coordination mode of $Zn(Cys)_4^{2-}$ than the two 12-6 nonbonded models even though both conserved the tetrahedral structure. Figure 69 shows that the loop/β-turns were distorted in simulations using the 12-6 LJ nonbonded models. The authors also discussed that inclusion of the local polarization and CT effects as well as appropriate VDW parameters are important to reproduce experimental structures.

Using CTPOL, Sakharov and Lim simulated a protein containing the $[CdZn_2Cys_9]^{3-}$ polynuclear metal site and the Hg^{2+}–MerP complex.[955] They showed that the CTPOL force field effectively simulated the polynuclear metal site, while the 12-6 LJ nonbonded model gave a too compact structure. Figure 70 shows the X-ray structure and average structure from the MD simulation using the new force field, indicating that the metal site is well conserved. Meanwhile, they found an angle restraint was necessary to preserve the linear coordinated Hg^{2+} site in the Hg^{2+}–MerP complex.

6.4.2. FQ-DCT Model. Rick and co-workers described the discrete charge-transfer (DCT) model for water and ion-aqueous systems.[948,956] In their formulation (see eq 140), an FQ model was used to model the polarization of water ($U_{self,FQ}$) in which the intramolecular charge interaction was represented by a Coulomb overlap integral based on Slater functions, and a DO model was used to describe the ion polarization ($U_{self,Drude}$). The Coulombic term was represented by the Coulomb equation multiplied by a damping function, and the VDW interaction was represented by a standard 12-6 LJ potential. The CT term was made distance dependent via a switching function, the maximum amount of CT occurs at short distances, and CT was prohibited between the Drude particle and the ion core. Dimer and bulk properties were used as targets for the ion–water parametrization effort. Additional ion–ion parameters were determined such that they reproduced experimental dipole moments of the ion pairs. Their results showed the average charges of the Na^+, K^+, and Cl^- ions in aqueous solution were +0.900e, +0.919e, and −0.775e, respectively, which are consistent with QM calculated results. Moreover, it was shown that the calculated HFEs and diffusion constants agreed with available experimental data. Their analysis also showed that the CT effect reduced the asymmetry of the first solvation shell of Cl^- ion and, for all ions studied, the first solvation shell waters carried a partial negative charge.

$$U_{total} = U_{LJ} + U_{Coulomb} + U_{CT} + U_{self,Drude} + U_{self,FQ} \quad (140)$$

Soniat et al., using the same model, parametrized Zn^{2+} and Mg^{2+} in aqueous solution.[555] They found that both CT and polarization effects influence the interaction of these divalent ions with water. Polarization increases the internal energy of the ion and water, but the ion–water interaction becomes stronger to compensate for this effect.[555] The CT effect decreases the

DOI: 10.1021/acs.chemrev.6b00440
Chem. Rev. 2017, 117, 1564–1686

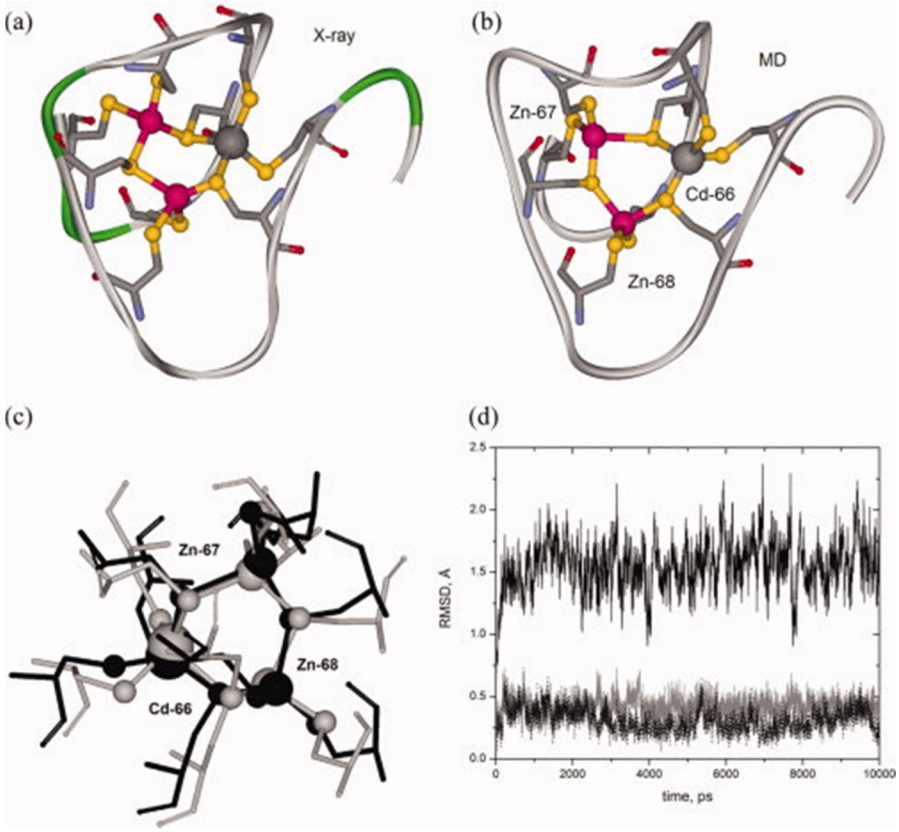

Figure 70. X-ray structure (panel a), average structure of MD simulation (panel b), superimposition of metal site of the former two structures (panel c), and RMSD values of the Cα atoms in protein backbone, Cd-Cys$_4$ complex, and average Zn-Cys$_4$ complex (solid, gray, and dotted curves in panel d, respectively). Reprinted with permission from ref 955. Copyright 2008 John Wiley and Sons.

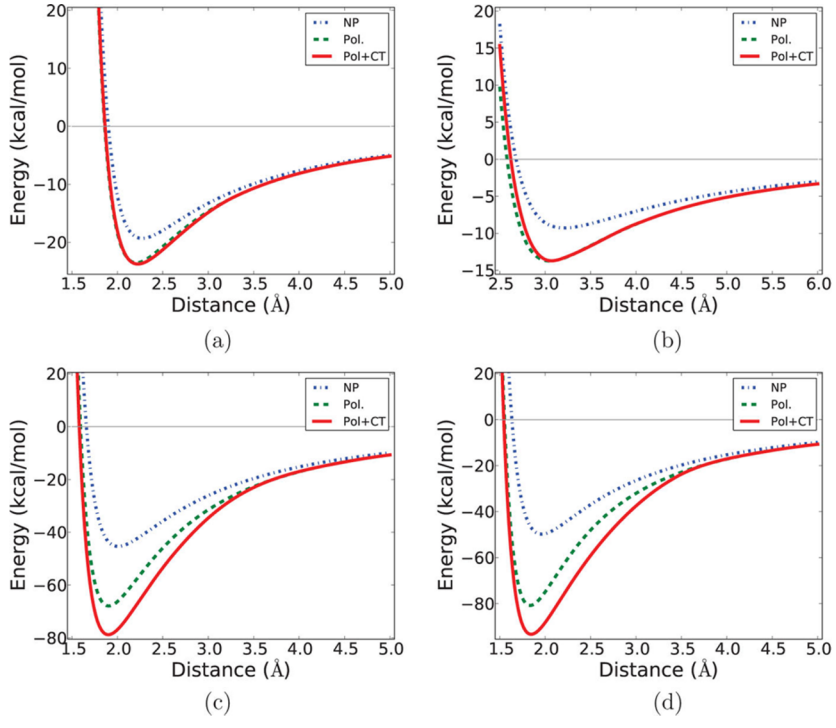

Figure 71. Nonpolar (NP), polarization (Pol.), and polarization plus charge-transfer (Pol+CT) energies in the energy decomposition of ion−water dimer system using the FQ-DCT model. Na^+−water, Cl^-−water, Mg^{2+}−water, and Zn^{2+}−water correspond to panels a, b, c, and d, respectively. Reprinted with permission from ref 555. Copyright 2015 American Chemical Society.

DOI: 10.1021/acs.chemrev.6b00440
Chem. Rev. 2017, 117, 1564−1686

ion−water interaction, but is counterbalanced by a decrease in energy of the system due to charge delocalization.[555] Figure 71 shows the energy decomposition results for a series of ion−water dimer systems using the FQ-DCT model. They found that for the monovalent ions, the polarization effect dominates the charge delocalization energy, while the CT effect is trivial. In comparison, the polarization decreases the binding energies to a greater extent (higher percentage) with the CT effect becoming considerable in the divalent ion−water dimer systems.

6.4.3. SIBFA Model. Gresh and co-workers have developed, over a number of years, the SIBFA method and have applied it to a number of systems. It has the following energy components: the permanent multipole term (E_{MTP}), the polarization term (E_{pol}), the CT term (E_{CT}), the repulsion term (E_{rep}), and the dispersion term (E_{disp}). An additional penetration term (E_{pen}) has been added in recent years because of the underestimation of E_{MTP} when compared to the Coulombic counterpart (E_C) of a QM energy decomposition analysis (EDA). Ultimately, it was shown that the summation of the multipole and penetration term better reproduced the E_C term from an EDA.[957] A Gaussian electrostatic model (GEM) SIBFA scheme has been developed and described in 2006.[958] This model connects the multipole distribution and electron densities, and includes the nonclassical penetration energy at short-range.

The SIBFA model places permanent multipoles (up to quadrupoles) on atoms and bond centers and induced dipole tensors on bond centers and lone pairs. The SIBFA model is usually parametrized to reproduce EDA results from QM calculations. The permanent multipole moments are derived on the basis of a QM-based multipolar analysis method described by Vigné-Maeder and Claverie.[927] The polarizability is represented as tensors based on the QM analysis of Garmer and Stevens.[925] The polarization term and charge-transfer term can be fit to their counterparts from a RVS or CSOV energy decomposition scheme, and the dispersion term can be fit to its counterpart from a SAPT analysis. The solvation free energy is incorporated into the SIBFA scheme through the Langlet−Claverie continuum reaction field procedure,[959] which represents the solvation free energy based on an aggregation of the electrostatic, repulsion, dispersion, polarization, and cavitation components.

The SIBFA model has been applied to a number of organic molecules,[960,961] ion−water systems (e.g., Pb^{2+}, La^{3+}, Lu^{3+}, and Th^{4+} ions in water),[935,962] and metal-containing biologically related systems (e.g., complexes involving Cu^+, Zn^{2+}, Ca^{2+}, or Mg^{2+} ions).[922,957,963−973] SIBFA can reproduce QM-derived interaction energies to very high accuracy (within 3% for some systems).[957,965,967,968,970−972] It showed little nonadditivity in the first-order term ($E_1 = E_{MTP} + E_{rep}$) but strong anticooperativity in E_{CT} and E_{pol}.[164] Moreover, because the model is parametrized against QM calculations, its accuracy depends on the level of QM theory employed.

Gresh et al. have developed a scheme to represent the interaction between two molecular fragments.[974] They discussed that in a SAPT analysis, the interaction energy is described as:

$$\Delta E = E_{el} + E_{rep} + E_{pol} + E_{disp} \tag{141}$$

Here, E_{el}, E_{rep}, E_{pol}, and E_{disp} are the electrostatic, repulsion, polarization, and dispersion parts of the interaction energy, respectively. In comparison, the interaction energy for a supramolecule in a SCF expansion can be represented by the following equation:

$$\Delta E_{SCF} = \Delta E_C + \Delta E_{ex} + \Delta E_{del} \tag{142}$$

Here, the ΔE_C, ΔE_{ex}, and ΔE_{del} are the Coulomb, exchange repulsion, and delocalization portions of the interaction energy. The delocalization part can be viewed as the sum of the polarization and charge-transfer energies. On the basis of these considerations, they proposed the following set of equations:

$$\Delta E_{MTP} = \Delta E_C - E_{pen} \tag{143}$$

$$\Delta E_{rep} = \Delta E_{ex} - E_{pen} \tag{144}$$

$$\Delta E_{SCF} = \Delta E_{MTP} + \Delta E_{rep} + \Delta E_{del} \tag{145}$$

$$\Delta E = \Delta E_{MTP} + \Delta E_{rep} + \Delta E_{pol} + \Delta E_{disp} \approx \Delta E_{SCF} \tag{146}$$

where ΔE_{MTP} represents the multipole expansion of the interaction energy and E_{pen} represents the penetration energy. The penetration energy is negative and is due to the overlap of electron clouds. It can be viewed as the interaction energy due to higher multipole terms. Finally, the interaction energy is represented by eq 146, as an approximation of the interaction energy based on the SCF calculations.

The multipole moments up to quadrupole of each fragment were evaluated on the basis of QM calculations, and both the atomic and the bond centers were modeled with multipole moments. The polarization energy of fragment A was calculated using:

$$E_{pol}^{A} = -\frac{1}{2}\sum_{i}^{A} \alpha_i \varepsilon_i^2 \tag{147}$$

Here, α_i represents the polarizability of the atomic/bond center i in molecule A, and ε_i is the electric field generated by all of the multipole moments on fragment B on each atom/bond center i of molecule A. The dispersion term was represented by r^{-6}, and to correct the nonphysical behavior of the polarization and dispersion functions at short-range, these interactions were scaled using modified distances instead of real distances between the atom centers. The repulsion term is calculated on the basis of the expansion of bond−bond repulsions (see eqs 148 and 149; a more detailed expansion is given in the original work).[974] They noted that the repulsion term depends on the square of the bond orbitals' overlap integrals.

$$E_{rep} = C \sum_{PQ}^{\text{bonds of A}} \sum_{RS}^{\text{bonds of B}} \text{rep}(PQ, RS) \tag{148}$$

$$\text{rep}(PQ, RS) = (M_{PR}\, e^{-\alpha d_{PR}} + M_{PS}\, e^{-\alpha d_{PS}} + M_{QR}\, e^{-\alpha d_{QR}} + M_{QS}\, e^{-\alpha d_{QS}})^2 \tag{149}$$

The authors pointed out that using additive functions to represent the interaction energy was a heuristic procedure and that they did not necessarily fit their model to the individual QM decomposition components.[974] They fit the parameters of H, N, O, Na^+, and K^+ to reproduce SCF calculated results for the water dimer, Na^+−water, K^+−water, and NH_4^+−water dimers.[974] It was shown that calculations based on their model showed good agreement with the SCF calculated binding energies and equilibrium distances. They also performed tests

DOI: 10.1021/acs.chemrev.6b00440
Chem. Rev. 2017, 117, 1564−1686

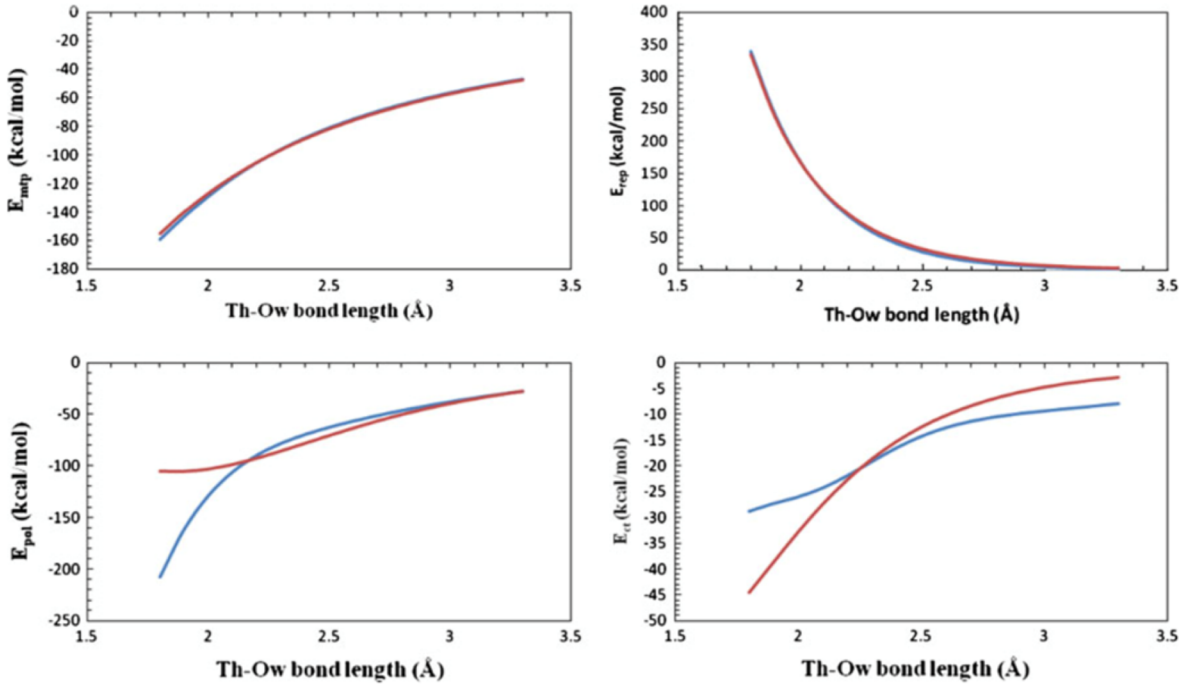

Figure 72. CSOV (blue) versus SIBFA (red) electrostatic (top left), repulsion (top right), polarization (bottom left), and charge-transfer (bottom right) energies as a function of the Th−O distance in Th^{4+}−H_2O. Reprinted with permission from ref 935. Copyright 2012 Springer.

on the Na^+−DMP^- (DMP^-, dimethyl-phosphate), K^+−DMP^-, Na^+−CH_3COO^-, Na^+−$CH_3COOCH_2CH_3$, and Na^+−CH_3CONH_2 systems. Importantly, the model reproduced the energy ordering for the different conformations of the Na^+−DMP^-, K^+−DMP^-, and Na^+−CH_3COO^- systems, and it predicted the stronger binding of Na^+ to CH_3CONH_2 than to $CH_3COOCH_2CH_3$.[974]

Gresh and co-workers have implemented an explicit CT term (see eq 150) into the interaction energy formula.[975] The CT term is based on the Murrell−Randic−Williams formula.[976]

$$E_{CT} = -2 \sum_{\alpha \in A} \sum_{\beta^* \in B} \frac{1}{\Delta E_{\alpha-\beta^*}} \left(\int \rho^{A}_{\alpha-\beta^*}(r) V^{B}(r)\, dr \right)^2 \tag{150}$$

Here, the factor 2 represents the double occupancy of the closed-shell MOs. α represents the electron donor orbitals, which are the ground-state MOs in fragment A. β represents the electron acceptor orbitals, which are the excited-state MOs in fragment B. V^B is the potential generated by fragment B. $\Delta E_{\alpha-\beta^*}$ is the difference of the IP of α in A and the EA of β^* in B. $\rho^{A}_{\alpha-\beta^*}$ is the overlap transition density:

$$\rho^{A}_{\alpha-\beta^*} = -(\alpha\beta^* - \alpha^2 S_{\alpha\beta^*}) \tag{151}$$

Here, the $S_{\alpha\beta^*}$ represents the overlap integral of MOs α and β^*. Details of the formal derivation can be found in the original publication.[975] A minimal valence Slater basis set was used for computing the necessary integrals. It was demonstrated that the proposed CT term agreed well with the CT energy values calculated using a SCF interaction energy analysis after counterpoise correction. It was also shown that the new formulation with an additional CT term offered improvement by showing better agreement with experimental and QM calculated results.

A number of application studies have been performed exploring the range of applicability of the SIBFA method.[922,935,957,960−973,977] For example, Gresh and Garmer studied the Mg^{2+}, Ca^{2+}, Zn^{2+}, and Cd^{2+} ions interacting with several biologically related functional groups (water, formamide, imidazole, methanethiol, formate, hydroxy, methoxy, methanethiolate) using the SIBFA method.[965] They showed that the SIBFA method could reproduce QM calculated binding energies and energy changes along with the intermolecular variables. They compared the SIBFA interaction analysis results for the (Mg^{2+} versus Ca^{2+}), (Zn^{2+} versus Cd^{2+}), and (Mg^{2+} versus Zn^{2+}) pairs against these ligands based on the softness of the ligands. While there were no clear correlations between the individual components and the total interaction energy for the (Mg^{2+} versus Ca^{2+}) pair, there were clear trends for the later two comparisons: the first-order term ($E_1 = E_{MTP} + E_{rep}$) is correlated with the total interaction energies, while the E_{CT} term follows the opposite trend. Moreover, their results indicated that the SIBFA scheme could reproduce the nonadditivity effects of the hexahydrates of these metal ions. Additionally, it was shown that the SIBFA method reproduced the nonadditivity of the E_{pol} and E_{CT} terms evaluated by EDA at the MP2 level of theory (the MP2 results showed that these two terms for the hexahydrates only increase by factors of ∼2.6 and ∼2, respectively, when compared to the monohydrates of these metal ions). Results showed that the interaction energy decreased from Mg^{2+} to Ca^{2+}, and from Zn^{2+} to Cd^{2+} (with six coordinated waters), because of the first-order term (the sum of E_{MTP} and E_{rep}), while the E_{CT} term followed the opposite trend. However, the increase in the interaction energy on going from Mg^{2+} to Zn^{2+} is more closely related to the second-order terms E_{CT} and E_{disp}.

Marjolin et al. parametrized the La^{3+}, Lu^{3+}, and Th^{4+} ions for aqueous phases using the SIBFA scheme.[935] They investigated different levels of theory, and HF with a mixed basis set (pseudopotential plus aug-cc-pVTZ) was chosen to use for the SIBFA parametrization between the metal ion and water. They noted that the underestimation of the energy at the minimum

DOI: 10.1021/acs.chemrev.6b00440
Chem. Rev. 2017, 117, 1564−1686

by the HF method, relative to MP2, can be partially compensated for by the suitable parametrization of the dispersion energy term. The E_{MTP}, E_{rep}, E_{pol}, and E_{CT} terms were fit to their counterparts obtained by CSOV analysis based on HF calculations. An example of Th^{4+}−water dimer is shown in Figure 72. Generally good agreement was obtained between the SIBFA and CSOV analysis results. Inconsistencies between the E_{pol} terms evaluated on the basis of the CSOV and SIBFA schemes were due to the overdamping of the latter method at short distance, which can be addressed using GEM. Finally, the difference between the MP2 and HF calculations was used to fit the E_{disp} component. However, the authors note that the correlation energy does not solely depend on the dispersion interactions, making the E_{disp} term less transferable than the other components.

6.4.4. Many-Body Polarizable Model. While the induced dipole model offers improved accuracy over the unpolarized model, its error at short-range is still considerable because the operative quantum effects are hard to model using simple classical representations. By applying related corrections (e.g., adding many-body terms) to the short-range region, further improvement can be obtained. In a series of papers, Paesani and co-workers explored water and monovalent ions based on a many-body polarizable model, and outstanding results were generally obtained. We briefly review the model and summarize the results in the following.

Paesani and co-workers have reported the development of the many-body polarizable (MB-pol) for water.[949−951] It contains 1-body, 2-body, and 3-body potentials explicitly combined with the "Thole-type model" (TTM) polarizable potential and a dispersion term (see eq 152). The 1-body potential inside an individual water molecule was based on the work of Partridge and Schwenke,[978] while the 2-body potential was fitted to the CCSD(T)/CBS calculated water dimer multidimensional PES (in total 42 508 dimers were considered),[949] and the 3-body potential was fitted to the CCSD(T)/aug-cc-pVTZ calculated water trimer energetics (in total 12 347 trimers were considered).[950]

$$E_N(x_1, ..., x_N) = \sum_a V^{1B}(x_a) + \sum_{a>b} V^{2B}(x_a, x_b) + \sum_{a>b>c} V^{3B}(x_a, x_b, x_c) + V_{TTM} + V_{disp} \quad (152)$$

As shown in eqs 153−155, the 2-body potential consists of the short-range term and the long-range term. The long-range term has electrostatic and induced dipole interaction terms from the TTM potential, as well as a dispersion term including r^{-6} and r^{-8} formulations. The short-range term can be viewed as a correction to the formulation of the long-range term. It is a polynomial that is invariant to permutation, which allows the potential to smoothly switch to zero when two water molecules separate each other beyond the assigned cutoff value. Overall, there are 1156 linear parameters and 16 nonlinear parameters in the 2-body potential that were fit.[949]

$$V^{2B}(x_a, x_b) = V^{2B}_{short}(x_a, x_b) + V^{2B}_{long}(x_a, x_b) \quad (153)$$

$$V^{2B}_{short}(x_a, x_b) = s_2\left(\frac{r_{OO} - R_i}{R_o - R_i}\right)V_{2S} \quad (154)$$

$$V^{2B}_{long}(x_a, x_b) = V^{2B}_{TTM,elec}(x_a, x_b) + V^{2B}_{TTM,ind}(x_a, x_b) + V^{2B}_{68}(x_a, x_b) \quad (155)$$

The 3-body potential used is shown in eqs 156 and 157. Similar to the 2-body potential, the short-range term in the 3-body potential has a switching function that makes the 3-body interaction switch to zero smoothly when one water molecule leaves from a trimer water cluster. In total, 1163 linear and 10 nonlinear parameters were fit in the 3-body potential.[950]

$$V^{3B}(x_a, x_b, x_c) = V^{3B}_{short}(x_a, x_b, x_c) + V^{3B}_{TMM,ind}(x_a, x_b, x_c) \quad (156)$$

$$V^{3B}_{short}(x_a, x_b, x_c) = [s(t_{ab})s(t_{ac}) + s(t_{ab})s(t_{bc}) + s(t_{ac})s(t_{bc})] \times V^{3B}_{poly}(x_a, x_b, x_c) \quad (157)$$

It was shown that the MB-pol model offered an outstanding model for simulating water in both the gas phase and the liquid phase, which represented a very important step toward a "universal model" of water. This water model has been thoroughly reviewed in recent publications by Paesani and co-workers.[979,980]

This team has also developed the i-TTM model for alkali metal ions[953] and halide ions,[952] which are compatible with their MB-pol water model. The total potential consists of a water molecule potential, and an i-TTM term for ion−water interactions (see eq 158). As shown in eq 159, the i-TTM term consists of a TTM electrostatic term, a TTM induction term, a repulsive term (which is described by a series of exponential potentials), and a dispersion term (which was represented by a series of r^{-6} potentials with damping functions). CCSD(T)/CBS calculated energetics were used for the parameter fitting. Accuracy of the i-TTM model was compared to those of QM and polarizable models for alkali metal ion−water clusters (with up to 4 water molecules),[953] and halide ion−water clusters (with up to 8 water molecules).[952] In general, the i-TTM potential provides an accurate and efficient way to model ion−water systems.

$$V_{total} = V^{intra}_{water} + V^{inter}_{water} + V^{i\text{-}TTM} \quad (158)$$

$$V^{i\text{-}TTM} = V^{TTM,elec} + V^{TTM,ind} + \sum_{i=1}^{n}(V_i^{rep} + V_i^{disp}) \quad (159)$$

Paesani and co-workers also developed a 2-body term inside the many-body-energy (MB-nrg) potential for halide ion−water dimers (see eq 160), which follows the MB-pol development strategy.[954] CCSD(T)-F12b/CBS calculated energies were used for parameter fitting. 12 773, 17 526, 17 738, and 13 783 halide−water dimers were used to fit the 2-body potentials of the H_2O-F^-, H_2O-Cl^-, H_2O-Br^-, and H_2O-I^- dimers, respectively. 874 linear and 9 nonlinear parameters were fitted for each halide−water dimer potential.

$$V^{2B}(H_2O-X^-) = V^{2B}_{short}(H_2O-X^-) + V^{2B}_{TTM}(H_2O-X^-) + V^{2B}_{disp}(H_2O-X^-) \quad (160)$$

Accuracy analysis of different methods was then performed, and their results show that the DFT models have considerable halide-dependent errors in describing the two-body interaction energies. Moreover, classical polarizable models could not well reproduce halide ion−water interactions at short-range, because

DOI: 10.1021/acs.chemrev.6b00440
Chem. Rev. 2017, 117, 1564−1686

these interactions are more quantum with considerable covalent characteristics.

Even though the MB-pol water model has achieved superb accuracy, the OH bond in water cannot be broken, which limits its ability to simulate chemical reactions. Furthermore, the MB-pol water model is highly parametrized, which increases its computational cost, when compared to the typical unpolarized or polarizable water models. The MD simulations reported so far only last for tens of nanoseconds for systems containing 216 or 512 water molecules.[980] Also, the complicated function form brings challenges to extend the MB-pol model to other systems. In comparing the i-TTM and MB-nrg potentials for ions, the latter has a better accuracy, while the former has fewer parameters, making it more easily extended. The many-body interactions in water tend to converge rapidly, but some covalent and metallic systems (e.g., Na, Si, Au) have many-body interactions that are oscillatory in nature.[981] It is not clear whether the MB-pol type model can be easily extended to these classes of systems.

6.5. Reactive Force Fields

Polarizable models offer improvements over unpolarized models, but they still do not address the need to model chemical reactivity using simpler models other than those based on QM methods. To fill this void, special purpose "reactive" force fields have been designed. These methods are typically based on the length−order−energy relationship of a chemical bond. The length−order−energy relationship of a chemical bond can be traced back to Pauling.[350] Johnston and Parr developed a related procedure for the prediction of activation energies and rate constants.[982] Tersoff developed an empirical force field (so-called the Tersoff potential), which uses the bond order concept to model covalent systems.[983] Benner developed the reactive empirical bond order (REBO) force field for hydrocarbons to model the chemistry of carbon.[984] Stuart et al. followed this work by developing the adaptive intermolecular REBO (AIREBO) force field for hydrocarbon systems.[985] Subsequently, Benner and co-workers created the second generation REBO force field for hydrocarbons.[986] van Duin, Goddard et al. developed the reactive force field (ReaxFF) in 2001.[987] Scaleable parallel ReaxFF has been implemented and is now available in the Purdue reactive molecular dynamics (PuPuReMD) open source software package[988−990] and the LAMMPS/User-ReaxC software package. Applications to metal-containing systems are well represented by ReaxFF, so, herein, we will focus on this methodology and some of its applications.

6.5.1. Model Introduction. Similar to nonreactive classical force field models, ReaxFF consists of two sets of terms: the bonded and nonbonded terms. However, ReaxFF allows bond formation and dissociation, and, hence, has much different bonded terms from classical harmonic potentials. The bonded terms are based on atomic connectivity, while the nonbonded terms are considered for each atom pair (see below for more details). During the MD simulation, bond orders are evaluated at each time-step and are used to determine the atomic connectivity at a user-defined cutoff. ReaxFF cannot simulate multiple spin states explicitly because it does not have the facility to incorporate electronic structure. However, because the ReaxFF is parametrized to the lowest energy spin state, it can model spin state changes along the bond formation/dissociation pathway implicitly. An explicit electron version of ReaxFF (eReaxFF) has been described recently,[991] in which the authors introduced an explicit treatment of holes and electrons in the potential function, while the ACKS2 method[873] was employed to calculate the atomic charges. A single atom type in ReaxFF defines each element: for example, there are no sp, sp^2, or sp^3 hybridized carbon atoms but only one carbon atom type. The energy curves are continuous throughout the simulation process, even at regions involving bond formation/breaking where favorable reactions can automatically occur without any restraint. A time-step of up to 0.5 fs could be used for simulations at low and normal temperatures, while a smaller time-step is needed for a higher temperature (>1500 K).[992]

$$E_{\text{total}} = E_{\text{bonded}} + E_{\text{nonbonded}} \tag{161}$$

$$E_{\text{bonded}} = E_{\text{bond}} + E_{\text{over}} + E_{\text{under}} + E_{\text{angle}} + E_{\text{lp}} + E_{\text{pen}} + E_{\text{tors}} + E_{\text{conj}} + E_{\text{hb}} \tag{162}$$

$$E_{\text{nonbonded}} = E_{\text{ele}} + E_{\text{VDW}} \tag{163}$$

The potential is summarized in eqs 161−163. The detailed expressions for the bonded terms and the other terms such as the overcoordination (E_{over}), undercoordination (E_{under}), penalty (E_{pen}), hydrogen bond (E_{hb}), and lone-pair (E_{lp}) terms can be found in the original articles. Moreover, the number of terms used depends on the application at hand. For example, for a system of pure gold, only E_{bond}, E_{over}, and E_{VDW} were considered.[993] For metal-catalyzed nanotube formation, an E_{C2} term (not contained in eqs 161−163) was added to destabilize the C_2 radial.[994]

The bond energy was represented as a function of the corrected bond order (see eq 164).[987] The uncorrected bond order is calculated on the basis of the bond distance directly (see eq 165 and an example shown in Figure 73) and consists

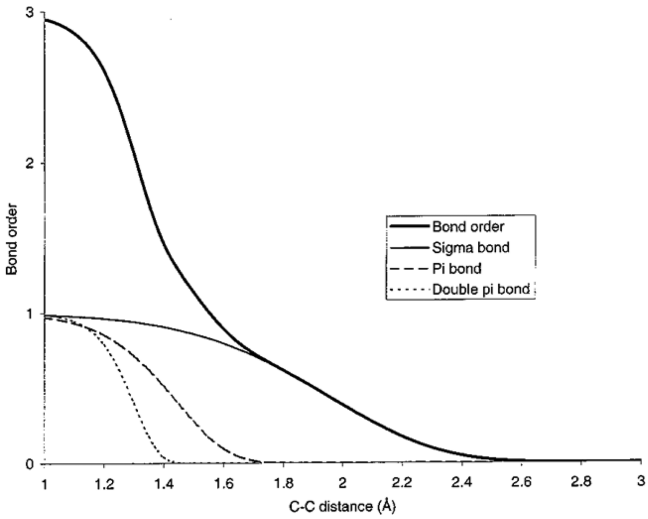

Figure 73. Interatomic distance dependency of the carbon−carbon bond order in ReaxFF. Reprinted with permission from ref 987. Copyright 2001 American Chemical Society.

of contributions from different types of bonds: the σ bond, the first π bond, and the second π bond ($\pi\pi$ here). All three terms in eq 165 are considered for a bond between two carbon atoms, while only the first term is used for the σ bond that forms between a carbon atom and a hydrogen atom. The uncorrected bond order equation (see eq 165) is an exponential decay function, which effectively considers the bond formation/

DOI: 10.1021/acs.chemrev.6b00440
Chem. Rev. 2017, 117, 1564−1686

breaking process. However, this representation will yield small bond orders for 1−3 interactions, causing a bond order overestimation between the relevant atoms. A correction equation (see eq 166) is utilized for this situation to minimize the long-range bond orders, where Δ_i' is the deviation of the uncorrected bond order summation (see eq 167) from the valence state of an atom (e.g., carbon and hydrogen have valencies of four and one, respectively). An example of the bond order correction is shown in Figure 74.

$$E_{\text{bond}} = -D_e \times BO_{ij} \times e^{C_{b1}(1-BO_{ij}^{C_{b2}})} \tag{164}$$

$$BO_{ij}' = e^{p_\sigma (r_{ij}/r_0^\sigma)^{C_\sigma}} + e^{C_{\pi 1}(r_{ij}/r_0^\pi)^{C_{\pi 2}}} + e^{C_{\pi\pi 1}(r_{ij}/r_0^{\pi\pi})^{C_{\pi\pi 2}}} \tag{165}$$

$$BO_{ij} = f(BO_{ij}', \Delta_i', \Delta_j') \tag{166}$$

$$\Delta_i' = \sum_{j=1}^{\text{nbond}} BO_{ij}' - Val_j \tag{167}$$

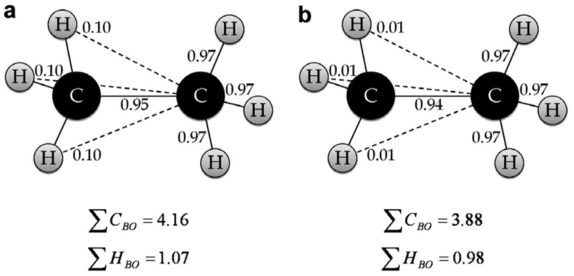

Figure 74. (a) Uncorrected bond orders for carbon and hydrogen within an ethane molecule. Carbon is overcoordinated due to second nearest neighbor interactions with hydrogen atoms. (b) Corrected bond orders. Weak interactions are negated due to carbon having its full bond order of 4. Reprinted with permission from ref 168. Copyright 2011 Elsevier.

The angle term in ReaxFF also depends on the bond orders (see eq 168) and diminishes smoothly as a bond involved in the angle breaks. A correction function $f(\Delta_j)$ may be applied to compensate for the effect of bond order overestimation/underestimation of the central atom j. Here, k_a, k_b, θ_o, and θ_{ijk} terms represent the depth, width, angle value, and equilibrium angle value for a given angle, respectively.

$$E_{\text{angle}} = f(BO_{ij}) \times f(BO_{jk}) \times f(\Delta_j) \times (k_a - k_a\, e^{-k_b(\theta_o - \theta_{ijk})^2}) \tag{168}$$

The dihedral term in ReaxFF is shown in eq 169. The first term reduces the dihedral interaction if the atoms forming the torsion angle are involved in a bond breaking process. When there are linear angles (180°) between atoms i, j, k, and/or atoms j, k, l, the two sine terms sets the i, j, k, l dihedral interaction to equal zero. The V_2 cosine term is related to the bond order of the central bond (j−k) and achieves a maximum when the bond order equals 2. The $f(\Delta_j, \Delta_k)$ indirectly corrects the overcoordination of atoms j and k.

$$E_{\text{dihedral}} = f(BO_{ij}, BO_{jk}, BO_{kl}) \times \sin\theta_{ijk} \times \sin\theta_{jkl} \times \left[\frac{1}{2}V_2 \times e^{C_l(BO_{jk}-3+f(\Delta_j,\Delta_k))^2} \times (1 - \cos 2\omega_{ijkl}) + \frac{1}{2}V_3 \times (1 + \cos 3\omega_{ijkl})\right] \tag{169}$$

To prevent energy jumps during bond formation/dissociation, there are nonbonded interactions between each atom pair (even for 1-2, 1-3 interactions) in ReaxFF. These equations are "shielded" to prevent unrealistic values at very short distances (see Figure 75). Electrostatic interactions are represented by a

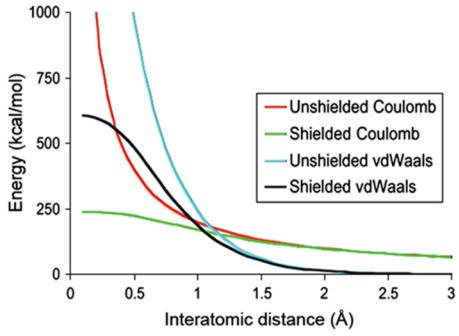

Figure 75. Plot of the Coulombic and VDW energies versus distance. A shielding term is applied to prevent these energies from becoming too large. Reprinted with permission from ref 168. Copyright 2011 Elsevier.

shielded Columbic term (see eq 170), and the VDW interaction uses a shielded Morse potential (see eqs 171 and 172). A FQ model (see eq 173) is used during the simulation, in which the electronegativity and chemical hardness parameters are optimized in the parametrization procedure. It was illustrated that the FQ model reproduced QM calculated

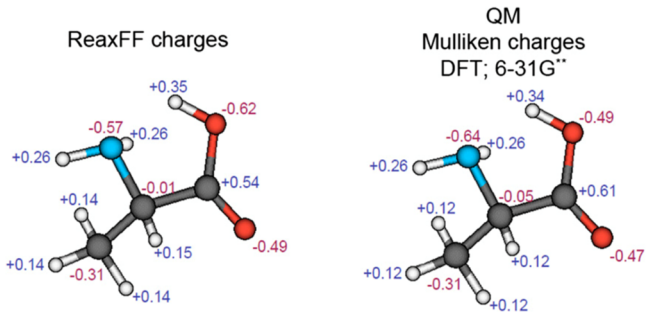

Figure 76. Comparison of the ReaxFF calculated charges versus QM values for the same molecule. The ReaxFF closely reproduces the Mullikan charges on each atom and models the polarizability of the molecule. Reprinted with permission from ref 168. Copyright 2011 Elsevier.

Mulliken charges (see Figure 76)[168] and the atomic charges are updated for each step during MD simulation.

$$E_{\text{ele}} = C \times \frac{q_i q_j}{\sqrt[3]{r_{ij}^3 + \left(\frac{1}{\gamma_{ij}}\right)^3}} \tag{170}$$

DOI: 10.1021/acs.chemrev.6b00440
Chem. Rev. 2017, 117, 1564−1686

$$E_{VDW} = D_{ij}\left\{e^{\alpha_{ij}(1-(f_s(r_{ij})/r_{VDW}))} - 2\,e^{[\frac{1}{2}\alpha_{ij}(1-(f_s(r_{ij})/r_{VDW}))]}\right\} \quad (171)$$

$$f_s = \sqrt[\frac{1}{C_{s1}}]{r_{ij}^{C_{s2}} + \left(\frac{1}{C_w}\right)^{C_{s1}}} \quad (172)$$

$$\frac{\partial E}{\partial q_n} = \chi_n + 2q_n\eta_n + C \times \sum_{j=1}^{n} \frac{q_j}{\sqrt[3]{r_{n,j}^3 + \left(\frac{1}{\gamma_{n,j}}\right)^3}}, \sum_{i=1}^{n} q_i = 0 \quad (173)$$

The ReaxFF force field is parametrized using the APM (see section 4.2.5) with the fitting being done against a variety of target properties from QM calculations. Different weights can be assigned to different data types during the parameter optimization process. Some recent works have been introduced to facilitate the parameter optimization of ReaxFF.[995−998] ReaxFF is not only able to simulate stable molecules but also relevant resonance structures, radical species, and reaction processes. ReaxFF is considerably faster than QM methods and can perform with good accuracy in carefully parametrized cases. For instance, the hydrocarbon reaction force field ($ReaxFF^{CH}$) offers an accuracy similar to that of the PM3 method, and is generally 100 times faster than PM3, which is itself ∼100 times faster than ab initio QM calculations.[987]

6.5.2. Examples. ReaxFFs have been developed for various metal-containing systems such as magnesium hydrides,[999] lithium-containing complexes,[1000] TM-catalyzed reactions,[994] platinum surfaces,[1001] gold,[993] vanadium oxide catalysts,[1002] zinc oxide,[1003] cobalt nanoparticles,[1004] etc. ReaxFF-based models have also been applied to biological systems including DNA[1005] and proteins.[1006] Three examples of ReaxFFs about modeling the TM related systems are summarized below.

Chenoweth et al. parametrized ReaxFF for the reactions of hydrocarbons catalyzed by vanadium oxide solids.[1002] 700 QM optimized structures and calculated energies were used to parametrize the reactive potential. These data points were related to bond dissociation processes, angle and dihedral distortions, energy changes of model reactions, bulk data on vanadium metals (BCC, FCC, A15, simple cubic, and diamond), and bulk data on vanadium oxides at different oxidation states. A MD simulation was carried out on a system consisting of a V_2O_5 slab (001) surface (containing 504 atoms), and 30 methanol molecules with a 0.25 fs time-step was used in the simulation. 250 ps of simulation was performed using a dual temperature thermostat algorithm (650 K for the slab to prevent it from melting and 2000 K for the methanol molecules). The resultant product distribution is shown in Figure 77. The simulation revealed CH_3OH molecules being converted to CH_2O molecules via two separate hydrogen absorption reactions by two surface V═O groups (with the CH_2OH radical as an intermediate species). Additional energy path scans indicated that the C−H dissociation path was preferred over O−H dissociation on the fully oxidized slab. Furthermore, water formation was observed during the simulation. Consistent with temperature-programmed desorption (TPD) experiments, the simulation results also supported interlayer bonding stabilization that facilitates water desorption at the vanadium oxide surface.

Nielson et al. investigated the branching process of carbon fragments catalyzed by metal atoms using a ReaxFF model.[994]

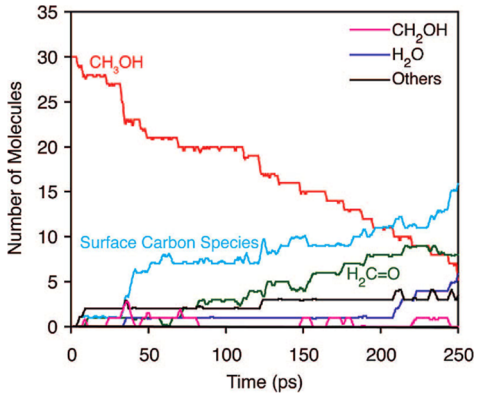

Figure 77. Product distribution observed during the NVT-MD simulation of CH_3OH exposed to V_2O_5 (001) using ReaxFF. Only major products are shown explicitly; minor intermediates are included as "others", and carbon-containing intermediates bound to the V_2O_5 surface are included as "surface carbon species". Reprinted with permission from ref 1002. Copyright 2008 American Chemical Society.

An E_{C2} term was added to the hydrogen carbon ReaxFF ($ReaxFF^{CH}$) to destabilize the C_2 radical. This is because the C−C bond in C_2 radical is weaker than a double bond, while $ReaxFF^{CH}$ makes this bond even stronger than a triple bond. A number of QM calculated structures and energies were used in the parametrization process. These data points were related to the ground and intermediate states of species relevant to the system being studied. A MD simulation was carried out with 0.1 fs time-step at 1500 K under the NVT ensemble. Five monocyclic C_{20} and 10 acyclic C_4 fragments were modeled in the system. No branching reactions were observed after 90 ps of simulation. Another three simulations were performed with each having 15 metal atoms added into the system (with 15 Co, Ni, and Cu atoms, respectively). To prevent metal clustering and facilitate metal carbon linkage, bond energies between the metal atoms were set to zero. As shown in Figure 78, considerable branching happens in the systems containing Co or Ni atoms, while the system containing Cu atoms showed less branching. This is consistent with experimental results. Figure 79 shows the structure of the system containing 15 Ni atoms after 750 ps of simulation, in which nanotude-like species were observed.

The CN of Cu^{2+} ion in aqueous solution has been the subject of some debate.[1007] The point of contention is whether the CN is equal to 5 or 6 in the first solvation shell of a Cu^{2+} ion. Moreover, the role of the Jahn−Teller effect is also an issue drawing attention. van Duin et al. parametrized ReaxFF for Cu/O/H mixed systems using a training set containing $Cu_x(OH)_y(H_2O)_z^{2-y}$ clusters, Cu, CuO, and Cu_2O crystals, along with various $Cu(H_2O)_5^{2+}$ and $Cu(H_2O)_6^{2+}$ structures.[1008] 133 ps of MD simulation was performed for a system containing one Cu^{2+} ion and 216 water molecules in the NVT ensemble at 300 K. It was shown that the ReaxFF model reproduced the Jahn−Teller effect in the first solvation shell. The dual-peak characteristic is clearly seen in the Cu−O RDF (see Figure 80). The ReaxFF simulation gave a 1.94 Å distance for the central copper to its equatorial oxygen and a 2.27 Å distance for the central copper to its axial oxygen. This agreed with available experimental data obtained from EXAFS and LAXS (distances of 1.95 and 2.29 Å, respectively). Meanwhile, the Jahn−Teller inversion rate was determined to be ∼5 ps

DOI: 10.1021/acs.chemrev.6b00440
Chem. Rev. 2017, 117, 1564−1686

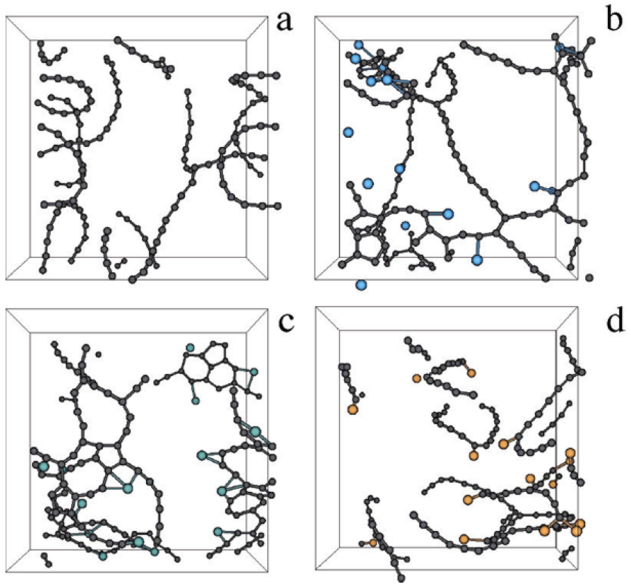

Figure 78. Configurations obtained after 90 ps of NVT-MD simulation using ReaxFF without metal (a) and with 15 Co (b), Ni (c), and Cu (d). Reprinted with permission from ref 994. Copyright 2005 American Chemical Society.

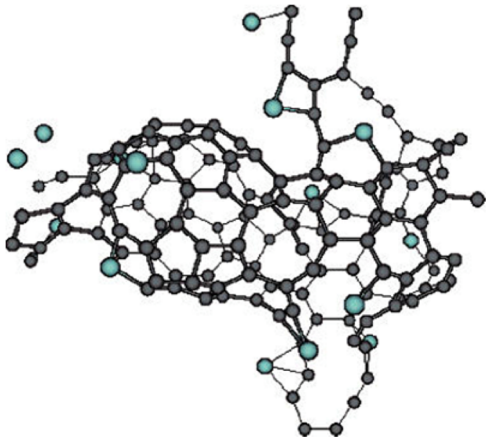

Figure 79. Configuration obtained from the NVT-MD simulation using ReaxFF with 15 Ni atoms after 750 ps. Reprinted with permission from ref 994. Copyright 2005 American Chemical Society.

from the ReaxFF simulation, which is in good agreement with the value of 5.1 ± 0.1 ps estimated from a ^{17}O NMR study. Additional simulations suggested that even with 6-coordination dominating, 5-coordinate structures do occasionally appear.

6.6. Advantages and Drawbacks: More Accurate but with More Parameters

It is reasonably well established that polarizable models afford better accuracy than unpolarized models, especially for metal-containing systems. One significant advantage of polarizable models is that they can accurately represent molecules in the gas, liquid, and interfacial phases due to their ability to respond to the surroundings. Unpolarized models, on the other hand, are typically designed for simulations in specific environments. However, the improvement of polarizable models over unpolarized ones is not always guaranteed and depends on parameter quality, which implies polarizable models still have room to improve. Because unpolarized models are usually designed for a single phase, only using them for simulations they were designed for can mitigate their disadvantages.

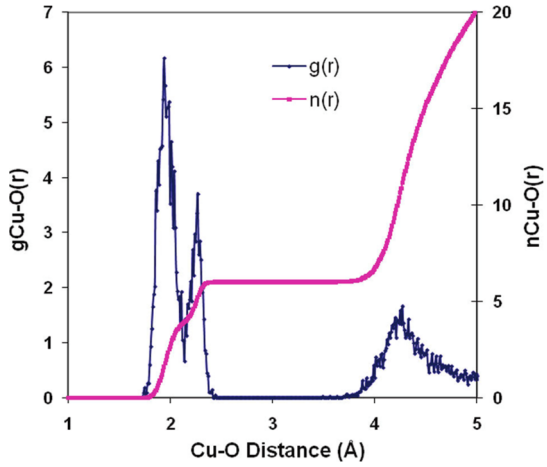

Figure 80. Cu−O RDF and integral as obtained from a ReaxFF MD simulation on a $[Cu(H_2O)_{216}]^{2+}$ system at T = 300 K. Reprinted with permission from ref 1008. Copyright 2010 American Chemical Society.

On the down side, polarizable models have more complicated parametrization schemes and usually require the determination of more parameters that add to their complexity. For polarizable models, the spectre of overfitting can rear its ugly head in complicated parametrization processes. Meanwhile, parameters in the polarizable models may afford limited transferability and reparametrization may be needed when applying to different systems. Furthermore, polarizable models also share some drawbacks with unpolarized models when modeling metal ions: for example, the balance of ion−water and ion−ion interactions in ionic solutions needs be considered to reproduce properties at high salt concentrations. Moreover, it is also hard to reproduce the Jahn−Teller effect using polarizable models (except for ReaxFF, which implicitly includes this effect). We have shown several examples in section 7.2 involving the incorporation of the AOM/VB approach into the AMOEBA force field and the LF model into the SIBFA approach. These examples all showed improvement in the representations of the Jahn−Teller effect.

7. MODELS BASED ON THE ANGULAR OVERLAP MODEL AND VALENCE BOND THEORY

The nonbonded and bonded models use atomic cores with charge and VDW interactions to represent each particle, while the polarizable models add the induction effect to the particle interactions. However, all of these models do not explicitly take the orbital effects into account and struggle to simulate the Jahn−Teller effect, which is related to the d-orbital splitting. The AOM,[1009,1010] a SE MO approach, and models based on the VB theory offer ways to effectively model the Jahn−Teller effect. These approaches are all based on the overlap between atomic/hybrid orbitals. Deeth and co-workers have developed and applied the LFMM approach,[1011] while Landis and co-workers have incorporated a Fourier angle term into the MM model to create the SHAPES force field.[197] The latter have also incorporated the VB theory into a force field (so-called the VALBOND model).[1012−1015] Xiang and Ponder have incorporated the AOM and VB approaches into the AMOEBA polarizable force field.[1016,1017] Piquemal et al. have merged the LFMM model into the SIBFA polarizable force field.[1018] These

DOI: 10.1021/acs.chemrev.6b00440
Chem. Rev. 2017, 117, 1564−1686

methods can model the Jahn−Teller effect, and offer more sophisticated approaches for ongoing and future force field development for TM complexes. In general, the AOM model is more suitable to systems with strong ionic characteristics, while the VB-based models can simulate systems with strong covalent effects. This is because the hybrid orbitals in the VB theory are based on covalent bonding, whereas the AOM-based models are atomic orbital based, which is more suitable for compounds that are more ionic. However, these models generally do not incorporate the electrostatic and polarization potential explicitly, which reduces their accuracy to represent long-range behavior (e.g., electrostatic, polarization) of metal centers. Electrostatic parameters can be incorporated to better account for long-range interactions, and they have a limited influence on geometric predictions but have a strong influence on energetic properties.[1019,1020] In what follows, we briefly review the approaches summarized above.

7.1. Applied to Unpolarized Models

7.1.1. LFMM Model. Deeth and co-workers described the LFMM (initially called CLFSE) model to incorporate the ligand field stabilization energy (LFSE) into the molecular modeling of TMs. Burton et al. created the Cellular LFSE (CLFSE)/MM model and applied it to Ni^{2+}- and Cu^{2+}-containing molecules.[1011] Its formulation is given in eq 174. It uses a Morse potential to represent bond stretching, and a 9-6 LJ potential for the nonbonded interactions (only for the 1-3 ligand−ligand interactions and between atoms separated by more than three bonds). Metal-containing angle and torsion interactions were assigned zero values. Electrostatic interactions were not included in the model. The CLFSE term was included in the total energy and was calculated on the basis of eq 175. Herein, $\varrho(d_i)$ is the occupation number (usually 0, 1, or 2), while $\varepsilon(d_i)$ is the d-orbital energies, which is obtained by diagonalization of the 5 × 5 d-orbital matrix (eq 176, where V_{LF} is the ligand field potential between d-orbitals i and j). Different spin states can be modeled by simply changing the occupancies of the d-orbitals. In the CLFSE model, each M−L interaction is divided into separate σ and π (including πx and πy) components, which are characterized by the e_σ, $e_{\pi x}$, and $e_{\pi y}$ energy parameters (count as different modes; see eq 176). The e_σ, $e_{\pi x}$, and $e_{\pi y}$ parameters are represented by eq 177, where $a_{n,k,ML}$ is the fitting parameter. The ligand field splitting energy (Δ_{oct}) is proportional to $1/r^5$, where r is the distance between the metal ion and its ligating atom. Because $\Delta_{oct} = 3e_\sigma$ for simple ligands with σ bonds to the metal ion (such as amines), e_σ should also be proportional to $1/r^5$. In their work, they only developed the e_σ parameter for Ni^{2+}/Cu^{2+} bound by a nitrogen atom. The e_σ parameter was represented by a linear equation (see eq 178) with r as the distance between the metal ion and its ligating atom.

$$E_{tot} = E_{bond} + E_{angle} + E_{torsion} + E_{VDW} + CLFSE \quad (174)$$

$$CLFSE = \sum_{i=1}^{n} \varrho(d_i)\varepsilon(d_i) \quad (175)$$

$$\langle d_i|V_{LF}|d_j\rangle = \sum_{l}^{cells} \sum_{k}^{modes} T_{ik}^{l*} T_{kj}^{l} e_k^{l} \quad (176)$$

$$e_k = \sum_{n=0}^{6} a_{n,k,ML} r_{ML}^{-n} \quad (177)$$

$$e_\sigma = 21629 - 8235r \ (cm^{-1}) \quad (178)$$

Results showed that CLFSE/MM model offered comparable or better results relative to conventional MM models. It effectively simulated the Jahn−Teller effect, and correctly reproduced geometries of Ni^{2+}−N and Cu^{2+}−N bonds regardless of the CNs, molecular geometries, and ligating ligand types used in their investigation.

The LFMM model can also be used to simulate Werner-type compounds (which are more ionic in character) that are affected by the Jahn−Teller effect (e.g., $[CuCl_4]^{2-}$)[1021] and complexes that have important contributions from bonds involving s orbitals (e.g., WH_6).[178] Covalent organometallic compounds WMe_6 and WH_6 have a d^0 electronic configuration but do not have octahedral geometries,[178] an effect that can be captured by VB-based method (summarized below) through inclusion of sd^n hybridization but can also be modeled by LFMM via inclusion of a stabilization energy term representing the contribution from the s orbitals.

Deeth et al. have implemented the LFMM model into the molecular operating environment (MOE) package in 2005, and, cleverly, called it DommiMOE (named after the Dommino program, which means "d-orbital in molecular mechanics for inorganics").[1022] Examples, combined with the MMFF94 force field, were shown in their work to validate the LFMM model. Results also showed that DFT calculations were useful in designing improved LFMM parameters.

Deeth has also applied the LFMM model to blue copper proteins.[1023] The AMBER ff94 force field was used to describe the organic ligands, while the Cu−S parameters for the LFMM model were fitted using DFT calculations. Results from cluster and protein calculations showed the good performance of the LFMM model (see Figures 81 and 82), allowing the authors to suggest that the LFMM method has "quantum-like" behavior and was ∼4 orders of magnitude faster than QM/MM calculations.

Deeth et al. designed Fe^{2+} complexes that have spin crossover and light-induced excited spin state-trapped properties.[1024] They employed the LFMM model combined with MD simulations. The parameters were fit to DFT calculated data, and the LFMM-based MD simulations reproduced the low-spin and high-spin states for complexes with the FeN_6 motif (see Figures 83 and 84). The method uses much less time than DFT calculations, but in the end offered similar accuracy.

More recently, Foscato et al. implemented the LFMM into the Tinker MM package.[1025] It was shown that LFMM could deal with both the static calculations and the dynamic simulations.

7.1.2. SHAPES Force Field. Allured et al. described the SHAPES force field in 1991.[197] It uses a single Fourier term (see eq 179) instead of the harmonic equation to represent the angle bending interaction.

$$E_{angle} = k^F[1 + \cos(n\phi + \varphi)] \quad (179)$$

Similar to the Fourier term for a dihedral angle, n is the periodicity, φ is the phase, and k^F is the energy minimum. It was shown the Fourier term allowed energy changes both close to and far from typical equilibrium bond angles. Figure 85 shows the PES for the HOH angle obtained from HF calculations, a normal harmonic potential, and the Fourier angle potential. From this figure, we see that the Fourier angle potential better matches the results from QM-based methods than does the standard harmonic potential. The parameters for

DOI: 10.1021/acs.chemrev.6b00440
Chem. Rev. 2017, 117, 1564−1686

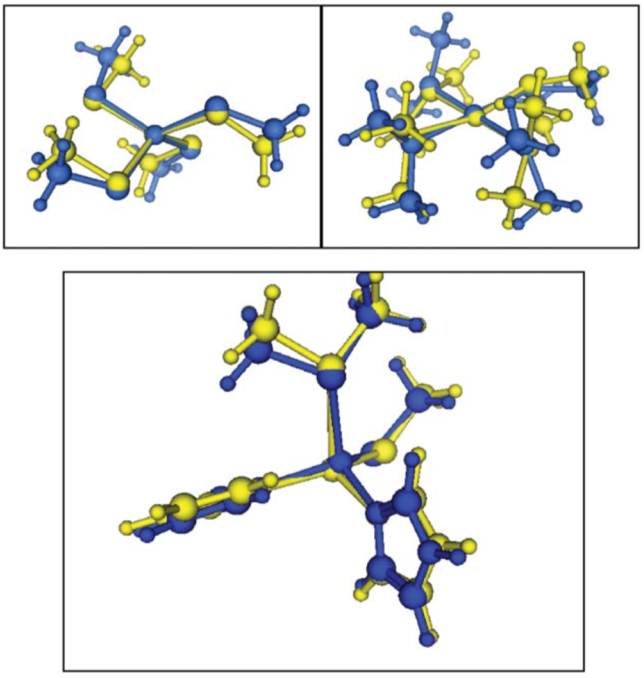

Figure 81. Overlay of LFMM (yellow) and DFT (blue) structures: top left, $[Cu(SMe)_4]^{2-}$, top right, $[Cu(SMe_2)_4]^{2+}$, and bottom, the Type I active site model $[Cu(im)_2(SMe)(SMe_2)]^{+}$. Reprinted with permission from ref 1023. Copyright 2006 Royal Society of Chemistry.

the Fourier angle potential can be calculated from parameters in a harmonic potential using the following equations:

$$n = \frac{\pi}{\pi - n\phi_0} \tag{180}$$

$$\varphi = \pi - n\phi_0 \tag{181}$$

$$k^{\mathrm{F}} = \frac{2k^{\mathrm{H}}}{n^2} \tag{182}$$

Moreover, the Fourier representation is consistent with the AOM (see the appendix from their work).[197] The geometry representation in SHAPES is based on spherical internal coordinates. As in many standard force fields, the bond term in the SHAPES force field is harmonic, the torsion term uses Fourier expansions, and the 12-6 LJ equation was used to represent the VDW interactions. Electrostatic interactions were not considered in the parametrization process, which was based on normal coordinate analysis and PES scans based on QM calculations. It was shown that the so-derived force field reproduced the molecular structures of different square-planar Rh complexes to good accuracy (RMSDs of bond lengths ±0.02 Å and of angles ±3°). Tests including electrostatic interactions based on the QEq formulation from Rappe et al.[868] demonstrated that inclusion of the electrostatic interactions had a trivial influence on structure prediction, implying that the derived parameters could be transferred to models including charge interactions. Using force constants based on normal coordinate analysis, they observed that the force constants inside ligands decreased when ligated to a metal ion. For example, k_b for the N−H bond decreases from 460 for a free ammonia to 410 kcal/mol·Å^{-2} for a coordinated ammonia, along with the k_θ for the H−N−H angle decreases from 44 to 40 kcal/mol·rad^{-2}. However, in later work, Cleveland and

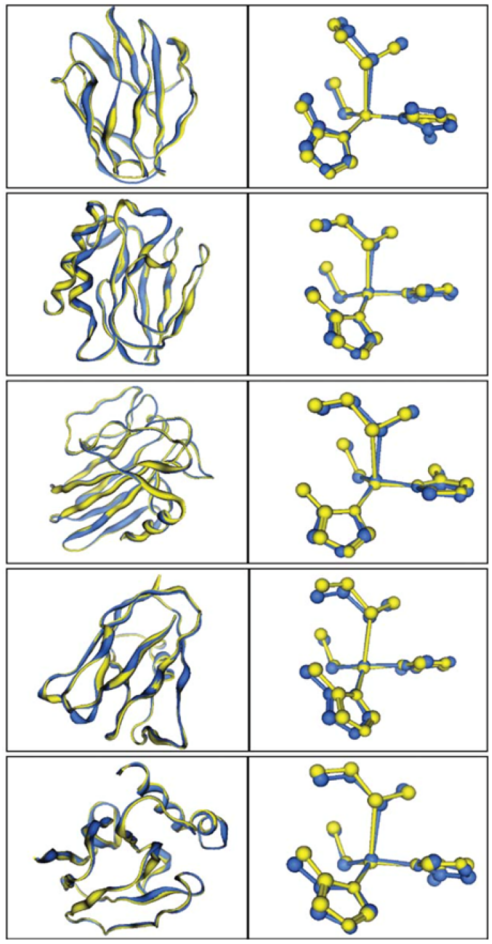

Figure 82. Overlay of XRD (yellow) and LFMM (blue) structures. Figures on the left show the superposition of the protein backbones, while those on the right show the optimal overlay of the trigonal [CuNNS] set. The proteins are given in the same order as Table 1 of ref 1023. Reprinted with permission from ref 1023. Copyright 2006 Royal Society of Chemistry.

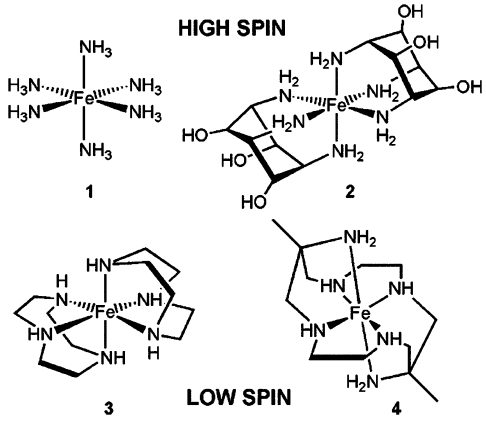

Figure 83. Schematic diagrams of Fe^{2+} am(m)ine complexes. In the solid state, 1 and 2 are high-spin while 3 and 4 are low-spin. Reprinted with permission from ref 1024. Copyright 2010 American Chemical Society.

Landis reported that the angular representation used in the SHAPES force field makes the bipyramidal geometry too rigid with respect to distortion to the square pyramidal geometry.[1013]

DOI: 10.1021/acs.chemrev.6b00440
Chem. Rev. 2017, 117, 1564−1686

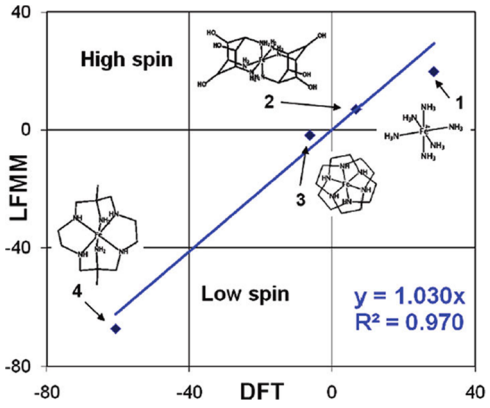

Figure 84. Comparison of theoretical spin-state energy differences (kJ/mol) for complexes 1−4. Reprinted with permission from ref 1024. Copyright 2010 American Chemical Society.

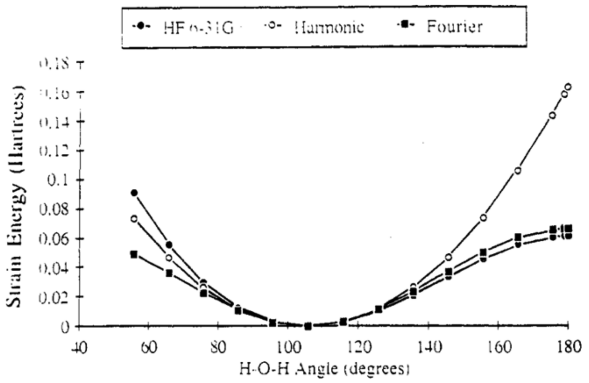

Figure 85. Comparison of PESs for angular distortion of water calculated by (●) the RHF method with a 6-31G* basis set, (○) a harmonic force field (k = 0.191 hartree/rad^2, θ_{eq} = 105.5°), and (■) a Fourier term (k^F = 0.0652 hartree, n = 2.42, φ = 74.50°). Reprinted with permission from ref 197. Copyright 1991 American Chemical Society.

Doman et al. created force field models for linear metallocenes [M(Cp)$_2$] (where Cp = cyclopentadienyl) for a series of TMs, where almost all of the force constants were obtained on the basis of experimental data.[1020] Fourier terms were used for the angles that have the metal ion as their center atom, while harmonic terms were used for the other angles. To model these sandwich compounds, dummy atoms were placed in the centers of the five-member rings of the Cp groups and then bound to the central metal ion. A dihedral term was used to model the 1-5 interaction between the Cp carbon-dummy-metal-dummy-Cp carbon, which represents the rotation along the ligand metal axis (see Figure 86). The Columbic equation was used with a distance-dependent dielectric constant, and atomic charges were determined on the basis of the FQ method and updated every 50 steps in the energy minimization. It was shown that inclusion of electrostatic interactions caused limited impact on the molecular geometry but exerted considerable influence on the molecular energy. The derived force field reproduced the geometries of the metallocenes, even for those highly strained examples.

7.1.3. Valence Bond-Based Models. Root et al. have developed the so-called VALBOND force field using concepts from the VB theory.[1012] They note that the conceptual foundation of MM aligns better with the localized bonds between hybrid orbitals (a perspective of VB theory) than it does with the delocalized LCAO picture from MO theory. The VALBOND model has an angular term based on the hybrid orbital strength function (see eqs 183−186). In these equations, α and Δ are the angle and overlap integral between two sp^{m}d^n hybrid orbitals, respectively. Functions of generalized strength $S(\alpha)$ and maximum possible strength S^{max} are shown in eqs 184 and 185, respectively. The final energy is determined on the basis of the pair defect approximation (PDA, see eq 183) where k is a scaling parameter.

$$E_{angle} = \sum_{i}^{\text{all ligands}} \sum_{j \neq i} k_i (S_i^{max} - S_i(\alpha_{ij})) \tag{183}$$

$$S(\alpha) = S^{max} \sqrt{1 - \frac{1 - \sqrt{1 - \Delta^2}}{2}} \tag{184}$$

$$S^{max} = \sqrt{\frac{1}{1 + m + n}} (1 + \sqrt{3m} + \sqrt{5n}) \tag{185}$$

$$\Delta = \frac{1}{1 + m + n} \left(1s + m \cos \alpha p_z + \frac{n}{2} (3 \cos^2 \alpha - 1)\, dz^2 \right) \tag{186}$$

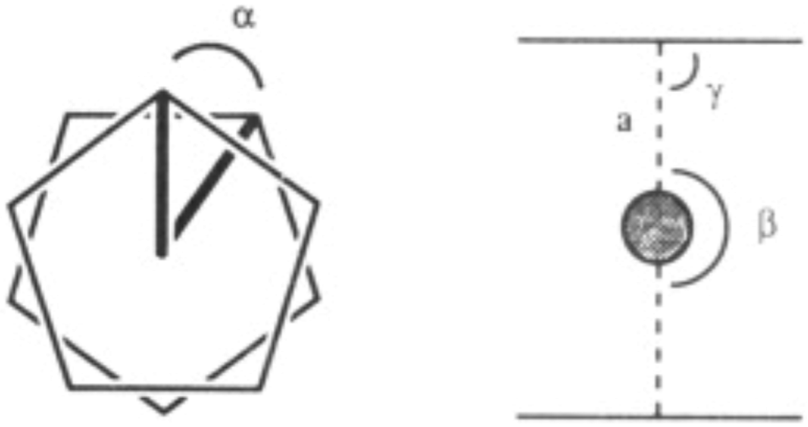

Figure 86. Representation of the skeletal modes of a linear metallocene. The Cp rings are represented by horizontal lines and the metal by a dark circle. The 1,5-dihedral angle, α, the M−D stretch, a, the D−M−D, β, and the C−D−M bend, γ, are shown. Reprinted with permission from ref 1020. Copyright 1992 American Chemical Society.

DOI: 10.1021/acs.chemrev.6b00440
Chem. Rev. 2017, 117, 1564−1686

Using sp^3 hybrid orbitals as an example, the value of $S^{max} = 2$ is obtained using eq 185, and $\Delta = \frac{1}{4}(1 + 3\cos\alpha)$ is derived using eq 186. When $\alpha = 109.5°$, $\Delta = 0.0$, which means the two orbitals are orthogonal, and $S(\alpha)$ equals S^{max}, yielding an E_{angle} (see eq 183) value of zero. The strength functions for sp^3, sp^2, sp^1, and pure p orbitals are shown in Figure 87.

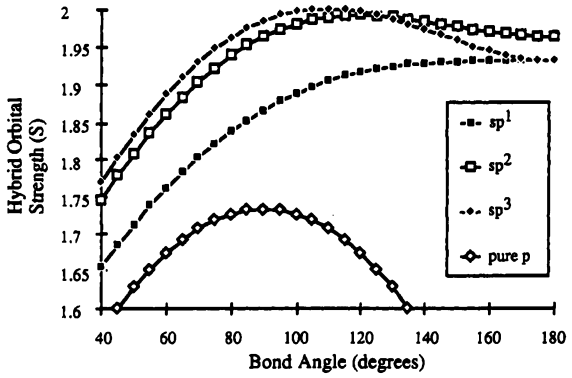

Figure 87. Strength functions for sp^3, sp^2, sp^1, and pure p orbitals. Reprinted with permission from ref 1012. Copyright 1993 American Chemical Society.

The only parameters that need to be determined in this formulation are the scaling parameter k and the hybridization of each bond orbital. They used simple Lewis structures and a quantitative representation of Bent's rule to determine the hybridization of an individual bond. In the VALBOND representation, there are weighting factors for each combination of elements, and these weighting factors were determined on the basis of several rules. Rather than delineate them, herein we refer the reader to the original literature for full details.[1012] The scaling parameters were determined such that experimental vibration frequencies were accurately reproduced, and via this process it was shown that the scaling parameters did not significantly vary. A value of ~163 kcal/mol for bonds containing hydrogen atoms and ~220 kcal/mol for the other bonds afforded a good estimation. Overall, it was shown that the VALBOND force field reproduced molecular geometries and vibrational frequencies to good accuracy with a small number of parameters.

The VB model can handle situations involving delocalized bonding arrangements, like that seen in 3-center-4-electron (3c4e) bonds, which are observed in hypervalent (HV) molecules. Modeling HV molecules is a challenge for traditional MM models. Cleveland and Landis extended the VALBOND force field to handle HV compounds involving p-block elements.[1013] Through the incorporation of resonance structures representing 3c4e bonds into VALBOND, these authors showed that it was possible to model HV molecules. To accomplish this, they added eq 187 to the VALBOND formulation to represent the 3c4e bond. In this equation, BOF stands for the bond order factor, and α and Δ are the bond angle and overlap integral between two interacting orbitals (e.g., for the F−Xe−F molecule, the two orbitals are the σ^* hybrid orbital of $[Xe-F]^+$ and the lone pair of F^-, respectively). This strength function favors the linear configuration: when $\alpha = 180°$, $\alpha + \pi = 360°$, making the overlap integral $\Delta = 0$, yielding a minimum value for $E(\alpha)$. k_α is a scaling parameter and was set to 260 kcal/mol in their work. The bond, dihedral, improper torsion, and VDW terms were all taken from the CHARMM force field.

$$E(\alpha) = BOF \times k_\alpha[1 - \Delta(\alpha + \pi)^2] \tag{187}$$

To model more complicated systems, such as ClF_3, which has both 2-center-3-electron (2c3e) and 3c4e bonds, different resonance configurations need to be considered. As shown in eqs 188 and 189, the total angle bending energy is represented by a mixture of energies of different resonance structures. Herein, c_n means the mixing coefficients, which are geometry dependent and determined on the basis of the HV angles inside each resonance configuration (see eq 189).

$$E_{angle} = \sum_n c_n E_n \tag{188}$$

$$c_j = \frac{\prod_{i=1}^{hype} \cos^2\theta_i}{\sum_{j=1}^{res\ config} \prod_{i=1}^{hype} \cos^2\theta_i} \tag{189}$$

An offset term was added for the nonhomoleptic HV molecules, and it is related to the electronegativities of the ligands in the 3c4e bond (see eqs 190 and 191).

$$E_{offset} = \sum_{i=1}^{config} c_j \sum_{j=1}^{hype} \frac{EN_{ija} + EN_{ijb}}{2} \tag{190}$$

$$EN_{ija} = 30 \times (en_{lig} - en_{c.a.}) \times ss \tag{191}$$

Herein, a and b represent two different atoms in the HV angle j of the ith MM configuration. en_{lig} and $en_{c.a.}$ are the electronegativities of the ligand and the central atom, respectively, while ss is a scaling factor. ss is 1 when the electronegativity difference is positive and is 2 when the difference is negative. This offset representation gives a lower energy when the electronegativity of the ligand is larger than the central atom, and a higher energy in the converse. Results showed this HV-VB scheme reproduced the PESs, geometries, vibrational frequencies, site-preference, and fluxional pathways and was able to manifest ligand site exchange processes.

Landis et al. extended the VALBOND force field to metal alkyls and hydrides.[1014] They used the 12-electron rule (based on sd^n hybridization) instead of the 18-electron rule to determine the hyper-valency of the TM complexes. This model can represent different configurations (such as square-planar, trigonal planar, octahedral) of TM complexes. It uses eq 192 to determine the mixing coefficients. This is because, while eq 189 is good for modeling sp^n hybridized orbitals, it is less suitable for orbitals with more than 67% d-character. The scaling factors (k, in eq 183) for some TMs were parametrized on the basis of QM calculated frequencies for their hydrides. On the basis of these values, the scaling factors for the other TMs investigated were determined through interpolation/extrapolation.

$$c_j = \frac{\prod_{i=1}^{hype} \Delta_i^2}{\sum_{j=1}^{res\ config} \prod_{i=1}^{hype} \Delta_i^2} \tag{192}$$

Finally, it was shown that VALBOND reproduced the angles of 36 TM complexes with an average RMSD of less than 5°.

Firman and Landis extended VALBOND to TM complexes involving π-bonds.[1015] When modeling π bonds in TM complexes, the VALBOND formulation becomes more complicated due to the incorporation $\sigma-\pi$ and $\pi-\pi$ bond

DOI: 10.1021/acs.chemrev.6b00440
Chem. Rev. 2017, 117, 1564−1686

pairs. Equation 193 calculates the torsion energy between a metal dπ orbital and a ligand dπ orbital (see Figure 88), where

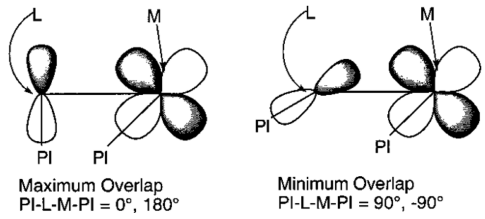

Figure 88. Scheme of π-bonding p−d atomic orbitals in the VALBOND model. Reprinted with permission from ref 1015. Copyright 2001 American Chemical Society.

ϕ is the torsion angle of PI−M−L−PI, with M, L, and PI represent the metal, ligand, and π-pseudoatom, respectively, r_m is 1.67 (whose value was empirically derived) times the distance between the two central atoms, and $bo2$ is the bond order of the M−L bond, whose value is 2 or 3. $e_{t\pi}$ is set to 260 kcal/mol, which was also empirically derived.

$$E_{t\pi} = -e_{t\pi} \times \cos^2\phi \times e^{-2r_m} \times\{1 + 2r_m[1 + 0.3r_m(1 + 0.3r_m)]\} \times [2 \times (bo2 - 1)] \quad (193)$$

To evaluate the bonds formed by the dπ orbital of a metal and a sd^n σ-hybrid orbital from a ligand, the equation given in Figure 89 is used. It is based on the consideration that a cloverleaf-shaped orbital can be represented by a linear combination of two d_{z^2}-shape orbitals (see Figure 90).

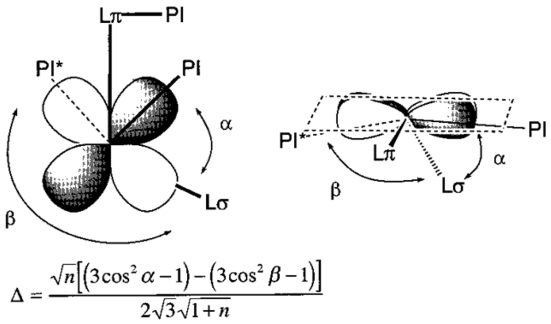

$$\Delta = \frac{\sqrt{n}\left[\left(3\cos^2\alpha - 1\right) - \left(3\cos^2\beta - 1\right)\right]}{2\sqrt{3}\sqrt{1+n}} \quad (6)$$

Figure 89. Overlap representation between a dπ orbital (left) and a σ bond with sd^n hybridization (right). Reprinted with permission from ref 1015. Copyright 2001 American Chemical Society.

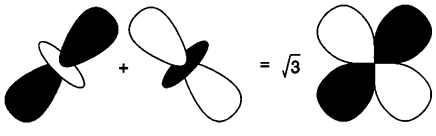

Figure 90. Representation of a cloverleaf shaped orbital by two d_{z2} shaped orbitals. Reprinted with permission from ref 1015. Copyright 2001 American Chemical Society.

The dπ−dπ overlap between two cloverleaf shaped orbitals was determined using:

$$\Delta = \{[(3\cos^2\alpha - 1) - (3\cos^2\beta - 1)] - [(3\cos^2\chi - 1) - (3\cos^2\delta - 1)]\}/6 \quad (194)$$

where the details for the α, β, χ, and δ terms can be found in the original article.[1015] In their work, a slightly modified formulation of the VALBOND force field was used. The new formulation gave the same results for homoleptic complexes and offered advantages when modeling nonhomoleptic complexes. Results reported by these authors show that the VALBOND force field can predict molecular structures for a number of TM complexes with metal−ligand multiple bonds.

To model situations where there is a trans influence, Tubert-Brohman et al. created the VALBOND-TRANS force field for octahedral complexes containing Ru, Os, Rh, and Ir.[1026] The trans influence (that is different from the trans effect, which is related to the substitution reaction rate[1027]) is a phenomenon affecting the electronic ground state of a complex where a ligand has the tendency to weaken the bond trans to it.[1028] It causes bond lengthening and can affect the relative stabilities of different diastereomers. It can be explained by a 3c4e bond formed between the metal ion and its ligands in which a "stronger" ligand prefers to bond in a trans orientation to a weaker ligand. They proposed eq 195 to model the energy changes due to the trans influence, which is based on the consideration that the trans influence is maximized at 180°.

$$E_{trans} = \sum_{i=1}^{hype} p_{AB}\Delta(\alpha + \pi)^2 \quad (195)$$

$$r_{A(B)} = r_A^0\left(1 + \frac{s_A \times \Delta(\alpha + \pi)^2 \times i_B}{100}\right) \quad (196)$$

Herein, p_{AB} is an adjustable parameter, which is related to the metal and ligand types. The harmonic equation was used for the bond stretching term, while the equilibrium bond distance was determined from eq 196, which represents bond length changes associated with the trans influence. Herein, i_B and s_A indicate the "trans influence intensity" and "lengthening sensitivity", respectively. The authors obtained parameters in eqs 195 and 196 for octahedral complexes containing Ru, Os, Rh, or Ir based on DFT calculated isomeric energies and optimized structures. Test calculations were carried out on two larger octahedral Ir complexes, and the obtained results showed that the VALBOND-TRANS force field was able to reproduce the DFT calculated isomeric energies and geometries, outperforming the VALBOND force field for the cases studied.

Recently, Jin et al. studied Cu oxidation/reduction in water and protein systems through MD simulations using the DFTB3/MM and VALBOND methods.[1029] DFTB3 is a SE QM method, which is able to study chemical reactions, while the VALBOND method is a fast MM method that can study structural properties but needs parametrization for specific oxidation states and coordination environments of the Cu ion. Both methods covered the nanosecond time scale during the MD simulations, and are more efficient than the QM/MM MD simulations based on ab initio or DFT methods. They found that DFTB3/MM and VALBOND all capture the coexistence of the five- and six-coordinated structures of Cu^{2+} in water, which is consistent with experiment. However, subtle differences exist between different approaches: the hybrid-DFT/MM, DFTB3/MM, and VALBOND methods favor a six-coordinated Cu^{2+} ion in water, as compared to that the five-coordinated structure is favored by the nonhybrid BLYP functional and experiment. MD simulations based on DFTB3/MM, the BLYP functional, and HSE functional support a two-coordinated Cu^{+} in water, while B3LYP/MM predicts a four-

DOI: 10.1021/acs.chemrev.6b00440
Chem. Rev. 2017, 117, 1564−1686

coordinated Cu^+ ion. They proposed that these subtle properties are worth further investigation by experiment and computation. These authors also showed that the DFTB3/MM and VALBOND methods performed well in simulating the $[Cu(NH_3)_4]^+$ and $[Cu(NH_3)_4]^{2+}$ complexes in aqueous solution. Furthermore, the DFTB3/MM method well simulated the active site of plastocyanin (where the Cu ion is coordinated to two His, one Cys, and one Met residue), and its predicted reduction potential and reorganization energy agreed with experiment. Meanwhile, the authors proposed that improved description of the charged species in DFTB3 was important for better modeling the Cu^+ ion in DFTB3/MM simulations.

7.2. Applied to Polarizable Models

7.2.1. SIBFA-LF Model. Piquemal et al. incorporated the ligand field (LF) effect based on the AOM model into SIBFA in 2003.[1018] The SIBFA-LF model was parametrized to model systems containing Cu^{2+}−O and Cu^{2+}−N bonds. It was found that the SIBFA-LF approach reproduced the Jahn−Teller effect, giving an improved geometric prediction when compared to the SIBFA approach. For example, the SIBFA-LF method predicts the elongated octahedral geometry of the $Cu^{2+}-(H_2O)_6$ complex with the axial and equatorial Cu−O distances at 2.17 and 1.99 Å, respectively. In comparison, SIBFA predicts the $Cu^{2+}-(H_2O)_6$ complex as octahedral with the six Cu−O distances all equal to 2.06 Å. As shown in Figure 91, the SIBFA

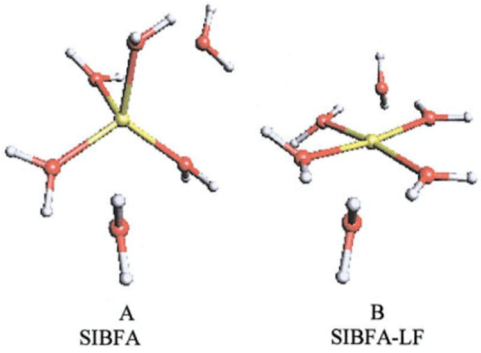

Figure 91. Minimized structure of $Cu^{2+}(H_2O)_4(H_2O)_2$ based on the SIBFA (panel A) and SIBFA-LF (panel B) models. Reprinted with permission from ref 1018. Copyright 2003 John Wiley and Sons.

model predicts that the inner four water molecules in $Cu^{2+}(H_2O)_4(H_2O)_2$ are tetrahedrally coordinated, while SIBFA-LF predicts them to be planar. The SIBFA-LF correctly predicts the quasi-planar D2d geometry for Cu^{2+} coordinated with four NH_3 groups, or four imidazole (ImH) groups (see Figure 92 for the latter case), while SIBFA predicts a tetrahedral geometry.

7.2.2. AMOEBA-VB and AMOEBA-AOM Models. Xiang and Ponder incorporated the VB model into the AMOEBA force field for the Zn^{2+} and Cu^{2+} ions in aqueous solution.[1017] The following representation was used:

$$U_{total} = U_{AMOEBA} + U_{VB} \quad (197)$$

$$U_{VB} = \sum_{k}^{resonance} W_k U_{resonance,k} = \sum_{k}^{angles} W_k (U_{VB\text{-}bond,k} + U_{VB\text{-}angle,k}) \quad (198)$$

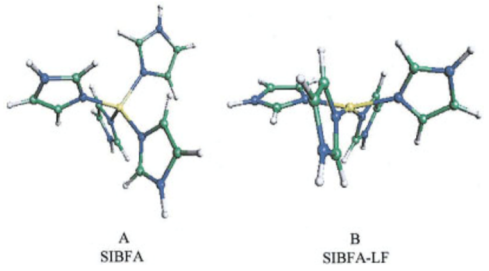

Figure 92. Minimized structure of $Cu^{2+}(ImH)_4$ based on the SIBFA (panel A) and SIBFA-LF (panel B) models. Reprinted with permission from ref 1018. Copyright 2003 John Wiley and Sons.

where the $U_{resonance}$ term represents the 3c4e bond, and the resonance structure number is equal to the number of O−M−O angles in the $M^{2+}(H2O)_6$ complex. Here, W_k is the weighting factor for different resonance structures and is calculated on the basis of an empirical function. The $U_{VB\text{-}angle}$ term is represented by the hybridization of the s, p, and d orbitals. The authors used an admixture of 10% s and 90% d to represent the bond formation between Cu^{2+} and its surrounding water molecules, while for Zn^{2+} 100% s orbital character was used. As shown in Figure 93, the VB angular potential for Cu^{2+} gives two energy

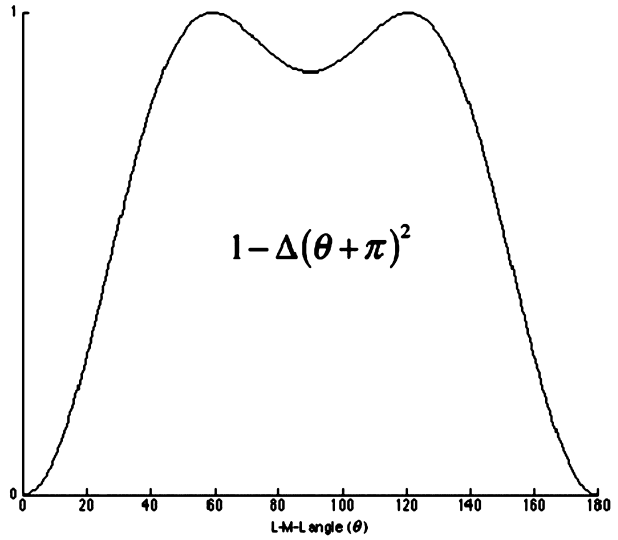

Figure 93. Schematic plot of VB angular potential for each 3c4e bond based on 10% s and 90% d hybridization. Reprinted with permission from ref 1017. Copyright 2012 John Wiley and Sons.

minima at 90° and 180°, which agreed with a previous AOM model from Carlsson.[1030] The parameters were fit on the basis of QM calculations on $M(H_2O)_4^{2+}$ and $M(H_2O)_6^{2+}$ systems. Addition of the Jahn−Teller stabilization energy function from Comba and Zimmer[1031] (see eqs 199 and 200, which are first-order harmonic equations, where r, r_0, Δ are the metal-ligand distance, average bonding distance, and a scaling parameter, respectively, with E_{JT}^{xy} applied to the in-plane ligands, and E_{JT}^{z} applied to the axial ligands) further improved the AMOEBA-VB model. However, this representation did not offer smooth transitions for axial−equatorial ligand interchange or coordination number changing, and therefore was not used in the subsequent MD simulation. Even with these modifications, the AMOEBA-VB model does not reproduce the dual peak in the first solvation shell of the Cu^{2+} ion during the aqueous phase

DOI: 10.1021/acs.chemrev.6b00440
Chem. Rev. 2017, 117, 1564−1686

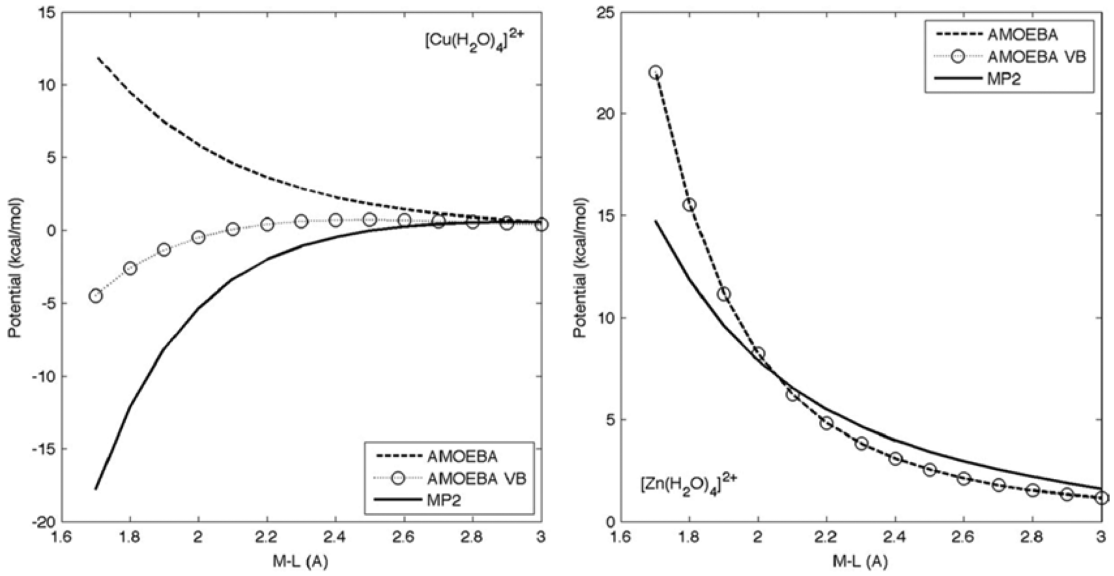

Figure 94. Energy difference between square-planar (sq) and tetrahedral (te) tetra-aqua TM complexes; energy calculated by (U_{sq} − U_{sq}/empty) − (U_{te} − U_{te}/empty); data points from AMOEBA and AMOEBA-VB methods for $[Zn(H_2O)_4]^{2+}$ overlap each other, as the differences in results are very small; see Tables 3 and 4 in the Supporting Information of ref 1017 for numerical values. U_{sq}/empty means system energy without considering the central ion. Reprinted with permission from ref 1017. Copyright 2012 John Wiley and Sons.

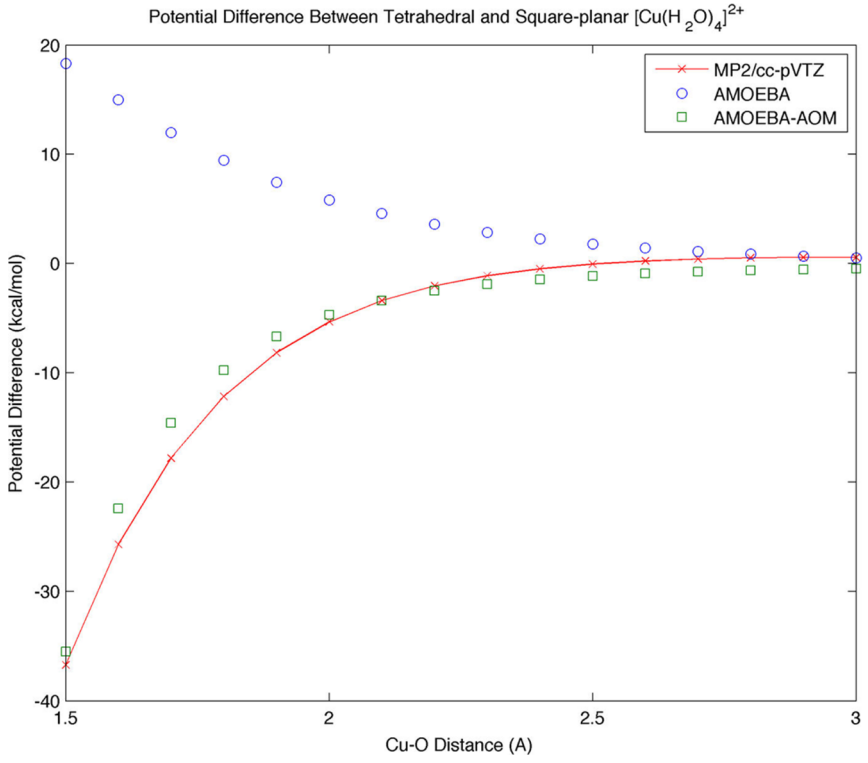

Figure 95. Potential energy difference between square-planar and tetrahedral tetra-aqua Cu^{2+} complexes with the water−water interaction removed. Negative values indicate that the square-planar structure is lower in potential energy than the tetrahedral geometry. Reprinted with permission from ref 1016. Copyright 2014 American Chemical Society.

MD simulation, and does not reproduce the two different bond lengths (elongation of the axial bond lengths) of the $Cu(H_2O)_6^{2+}$ complex, but AMOEBA-VB predicts the square planar structure of the $Cu(H_2O)_4^{2+}$ complex to be more stable than the tetrahedral one, offering an improved description over the AMOEBA model (see Figure 94). Meanwhile, their work showed that AMOEBA-VB gave results similar to those of the AMOEBA model for systems containing Zn^{2+}.

$$E_{JT}^{xy} = -(r - r_0)\Delta/r_0 \quad (199)$$

$$E_{JT}^{z} = -2(r - r_0)\Delta/r_0 \quad (200)$$

These authors have also incorporated the ligand field effect using the AOM for the Cu^{2+} ion in the AMOEBA force field.[1016] In their work, they used MP2 calculated results as their benchmark data, because the DFT functionals, B3LYP and

DOI: 10.1021/acs.chemrev.6b00440
Chem. Rev. 2017, 117, 1564−1686

B2PLYP-D, gave divergent results. Similar to the AMOEBA-VB model described above, the AMOEBA-AOM model also effectively simulated the square-planar structure of the $Cu(H_2O)_4^{2+}$ complex, giving it a lower energy than the tetrahedral one, while standard AMOEBA could not reproduce this effect (see Figure 95). The Jahn−Teller effect was well reproduced using this model in the gas phase for the $Cu(H_2O)_6^{2+}$ complex, but in the aqueous phase this was not apparent because the dual peak was not observed in the Cu−O RDF in aqueous solution. The AMOBEA-AOM model predicted that the mean residence time of the first solvation shell water molecules for Cu^{2+} was 0.6−1.8 ns at room temperature, which was in accord with available experimental data (~5 ns). In general, the AMOEBA-AOM force field was shown to outperform AMOEBA, when compared to QM calculated results. However, it elongates the Cu^{2+}−S distance between the metal ion and Met group and could not well reproduce the sulfur ligand binding energies. The authors also proposed that AMOEBA-AOM might not be suitable for simulating system with strong covalent interactions, while the AMOEBA-VB model would be more appropriate.

8. CONCLUSIONS AND PERSPECTIVES

8.1. Conclusions

There are a broad range of options to model metal ion-containing systems. However, for the uninitiated, the range of choices can be truly bewildering. The best way to proceed depends on a number of factors coupled with what exactly someone is trying to accomplish. To address this issue, we attempt to simplify the structure of the extensive discussion present in this Review by summarizing our suggestions for modeling TM-containing systems using QM and MM models. These suggestions are only meant to help initiate a study on metal ion-containing systems, and the reader is urged to review the sections most appropriate to their choice of model to understand their strengths and weaknesses and range of applicability in more detail. It is easy to go astray when modeling metal ions (even for so-called "experts"), so caveat emptor!

8.1.1. Quantum Mechanical Methods. Generally, the main group metal elements and Zn (it is easy to model zinc complexes as normal organic molecules) are well represented using DFT and post-HF methods with large basis sets. However, it is really challenging to model TMs, especially the middle series, in the periodic table due to their various spin states. Overall, the HF method is not suggested to use to study TM-containing systems due to the use of a single-determinant and omission of correlation effects. Care should be taken when one uses semiempirical methods to study such systems due to their minimal basis set. Moreover, attention should also be paid when using post-HF methods (e.g., MP2, CCSD, and CCSD(T) methods) to model TM species again because of their use of a single-determinant. Multiple reference methods such as CASSCF offer significant improvement in describing multireference systems like many TM species but are not practical for the study of large systems due to their extraordinary computational needs. Meanwhile, the DMRG method is a promising approach to model TM-containing systems with strong multireference characteristics.

The ccCA composite approach is recommended to obtain reference energy properties (e.g., HOFs) for TM species. DFT methods with their high computational speed could be very good choices to computationally study TM-containing systems. However, a large number of DFT functionals are available, and attention should be paid to choosing the appropriate one. In general, for pure metal systems, the functionals that approach the noble gas limit are recommended, while for multireference systems nonhybrid functionals are the best choice. For TM complexes containing organic ligands, the hybrid functionals may offer some improvements. However, the hybrid functionals with more than 40% HF exchange energy are not recommended. In terms of basis set choices, the basis sets of the ligands play a larger role than the basis set of the metal ions. All electron basis sets are recommended for the ligands, while effective core potentials can be used on the TMs. This is because the effective core potential considers the relativistic effect (which can be large for heavy metal elements) to some extent at a reduced computational cost. However, we note that the optimal basis set is also dependent on the DFT functional choice.

8.1.2. Force Field Models. For ions that have strong ionic characteristics (e.g., Na^+, K^+, F^-, Cl^-, Mg^{2+}, Ca^{2+}), the electrostatic term dominates its interaction with surrounding ligands. A nonbonded approach including electrostatic and VDW interactions is recommended for these situations, while charge scaling may be needed to better reproduce structural and dynamic properties in high salt concentrations. There are several classifications for nonbonded models: (1) The widely used 12-6 nonbonded model offers generally excellent results for the alkali metal ions except Li^+. This is because the partial charges on these ions are close to the formal charge (+1e), making a point charge model an appropriate representation. (2) The 12-6-4, CDAM, DO, IDM, and LFMM models are suggested for use for the remaining monovalent ions as well as with divalent ions. This is because the 12-6 nonbonded model fails to describe the non-negligible polarization and CT effects for these ions, making it hard to reproduce multiple properties simultaneously. Meanwhile, the models listed above, which incorporate the polarization and CT interactions to some extent, can offer significant improvements. (3) The 12-6-4 and IDM models are suggested for highly charged ions. A combined model can also be used if the metal ion is only coordinated by water molecules.

The VALBOND and bonded models are recommended for use with TM complexes with strong covalent character or those that contain strong ion-ligand binding interactions that are largely invariant with time (i.e., no exchange or CN change). For the bonded model, the Seminario method is preferred because of its ease of use and good accuracy. An automatic parametrization method can be used for a metal site of specific interest. However, because the 1-3 nonbonded interaction is usually not included in the bonded model, it can fail for systems in which there are only attractive 1-4 electrostatic interactions (e.g., two adjacent coordinated water molecules). Hence, a bonded model with additional 1-3 terms or a nonbonded model with restrained interactions can be utilized in these situations. If one wants to study ligand switching at a specific coordination site, a hybrid unpolarized model can be used. To model the Jahn−Teller effect, the CDAM, bonded, LFMM, and ReaxFF models can be used. If one wants to study chemical reactions around metal ion-containing reactive centers, the cluster QM, QM/MM, or ReaxFF approaches are viable choices. The FQ model is the best approach to rapidly determine atomic charges and for screening large databases for ligand/material design. We have listed the availability of various

DOI: 10.1021/acs.chemrev.6b00440
Chem. Rev. 2017, 117, 1564−1686

Table 5. Availability of Various Models in Several Popular MD Simulation Packages[a]

	model/software package						
	AMBER[1032]	CHARMM[1033]	GROMACS[1034]	OpenMM[1035]	TINKER[1036]	Material Studio[1037]	LAMMPS[1038]
unpolarized[a]	yes	yes	yes	yes	yes	yes	yes
FQ	no	yes	no	no	no	no	yes
DO	no	yes	yes	yes[1039]	no	no	yes
IDP	yes	yes	no	yes	yes	no	no
ReaxFF	no	no	no	no	no	yes	yes
LFMM	no	no	no	no	yes[1025]	no	no
VALBOND	no	yes[1029]	no	no	no	no	no

[a]The unpolarized models consist of the bonded, nonbonded, cationic dummy atom, combined, and coarse-grained models. All of these models have similar functional forms, and most MD simulation packages can handle all of them.

Table 6. Availability of Some Parametrization Tools To Facilitate Building Bonded Models of Metal-Containing Systems

	language	method	support software	ref
Hess2FF[a]	Perl	Seminario	Gaussian	669
MCPB[b]	C++	Seminario/Z-matrix	Gaussian	1
parafreq[c]	Python	Burger	Gaussian	682
MCPB.py[d]	Python	Seminario/Z-marix	Gaussian/GAMESS-US	671
CartHess2FC.py[e]	Python	Seminario/Z-marix	Gaussian/GAMESS-US	1040
VFFDT[f]	C++	Seminario	Gaussian/GAMESS-US/ORCA/Q-Chem/MOPAC	672

[a]Can be downloaded from http://www.theochem.kth.se/~lixin/course/Hess2FF.pl. [b]Available in AmberTools from AmberTools1.5 to AmberTools16. [c]Available at http://www.chemistry.mcmaster.ca/ayers/5_software/para_freqv_1.3.tgz. [d]Available in AmberTools15, AmberTools16, and GitHub: https://github.com/Amber-MD/pymsmt. [e]Avaliable in AmberTools16 and GitHub: https://github.com/Amber-MD/pymsmt. [f]Avaliable at Dropbox, https://www.dropbox.com/sh/hlefz8xy8o23q44/AADZGTBN-aJ07flZ-kM0s4U6a?dl=0, and Baidu Cloud, https://pan.baidu.com/share/home?uk=2642812499.

models in several popular MD simulation packages in Table 5, and several parametrization tools for building up the bonded model are summarized in Table 6.

8.2. Perspectives

Overall, it is still challenging to accurately model metal ion-containing systems, especially those containing TMs. Experimental studies, development of novel models and algorithms, as well as software development and application studies are all important to further facilitate research in this area. First, theoretical research of metal containing systems is being held back by the dearth of experimental data. With more and higher quality experimental data, computational methods (both QM and MM) could be better parametrized. With extensive experimental information at hand, benchmark studies to better understand the pros and cons of existing models can be carried out guiding the development of next generation models. Second, it is important to develop new models that better encapsulate the physics of metal ion-containing systems at an affordable cost. For example, models that accurately represent the structural dynamics of metal centers and bond breaking/formation processes are needed to accurately model TM-containing systems. Third, advanced algorithms that bridge the gap between quantum and classical models are needed. Current algorithms could be refined or new algorithms could be proposed that better reproduce the quantum effects in classical models. For example, algorithms that could allow classical models to better reproduce quantum calculated Hessian matrixes (like the Seminario method versus the Z-matrix method) would be beneficial. Finally, software development also plays an important role in facilitating model development, allowing for the rapid prototyping of various models to examine their applicability to a given problem.

AUTHOR INFORMATION

Corresponding Author

*E-mail: kmerz1@gmail.com.

ORCID

Pengfei Li: 0000-0002-2572-5935

Kenneth M. Merz Jr.: 0000-0001-9139-5893

Present Address

[†]Department of Chemistry, University of Illinois at Urbana-Champaign, Urbana, Illinois 61801, United States.

Notes

The authors declare no competing financial interest.

Biographies

Pengfei Li graduated from Xiamen University in China with a B.S. degree in Chemistry in 2011. During his undergraduate studies, he obtained training in quantum chemistry in the laboratory of Prof. Zexing Cao. In 2011, he enrolled in the Ph.D. program at the University of Florida and entered Prof. Kenneth M. Merz Jr.'s lab. In 2013 the Merz laboratory transferred to Michigan State University where he obtained his Ph.D. degree in Chemistry in the summer of 2016. His Ph.D. research concentrated on the development of models and software tools for metal ion modeling. Currently, he is a Postdoctoral Research Associate in Professor Sharon Hammes-Schiffer's lab at the University of Illinois at Urbana−Champaign.

Kenneth M. Merz Jr. is the Joseph Zichis Chair in Chemistry and Director of the Institute for Cyber Enabled Research (iCER) at Michigan State University. His research interest lies in the development of theoretical and computational tools and their application to biological problems including structure and ligand-based drug design, mechanistic enzymology, and methodological verification and validation. He has received a number of honors including election as an ACS Fellow, the 2010 ACS Award for Computers in Chemical and

DOI: 10.1021/acs.chemrev.6b00440
Chem. Rev. 2017, 117, 1564−1686

Pharmaceutical Research, election as a fellow of the American Association for the Advancement of Science, and a John Simon Guggenheim Fellowship.

ACKNOWLEDGMENTS

We acknowledge financial support from the National Institutes of Heath (RO1's GM044974 and GM066859). We thank Dr. David Cerutti (MSU) for his edits of the prose in the Introduction. We acknowledge Dr. Metin Aktulga (MSU) and the referees for their suggestions to improve the manuscript.

ABBREVIATIONS

ABEEM	atom-bond electronegativity equalization method
AC	activity coefficient
AIREBO	adaptive intermolecular REBO
AM1	Austin model 1
AM1-BCC	AM1 with bond charge correction
AMBER	assisted model building with energy refinement
AMOEBA	atomic multipole optimized energetics for biomolecular simulation
AOM	angular overlap model
BAR	Bennett acceptance ratio
BCC	body-centered cubic
BDE	bond dissociation energy
BOF	bond order factor
CASSCF	complete active space consistent field
CBAC	connectivity-based atom contribution
CBS	complete basis set
CC	coupled cluster
CCSD	coupled cluster with single and double excitations
CCSD(T)	coupled cluster with single, double, and perturbative triple excitations
CDAM	cationic dummy atom model
CFF	consistent force field
CG	coarse-grained
CHARMM	Chemistry at Harvard macromolecular mechanics
CHELP	charges from electrostatic potentials
CI	configuration interaction
CID	configuration interaction in the space of double substitutions
CLFSE	cellular LFSE
CMO	canonical molecular orbital
CN	coordination number
CNDO	complete neglect of differential overlap
CNS	crystallography and NMR system
COMB	charge-optimized-many-body
COMPASS	condensed-phase optimized molecular potentials for atomistic simulation studies
CPA	carboxypeptidase A
CPE	chemical potential equilibration
CPMD	Car−Parrinello molecular dynamics
CPU	central processing unit
CS	charge scaling
CSOV	constrained space orbital variation
CT	charge transfer
CTPOL	charge-transfer polarizable
CVFF	consistent valence force field
DC	diffusion coefficient
DDAP	density-derived atomic point
DDEC	density-derived electrostatic and chemical
DFT	density functional theory
DFTB	density functional tight binding
DMA	distributed multipole analysis
DMD	discrete molecular dynamics
DMRG	density matrix renormalization group
DNA	deoxyribonucleic acid
DO	Drude oscillator
DR	Drude rod
DREIDING	a generic force field developed by Mayo et al.
EA	electron affinity
EAM	embedded atom model
ECP	effective core potential
EDA	energy decomposition analysis
EEM	electronegativity equalization method
EPM	electrostatic potential map
EQeq	extended charge equilibration
ESP	electrostatic potential
EVB	empirical valence bond
EXAFS	extended X-ray absorption fine structure
FCC	face centered cubic
FEP	free-energy perturbation
FQ	fluctuating charge
FQ-DCT	FQ discrete charge-transfer
FS	Finnis−Sinclair
G1	Gaussian-1
G2	Gaussian-2
G3	Gaussian-3
G4	Gaussian-4
GAFF	general AMBER force field
GAM	gradient approximation for molecules
GEM	Gaussian electrostatic model
GGA	generalized gradient approximation
GME	Gmelinite
GPU	graphic processing unit
GROMOS	a force field associated with Groningen Machine for Chemical Simulations (GROMACS) software package
GSK3β	glycogen synthase kinase 3β
GolP	gold-protein
HCAI	human carbonic anhydrase I
HCAII	human carbonic anhydrase II
HCP	hexagonal close packed
HF	Hartree−Fock
HFE	hydration free energy
HO	hybrid orbital
HOF	heat of formation
HSAB	hard soft acid base
HV	hypervalent
Hp	*Helicobacter pylori*
IDM	induced dipole model
INDO	intermediate neglect of differential overlap
IOD	ion−oxygen distance of first solvation shell
IRF	interaction round a face
IP	ionization potential
IR	infrared
KA	Klebsella aerogenes
KBI	Kirkwood−Buff integral
LAXS	large-angle X-ray scattering
LB	Lorentz−Berthelot
LC	crystal lattice constant
LCAO	linear combination of atomic orbitals

DOI: 10.1021/acs.chemrev.6b00440
Chem. Rev. 2017, 117, 1564−1686

LDA	local density approximation
LE	crystal lattice energy
LF	ligand field
LFMM	ligand field molecular mechanics
LFSE	ligand field stabilization energy
LIE	linear interaction energy
LJ	Lennard-Jones
LSDA	local spin density approximation
MAD	mean absolute deviation
MAPE	mean absolute percentage error
MARTINI	a coarse-grained force field developed by Marrink et al. for biomolecular simulations
MB-nrg	many-body-energy
MC	Monte Carlo
MCPB	metal center parameter builder
MD	molecular dynamics
MDEC	molecular dynamics electronic continuum
MIL	Material from Institute Lavoisier
MINDO	modified intermediate neglect differential overlap
MM	molecular mechanics
MM/GBSA	molecular mechanics generalized Born surface area
MM/PBSA	molecular mechanics Poisson−Boltzmann surface area
MMFF	Merck molecular force field
MMP	matrix metalloproteinase
MNDO	modified neglect of diatomic overlap
MO	molecular orbital
MOE	molecular operating environment
MOF	metal−organic framework
MOLPRO	a quantum chemistry software package developed by Knowles, Werner, and co-workers
MP2	Møller−Plesset perturbation theory to the second order
MP3	Møller−Plesset perturbation theory to the third order
MP4	Møller−Plesset perturbation theory to the fourth order
MS-EVB	multistate empirical valence bond
MSINDO	modified SINDO
NMR	nuclear magnetic resonance
NNLC	nearest neighbor ligands correction
NPA	natural population analysis
OPC	optimal point charge
OPLS	optimized potentials for liquid simulations
OPLS-AA	OPLS with all atom representation
OPLS-AAP	OPLS-AA with induced dipoles
OPLS-CM1AP	OPLS with with CM1A charge and induced dipoles
ORCA	a quantum chemistry software package developed by Neese and co-workers
PBC	periodic boundary condition
PBF	Poisson−Boltzmann finite element continuum solvation model
PCFF	polymer consistent force field
PCM	polarizable continuum model
PDA	pair defect approximation
PDB	protein databank
PEOE	partial equalization of orbital electronegativity
PES	potential energy surface
PFF	polarizable force field
PHF	partial Hessian fitting
PIPF	polarizable intermolecular potential function
PM3	parametric method 3
PME	particle mesh Ewald
PMF	potential of mean force
POL	polarization
PQEq	periodic charge equilibration
Q-Chem	a quantum chemistry software package developed by Q-Chem Inc.
QCISD	quadratic configuration interaction singles doubles
QEq	charge equilibration
QM	quantum mechanics
QM/MM	quantum mechanics/molecular mechanics
QPCT	quantum calibrated polarizable-charge transfer
QSAR	quantitative structure-acitivity relationship
RASSCF	restricted active space consistent field
RDF	radial distribution function
REBO	reactive empirical bond order
REPEAT	repeating electrostatic potential extracted atomic
RESP	restrained electrostatic potential
RG	renormalization group
RHF	restricted Hartree−Fock
RMS	root mean square
RMSD	root mean square deviation
RMSF	root mean square fluctation
RNA	ribonucleic acid
ROHF	restricted-open-shell-Hartree−Fock
RVS	reduced variational space
ReaxFF	reactive force field
SAPT	symmetry-adapted perturbation theory
SC	Sutton−Chen
SCC-DFTB	self-consistent charge density functional tight binding
SCF	self-consistent field
SCS	spin component scaled
SE	semiempirical
SFC	semifluctuating charge
SHAPES	a classical force field developed by Landis et al.
SIBFA	sum of interactions between fragments computed ab initio
SINDO	symmetrically orthogonalized INDO
SINDO1	a semiempirical quantum mechanics method developed by Jug et al.
SLEF	short−long effective function
SNase	staphylococcal nuclease
SOD	sodalite
SPC	simple point charge water model
SPC/E	extended simple point charge water model
SWM4-DP	simple water model with four sites and Drude polarizability
SWM4-NDP	simple water model with four sites and negative Drude polarizability
TB	tight-binding
TB-SMA	tight-binding with second moment approximation
TI	thermodynamic integration
TIP3P	transferable intermolecular potential 3-point charges
TIP4P	transferable intermolecular potential 4-point charges
$TIP4P_{EW}$	TIP4P water model for Ewald summation
TIPS	transferable intermolecular potential function

DOI: 10.1021/acs.chemrev.6b00440
Chem. Rev. 2017, 117, 1564−1686

TM	transition metal
TPD	temperature-programmed desorption
TraPPE	transferable potentials for phase equilibria
TST	transition state theory
TTM	Thole-type model
UFF	Universal force field UNRES United residue
VALBOND	a force field developed by Landis et al. based on the VB theory
VB	valence bond
VDW	van der Waals
VESPR	valence shell electron pair repulsion
VFFDT	visual force field derivation toolkit
XRD	X-ray diffraction
ZAFF	zinc AMBER force field
ZIF	zeolitic imidazolate framework
ZINDO	Zerner INDO method
ccCA	correlation consistent composite approach
ccCA-TM	ccCA for transition metals
pyMSMT	python metal site modeling toolbox
rp-ccCA	relativistic pseudopotential ccCA

REFERENCES

(1) Peters, M. B.; Yang, Y.; Wang, B.; Füsti-Molnár, L.; Weaver, M. N.; Merz, K. M., Jr Structural Survey of Zinc-Containing Proteins and Development of the Zinc Amber Force Field (Zaff). *J. Chem. Theory Comput.* **2010**, *6*, 2935−2947.

(2) Perez, V.; Chang, E. T. Sodium-to-Potassium Ratio and Blood Pressure, Hypertension, and Related Factors. *Adv. Nutr.* **2014**, *5*, 712−741.

(3) Haddy, F. J.; Vanhoutte, P. M.; Feletou, M. Role of Potassium in Regulating Blood Flow and Blood Pressure. *Am. J. Physiol. Regul. Integr. Comp. Physiol.* **2005**, *290*, R546−R552.

(4) Altura, B.; Altura, B. Interactions of Mg and K on Blood Vessels–Aspects in View of Hypertension. Review of Present Status and New Findings. *Magnesium* **1983**, *3*, 175−194.

(5) Bukoski, R. D. Dietary Ca2+ and Blood Pressure: Evidence That Ca2+-Sensing Receptor Activated, Sensory Nerve Dilator Activity Couples Changes in Interstitial Ca2+ with Vascular Tone. *Nephrol. Dial. Transplant.* **2001**, *16*, 218−221.

(6) Page, M. J.; Di Cera, E. Role of Na+ and K+ in Enzyme Function. *Physiol. Rev.* **2006**, *86*, 1049−1092.

(7) Aperia, A.; Holtbäck, U.; Syren, M.; Svensson, L.; Fryckstedt, J.; Greengard, P. Activation/Deactivation of Renal Na+, K (+)-Atpase: A Final Common Pathway for Regulation of Natriuresis. *FASEB J.* **1994**, *8*, 436−439.

(8) Møller, J.; Lind, K.; Andersen, J. Enzyme Kinetics and Substrate Stabilization of Detergent-Solubilized and Membraneous (Ca2+ + Mg2+)-Activated Atpase from Sarcoplasmic Reticulum. Effect of Protein-Protein Interactions. *J. Biol. Chem.* **1980**, *255*, 1912−1920.

(9) Lee, S. H.; Johnson, J. D.; Walsh, M. P.; Van Lierop, J. E.; SUTHERLAND, C.; Ande, X.; Snedden, W. A.; Danuta, K.-K.; Fromm, H.; Narayanan, N. Differential Regulation of Ca2+/Calmodulin-Dependent Enzymes by Plant Calmodulin Isoforms and Free Ca2+ Concentration. *Biochem. J.* **2000**, *350*, 299−306.

(10) Ahvazi, B.; Boeshans, K. M.; Idler, W.; Baxa, U.; Steinert, P. M. Roles of Calcium Ions in the Activation and Activity of the Transglutaminase 3 Enzyme. *J. Biol. Chem.* **2003**, *278*, 23834−23841.

(11) Robinson, R. Structure of Signaling Enzyme Reveals How Calcium Turns It On. *PLoS Biol.* **2010**, *8*.

(12) Beinert, H.; Kennedy, M. C.; Stout, C. D. Aconitase as Iron−Sulfur Protein, Enzyme, and Iron-Regulatory Protein. *Chem. Rev.* **1996**, *96*, 2335−2374.

(13) Stephens, P. J.; Jollie, D. R.; Warshel, A. Protein Control of Redox Potentials of Iron−Sulfur Proteins. *Chem. Rev.* **1996**, *96*, 2491−2514.

(14) Ferguson-Miller, S.; Babcock, G. T. Heme/Copper Terminal Oxidases. *Chem. Rev.* **1996**, *96*, 2889−2908.

(15) Solomon, E. I.; Sundaram, U. M.; Machonkin, T. E. Multicopper Oxidases and Oxygenases. *Chem. Rev.* **1996**, *96*, 2563−2606.

(16) Jacoby, M. How Computers Are Helping Chemists Discover Materials That Don't yet Exist. *Chem. Eng. News* **2015**, *93*, 8−11.

(17) Schaller, R. R. Moore's Law: Past, Present and Future. *IEEE Spectrum* **1997**, *34*, 52−59.

(18) Jacoby, M. Chemistry by the Numbers. *Chem. Eng. News* **2013**, *91*, 51−55.

(19) Götz, A. W.; Williamson, M. J.; Xu, D.; Poole, D.; Le Grand, S.; Walker, R. C. Routine Microsecond Molecular Dynamics Simulations with Amber on Gpus. 1. Generalized Born. *J. Chem. Theory Comput.* **2012**, *8*, 1542−1555.

(20) Salomon-Ferrer, R.; Götz, A. W.; Poole, D.; Le Grand, S.; Walker, R. C. Routine Microsecond Molecular Dynamics Simulations with Amber on Gpus. 2. Explicit Solvent Particle Mesh Ewald. *J. Chem. Theory Comput.* **2013**, *9*, 3878−3888.

(21) Shaw, D. E.; Maragakis, P.; Lindorff-Larsen, K.; Piana, S.; Dror, R. O.; Eastwood, M. P.; Bank, J. A.; Jumper, J. M.; Salmon, J. K.; Shan, Y.; et al. Atomic-Level Characterization of the Structural Dynamics of Proteins. *Science* **2010**, *330*, 341−346.

(22) Jorgensen, W. L.; Ruiz-Caro, J.; Tirado-Rives, J.; Basavapathruni, A.; Anderson, K. S.; Hamilton, A. D. Computer-Aided Design of Non-Nucleoside Inhibitors of Hiv-1 Reverse Transcriptase. *Bioorg. Med. Chem. Lett.* **2006**, *16*, 663−667.

(23) Bollini, M.; Domaoal, R. A.; Thakur, V. V.; Gallardo-Macias, R.; Spasov, K. A.; Anderson, K. S.; Jorgensen, W. L. Computationally-Guided Optimization of a Docking Hit to Yield Catechol Diethers as Potent Anti-Hiv Agents. *J. Med. Chem.* **2011**, *54*, 8582−8591.

(24) Dziedzic, P.; Cisneros, J. A.; Robertson, M. J.; Hare, A. A.; Danford, N. E.; Baxter, R. H.; Jorgensen, W. L. Design, Synthesis, and Protein Crystallography of Biaryltriazoles as Potent Tautomerase Inhibitors of Macrophage Migration Inhibitory Factor. *J. Am. Chem. Soc.* **2015**, *137*, 2996−3003.

(25) Gray, W. T.; Frey, K. M.; Laskey, S. B.; Mislak, A. C.; Spasov, K. A.; Lee, W.-G.; Bollini, M.; Siliciano, R. F.; Jorgensen, W. L.; Anderson, K. S. Potent Inhibitors Active against Hiv Reverse Transcriptase with K101p, a Mutation Conferring Rilpivirine Resistance. *ACS Med. Chem. Lett.* **2015**, *6*, 1075−1079.

(26) Mak, L.; Liggi, S.; Tan, L.; Kusonmano, K.; M Rollinger, J.; Koutsoukas, A.; C Glen, R.; Kirchmair, J. Anti-Cancer Drug Development: Computational Strategies to Identify and Target Proteins Involved in Cancer Metabolism. *Curr. Pharm. Des.* **2013**, *19*, 532−577.

(27) Wood, J. M.; Maibaum, J.; Rahuel, J.; Grutter, M. G.; Cohen, N. C.; Rasetti, V.; Ruger, H.; Goschke, R.; Stutz, S.; Fuhrer, W.; et al. Structure-Based Design of Aliskiren, a Novel Orally Effective Renin Inhibitor. *Biochem. Biophys. Res. Commun.* **2003**, *308*, 698−705.

(28) Cole, J. M.; Low, K. S.; Ozoe, H.; Stathi, P.; Kitamura, C.; Kurata, H.; Rudolf, P.; Kawase, T. Data Mining with Molecular Design Rules Identifies New Class of Dyes for Dye-Sensitised Solar Cells. *Phys. Chem. Chem. Phys.* **2014**, *16*, 26684−26690.

(29) Studt, F.; Sharafutdinov, I.; Abild-Pedersen, F.; Elkjær, C. F.; Hummelshøj, J. S.; Dahl, S.; Chorkendorff, I.; Nørskov, J. K. Discovery of a Ni-Ga Catalyst for Carbon Dioxide Reduction to Methanol. *Nat. Chem.* **2014**, *6*, 320−324.

(30) Kibsgaard, J.; Tsai, C.; Chan, K.; Benck, J. D.; Nørskov, J. K.; Abild-Pedersen, F.; Jaramillo, T. F. Designing an Improved Transition Metal Phosphide Catalyst for Hydrogen Evolution Using Experimental and Theoretical Trends. *Energy Environ. Sci.* **2015**, *8*, 3022−3029.

(31) Shamp, A.; Zurek, E. Superconducting High-Pressure Phases Composed of Hydrogen and Iodine. *J. Phys. Chem. Lett.* **2015**, *6*, 4067−4072.

(32) Yan, F.; Zhang, X.; Yu, Y. G.; Yu, L.; Nagaraja, A.; Mason, T. O.; Zunger, A. Design and Discovery of a Novel Half-Heusler Transparent Hole Conductor Made of All-Metallic Heavy Elements. *Nat. Commun.* **2015**, *6*, 7308.

(33) Zurek, E.; Yao, Y. Theoretical Predictions of Novel Superconducting Phases of Bage3 Stable at Atmospheric and High Pressures. *Inorg. Chem.* **2015**, *54*, 2875−2884.

DOI: 10.1021/acs.chemrev.6b00440
Chem. Rev. 2017, 117, 1564−1686

(34) Riedel, S.; Kaupp, M. The Highest Oxidation States of the Transition Metal Elements. *Coord. Chem. Rev.* **2009**, *253*, 606−624.
(35) Wang, G.; Zhou, M.; Goettel, J. T.; Schrobilgen, G. J.; Su, J.; Li, J.; Schlöder, T.; Riedel, S. Identification of an Iridium-Containing Compound with a Formal Oxidation State of Ix. *Nature* **2014**, *514*, 475−477.
(36) Yu, H. S.; Truhlar, D. G. Oxidation State 10 Exists. *Angew. Chem., Int. Ed.* **2016**, *55*, 9004.
(37) Megyes, T.; Grosz, T.; Radnai, T.; Bakó, I.; Pálinkás, G. Solvation of Calcium Ion in Polar Solvents: An X-Ray Diffraction and Ab Initio Study. *J. Phys. Chem. A* **2004**, *108*, 7261−7271.
(38) Cotton, F.; Curtis, N.; Harris, C.; Johnson, B.; Lippard, S.; Mague, J.; Robinson, W.; Wood, J. Mononuclear and Polynuclear Chemistry of Rhenium (Iii): Its Pronounced Homophilicity. *Science* **1964**, *145*, 1305−1307.
(39) Gagliardi, L.; Roos, B. O. Quantum Chemical Calculations Show That the Uranium Molecule U2 Has a Quintuple Bond. *Nature* **2005**, *433*, 848−851.
(40) Nguyen, T.; Sutton, A. D.; Brynda, M.; Fettinger, J. C.; Long, G. J.; Power, P. P. Synthesis of a Stable Compound with Fivefold Bonding between Two Chromium (I) Centers. *Science* **2005**, *310*, 844−847.
(41) Clark, D.; Schrock, R. Multiple Metal-Carbon Bonds. 12. Tungsten and Molybdenum Neopentylidyne and Some Tungsten Neopentylidene Complexes. *J. Am. Chem. Soc.* **1978**, *100*, 6774−6776.
(42) Churchill, M. R.; Youngs, W. J. Crystal Structure and Molecular Geometry of W (. Tplbond. Ccme3)(: Chcme3) (Ch2cme3) (Dmpe), a Mononuclear Tungsten (Vi) Complex with Metal-Alkylidyne, Metal-Alkylidene, and Metal-Alkyl Linkages. *Inorg. Chem.* **1979**, *18*, 2454−2458.
(43) Beaumier, E. P.; Billow, B. S.; Singh, A. K.; Biros, S. M.; Odom, A. L. A Complex with Nitrogen Single, Double, and Triple Bonds to the Same Chromium Atom: Synthesis, Structure, and Reactivity. *Chem. Sci.* **2016**, *7*, 2532−2536.
(44) Chaboy, J.; Muñoz-Páez, A.; Merkling, P. J.; Marcos, E. S. The Hydration of Cu2+: Can the Jahn-Teller Effect Be Detected in Liquid Solution? *J. Chem. Phys.* **2006**, *124*, 064509.
(45) Lipscomb, W. N.; Sträter, N. Recent Advances in Zinc Enzymology. *Chem. Rev.* **1996**, *96*, 2375−2434.
(46) Danopoulos, A. A.; Wilkinson, G.; Sweet, T. K.; Hursthouse, M. B. Tert-Butylimido Compounds of Manganese-(Vii),-(Vi),-(V) and-(Ii); Nitrido, Amido, Alkyl, Zinc and Aluminium Compounds. *J. Chem. Soc., Dalton Trans.* **1995**, 205−216.
(47) Jiang, W.; DeYonker, N. J.; Determan, J. J.; Wilson, A. K. Toward Accurate Theoretical Thermochemistry of First Row Transition Metal Complexes. *J. Phys. Chem. A* **2012**, *116*, 870−885.
(48) Grossfield, A.; Ren, P.; Ponder, J. W. Ion Solvation Thermodynamics from Simulation with a Polarizable Force Field. *J. Am. Chem. Soc.* **2003**, *125*, 15671−15682.
(49) Lamoureux, G.; Roux, B. Absolute Hydration Free Energy Scale for Alkali and Halide Ions Established from Simulations with a Polarizable Force Field. *J. Phys. Chem. B* **2006**, *110*, 3308−3322.
(50) Norrby, P. O.; Liljefors, T. Automated Molecular Mechanics Parameterization with Simultaneous Utilization of Experimental and Quantum Mechanical Data. *J. Comput. Chem.* **1998**, *19*, 1146−1166.
(51) Allinger, N. L.; Zhou, X.; Bergsma, J. Molecular Mechanics Parameters. *J. Mol. Struct.: THEOCHEM* **1994**, *312*, 69−83.
(52) Holm, R. H.; Solomon, E. I. Preface: Bioinorganic Enzymology. *Chem. Rev.* **1996**, *96*, 2237−2238.
(53) Averill, B. A. Dissimilatory Nitrite and Nitric Oxide Reductases. *Chem. Rev.* **1996**, *96*, 2951−2964.
(54) Burgess, B. K.; Lowe, D. J. Mechanism of Molybdenum Nitrogenase. *Chem. Rev.* **1996**, *96*, 2983−3012.
(55) Dismukes, G. C. Manganese Enzymes with Binuclear Active Sites. *Chem. Rev.* **1996**, *96*, 2909−2926.
(56) Eady, R. R. Structure-Function Relationships of Alternative Nitrogenases. *Chem. Rev.* **1996**, *96*, 3013−3030.
(57) Flint, D. H.; Allen, R. M. Iron-Sulfur Proteins with Nonredox Functions. *Chem. Rev.* **1996**, *96*, 2315−2334.
(58) Hille, R. The Mononuclear Molybdenum Enzymes. *Chem. Rev.* **1996**, *96*, 2757−2816.
(59) Holm, R. H.; Kennepohl, P.; Solomon, E. I. Structural and Functional Aspects of Metal Sites in Biology. *Chem. Rev.* **1996**, *96*, 2239−2314.
(60) Howard, J. B.; Rees, D. C. Structural Basis of Biological Nitrogen Fixation. *Chem. Rev.* **1996**, *96*, 2965−2982.
(61) Johnson, M. K.; Rees, D. C.; Adams, M. W. W. Tungstoenzymes. *Chem. Rev.* **1996**, *96*, 2817−2840.
(62) Kappock, T. J.; Caradonna, J. P. Pterin-Dependent Amino Acid Hydroxylases. *Chem. Rev.* **1996**, *96*, 2659−2756.
(63) Klinman, J. P. Mechanisms Whereby Mononuclear Copper Proteins Functionalize Organic Substrates. *Chem. Rev.* **1996**, *96*, 2541−2562.
(64) Nocek, J. M.; Zhou, J. S.; De Forest, S.; Priyadarshy, S.; Beratan, D. N.; Onuchic, J. N.; Hoffman, B. M. Theory and Practice of Electron Transfer within Protein−Protein Complexes: Application to the Multidomain Binding of Cytochrome C by Cytochrome C Peroxidase. *Chem. Rev.* **1996**, *96*, 2459−2490.
(65) Que, L.; Ho, R. Y. N. Dioxygen Activation by Enzymes with Mononuclear Non-Heme Iron Active Sites. *Chem. Rev.* **1996**, *96*, 2607−2624.
(66) Ragsdale, S. W.; Kumar, M. Nickel-Containing Carbon Monoxide Dehydrogenase/Acetyl-Coa Synthase. *Chem. Rev.* **1996**, *96*, 2515−2540.
(67) Sono, M.; Roach, M. P.; Coulter, E. D.; Dawson, J. H. Heme-Containing Oxygenases. *Chem. Rev.* **1996**, *96*, 2841−2888.
(68) Thauer, R. K.; Klein, A. R.; Hartmann, G. C. Reactions with Molecular Hydrogen in Microorganisms: Evidence for a Purely Organic Hydrogenation Catalyst. *Chem. Rev.* **1996**, *96*, 3031−3042.
(69) Wallar, B. J.; Lipscomb, J. D. Dioxygen Activation by Enzymes Containing Binuclear Non-Heme Iron Clusters. *Chem. Rev.* **1996**, *96*, 2625−2658.
(70) Wilcox, D. E. Binuclear Metallohydrolases. *Chem. Rev.* **1996**, *96*, 2435−2458.
(71) Yachandra, V. K.; Sauer, K.; Klein, M. P. Manganese Cluster in Photosynthesis: Where Plants Oxidize Water to Dioxygen. *Chem. Rev.* **1996**, *96*, 2927−2950.
(72) Davidson, E. R. Computational Transition Metal Chemistry. *Chem. Rev.* **2000**, *100*, 351−352.
(73) Alonso, J. A. Electronic and Atomic Structure, and Magnetism of Transition-Metal Clusters. *Chem. Rev.* **2000**, *100*, 637−678.
(74) Ceulemans, A.; Chibotaru, L. F.; Heylen, G. A.; Pierloot, K.; Vanquickenborne, L. G. Theoretical Models of Exchange Interactions in Dimeric Transition-Metal Complexes. *Chem. Rev.* **2000**, *100*, 787−806.
(75) Cundari, T. R. Computational Studies of Transition Metal−Main Group Multiple Bonding. *Chem. Rev.* **2000**, *100*, 807−818.
(76) Dedieu, A. Theoretical Studies in Palladium and Platinum Molecular Chemistry. *Chem. Rev.* **2000**, *100*, 543−600.
(77) Frenking, G.; Fröhlich, N. The Nature of the Bonding in Transition-Metal Compounds. *Chem. Rev.* **2000**, *100*, 717−774.
(78) Harrison, J. F. Electronic Structure of Diatomic Molecules Composed of a First-Row Transition Metal and Main-Group Element (H−F). *Chem. Rev.* **2000**, *100*, 679−716.
(79) Hush, N. S.; Reimers, J. R. Solvent Effects on the Electronic Spectra of Transition Metal Complexes. *Chem. Rev.* **2000**, *100*, 775−786.
(80) Loew, G. H.; Harris, D. L. Role of the Heme Active Site and Protein Environment in Structure, Spectra, and Function of the Cytochrome P450s. *Chem. Rev.* **2000**, *100*, 407−420.
(81) Maseras, F.; Lledós, A.; Clot, E.; Eisenstein, O. Transition Metal Polyhydrides: From Qualitative Ideas to Reliable Computational Studies. *Chem. Rev.* **2000**, *100*, 601−636.
(82) Niu, S.; Hall, M. B. Theoretical Studies on Reactions of Transition-Metal Complexes. *Chem. Rev.* **2000**, *100*, 353−406.
(83) Rohmer, M.-M.; Bénard, M.; Poblet, J.-M. Structure, Reactivity, and Growth Pathways of Metallocarbohedrenes M8c12 and Transition

DOI: 10.1021/acs.chemrev.6b00440
Chem. Rev. 2017, 117, 1564−1686

Metal/Carbon Clusters and Nanocrystals: A Challenge to Computational Chemistry. *Chem. Rev.* **2000**, *100*, 495−542.
(84) Siegbahn, P. E.; Blomberg, M. R. Transition-Metal Systems in Biochemistry Studied by High-Accuracy Quantum Chemical Methods. *Chem. Rev.* **2000**, *100*, 421−438.
(85) Torrent, M.; Solà, M.; Frenking, G. Theoretical Studies of Some Transition-Metal-Mediated Reactions of Industrial and Synthetic Importance. *Chem. Rev.* **2000**, *100*, 439−494.
(86) Holm, R. H.; Solomon, E. I. Preface: Biomimetic Inorganic Chemistry. *Chem. Rev.* **2004**, *104*, 347−348.
(87) Aoki, S.; Kimura, E. Zinc−Nucleic Acid Interaction. *Chem. Rev.* **2004**, *104*, 769−788.
(88) Collman, J. P.; Boulatov, R.; Sunderland, C. J.; Fu, L. Functional Analogues of Cytochrome C Oxidase, Myoglobin, and Hemoglobin. *Chem. Rev.* **2004**, *104*, 561−588.
(89) Costas, M.; Mehn, M. P.; Jensen, M. P.; Que, L. Dioxygen Activation at Mononuclear Nonheme Iron Active Sites: Enzymes, Models, and Intermediates. *Chem. Rev.* **2004**, *104*, 939−986.
(90) Crans, D. C.; Smee, J. J.; Gaidamauskas, E.; Yang, L. The Chemistry and Biochemistry of Vanadium and the Biological Activities Exerted by Vanadium Compounds. *Chem. Rev.* **2004**, *104*, 849−902.
(91) Dos Santos, P. C.; Dean, D. R.; Hu, Y.; Ribbe, M. W. Formation and Insertion of the Nitrogenase Iron−Molybdenum Cofactor. *Chem. Rev.* **2004**, *104*, 1159−1174.
(92) Enemark, J. H.; Cooney, J. J. A.; Wang, J.-J.; Holm, R. H. Synthetic Analogues and Reaction Systems Relevant to the Molybdenum and Tungsten Oxotransferases. *Chem. Rev.* **2004**, *104*, 1175−1200.
(93) Gavrilova, A. L.; Bosnich, B. Principles of Mononucleating and Binucleating Ligand Design. *Chem. Rev.* **2004**, *104*, 349−384.
(94) Henkel, G.; Krebs, B. Metallothioneins: Zinc, Cadmium, Mercury, and Copper Thiolates and Selenolates Mimicking Protein Active Site Features − Structural Aspects and Biological Implications. *Chem. Rev.* **2004**, *104*, 801−824.
(95) Jantz, D.; Amann, B. T.; Gatto, G. J.; Berg, J. M. The Design of Functional DNA-Binding Proteins Based on Zinc Finger Domains. *Chem. Rev.* **2004**, *104*, 789−800.
(96) Kim, E.; Chufán, E. E.; Kamaraj, K.; Karlin, K. D. Synthetic Models for Heme−Copper Oxidases. *Chem. Rev.* **2004**, *104*, 1077−1134.
(97) Kovacs, J. A. Synthetic Analogues of Cysteinate-Ligated Non-Heme Iron and Non-Corrinoid Cobalt Enzymes. *Chem. Rev.* **2004**, *104*, 825−848.
(98) Kuchar, J.; Hausinger, R. P. Biosynthesis of Metal Sites. *Chem. Rev.* **2004**, *104*, 509−526.
(99) Lee, S. C.; Holm, R. H. The Clusters of Nitrogenase: Synthetic Methodology in the Construction of Weak-Field Clusters. *Chem. Rev.* **2004**, *104*, 1135−1158.
(100) Lewis, E. A.; Tolman, W. B. Reactivity of Dioxygen−Copper Systems. *Chem. Rev.* **2004**, *104*, 1047−1076.
(101) MacKay, B. A.; Fryzuk, M. D. Dinitrogen Coordination Chemistry: On the Biomimetic Borderlands. *Chem. Rev.* **2004**, *104*, 385−402.
(102) McCleverty, J. A. Chemistry of Nitric Oxide Relevant to Biology. *Chem. Rev.* **2004**, *104*, 403−418.
(103) Mirica, L. M.; Ottenwaelder, X.; Stack, T. D. P. Structure and Spectroscopy of Copper−Dioxygen Complexes. *Chem. Rev.* **2004**, *104*, 1013−1046.
(104) Noodleman, L.; Lovell, T.; Han, W.-G.; Li, J.; Himo, F. Quantum Chemical Studies of Intermediates and Reaction Pathways in Selected Enzymes and Catalytic Synthetic Systems. *Chem. Rev.* **2004**, *104*, 459−508.
(105) Parkin, G. Synthetic Analogues Relevant to the Structure and Function of Zinc Enzymes. *Chem. Rev.* **2004**, *104*, 699−768.
(106) Reedy, C. J.; Gibney, B. R. Heme Protein Assemblies. *Chem. Rev.* **2004**, *104*, 617−650.
(107) Rorabacher, D. B. Electron Transfer by Copper Centers. *Chem. Rev.* **2004**, *104*, 651−698.
(108) Solomon, E. I.; Szilagyi, R. K.; DeBeer George, S.; Basumallick, L. Electronic Structures of Metal Sites in Proteins and Models: Contributions to Function in Blue Copper Proteins. *Chem. Rev.* **2004**, *104*, 419−458.
(109) Tshuva, E. Y.; Lippard, S. J. Synthetic Models for Non-Heme Carboxylate-Bridged Diiron Metalloproteins: Strategies and Tactics. *Chem. Rev.* **2004**, *104*, 987−1012.
(110) Venkateswara Rao, P.; Holm, R. H. Synthetic Analogues of the Active Sites of Iron−Sulfur Proteins. *Chem. Rev.* **2004**, *104*, 527−560.
(111) Walker, F. A. Models of the Bis-Histidine-Ligated Electron-Transferring Cytochromes. Comparative Geometric and Electronic Structure of Low-Spin Ferro- and Ferrihemes. *Chem. Rev.* **2004**, *104*, 589−616.
(112) Wu, A. J.; Penner-Hahn, J. E.; Pecoraro, V. L. Structural, Spectroscopic, and Reactivity Models for the Manganese Catalases. *Chem. Rev.* **2004**, *104*, 903−938.
(113) Holm, R. H.; Solomon, E. I. Introduction: Bioinorganic Enzymology Ii. *Chem. Rev.* **2014**, *114*, 3367−3368.
(114) Blomberg, M. R. A.; Borowski, T.; Himo, F.; Liao, R.-Z.; Siegbahn, P. E. M. Quantum Chemical Studies of Mechanisms for Metalloenzymes. *Chem. Rev.* **2014**, *114*, 3601−3658.
(115) Hille, R.; Hall, J.; Basu, P. The Mononuclear Molybdenum Enzymes. *Chem. Rev.* **2014**, *114*, 3963−4038.
(116) Layfield, J. P.; Hammes-Schiffer, S. Hydrogen Tunneling in Enzymes and Biomimetic Models. *Chem. Rev.* **2014**, *114*, 3466−3494.
(117) Lee, S. C.; Lo, W.; Holm, R. H. Developments in the Biomimetic Chemistry of Cubane-Type and Higher Nuclearity Iron−Sulfur Clusters. *Chem. Rev.* **2014**, *114*, 3579−3600.
(118) Migliore, A.; Polizzi, N. F.; Therien, M. J.; Beratan, D. N. Biochemistry and Theory of Proton-Coupled Electron Transfer. *Chem. Rev.* **2014**, *114*, 3381−3465.
(119) Poulos, T. L. Heme Enzyme Structure and Function. *Chem. Rev.* **2014**, *114*, 3919−3962.
(120) Sheng, Y.; Abreu, I. A.; Cabelli, D. E.; Maroney, M. J.; Miller, A.-F.; Teixeira, M.; Valentine, J. S. Superoxide Dismutases and Superoxide Reductases. *Chem. Rev.* **2014**, *114*, 3854−3918.
(121) Solomon, E. I.; Heppner, D. E.; Johnston, E. M.; Ginsbach, J. W.; Cirera, J.; Qayyum, M.; Kieber-Emmons, M. T.; Kjaergaard, C. H.; Hadt, R. G.; Tian, L. Copper Active Sites in Biology. *Chem. Rev.* **2014**, *114*, 3659−3853.
(122) Winkler, J. R.; Gray, H. B. Electron Flow through Metalloproteins. *Chem. Rev.* **2014**, *114*, 3369−3380.
(123) Yu, F.; Cangelosi, V. M.; Zastrow, M. L.; Tegoni, M.; Plegaria, J. S.; Tebo, A. G.; Mocny, C. S.; Ruckthong, L.; Qayyum, H.; Pecoraro, V. L. Protein Design: Toward Functional Metalloenzymes. *Chem. Rev.* **2014**, *114*, 3495−3578.
(124) Gordon, M. S.; Slipchenko, L. V. Introduction: Calculations on Large Systems. *Chem. Rev.* **2015**, *115*, 5605−5606.
(125) Fernando, A.; Weerawardene, K. L. D. M.; Karimova, N. V.; Aikens, C. M. Quantum Mechanical Studies of Large Metal, Metal Oxide, and Metal Chalcogenide Nanoparticles and Clusters. *Chem. Rev.* **2015**, *115*, 6112−6216.
(126) Odoh, S. O.; Cramer, C. J.; Truhlar, D. G.; Gagliardi, L. Quantum-Chemical Characterization of the Properties and Reactivities of Metal−Organic Frameworks. *Chem. Rev.* **2015**, *115*, 6051−6111.
(127) Rode, B. M.; Schwenk, C. F.; Tongraar, A. Structure and Dynamics of Hydrated Ions—New Insights through Quantum Mechanical Simulations. *J. Mol. Liq.* **2004**, *110*, 105−122.
(128) Deeth, R. J. Recent Developments in Computational Bioinorganic Chemistry. *Principles and Applications of Density Functional Theory in Inorganic Chemistry II*; Springer-Verlag: Berlin, Germany, 2004; pp 37−70.
(129) Shaik, S.; Kumar, D.; de Visser, S. P.; Altun, A.; Thiel, W. Theoretical Perspective on the Structure and Mechanism of Cytochrome P450 Enzymes. *Chem. Rev.* **2005**, *105*, 2279−2328.
(130) Noodleman, L.; Han, W.-G. Structure, Redox, Pka, Spin. A Golden Tetrad for Understanding Metalloenzyme Energetics and Reaction Pathways. *JBIC, J. Biol. Inorg. Chem.* **2006**, *11*, 674−694.

DOI: 10.1021/acs.chemrev.6b00440
Chem. Rev. 2017, 117, 1564−1686

(131) Neese, F. A Critical Evaluation of Dft, Including Time-Dependent Dft, Applied to Bioinorganic Chemistry. *JBIC, J. Biol. Inorg. Chem.* **2006**, *11*, 702−711.
(132) Hallberg, K. A. New Trends in Density Matrix Renormalization. *Adv. Phys.* **2006**, *55*, 477−526.
(133) Cramer, C. J.; Truhlar, D. G. Density Functional Theory for Transition Metals and Transition Metal Chemistry. *Phys. Chem. Chem. Phys.* **2009**, *11*, 10757−10816.
(134) Aullón, G.; Alvarez, S. Oxidation States, Atomic Charges and Orbital Populations in Transition Metal Complexes. *Theor. Chem. Acc.* **2009**, *123*, 67−73.
(135) Shaik, S.; Cohen, S.; Wang, Y.; Chen, H.; Kumar, D.; Thiel, W. P450 Enzymes: Their Structure, Reactivity, and Selectivity—Modeled by Qm/Mm Calculations. *Chem. Rev.* **2010**, *110*, 949−1017.
(136) Hofer, T. S.; Weiss, A. K.; Randolf, B. R.; Rode, B. M. Hydration of Highly Charged Ions. *Chem. Phys. Lett.* **2011**, *512*, 139−145.
(137) Sameera, W.; Maseras, F. Transition Metal Catalysis by Density Functional Theory and Density Functional Theory/Molecular Mechanics. *Wiley Interdiscip. Rev. Comput. Mol. Sci.* **2012**, *2*, 375−385.
(138) Tsipis, A. C. Dft Flavor of Coordination Chemistry. *Coord. Chem. Rev.* **2014**, *272*, 1−29.
(139) Brubaker, G. R.; Johnson, D. W. Molecular Mechanics Calculations in Coordination Chemistry. *Coord. Chem. Rev.* **1984**, *53*, 1−36.
(140) Hancock, R. D.; Martell, A. E. Ligand Design for Selective Complexation of Metal Ions in Aqueous Solution. *Chem. Rev.* **1989**, *89*, 1875−1914.
(141) Comba, P. Metal Ion Selectivity and Molecular Modeling. *Coord. Chem. Rev.* **1999**, *185*−*186*, 81−98.
(142) Norrby, P.-O.; Brandt, P. Deriving Force Field Parameters for Coordination Complexes. *Coord. Chem. Rev.* **2001**, *212*, 79−109.
(143) Banci, L. Molecular Dynamics Simulations of Metalloproteins. *Curr. Opin. Chem. Biol.* **2003**, *7*, 143−149.
(144) Comba, P.; Remenyi, R. Inorganic and Bioinorganic Molecular Mechanics Modeling - the Problem of the Force Field Parameterization. *Coord. Chem. Rev.* **2003**, *238*−*239*, 9−20.
(145) Jungwirth, P.; Tobias, D. J. Specific Ion Effects at the Air/Water Interface. *Chem. Rev.* **2006**, *106*, 1259−1281.
(146) Comba, P.; Hambley, T. W.; Martin, B. *Molecular Modeling of Inorganic Compounds*; John Wiley & Sons: Weinheim, Germany, 2009.
(147) Zimmer, M. Are Classical Molecular Mechanics Calculations Still Useful in Bioinorganic Simulations? *Coord. Chem. Rev.* **2009**, *253*, 817−826.
(148) Sousa, S. F.; Fernandes, P. A.; Ramos, M. J. Molecular Dynamics Simulations: Difficulties, Solutions and Strategies for Treating Metalloenzymes. In *Kinetics and Dynamics*; Paneth, P., Dybala-Defratyka, A., Eds.; Springer Science+Business Media B.V.: New York, 2010; Vol. *12*, Chapter 11, pp 299−330.
(149) Leontyev, I.; Stuchebrukhov, A. Accounting for Electronic Polarization in Non-Polarizable Force Fields. *Phys. Chem. Chem. Phys.* **2011**, *13*, 2613−2626.
(150) Dommert, F.; Wendler, K.; Berger, R.; Delle Site, L.; Holm, C. Force Fields for Studying the Structure and Dynamics of Ionic Liquids: A Critical Review of Recent Developments. *ChemPhysChem* **2012**, *13*, 1625−1637.
(151) Riniker, S.; Allison, J. R.; van Gunsteren, W. F. On Developing Coarse-Grained Models for Biomolecular Simulation: A Review. *Phys. Chem. Chem. Phys.* **2012**, *14*, 12423−12430.
(152) Marrink, S. J.; Tieleman, D. P. Perspective on the Martini Model. *Chem. Soc. Rev.* **2013**, *42*, 6801−6822.
(153) Nechay, M. R.; Valdez, C. E.; Alexandrova, A. N. Computational Treatment of Metalloproteins. *J. Phys. Chem. B* **2015**, *119*, 5945−56.
(154) Li, W.; Wang, J.; Zhang, J.; Wang, W. Molecular Simulations of Metal-Coupled Protein Folding. *Curr. Opin. Struct. Biol.* **2015**, *30*, 25−31.
(155) Heinz, H.; Ramezani-Dakhel, H. Simulations of Inorganic−Bioorganic Interfaces to Discover New Materials: Insights, Comparisons to Experiment, Challenges, and Opportunities. *Chem. Soc. Rev.* **2016**, *45*, 412−448.
(156) Kmiecik, S.; Gront, D.; Kolinski, M.; Wieteska, L.; Dawid, A. E.; Kolinski, A. Coarse-Grained Protein Models and Their Applications. *Chem. Rev.* **2016**, *116*, 7898−7936.
(157) Cho, A. E.; Goddard, W. A., III. *Metalloproteins: Theory, Calculations, and Experiments*; CRC Press: Taylor & Francis Group: Boca Raton, FL, 2015.
(158) Halgren, T. A.; Damm, W. Polarizable Force Fields. *Curr. Opin. Struct. Biol.* **2001**, *11*, 236−242.
(159) Rick, S. W.; Stuart, S. J. Potentials and Algorithms for Incorporating Polarizability in Computer Simulations. In *Reviews in Computational Chemistry*; Lipkowitz, K. B., Boyd, D. B., Eds.; John Wiley & Sons, Inc.: Hoboken, NJ, 2002; Vol. *18*, pp 89−146.
(160) Ponder, J. W.; Case, D. A. Force Fields for Protein Simulations. *Adv. Protein Chem.* **2003**, *66*, 27−85.
(161) Mackerell, A. D. Empirical Force Fields for Biological Macromolecules: Overview and Issues. *J. Comput. Chem.* **2004**, *25*, 1584−1604.
(162) Friesner, R. A. Modeling Polarization in Proteins and Protein−Ligand Complexes: Methods and Preliminary Results. *Adv. Protein Chem.* **2005**, *72*, 79−104.
(163) Patel, S.; Brooks, C. L., III Fluctuating Charge Force Fields: Recent Developments and Applications from Small Molecules to Macromolecular Biological Systems. *Mol. Simul.* **2006**, *32*, 231−249.
(164) Gresh, N.; Cisneros, G. A.; Darden, T. A.; Piquemal, J.-P. Anisotropic, Polarizable Molecular Mechanics Studies of Inter-and Intramolecular Interactions and Ligand-Macromolecule Complexes. A Bottom-up Strategy. *J. Chem. Theory Comput.* **2007**, *3*, 1960−1986.
(165) Warshel, A.; Kato, M.; Pisliakov, A. V. Polarizable Force Fields: History, Test Cases, and Prospects. *J. Chem. Theory Comput.* **2007**, *3*, 2034−2045.
(166) Cieplak, P.; Dupradeau, F.-Y.; Duan, Y.; Wang, J. Polarization Effects in Molecular Mechanical Force Fields. *J. Phys.: Condens. Matter* **2009**, *21*, 333102.
(167) Lopes, P. E.; Roux, B.; MacKerell, A. D., Jr Molecular Modeling and Dynamics Studies with Explicit Inclusion of Electronic Polarizability: Theory and Applications. *Theor. Chem. Acc.* **2009**, *124*, 11−28.
(168) Russo, M. F.; van Duin, A. C. Atomistic-Scale Simulations of Chemical Reactions: Bridging from Quantum Chemistry to Engineering. *Nucl. Instrum. Methods Phys. Res., Sect. B* **2011**, *269*, 1549−1554.
(169) Gong, L. Development and Applications of the Abeem Fluctuating Charge Molecular Force Field in the Ion-Containing Systems. *Sci. China: Chem.* **2012**, *55*, 2471−2484.
(170) Lamoureux, G.; Orabi, E. A. Molecular Modelling of Cation−Π Interactions. *Mol. Simul.* **2012**, *38*, 704−722.
(171) Shin, Y. K.; Shan, T.-R.; Liang, T.; Noordhoek, M. J.; Sinnott, S. B.; Van Duin, A. C.; Phillpot, S. R. Variable Charge Many-Body Interatomic Potentials. *MRS Bull.* **2012**, *37*, 504−512.
(172) Liang, T.; Shin, Y. K.; Cheng, Y.-T.; Yilmaz, D. E.; Vishnu, K. G.; Verners, O.; Zou, C.; Phillpot, S. R.; Sinnott, S. B.; van Duin, A. C. Reactive Potentials for Advanced Atomistic Simulations. *Annu. Rev. Mater. Res.* **2013**, *43*, 109−129.
(173) Shi, Y.; Ren, P.; Schnieders, M.; Piquemal, J. P. Polarizable Force Fields for Biomolecular Modeling. In *Reviews in Computational Chemistry*; Parrill, A. L., Lipkowitz, K. B., Eds.; John Wiley & Sons, Inc.: Hoboken, NJ, 2015; Vol. *28*, pp 51−86.
(174) Vanommeslaeghe, K.; MacKerell, A. Charmm Additive and Polarizable Force Fields for Biophysics and Computer-Aided Drug Design. *Biochim. Biophys. Acta, Gen. Subj.* **2015**, *1850*, 861−871.
(175) Lemkul, J. A.; Huang, J.; Roux, B.; MacKerell, A. D., Jr An Empirical Polarizable Force Field Based on the Classical Drude Oscillator Model: Development History and Recent Applications. *Chem. Rev.* **2016**, *116*, 4983.
(176) Senftle, T. P.; Hong, S.; Islam, M. M.; Kylasa, S. B.; Zheng, Y.; Shin, Y. K.; Junkermeier, C.; Engel-Herbert, R.; Janik, M. J.; Aktulga, H. M. The Reaxff Reactive Force-Field: Development, Applications and Future Directions. *NPJ. Comput. Mater.* **2016**, *2*, 15011.

DOI: 10.1021/acs.chemrev.6b00440
Chem. Rev. 2017, 117, 1564−1686

(177) Landis, C. R.; Root, D. M.; Cleveland, T. Molecular Mechanics Force Fields for Modeling Inorganic and Organometallic Compounds. In *Reviews in Computational Chemistry*; Lipkowitz, K. B., Boyd, D. B., Eds.; John Wiley & Sons, Inc.: New York, 1995; Vol. *6*, pp 73−148.
(178) Deeth, R. J. The Ligand Field Molecular Mechanics Model and the Stereoelectronic Effects of D and S Electrons. *Coord. Chem. Rev.* **2001**, *212*, 11−34.
(179) Deeth, R. J.; Anastasi, A.; Diedrich, C.; Randell, K. Molecular Modelling for Transition Metal Complexes: Dealing with D-Electron Effects. *Coord. Chem. Rev.* **2009**, *253*, 795−816.
(180) Deeth, R. J. Molecular Mechanics for Transition Metal Centers: From Coordination Complexes to Metalloproteins. *Adv. Inorg. Chem.* **2010**, *62*, 1−39.
(181) Deeth, R. J. Molecular Modelling for Systems Containing Transition Metal Centres. In *Structure and Function*; Comba, P., Ed.; Springer Science+Business Media B.V.: New York, 2010; pp 21−51.
(182) Deeth, R. J. Transition Metal Systems. *Drug Design Strategies: Computational Techniques and Applications* **2012**, 27−55.
(183) Radom, L.; Schleyer, P. v. R.; Pople, J.; Hehre, W. Wiley: New York, 1986.
(184) Parr, R. G.; Yang, W. Oxford University Press: New York, 1989.
(185) Szabo, A.; Ostlund, N. S. *Modern Quantum Chemistry: Introduction to Advanced Electronic Structure Theory*; McGraw-Hill, Inc.: New York, 1989.
(186) Martin, R. L.; Hay, P. J. Relativistic Contributions to the Low-Lying Excitation Energies and Ionization Potentials of the Transition Metals. *J. Chem. Phys.* **1981**, *75*, 4539−4545.
(187) Cowan, R. D.; Griffin, D. C. Approximate Relativistic Corrections to Atomic Radial Wave Functions. *J. Opt. Soc. Am.* **1976**, *66*, 1010−1014.
(188) Bauschlicher, C. W., Jr; Siegbahn, P.; Pettersson, L. G. The Atomic States of Nickel. *Theor. Chim. Acta* **1988**, *74*, 479−491.
(189) Moore, C. E. Atomic Energy Levels, Nbs Circular No. 467; US Govt. Printing Office: Washington, DC, 1949.
(190) Zhao, S.; Li, Z.-H.; Wang, W.-N.; Liu, Z.-P.; Fan, K.-N.; Xie, Y.; Schaefer, H. F., III Is the Uniform Electron Gas Limit Important for Small Ag Clusters? Assessment of Different Density Functionals for Agn (N⩽4). *J. Chem. Phys.* **2006**, *124*, 184102.
(191) Paier, J.; Marsman, M.; Kresse, G. Why Does the B3lyp Hybrid Functional Fail for Metals? *J. Chem. Phys.* **2007**, *127*, 024103.
(192) Hartree, D. R. The Wave Mechanics of an Atom with a Non-Coulomb Central Field. Part I. Theory and Methods. *Math. Proc. Cambridge Philos. Soc.* **1928**, *24*, 89−110.
(193) Hartree, D. R. The Wave Mechanics of an Atom with a Non-Coulomb Central Field. Part Ii. Some Results and Discussion. *Math. Proc. Cambridge Philos. Soc.* **1928**, *24*, 111−132.
(194) Fock, V. Selfconsistent Field "Mit Austausch Für Natrium. *Eur. Phys. J. A* **1930**, *62*, 795−805.
(195) Slater, J. C. Note on Hartree's Method. *Phys. Rev.* **1930**, *35*, 210−211.
(196) Slater, J. C. A Simplification of the Hartree-Fock Method. *Phys. Rev.* **1951**, *81*, 385−390.
(197) Allured, V. S.; Kelly, C. M.; Landis, C. R. Shapes Empirical Force Field: New Treatment of Angular Potentials and Its Application to Square-Planar Transition-Metal Complexes. *J. Am. Chem. Soc.* **1991**, *113*, 1−12.
(198) Řezáč, J.; Hobza, P. Describing Noncovalent Interactions Beyond the Common Approximations: How Accurate Is the "Gold Standard," Ccsd (T) at the Complete Basis Set Limit? *J. Chem. Theory Comput.* **2013**, *9*, 2151−2155.
(199) Helgaker, T.; Ruden, T. A.; Jørgensen, P.; Olsen, J.; Klopper, W. A Priori Calculation of Molecular Properties to Chemical Accuracy. *J. Phys. Org. Chem.* **2004**, *17*, 913−933.
(200) Weaver, M. N.; Merz, K. M., Jr; Ma, D.; Kim, H. J.; Gagliardi, L. Calculation of Heats of Formation for Zn Complexes: Comparison of Density Functional Theory, Second Order Perturbation Theory, Coupled-Cluster and Complete Active Space Methods. *J. Chem. Theory Comput.* **2013**, *9*, 5277−5285.
(201) Roos, B. O. The Ground State Potential for the Chromium Dimer Revisited. *Collect. Czech. Chem. Commun.* **2003**, *68*, 265−274.
(202) Abrams, M. L.; Sherrill, C. D. Full Configuration Interaction Potential Energy Curves for the X1σg+, B1δg, and B′σ1g+ States of C2: A Challenge for Approximate Methods. *J. Chem. Phys.* **2004**, *121*, 9211−9219.
(203) Jiang, W.; DeYonker, N. J.; Wilson, A. K. Multireference Character for 3d Transition-Metal-Containing Molecules. *J. Chem. Theory Comput.* **2012**, *8*, 460−468.
(204) Wang, J.; Manivasagam, S.; Wilson, A. K. Multireference Character for 4d Transition Metal-Containing Molecules. *J. Chem. Theory Comput.* **2015**, *11*, 5865−5872.
(205) Weaver, M. N.; Yang, Y.; Merz, K. M., Jr Assessment of the Ccsd and Ccsd (T) Coupled-Cluster Methods in Calculating Heats of Formation for Zn Complexes. *J. Phys. Chem. A* **2009**, *113*, 10081−10088.
(206) Weaver, M. N.; Merz, K. M., Jr Assessment of the Ccsd and Ccsd (T) Coupled-Cluster Methods in Calculating Heats of Formation for Cu Complexes. *Mol. Phys.* **2009**, *107*, 1251−1259.
(207) Xu, X.; Zhang, W.; Tang, M.; Truhlar, D. G. Do Practical Standard Coupled Cluster Calculations Agree Better Than Kohn−Sham Calculations with Currently Available Functionals When Compared to the Best Available Experimental Data for Dissociation Energies of Bonds to 3 D Transition Metals? *J. Chem. Theory Comput.* **2015**, *11*, 2036−2052.
(208) Hyla-Kryspin, I.; Grimme, S. Comprehensive Study of the Thermochemistry of First-Row Transition Metal Compounds by Spin Component Scaled Mp2 and Mp3Methods. *Organometallics* **2004**, *23*, 5581−5592.
(209) Carlson, R. K.; Odoh, S. O.; Tereniak, S. J.; Lu, C. C.; Gagliardi, L. Can Multiconfigurational Self-Consistent Field Theory and Density Functional Theory Correctly Predict the Ground State of Metal−Metal-Bonded Complexes? *J. Chem. Theory Comput.* **2015**, *11*, 4093−4101.
(210) DeYonker, N. J.; Cundari, T. R.; Wilson, A. K. The Correlation Consistent Composite Approach (Ccca): An Alternative to the Gaussian-N Methods. *J. Chem. Phys.* **2006**, *124*, 114104.
(211) Pople, J. A.; Head-Gordon, M.; Fox, D. J.; Raghavachari, K.; Curtiss, L. A. Gaussian-1 Theory: A General Procedure for Prediction of Molecular Energies. *J. Chem. Phys.* **1989**, *90*, 5622−5629.
(212) Curtiss, L. A.; Jones, C.; Trucks, G. W.; Raghavachari, K.; Pople, J. A. Gaussian-1 Theory of Molecular Energies for Second-Row Compounds. *J. Chem. Phys.* **1990**, *93*, 2537−2545.
(213) Curtiss, L. A.; Raghavachari, K.; Trucks, G. W.; Pople, J. A. Gaussian-2 Theory for Molecular Energies of First-and Second-Row Compounds. *J. Chem. Phys.* **1991**, *94*, 7221−7230.
(214) Curtiss, L. A.; Raghavachari, K.; Redfern, P. C.; Rassolov, V.; Pople, J. A. Gaussian-3 (G3) Theory for Molecules Containing First and Second-Row Atoms. *J. Chem. Phys.* **1998**, *109*, 7764−7776.
(215) Curtiss, L. A.; Redfern, P. C.; Raghavachari, K. Gaussian-4 Theory. *J. Chem. Phys.* **2007**, *126*, 084108.
(216) Mayhall, N. J.; Raghavachari, K.; Redfern, P. C.; Curtiss, L. A. Investigation of Gaussian4 Theory for Transition Metal Thermochemistry. *J. Phys. Chem. A* **2009**, *113*, 5170−5175.
(217) DeYonker, N. J.; Grimes, T.; Yockel, S.; Dinescu, A.; Mintz, B.; Cundari, T. R.; Wilson, A. K. The Correlation-Consistent Composite Approach: Application to the G3/99 Test Set. *J. Chem. Phys.* **2006**, *125*, 104111.
(218) Ho, D. S.; DeYonker, N. J.; Wilson, A. K.; Cundari, T. R. Accurate Enthalpies of Formation of Alkali and Alkaline Earth Metal Oxides and Hydroxides: Assessment of the Correlation Consistent Composite Approach (Ccca). *J. Phys. Chem. A* **2006**, *110*, 9767−9770.
(219) DeYonker, N. J.; Ho, D. S.; Wilson, A. K.; Cundari, T. R. Computational S-Block Thermochemistry with the Correlation Consistent Composite Approach. *J. Phys. Chem. A* **2007**, *111*, 10776−10780.
(220) DeYonker, N. J.; Peterson, K. A.; Steyl, G.; Wilson, A. K.; Cundari, T. R. Quantitative Computational Thermochemistry of Transition Metal Species. *J. Phys. Chem. A* **2007**, *111*, 11269−11277.

DOI: 10.1021/acs.chemrev.6b00440
Chem. Rev. 2017, 117, 1564−1686

(221) DeYonker, N. J.; Williams, T. G.; Imel, A. E.; Cundari, T. R.; Wilson, A. K. Accurate Thermochemistry for Transition Metal Complexes from First-Principles Calculations. *J. Chem. Phys.* **2009**, *131*, 024106.
(222) Laury, M. L.; DeYonker, N. J.; Jiang, W.; Wilson, A. K. A Pseudopotential-Based Composite Method: The Relativistic Pseudopotential Correlation Consistent Composite Approach for Molecules Containing 4d Transition Metals (Y−Cd). *J. Chem. Phys.* **2011**, *135*, 214103.
(223) Thiel, W. Semiempirical Quantum−Chemical Methods. *Wiley Interdiscip. Rev. Comput. Mol. Sci.* **2014**, *4*, 145−157.
(224) Pople, J. A.; Segal, G. A. Approximate Self-Consistent Molecular Orbital Theory. Ii. Calculations with Complete Neglect of Differential Overlap. *J. Chem. Phys.* **1965**, *43*, S136−S151.
(225) Pople, J. A.; Segal, G. A. Approximate Self-Consistent Molecular Orbital Theory. Iii. Cndo Results for Ab2 and Ab3 Systems. *J. Chem. Phys.* **1966**, *44*, 3289−3296.
(226) Pople, J.; Beveridge, D.; Dobosh, P. Approximate Self-Consistent Molecular-Orbital Theory. V. Intermediate Neglect of Differential Overlap. *J. Chem. Phys.* **1967**, *47*, 2026−2033.
(227) Pople, J. A.; Santry, D. P.; Segal, G. A. Approximate Self-Consistent Molecular Orbital Theory. I. Invariant Procedures. *J. Chem. Phys.* **1965**, *43*, S129−S135.
(228) Ridley, J.; Zerner, M. An Intermediate Neglect of Differential Overlap Technique for Spectroscopy: Pyrrole and the Azines. *Theor. Chim. Acta* **1973**, *32*, 111−134.
(229) Ridley, J. E.; Zerner, M. C. Triplet States Via Intermediate Neglect of Differential Overlap: Benzene, Pyridine and the Diazines. *Theor. Chim. Acta* **1976**, *42*, 223−236.
(230) Bacon, A. D.; Zerner, M. C. An Intermediate Neglect of Differential Overlap Theory for Transition Metal Complexes: Fe, Co and Cu Chlorides. *Theor. Chim. Acta* **1979**, *53*, 21−54.
(231) Zerner, M. C.; Loew, G. H.; Kirchner, R. F.; Mueller-Westerhoff, U. T. An Intermediate Neglect of Differential Overlap Technique for Spectroscopy of Transition-Metal Complexes. Ferrocene. *J. Am. Chem. Soc.* **1980**, *102*, 589−599.
(232) Anderson, W. P.; Edwards, W. D.; Zerner, M. C. Calculated Spectra of Hydrated Ions of the First Transition-Metal Series. *Inorg. Chem.* **1986**, *25*, 2728−2732.
(233) Edwards, W. D.; Weiner, B.; Zerner, M. C. On the Low-Lying States and Electronic Spectroscopy of Iron (Ii) Porphine. *J. Am. Chem. Soc.* **1986**, *108*, 2196−2204.
(234) Anderson, W. P.; Cundari, T. R.; Drago, R. S.; Zerner, M. C. Utility of the Semiempirical Indo/1 Method for the Calculation of the Geometries of Second-Row Transition-Metal Species. *Inorg. Chem.* **1990**, *29*, 1−3.
(235) Kotzian, M.; Rösch, N.; Zerner, M. Intermediate Neglect of Differential Overlap Spectroscopic Studies on Lanthanide Complexes. *Theor. Chim. Acta* **1992**, *81*, 201−222.
(236) Cory, M. G.; Köstlmeier, S.; Kotzian, M.; Rösch, N.; Zerner, M. C. An Intermediate Neglect of Differential Overlap Technique for Actinide Compounds. *J. Chem. Phys.* **1994**, *100*, 1353−1365.
(237) Voityuk, A. A. Intermediate Neglect of Differential Overlap for Spectroscopy. *Wiley Interdiscip. Rev. Comput. Mol. Sci.* **2013**, *3*, 515−527.
(238) Filatov, M. J.; Gritsenko, O. V.; Zhidomirov, G. M. Cndo-S2—a Semiempirical Scf Mo Method for Transition Metal Organometallics. *Theor. Chim. Acta* **1987**, *72*, 211−222.
(239) Nieke, C.; Reinhold, J. Application of the Nddo Method to Transition Metal Compounds. *Theor. Chim. Acta* **1984**, *65*, 99−108.
(240) Filatov, M. J.; Zilberberg, I. L.; Zhidomirov, G. M. Nddo/Mc: A New Semiempirical Scfmo Method for Transition Metal Complexes. *Int. J. Quantum Chem.* **1992**, *44*, 565−585.
(241) Jug, K.; Nanda, D. Sindo1 Ii. Application to Ground States of Molecules Containing Carbon, Nitrogen and Oxygen Atoms. *Theor. Chim. Acta* **1980**, *57*, 107−130.
(242) Jug, K.; Nanda, D. Sindo1 Iii. Application to Ground States of Molecules Containing Fluorine, Boron, Beryllium and Lithium Atoms. *Theor. Chim. Acta* **1980**, *57*, 131−144.
(243) Nanda, D.; Jug, K. Sindo1. A Semiempirical Scf Mo Method for Molecular Binding Energy and Geometry I. Approximations and Parametrization. *Theor. Chim. Acta* **1980**, *57*, 95−106.
(244) Li, J.; De Mello, P. C.; Jug, K. Extension of Sindo1 to Transition Metal Compounds. *J. Comput. Chem.* **1992**, *13*, 85−92.
(245) Ahlswede, B.; Jug, K. Consistent Modifications of Sindo1: I. Approximations and Parameters. *J. Comput. Chem.* **1999**, *20*, 563−571.
(246) Ahlswede, B.; Jug, K. Consistent Modifications of Sindo1: Ii. Applications to First-and Second-Row Elements. *J. Comput. Chem.* **1999**, *20*, 572−578.
(247) Jug, K.; Geudtner, G.; Homann, T. Msindo Parameterization for Third-Row Main Group Elements. *J. Comput. Chem.* **2000**, *21*, 974−987.
(248) Bredow, T.; Geudtner, G.; Jug, K. Msindo Parameterization for Third-Row Transition Metals. *J. Comput. Chem.* **2001**, *22*, 861−887.
(249) Baird, N. C.; Dewar, M. J. Ground States of Σ-Bonded Molecules. Iv. The Mindo Method and Its Application to Hydrocarbons. *J. Chem. Phys.* **1969**, *50*, 1262−1274.
(250) Dewar, M. J.; Haselbach, E. Ground States Of. Sigma.-Bonded Molecules. Ix. Mindo [Modified Intermediate Neglect of Differential Overlap]/2 Method. *J. Am. Chem. Soc.* **1970**, *92*, 590−598.
(251) Bingham, R. C.; Dewar, M. J.; Lo, D. H. Ground States of Molecules. Xxv. Mindo/3. Improved Version of the Mindo Semiempirical Scf-Mo Method. *J. Am. Chem. Soc.* **1975**, *97*, 1285−1293.
(252) Dewar, M. J.; Thiel, W. Ground States of Molecules. 38. The Mndo Method. Approximations and Parameters. *J. Am. Chem. Soc.* **1977**, *99*, 4899−4907.
(253) Dewar, M. J.; Grady, G. L.; Stewart, J. J. Mndo Calculations for Compounds Containing Tim. *J. Am. Chem. Soc.* **1984**, *106*, 6771−6773.
(254) Dewar, M. J.; Grady, G. L.; Merz, K. M., Jr; Stewart, J. J. Mndo Calculations for Compounds Containing Mercury. *Organometallics* **1985**, *4*, 1964−1966.
(255) Dewar, M. J.; Merz, K. M., Jr Ground States of Molecules. Part 84. Mndo Calculations for Compounds Containing Zinc. *Organometallics* **1986**, *5*, 1494−1496.
(256) Thiel, W.; Voityuk, A. A. Extension of the Mndo Formalism to D Orbitals: Integral Approximations and Preliminary Numerical Results. *Theor. Chim. Acta* **1992**, *81*, 391−404.
(257) Thiel, W.; Voityuk, A. A. Extension of the Mndo Formalism Tod Orbitals: Integral Approximations and Preliminary Numerical Results. *Theor. Chim. Acta* **1996**, *93*, 315−315.
(258) Thiel, W.; Voityuk, A. A. Extension of Mndo to D Orbitals: Parameters and Results for the Second-Row Elements and for the Zinc Group. *J. Phys. Chem.* **1996**, *100*, 616−626.
(259) Dewar, M. J.; Zoebisch, E. G.; Healy, E. F.; Stewart, J. J. Development and Use of Quantum Mechanical Molecular Models. 76. Am1: A New General Purpose Quantum Mechanical Molecular Model. *J. Am. Chem. Soc.* **1985**, *107*, 3902−3909.
(260) Dewar, M. J.; Merz, K. M., Jr Am1 Parameters for Zinc. *Organometallics* **1988**, *7*, 522−524.
(261) Voityuk, A. A.; Rösch, N. Am1/D Parameters for Molybdenum. *J. Phys. Chem. A* **2000**, *104*, 4089−4094.
(262) Imhof, P.; Noé, F.; Fischer, S.; Smith, J. C. Am1/D Parameters for Magnesium in Metalloenzymes. *J. Chem. Theory Comput.* **2006**, *2*, 1050−1056.
(263) Winget, P.; Clark, T. Am1* Parameters for Aluminum, Silicon, Titanium and Zirconium. *J. Mol. Model.* **2005**, *11*, 439−456.
(264) Kayi, H.; Clark, T. Am1* Parameters for Copper and Zinc. *J. Mol. Model.* **2007**, *13*, 965−979.
(265) Kayi, H.; Clark, T. Am1* Parameters for Vanadium and Chromium. *J. Mol. Model.* **2009**, *15*, 1253−1269.
(266) Kayi, H. Am1* Parameters for Gold. *J. Mol. Model.* **2010**, *16*, 1029−1038.
(267) Kayi, H.; Clark, T. Am1* Parameters for Cobalt and Nickel. *J. Mol. Model.* **2010**, *16*, 29−47.
(268) Kayi, H.; Clark, T. Am1* Parameters for Manganese and Iron. *J. Mol. Model.* **2010**, *16*, 1109−1126.

DOI: 10.1021/acs.chemrev.6b00440
Chem. Rev. 2017, 117, 1564−1686

(269) Kayi, H.; Clark, T. Am1* Parameters for Palladium and Silver. *J. Mol. Model.* **2011**, *17*, 2585−2600.
(270) Stewart, J. J. Optimization of Parameters for Semiempirical Methods I. Method. *J. Comput. Chem.* **1989**, *10*, 209−220.
(271) Stewart, J. J. Optimization of Parameters for Semiempirical Methods Ii. Applications. *J. Comput. Chem.* **1989**, *10*, 221−264.
(272) Stewart, J. J. Optimization of Parameters for Semiempirical Methods. Iii Extension of Pm3 to Be, Mg, Zn, Ga, Ge, as, Se, Cd, in, Sn, Sb, Te, Hg, Tl, Pb, and Bi. *J. Comput. Chem.* **1991**, *12*, 320−341.
(273) Ignatov, S.; Razuvaev, A.; Kokorev, V.; Alexandrov, Y. A. Extension of the Pm3Method on S, P, D Basis. Test Calculations on Organochromium Compounds. *J. Phys. Chem.* **1996**, *100*, 6354−6358.
(274) Børve, K. J.; Jensen, V. R.; Karlsen, T.; Støvneng, J. A.; Swang, O. Evaluation of Pm3(Tm) as a Geometry Generator in Theoretical Studies of Transition-Metal-Based Catalysts for Polymerizing Olefins. *J. Mol. Model.* **1997**, *3*, 193−202.
(275) Cundari, T. R.; Deng, J. Pm3 (Tm) Analysis of Transition-Metal Complexes. *J. Chem. Inf. Comput. Sci.* **1999**, *39*, 376−381.
(276) Stewart, J. J. Optimization of Parameters for Semiempirical Methods V: Modification of Nddo Approximations and Application to 70 Elements. *J. Mol. Model.* **2007**, *13*, 1173−1213.
(277) Stewart, J. J. Optimization of Parameters for Semiempirical Methods Vi: More Modifications to the Nddo Approximations and Re-Optimization of Parameters. *J. Mol. Model.* **2013**, *19*, 1−32.
(278) Seitz, M.; Alzakhem, N. Computational Estimation of Lanthanoid− Water Bond Lengths by Semiempirical Methods. *J. Chem. Inf. Model.* **2010**, *50*, 217−220.
(279) Daw, M. S.; Baskes, M. I. Semiempirical, Quantum Mechanical Calculation of Hydrogen Embrittlement in Metals. *Phys. Rev. Lett.* **1983**, *50*, 1285−1288.
(280) Finnis, M.; Sinclair, J. A Simple Empirical N-Body Potential for Transition Metals. *Philos. Mag. A* **1984**, *50*, 45−55.
(281) Sutton, A.; Chen, J. Long-Range Finnis-Sinclair Potentials. *Philos. Mag. Lett.* **1990**, *61*, 139−146.
(282) Cleri, F.; Rosato, V. Tight-Binding Potentials for Transition Metals and Alloys. *Phys. Rev. B: Condens. Matter Mater. Phys.* **1993**, *48*, 22−33.
(283) Daw, M. S.; Baskes, M. I. Embedded-Atom Method: Derivation and Application to Impurities, Surfaces, and Other Defects in Metals. *Phys. Rev. B: Condens. Matter Mater. Phys.* **1984**, *29*, 6443−6453.
(284) Foiles, S. M.; Baskes, M. I.; Daw, M. S. Embedded-Atom-Method Functions for the Fcc Metals Cu, Ag, Au, Ni, Pd, Pt, and Their Alloys. *Phys. Rev. B: Condens. Matter Mater. Phys.* **1986**, *33*, 7983−7991.
(285) Seifert, G.; Eschrig, H.; Bieger, W. An Approximation Variant of Lcao-X-Alpha Methods. *Z. Phys. Chem.-Leipzig* **1986**, *267*, 529−539.
(286) Elstner, M.; Porezag, D.; Jungnickel, G.; Elsner, J.; Haugk, M.; Frauenheim, T.; Suhai, S.; Seifert, G. Self-Consistent-Charge Density-Functional Tight-Binding Method for Simulations of Complex Materials Properties. *Phys. Rev. B: Condens. Matter Mater. Phys.* **1998**, *58*, 7260.
(287) Elstner, M.; Cui, Q.; Munih, P.; Kaxiras, E.; Frauenheim, T.; Karplus, M. Modeling Zinc in Biomolecules with the Self Consistent Charge-Density Functional Tight Binding (Scc-Dftb) Method: Applications to Structural and Energetic Analysis. *J. Comput. Chem.* **2003**, *24*, 565−581.
(288) Sattelmeyer, K. W.; Tirado-Rives, J.; Jorgensen, W. L. Comparison of Scc-Dftb and Nddo-Based Semiempirical Molecular Orbital Methods for Organic Molecules. *J. Phys. Chem. A* **2006**, *110*, 13551−13559.
(289) Zheng, G.; Witek, H. A.; Bobadova-Parvanova, P.; Irle, S.; Musaev, D. G.; Prabhakar, R.; Morokuma, K.; Lundberg, M.; Elstner, M.; Köhler, C. Parameter Calibration of Transition-Metal Elements for the Spin-Polarized Self-Consistent-Charge Density-Functional Tight-Binding (Dftb) Method: Sc, Ti, Fe, Co, and Ni. *J. Chem. Theory Comput.* **2007**, *3*, 1349−1367.
(290) Bruschi, M.; Bertini, L.; Bonačić-Koutecký, V.; De Gioia, L.; Mitrić, R.; Zampella, G.; Fantucci, P. Speciation of Copper−Peptide Complexes in Water Solution Using Dftb and Dft Approaches: Case of the [Cu (Hggg) (Py)] Complex. *J. Phys. Chem. B* **2012**, *116*, 6250−6260.
(291) Gaus, M.; Cui, Q.; Elstner, M. Dftb3: Extension of the Self-Consistent-Charge Density-Functional Tight-Binding Method (Scc-Dftb). *J. Chem. Theory Comput.* **2011**, *7*, 931−948.
(292) Gaus, M.; Goez, A.; Elstner, M. Parametrization and Benchmark of Dftb3 for Organic Molecules. *J. Chem. Theory Comput.* **2013**, *9*, 338−354.
(293) Kubillus, M.; Kubař, T. s.; Gaus, M.; Řezáč, J.; Elstner, M. Parameterization of the Dftb3Method for Br, Ca, Cl, F, I, K, and Na in Organic and Biological Systems. *J. Chem. Theory Comput.* **2015**, *11*, 332−342.
(294) Lu, X.; Gaus, M.; Elstner, M.; Cui, Q. Parametrization of Dftb3/3ob for Magnesium and Zinc for Chemical and Biological Applications. *J. Phys. Chem. B* **2015**, *119*, 1062−1082.
(295) Gaus, M.; Jin, H.; Demapan, D.; Christensen, A. S.; Goyal, P.; Elstner, M.; Cui, Q. Dftb3 Parametrization for Copper: The Importance of Orbital Angular Momentum Dependence of Hubbard Parameters. *J. Chem. Theory Comput.* **2015**, *11*, 4205−4219.
(296) Christensen, A. S.; Elstner, M.; Cui, Q. Improving Intermolecular Interactions in Dftb3 Using Extended Polarization from Chemical-Potential Equalization. *J. Chem. Phys.* **2015**, *143*, 084123.
(297) Lukose, B.; Supronowicz, B., St; Petkov, P.; Frenzel, J.; Kuc, A. B.; Seifert, G.; Vayssilov, G. N.; Heine, T. Structural Properties of Metal-Organic Frameworks within the Density-Functional Based Tight-Binding Method. *Phys. Status Solidi B* **2012**, *249*, 335−342.
(298) Fermi, E. Un Metodo Statistico Per La Determinazione Di Alcune Priorieta Dell'atome. *Rend. Accad. Naz. Lincei* **1927**, *6*, 602−607.
(299) Thomas, L. H. The Calculation of Atomic Fields. *Math. Proc. Cambridge Philos. Soc.* **1927**, *23*, 542−548.
(300) Hohenberg, P.; Kohn, W. Inhomogeneous Electron Gas. *Phys. Rev.* **1964**, *136*, B864−B871.
(301) Kohn, W.; Sham, L. J. Self-Consistent Equations Including Exchange and Correlation Effects. *Phys. Rev.* **1965**, *140*, A1133−A1138.
(302) Perdew, J. P.; Schmidt, K. Jacob's Ladder of Density Functional Approximations for the Exchange-Correlation Energy. *AIP Conf. Proc.*; IOP Institute of Physics Publishing Ltd.: 2001; Vol. *577*, pp 1−20.
(303) Becke, A. D. Density-Functional Thermochemistry. Iii. The Role of Exact Exchange. *J. Chem. Phys.* **1993**, *98*, 5648−5652.
(304) Perdew, J. P.; Burke, K.; Ernzerhof, M. Generalized Gradient Approximation Made Simple. *Phys. Rev. Lett.* **1996**, *77*, 3865.
(305) Faver, J. C.; Benson, M. L.; He, X.; Roberts, B. P.; Wang, B.; Marshall, M. S.; Kennedy, M. R.; Sherrill, C. D.; Merz, K. M., Jr Formal Estimation of Errors in Computed Absolute Interaction Energies of Protein− Ligand Complexes. *J. Chem. Theory Comput.* **2011**, *7*, 790−797.
(306) Luo, S.; Truhlar, D. G. How Evenly Can Approximate Density Functionals Treat the Different Multiplicities and Ionization States of 4d Transition Metal Atoms? *J. Chem. Theory Comput.* **2012**, *8*, 4112−4126.
(307) Zhang, W.; Truhlar, D. G.; Tang, M. Tests of Exchange-Correlation Functional Approximations against Reliable Experimental Data for Average Bond Energies of 3d Transition Metal Compounds. *J. Chem. Theory Comput.* **2013**, *9*, 3965−3977.
(308) Jensen, K. P.; Roos, B. O.; Ryde, U. Performance of Density Functionals for First Row Transition Metal Systems. *J. Chem. Phys.* **2007**, *126*, 014103.
(309) Luo, S.; Averkiev, B.; Yang, K. R.; Xu, X.; Truhlar, D. G. Density Functional Theory of Open-Shell Systems. The 3d-Series Transition-Metal Atoms and Their Cations. *J. Chem. Theory Comput.* **2014**, *10*, 102−121.
(310) Gorelsky, S. I. Complexes with a Single Metal−Metal Bond as a Sensitive Probe of Quality of Exchange-Correlation Functionals. *J. Chem. Theory Comput.* **2012**, *8*, 908−914.

DOI: 10.1021/acs.chemrev.6b00440
Chem. Rev. 2017, 117, 1564−1686

(311) Schultz, N. E.; Zhao, Y.; Truhlar, D. G. Databases for Transition Element Bonding: Metal-Metal Bond Energies and Bond Lengths and Their Use to Test Hybrid, Hybrid Meta, and Meta Density Functionals and Generalized Gradient Approximations. *J. Phys. Chem. A* **2005**, *109*, 4388−4403.
(312) Bühl, M.; Kabrede, H. Geometries of Transition-Metal Complexes from Density-Functional Theory. *J. Chem. Theory Comput.* **2006**, *2*, 1282−1290.
(313) Tekarli, S. M.; Drummond, M. L.; Williams, T. G.; Cundari, T. R.; Wilson, A. K. Performance of Density Functional Theory for 3d Transition Metal-Containing Complexes: Utilization of the Correlation Consistent Basis Sets. *J. Phys. Chem. A* **2009**, *113*, 8607−8614.
(314) Laury, M. L.; Wilson, A. K. Performance of Density Functional Theory for Second Row (4 D) Transition Metal Thermochemistry. *J. Chem. Theory Comput.* **2013**, *9*, 3939−3946.
(315) Weymuth, T.; Couzijn, E. P.; Chen, P.; Reiher, M. New Benchmark Set of Transition-Metal Coordination Reactions for the Assessment of Density Functionals. *J. Chem. Theory Comput.* **2014**, *10*, 3092−3103.
(316) Riley, K. E.; Merz, K. M., Jr Assessment of Density Functional Theory Methods for the Computation of Heats of Formation and Ionization Potentials of Systems Containing Third Row Transition Metals. *J. Phys. Chem. A* **2007**, *111*, 6044−6053.
(317) Liu, C.; Peterson, C.; Wilson, A. K. C−O Bond Cleavage of Dimethyl Ether by Transition Metal Ions: A Systematic Study on Catalytic Properties of Metals and Performance of Dft Functionals. *J. Phys. Chem. A* **2013**, *117*, 5140−5148.
(318) Shil, S.; Bhattacharya, D.; Sarkar, S.; Misra, A. Performance of the Widely Used Minnesota Density Functionals for the Prediction of Heat of Formations, Ionization Potentials of Some Benchmarked First Row Transition Metal Complexes. *J. Phys. Chem. A* **2013**, *117*, 4945−4955.
(319) Zhao, Y.; Truhlar, D. G. Comparative Assessment of Density Functional Methods for 3d Transition-Metal Chemistry. *J. Chem. Phys.* **2006**, *124*, 224105.
(320) Furche, F.; Perdew, J. P. The Performance of Semilocal and Hybrid Density Functionals in 3d Transition-Metal Chemistry. *J. Chem. Phys.* **2006**, *124*, 044103.
(321) Yang, Y.; Weaver, M. N.; Merz, K. M., Jr Assessment of the "6-31+ G**+ Lanl2dz" Mixed Basis Set Coupled with Density Functional Theory Methods and the Effective Core Potential: Prediction of Heats of Formation and Ionization Potentials for First-Row-Transition-Metal Complexes. *J. Phys. Chem. A* **2009**, *113*, 9843−9851.
(322) Zhao, Y.; Truhlar, D. G. The M06 Suite of Density Functionals for Main Group Thermochemistry, Thermochemical Kinetics, Noncovalent Interactions, Excited States, and Transition Elements: Two New Functionals and Systematic Testing of Four M06-Class Functionals and 12 Other Functionals. *Theor. Chem. Acc.* **2008**, *120*, 215−241.
(323) Alipour, M. Validation of Double-Hybrid Density Functionals for Electric Response Properties of Transition-Metal Systems: A New Paradigm Based on Physical Considerations. *J. Phys. Chem. A* **2013**, *117*, 2884−2890.
(324) Yu, H. S.; Zhang, W.; Verma, P.; He, X.; Truhlar, D. G. Nonseparable Exchange−Correlation Functional for Molecules, Including Homogeneous Catalysis Involving Transition Metals. *Phys. Chem. Chem. Phys.* **2015**, *17*, 12146−12160.
(325) Janthon, P.; Luo, S.; Kozlov, S. M.; Viñes, F.; Limtrakul, J.; Truhlar, D. G.; Illas, F. Bulk Properties of Transition Metals: A Challenge for the Design of Universal Density Functionals. *J. Chem. Theory Comput.* **2014**, *10*, 3832−3839.
(326) Jiang, W.; Laury, M. L.; Powell, M.; Wilson, A. K. Comparative Study of Single and Double Hybrid Density Functionals for the Prediction of 3d Transition Metal Thermochemistry. *J. Chem. Theory Comput.* **2012**, *8*, 4102−4111.
(327) Janthon, P.; Kozlov, S. M.; Viñes, F.; Limtrakul, J.; Illas, F. Establishing the Accuracy of Broadly Used Density Functionals in Describing Bulk Properties of Transition Metals. *J. Chem. Theory Comput.* **2013**, *9*, 1631−1640.
(328) Waller, M. P.; Braun, H.; Hojdis, N.; Bühl, M. Geometries of Second-Row Transition-Metal Complexes from Density-Functional Theory. *J. Chem. Theory Comput.* **2007**, *3*, 2234−2242.
(329) Grimmel, S.; Schoendorff, G.; Wilson, A. K. Gauging the Performance of Density Functionals for Lanthanide-Containing Molecules. *J. Chem. Theory Comput.* **2016**, *12*, 1259−1266.
(330) White, S. R. Density Matrix Formulation for Quantum Renormalization Groups. *Phys. Rev. Lett.* **1992**, *69*, 2863.
(331) White, S. R. Density-Matrix Algorithms for Quantum Renormalization Groups. *Phys. Rev. B: Condens. Matter Mater. Phys.* **1993**, *48*, 10345.
(332) Wilson, K. G. The Renormalization Group: Critical Phenomena and the Kondo Problem. *Rev. Mod. Phys.* **1975**, *47*, 773.
(333) Wilson, K. G. The Renormalization Group and Critical Phenomena. *Rev. Mod. Phys.* **1983**, *55*, 583.
(334) Chan, G. K.-L.; Head-Gordon, M. Highly Correlated Calculations with a Polynomial Cost Algorithm: A Study of the Density Matrix Renormalization Group. *J. Chem. Phys.* **2002**, *116*, 4462−4476.
(335) Daul, S.; Ciofini, I.; Daul, C.; White, S. R. Full-Ci Quantum Chemistry Using the Density Matrix Renormalization Group. *Int. J. Quantum Chem.* **2000**, *79*, 331−342.
(336) Zgid, D.; Nooijen, M. The Density Matrix Renormalization Group Self-Consistent Field Method: Orbital Optimization with the Density Matrix Renormalization Group Method in the Active Space. *J. Chem. Phys.* **2008**, *128*, 144116.
(337) White, S. R.; Noack, R. Real-Space Quantum Renormalization Groups. *Phys. Rev. Lett.* **1992**, *68*, 3487.
(338) Nishino, T. Density Matrix Renormalization Group Method for 2d Classical Models. *J. Phys. Soc. Jpn.* **1995**, *64*, 3598−3601.
(339) Fano, G.; Ortolani, F.; Ziosi, L. The Density Matrix Renormalization Group Method: Application to the Ppp Model of a Cyclic Polyene Chain. *J. Chem. Phys.* **1998**, *108*, 9246−9252.
(340) White, S. R.; Martin, R. L. Ab Initio Quantum Chemistry Using the Density Matrix Renormalization Group. *J. Chem. Phys.* **1999**, *110*, 4127−4130.
(341) Marti, K. H.; Ondík, I. M.; Moritz, G.; Reiher, M. Density Matrix Renormalization Group Calculations on Relative Energies of Transition Metal Complexes and Clusters. *J. Chem. Phys.* **2008**, *128*, 014104.
(342) Kurashige, Y.; Yanai, T. High-Performance Ab Initio Density Matrix Renormalization Group Method: Applicability to Large-Scale Multireference Problems for Metal Compounds. *J. Chem. Phys.* **2009**, *130*, 234114.
(343) Yan, S.; Huse, D. A.; White, S. R. Spin-Liquid Ground State of the S= 1/2 Kagome Heisenberg Antiferromagnet. *Science* **2011**, *332*, 1173−1176.
(344) Kurashige, Y.; Chan, G. K.-L.; Yanai, T. Entangled Quantum Electronic Wavefunctions of the Mn4cao5 Cluster in Photosystem Ii. *Nat. Chem.* **2013**, *5*, 660−666.
(345) Sharma, S.; Sivalingam, K.; Neese, F.; Chan, G. K.-L. Low-Energy Spectrum of Iron−Sulfur Clusters Directly from Many-Particle Quantum Mechanics. *Nat. Chem.* **2014**, *6*, 927−933.
(346) Olivares-Amaya, R.; Hu, W.; Nakatani, N.; Sharma, S.; Yang, J.; Chan, G. K.-L. The Ab-Initio Density Matrix Renormalization Group in Practice. *J. Chem. Phys.* **2015**, *142*, 034102.
(347) Neese, F. The Orca Program System. *Wiley Interdiscip. Rev. Comput. Mol. Sci.* **2012**, *2*, 73−78.
(348) Krylov, A. I.; Gill, P. M. Q-Chem: An Engine for Innovation. *Wiley Interdiscip. Rev. Comput. Mol. Sci.* **2013**, *3*, 317−326.
(349) Werner, H. J.; Knowles, P. J.; Knizia, G.; Manby, F. R.; Schütz, M. Molpro: A General-Purpose Quantum Chemistry Program Package. *Wiley Interdiscip. Rev. Comput. Mol. Sci.* **2012**, *2*, 242−253.
(350) Pauling, L. *The Nature of the Chemical Bond*, 3rd ed.; Cornell University Press: Ithaca, NY, 1960.
(351) Glendening, E. D.; Landis, C. R.; Weinhold, F. Natural Bond Orbital Methods. *Wiley Interdiscip. Rev. Comput. Mol. Sci.* **2012**, *2*, 1−42.

DOI: 10.1021/acs.chemrev.6b00440
Chem. Rev. 2017, 117, 1564−1686

(352) Glendening, E. D.; Weinhold, F. Natural Resonance Theory: I. General Formalism. *J. Comput. Chem.* **1998**, *19*, 593−609.
(353) Glendening, E. D.; Weinhold, F. Natural Resonance Theory: Ii. Natural Bond Order and Valency. *J. Comput. Chem.* **1998**, *19*, 610−627.
(354) Glendening, E. D.; Badenhoop, J. K.; Weinhold, F. Natural Resonance Theory: Iii. Chemical Applications. *J. Comput. Chem.* **1998**, *19*, 628−646.
(355) Goddard, W. A., III; Dunning, T. H., Jr; Hunt, W. J.; Hay, P. J. Generalized Valence Bond Description of Bonding in Low-Lying States of Molecules. *Acc. Chem. Res.* **1973**, *6*, 368−376.
(356) Ohanessian, G.; Goddard, W. A., III Valence-Bond Concepts in Transition Metals: Metal Hydride Diatomic Cations. *Acc. Chem. Res.* **1990**, *23*, 386−392.
(357) Åqvist, J.; Warshel, A. Simulation of Enzyme Reactions Using Valence Bond Force Fields and Other Hybrid Quantum/Classical Approaches. *Chem. Rev.* **1993**, *93*, 2523−2544.
(358) Maupin, C. M.; McKenna, R.; Silverman, D. N.; Voth, G. A. Elucidation of the Proton Transport Mechanism in Human Carbonic Anhydrase Ii. *J. Am. Chem. Soc.* **2009**, *131*, 7598−7608.
(359) Maupin, C. M.; Castillo, N.; Taraphder, S.; Tu, C.; McKenna, R.; Silverman, D. N.; Voth, G. A. Chemical Rescue of Enzymes: Proton Transfer in Mutants of Human Carbonic Anhydrase Ii. *J. Am. Chem. Soc.* **2011**, *133*, 6223−6234.
(360) Wu, W.; Su, P.; Shaik, S.; Hiberty, P. C. Classical Valence Bond Approach by Modern Methods. *Chem. Rev.* **2011**, *111*, 7557−7593.
(361) Cundari, T. R.; Leza, H. A. R.; Grimes, T.; Steyl, G.; Waters, A.; Wilson, A. K. Calculation of the Enthalpies of Formation for Transition Metal Complexes. *Chem. Phys. Lett.* **2005**, *401*, 58−61.
(362) Williams, T. G.; Wilson, A. K. Importance of the Quality of Metal and Ligand Basis Sets in Transition Metal Species. *J. Chem. Phys.* **2008**, *129*, 054108.
(363) Xu, X.; Truhlar, D. G. Performance of Effective Core Potentials for Density Functional Calculations on 3d Transition Metals. *J. Chem. Theory Comput.* **2012**, *8*, 80−90.
(364) Amin, E. A.; Truhlar, D. G. Zn Coordination Chemistry: Development of Benchmark Suites for Geometries, Dipole Moments, and Bond Dissociation Energies and Their Use to Test and Validate Density Functionals and Molecular Orbital Theory. *J. Chem. Theory Comput.* **2008**, *4*, 75−85.
(365) Jiang, J.; Wu, Y.; Wang, Z.-X.; Wu, C. Assessing the Performance of Popular Quantum Mechanics and Molecular Mechanics Methods and Revealing the Sequence-Dependent Energetic Features Using 100 Tetrapeptide Models. *J. Chem. Theory Comput.* **2010**, *6*, 1199−1209.
(366) Faver, J. C.; Benson, M. L.; He, X.; Roberts, B. P.; Wang, B.; Marshall, M. S.; Sherrill, C. D.; Merz, K. M., Jr The Energy Computation Paradox and Ab Initio Protein Folding. *PLoS One* **2011**, *6*, e18868.
(367) Car, R.; Parrinello, M. Unified Approach for Molecular Dynamics and Density-Functional Theory. *Phys. Rev. Lett.* **1985**, *55*, 2471−2474.
(368) Wang, L.-P.; Titov, A.; McGibbon, R.; Liu, F.; Pande, V. S.; Martínez, T. J. Discovering Chemistry with an Ab Initio Nanoreactor. *Nat. Chem.* **2014**, *6*, 1044−1048.
(369) Hirschfelder, J.; Ewell, R. Roebuck, J., Determination of Intermolecular Forces from the Joule-Thomson Coefficients. *J. Chem. Phys.* **1938**, *6*, 205−218.
(370) Born, M.; Mayer, J. E. Zur Gittertheorie Der Ionenkristalle. *Eur. Phys. J. A* **1932**, *75*, 1−18.
(371) Mie, G. Zur Kinetischen Theorie Der Einatomigen Körper. *Ann. Phys. (Berlin, Ger.)* **1903**, *316*, 657−697.
(372) Ewald, P. P. Die Berechnung Optischer Und Elektrostatischer Gitterpotentiale. *Ann. Phys. (Berlin, Ger.)* **1921**, *369*, 253−287.
(373) Darden, T.; York, D.; Pedersen, L. Particle Mesh Ewald: An N·Log(N) Method for Ewald Sums in Large Systems. *J. Chem. Phys.* **1993**, *98*, 10089−10092.
(374) Jones, J. E. On the Determination of Molecular Fields. I. From the Variation of the Viscosity of a Gas with Temperature. *Proc. R. Soc. London, Ser. A* **1924**, *106*, 441−462.
(375) Jones, J. E. On the Determination of Molecular Fields. Ii. From the Equation of State of a Gas. *Proc. R. Soc. London, Ser. A* **1924**, *106*, 463−477.
(376) London, F. Zur Theorie Und Systematik Der Molekularkräfte. *Eur. Phys. J. A* **1930**, *63*, 245−279.
(377) Slater, J. C.; Kirkwood, J. G. The Van Der Waals Forces in Gases. *Phys. Rev.* **1931**, *37*, 682−697.
(378) Buckingham, R. A. The Classical Equation of State of Gaseous Helium, Neon and Argon. *Proc. R. Soc. London, Ser. A* **1938**, *168*, 264−283.
(379) Born, M.; Landé, A. Ueber Die Absolute Berechnung Der Kristalleigenschaften Mit Hilfe Bohrscher Atommodelle. *Preuss. Akad.* **1918**, *45*, 1048−1068.
(380) Pauling, L. *Linus Pauling Selected Scientific Papers, Vol. 1 Physical Sciences*; World Scientific Publishing Co. Pte. Ltd.: Singapore, 2001; Vol. *1*.
(381) Mayer, J. E. Dispersion and Polarizability and the Van Der Waals Potential in the Alkali Halides. *J. Chem. Phys.* **1933**, *1*, 270−279.
(382) Margenau, H. The Role of Quadrupole Forces in Van Der Waals Attractions. *Phys. Rev.* **1931**, *38*, 747−756.
(383) Huggins, M. L.; Mayer, J. E. Interatomic Distances in Crystals of the Alkali Halides. *J. Chem. Phys.* **1933**, *1*, 643−646.
(384) Fumi, F. G.; Tosi, M. Ionic Sizes and Born Repulsive Parameters in the Nacl-Type Alkali Halides—I: The Huggins-Mayer and Pauling Forms. *J. Phys. Chem. Solids* **1964**, *25*, 31−43.
(385) Tosi, M.; Fumi, F. Ionic Sizes and Born Repulsive Parameters in the Nacl-Type Alkali Halides—Ii: The Generalized Huggins-Mayer Form. *J. Phys. Chem. Solids* **1964**, *25*, 45−52.
(386) Zgarbová, M.; Otyepka, M.; Šponer, J.; Hobza, P.; Jurečka, P. Large-Scale Compensation of Errors in Pairwise-Additive Empirical Force Fields: Comparison of Amber Intermolecular Terms with Rigorous Dft-Sapt Calculations. *Phys. Chem. Chem. Phys.* **2010**, *12*, 10476−10493.
(387) White, D. N. A Computationally Efficient Alternative to the Buckingham Potential for Molecular Mechanics Calculations. *J. Comput.-Aided Mol. Des.* **1997**, *11*, 517−521.
(388) Lifson, S.; Warshel, A. Consistent Force Field for Calculations of Conformations, Vibrational Spectra, and Enthalpies of Cycloalkane and N-Alkane Molecules. *J. Chem. Phys.* **1968**, *49*, 5116−5129.
(389) Jorgensen, W. L. Quantum and Statistical Mechanical Studies of Liquids. 3. Deriving Intermolecular Potential Functions for the Water Dimer from Ab Initio Calculations. *J. Am. Chem. Soc.* **1979**, *101*, 2011−2016.
(390) Li, P.; Roberts, B. P.; Chakravorty, D. K.; Merz, K. M., Jr Rational Design of Particle Mesh Ewald Compatible Lennard-Jones Parameters for + 2 Metal Cations in Explicit Solvent. *J. Chem. Theory Comput.* **2013**, *9*, 2733−2748.
(391) Li, P.; Song, L. F.; Merz, K. M., Jr Parameterization of Highly Charged Metal Ions Using the 12−6-4 Lj-Type Nonbonded Model in Explicit Water. *J. Phys. Chem. B* **2015**, *119*, 883−895.
(392) Weiner, S. J.; Kollman, P. A.; Case, D. A.; Singh, U. C.; Ghio, C.; Alagona, G.; Profeta, S.; Weiner, P. A New Force Field for Molecular Mechanical Simulation of Nucleic Acids and Proteins. *J. Am. Chem. Soc.* **1984**, *106*, 765−784.
(393) Weiner, S. J.; Kollman, P. A.; Nguyen, D. T.; Case, D. A. An All Atom Force Field for Simulations of Proteins and Nucleic Acids. *J. Comput. Chem.* **1986**, *7*, 230−252.
(394) Cornell, W. D.; Cieplak, P.; Bayly, C. I.; Gould, I. R.; Merz, K. M., Jr; Ferguson, D. M.; Spellmeyer, D. C.; Fox, T.; Caldwell, J. W.; Kollman, P. A. A Second Generation Force Field for the Simulation of Proteins, Nucleic Acids, and Organic Molecules. *J. Am. Chem. Soc.* **1995**, *117*, 5179−5197.
(395) Cheatham, T. E., III; Cieplak, P.; Kollman, P. A. A Modified Version of the Cornell Et Al. Force Field with Improved Sugar Pucker Phases and Helical Repeat. *J. Biomol. Struct. Dyn.* **1999**, *16*, 845−862.

DOI: 10.1021/acs.chemrev.6b00440
Chem. Rev. 2017, 117, 1564−1686

(396) Duan, Y.; Wu, C.; Chowdhury, S.; Lee, M. C.; Xiong, G.; Zhang, W.; Yang, R.; Cieplak, P.; Luo, R.; Lee, T. A Point-Charge Force Field for Molecular Mechanics Simulations of Proteins Based on Condensed-Phase Quantum Mechanical Calculations. *J. Comput. Chem.* **2003**, *24*, 1999−2012.
(397) Wang, J.; Wolf, R. M.; Caldwell, J. W.; Kollman, P. A.; Case, D. A. Development and Testing of a General Amber Force Field. *J. Comput. Chem.* **2004**, *25*, 1157−1174.
(398) Hornak, V.; Abel, R.; Okur, A.; Strockbine, B.; Roitberg, A.; Simmerling, C. Comparison of Multiple Amber Force Fields and Development of Improved Protein Backbone Parameters. *Proteins: Struct., Funct., Genet.* **2006**, *65*, 712−725.
(399) Cerutti, D. S.; Swope, W. C.; Rice, J. E.; Case, D. A. Ff14ipq: A Self-Consistent Force Field for Condensed-Phase Simulations of Proteins. *J. Chem. Theory Comput.* **2014**, *10*, 4515−4534.
(400) Maier, J. A.; Martinez, C.; Kasavajhala, K.; Wickstrom, L.; Hauser, K. E.; Simmerling, C. Ff14sb: Improving the Accuracy of Protein Side Chain and Backbone Parameters from Ff99sb. *J. Chem. Theory Comput.* **2015**, *11*, 3696−3713.
(401) MacKerell, A. D.; Bashford, D.; Bellott, M.; Dunbrack, R.; Evanseck, J.; Field, M. J.; Fischer, S.; Gao, J.; Guo, H.; Ha, S. a. All-Atom Empirical Potential for Molecular Modeling and Dynamics Studies of Proteins. *J. Phys. Chem. B* **1998**, *102*, 3586−3616.
(402) MacKerell, A. D.; Banavali, N.; Foloppe, N. Development and Current Status of the Charmm Force Field for Nucleic Acids. *Biopolymers* **2000**, *56*, 257−265.
(403) MacKerell, A. D.; Feig, M.; Brooks, C. L. Improved Treatment of the Protein Backbone in Empirical Force Fields. *J. Am. Chem. Soc.* **2004**, *126*, 698−699.
(404) Klauda, J. B.; Venable, R. M.; Freites, J. A.; O'Connor, J. W.; Tobias, D. J.; Mondragon-Ramirez, C.; Vorobyov, I.; MacKerell, A. D., Jr; Pastor, R. W. Update of the Charmm All-Atom Additive Force Field for Lipids: Validation on Six Lipid Types. *J. Phys. Chem. B* **2010**, *114*, 7830−7843.
(405) Vanommeslaeghe, K.; Hatcher, E.; Acharya, C.; Kundu, S.; Zhong, S.; Shim, J.; Darian, E.; Guvench, O.; Lopes, P.; Vorobyov, I. Charmm General Force Field: A Force Field for Drug-Like Molecules Compatible with the Charmm All-Atom Additive Biological Force Fields. *J. Comput. Chem.* **2010**, *31*, 671−690.
(406) Vanommeslaeghe, K.; Raman, E. P.; MacKerell, A. D., Jr Automation of the Charmm General Force Field (Cgenff) Ii: Assignment of Bonded Parameters and Partial Atomic Charges. *J. Chem. Inf. Model.* **2012**, *52*, 3155−3168.
(407) Jorgensen, W. L.; Maxwell, D. S.; Tirado-Rives, J. Development and Testing of the Opls All-Atom Force Field on Conformational Energetics and Properties of Organic Liquids. *J. Am. Chem. Soc.* **1996**, *118*, 11225−11236.
(408) Damm, W.; Frontera, A.; Tirado−Rives, J.; Jorgensen, W. L. Opls All-Atom Force Field for Carbohydrates. *J. Comput. Chem.* **1997**, *18*, 1955−1970.
(409) Rizzo, R. C.; Jorgensen, W. L. Opls All-Atom Model for Amines: Resolution of the Amine Hydration Problem. *J. Am. Chem. Soc.* **1999**, *121*, 4827−4836.
(410) Kaminski, G. A.; Friesner, R. A.; Tirado-Rives, J.; Jorgensen, W. L. Evaluation and Reparametrization of the Opls-Aa Force Field for Proteins Via Comparison with Accurate Quantum Chemical Calculations on Peptides. *J. Phys. Chem. B* **2001**, *105*, 6474−6487.
(411) Robertson, M. J.; Tirado-Rives, J.; Jorgensen, W. L. Improved Peptide and Protein Torsional Energetics with the Opls-Aa Force Field. *J. Chem. Theory Comput.* **2015**, *11*, 3499−3509.
(412) Metropolis, N.; Ulam, S. The Monte Carlo Method. *J. Am. Stat. Assoc.* **1949**, *44*, 335−341.
(413) Alder, B. J.; Wainwright, T. E. Phase Transition for a Hard Sphere System. *J. Chem. Phys.* **1957**, *27*, 1208−1209.
(414) Probst, M.; Spohr, E.; Heinzinger, K. On the Hydration of the Beryllium Ion. *Chem. Phys. Lett.* **1989**, *161*, 405−408.
(415) Cordeiro, M. N. D.; Gomes, J. A.; González-Lafont, A.; Lluch, J. M.; Bertrán, J. The Role of Many-Body Interactions in the Stability of Hydrated Cu2+ Clusters. *Chem. Phys.* **1990**, *141*, 379−392.
(416) Rode, B. M.; Islam, S. M. Monte Carlo Simulations with an Improved Potential Function for Cu(Ii)-Water Including Neighbour Ligand Corrections. *Z. Naturforsch., A: Phys. Sci.* **1991**, *46*, 357−362.
(417) Cordeiro, M.; Gomes, J. A. Ab Initio Copper−Water Interaction Potential for the Simulation of Aqueous Solutions. *J. Comput. Chem.* **1993**, *14*, 629−638.
(418) Kennedy, T. *Electronic Computer Flashes Answers, May Speed Engineering*; New York Times, Feb. 15, 1946; p 15.
(419) Rosenbluth, M. N.; Rosenbluth, A. W. Further Results on Monte Carlo Equations of State. *J. Chem. Phys.* **1954**, *22*, 881−884.
(420) Wood, W.; Parker, F. Monte Carlo Equation of State of Molecules Interacting with the Lennard-Jones Potential. I. A Supercritical Isotherm at About Twice the Critical Temperature. *J. Chem. Phys.* **1957**, *27*, 720−733.
(421) Barker, A. Monte Carlo Calculations of the Radial Distribution Functions for a Proton? Electron Plasma. *Aust. J. Phys.* **1965**, *18*, 119−134.
(422) Woodcock, L.; Singer, K. Thermodynamic and Structural Properties of Liquid Ionic Salts Obtained by Monte Carlo Computation. Part 1.—Potassium Chloride. *Trans. Faraday Soc.* **1971**, *67*, 12−30.
(423) Clementi, E.; Popkie, H. Study of the Structure of Molecular Complexes. I. Energy Surface of a Water Molecule in the Field of a Lithium Positive Ion. *J. Chem. Phys.* **1972**, *57*, 1077−1094.
(424) Kistenmacher, H.; Popkie, H.; Clementi, E. Study of the Structure of Molecular Complexes. Ii. Energy Surfaces for a Water Molecule in the Field of a Sodium or Potassium Cation. *J. Chem. Phys.* **1973**, *58*, 1689−1699.
(425) Kistenmacher, H.; Popkie, H.; Clementi, E. Study of the Structure of Molecular Complexes. Iii. Energy Surface of a Water Molecule in the Field of a Fluorine or Chlorine Anion. *J. Chem. Phys.* **1973**, *58*, 5627−5638.
(426) Watts, R.; Clementi, E.; Fromm, J. A Theoretical Study of the Lithium Fluoride Molecule in Water. *J. Chem. Phys.* **1974**, *61*, 2550−2555.
(427) Fromm, J.; Clementi, E.; Watts, R. O. Coordination Number for the Li+−F− Ion Pair in Water. *J. Chem. Phys.* **1975**, *62*, 1388−1398.
(428) Clementi, E.; Barsotti, R.; Fromm, J.; Watts, R. Study of the Structure of Molecular Complexes. *Theor. Chim. Acta.* **1976**, *43*, 101−120.
(429) Clementi, E.; Barsotti, R. Study of the Structure of Molecular Complexes. Coordination Numbers for Li+, Na+, K+, F− and Cl− in Water. *Chem. Phys. Lett.* **1978**, *59*, 21−25.
(430) Clementi, E.; Corongiu, G. Simulations of the Solvent Structure for Macromolecules: Solvation Model for B-DNA and Na +-B-DNA Double Helix at 300° K. *Ann. N. Y. Acad. Sci.* **1981**, *367*, 83−107.
(431) Corongiu, G.; Clementi, E. Simulations of the Solvent Structure for Macromolecules. Ii. Structure of Water Solvating Na +-B-DNA at 300 K and a Model for Conformational Transitions Induced by Solvent Variations. *Biopolymers* **1981**, *20*, 2427−2483.
(432) Clementi, E.; Corongiu, G. Simulations of the Solvent Structure for Macromolecules. Iii. Determination of the Na+ Counter Ion Structure. *Biopolymers* **1982**, *21*, 763−777.
(433) Clementi, E.; Corongiu, G. B-DNA Structural Determination of Na+ Counterions at Different Humidities, Ionic Concentrations, and Temperatures. *Int. J. Quantum Chem.* **1982**, *22*, 595−630.
(434) Clementi, E.; Corongiu, G. Structure of Aggregates of Water and Li+, Na+, or K+ Counterions with Nucleic Acid in Solution. *J. Biol. Phys.* **1983**, *11*, 33−42.
(435) Kim, K.; Nguyen, H.; Swaminathan, P.; Clementi, E. Na+ and K+ Ion Transport through a Solvated Gramicidin a Transmembrane Channel: Molecular Dynamics Studies Using Parallel Processors. *J. Phys. Chem.* **1985**, *89*, 2870−2876.
(436) Kim, K. S.; Clementi, E. Energetics and Hydration Structures of a Solvated Gramicidin a Transmembrane Channel for Potassium and Sodium Cations. *J. Am. Chem. Soc.* **1985**, *107*, 5504−5513.

DOI: 10.1021/acs.chemrev.6b00440
Chem. Rev. 2017, 117, 1564−1686

(437) Kim, K. S.; Vercauteren, D. P.; Welti, M.; Chin, S.; Clementi, E. Interaction of K+ Ion with the Solvated Gramicidin a Transmembrane Channel. *Biophys. J.* **1985**, *47*, 327−335.
(438) Kim, K. S.; Vercauteren, D. P.; Welti, M.; Fornili, S. L.; Clementi, E. Interaction of Na+ Ion with the Solvated Gramicidin-a Transmembrane Channel. *Croat. Chem. Acta* **1986**, *59*, 369−381.
(439) Alder, B. J.; Wainwright, T. Studies in Molecular Dynamics. I. General Method. *J. Chem. Phys.* **1959**, *31*, 459−466.
(440) Gibson, J. B.; Goland, A. N.; Milgram, M. Vineyard, G. H., Dynamics of Radiation Damage. *Phys. Rev.* **1960**, *120*, 1229−1253.
(441) Rahman, A. Correlations in the Motion of Atoms in Liquid Argon. *Phys. Rev.* **1964**, *136*, A405−A411.
(442) Woodcock, L.-V. Isothermal Molecular Dynamics Calculations for Liquid Salts. *Chem. Phys. Lett.* **1971**, *10*, 257−261.
(443) Rahman, A.; Stillinger, F. H. Molecular Dynamics Study of Liquid Water. *J. Chem. Phys.* **1971**, *55*, 3336−3359.
(444) Heinzinger, K.; Vogel, P. A Molecular Dynamics Study of Aqueous Solutions I. First Results for Licl in H2o. *Z. Naturforsch., A: Phys. Sci.* **1974**, *29*, 1164−1171.
(445) Hogervorst, W. Transport and Equilibrium Properties of Simple Gases and Forces between Like and Unlike Atoms. *Physica* **1971**, *51*, 77−89.
(446) Kong, C. L. Combining Rules for Intermolecular Potential Parameters. Ii. Rules for the Lennard-Jones (12−6) Potential and the Morse Potential. *J. Chem. Phys.* **1973**, *59*, 2464−2467.
(447) Jorgensen, W. L.; Bigot, B.; Chandrasekhar, J. Quantum and Statistical Mechanical Studies of Liquids. 21. The Nature of Dilute Solutions of Sodium and Methoxide Ions in Methanol. *J. Am. Chem. Soc.* **1982**, *104*, 4584−4591.
(448) Chandrasekhar, J.; Spellmeyer, D. C.; Jorgensen, W. L. Energy Component Analysis for Dilute Aqueous Solutions of Lithium (1+), Sodium (1+), Fluoride (1-), and Chloride (1-) Ions. *J. Am. Chem. Soc.* **1984**, *106*, 903−910.
(449) Jorgensen, W. L.; Chandrasekhar, J.; Madura, J. D.; Impey, R. W.; Klein, M. L. Comparison of Simple Potential Functions for Simulating Liquid Water. *J. Chem. Phys.* **1983**, *79*, 926−935.
(450) Bounds, D. A Molecular Dynamics Study of the Structure of Water around the Ions Li+, Na+, K+, Ca++, Ni++ and Cl. *Mol. Phys.* **1985**, *54*, 1335−1355.
(451) Teleman, O.; Ahlstroem, P. Molecular Dynamics Simulation of a Small Calcium Complex in Aqueous Solution. *J. Am. Chem. Soc.* **1986**, *108*, 4333−4341.
(452) Migliore, M.; Corongiu, G.; Clementi, E.; Lie, G. Monte Carlo Study of Free Energy of Hydration for Li+, Na+, K+, F−, and Cl− with Abinitio Potentials. *J. Chem. Phys.* **1988**, *88*, 7766−7771.
(453) Straatsma, T.; Berendsen, H. Free Energy of Ionic Hydration: Analysis of a Thermodynamic Integration Technique to Evaluate Free Energy Differences by Molecular Dynamics Simulations. *J. Chem. Phys.* **1988**, *89*, 5876−5886.
(454) Floris, F.; Persico, M.; Tani, A.; Tomasi, J. Free Energies and Structures of Hydrated Cations, Based on Effective Pair Potentials. *Chem. Phys.* **1995**, *195*, 207−220.
(455) Marcos, E. S.; Pappalardo, R. R.; Barthelat, J.-C.; Gadea, F. X. Theoretical Suggestion for the Zn2+(H2o) Formation. *J. Phys. Chem.* **1992**, *96*, 516−518.
(456) Curtiss, L. A.; Halley, J. W.; Hautman, J.; Rahman, A. Nonadditivity of Abinitio Pair Potentials for Molecular Dynamics of Multivalent Transition Metal Ions in Water. *J. Chem. Phys.* **1987**, *86*, 2319−2327.
(457) Clementi, E.; Kistenmacher, H.; Kołos, W.; Romano, S. Non-Additivity in Water-Ion-Water Interactions. *Theor. Chim. Acta* **1980**, *55*, 257−266.
(458) Corongiu, G.; Migliore, M.; Clementi, E. Hydration Free Energy for Li+ at Infinite Dilution with a Three-Body Abinitio Potential. *J. Chem. Phys.* **1989**, *90*, 4629−4630.
(459) González-Lafont, A.; Lluch, J.; Oliva, A.; Bertrágn, J. Theoretical Study of Several Fe(H2o)N2+ Clusters at Different Temperatures. *Int. J. Quantum Chem.* **1986**, *29*, 1373−1382.
(460) Natália, M.; Cordeiro, D.; Ignaczak, A.; Gomes, J. A. Simulation of Water Solutions of Ni2+ at Infinite Dilution. *Chem. Phys.* **1993**, *176*, 97−108.
(461) Yamaguchi, T.; Ohtaki, H.; Spohr, E.; Palinkas, G.; Heinzinger, K.; Probst, M. Molecular Dynamics and X-Ray Diffraction Study of Aqueous Beryllium (Ii) Chloride Solutions. *Z. Naturforsch., A: Phys. Sci.* **1986**, *41*, 1175−1185.
(462) Åqvist, J. Ion-Water Interaction Potentials Derived from Free Energy Perturbation Simulations. *J. Phys. Chem.* **1990**, *94*, 8021−8024.
(463) Floris, F.; Persico, M.; Tani, A.; Tomasi, J. Ab Initio Effective Pair Potentials for Simulations of the Liquid State, Based on the Polarizable Continuum Model of the Solvent. *Chem. Phys. Lett.* **1992**, *199*, 518−524.
(464) Periole, X.; Allouche, D.; Daudey, J.-P.; Sanejouand, Y.-H. Simple Two-Body Cation-Water Interaction Potentials Derived from Ab Initio Calculations. Comparison to Results Obtained with an Empirical Approach. *J. Phys. Chem. B* **1997**, *101*, 5018−5025.
(465) Cramer, C. J.; Truhlar, D. G. Implicit Solvation Models: Equilibria, Structure, Spectra, and Dynamics. *Chem. Rev.* **1999**, *99*, 2161−2200.
(466) Floris, F. M.; Persico, M.; Tani, A.; Tomasi, J. Hydration Shell Structure of the Calcium Ion from Simulations with Ab Initio Effective Pair Potentials. *Chem. Phys. Lett.* **1994**, *227*, 126−132.
(467) Floris, F. M.; Tani, A. A Study of Aqueous Solutions of Lanthanide Ions by Molecular Dynamics Simulation with Ab Initio Effective Pair Potentials. *J. Chem. Phys.* **2001**, *115*, 4750−4765.
(468) D'Angelo, P.; Barone, V.; Chillemi, G.; Sanna, N.; Meyer-Klaucke, W.; Pavel, N. V. Hydrogen and Higher Shell Contributions in Zn2+, Ni2+, and Co2+ Aqueous Solutions: An X-Ray Absorption Fine Structure and Molecular Dynamics Study. *J. Am. Chem. Soc.* **2002**, *124*, 1958−1967.
(469) Chillemi, G.; D'Angelo, P.; Pavel, N. V.; Sanna, N.; Barone, V. Development and Validation of an Integrated Computational Approach for the Study of Ionic Species in Solution by Means of Effective Two-Body Potentials. The Case of Zn2+, Ni2+, and Co2+ in Aqueous Solutions. *J. Am. Chem. Soc.* **2002**, *124*, 1968−1976.
(470) Mancini, G.; Sanna, N.; Barone, V.; Migliorati, V.; D'Angelo, P.; Chillemi, G. Structural and Dynamical Properties of the Hg2+ Aqua Ion: A Molecular Dynamics Study. *J. Phys. Chem. B* **2008**, *112*, 4694−4702.
(471) Spezia, R.; Duvail, M.; Vitorge, P.; D'Angelo, P. Molecular Dynamics to Rationalize Exafs Experiments: A Dynamical Model Explaining Hydration Behaviour across the Lanthanoid (Iii) Series. *J. Phys.: Conf. Ser.* **2009**, *190*, 012056.
(472) D'Angelo, P.; Zitolo, A.; Migliorati, V.; Persson, I. Analysis of the Detailed Configuration of Hydrated Lanthanoid (Iii) Ions in Aqueous Solution and Crystalline Salts by Using K-and L3-Edge Xanes Spectroscopy. *Chem. - Eur. J.* **2010**, *16*, 684−692.
(473) D'Angelo, P.; Zitolo, A.; Migliorati, V.; Chillemi, G.; Duvail, M.; Vitorge, P.; Abadie, S.; Spezia, R. Revised Ionic Radii of Lanthanoid(Iii) Ions in Aqueous Solution. *Inorg. Chem.* **2011**, *50*, 4572−4579.
(474) D'Angelo, P.; Spezia, R. Hydration of Lanthanoids (Iii) and Actinoids (Iii): An Experimental/Theoretical Saga. *Chem. - Eur. J.* **2012**, *18*, 11162−11178.
(475) D'Angelo, P.; Martelli, F.; Spezia, R.; Filipponi, A.; Denecke, M. A. Hydration Properties and Ionic Radii of Actinide (Iii) Ions in Aqueous Solution. *Inorg. Chem.* **2013**, *52*, 10318−10324.
(476) Migliorati, V.; Chillemi, G.; D'Angelo, P. On the Solvation of the Zn2+ Ion in Methanol: A Combined Quantum Mechanics, Molecular Dynamics, and Exafs Approach. *Inorg. Chem.* **2011**, *50*, 8509−8515.
(477) Migliorati, V.; D'Angelo, P. A Quantum Mechanics, Molecular Dynamics and Exafs Investigation into the Hg2+ Ion Solvation Properties in Methanol Solution. *RSC Adv.* **2013**, *3*, 21118−21126.
(478) Pang, X.; Han, K.; Cui, Q. A Simple but Effective Modeling Strategy for Structural Properties of Non-Heme Fe (Ii) Sites in Proteins: Test of Force Field Models and Application to Proteins in the Alkb Family. *J. Comput. Chem.* **2013**, *34*, 1620−1635.

DOI: 10.1021/acs.chemrev.6b00440
Chem. Rev. 2017, 117, 1564−1686

(479) Wu, R.; Lu, Z.; Cao, Z.; Zhang, Y. A Transferable Nonbonded Pairwise Force Field to Model Zinc Interactions in Metalloproteins. *J. Chem. Theory Comput.* **2011**, *7*, 433−443.
(480) Gong, W.; Wu, R.; Zhang, Y. Thiol Versus Hydroxamate as Zinc Binding Group in Hdac Inhibition: An Ab Initio Qm/Mm Molecular Dynamics Study. *J. Comput. Chem.* **2015**, *36*, 2228−2235.
(481) Zhu, T.; Xiao, X.; Ji, C.; Zhang, J. Z. A New Quantum Calibrated Force Field for Zinc−Protein Complex. *J. Chem. Theory Comput.* **2013**, *9*, 1788−1798.
(482) Xiao, X.; Zhu, T.; Ji, C. G.; Zhang, J. Z. Development of an Effective Polarizable Bond Method for Biomolecular Simulation. *J. Phys. Chem. B* **2013**, *117*, 14885−14893.
(483) Zwanzig, R. W. High-Temperature Equation of State by a Perturbation Method. I. Nonpolar Gases. *J. Chem. Phys.* **1954**, *22*, 1420−1426.
(484) Fogolari, F.; Brigo, A.; Molinari, H. Protocol for Mm/Pbsa Molecular Dynamics Simulations of Proteins. *Biophys. J.* **2003**, *85*, 159−166.
(485) Kollman, P. Free Energy Calculations: Applications to Chemical and Biochemical Phenomena. *Chem. Rev.* **1993**, *93*, 2395−2417.
(486) Valleau, J.; Card, D. Monte Carlo Estimation of the Free Energy by Multistage Sampling. *J. Chem. Phys.* **1972**, *57*, 5457−5462.
(487) Torrie, G. M.; Valleau, J. P. Monte Carlo Free Energy Estimates Using Non-Boltzmann Sampling: Application to the Sub-Critical Lennard-Jones Fluid. *Chem. Phys. Lett.* **1974**, *28*, 578−581.
(488) Mezei, M.; Swaminathan, S.; Beveridge, D. L. Ab Initio Calculation of the Free Energy of Liquid Water. *J. Am. Chem. Soc.* **1978**, *100*, 3255−3256.
(489) Tembe, B. L.; McCammon, J. A. Ligand-Receptor Interactions. *Comput. Chem.* **1984**, *8*, 281−283.
(490) Jorgensen, W. L.; Ravimohan, C. Monte Carlo Simulation of Differences in Free Energies of Hydration. *J. Chem. Phys.* **1985**, *83*, 3050−3054.
(491) Lybrand, T. P.; Ghosh, I.; McCammon, J. A. Hydration of Chloride and Bromide Anions: Determination of Relative Free Energy by Computer Simulation. *J. Am. Chem. Soc.* **1985**, *107*, 7793−7794.
(492) Berendsen, H. J.; Postma, J. P.; van Gunsteren, W. F.; Hermans, J. *Interaction Models for Water in Relation to Protein Hydration*; Springer Netherlands: Dordrecht, Netherlands, 1981; Vol. *14*, pp 331−342.
(493) Lybrand, T. P.; McCammon, J. A.; Wipff, G. Theoretical Calculation of Relative Binding Affinity in Host-Guest Systems. *Proc. Natl. Acad. Sci. U. S. A.* **1986**, *83*, 833−835.
(494) Mazor, M. H.; McCammon, J. A.; Lybrand, T. P. Molecular Recognition in Nonaqueous Solvents: Sodium Ion, Potassium Ion, and 18-Crown-6 in Methanol. *J. Am. Chem. Soc.* **1989**, *111*, 55−56.
(495) Jorgensen, W. L.; Blake, J. F.; Buckner, J. K. Free Energy of Tip4p Water and the Free Energies of Hydration of Ch4 and Cl- from Statistical Perturbation Theory. *Chem. Phys.* **1989**, *129*, 193−200.
(496) Stote, R. H.; Karplus, M. Zinc Binding in Proteins and Solution: A Simple but Accurate Nonbonded Representation. *Proteins: Struct., Funct., Genet.* **1995**, *23*, 12−31.
(497) Donini, O. A.; Kollman, P. A. Calculation and Prediction of Binding Free Energies for the Matrix Metalloproteinases. *J. Med. Chem.* **2000**, *43*, 4180−4188.
(498) Halgren, T. A. Merck Molecular Force Field. V. Extension of Mmff94 Using Experimental Data, Additional Computational Data, and Empirical Rules. *J. Comput. Chem.* **1996**, *17*, 616−641.
(499) Peng, Z.; Ewig, C. S.; Hwang, M.-J.; Waldman, M.; Hagler, A. T. Derivation of Class Ii Force Fields. 4. Van Der Waals Parameters of Alkali Metal Cations and Halide Anions. *J. Phys. Chem. A* **1997**, *101*, 7243−7252.
(500) Jensen, K. P.; Jorgensen, W. L. Halide, Ammonium, and Alkali Metal Ion Parameters for Modeling Aqueous Solutions. *J. Chem. Theory Comput.* **2006**, *2*, 1499−1509.
(501) Babu, C. S.; Lim, C. Empirical Force Fields for Biologically Active Divalent Metal Cations in Water†. *J. Phys. Chem. A* **2006**, *110*, 691−699.
(502) Marcus, Y. Thermodynamics of Solvation of Ions. Part 5.-Gibbs Free Energy of Hydration at 298.15 K. *J. Chem. Soc., Faraday Trans.* **1991**, *87*, 2995−2999.
(503) Carlsson, J.; Åqvist, J. Absolute Hydration Entropies of Alkali Metal Ions from Molecular Dynamics Simulations. *J. Phys. Chem. B* **2009**, *113*, 10255−10260.
(504) Won, Y. Force Field for Monovalent, Divalent, and Trivalent Cations Developed under the Solvent Boundary Potential. *J. Phys. Chem. A* **2012**, *116*, 11763−11767.
(505) Mao, A. H.; Pappu, R. V. Crystal Lattice Properties Fully Determine Short-Range Interaction Parameters for Alkali and Halide Ions. *J. Chem. Phys.* **2012**, *137*, 064104.
(506) Joung, I. S.; Cheatham, T. E. Determination of Alkali and Halide Monovalent Ion Parameters for Use in Explicitly Solvated Biomolecular Simulations. *J. Phys. Chem. B* **2008**, *112*, 9020−9041.
(507) Schmid, R.; Miah, A. M.; Sapunov, V. N. A New Table of the Thermodynamic Quantities of Ionic Hydration: Values and Some Applications (Enthalpy-Entropy Compensation and Born Radii). *Phys. Chem. Chem. Phys.* **2000**, *2*, 97−102.
(508) Cheatham, T. E., III; Miller, J. L.; Fox, T.; Darden, T. A.; Kollman, P. A. Molecular Dynamics Simulations on Solvated Biomolecular Systems: The Particle Mesh Ewald Method Leads to Stable Trajectories of DNA, Rna, and Proteins. *J. Am. Chem. Soc.* **1995**, *117*, 4193−4194.
(509) Cisneros, G. A. s.; Karttunen, M.; Ren, P.; Sagui, C. Classical Electrostatics for Biomolecular Simulations. *Chem. Rev.* **2014**, *114*, 779−814.
(510) Li, P.; Song, L. F.; Merz, K. M., Jr Systematic Parameterization of Monovalent Ions Employing the Nonbonded Model. *J. Chem. Theory Comput.* **2015**, *11*, 1645−1657.
(511) Li, P. *Advances in Metal Ion Modeling*; Michigan State University, 2016.
(512) Heinz, H.; Vaia, R.; Farmer, B.; Naik, R. Accurate Simulation of Surfaces and Interfaces of Face-Centered Cubic Metals Using 12− 6 and 9− 6 Lennard-Jones Potentials. *J. Phys. Chem. C* **2008**, *112*, 17281−17290.
(513) Iori, F.; Di Felice, R.; Molinari, E.; Corni, S. Golp: An Atomistic Force-Field to Describe the Interaction of Proteins with Au (111) Surfaces in Water. *J. Comput. Chem.* **2009**, *30*, 1465−1476.
(514) Marrone, T. J.; Merz, K. M., Jr Transferability of Ion Models. *J. Phys. Chem.* **1993**, *97*, 6524−6529.
(515) Åqvist, J. Comment on "Transferability of Ion Models". *J. Phys. Chem.* **1994**, *98*, 8253−8255.
(516) Marrone, T. J.; Merz, K. M., Jr Reply to Comment on "Transferability of Ion Models". *J. Phys. Chem.* **1994**, *98*, 8256−8257.
(517) Dang, L. X.; Kollman, P. A. Free Energy of Association of the K+: 18-Crown-6 Complex in Water: A New Molecular Dynamics Study. *J. Phys. Chem.* **1995**, *99*, 55−58.
(518) Auffinger, P.; Cheatham, T. E.; Vaiana, A. C. Spontaneous Formation of Kcl Aggregates in Biomolecular Simulations: A Force Field Issue? *J. Chem. Theory Comput.* **2007**, *3*, 1851−1859.
(519) Dang, L. X.; Garrett, B. C. Photoelectron Spectra of the Hydrated Iodine Anion from Molecular Dynamics Simulations. *J. Chem. Phys.* **1993**, *99*, 2972−2977.
(520) Dang, L. X. Free Energies for Association of Cs+ to 18-Crown-6 in Water. A Molecular Dynamics Study Including Counter Ions. *Chem. Phys. Lett.* **1994**, *227*, 211−214.
(521) Dang, L. X. Mechanism and Thermodynamics of Ion Selectivity in Aqueous Solutions of 18-Crown-6 Ether: A Molecular Dynamics Study. *J. Am. Chem. Soc.* **1995**, *117*, 6954−6960.
(522) Chang, T.-M.; Dang, L. X. Detailed Study of Potassium Solvation Using Molecular Dynamics Techniques. *J. Phys. Chem. B* **1999**, *103*, 4714−4720.
(523) Dang, L. X. Computational Study of Ion Binding to the Liquid Interface of Water. *J. Phys. Chem. B* **2002**, *106*, 10388−10394.
(524) Peng, T.; Chang, T.-M.; Sun, X.; Nguyen, A. V.; Dang, L. X. Development of Ions-Tip4p-Ew Force Fields for Molecular Processes in Bulk and at the Aqueous Interface Using Molecular Simulations. *J. Mol. Liq.* **2012**, *173*, 47−54.

DOI: 10.1021/acs.chemrev.6b00440
Chem. Rev. 2017, 117, 1564−1686

(525) Stokes, R. The Van Der Waals Radii of Gaseous Ions of the Noble Gas Structure in Relation to Hydration Energies. *J. Am. Chem. Soc.* **1964**, *86*, 979−982.
(526) Bondi, A. Van Der Waals Volumes and Radii. *J. Phys. Chem.* **1964**, *68*, 441−451.
(527) Radëtìsig, A.; Smirnov, B. *Reference Data on Atoms, Molecules, and Ions*; Springer-Verlag: Berlin and Heidelberg, 1985.
(528) Ramaniah, L. M.; Bernasconi, M.; Parrinello, M. Ab Initio Molecular-Dynamics Simulation of K+ Solvation in Water. *J. Chem. Phys.* **1999**, *111*, 1587−1591.
(529) Lorentz, H. Ueber Die Anwendung Des Satzes Vom Virial in Der Kinetischen Theorie Der Gase. *Ann. Phys. (Berlin, Ger.)* **1881**, *248*, 127−136.
(530) Berthelot, D. Sur Le Mélange Des Gaz. *Compt. Rendus.* **1898**, *126*, 1703−1706.
(531) Hudson, G.; McCoubrey, J. Intermolecular Forces between Unlike Molecules. A More Complete Form of the Combining Rules. *Trans. Faraday Soc.* **1960**, *56*, 761−766.
(532) Fender, B.; Halsey, G., Jr Second Virial Coefficients of Argon, Krypton, and Argon-Krypton Mixtures at Low Temperatures. *J. Chem. Phys.* **1962**, *36*, 1881−1888.
(533) Sikora, P. T. Combining Rules for Spherically Symmetric Intermolecular Potentials. *J. Phys. B: At. Mol. Phys.* **1970**, *3*, 1475.
(534) Pena, M. D.; Pando, C.; Renuncio, J. Combination Rules for Intermolecular Potential Parameters. I. Rules Based on Approximations for the Long-Range Dispersion Energy. *J. Chem. Phys.* **1982**, *76*, 325−332.
(535) Pena, M. D.; Pando, C.; Renuncio, J. Combination Rules for Intermolecular Potential Parameters. Ii. Rules Based on Approximations for the Long-Range Dispersion Energy and an Atomic Distortion Model for the Repulsive Interactions. *J. Chem. Phys.* **1982**, *76*, 333−339.
(536) Tang, K.; Toennies, J. P. New Combining Rules for Well Parameters and Shapes of the Van Der Waals Potential of Mixed Rare Gas Systems. *Z. Phys. D: At., Mol. Clusters* **1986**, *1*, 91−101.
(537) Waldman, M.; Hagler, A. New Combining Rules for Rare Gas Van Der Waals Parameters. *J. Comput. Chem.* **1993**, *14*, 1077−1084.
(538) Fyta, M.; Netz, R. R. Ionic Force Field Optimization Based on Single-Ion and Ion-Pair Solvation Properties: Going Beyond Standard Mixing Rules. *J. Chem. Phys.* **2012**, *136*, 124103.
(539) Luo, Y.; Roux, B. Simulation of Osmotic Pressure in Concentrated Aqueous Salt Solutions. *J. Phys. Chem. Lett.* **2010**, *1*, 183−189.
(540) Beglov, D.; Roux, B. Finite Representation of an Infinite Bulk System: Solvent Boundary Potential for Computer Simulations. *J. Chem. Phys.* **1994**, *100*, 9050−9063.
(541) Noskov, S. Y.; Roux, B. Control of Ion Selectivity in Leut: Two Na+ Binding Sites with Two Different Mechanisms. *J. Mol. Biol.* **2008**, *377*, 804−818.
(542) Joung, I. S.; Cheatham, T. E., III Molecular Dynamics Simulations of the Dynamic and Energetic Properties of Alkali and Halide Ions Using Water-Model-Specific Ion Parameters. *J. Phys. Chem. B* **2009**, *113*, 13279−13290.
(543) Allnér, O.; Nilsson, L.; Villa, A. Magnesium Ion−Water Coordination and Exchange in Biomolecular Simulations. *J. Chem. Theory Comput.* **2012**, *8*, 1493−1502.
(544) Yoo, J.; Aksimentiev, A. Improved Parametrization of Li+, Na +, K+, and Mg2+ Ions for All-Atom Molecular Dynamics Simulations of Nucleic Acid Systems. *J. Phys. Chem. Lett.* **2012**, *3*, 45−50.
(545) Venable, R. M.; Luo, Y.; Gawrisch, K.; Roux, B.; Pastor, R. W. Simulations of Anionic Lipid Membranes: Development of Interaction-Specific Ion Parameters and Validation Using Nmr Data. *J. Phys. Chem. B* **2013**, *117*, 10183−10192.
(546) Torras, J.; Alemán, C. Determination of New Cu+, Cu2+, and Zn2+ Lennard-Jones Ion Parameters in Acetonitrile. *J. Phys. Chem. B* **2013**, *117*, 10513−10522.
(547) de Araujo, A. S.; Sonoda, M. T.; Piro, O. E.; Castellano, E. E. Development of New Cd2+ and Pb2+ Lennard-Jones Parameters for Liquid Simulations. *J. Phys. Chem. B* **2007**, *111*, 2219−2224.
(548) Williams, C. D.; Burton, N. A.; Travis, K. P.; Harding, J. H. The Development of a Classical Force Field to Determine the Selectivity of an Aqueous Fe3+−Eda Complex for Tco4−and So42−. *J. Chem. Theory Comput.* **2014**, *10*, 3345−3353.
(549) Li, P.; Merz, K. M., Jr Taking into Account the Ion-Induced Dipole Interaction in the Nonbonded Model of Ions. *J. Chem. Theory Comput.* **2014**, *10*, 289−297.
(550) Panteva, M. T.; Giambaşu, G. M.; York, D. M. Comparison of Structural, Thermodynamic, Kinetic and Mass Transport Properties of Mg2+ Ion Models Commonly Used in Biomolecular Simulations. *J. Comput. Chem.* **2015**, *36*, 970−982.
(551) Lightstone, F. C.; Schwegler, E.; Hood, R. Q.; Gygi, F.; Galli, G. A First Principles Molecular Dynamics Simulation of the Hydrated Magnesium Ion. *Chem. Phys. Lett.* **2001**, *343*, 549−555.
(552) Yu, H.; Whitfield, T. W.; Harder, E.; Lamoureux, G.; Vorobyov, I.; Anisimov, V. M.; MacKerell, A. D.; Roux, B. t. Simulating Monovalent and Divalent Ions in Aqueous Solution Using a Drude Polarizable Force Field. *J. Chem. Theory Comput.* **2010**, *6*, 774−786.
(553) Jiao, D.; King, C.; Grossfield, A.; Darden, T. A.; Ren, P. Simulation of Ca2+ and Mg2+ Solvation Using Polarizable Atomic Multipole Potential. *J. Phys. Chem. B* **2006**, *110*, 18553−18559.
(554) Piquemal, J.-P.; Perera, L.; Cisneros, G. A.; Ren, P.; Pedersen, L. G.; Darden, T. A. Towards Accurate Solvation Dynamics of Divalent Cations in Water Using the Polarizable Amoeba Force Field: From Energetics to Structure. *J. Chem. Phys.* **2006**, *125*, 054511.
(555) Soniat, M.; Hartman, L.; Rick, S. W. Charge Transfer Models of Zinc and Magnesium in Water. *J. Chem. Theory Comput.* **2015**, *11*, 1658−1667.
(556) Marcus, Y. Ionic Radii in Aqueous Solutions. *Chem. Rev.* **1988**, *88*, 1475−1498.
(557) Bleuzen, A.; Pittet, P. A.; Helm, L.; Merbach, A. E. Water Exchange on Magnesium (Ii) in Aqueous Solution: A Variable Temperature and Pressure 17o Nmr Study. *Magn. Reson. Chem.* **1997**, *35*, 765−773.
(558) Struis, R.; De Bleijser, J.; Leyte, J. An Nmr Contribution to the Interpretation of the Dynamical Behavior of Water Molecules as a Function of the Magnesium Chloride Concentration at 25. Degree. C. *J. Phys. Chem.* **1987**, *91*, 6309−6315.
(559) Panteva, M. T.; Giambaşu, G. M.; York, D. M. Force Field for Mg2+, Mn2+, Zn2+, and Cd2+ Ions That Have Balanced Interactions with Nucleic Acids. *J. Phys. Chem. B* **2015**, *119*, 15460−15470.
(560) Leontyev, I.; Stuchebrukhov, A. Electronic Continuum Model for Molecular Dynamics Simulations. *J. Chem. Phys.* **2009**, *130*, 085102.
(561) Leontyev, I.; Stuchebrukhov, A. Electronic Polarizability and the Effective Pair Potentials of Water. *J. Chem. Theory Comput.* **2010**, *6*, 3153−3161.
(562) Leontyev, I.; Stuchebrukhov, A. Electronic Continuum Model for Molecular Dynamics Simulations of Biological Molecules. *J. Chem. Theory Comput.* **2010**, *6*, 1498−1508.
(563) Berendsen, H. J. C.; Grigera, J. R.; Straatsma, T. P. The Missing Term in Effective Pair Potentials. *J. Phys. Chem.* **1987**, *91*, 6269−6271.
(564) Abascal, J. L.; Vega, C. A General Purpose Model for the Condensed Phases of Water: Tip4p/2005. *J. Chem. Phys.* **2005**, *123*, 234505.
(565) Horn, H. W.; Swope, W. C.; Pitera, J. W.; Madura, J. D.; Dick, T. J.; Hura, G. L.; Head-Gordon, T. Development of an Improved Four-Site Water Model for Biomolecular Simulations: Tip4p-Ew. *J. Chem. Phys.* **2004**, *120*, 9665−9678.
(566) Mahoney, M. W.; Jorgensen, W. L. A Five-Site Model for Liquid Water and the Reproduction of the Density Anomaly by Rigid, Nonpolarizable Potential Functions. *J. Chem. Phys.* **2000**, *112*, 8910−8922.
(567) Leontyev, I. V.; Stuchebrukhov, A. A. Polarizable Molecular Interactions in Condensed Phase and Their Equivalent Nonpolarizable Models. *J. Chem. Phys.* **2014**, *141*, 014103.

DOI: 10.1021/acs.chemrev.6b00440
Chem. Rev. 2017, 117, 1564−1686

(568) Leontyev, I. V.; Stuchebrukhov, A. A. Polarizable Mean-Field Model of Water for Biological Simulations with Amber and Charmm Force Fields. *J. Chem. Theory Comput.* **2012**, *8*, 3207−3216.
(569) Wendler, K.; Dommert, F.; Zhao, Y. Y.; Berger, R.; Holm, C.; Delle Site, L. Ionic Liquids Studied across Different Scales: A Computational Perspective. *Faraday Discuss.* **2012**, *154*, 111−132.
(570) Kann, Z.; Skinner, J. A Scaled-Ionic-Charge Simulation Model That Reproduces Enhanced and Suppressed Water Diffusion in Aqueous Salt Solutions. *J. Chem. Phys.* **2014**, *141*, 104507.
(571) Mason, P. E.; Wernersson, E.; Jungwirth, P. Accurate Description of Aqueous Carbonate Ions: An Effective Polarization Model Verified by Neutron Scattering. *J. Phys. Chem. B* **2012**, *116*, 8145−8153.
(572) Vazdar, M.; Pluhařová, E.; Mason, P. E.; Vácha, R.; Jungwirth, P. Ions at Hydrophobic Aqueous Interfaces: Molecular Dynamics with Effective Polarization. *J. Phys. Chem. Lett.* **2012**, *3*, 2087−2091.
(573) Kim, J. S.; Wu, Z.; Morrow, A. R.; Yethiraj, A.; Yethiraj, A. Self-Diffusion and Viscosity in Electrolyte Solutions. *J. Phys. Chem. B* **2012**, *116*, 12007−12013.
(574) Zhang, Y.; Yang, W. Comment on "Generalized Gradient Approximation Made Simple. *Phys. Rev. Lett.* **1998**, *80*, 890.
(575) Ding, Y.; Hassanali, A. A.; Parrinello, M. Anomalous Water Diffusion in Salt Solutions. *Proc. Natl. Acad. Sci. U. S. A.* **2014**, *111*, 3310−3315.
(576) Tainter, C.; Pieniazek, P.; Lin, Y.-S.; Skinner, J. Robust Three-Body Water Simulation Model. *J. Chem. Phys.* **2011**, *134*, 184501.
(577) Li, J.; Wang, F. Pairwise-Additive Force Fields for Selected Aqueous Monovalent Ions from Adaptive Force Matching. *J. Chem. Phys.* **2015**, *143*, 194505.
(578) Li, J.; Wang, F. Erratum:"Pairwise-Additive Force Fields for Selected Aqueous Monovalent Ions from Adaptive Force Matching"[J. Chem. Phys. 143, 194505 (2015)]. *J. Chem. Phys.* **2015**, *143*, 219901.
(579) Yao, Y.; Berkowitz, M. L.; Kanai, Y. Communication: Modeling of Concentration Dependent Water Diffusivity in Ionic Solutions: Role of Intermolecular Charge Transfer. *J. Chem. Phys.* **2015**, *143*, 241101.
(580) Schröder, C. Comparing Reduced Partial Charge Models with Polarizable Simulations of Ionic Liquids. *Phys. Chem. Chem. Phys.* **2012**, *14*, 3089−3102.
(581) Pegado, L.; Marsalek, O.; Jungwirth, P.; Wernersson, E. Solvation and Ion-Pairing Properties of the Aqueous Sulfate Anion: Explicit Versus Effective Electronic Polarization. *Phys. Chem. Chem. Phys.* **2012**, *14*, 10248−10257.
(582) Marrink, S. J.; Risselada, H. J.; Yefimov, S.; Tieleman, D. P.; De Vries, A. H. The Martini Force Field: Coarse Grained Model for Biomolecular Simulations. *J. Phys. Chem. B* **2007**, *111*, 7812−7824.
(583) Sokkar, P.; Boulanger, E.; Thiel, W.; Sanchez-Garcia, E. Hybrid Quantum Mechanics/Molecular Mechanics/Coarse Grained Modeling: A Triple-Resolution Approach for Biomolecular Systems. *J. Chem. Theory Comput.* **2015**, *11*, 1809−1818.
(584) Marrink, S. J.; De Vries, A. H.; Mark, A. E. Coarse Grained Model for Semiquantitative Lipid Simulations. *J. Phys. Chem. B* **2004**, *108*, 750−760.
(585) Singh, U.; Weiner, S. J.; Kollman, P. Molecular Dynamics Simulations of D(C-G-C-G-a).D(T-C-G-C-G) with and without" Hydrated" Counterions. *Proc. Natl. Acad. Sci. U. S. A.* **1985**, *82*, 755−759.
(586) Khalili, M.; Saunders, J. A.; Liwo, A.; Ołdziej, S.; Scheraga, H. A. A United Residue Force-Field for Calcium-Protein Interactions. *Protein Sci.* **2004**, *13*, 2725−2735.
(587) Bixon, M.; Lifson, S. Potential Functions and Conformations in Cycloalkanes. *Tetrahedron* **1967**, *23*, 769−784.
(588) Warshel, A.; Levitt, M.; Lifson, S. Consistent Force Field for Calculation of Vibrational Spectra and Conformations of Some Amides and Lactam Rings. *J. Mol. Spectrosc.* **1970**, *33*, 84−99.
(589) Warshel, A.; Lifson, S. Consistent Force Field Calculations. Ii. Crystal Structures, Sublimation Energies, Molecular and Lattice Vibrations, Molecular Conformations, and Enthalpies of Alkanes. *J. Chem. Phys.* **1970**, *53*, 582−594.
(590) Ermer, O.; Lifson, S. Consistent Force Field Calculations. Iii. Vibrations, Conformations, and Heats of Hydrogenation of Non-conjugated Olefins. *J. Am. Chem. Soc.* **1973**, *95*, 4121−4132.
(591) Hagler, A.; Huler, E.; Lifson, S. Energy Functions for Peptides and Proteins. I. Derivation of a Consistent Force Field Including the Hydrogen Bond from Amide Crystals. *J. Am. Chem. Soc.* **1974**, *96*, 5319−5327.
(592) Hagler, A.; Lifson, S. Energy Functions for Peptides and Proteins. Ii. Amide Hydrogen Bond and Calculation of Amide Crystal Properties. *J. Am. Chem. Soc.* **1974**, *96*, 5327−5335.
(593) Hagler, A.; Dauber, P.; Lifson, S. Consistent Force Field Studies of Intermolecular Forces in Hydrogen-Bonded Crystals. 3. The C: O. Cntdot.. Cntdot.. Cntdot. Ho Hydrogen Bond and the Analysis of the Energetics and Packing of Carboxylic Acids. *J. Am. Chem. Soc.* **1979**, *101*, 5131−5141.
(594) Hagler, A.; Lifson, S.; Dauber, P. Consistent Force Field Studies of Intermolecular Forces in Hydrogen-Bonded Crystals. 2. A Benchmark for the Objective Comparison of Alternative Force Fields. *J. Am. Chem. Soc.* **1979**, *101*, 5122−5130.
(595) Lifson, S.; Hagler, A.; Dauber, P. Consistent Force Field Studies of Intermolecular Forces in Hydrogen-Bonded Crystals. 1. Carboxylic Acids, Amides, and the C: O. Cntdot.. Cntdot.. Cntdot. H-Hydrogen Bonds. *J. Am. Chem. Soc.* **1979**, *101*, 5111−5121.
(596) Levitt, M. The Birth of Computational Structural Biology. *Nat. Struct. Biol.* **2001**, *8*, 392−393.
(597) Levitt, M.; Lifson, S. Refinement of Protein Conformations Using a Macromolecular Energy Minimization Procedure. *J. Mol. Biol.* **1969**, *46*, 269−279.
(598) Heinz, H.; Lin, T.-J.; Kishore Mishra, R.; Emami, F. S. Thermodynamically Consistent Force Fields for the Assembly of Inorganic, Organic, and Biological Nanostructures: The Interface Force Field. *Langmuir* **2013**, *29*, 1754−1765.
(599) Ott, K. H.; Meyer, B. Parametrization of Gromos Force Field for Oligosaccharides and Assessment of Efficiency of Molecular Dynamics Simulations. *J. Comput. Chem.* **1996**, *17*, 1068−1084.
(600) Daura, X.; Mark, A. E.; van Gunsteren, W. F. Parametrization of Aliphatic Chn United Atoms of Gromos96 Force Field. *J. Comput. Chem.* **1998**, *19*, 535−547.
(601) Schuler, L. D.; Daura, X.; van Gunsteren, W. F. An Improved Gromos96 Force Field for Aliphatic Hydrocarbons in the Condensed Phase. *J. Comput. Chem.* **2001**, *22*, 1205−1218.
(602) Oostenbrink, C.; Villa, A.; Mark, A. E.; van Gunsteren, W. F. A Biomolecular Force Field Based on the Free Enthalpy of Hydration and Solvation: The Gromos Force-Field Parameter Sets 53a5 and 53a6. *J. Comput. Chem.* **2004**, *25*, 1656−1676.
(603) Lins, R. D.; Hünenberger, P. H. A New Gromos Force Field for Hexopyranose-Based Carbohydrates. *J. Comput. Chem.* **2005**, *26*, 1400−1412.
(604) Soares, T. A.; Hünenberger, P. H.; Kastenholz, M. A.; Kräutler, V.; Lenz, T.; Lins, R. D.; Oostenbrink, C.; van Gunsteren, W. F. An Improved Nucleic Acid Parameter Set for the Gromos Force Field. *J. Comput. Chem.* **2005**, *26*, 725−737.
(605) Schmid, N.; Eichenberger, A. P.; Choutko, A.; Riniker, S.; Winger, M.; Mark, A. E.; van Gunsteren, W. F. Definition and Testing of the Gromos Force-Field Versions 54a7 and 54b7. *Eur. Biophys. J.* **2011**, *40*, 843−856.
(606) Sun, H. Compass: An Ab Initio Force-Field Optimized for Condensed-Phase Applications Overview with Details on Alkane and Benzene Compounds. *J. Phys. Chem. B* **1998**, *102*, 7338−7364.
(607) Bunte, S. W.; Sun, H. Molecular Modeling of Energetic Materials: The Parameterization and Validation of Nitrate Esters in the Compass Force Field. *J. Phys. Chem. B* **2000**, *104*, 2477−2489.
(608) Dauber-Osguthorpe, P.; Roberts, V. A.; Osguthorpe, D. J.; Wolff, J.; Genest, M.; Hagler, A. T. Structure and Energetics of Ligand Binding to Proteins: Escherichia Coli Dihydrofolate Reductase-Trimethoprim, a Drug-Receptor System. *Proteins: Struct., Funct., Genet.* **1988**, *4*, 31−47.

DOI: 10.1021/acs.chemrev.6b00440
Chem. Rev. 2017, 117, 1564−1686

(609) Sun, H. Force Field for Computation of Conformational Energies, Structures, and Vibrational Frequencies of Aromatic Polyesters. *J. Comput. Chem.* **1994**, *15*, 752−768.
(610) Rai, N.; Siepmann, J. I. Transferable Potentials for Phase Equilibria. 9. Explicit Hydrogen Description of Benzene and Five-Membered and Six-Membered Heterocyclic Aromatic Compounds. *J. Phys. Chem. B* **2007**, *111*, 10790−10799.
(611) Gelin, B. R.; Karplus, M. Mechanism of Tertiary Structural Change in Hemoglobin. *Proc. Natl. Acad. Sci. U. S. A.* **1977**, *74*, 801−805.
(612) Case, D.; Karplus, M. Dynamics of Ligand Binding to Heme Proteins. *J. Mol. Biol.* **1979**, *132*, 343−368.
(613) Case, D. A.; McCammon, J. A. Dynamic Simulations of Oxygen Binding to Myoglobin. *Ann. N. Y. Acad. Sci.* **1986**, *482*, 222−233.
(614) Kottalam, J.; Case, D. A. Dynamics of Ligand Escape from the Heme Pocket of Myoglobin. *J. Am. Chem. Soc.* **1988**, *110*, 7690−7697.
(615) Mayo, S. L.; Olafson, B. D.; Goddard, W. A. Dreiding: A Generic Force Field for Molecular Simulations. *J. Phys. Chem.* **1990**, *94*, 8897−8909.
(616) Allinger, N. L. Conformational Analysis. 130. Mm2. A Hydrocarbon Force Field Utilizing V1 and V2 Torsional Terms. *J. Am. Chem. Soc.* **1977**, *99*, 8127−8134.
(617) Allinger, N. L.; Yuh, Y. H.; Lii, J. H. Molecular Mechanics. The Mm3 Force Field for Hydrocarbons. 1. *J. Am. Chem. Soc.* **1989**, *111*, 8551−8566.
(618) Lii, J. H.; Allinger, N. L. Molecular Mechanics. The Mm3 Force Field for Hydrocarbons. 2. Vibrational Frequencies and Thermodynamics. *J. Am. Chem. Soc.* **1989**, *111*, 8566−8575.
(619) Lii, J. H.; Allinger, N. L. Molecular Mechanics. The Mm3 Force Field for Hydrocarbons. 3. The Van Der Waals' Potentials and Crystal Data for Aliphatic and Aromatic Hydrocarbons. *J. Am. Chem. Soc.* **1989**, *111*, 8576−8582.
(620) Allinger, N. L.; Li, F.; Yan, L. Molecular Mechanics. The Mm3 Force Field for Alkenes. *J. Comput. Chem.* **1990**, *11*, 848−867.
(621) Lii, J. H.; Allinger, N. L. The Mm3 Force Field for Amides, Polypeptides and Proteins. *J. Comput. Chem.* **1991**, *12*, 186−199.
(622) Allinger, N. L.; Chen, K.; Lii, J. H. An Improved Force Field (Mm4) for Saturated Hydrocarbons. *J. Comput. Chem.* **1996**, *17*, 642−668.
(623) Allinger, N. L.; Chen, K. H.; Lii, J. H.; Durkin, K. A. Alcohols, Ethers, Carbohydrates, and Related Compounds. I. The Mm4 Force Field for Simple Compounds. *J. Comput. Chem.* **2003**, *24*, 1447−1472.
(624) Lii, J. H.; Chen, K. H.; Allinger, N. L. Alcohols, Ethers, Carbohydrates, and Related Compounds. Iv. Carbohydrates. *J. Comput. Chem.* **2003**, *24*, 1504−1513.
(625) Lii, J. H.; Chen, K. H.; Durkin, K. A.; Allinger, N. L. Alcohols, Ethers, Carbohydrates, and Related Compounds. Ii. The Anomeric Effect. *J. Comput. Chem.* **2003**, *24*, 1473−1489.
(626) Lii, J. H.; Chen, K. H.; Grindley, T. B.; Allinger, N. L. Alcohols, Ethers, Carbohydrates, and Related Compounds. Iii. The 1, 2-Dimethoxyethane System. *J. Comput. Chem.* **2003**, *24*, 1490−1503.
(627) Lii, J.-H.; Chen, K.-H.; Allinger, N. L. Alcohols, Ethers, Carbohydrates, and Related Compounds Part V. 2 the Bohlmann Torsional Effect. *J. Phys. Chem. A* **2004**, *108*, 3006−3015.
(628) Halgren, T. A. Merck Molecular Force Field. I. Basis, Form, Scope, Parameterization, and Performance of Mmff94. *J. Comput. Chem.* **1996**, *17*, 490−519.
(629) Halgren, T. A. Merck Molecular Force Field. Ii. Mmff94 Van Der Waals and Electrostatic Parameters for Intermolecular Interactions. *J. Comput. Chem.* **1996**, *17*, 520−552.
(630) Halgren, T. A. Merck Molecular Force Field. Iii. Molecular Geometries and Vibrational Frequencies for Mmff94. *J. Comput. Chem.* **1996**, *17*, 553−586.
(631) Halgren, T. A.; Nachbar, R. B. Merck Molecular Force Field. Iv. Conformational Energies and Geometries for Mmff94. *J. Comput. Chem.* **1996**, *17*, 587−615.
(632) Halgren, T. A. Mmff Vi. Mmff94s Option for Energy Minimization Studies. *J. Comput. Chem.* **1999**, *20*, 720−729.
(633) Halgren, T. A. Mmff Vii. Characterization of Mmff94, Mmff94s, and Other Widely Available Force Fields for Conformational Energies and for Intermolecular-Interaction Energies and Geometries. *J. Comput. Chem.* **1999**, *20*, 730−748.
(634) Urey, H. C.; Bradley, C. A. The Vibrations of Pentatonic Tetrahedral Molecules. *Phys. Rev.* **1931**, *38*, 1969−1978.
(635) Wilson, E. B., Jr A Method of Obtaining the Expanded Secular Equation for the Vibration Frequencies of a Molecule. *J. Chem. Phys.* **1939**, *7*, 1047−1052.
(636) Simanouti, T. The Normal Vibrations of Polyatomic Molecules as Treated by Urey-Bradley Field. *J. Chem. Phys.* **1949**, *17*, 245−248.
(637) Simanouti, T. The Normal Vibrations of Polyatomic Molecules as Calculated by Urey-Bradley Field. Ii. Vibrations of Polythene, Ethane, and Their Deuterium Compounds. *J. Chem. Phys.* **1949**, *17*, 734−737.
(638) Simanouti, T. The Normal Vibrations of Polyatomic Molecules as Calculated by Urey-Bradley Field. Iii. A Table of Force Constants. *J. Chem. Phys.* **1949**, *17*, 848−851.
(639) Nakagawa, I.; Shimanouchi, T. Infrared Absorption Spectra of Aquo Complexes and the Nature of Co-Ordination Bonds. *Spectrochim. Acta* **1964**, *20*, 429−439.
(640) Shahrokh, K.; Orendt, A.; Yost, G. S.; Cheatham, T. E. Quantum Mechanically Derived Amber-Compatible Heme Parameters for Various States of the Cytochrome P450 Catalytic Cycle. *J. Comput. Chem.* **2012**, *33*, 119−133.
(641) Neves, R. P.; Sousa, S. F.; Fernandes, P. A.; Ramos, M. J. Parameters for Molecular Dynamics Simulations of Manganese-Containing Metalloproteins. *J. Chem. Theory Comput.* **2013**, *9*, 2718−2732.
(642) Pople, J. A.; Krishnan, R.; Schlegel, H.; Binkley, J. S. Derivative Studies in Hartree-Fock and Møller-Plesset Theories. *Int. J. Quantum Chem.* **1979**, *16*, 225−241.
(643) Cramer, C. J. *Essentials of Computational Chemistry: Theories and Models*; John Wiley & Sons: West Sussex, UK, 2013.
(644) Pulay, P. Ab Initio Calculation of Force Constants and Equilibrium Geometries in Polyatomic Molecules: I. Theory. *Mol. Phys.* **1969**, *17*, 197−204.
(645) Pulay, P.; Fogarasi, G.; Pang, F.; Boggs, J. E. Systematic Ab Initio Gradient Calculation of Molecular Geometries, Force Constants, and Dipole Moment Derivatives. *J. Am. Chem. Soc.* **1979**, *101*, 2550−2560.
(646) Rauhut, G.; Pulay, P. Transferable Scaling Factors for Density Functional Derived Vibrational Force Fields. *J. Phys. Chem.* **1995**, *99*, 3093−3100.
(647) Person, W. B.; Szczepaniak, K.; Szczesniak, M.; Del Bene, J. E. Experimental and Ab Initio Quantum Mechanical Studies of the Vibrational Spectra of Isolated Pyrimidine Bases. *Recent Experimental and Computational Advances in Molecular Spectroscopy*; Springer: Dordrecht, Netherlands, 1993; pp 141−169.
(648) Ryde, U. Molecular Dynamics Simulations of Alcohol Dehydrogenase with a Four-or Five-Coordinate Catalytic Zinc Ion. *Proteins: Struct., Funct., Genet.* **1995**, *21*, 40−56.
(649) Hehre, W.; Radom, L.; Schleyer, P. v. R.; Pople, J. *Ab Initio Molecular Orbital Theory*; John Wiley & Sons: New York, 1986.
(650) Seminario, J. M. Calculation of Intramolecular Force Fields from Second-Derivative Tensors. *Int. J. Quantum Chem.* **1996**, *60*, 1271−1277.
(651) Tuccinardi, T.; Martinelli, A.; Nuti, E.; Carelli, P.; Balzano, F.; Uccello-Barretta, G.; Murphy, G.; Rossello, A. Amber Force Field Implementation, Molecular Modelling Study, Synthesis and Mmp-1/Mmp-2 Inhibition Profile of (R)-and (S)-N-Hydroxy-2-(N-Isopropoxybiphenyl-4-Ylsulfonamido)-3-Methylbutanamides. *Bioorg. Med. Chem.* **2006**, *14*, 4260−4276.
(652) Suárez, D.; Merz, K. M., Jr Molecular Dynamics Simulations of the Mononuclear Zinc-B-Lactamase from Bacillus Cereus. *J. Am. Chem. Soc.* **2001**, *123*, 3759−3770.
(653) Cui, G.; Wang, B.; Merz, K. M., Jr Computational Studies of the Farnesyltransferase Ternary Complex Part I: Substrate Binding. *Biochemistry* **2005**, *44*, 16513−16523.

DOI: 10.1021/acs.chemrev.6b00440
Chem. Rev. 2017, 117, 1564−1686

(654) Op't Holt, B. T.; Merz, K. M., Jr Insights into Cu (I) Exchange in Hah1 Using Quantum Mechanical and Molecular Simulations. *Biochemistry* **2007**, *46*, 8816−8826.
(655) Lin, F.; Wang, R. Systematic Derivation of Amber Force Field Parameters Applicable to Zinc-Containing Systems. *J. Chem. Theory Comput.* **2010**, *6*, 1852−1870.
(656) Chakravorty, D. K.; Wang, B.; Lee, C. W.; Giedroc, D. P.; Merz, K. M., Jr Simulations of Allosteric Motions in the Zinc Sensor Czra. *J. Am. Chem. Soc.* **2012**, *134*, 3367−3376.
(657) Chakravorty, D. K.; Wang, B.; Ucisik, M. N.; Merz, K. M., Jr Insight into the Cation-Π Interaction at the Metal Binding Site of the Copper Metallochaperone Cusf. *J. Am. Chem. Soc.* **2011**, *133*, 19330−19333.
(658) Ucisik, M. N.; Chakravorty, D. K.; Merz, K. M., Jr Structure and Dynamics of the N-Terminal Domain of the Cu (I) Binding Protein Cusb. *Biochemistry* **2013**, *52*, 6911−6923.
(659) Roberts, B. P.; Miller, B. R., III; Roitberg, A. E.; Merz, K. M., Jr Wide-Open Flaps Are Key to Urease Activity. *J. Am. Chem. Soc.* **2012**, *134*, 9934−9937.
(660) Minkara, M. S.; Ucisik, M. N.; Weaver, M. N.; Merz, K. M., Jr Molecular Dynamics Study of Helicobacter Pylori Urease. *J. Chem. Theory Comput.* **2014**, *10*, 1852−1862.
(661) Bautista, E. J.; Seminario, J. M. Harmonic Force Field for Glycine Oligopeptides. *Int. J. Quantum Chem.* **2008**, *108*, 180−188.
(662) Reyes, L. H.; Seminario, J. M. Determination of Precise Harmonic Force Constants for Alanine Polypeptides. *J. Mol. Struct.: THEOCHEM* **2007**, *818*, 125−129.
(663) Bellido, E. P.; Seminario, J. M. Harmonic Force Field for Nitro Compounds. *J. Mol. Model.* **2012**, *18*, 2805−2811.
(664) Aguilera-Segura, S. M.; Seminario, J. M. Ab Initio Analysis of Silicon Nano-Clusters. *J. Phys. Chem. C* **2014**, *118*, 1397−1406.
(665) Perez-Angel, E. C.; Seminario, J. M. Ab Initio Analysis and Harmonic Force Fields of Gallium Nitride Nanoclusters. *J. Phys. Chem. C* **2011**, *115*, 6467−6477.
(666) Lee, S. U.; Jung, J.; Han, Y.-K. Molecular Dynamics Study of the Ionic Conductivity of 1-N-Butyl-3-Methylimidazolium Salts as Ionic Liquids. *Chem. Phys. Lett.* **2005**, *406*, 332−340.
(667) Kaukonen, M.; Gulans, A.; Havu, P.; Kauppinen, E. Lennard-Jones Parameters for Small Diameter Carbon Nanotubes and Water for Molecular Mechanics Simulations from Van Der Waals Density Functional Calculations. *J. Comput. Chem.* **2012**, *33*, 652−658.
(668) Krokidas, P.; Castier, M.; Moncho, S.; Brothers, E.; Economou, I. G. Molecular Simulation Studies of the Diffusion of Methane, Ethane, Propane, and Propylene in Zif-8. *J. Phys. Chem. C* **2015**, *119*, 27028−27037.
(669) Nilsson, K.; Lecerof, D.; Sigfridsson, E.; Ryde, U. An Automatic Method to Generate Force-Field Parameters for Hetero-Compounds. *Acta Crystallogr., Sect. D: Biol. Crystallogr.* **2003**, *59*, 274−289.
(670) Humphrey, W.; Dalke, A.; Schulten, K. Vmd: Visual Molecular Dynamics. *J. Mol. Graphics* **1996**, *14*, 33−38.
(671) Li, P.; Merz, K. M., Jr Mcpb.Py: A Python Based Metal Center Parameter Builder. *J. Chem. Inf. Model.* **2016**, *56*, 599−604.
(672) Zheng, S.; Tang, Q.; He, J.; Du, S.; Xu, S.; Wang, C.; Xu, Y.; Lin, F. Vffdt: A New Software for Preparing Amber Force Field Parameters for Metal-Containing Molecular Systems. *J. Chem. Inf. Model.* **2016**, *56*, 811−818.
(673) Frisch, M.; Trucks, G.; Schlegel, H.; Scuseria, G.; Robb, M.; Cheeseman, J.; Montgomery, J., Jr.; Vreven, T.; Kudin, K.; Burant, J. *Gaussian 03*; Gaussian, Inc.: Wallingford, CT, 2004.
(674) Frisch, M. J.; Trucks, G. W.; Schlegel, H. B.; Scuseria, G. E.; Robb, M. A.; Cheeseman, J. R.; Scalmani, G.; Barone, V.; Mennucci, B.; Petersson, G. A.; et al. *Gaussian 09*, revision C.01; Gaussian, Inc.: Wallingford, CT, 2009.
(675) Schmidt, M. W.; Baldridge, K. K.; Boatz, J. A.; Elbert, S. T.; Gordon, M. S.; Jensen, J. H.; Koseki, S.; Matsunaga, N.; Nguyen, K. A.; Su, S. General Atomic and Molecular Electronic Structure System. *J. Comput. Chem.* **1993**, *14*, 1347−1363.
(676) Stewart, J. J. Mopac: A Semiempirical Molecular Orbital Program. *J. Comput.-Aided Mol. Des.* **1990**, *4*, 1−103.
(677) Hu, L.; Ryde, U. Comparison of Methods to Obtain Force-Field Parameters for Metal Sites. *J. Chem. Theory Comput.* **2011**, *7*, 2452−2463.
(678) Izadi, S.; Anandakrishnan, R.; Onufriev, A. V. Building Water Models: A Different Approach. *J. Phys. Chem. Lett.* **2014**, *5*, 3863−3871.
(679) Betz, R. M.; Walker, R. C. Paramfit: Automated Optimization of Force Field Parameters for Molecular Dynamics Simulations. *J. Comput. Chem.* **2015**, *36*, 79−87.
(680) Wang, L.-P.; Martinez, T. J.; Pande, V. S. Building Force Fields: An Automatic, Systematic, and Reproducible Approach. *J. Phys. Chem. Lett.* **2014**, *5*, 1885−1891.
(681) Rydberg, P.; Olsen, L.; Norrby, P.-O.; Ryde, U. General Transition-State Force Field for Cytochrome P450 Hydroxylation. *J. Chem. Theory Comput.* **2007**, *3*, 1765−1773.
(682) Burger, S. K.; Lacasse, M.; Verstraelen, T.; Drewry, J.; Gunning, P.; Ayers, P. W. Automated Parametrization of Amber Force Field Terms from Vibrational Analysis with a Focus on Functionalizing Dinuclear Zinc (Ii) Scaffolds. *J. Chem. Theory Comput.* **2012**, *8*, 554−562.
(683) Wang, R.; Ozhgibesov, M.; Hirao, H. Partial Hessian Fitting for Determining Force Constant Parameters in Molecular Mechanics. *J. Comput. Chem.* **2016**, *37*, 2349−2359.
(684) Badger, R. M. A Relation between Internuclear Distances and Bond Force Constants. *J. Chem. Phys.* **1934**, *2*, 128−131.
(685) Mecke, R. Zum Aufbau Der Bandenspektra. *Eur. Phys. J. A* **1925**, *32*, 823−834.
(686) Morse, P. M. Diatomic Molecules According to the Wave Mechanics. Ii. Vibrational Levels. *Phys. Rev.* **1929**, *34*, 57.
(687) Badger, R. M. The Relation between the Internuclear Distances and Force Constants of Molecules and Its Application to Polyatomic Molecules. *J. Chem. Phys.* **1935**, *3*, 710−714.
(688) Halgren, T. A. Maximally Diagonal Force Constants in Dependent Angle-Bending Coordinates: Part I. Mathematical Formulation. *J. Mol. Struct.: THEOCHEM* **1988**, *163*, 431−446.
(689) Halgren, T. A. Maximally Diagonal Force Constants in Dependent Angle-Bending Coordinates. Ii. Implications for the Design of Empirical Force Fields. *J. Am. Chem. Soc.* **1990**, *112*, 4710−4723.
(690) Wang, J.; Wolf, R. M.; Caldwell, J. W.; Kollman, P. A.; Case, D. A.; Wang, Junmei; Wolf, Romain M.; Caldwell, James W.; Kollman, Peter A.; David, A. Case,″ Development and Testing of a General Amber Force Field″ Journal of Computational Chemistry (2004) 25 (9) 1157−1174. *J. Comput. Chem.* **2005**, *26*, 114−114.
(691) Hancock, R. D. Molecular Mechanics Calculations as a Tool in Coordination Chemistry. *Progress in Inorganic Chemistry*; John Wiley & Sons, Inc.: New York, 1989; Vol. *37*, pp 187−291.
(692) Cornell, W. D.; Cieplak, P.; Bayly, C. I.; Kollmann, P. A. Application of Resp Charges to Calculate Conformational Energies, Hydrogen Bond Energies, and Free Energies of Solvation. *J. Am. Chem. Soc.* **1993**, *115*, 9620−9631.
(693) Kirschner, K. N.; Yongye, A. B.; Tschampel, S. M.; González-Outeiriño, J.; Daniels, C. R.; Foley, B. L.; Woods, R. J. Glycam06: A Generalizable Biomolecular Force Field. Carbohydrates. *J. Comput. Chem.* **2008**, *29*, 622−655.
(694) Reiher, W. E., III. *Theoretical Studies of Hydrogen Bonding*; Harvard University: MA, 1985.
(695) Neria, E.; Fischer, S.; Karplus, M. Simulation of Activation Free Energies in Molecular Systems. *J. Chem. Phys.* **1996**, *105*, 1902−1921.
(696) Yin, D.; MacKerell, A. D. Combined Ab Initio/Empirical Approach for Optimization of Lennard−Jones Parameters. *J. Comput. Chem.* **1998**, *19*, 334−348.
(697) Feller, S. E.; MacKerell, A. D. An Improved Empirical Potential Energy Function for Molecular Simulations of Phospholipids. *J. Phys. Chem. B* **2000**, *104*, 7510−7515.
(698) Wang, Z. X.; Zhang, W.; Wu, C.; Lei, H.; Cieplak, P.; Duan, Y. Strike a Balance: Optimization of Backbone Torsion Parameters of

DOI: 10.1021/acs.chemrev.6b00440
Chem. Rev. 2017, 117, 1564−1686

Amber Polarizable Force Field for Simulations of Proteins and Peptides. *J. Comput. Chem.* **2006**, *27*, 781−790.
(699) Hambley, T.; Searle, G. The Structure of U-Fac-(Diethylenetriamine)[Di(3-Aminopropyl)Amine] Cobalt(Iii) Perchlorate,[Co(Dien) (Dpt)](Clo4)3, and an Energy Minimization Analysis of the [Co(Dien) (Dpt)]3+ System. *Aust. J. Chem.* **1984**, *37*, 249−256.
(700) Hyon Kim, P. On the Proton Resonance of Several Hexammine Complex Salts. *J. Phys. Soc. Jpn.* **1960**, *15*, 445−455.
(701) Hambley, T. W. Molecular Mechanics Analysis of the Influence of Interligand Interactions on Isomer Stabilities and Barriers to Isomer Interconversion in Diammine-and Bis (Amine) Bis (Purine) Platinum (Ii) Complexes. *Inorg. Chem.* **1988**, *27*, 1073−1077.
(702) Hoops, S. C.; Anderson, K. W.; Merz, K. M., Jr Force Field Design for Metalloproteins. *J. Am. Chem. Soc.* **1991**, *113*, 8262−8270.
(703) Jorgensen, W. L.; Tirado-Rives, J. The Opls [Optimized Potentials for Liquid Simulations] Potential Functions for Proteins, Energy Minimizations for Crystals of Cyclic Peptides and Crambin. *J. Am. Chem. Soc.* **1988**, *110*, 1657−1666.
(704) Pranata, J.; Wierschke, S. G.; Jorgensen, W. L. Opls Potential Functions for Nucleotide Bases. Relative Association Constants of Hydrogen-Bonded Base Pairs in Chloroform. *J. Am. Chem. Soc.* **1991**, *113*, 2810−2819.
(705) Mulliken, R. S. Electronic Population Analysis on Lcao-Mo Molecular Wave Functions. I. *J. Chem. Phys.* **1955**, *23*, 1833−1840.
(706) Mulliken, R. Electronic Population Analysis on Lcao−Mo Molecular Wave Functions. Ii. Overlap Populations, Bond Orders, and Covalent Bond Energies. *J. Chem. Phys.* **1955**, *23*, 1841−1846.
(707) Mulliken, R. Electronic Population Analysis on Lcao-Mo Molecular Wave Functions. Iii. Effects of Hybridization on Overlap and Gross Ao Populations. *J. Chem. Phys.* **1955**, *23*, 2338−2342.
(708) Mulliken, R. Electronic Population Analysis on Lcao-Mo Molecular Wave Functions. Iv. Bonding and Antibonding in Lcao and Valence-Bond Theories. *J. Chem. Phys.* **1955**, *23*, 2343−2346.
(709) Reed, A. E.; Weinstock, R. B.; Weinhold, F. Natural Population Analysis. *J. Chem. Phys.* **1985**, *83*, 735−746.
(710) Lu, H.; Dai, D.; Yang, P.; Li, L. Atomic Orbitals in Molecules: General Electronegativity and Improvement of Mulliken Population Analysis. *Phys. Chem. Chem. Phys.* **2006**, *8*, 340−346.
(711) Singh, U. C.; Kollman, P. A. An Approach to Computing Electrostatic Charges for Molecules. *J. Comput. Chem.* **1984**, *5*, 129−145.
(712) Chirlian, L. E.; Francl, M. M. Atomic Charges Derived from Electrostatic Potentials: A Detailed Study. *J. Comput. Chem.* **1987**, *8*, 894−905.
(713) Breneman, C. M.; Wiberg, K. B. Determining Atom-Centered Monopoles from Molecular Electrostatic Potentials. The Need for High Sampling Density in Formamide Conformational Analysis. *J. Comput. Chem.* **1990**, *11*, 361−373.
(714) Bader, R. F.; Beddall, P. Virial Field Relationship for Molecular Charge Distributions and the Spatial Partitioning of Molecular Properties. *J. Chem. Phys.* **1972**, *56*, 3320−3329.
(715) Hirshfeld, F. Bonded-Atom Fragments for Describing Molecular Charge Densities. *Theor. Chim. Acta* **1977**, *44*, 129−138.
(716) Lu, T.; Chen, F. Atomic Dipole Moment Corrected Hirshfeld Population Method. *J. Theor. Comput. Chem.* **2012**, *11*, 163−183.
(717) Jakalian, A.; Bush, B. L.; Jack, D. B.; Bayly, C. I. Fast, Efficient Generation of High-Quality Atomic Charges. Am1-Bcc Model: I. Method. *J. Comput. Chem.* **2000**, *21*, 132−146.
(718) Jakalian, A.; Jack, D. B.; Bayly, C. I. Fast, Efficient Generation of High-Quality Atomic Charges. Am1-Bcc Model: Ii. Parameterization and Validation. *J. Comput. Chem.* **2002**, *23*, 1623−1641.
(719) Storer, J. W.; Giesen, D. J.; Cramer, C. J.; Truhlar, D. G. Class Iv Charge Models: A New Semiempirical Approach in Quantum Chemistry. *J. Comput.-Aided Mol. Des.* **1995**, *9*, 87−110.
(720) Li, J.; Zhu, T.; Cramer, C. J.; Truhlar, D. G. New Class Iv Charge Model for Extracting Accurate Partial Charges from Wave Functions. *J. Phys. Chem. A* **1998**, *102*, 1820−1831.
(721) Winget, P.; Thompson, J. D.; Xidos, J. D.; Cramer, C. J.; Truhlar, D. G. Charge Model 3: A Class Iv Charge Model Based on Hybrid Density Functional Theory with Variable Exchange. *J. Phys. Chem. A* **2002**, *106*, 10707−10717.
(722) Kelly, C. P.; Cramer, C. J.; Truhlar, D. G. Sm6: A Density Functional Theory Continuum Solvation Model for Calculating Aqueous Solvation Free Energies of Neutrals, Ions, and Solute-Water Clusters. *J. Chem. Theory Comput.* **2005**, *1*, 1133−1152.
(723) Marenich, A. V.; Jerome, S. V.; Cramer, C. J.; Truhlar, D. G. Charge Model 5: An Extension of Hirshfeld Population Analysis for the Accurate Description of Molecular Interactions in Gaseous and Condensed Phases. *J. Chem. Theory Comput.* **2012**, *8*, 527−541.
(724) Bonaccorsi, R.; Petrolongo, C.; Scrocco, E.; Tomasi, J. Quantum Aspects of Heterocyclic Compounds Minimal Basis Set SCF Calculations for the Three-Membered Ring Molecules C3h6, C2h4nh, C2h4o, C2h4nh2+, C3h4. Jerusalem Symposia "Quantum Aspects of Heterocyclic Compounds in Chemistry and Biochemistry. Pullman, B, Bergman, E., Eds.; Israeli Academy of Science: Jerusalem, 1970.
(725) Bonaccorsi, R.; Scrocco, E.; Tomasi, J. Molecular Scf Calculations for the Ground State of Some Three-Membered Ring Molecules:(Ch2) 3,(Ch2) 2nh,(Ch2) 2nh2+,(Ch2) 2o,(Ch2) 2s,(Ch) 2ch2, and N2ch2. *J. Chem. Phys.* **1970**, *52*, 5270−5284.
(726) Bonaccorsi, R.; Scrocco, E.; Tomasi, J. *Theoretical Section Progress Report*; Laboratorio di Chimica Quantistica del CNR e Istituto di Chimica Fisica dell'Universita, 1970; p 35.
(727) Bonaccorsi, R.; Petrongolo, C.; Scrocco, E.; Tomasi, J. Theoretical Investigations on the Solvation Process. *Theor. Chim. Acta* **1971**, *20*, 331−342.
(728) Bonaccorsi, R.; Scrocco, E.; Tomasi, J. Molecular Scf Calculations for the Ground State of Some Three-Membered Ring Molecules: Cis and Trans Diaziridine, Oxaziridine and the Corresponding Imminium Ions. *Theor. Chim. Acta* **1971**, *21*, 17−27.
(729) Bonaccorsi, R.; Pullman, A.; Scrocco, E.; Tomasi, J. N-Versus O-Proton Affinities of the Amide Group: Ab Initio Electrostatic Molecular Potentials. *Chem. Phys. Lett.* **1972**, *12*, 622−624.
(730) Bonaccorsi, R.; Pullman, A.; Scrocco, E.; Tomasi, J. The Molecular Electrostatic Potentials for the Nucleic Acid Bases: Adenine, Thymine, and Cytosine. *Theor. Chim. Acta* **1972**, *24*, 51−60.
(731) Kollman, P.; McKelvey, J.; Johansson, A.; Rothenberg, S. Theoretical Studies of Hydrogen-Bonded Dimers. Complexes Involving Hf, H2o, Nh3, Hc1, H2s, Ph3, Hcn, Hnc, Hcp, Ch2nh, H2cs, H2co, Ch4, Cf3h, C2h2, C2h4, C6h6, F-and H3O+. *J. Am. Chem. Soc.* **1975**, *97*, 955−965.
(732) Iwata, S.; Morokuma, K. Molecular Orbital Studies of Hydrogen Bonds. Vi. Origin of Red Shift Of. Pi.-. Pi.* Transitions. Trans-Acrolein-Water Complex. *J. Am. Chem. Soc.* **1975**, *97*, 966−970.
(733) Lathan, W. A.; Morokuma, K. Molecular Orbital Studies of Electron Donor-Acceptor Complexes. I. Carbonyl Cyanide-Ror and Tetracyanoethylene-Ror Complexes. *J. Am. Chem. Soc.* **1975**, *97*, 3615−3622.
(734) Hayes, D. M.; Kollman, P. A. Electrostatic Potentials of Proteins. 1. Carboxypeptidase A. *J. Am. Chem. Soc.* **1976**, *98*, 3335−3345.
(735) Hayes, D. M.; Kollman, P. A. Electrostatic Potentials of Proteins. 2. Role of Electrostatics in a Possible Catalytic Mechanism for Carboxypeptidase A. *J. Am. Chem. Soc.* **1976**, *98*, 7811−7816.
(736) Nuss, M. E.; Kollman, P. A. Electrostatic Potentials of Deoxydinucleoside Monophosphates. 1. Deoxydinucleoside Monophosphates and Actinomycin Chromophore Interactions. *J. Med. Chem.* **1979**, *22*, 1517−1524.
(737) Almlöf, J.; Wahlgren, U. Hydrogen Bond Studies. *Theor. Chim. Acta* **1973**, *28*, 161−168.
(738) Momany, F. A. Determination of Partial Atomic Charges from Ab Initio Molecular Electrostatic Potentials. Application to Formamide, Methanol, and Formic Acid. *J. Phys. Chem.* **1978**, *82*, 592−601.
(739) Scrocco, E.; Tomasi, J. Interpretation by Means of Electrostatic Molecular Potentials. *Adv. Quantum Chem.* **1978**, *11*, 115.

DOI: 10.1021/acs.chemrev.6b00440
Chem. Rev. 2017, 117, 1564−1686

(740) Cox, S.; Williams, D. Representation of the Molecular Electrostatic Potential by a Net Atomic Charge Model. *J. Comput. Chem.* **1981**, *2*, 304−323.
(741) Smit, P. H.; Derissen, J. L.; van Duijneveldt, F. B. Intermolecular Interactions in Crystals of Carboxylic Acids: Iii. Non-Empirical Interatomic Potential Functions. *Mol. Phys.* **1979**, *37*, 521−539.
(742) Sigfridsson, E.; Ryde, U. Comparison of Methods for Deriving Atomic Charges from the Electrostatic Potential and Moments. *J. Comput. Chem.* **1998**, *19*, 377−395.
(743) Besler, B. H.; Merz, K. M., Jr; Kollman, P. A. Atomic Charges Derived from Semiempirical Methods. *J. Comput. Chem.* **1990**, *11*, 431−439.
(744) Merz, K. M., Jr Carbon Dioxide Binding to Human Carbonic Anhydrase Ii. *J. Am. Chem. Soc.* **1991**, *113*, 406−411.
(745) Merz, K. M., Jr; Murcko, M. A.; Kollman, P. A. Inhibition of Carbonic Anhydrase. *J. Am. Chem. Soc.* **1991**, *113*, 4484−4490.
(746) Merz, K. M., Jr Analysis of a Large Data Base of Electrostatic Potential Derived Atomic Charges. *J. Comput. Chem.* **1992**, *13*, 749−767.
(747) Williams, D. E. Alanyl Dipeptide Potential-Derived Net Atomic Charges and Bond Dipoles, and Their Variation with Molecular Conformation. *Biopolymers* **1990**, *29*, 1367−1386.
(748) Bayly, C. I.; Cieplak, P.; Cornell, W.; Kollman, P. A. A Well-Behaved Electrostatic Potential Based Method Using Charge Restraints for Deriving Atomic Charges: The Resp Model. *J. Phys. Chem.* **1993**, *97*, 10269−10280.
(749) Cieplak, P.; Cornell, W. D.; Bayly, C.; Kollman, P. A. Application of the Multimolecule and Multiconformational Resp Methodology to Biopolymers: Charge Derivation for DNA, Rna, and Proteins. *J. Comput. Chem.* **1995**, *16*, 1357−1377.
(750) Wang, J.; Cieplak, P.; Kollman, P. A. How Well Does a Restrained Electrostatic Potential (Resp) Model Perform in Calculating Conformational Energies of Organic and Biological Molecules? *J. Comput. Chem.* **2000**, *21*, 1049−1074.
(751) Ryde, U. The Coordination Chemistry of the Structural Zinc Ion in Alcohol Dehydrogenase Studied by Ab Initio Quantum Chemical Calculations. *Eur. Biophys. J.* **1996**, *24*, 213−221.
(752) Heinz, H.; Suter, U. W. Atomic Charges for Classical Simulations of Polar Systems. *J. Phys. Chem. B* **2004**, *108*, 18341−18352.
(753) Heinz, H.; Koerner, H.; Anderson, K. L.; Vaia, R. A.; Farmer, B. Force Field for Mica-Type Silicates and Dynamics of Octadecylammonium Chains Grafted to Montmorillonite. *Chem. Mater.* **2005**, *17*, 5658−5669.
(754) Pearlman, D. A.; Kim, S.-H. Atomic Charges for DNA Constituents Derived from Single-Crystal X-Ray Diffraction Data. *J. Mol. Biol.* **1990**, *211*, 171−187.
(755) Hansen, N. K.; Coppens, P. Testing Aspherical Atom Refinements on Small-Molecule Data Sets. *Acta Crystallogr., Sect. A: Cryst. Phys., Diffr., Theor. Gen. Crystallogr.* **1978**, *34*, 909−921.
(756) Coppens, P.; Guru Row, T.; Leung, P.; Stevens, E.; Becker, P. t.; Yang, Y. Net Atomic Charges and Molecular Dipole Moments from Spherical-Atom X-Ray Refinements, and the Relation between Atomic Charge and Shape. *Acta Crystallogr., Sect. A: Cryst. Phys., Diffr., Theor. Gen. Crystallogr.* **1979**, *35*, 63−72.
(757) Pichon-Pesme, V.; Lecomte, C.; Lachekar, H. On Building a Data Bank of Transferable Experimental Electron Density Parameters Applicable to Polypeptides. *J. Phys. Chem.* **1995**, *99*, 6242−6250.
(758) Jelsch, C.; Pichon-Pesme, V.; Lecomte, C.; Aubry, A. Transferability of Multipole Charge-Density Parameters: Application to Very High Resolution Oligopeptide and Protein Structures. *Acta Crystallogr., Sect. D: Biol. Crystallogr.* **1998**, *54*, 1306−1318.
(759) Jelsch, C.; Teeter, M. M.; Lamzin, V.; Pichon-Pesme, V.; Blessing, R. H.; Lecomte, C. Accurate Protein Crystallography at Ultra-High Resolution: Valence Electron Distribution in Crambin. *Proc. Natl. Acad. Sci. U. S. A.* **2000**, *97*, 3171−3176.
(760) Pearlman, D. A.; Kim, S. H. Determinations of Atomic Partial Charges for Nucleic Acid Constituents from X-Ray Diffraction Data. I. 2′-Deoxycytidine-5′-Monophosphate. *Biopolymers* **1985**, *24*, 327−357.
(761) Hill, R. J. Crystal Structure Refinement and Electron Density Distribution in Diaspore. *Phys. Chem. Miner.* **1979**, *5*, 179−200.
(762) Thong, N.; Schwarzenbach, D. The Use of Electric Field Gradient Calculations in Charge Density Refinements. Ii. Charge Density Refinement of the Low-Quartz Structure of Aluminum Phosphate. *Acta Crystallogr., Sect. A: Cryst. Phys., Diffr., Theor. Gen. Crystallogr.* **1979**, *35*, 658−664.
(763) Lewis, J.; Schwarzenbach, D.; Flack, H. D. Electric Field Gradients and Charge Density in Corundum, A-Al2o3. *Acta Crystallogr., Sect. A: Cryst. Phys., Diffr., Theor. Gen. Crystallogr.* **1982**, *38*, 733−739.
(764) Belokoneva, E.; Gubina, Y. K.; Forsyth, J.; Brown, P. The Charge-Density Distribution, Its Multipole Refinement and the Antiferromagnetic Structure of Dioptase, Cu6 [Si6o18]· 6h2o. *Phys. Chem. Miner.* **2002**, *29*, 430−438.
(765) Souhassou, M.; Blessing, R. H. Topological Analysis of Experimental Electron Densities. *J. Appl. Crystallogr.* **1999**, *32*, 210−217.
(766) Ghermani, N.-E.; Bouhmaida, N.; Lecomte, C. Modelling Electrostatic Potential from Experimentally Determined Charge Densities. I. Spherical-Atom Approximation. *Acta Crystallogr., Sect. A: Found. Crystallogr.* **1993**, *49*, 781−789.
(767) Bouhmaida, N.; Ghermani, N.-E.; Lecomte, C.; Thalal, A. Modelling Electrostatic Potential from Experimentally Determined Charge Densities. Ii. Total Potential. *Acta Crystallogr., Sect. A: Found. Crystallogr.* **1997**, *53*, 556−563.
(768) Hamad, S.; Balestra, S. R.; Bueno-Perez, R.; Calero, S.; Ruiz-Salvador, A. R. Atomic Charges for Modeling Metal−Organic Frameworks: Why and How. *J. Solid State Chem.* **2015**, *223*, 144−151.
(769) Manz, T. A.; Sholl, D. S. Improved Atoms-in-Molecule Charge Partitioning Functional for Simultaneously Reproducing the Electrostatic Potential and Chemical States in Periodic and Nonperiodic Materials. *J. Chem. Theory Comput.* **2012**, *8*, 2844−2867.
(770) Campaná, C.; Mussard, B.; Woo, T. K. Electrostatic Potential Derived Atomic Charges for Periodic Systems Using a Modified Error Functional. *J. Chem. Theory Comput.* **2009**, *5*, 2866−2878.
(771) Blöchl, P. Electrostatic Decoupling of Periodic Images of Plane-Wave-Expanded Densities and Derived Atomic Point Charges. *J. Chem. Phys.* **1995**, *103*, 7422−7428.
(772) Wilmer, C. E.; Kim, K. C.; Snurr, R. Q. An Extended Charge Equilibration Method. *J. Phys. Chem. Lett.* **2012**, *3*, 2506−2511.
(773) Xu, Q.; Zhong, C. A General Approach for Estimating Framework Charges in Metal− Organic Frameworks. *J. Phys. Chem. C* **2010**, *114*, 5035−5042.
(774) Bourrelly, S.; Llewellyn, P. L.; Serre, C.; Millange, F.; Loiseau, T.; Férey, G. Different Adsorption Behaviors of Methane and Carbon Dioxide in the Isotypic Nanoporous Metal Terephthalates Mil-53 and Mil-47. *J. Am. Chem. Soc.* **2005**, *127*, 13519−13521.
(775) Šebesta, F.; Sláma, V.; Melcr, J.; Futera, Z.; Burda, J. V. Estimation of Transition-Metal Empirical Parameters for Molecular Mechanical Force Fields. *J. Chem. Theory Comput.* **2016**, *12*, 3681−3688.
(776) Batsanov, S. Van Der Waals Radii of Elements. *Inorg. Mater.* **2001**, *37*, 871−885.
(777) Handbook, C. *Handbook of Chemistry and Physics*; CRC Press LLC: Boca Raton, FL, 2002.
(778) Rappé, A. K.; Casewit, C. J.; Colwell, K. S.; Goddard, W. A., III; Skiff, W. M. Uff, a Full Periodic Table Force Field for Molecular Mechanics and Molecular Dynamics Simulations. *J. Am. Chem. Soc.* **1992**, *114*, 10024−10035.
(779) Clark, M.; Cramer, R. D.; van Opdenbosch, N. Validation of the General Purpose Tripos 5.2 Force Field. *J. Comput. Chem.* **1989**, *10*, 982−1012.
(780) Callomon, J. H.; Hirota, E.; Kuchitsu, K.; Lafferty, W. J.; Maki, A. G.; Pote, C. S. Springer-Verlag: Berlin−Heidelberg, 1976.

DOI: 10.1021/acs.chemrev.6b00440
Chem. Rev. 2017, 117, 1564−1686

(781) Harmony, M. D.; Laurie, V. W.; Kuczkowski, R. L.; Schwendeman, R. H.; Ramsay, D. A.; Lovas, F. J.; Lafferty, W. J.; Maki, A. G. Molecular Structures of Gas-Phase Polyatomic Molecules Determined by Spectroscopic Methods. *J. Phys. Chem. Ref. Data* **1979**, *8*, 619−722.
(782) Huber, K. P.; Herzberg, G. *Constants of Diatomic Molecules*; Van Nostrand Reinhold: New York, 1979; Vol. 4.
(783) Well, A. F. *Structural Inorganic Chemistry*; Clarendon: Oxford, 1984.
(784) Rappé, A. K.; Colwell, K. S.; Casewit, C. J. Application of a Universal Force Field to Metal Complexes. *Inorg. Chem.* **1993**, *32*, 3438−3450.
(785) Åqvist, J.; Warshel, A. Free Energy Relationships in Metalloenzyme-Catalyzed Reactions. Calculations of the Effects of Metal Ion Substitutions in Staphylococcal Nuclease. *J. Am. Chem. Soc.* **1990**, *112*, 2860−2868.
(786) Jiang, Y.; Zhang, H.; Tan, T. Rational Design of Methodology-Independent Metal Parameters Using a Nonbonded Dummy Model. *J. Chem. Theory Comput.* **2016**, *12*, 3250−60.
(787) Duarte, F.; Bauer, P.; Barrozo, A.; Amrein, B. A.; Purg, M.; Åqvist, J.; Kamerlin, S. C. L. Force Field Independent Metal Parameters Using a Nonbonded Dummy Model. *J. Phys. Chem. B* **2014**, *118*, 4351−4362.
(788) Lu, S. Y.; Huang, Z. M.; Huang, W. K.; Liu, X. Y.; Chen, Y. Y.; Shi, T.; Zhang, J. How Calcium Inhibits the Magnesium-Dependent Kinase Gsk3β: A Molecular Simulation Study. *Proteins: Struct., Funct., Genet.* **2013**, *81*, 740−753.
(789) Burgess, J. *Metal Ions in Solution*; Ellis Horwood Ltd.: Chichester, UK, 1978.
(790) Åqvist, J.; Warshel, A. Computer Simulation of the Initial Proton Transfer Step in Human Carbonic Anhydrase I. *J. Mol. Biol.* **1992**, *224*, 7−14.
(791) Oelschlaeger, P.; Klahn, M.; Beard, W. A.; Wilson, S. H.; Warshel, A. Magnesium-Cationic Dummy Atom Molecules Enhance Representation of DNA Polymerase B in Molecular Dynamics Simulations: Improved Accuracy in Studies of Structural Features and Mutational Effects. *J. Mol. Biol.* **2007**, *366*, 687−701.
(792) Saxena, A.; Sept, D. Multisite Ion Models That Improve Coordination and Free Energy Calculations in Molecular Dynamics Simulations. *J. Chem. Theory Comput.* **2013**, *9*, 3538−3542.
(793) Saxena, A.; García, A. E. Multisite Ion Model in Concentrated Solutions of Divalent Cations (Mgcl2 and Cacl2): Osmotic Pressure Calculations. *J. Phys. Chem. B* **2015**, *119*, 219−227.
(794) Liao, Q.; Kamerlin, S. C. L.; Strodel, B. Development and Application of a Non-Bonded Cu2+ Model That Includes the Jahn-Teller Effect. *J. Phys. Chem. Lett.* **2015**, *6*, 2657−2662.
(795) Pang, Y.-P. Novel Zinc Protein Molecular Dynamics Simulations: Steps toward Antiangiogenesis for Cancer Treatment. *J. Mol. Model.* **1999**, *5*, 196−202.
(796) Pang, Y.-P.; Xu, K.; Yazal, J. E.; Prendergast, F. G. Successful Molecular Dynamics Simulation of the Zinc-Bound Farnesyltransferase Using the Cationic Dummy Atom Approach. *Protein Sci.* **2000**, *9*, 1857−1865.
(797) Pang, Y.-P. Successful Molecular Dynamics Simulation of Two Zinc Complexes Bridged by a Hydroxide in Phosphotriesterase Using the Cationic Dummy Atom Method. *Proteins: Struct., Funct., Genet.* **2001**, *45*, 183−189.
(798) Park, J. G.; Sill, P. C.; Makiyi, E. F.; Garcia-Sosa, A. T.; Millard, C. B.; Schmidt, J. J.; Pang, Y.-P. Serotype-Selective, Small-Molecule Inhibitors of the Zinc Endopeptidase of Botulinum Neurotoxin Serotype A. *Bioorg. Med. Chem.* **2006**, *14*, 395−408.
(799) Tang, J.; Park, J. G.; Millard, C. B.; Schmidt, J. J.; Pang, Y.-P. Computer-Aided Lead Optimization: Improved Small-Molecule Inhibitor of the Zinc Endopeptidase of Botulinum Neurotoxin Serotype A. *PLoS One* **2007**, *2*, e761.
(800) Pang, Y.-P.; Vummenthala, A.; Mishra, R. K.; Park, J. G.; Wang, S.; Davis, J.; Millard, C. B.; Schmidt, J. J. Potent New Small-Molecule Inhibitor of Botulinum Neurotoxin Serotype a Endopeptidase Developed by Synthesis-Based Computer-Aided Molecular Design. *PLoS One* **2009**, *4*, e7730.
(801) Pang, Y.-P.; Davis, J.; Wang, S.; Park, J. G.; Nambiar, M. P.; Schmidt, J. J.; Millard, C. B. Small Molecules Showing Significant Protection of Mice against Botulinum Neurotoxin Serotype A. *PLoS One* **2010**, *5*, e10129.
(802) Jiang, Y.; Zhang, H.; Feng, W.; Tan, T. Refined Dummy Atom Model of Mg2+ by Simple Parameter Screening Strategy with Revised Experimental Solvation Free Energy. *J. Chem. Inf. Model.* **2015**, *55*, 2575−2586.
(803) Martínez, J. M.; Hernández-Cobos, J.; Saint-Martin, H.; Pappalardo, R. R.; Ortega-Blake, I.; Marcos, E. S. Coupling a Polarizable Water Model to the Hydrated Ion−Water Interaction Potential: A Test on the Cr3+ Hydration. *J. Chem. Phys.* **2000**, *112*, 2339−2347.
(804) Martínez, J. M.; Pappalardo, R. R.; Sánchez Marcos, E. First-Principles Ion-Water Interaction Potentials for Highly Charged Monatomic Cations. Computer Simulations of Al3+, Mg2+, and Be2+ in Water. *J. Am. Chem. Soc.* **1999**, *121*, 3175−3184.
(805) Wasserman, E.; Rustad, J. R.; Xantheas, S. S. Interaction Potential of Al3+ in Water from First Principles Calculations. *J. Chem. Phys.* **1997**, *106*, 9769−9780.
(806) Bleuzen, A.; Foglia, F.; Furet, E.; Helm, L.; Merbach, A. E.; Weber, J. Second Coordination Shell Water Exchange Rate and Mechanism: Experiments and Modeling on Hexaaquachromium (Iii). *J. Am. Chem. Soc.* **1996**, *118*, 12777−12787.
(807) Pappalardo, R. R.; Martínez, J. M.; Marcos, E. S. Application of the Hydrated Ion Concept for Modeling Aqueous Solutions Containing Highly Charged Ions: A Monte Carlo Simulation of Cr3+ in Water Using an Ab Initio Intermolecular Potential. *J. Phys. Chem.* **1996**, *100*, 11748−11754.
(808) Martínez, J. M.; Pappalardo, R. R.; Marcos, E. S.; Refson, K.; Díaz-Moreno, S.; Muñoz-Páez, A. Dynamics of a Highly Charged Ion in Aqueous Solutions: Md Simulations of Dilute Crcl3 Aqueous Solutions Using Interaction Potentials Based on the Hydrated Ion Concept. *J. Phys. Chem. B* **1998**, *102*, 3272−3282.
(809) Martínez, J. M.; Pappalardo, R. R.; Sánchez Marcos, E. A Molecular Dynamics Study of the Cr3+ Hydration Based on a Fully Flexible Hydrated Ion Model. *J. Chem. Phys.* **1998**, *109*, 1445−1455.
(810) Pappalardo, R. R.; Sanchez Marcos, E. Recovering the Concept of the Hydrated Ion for Modeling Ionic Solutions: A Monte Carlo Study of Zinc (2+) in Water. *J. Phys. Chem.* **1993**, *97*, 4500−4504.
(811) Bernal-Uruchurtu, M.; Hernández-Cobos, J.; Ortega-Blake, I. Comment on " Examining the Influence of the [Zn(H2o)6]2+ Geometry Change on the Monte Carlo Simulations of Zn2+ in Water" [J. Chem. Phys. 105, 5968 (1996)]. *J. Chem. Phys.* **1998**, *108*, 1750−1751.
(812) Marcos, E. S.; Martínez, J. M.; Pappalardo, R. R. Response to "Comment on 'Examining the Influence of the [Zn(H2o)6]2+ Geometry Change on the Monte Carlo Simulations of Zn2+ in Water'" [J. Chem. Phys. 108, 1750 (1998)]. *J. Chem. Phys.* **1998**, *108*, 1752−1753.
(813) Martínez, J. M.; Torrico, F.; Pappalardo, R. R.; Sanchez Marcos, E. Understanding the Hydration Structure of Square-Planar Aquaions: The [Pd(H2o)4]2+ Case. *J. Phys. Chem. B* **2004**, *108*, 15851−15855.
(814) Torrico, F.; Pappalardo, R. R.; Marcos, E. S.; Martínez, J. M. Hydration Structure and Dynamic Properties of the Square Planar Pt (Ii) Aquaion Compared to the Pd (Ii) Case. *Theor. Chem. Acc.* **2006**, *115*, 196−203.
(815) Yang, T.; Tsushima, S.; Suzuki, A. Quantum Mechanical and Molecular Dynamical Simulations on Thorium (Iv) Hydrates in Aqueous Solution. *J. Phys. Chem. A* **2001**, *105*, 10439−10445.
(816) Marcos, E. S.; Martínez, J. M.; Pappalardo, R. R. Examining the Influence of the [Zn(H2o)6]2+ Geometry Change on the Monte Carlo Simulations of Zn2+ in Water. *J. Chem. Phys.* **1996**, *105*, 5968−5970.

DOI: 10.1021/acs.chemrev.6b00440
Chem. Rev. 2017, 117, 1564−1686

(817) Jeziorski, B.; Moszynski, R.; Szalewicz, K. Perturbation Theory Approach to Intermolecular Potential Energy Surfaces of Van Der Waals Complexes. *Chem. Rev.* **1994**, *94*, 1887−1930.
(818) van Belle, D.; Couplet, I.; Prevost, M.; Wodak, S. J. Calculations of Electrostatic Properties in Proteins: Analysis of Contributions from Induced Protein Dipoles. *J. Mol. Biol.* **1987**, *198*, 721−735.
(819) Svishchev, I. M.; Kusalik, P. G.; Wang, J.; Boyd, R. J. Polarizable Point-Charge Model for Water: Results under Normal and Extreme Conditions. *J. Chem. Phys.* **1996**, *105*, 4742−4750.
(820) van Maaren, P. J.; van der Spoel, D. Molecular Dynamics Simulations of Water with Novel Shell-Model Potentials. *J. Phys. Chem. B* **2001**, *105*, 2618−2626.
(821) Bernardo, D. N.; Ding, Y.; Krogh-Jespersen, K.; Levy, R. M. An Anisotropic Polarizable Water Model: Incorporation of All-Atom Polarizabilities into Molecular Mechanics Force Fields. *J. Phys. Chem.* **1994**, *98*, 4180−4187.
(822) Medeiros, M.; Costas, M. E. Gibbs Ensemble Monte Carlo Simulation of the Properties of Water with a Fluctuating Charges Model. *J. Chem. Phys.* **1997**, *107*, 2012−2019.
(823) Campbell, T.; Kalia, R. K.; Nakano, A.; Vashishta, P.; Ogata, S.; Rodgers, S. Dynamics of Oxidation of Aluminum Nanoclusters Using Variable Charge Molecular-Dynamics Simulations on Parallel Computers. *Phys. Rev. Lett.* **1999**, *82*, 4866.
(824) van Belle, D.; Wodak, S. Extended Lagrangian Formalism Applied to Temperature Control and Electronic Polarization Effects in Molecular Dynamics Simulations. *Comput. Phys. Commun.* **1995**, *91*, 253−262.
(825) Tuckerman, M. E.; Martyna, G. J. Understanding Modern Molecular Dynamics: Techniques and Applications. *J. Phys. Chem. B* **2000**, *104*, 159−178.
(826) Tuckerman, M. E.; Martyna, G. J. Understanding Modern Molecular Dynamics: Techniques and Applications. *J. Phys. Chem. B* **2001**, *105*, 7598−7598.
(827) Souaille, M.; Loirat, H.; Borgis, D.; Gaigeot, M. Mdvry: A Polarizable Classical Molecular Dynamics Package for Biomolecules. *Comput. Phys. Commun.* **2009**, *180*, 276−301.
(828) Patel, S.; Brooks, C. L. Charmm Fluctuating Charge Force Field for Proteins: I Parameterization and Application to Bulk Organic Liquid Simulations. *J. Comput. Chem.* **2004**, *25*, 1−16.
(829) Mortier, W. J.; van Genechten, K.; Gasteiger, J. Electronegativity Equalization: Application and Parametrization. *J. Am. Chem. Soc.* **1985**, *107*, 829−835.
(830) Mortier, W. J.; Ghosh, S. K.; Shankar, S. Electronegativity-Equalization Method for the Calculation of Atomic Charges in Molecules. *J. Am. Chem. Soc.* **1986**, *108*, 4315−4320.
(831) De Proft, F.; Langenaeker, W.; Geerlings, P. A Non-Empirical Electronegativity Equalization Scheme. Theory and Applications Using Isolated Atom Properties. *J. Mol. Struct.: THEOCHEM* **1995**, *339*, 45−55.
(832) Smirnov, K. S.; van de Graaf, B. Consistent Implementation of the Electronegativity Equalization Method in Molecular Mechanics and Molecular Dynamics. *J. Chem. Soc., Faraday Trans.* **1996**, *92*, 2469−2474.
(833) Banks, J. L.; Kaminski, G. A.; Zhou, R.; Mainz, D. T.; Berne, B. J.; Friesner, R. A. Parametrizing a Polarizable Force Field from Ab Initio Data. I. The Fluctuating Point Charge Model. *J. Chem. Phys.* **1999**, *110*, 741−754.
(834) Patel, S.; Mackerell, A. D.; Brooks, C. L. Charmm Fluctuating Charge Force Field for Proteins: Ii Protein/Solvent Properties from Molecular Dynamics Simulations Using a Nonadditive Electrostatic Model. *J. Comput. Chem.* **2004**, *25*, 1504−1514.
(835) Yang, Z.-Z.; Wang, C.-S. Atom-Bond Electronegativity Equalization Method. 1. Calculation of the Charge Distribution in Large Molecules. *J. Phys. Chem. A* **1997**, *101*, 6315−6321.
(836) Wang, C.-S.; Yang, Z.-Z. Atom−Bond Electronegativity Equalization Method. Ii. Lone-Pair Electron Model. *J. Chem. Phys.* **1999**, *110*, 6189−6197.
(837) Cong, Y.; Yang, Z.-Z. General Atom-Bond Electronegativity Equalization Method and Its Application in Prediction of Charge Distributions in Polypeptide. *Chem. Phys. Lett.* **2000**, *316*, 324−329.
(838) Yang, Z.-Z.; Wang, C.-S. Atom-Bond Electronegativity Equalization Method and Its Applications Based on Density Functional Theory. *J. Theor. Comput. Chem.* **2003**, *2*, 273−299.
(839) Wu, Y.; Yang, Z.-Z. Atom-Bond Electronegativity Equalization Method Fused into Molecular Mechanics. Ii. A Seven-Site Fluctuating Charge and Flexible Body Water Potential Function for Liquid Water. *J. Phys. Chem. A* **2004**, *108*, 7563−7576.
(840) Yang, Z.-Z.; Wu, Y.; Zhao, D.-X. Atom-Bond Electronegativity Equalization Method Fused into Molecular Mechanics. I. A Seven-Site Fluctuating Charge and Flexible Body Water Potential Function for Water Clusters. *J. Chem. Phys.* **2004**, *120*, 2541−2557.
(841) Li, X.; Yang, Z.-Z. Study of Lithium Cation in Water Clusters: Based on Atom-Bond Electronegativity Equalization Method Fused into Molecular Mechanics. *J. Phys. Chem. A* **2005**, *109*, 4102−4111.
(842) Li, X.; Yang, Z.-Z. Hydration of Li+-Ion in Atom-Bond Electronegativity Equalization Method-7p Water: A Molecular Dynamics Simulation Study. *J. Chem. Phys.* **2005**, *122*, 84514.
(843) Yang, Z.-Z.; Li, X. Ion Solvation in Water from Molecular Dynamics Simulation with the Abeem/Mm Force Field. *J. Phys. Chem. A* **2005**, *109*, 3517−3520.
(844) Yang, Z.-Z.; Li, X. Molecular-Dynamics Simulations of Alkaline-Earth Metal Cations in Water by Atom-Bond Electronegativity Equalization Method Fused into Molecular Mechanics. *J. Chem. Phys.* **2005**, *123*, 094507.
(845) Zhang, Q.; Yang, Z.-Z. An Investigation of Alkane Conformations Based on the Abeem/Mm Model. *Chem. Phys. Lett.* **2005**, *403*, 242−247.
(846) Yang, Z.-Z.; Qian, P. A Study of N-Methylacetamide in Water Clusters: Based on Atom-Bond Electronegativity Equalization Method Fused into Molecular Mechanics. *J. Chem. Phys.* **2006**, *125*, 064311.
(847) Yang, Z. Z.; Zhang, Q. Study of Peptide Conformation in Terms of the Abeem/Mm Method. *J. Comput. Chem.* **2006**, *27*, 1−10.
(848) Yang, Z.-Z.; Cui, B.-Q. Atomic Charge Calculation of Metallobiomolecules in Terms of the Abeem Method. *J. Chem. Theory Comput.* **2007**, *3*, 1561−1568.
(849) Cui, B. Q.; Guan, Q. M.; Gong, L. D.; Zhao, D. X.; Yang, Z. Z. Studies on the Heme Prosthetic Group's Geometry by Abeem/Mm Method. *Chem. J. Chin. Univ.* **2008**, *29*, 585−590.
(850) QingMei, G.; BaoQiu, C.; DongXia, Z.; LiDong, G.; ZhongZhi, Y. Molecular Dynamics Study on Bpti Aqueous Solution by Abeem/Mm Fluctuating Charge Model. *Chin. Sci. Bull.* **2008**, *53*, 1171−1174.
(851) Zhao, D.-X.; Liu, C.; Wang, F.-F.; Yu, C.-Y.; Gong, L.-D.; Liu, S.-B.; Yang, Z.-Z. Development of a Polarizable Force Field Using Multiple Fluctuating Charges Per Atom. *J. Chem. Theory Comput.* **2010**, *6*, 795−804.
(852) Yang, Z. Z.; Wang, J. J.; Zhao, D. X. Valence State Parameters of All Transition Metal Atoms in Metalloproteins—Development of Abeem$\sigma\pi$ Fluctuating Charge Force Field. *J. Comput. Chem.* **2014**, *35*, 1690−1706.
(853) Jensen, W. B. Electronegativity from Avogadro to Pauling: Part 1: Origins of the Electronegativity Concept. *J. Chem. Educ.* **1996**, *73*, 11−20.
(854) Jensen, W. B. Electronegativity from Avogadro to Pauling: Ii. Late Nineteenth-and Early Twentieth-Century Developments. *J. Chem. Educ.* **2003**, *80*, 279−287.
(855) Hund, F. Zur Frage Der Chemischen Bindung. *Eur. Phys. J. A* **1932**, *73*, 1−30.
(856) Pauling, L. The Nature of the Chemical Bond. Iv. The Energy of Single Bonds and the Relative Electronegativity of Atoms. *J. Am. Chem. Soc.* **1932**, *54*, 3570−3582.
(857) Mulliken, R. S. A New Electroaffinity Scale; Together with Data on Valence States and on Valence Ionization Potentials and Electron Affinities. *J. Chem. Phys.* **1934**, *2*, 782−793.
(858) Sanderson, R. An Interpretation of Bond Lengths and a Classification of Bonds. *Science* **1951**, *114*, 670−672.

DOI: 10.1021/acs.chemrev.6b00440
Chem. Rev. 2017, 117, 1564−1686

(859) Sanderson, R. An Interpretation of Bond Lengths in Alkali Halide Gas Molecules. *J. Am. Chem. Soc.* **1952**, *74*, 272−274.
(860) Parr, R. G.; Donnelly, R. A.; Levy, M.; Palke, W. E. Electronegativity: The Density Functional Viewpoint. *J. Chem. Phys.* **1978**, *68*, 3801−3807.
(861) Parr, R. G.; Pearson, R. G. Absolute Hardness: Companion Parameter to Absolute Electronegativity. *J. Am. Chem. Soc.* **1983**, *105*, 7512−7516.
(862) Hinze, J.; Jaffe, H. H.; Electronegativity, I. Orbital Electronegativity of Neutral Atoms. *J. Am. Chem. Soc.* **1962**, *84*, 540−546.
(863) Hinze, J.; Whitehead, M.; Jaffe, H. H. Electronegativity. Ii. Bond and Orbital Electronegativities. *J. Am. Chem. Soc.* **1963**, *85*, 148−154.
(864) Hinze, J.; Jaffé, H. Electronegativity. Iii. Orbital Electronegativities and Electron Affinities of Transition Metals. *Can. J. Chem.* **1963**, *41*, 1315−1328.
(865) Hinze, J.; Jaffe, H. Electronegativity. Iv. Orbital Electronegativities of the Neutral Atoms of the Periods Three a and Four a and of Positive Ions of Periods One and Two. *J. Phys. Chem.* **1963**, *67*, 1501−1506.
(866) Gasteiger, J.; Marsili, M. A New Model for Calculating Atomic Charges in Molecules. *Tetrahedron Lett.* **1978**, *19*, 3181−3184.
(867) Gasteiger, J.; Marsili, M. Iterative Partial Equalization of Orbital Electronegativity - a Rapid Access to Atomic Charges. *Tetrahedron* **1980**, *36*, 3219−3228.
(868) Rappé, A. K.; Goddard, W. A., III Charge Equilibration for Molecular Dynamics Simulations. *J. Phys. Chem.* **1991**, *95*, 3358−3363.
(869) Casewit, C.; Colwell, K.; Rappe, A. Application of a Universal Force Field to Organic Molecules. *J. Am. Chem. Soc.* **1992**, *114*, 10035−10046.
(870) Casewit, C.; Colwell, K.; Rappe, A. Application of a Universal Force Field to Main Group Compounds. *J. Am. Chem. Soc.* **1992**, *114*, 10046−10053.
(871) Nistor, R. A.; Polihronov, J. G.; Müser, M. H.; Mosey, N. J. A Generalization of the Charge Equilibration Method for Nonmetallic Materials. *J. Chem. Phys.* **2006**, *125*, 094108.
(872) Verstraelen, T.; Van Speybroeck, V.; Waroquier, M. The Electronegativity Equalization Method and the Split Charge Equilibration Applied to Organic Systems: Parametrization, Validation, and Comparison. *J. Chem. Phys.* **2009**, *131*, 044127.
(873) Verstraelen, T.; Ayers, P.; Van Speybroeck, V.; Waroquier, M. Acks2: Atom-Condensed Kohn-Sham Dft Approximated to Second Order. *J. Chem. Phys.* **2013**, *138*, 074108.
(874) Rick, S. W.; Stuart, S. J.; Berne, B. J. Dynamical Fluctuating Charge Force Fields: Application to Liquid Water. *J. Chem. Phys.* **1994**, *101*, 6141−6156.
(875) Stuart, S. J.; Berne, B. Effects of Polarizability on the Hydration of the Chloride Ion. *J. Phys. Chem.* **1996**, *100*, 11934−11943.
(876) Stuart, S. J.; Berne, B. Surface Curvature Effects in the Aqueous Ionic Solvation of the Chloride Ion. *J. Phys. Chem. A* **1999**, *103*, 10300−10307.
(877) Comba, P.; Martin, B.; Sanyal, A. An Efficient Fluctuating Charge Model for Transition Metal Complexes. *J. Comput. Chem.* **2013**, *34*, 1598−1608.
(878) Comba, P.; Martin, B.; Sanyal, A.; Stephan, H. The Computation of Lipophilicities of 64 Cu Pet Systems Based on a Novel Approach for Fluctuating Charges. *Dalton Transactions* **2013**, *42*, 11066−11073.
(879) Ramachandran, S.; Lenz, T.; Skiff, W.; Rappe, A. Toward an Understanding of Zeolite Y as a Cracking Catalyst with the Use of Periodic Charge Equilibration. *J. Phys. Chem.* **1996**, *100*, 5898−5907.
(880) Martin-Noble, G. C.; Reilley, D.; Rivas, L. M.; Smith, M. D.; Schrier, J. Eqeq+ C: An Empirical Bond-Order-Corrected Extended Charge Equilibration Method. *J. Chem. Theory Comput.* **2015**, *11*, 3364−3374.
(881) Brown, I. D. Recent Developments in the Methods and Applications of the Bond Valence Model. *Chem. Rev.* **2009**, *109*, 6858−6919.
(882) Drude, P. *The Theory of Optics*; Dover Publications Inc.: New York, 1902.
(883) Galbis, E.; Hernández-Cobos, J.; Pappalardo, R. R.; Marcos, E. S. Collecting High-Order Interactions in an Effective Pairwise Intermolecular Potential Using the Hydrated Ion Concept: The Hydration of Cf3+. *J. Chem. Phys.* **2014**, *140*, 214104.
(884) Iori, F.; Corni, S. Including Image Charge Effects in the Molecular Dynamics Simulations of Molecules on Metal Surfaces. *J. Comput. Chem.* **2008**, *29*, 1656−1666.
(885) Dick, B. G.; Overhauser, A. W. Theory of the Dielectric Constants of Alkali Halide Crystals. *Phys. Rev.* **1958**, *112*, 90−103.
(886) Szigeti, B. Polarisability and Dielectric Constant of Ionic Crystals. *Trans. Faraday Soc.* **1949**, *45*, 155−166.
(887) Szigeti, B. Compressibility and Absorption Frequency of Ionic Crystals. *Proc. R. Soc. A*; The Royal Society: UK, 1950; Vol. *204*, pp 51−62.
(888) Hanlon, J. E.; Lawson, A. W. Effective Ionic Charge in Alkali Halides. *Phys. Rev.* **1959**, *113*, 472−478.
(889) Jacucci, G.; McDonald, I.; Singer, K. Introduction of the Shell Model of Ionic Polarizability into Molecular Dynamics Calculations. *Phys. Lett. A* **1974**, *50*, 141−143.
(890) Lindan, P.; Gillan, M. Shell-Model Molecular Dynamics Simulation of Superionic Conduction in Caf2. *J. Phys.: Condens. Matter* **1993**, *5*, 1019−1031.
(891) Mitchell, P.; Fincham, D. Shell Model Simulations by Adiabatic Dynamics. *J. Phys.: Condens. Matter* **1993**, *5*, 1031−1038.
(892) Lamoureux, G.; MacKerell, A. D., Jr; Roux, B. A Simple Polarizable Model of Water Based on Classical Drude Oscillators. *J. Chem. Phys.* **2003**, *119*, 5185−5197.
(893) Lamoureux, G.; Harder, E.; Vorobyov, I. V.; Roux, B.; MacKerell, A. D. A Polarizable Model of Water for Molecular Dynamics Simulations of Biomolecules. *Chem. Phys. Lett.* **2006**, *418*, 245−249.
(894) Orabi, E. A.; Lamoureux, G. Cation− Π and Π−Π Interactions in Aqueous Solution Studied Using Polarizable Potential Models. *J. Chem. Theory Comput.* **2012**, *8*, 182−193.
(895) Orabi, E. A.; Lamoureux, G. Molecular Dynamics Investigation of Alkali Metal Ions in Liquid and Aqueous Ammonia. *J. Chem. Theory Comput.* **2013**, *9*, 2324−2338.
(896) Luo, Y.; Jiang, W.; Yu, H.; MacKerell, A. D.; Roux, B. Simulation Study of Ion Pairing in Concentrated Aqueous Salt Solutions with a Polarizable Force Field. *Faraday Discuss.* **2013**, *160*, 135−149.
(897) Vorobyov, I. V.; Anisimov, V. M.; MacKerell, A. D. Polarizable Empirical Force Field for Alkanes Based on the Classical Drude Oscillator Model. *J. Phys. Chem. B* **2005**, *109*, 18988−18999.
(898) Anisimov, V. M.; Vorobyov, I. V.; Roux, B.; MacKerell, A. D. Polarizable Empirical Force Field for the Primary and Secondary Alcohol Series Based on the Classical Drude Model. *J. Chem. Theory Comput.* **2007**, *3*, 1927−1946.
(899) Lopes, P. E.; Lamoureux, G.; Roux, B.; MacKerell, A. D. Polarizable Empirical Force Field for Aromatic Compounds Based on the Classical Drude Oscillator. *J. Phys. Chem. B* **2007**, *111*, 2873−2885.
(900) Vorobyov, I.; Anisimov, V. M.; Greene, S.; Venable, R. M.; Moser, A.; Pastor, R. W.; MacKerell, A. D. Additive and Classical Drude Polarizable Force Fields for Linear and Cyclic Ethers. *J. Chem. Theory Comput.* **2007**, *3*, 1120−1133.
(901) Lamoureux, G.; Faraldo-Gómez, J. D.; Krupin, S.; Noskov, S. Y. Polarizable Model of Chloroform Based on Classical Drude Oscillators. *Chem. Phys. Lett.* **2009**, *468*, 270−274.
(902) Lopes, P. E.; Lamoureux, G.; Mackerell, A. D. Polarizable Empirical Force Field for Nitrogen-Containing Heteroaromatic Compounds Based on the Classical Drude Oscillator. *J. Comput. Chem.* **2009**, *30*, 1821−1838.
(903) Baker, C. M.; MacKerell, A. D., Jr Polarizability Rescaling and Atom-Based Thole Scaling in the Charmm Drude Polarizable Force Field for Ethers. *J. Mol. Model.* **2010**, *16*, 567−576.

DOI: 10.1021/acs.chemrev.6b00440
Chem. Rev. 2017, 117, 1564−1686

(904) Zhu, X.; Mackerell, A. D. Polarizable Empirical Force Field for Sulfur-Containing Compounds Based on the Classical Drude Oscillator Model. *J. Comput. Chem.* **2010**, *31*, 2330−2341.
(905) Lopes, P. E.; Huang, J.; Shim, J.; Luo, Y.; Li, H.; Roux, B.; MacKerell, A. D., Jr Polarizable Force Field for Peptides and Proteins Based on the Classical Drude Oscillator. *J. Chem. Theory Comput.* **2013**, *9*, 5430−5449.
(906) Baker, C. M.; Anisimov, V. M.; MacKerell, A. D., Jr Development of Charmm Polarizable Force Field for Nucleic Acid Bases Based on the Classical Drude Oscillator Model. *J. Phys. Chem. B* **2011**, *115*, 580−596.
(907) Savelyev, A.; MacKerell, A. D. All-Atom Polarizable Force Field for DNA Based on the Classical Drude Oscillator Model. *J. Comput. Chem.* **2014**, *35*, 1219−1239.
(908) Chowdhary, J.; Harder, E.; Lopes, P. E.; Huang, L.; MacKerell, A. D., Jr; Roux, B. A Polarizable Force Field of Dipalmitoylphosphatidylcholine Based on the Classical Drude Model for Molecular Dynamics Simulations of Lipids. *J. Phys. Chem. B* **2013**, *117*, 9142−9160.
(909) Patel, D. S.; He, X.; MacKerell, A. D., Jr Polarizable Empirical Force Field for Hexopyranose Monosaccharides Based on the Classical Drude Oscillator. *J. Phys. Chem. B* **2015**, *119*, 637−652.
(910) Lamoureux, G.; Roux, B. t. Modeling Induced Polarization with Classical Drude Oscillators: Theory and Molecular Dynamics Simulation Algorithm. *J. Chem. Phys.* **2003**, *119*, 3025−3039.
(911) Noyes, R. M. Thermodynamics of Ion Hydration as a Measure of Effective Dielectric Properties of Water. *J. Am. Chem. Soc.* **1962**, *84*, 513−522.
(912) Archontis, G.; Leontidis, E.; Andreou, G. Attraction of Iodide Ions by the Free Water Surface, Revealed by Simulations with a Polarizable Force Field Based on Drude Oscillators. *J. Phys. Chem. B* **2005**, *109*, 17957−17966.
(913) Saint-Martin, H.; Hernández-Cobos, J.; Bernal-Uruchurtu, M. I.; Ortega-Blake, I.; Berendsen, H. J. A Mobile Charge Densities in Harmonic Oscillators (Mcdho) Molecular Model for Numerical Simulations: The Water−Water Interaction. *J. Chem. Phys.* **2000**, *113*, 10899−10912.
(914) Yu, K.; McDaniel, J. G.; Schmidt, J. Physically Motivated, Robust, Ab Initio Force Fields for Co2 and N2. *J. Phys. Chem. B* **2011**, *115*, 10054−10063.
(915) McDaniel, J. G.; Schmidt, J. Robust, Transferable, and Physically Motivated Force Fields for Gas Adsorption in Functionalized Zeolitic Imidazolate Frameworks. *J. Phys. Chem. C* **2012**, *116*, 14031−14039.
(916) Barker, J. A. Statistical Mechanics of Interacting Dipoles. *Proc. R. Soc. London, Ser. A* **1953**, *219*, 367−372.
(917) Warshel, A.; Levitt, M. Theoretical Studies of Enzymic Reactions: Dielectric, Electrostatic and Steric Stabilization of the Carbonium Ion in the Reaction of Lysozyme. *J. Mol. Biol.* **1976**, *103*, 227−249.
(918) David, C. W. Applying the Polarization Model to the Hydrated Lithium Cation. *Computer Modeling of Matter*; American Chemical Society: Washington, DC, 1978; Vol. *86*, pp 35−61.
(919) Jorgensen, W. L.; Jensen, K. P.; Alexandrova, A. N. Polarization Effects for Hydrogen-Bonded Complexes of Substituted Phenols with Water and Chloride Ion. *J. Chem. Theory Comput.* **2007**, *3*, 1987−1992.
(920) Cieplak, P.; Caldwell, J.; Kollman, P. Molecular Mechanical Models for Organic and Biological Systems Going Beyond the Atom Centered Two Body Additive Approximation: Aqueous Solution Free Energies of Methanol and N-Methyl Acetamide, Nucleic Acid Base, and Amide Hydrogen Bonding and Chloroform/Water Partition Coefficients of the Nucleic Acid Bases. *J. Comput. Chem.* **2001**, *22*, 1048−1057.
(921) Ren, P.; Ponder, J. W. Polarizable Atomic Multipole Water Model for Molecular Mechanics Simulation. *J. Phys. Chem. B* **2003**, *107*, 5933−5947.
(922) Gresh, N.; Policar, C.; Giessner-Prettre, C. Modeling Copper (I) Complexes: Sibfa Molecular Mechanics Versus Ab Initio Energetics and Geometrical Arrangements. *J. Phys. Chem. A* **2002**, *106*, 5660−5670.
(923) Xie, W.; Pu, J.; MacKerell, A. D.; Gao, J. Development of a Polarizable Intermolecular Potential Function (Pipf) for Liquid Amides and Alkanes. *J. Chem. Theory Comput.* **2007**, *3*, 1878−1889.
(924) Sakharov, D. V.; Lim, C. Zn Protein Simulations Including Charge Transfer and Local Polarization Effects. *J. Am. Chem. Soc.* **2005**, *127*, 4921−4929.
(925) Garmer, D. R.; Stevens, W. J. Transferability of Molecular Distributed Polarizabilities from a Simple Localized Orbital Based Method. *J. Phys. Chem.* **1989**, *93*, 8263−8270.
(926) Stone, A. Distributed Multipole Analysis, or How to Describe a Molecular Charge Distribution. *Chem. Phys. Lett.* **1981**, *83*, 233−239.
(927) Vigné - Maeder, F.; Claverie, P. The Exact Multicenter Multipolar Part of a Molecular Charge Distribution and Its Simplified Representations. *J. Chem. Phys.* **1988**, *88*, 4934−4948.
(928) Bagus, P. S.; Hermann, K.; Bauschlicher, C. W., Jr A New Analysis of Charge Transfer and Polarization for Ligand−Metal Bonding: Model Studies of Al4co and Al4nh3. *J. Chem. Phys.* **1984**, *80*, 4378−4386.
(929) Bagus, P. S.; Illas, F. Decomposition of the Chemisorption Bond by Constrained Variations: Order of the Variations and Construction of the Variational Spaces. *J. Chem. Phys.* **1992**, *96*, 8962−8970.
(930) Piquemal, J. P.; Marquez, A.; Parisel, O.; Giessner−Prettre, C. A Csov Study of the Difference between Hf and Dft Intermolecular Interaction Energy Values: The Importance of the Charge Transfer Contribution. *J. Comput. Chem.* **2005**, *26*, 1052−1062.
(931) Stevens, W. J.; Fink, W. H. Frozen Fragment Reduced Variational Space Analysis of Hydrogen Bonding Interactions. Application to the Water Dimer. *Chem. Phys. Lett.* **1987**, *139*, 15−22.
(932) Caldwell, J. W.; Kollman, P. A. Cation-. Pi. Interactions: Nonadditive Effects Are Critical in Their Accurate Representation. *J. Am. Chem. Soc.* **1995**, *117*, 4177−4178.
(933) Shi, Y.; Xia, Z.; Zhang, J.; Best, R.; Wu, C.; Ponder, J. W.; Ren, P. Polarizable Atomic Multipole-Based Amoeba Force Field for Proteins. *J. Chem. Theory Comput.* **2013**, *9*, 4046−4063.
(934) Wu, J. C.; Piquemal, J.-P.; Chaudret, R.; Reinhardt, P.; Ren, P. Polarizable Molecular Dynamics Simulation of Zn (Ii) in Water Using the Amoeba Force Field. *J. Chem. Theory Comput.* **2010**, *6*, 2059−2070.
(935) Marjolin, A.; Gourlaouen, C.; Clavaguéra, C.; Ren, P. Y.; Wu, J. C.; Gresh, N.; Dognon, J.-P.; Piquemal, J.-P. Toward Accurate Solvation Dynamics of Lanthanides and Actinides in Water Using Polarizable Force Fields: From Gas-Phase Energetics to Hydration Free Energies. *Theor. Chem. Acc.* **2012**, *131*, 1−14.
(936) Zhang, J.; Yang, W.; Piquemal, J.-P.; Ren, P. Modeling Structural Coordination and Ligand Binding in Zinc Proteins with a Polarizable Potential. *J. Chem. Theory Comput.* **2012**, *8*, 1314−1324.
(937) Naor, M. M.; Van Nostrand, K.; Dellago, C. Car−Parrinello Molecular Dynamics Simulation of the Calcium Ion in Liquid Water. *Chem. Phys. Lett.* **2003**, *369*, 159−164.
(938) Lightstone, F. C.; Schwegler, E.; Allesch, M.; Gygi, F.; Galli, G. A First-Principles Molecular Dynamics Study of Calcium in Water. *ChemPhysChem* **2005**, *6*, 1745−1749.
(939) Ikeda, T.; Boero, M.; Terakura, K. Hydration Properties of Magnesium and Calcium Ions from Constrained First Principles Molecular Dynamics. *J. Chem. Phys.* **2007**, *127*, 074503.
(940) Ren, P.; Wu, C.; Ponder, J. W. Polarizable Atomic Multipole-Based Molecular Mechanics for Organic Molecules. *J. Chem. Theory Comput.* **2011**, *7*, 3143−3161.
(941) Shi, Y.; Wu, C.; Ponder, J. W.; Ren, P. Multipole Electrostatics in Hydration Free Energy Calculations. *J. Comput. Chem.* **2011**, *32*, 967−977.
(942) Wu, J. C.; Chattree, G.; Ren, P. Automation of Amoeba Polarizable Force Field Parameterization for Small Molecules. *Theor. Chem. Acc.* **2012**, *131*, 1−11.
(943) Semrouni, D.; Isley, W. C., III; Clavaguéra, C.; Dognon, J.-P.; Cramer, C. J.; Gagliardi, L. Ab Initio Extension of the Amoeba

DOI: 10.1021/acs.chemrev.6b00440
Chem. Rev. 2017, 117, 1564−1686

Polarizable Force Field to Fe2+. *J. Chem. Theory Comput.* **2013**, *9*, 3062−3071.
(944) Kaminski, G. A.; Stern, H. A.; Berne, B. J.; Friesner, R. A.; Cao, Y. X.; Murphy, R. B.; Zhou, R.; Halgren, T. A. Development of a Polarizable Force Field for Proteins Via Ab Initio Quantum Chemistry: First Generation Model and Gas Phase Tests. *J. Comput. Chem.* **2002**, *23*, 1515−1531.
(945) Kaminski, G. A. Accurate Prediction of Absolute Acidity Constants in Water with a Polarizable Force Field: Substituted Phenols, Methanol, and Imidazole. *J. Phys. Chem. B* **2005**, *109*, 5884−5890.
(946) Ponomarev, S. Y.; Click, T. H.; Kaminski, G. A. Electrostatic Polarization Is Crucial in Reproducing Cu(I) Interaction Energies and Hydration. *J. Phys. Chem. B* **2011**, *115*, 10079−10085.
(947) Click, T. H.; Ponomarev, S. Y.; Kaminski, G. A. Importance of Electrostatic Polarizability in Calculating Cysteine Acidity Constants and Copper (I) Binding Energy of Bacillus Subtilis Copz. *J. Comput. Chem.* **2012**, *33*, 1142−1151.
(948) Soniat, M.; Rick, S. W. The Effects of Charge Transfer on the Aqueous Solvation of Ions. *J. Chem. Phys.* **2012**, *137*, 044511.
(949) Babin, V.; Leforestier, C.; Paesani, F. Development of a "First Principles" Water Potential with Flexible Monomers: Dimer Potential Energy Surface, Vrt Spectrum, and Second Virial Coefficient. *J. Chem. Theory Comput.* **2013**, *9*, 5395−5403.
(950) Babin, V.; Medders, G. R.; Paesani, F. Development of a "First Principles" Water Potential with Flexible Monomers. Ii: Trimer Potential Energy Surface, Third Virial Coefficient, and Small Clusters. *J. Chem. Theory Comput.* **2014**, *10*, 1599−1607.
(951) Medders, G. R.; Babin, V.; Paesani, F. Development of a "First-Principles" Water Potential with Flexible Monomers. Iii. Liquid Phase Properties. *J. Chem. Theory Comput.* **2014**, *10*, 2906−2910.
(952) Arismendi-Arrieta, D. J.; Riera, M.; Bajaj, P.; Prosmiti, R.; Paesani, F. I-Ttm Model for Ab Initio-Based Ion−Water Interaction Potentials. 1. Halide−Water Potential Energy Functions. *J. Phys. Chem. B* **2016**, *120*, 1822−1832.
(953) Riera, M.; Götz, A. W.; Paesani, F. I-Ttm Model for Ab Initio-Based Ion-Water Interaction Potentials. Ii. Alkali Metal Ion−Water Potential Energy Functions. *Phys. Chem. Chem. Phys.* **2016**, *18*, 30334−30343.
(954) Bajaj, P.; Götz, A. W.; Paesani, F. Toward Chemical Accuracy in the Description of Ion-Water Interactions through Many-Body Representations. I. Halide-Water Dimer Potential Energy Surfaces. *J. Chem. Theory Comput.* **2016**, *12*, 2698−2705.
(955) Sakharov, D. V.; Lim, C. Force Fields Including Charge Transfer and Local Polarization Effects: Application to Proteins Containing Multi/Heavy Metal Ions. *J. Comput. Chem.* **2009**, *30*, 191−202.
(956) Lee, A. J.; Rick, S. W. The Effects of Charge Transfer on the Properties of Liquid Water. *J. Chem. Phys.* **2011**, *134*, 184507.
(957) Gresh, N.; Piquemal, J. P.; Krauss, M. Representation of Zn (Ii) Complexes in Polarizable Molecular Mechanics. Further Refinements of the Electrostatic and Short-Range Contributions. Comparisons with Parallel Ab Initio Computations. *J. Comput. Chem.* **2005**, *26*, 1113−1130.
(958) Piquemal, J.-P.; Cisneros, G. A.; Reinhardt, P.; Gresh, N.; Darden, T. A. Towards a Force Field Based on Density Fitting. *J. Chem. Phys.* **2006**, *124*, 104101.
(959) Langlet, J.; Claverie, P.; Caillet, J.; Pullman, A. Improvements of the Continuum Model 0.1. Application to the Calculation of the Vaporization Thermodynamic Quantities of Nonassociated Liquids. *J. Phys. Chem.* **1988**, *92*, 1617−1631.
(960) Gresh, N.; Claverie, P.; Pullman, A. Theoretical Studies of Molecular Conformation. Derivation of an Additive Procedure for the Computation of Intramolecular Interaction Energies. Comparison Withab Initio Scf Computations. *Theor. Chim. Acta* **1984**, *66*, 1−20.
(961) Gresh, N.; Pullman, A.; Claverie, P. Theoretical Studies of Molecular Conformation. Ii: Application of the Sibfa Procedure to Molecules Containing Carbonyl and Carboxylate Oxygens and Amide Nitrogens. *Theor. Chim. Acta* **1985**, *67*, 11−32.
(962) Devereux, M.; van Severen, M.-C.; Parisel, O.; Piquemal, J.-P.; Gresh, N. Role of Cation Polarization in Holo-and Hemi-Directed [Pb(H2o)N]2+ Complexes and Development of a Pb2+ Polarizable Force Field. *J. Chem. Theory Comput.* **2011**, *7*, 138−147.
(963) Gresh, N.; Pullman, A.; Claverie, P. Cation−Ligand Interactions: Reproduction of Extended Basis Set Ab Initio Scf Computations by the Sibfa 2 Additive Procedure. *Int. J. Quantum Chem.* **1985**, *28*, 757−771.
(964) Gresh, N. Energetics of Zn2+ Binding to a Series of Biologically Relevant Ligands: A Molecular Mechanics Investigation Grounded on Ab Initio Self-Consistent Field Supermolecular Computations. *J. Comput. Chem.* **1995**, *16*, 856−882.
(965) Gresh, N.; Garmer, D. R. Comparative Binding Energetics of Mg2+, Ca2+, Zn2+, and Cd2+ to Biologically Relevant Ligands: Combined Ab Initio Scf Supermolecule and Molecular Mechanics Investigation. *J. Comput. Chem.* **1996**, *17*, 1481−1495.
(966) Tiraboschi, G.; Roques, B. P.; Gresh, N. Joint Quantum Chemical and Polarizable Molecular Mechanics Investigation of Formate Complexes with Penta-and Hexahydrated Zn2+: Comparison between Energetics of Model Bidentate, Monodentate, and through-Water Zn2+ Binding Modes and Evaluation of Nonadditivity Effects. *J. Comput. Chem.* **1999**, *20*, 1379−1390.
(967) Tiraboschi, G.; Gresh, N.; Giessner-Prettre, C.; Pedersen, L. G.; Deerfield, D. W. Parallel Ab Initio and Molecular Mechanics Investigation of Polycoordinated Zn (Ii) Complexes with Model Hard and Soft Ligands: Variations of Binding Energy and of Its Components with Number and Charges of Ligands. *J. Comput. Chem.* **2000**, *21*, 1011−1039.
(968) Antony, J.; Piquemal, J. P.; Gresh, N. Complexes of Thiomandelate and Captopril Mercaptocarboxylate Inhibitors to Metallo-B-Lactamase by Polarizable Molecular Mechanics. Validation on Model Binding Sites by Quantum Chemistry. *J. Comput. Chem.* **2005**, *26*, 1131−1147.
(969) de Courcy, B.; Piquemal, J.-P.; Gresh, N. Energy Analysis of Zn Polycoordination in a Metalloprotein Environment and of the Role of a Neighboring Aromatic Residue. What Is the Impact of Polarization? *J. Chem. Theory Comput.* **2008**, *4*, 1659−1668.
(970) Gresh, N.; Audiffren, N.; Piquemal, J.-P.; de Ruyck, J.; Ledecq, M.; Wouters, J. Analysis of the Interactions Taking Place in the Recognition Site of a Bimetallic Mg (Ii)-Zn(Ii) Enzyme, Isopentenyl Diphosphate Isomerase. A Parallel Quantum-Chemical and Polarizable Molecular Mechanics Study. *J. Phys. Chem. B* **2010**, *114*, 4884−4895.
(971) De Courcy, B.; Dognon, J. P.; Clavaguéra, C.; Gresh, N.; Piquemal, J. P. Interactions within the Alcohol Dehydrogenase Zn (Ii)-Metalloenzyme Active Site: Interplay between Subvalence, Electron Correlation/Dispersion, and Charge Transfer/Induction Effects. *Int. J. Quantum Chem.* **2011**, *111*, 1213−1221.
(972) Gresh, N.; de Courcy, B.; Piquemal, J.-P.; Foret, J.; Courtiol-Legourd, S.; Salmon, L. Polarizable Water Networks in Ligand−Metalloprotein Recognition. Impact on the Relative Complexation Energies of Zn-Dependent Phosphomannose Isomerase with D-Mannose 6-Phosphate Surrogates. *J. Phys. Chem. B* **2011**, *115*, 8304−8316.
(973) Gresh, N.; El Hage, K.; Perahia, D.; Piquemal, J. P.; Berthomieu, C.; Berthomieu, D. Polarizable Molecular Mechanics Studies of Cu (I)/Zn (Ii) Superoxide Dismutase: Bimetallic Binding Site and Structured Waters. *J. Comput. Chem.* **2014**, *35*, 2096−2106.
(974) Gresh, N.; Claverie, P.; Pullman, A. Intermolecular Interactions: Reproduction of the Results of Ab Initio Supermolecule Computations by an Additive Procedure. *Int. J. Quantum Chem.* **1979**, *16*, 243−253.
(975) Gresh, N.; Claverie, P.; Pullman, A. Computations of Intermolecular Interactions: Expansion of a Charge-Transfer Energy Contribution in the Framework of an Additive Procedure. Applications to Hydrogen-Bonded Systems. *Int. J. Quantum Chem.* **1982**, *22*, 199−215.
(976) Murrell, J.; Randic, M.; Williams, D. The Theory of Intermolecular Forces in the Region of Small Orbital Overlap. *Proc. R. Soc. A*; The Royal Society: UK, 1965; Vol. *284*, pp 566−581.

DOI: 10.1021/acs.chemrev.6b00440
Chem. Rev. 2017, 117, 1564−1686

(977) de Courcy, B.; Piquemal, J.-P.; Garbay, C.; Gresh, N. Polarizable Water Molecules in Ligand− Macromolecule Recognition. Impact on the Relative Affinities of Competing Pyrrolopyrimidine Inhibitors for Fak Kinase. *J. Am. Chem. Soc.* **2010**, *132*, 3312−3320.
(978) Partridge, H.; Schwenke, D. W. The Determination of an Accurate Isotope Dependent Potential Energy Surface for Water from Extensive Ab Initio Calculations and Experimental Data. *J. Chem. Phys.* **1997**, *106*, 4618−4639.
(979) Cisneros, G. A. s.; Wikfeldt, K. T.; Ojamäe, L.; Lu, J.; Xu, Y.; Torabifard, H.; Bartók, A. P.; Csányi, G. b.; Molinero, V.; Paesani, F. Modeling Molecular Interactions in Water: From Pairwise to Many-Body Potential Energy Functions. *Chem. Rev.* **2016**, *116*, 7501−7528.
(980) Paesani, F. Getting the Right Answers for the Right Reasons: Toward Predictive Molecular Simulations of Water with Many-Body Potential Energy Functions. *Acc. Chem. Res.* **2016**, *49*, 1844−1851.
(981) Hermann, A.; Krawczyk, R. P.; Lein, M.; Schwerdtfeger, P.; Hamilton, I. P.; Stewart, J. J. Convergence of the Many-Body Expansion of Interaction Potentials: From Van Der Waals to Covalent and Metallic Systems. *Phys. Rev. A: At., Mol., Opt. Phys.* **2007**, *76*, 013202.
(982) Johnston, H. S.; Parr, C. Activation Energies from Bond Energies. I. Hydrogen Transfer Reactions. *J. Am. Chem. Soc.* **1963**, *85*, 2544−2551.
(983) Tersoff, J. New Empirical Approach for the Structure and Energy of Covalent Systems. *Phys. Rev. B: Condens. Matter Mater. Phys.* **1988**, *37*, 6991−7000.
(984) Brenner, D. W. Empirical Potential for Hydrocarbons for Use in Simulating the Chemical Vapor Deposition of Diamond Films. *Phys. Rev. B: Condens. Matter Mater. Phys.* **1990**, *42*, 9458−9471.
(985) Stuart, S. J.; Tutein, A. B.; Harrison, J. A. A Reactive Potential for Hydrocarbons with Intermolecular Interactions. *J. Chem. Phys.* **2000**, *112*, 6472−6486.
(986) Brenner, D. W.; Shenderova, O. A.; Harrison, J. A.; Stuart, S. J.; Ni, B.; Sinnott, S. B. A Second-Generation Reactive Empirical Bond Order (Rebo) Potential Energy Expression for Hydrocarbons. *J. Phys.: Condens. Matter* **2002**, *14*, 783−802.
(987) van Duin, A. C.; Dasgupta, S.; Lorant, F.; Goddard, W. A. Reaxff: A Reactive Force Field for Hydrocarbons. *J. Phys. Chem. A* **2001**, *105*, 9396−9409.
(988) Aktulga, H. M.; Fogarty, J. C.; Pandit, S. A.; Grama, A. Y. Parallel Reactive Molecular Dynamics: Numerical Methods and Algorithmic Techniques. *Parallel Computing* **2012**, *38*, 245−259.
(989) Aktulga, H. M.; Pandit, S. A.; van Duin, A. C.; Grama, A. Y. Reactive Molecular Dynamics: Numerical Methods and Algorithmic Techniques. *SIAM Journal on Scientific Computing* **2012**, *34*, C1−C23.
(990) Kylasa, S. B.; Aktulga, H. M.; Grama, A. Y. Reactive Molecular Dynamics on Massively Parallel Heterogeneous Architectures. *IEEE Transactions on Parallel and Distributed Systems* **2016**, *27*, 1.
(991) Islam, M. M.; Kolesov, G.; Verstraelen, T.; Kaxiras, E.; van Duin, A. C. Ereaxff: A Pseudo-Classical Treatment of Explicit Electrons within Reactive Force Field Simulations. *J. Chem. Theory Comput.* **2016**, *12*, 3462−3472.
(992) van Duin, A. *Reaxff User Manual*; California Institute of Technology: 2002.
(993) Järvi, T.; Kuronen, A.; Hakala, M.; Nordlund, K.; Van Duin, A.; Goddard, W., III; Jacob, T. Development of a Reaxff Description for Gold. *Eur. Phys. J. B* **2008**, *66*, 75−79.
(994) Nielson, K. D.; van Duin, A. C.; Oxgaard, J.; Deng, W.-Q.; Goddard, W. A. Development of the Reaxff Reactive Force Field for Describing Transition Metal Catalyzed Reactions, with Application to the Initial Stages of the Catalytic Formation of Carbon Nanotubes. *J. Phys. Chem. A* **2005**, *109*, 493−499.
(995) Larsson, H. R.; Duin, A. C.; Hartke, B. Global Optimization of Parameters in the Reactive Force Field Reaxff for Sioh. *J. Comput. Chem.* **2013**, *34*, 2178−2189.
(996) Deetz, J. D.; Faller, R. Parallel Optimization of a Reactive Force Field for Polycondensation of Alkoxysilanes. *J. Phys. Chem. B* **2014**, *118*, 10966−10978.
(997) Jaramillo-Botero, A.; Naserifar, S.; Goddard, W. A., III General Multiobjective Force Field Optimization Framework, with Application to Reactive Force Fields for Silicon Carbide. *J. Chem. Theory Comput.* **2014**, *10*, 1426−1439.
(998) Dittner, M.; Müller, J.; Aktulga, H. M.; Hartke, B. Efficient Global Optimization of Reactive Force-Field Parameters. *J. Comput. Chem.* **2015**, *36*, 1550−1561.
(999) Cheung, S.; Deng, W.-Q.; van Duin, A. C.; Goddard, W. A. Reaxffmgh Reactive Force Field for Magnesium Hydride Systems. *J. Phys. Chem. A* **2005**, *109*, 851−859.
(1000) Han, S. S.; van Duin, A. C.; Goddard, W. A.; Lee, H. M. Optimization and Application of Lithium Parameters for the Reactive Force Field, Reaxff. *J. Phys. Chem. A* **2005**, *109*, 4575−4582.
(1001) Ludwig, J.; Vlachos, D. G.; Van Duin, A. C.; Goddard, W. A. Dynamics of the Dissociation of Hydrogen on Stepped Platinum Surfaces Using the Reaxff Reactive Force Field. *J. Phys. Chem. B* **2006**, *110*, 4274−4282.
(1002) Chenoweth, K.; Duin, A. C. v.; Persson, P.; Cheng, M.-J.; Oxgaard, J.; Goddard, I.; William, A. Development and Application of a Reaxff Reactive Force Field for Oxidative Dehydrogenation on Vanadium Oxide Catalysts. *J. Phys. Chem. C* **2008**, *112*, 14645−14654.
(1003) Raymand, D.; van Duin, A. C.; Baudin, M.; Hermansson, K. A Reactive Force Field (Reaxff) for Zinc Oxide. *Surf. Sci.* **2008**, *602*, 1020−1031.
(1004) Zhang, X.-Q.; Iype, E.; Nedea, S. V.; Jansen, A. P.; Szyja, B. M.; Hensen, E. J.; van Santen, R. A. Site Stability on Cobalt Nanoparticles: A Molecular Dynamics Reaxff Reactive Force Field Study. *J. Phys. Chem. C* **2014**, *118*, 6882−6886.
(1005) Abolfath, R. M.; Van Duin, A.; Brabec, T. Reactive Molecular Dynamics Study on the First Steps of DNA Damage by Free Hydroxyl Radicals. *J. Phys. Chem. A* **2011**, *115*, 11045−11049.
(1006) Monti, S.; Corozzi, A.; Fristrup, P.; Joshi, K. L.; Shin, Y. K.; Oelschlaeger, P.; van Duin, A. C.; Barone, V. Exploring the Conformational and Reactive Dynamics of Biomolecules in Solution Using an Extended Version of the Glycine Reactive Force Field. *Phys. Chem. Chem. Phys.* **2013**, *15*, 15062−15077.
(1007) Smirnov, P.; Trostin, V. Structural Parameters of Cu2+ Aqua Complexes in Aqueous Solutions of Its Salts. *Russ. J. Gen. Chem.* **2009**, *79*, 1591−1599.
(1008) van Duin, A. C.; Bryantsev, V. S.; Diallo, M. S.; Goddard, W. A.; Rahaman, O.; Doren, D. J.; Raymand, D.; Hermansson, K. Development and Validation of a Reaxff Reactive Force Field for Cu Cation/Water Interactions and Copper Metal/Metal Oxide/Metal Hydroxide Condensed Phases. *J. Phys. Chem. A* **2010**, *114*, 9507−9514.
(1009) Schäffer, C. E.; Jørgensen, C. K. The Angular Overlap Model, an Attempt to Revive the Ligand Field Approaches. *Mol. Phys.* **1965**, *9*, 401−412.
(1010) Larsen, E.; La Mar, G. N. The Angular Overlap Model. How to Use It and Why. *J. Chem. Educ.* **1974**, *51*, 633−640.
(1011) Burton, V. J.; Deeth, R. J.; Kemp, C. M.; Gilbert, P. J. Molecular Mechanics for Coordination Complexes: The Impact of Adding D-Electron Stabilization Energies. *J. Am. Chem. Soc.* **1995**, *117*, 8407−8415.
(1012) Root, D. M.; Landis, C. R.; Cleveland, T. Valence Bond Concepts Applied to the Molecular Mechanics Description of Molecular Shapes. 1. Application to Nonhypervalent Molecules of the P-Block. *J. Am. Chem. Soc.* **1993**, *115*, 4201−4209.
(1013) Cleveland, T.; Landis, C. R. Valence Bond Concepts Applied to the Molecular Mechanics Description of Molecular Shapes. 2. Applications to Hypervalent Molecules of the P-Block. *J. Am. Chem. Soc.* **1996**, *118*, 6020−6030.
(1014) Landis, C. R.; Cleveland, T.; Firman, T. K. Valence Bond Concepts Applied to the Molecular Mechanics Description of Molecular Shapes. 3. Applications to Transition Metal Alkyls and Hydrides. *J. Am. Chem. Soc.* **1998**, *120*, 2641−2649.
(1015) Firman, T. K.; Landis, C. R. Valence Bond Concepts Applied to the Molecular Mechanics Description of Molecular Shapes. 4.

DOI: 10.1021/acs.chemrev.6b00440
Chem. Rev. 2017, 117, 1564−1686

Transition Metals with Π-Bonds. *J. Am. Chem. Soc.* **2001**, *123*, 11728−11742.
(1016) Xiang, J. Y.; Ponder, J. W. An Angular Overlap Model for Cu (Ii) Ion in the Amoeba Polarizable Force Field. *J. Chem. Theory Comput.* **2014**, *10*, 298−311.
(1017) Xiang, J. Y.; Ponder, J. W. A Valence Bond Model for Aqueous Cu (Ii) and Zn (Ii) Ions in the Amoeba Polarizable Force Field. *J. Comput. Chem.* **2013**, *34*, 739−749.
(1018) Piquemal, J. P.; Williams-Hubbard, B.; Fey, N.; Deeth, R. J.; Gresh, N.; Giessner-Prettre, C. Inclusion of the Ligand Field Contribution in a Polarizable Molecular Mechanics: Sibfa-Lf. *J. Comput. Chem.* **2003**, *24*, 1963−1970.
(1019) Pettitt, B. M.; Karplus, M. Role of Electrostatics in the Structure, Energy and Dynamics of Biomolecules: A Model Study of N-Methylalanylacetamide. *J. Am. Chem. Soc.* **1985**, *107*, 1166−1173.
(1020) Doman, T. N.; Landis, C. R.; Bosnich, B. Molecular Mechanics Force Fields for Linear Metallocenes. *J. Am. Chem. Soc.* **1992**, *114*, 7264−7272.
(1021) Deeth, R. J.; Foulis, D. L. Analytical Derivatives, Π Bonding and D−S Mixing in the Ligand Field Molecular Mechanics Method. *Phys. Chem. Chem. Phys.* **2002**, *4*, 4292−4297.
(1022) Deeth, R. J.; Fey, N.; Williams−Hubbard, B. Dommimoe: An Implementation of Ligand Field Molecular Mechanics in the Molecular Operating Environment. *J. Comput. Chem.* **2005**, *26*, 123−130.
(1023) Deeth, R. J. A Test of Ligand Field Molecular Mechanics as an Efficient Alternative to Qm/Mm for Modelling Metalloproteins: The Structures of Oxidised Type I Copper Centres. *Chem. Commun.* **2006**, 2551−2553.
(1024) Deeth, R. J.; Anastasi, A. E.; Wilcockson, M. J. An in Silico Design Tool for Fe(Ii) Spin Crossover and Light-Induced Excited Spin State-Trapped Complexes. *J. Am. Chem. Soc.* **2010**, *132*, 6876−6877.
(1025) Foscato, M.; Deeth, R. J.; Jensen, V. R. Integration of Ligand Field Molecular Mechanics in Tinker. *J. Chem. Inf. Model.* **2015**, *55*, 1282−1290.
(1026) Tubert-Brohman, I.; Schmid, M.; Meuwly, M. Molecular Mechanics Force Field for Octahedral Organometallic Compounds with Inclusion of the Trans Influence. *J. Chem. Theory Comput.* **2009**, *5*, 530−539.
(1027) Coe, B. J.; Glenwright, S. J. Trans-Effects in Octahedral Transition Metal Complexes. *Coord. Chem. Rev.* **2000**, *203*, 5−80.
(1028) Pidcock, A.; Richards, R.; Venanzi, L. 195 Pt−31 P Nuclear Spin Coupling Constants and the Nature of the Trans-Effect in Platinum Complexes. *J. Chem. Soc. A* **1966**, *0*, 1707−1710.
(1029) Jin, H.; Goyal, P.; Das, A. K.; Gaus, M.; Meuwly, M.; Cui, Q. Copper Oxidation/Reduction in Water and Protein: Studies with Dftb3/Mm and Valbond Molecular Dynamics Simulations. *J. Phys. Chem. B* **2016**, *120*, 1894−1910.
(1030) Carlsson, A. Angular Forces around Transition Metals in Biomolecules. *Phys. Rev. Lett.* **1998**, *81*, 477.
(1031) Comba, P.; Zimmer, M. Molecular Mechanics and the Jahn-Teller Effect. *Inorg. Chem.* **1994**, *33*, 5368−5369.
(1032) Salomon - Ferrer, R.; Case, D. A.; Walker, R. C. An Overview of the Amber Biomolecular Simulation Package. *Wiley Interdiscip. Rev. Comput. Mol. Sci.* **2013**, *3*, 198−210.
(1033) Brooks, B. R.; Brooks, C. L.; MacKerell, A. D.; Nilsson, L.; Petrella, R. J.; Roux, B.; Won, Y.; Archontis, G.; Bartels, C.; Boresch, S. Charmm: The Biomolecular Simulation Program. *J. Comput. Chem.* **2009**, *30*, 1545−1614.
(1034) van der Spoel, D.; Lindahl, E.; Hess, B.; Groenhof, G.; Mark, A. E.; Berendsen, H. J. Gromacs: Fast, Flexible, and Free. *J. Comput. Chem.* **2005**, *26*, 1701−1718.
(1035) Eastman, P.; Pande, V. Openmm: A Hardware-Independent Framework for Molecular Simulations. *Comput. Sci. Eng.* **2010**, *12*, 34−39.
(1036) Ponder, J. W. *Tinker: Software Tools for Molecular Design*, 2004.
(1037) Module, F. *Material Studio 6.0*, 2011.
(1038) Plimpton, S.; Crozier, P.; Thompson, A. *Lammps-Large-Scale Atomic/Molecular Massively Parallel Simulator*, 2007.
(1039) Eastman, P.; Swails, J.; Chodera, J. D.; McGibbon, R. T.; Zhao, Y.; Beauchamp, K. A.; Wang, L.-P.; Simmonett, A. C.; Harrigan, M. P.; Brooks, B. R. OpenMM 7: Rapid Development of High Performance Algorithms for Molecular Dynamics. *bioRxiv* **2016**, 091801.
(1040) Case, D. A.; Betz, R. M.; Botello-Smith, W.; Cerutti, D. S.; Cheatham, I. T. E.; Darden, T. A.; Duke, R. E.; Giese, T. J.; Gohlke, H.; Goetz, A. W.; et al. *AMBER 2016*; University of California: San Francisco, CA, 2016.

DOI: 10.1021/acs.chemrev.6b00440
Chem. Rev. 2017, 117, 1564−1686